

Dynamic Modelling and Control of District Heating and Cooling Systems



Jose Hector Bastida Hernandez
School of Engineering
Cardiff University

A thesis submitted for the degree of
Doctor of Philosophy
2021



Abstract

District heating and cooling systems (DHCSs) provide thermal energy to a wide range of users. The efficient performance of DHCSs is critical for the reliability of the generation, supply and consumption of energy processes. Moreover, improvement of the energy management within DHCSs helps to tackle the greenhouse gas emission issue. Therefore, accurate models to analyse the thermal and hydraulic behaviours presented in a DHCS become essential to enhance the energy efficiency of heating and cooling processes. A substantial number of studies rely on steady-state models, in which the transient responses and their influence on the whole system are often ignored. The results and conclusions derived from these studies are based on assumptions that neglect critical dynamics under changes of operating conditions. Moreover, some studies only consider the energy dispatch ignoring how energy is transported, transferred and consumed. Thus, the fundamental variables that describe the behaviour of DHCS have not been considered in detail.

To bridge this research gap, one-dimensional hydraulic and thermal dynamic modelling approaches capable of providing a detailed understanding of the different underlying physics phenomena are presented in this thesis. The prediction of the dynamic behaviour of fundamental variables such as temperature, pressure and mass flow rate afforded through the presented mathematical models allows analysing different operating scenarios. The well-described heat transfer process in the heat and cold supply processes is one of the key properties of the proposed approaches. For the hydraulic side, linear momentum and Newton's second law of motion are used to describe the pressure and fluid velocities of the DHCS's pipe network, considering critical parameters such as the friction factor and loss coefficients of valves and pipes. Thus, the modelling approach is employed to develop non-linear one-dimensional (1-D) models of essential DHCS's components such as pipe networks, heat exchangers, thermal energy storage tanks and buildings. High-fidelity of the dynamic models is based on the physics principles and the dynamic changes of thermophysical properties of the fluids and materials involved in the energy supply process. Following this, the enthalpy-specific heat relation of phase change materials is analysed to obtain accurate dynamic models of latent thermal energy storage tanks.

The accuracy and simplicity achieved by the 1-D dynamic models allow designing basic PI controllers to regulate the operating conditions of the DHCSs. A linearisation method is used to design the controllers following a well-explained proposed control design process based on loop-shaping of the frequency response. Hence, the design and implementation of adequate controllers can significantly enhance the efficiency of the heating and cooling supply processes within DHCSs.

The research outcomes shed light on the use of 1-D dynamic models to analyse DHCSs considering their fundamental physical variables. The description of control schemes implementation to improve the overall DHCS's performance using non-linear models has been provided and demonstrated through the presented case studies.



Acknowledgements

My first and foremost thanks go to my main supervisor Dr Carlos Ugalde-Loo, for his continuous and invaluable guidance, support, patience, and for believing in me. I really appreciated and enjoyed all our meetings discussing my progress, new ideas about my research and heavy metal music. It has been a great pleasure to work with you.

My gratitude also goes to my co-supervisor Dr. Meysam Qadran for his comments and suggestions on my work. I would like to acknowledge my co-supervisor Dr Muditha Abeysekera for his help during my first steps in the energy systems field and his contributions to my research outcomes. I am also grateful to Prof. Nick Jenkins for his advice and support; I am sure that I would not have achieved this goal if I hadn't had all the opportunities he gave me. Many thanks to Prof. Jianzhong Wu for all his support and his comments about my research progress during our weekly group meetings.

My gratitude also goes to Dr. Pedro Ponce-Cruz for pushing me to continue my postgraduate studies and for all his support and advice during my PhD position search. You have been an inspiration for my academic career.

I would also thank Dr. Karolina Rucinska for always taking care about the PhD students in the CIREGS, your help in the last part of my PhD was key for this achievement. I want to include in these acknowledgements my office mates and friends: Davide Pinzan, Emmanuel Fasina, Rilwan Oliyide, Oscar Utomo, Sofia Mavidou, Athanasios Mermigkas, Manon Davies, Kudzie Craig, Saad Khalaf and Ye-Obong Udoakah. Guys! thank you for your time, our chats, your jokes and for having made our office a really nice working environment.

I would like to express my thankfulness to my friends and colleagues, Victor Castaneda, Roberto Loza, Edith Rojo, Maria Cruz, Haydee Martinez, Julian Medina, Carlos Azua, Andres Quichimbo, Tattiana Hernandez and Mohamed Abdelrahman for the time spent together, the talks and outdoors experiences. I also want to include in this gratefulness the new mexican team arrived recently at Cardiff: Daniel Morales, Miguel Blas, Ivan de la Cruz and Cecilia Contreras for your online companionship during this hard time due to the world pandemic situation.

I have been abroad for so many years, but there are old friends whose companionship transcends the distance and time. Thank you Manuel Arias for the friendship. No matter the distance, you have been supportive during this PhD journey.

I want to especially thank my parents Esther and Jose, who have given me their constant and unquestionable support throughout my life. Thank you *Ma y Pa* for your infinite love. To my sister Ceci and the young Nova for being there every time I need your help.

My dear wife, Claudia, for all your love, comprehension and support. Thank you for being during the highs and the lows. This achievement is as much mine as it is yours.

Finally, I want to acknowledge the SENER-CONACyT (Secretaría de Energía-Consejo Nacional de Ciencia y Tecnología, Mexico) for the scholarship given to me during my PhD studies.



Contents

Abstract	iii
Acknowledgements	v
Contents	vii
List of Figures	xi
List of Tables	xix
Nomenclature	xxi
1 Introduction	1
1.1 Motivation	1
1.2 Research objectives	2
1.3 Challenges and research gaps	3
1.3.1 Challenges	3
1.3.2 Reserach gaps	3
1.4 Main contributions	4
1.5 Conference and journal publications	5
1.6 Thesis outline	6
1.7 References	8
2 Literature review	9
2.1 Introduction	9
2.2 District heating and cooling systems	9
2.2.1 DHCSs tackling climate change	11
2.2.2 Potential solutions	12
2.3 District heating and cooling system operation description	15
2.3.1 Heating and cooling sources	17
2.3.2 Distribution network	19
2.3.3 Thermal energy storage	20

2.3.4	Thermal loads	23
2.4	Benefits and disadvantages of DHCSs	23
2.5	Modelling challenges	24
2.5.1	Thermal behaviour	24
2.5.2	Hydraulic behaviour	26
2.5.3	Dynamic or steady-state models of DHCSs	27
2.6	Classical control for DHCSs	29
2.7	Modelling tools for dynamic simulation of DHCSs	31
2.8	Summary	32
2.9	References	33
3	Hydraulic and thermal dynamic modelling approaches for district heating and cooling systems	43
3.1	Introduction	43
3.2	Thermal dynamic modelling	43
3.2.1	Energy balance	44
3.2.2	Heat transfer: conduction and convection	50
3.2.3	Discretisation/stratification method	58
3.3	Hydraulic dynamic modelling	61
3.4	Electric-thermal analogy for thermal dynamic building models	64
3.5	Summary	67
3.6	References	67
4	Dynamic models of district heating and cooling system's elements	69
4.1	Introduction	69
4.2	Pipe networks	69
4.2.1	Pump	70
4.2.2	Valve model	74
4.2.3	Pipe	75
4.2.4	Verification of pipe network element models	80
4.2.5	Dynamic modelling of pipe network	82
4.3	Heat exchangers	86
4.3.1	Parallel-flow heat exchanger	86
4.3.2	Counter-flow heat exchanger	101
4.4	Thermal energy storage tanks	109
4.4.1	Sensible heat-TES	109
4.4.2	Latent heat-thermal energy storage	114
4.5	Buildings	143
4.5.1	Dynamic model of a single house	143
4.5.2	Simulations	146
4.6	Summary	148
4.7	References	149

5	Design and implementation of local controllers for district heating and cooling systems	153
5.1	Introduction	153
5.2	Design and implementation of local controllers	154
5.2.1	Differential pressure controller for a pipe network	154
5.2.2	Temperature controller for a flat plate heat exchanger	161
5.2.3	Temperature controller for a shell-and-tube heat exchanger	169
5.2.4	Charging process controller for a sensible TES	175
5.2.5	Single house temperature controller	180
5.3	Summary	185
5.4	References	185
6	Case studies of district heating and cooling systems	187
6.1	Introduction	187
6.2	Case study 1	188
6.2.1	Description	188
6.2.2	PI controllers	192
6.2.3	Assessment methodology of the designed controllers	196
6.2.4	Apros model	198
6.2.5	Simulation results	202
6.3	Case study 2	215
6.3.1	Description	215
6.3.2	Setup of thermal energy storage model	215
6.3.3	Co-simulation between MATLAB/Simulink and Apros software	218
6.3.4	Apros model	219
6.3.5	Simulation results	219
6.4	Summary	225
6.5	References	225
7	Conclusions	227
7.1	Conclusions	227
7.2	Future work	232
	Appendices	235
A	MATLAB/Simulink s-functions	237
B	Conversion factor of valve's flow coefficient	241
C	Systems' parameters	243
C.1	Pump's head-volumetric curve and valve's flow coefficient of section 4.2.4	243
C.2	Pipe network of section 4.2.5	244
C.3	Flat plate heat exchanger of sections 4.3.1 and 5.2.2	245
C.4	Shell-and-tube heat exchanger of section 4.3.1	245
C.5	Water tank-based TES of section 4.4.1	246
C.6	Latent thermal energy storage tank of section 4.4.2	246
C.7	Latent thermal energy storage tank of section 4.4.2	247

C.8	Material properties of single house of section 4.5.2	248
C.9	Shell-and-tube heat exchanger of section 5.2.3	249
D	Coefficient of the matrices of linearised heat exchanger model	251
E	Calculation of thermal resistance on shell-and-tube heat exchanger	253
F	Thermophysical properties of Glycol 34%	255
G	Control design procedure	257
G.1	System linearisation	258
G.2	PI controller design	260
G.3	Second-order equivalent system	262
G.4	Loop-shaping	262
G.5	Controller test	263
G.6	References	264
H	Design of PI controllers for case studies	265
H.1	Differential pressure control for DHS	265
H.2	Temperature control for DHS and energy cooling centre	267

List of Figures

1.1	Structure of the thesis.	6
2.1	Percentages of residential, service and industry shares of district heating. . .	10
2.2	Fuels used for heating and cooling in EU	10
2.3	Greenhouse gas emissions by source sector [16].	11
2.4	Scheme of district heating system components [4].	15
2.5	Scheme of district cooling system components [33].	16
2.6	Schematic diagram of a district heating system.	16
2.7	Stages of absorption chiller cycle.	19
2.8	Scheme of a heating and cooling pipe network of a DHCS.	20
2.9	Schematic diagram of a DHCS's substation.	20
2.10	Classification of thermal energy storage [66].	21
2.11	Water tank-based TES schematic diagram.	22
2.12	Left: Dynamic model block diagram. Right: comparison between scopes of dynamic and steady state models.	27
2.13	Overview of the four control systems in DHCS.	31
2.14	Communication between MATLAB and AproS.	32
3.1	Framework of the thermal dynamic modelling approach.	44
3.2	General form of conservation law in a control volume.	45
3.3	Conservation of energy within a control volume.	47
3.4	Control volume reduction from three to 1-D analysis.	49
3.5	Convective flux contribution to internal energy of a control volume.	49
3.6	Convection from a surface to a moving fluid	50
3.7	Boundary layer development in convection heat transfer.	51
3.8	Temperature profiles with and without boundary layers.	53
3.9	Association of conduction heat transfer with diffusion of energy due to molecular activity.	54
3.10	Thermophysical properties of saturated water. Left from top to bottom: density, thermal conductivity. Right from top to bottom: viscosity, Prandtl number .	56

3.11	Equivalent thermal circuit for a series heat transfer composite.	58
3.12	Control volume of two fluids flowing in square channels.	59
3.13	Framework of the dynamic hydraulic modelling approach.	61
3.14	Control volume and system at three different moments.	62
3.15	External forces over cylindrical control volume.	63
3.16	Simple pipe network comprises of a pump, a heat exchanger and three pipes connected in series.	64
3.17	Electric circuit analogy of convection and conduction heat transfers presented in a wall.	65
3.18	Electric circuit analogy of convection and conduction heat transfer presented in an insulator-wall.	66
4.1	Schematic diagram of a centrifugal pump.	70
4.2	Losses of the head-flow rate curve of the pump.	71
4.3	Experimental (right) and computed (left) volumetric flow-head curves of real impeller.	73
4.4	Efficiency curve of the pump's impeller model C2145WRT1 [2]	73
4.5	Schematic of the flow through a valve.	74
4.6	Flow-valve opening curves of different type of valves.	75
4.7	Schematic of circular pipe.	76
4.8	Viscous sublayer on rough and smooth wall of a pipe.	77
4.9	Friction factor computed by equation (4.27) which is defined in terms of Re and relative roughness or circular pipes.	78
4.10	Comparison between original Moody chart (blue dashed traces) and the friction factor computed by Apros's method (orange traces).	79
4.11	Simple hydraulic line built-up in Apros.	80
4.12	Left: Operating conditions of Apros' simulation of hydraulic line. Right: Comparison of the pump's performance curve between Apros' simulation and pump's model equation.	81
4.13	Comparison between Apros' simulation and model equations results of Δp of pump (top), valve (middle) and pipe (bottom).	81
4.14	Schematic of the pipe network.	82
4.15	Analogue electric circuit of the pipe network system.	83
4.16	Overview of the developed Apros model of the pipe network.	84
4.17	Comparison of simulation results of the pipe network. Changes in flow velocities (bottom) due to pump's speed (top) and valve openings (middle)	85
4.18	Simulation results with different initial conditions of the flow velocities (bottom) under the same variations of pump's speed (top) and valve openings (middle).	85
4.19	Stream directions and typical output temperature of Parallel-flow heat exchanger.	86
4.20	Schematic of flat plates heat exchanger.	87
4.21	Schematic of the discretization of the flat plate heat exchanger.	88
4.22	Heat transferred (Q) and the cold and hot volumes next to a plate in a node.	88
4.23	Node division modelling approach.	89
4.24	Simulation results of the parallel-flow configuration of flat plate heat exchanger with $n = 10$	91

4.25 Flat plate heat exchanger response under mass flow rate and input temperature variations.	91
4.26 Input and internal temperatures of heat exchanger under mass flow rate variations.	91
4.27 Output temperatures (T_c and T_h) of flat plate heat exchanger divided into 3, 10, 20, 30, 50 and 100 nodes.	92
4.28 Flat plate heat exchanger implementation in Apros.	92
4.29 Comparison between MATLAB (M) and Apros (A) simulation results of the flat plate heat exchanger with different number of nodes.	93
4.30 Shell-and-tube heat exchanger with one shell pass.	94
4.31 Internal and external heat transfer areas of the tubes.	95
4.32 Types of tubes arrangement of shell-and-tube heat exchanger.	96
4.33 Flow areas and wetted perimeters of shell-and-tube heat exchanger.	97
4.34 Thermal resistances of heat transfer coefficient of shell-and-tube heat exchanger.	98
4.35 Simulation results of shell and tube heat exchanger with $n = 10$	99
4.36 Top: mass flow rate variations. Bottom: Simulation results of the shell-and-tube heat exchanger under variations of input temperature and mass flow rates.	100
4.37 Input and internal temperatures of heat exchanger.	100
4.38 Comparison between MATLAB (M) and Apros (A) simulation results of the shell-and-tube heat exchanger with different number of nodes.	101
4.39 Stream directions and output temperature of counter-flow heat exchanger. . .	102
4.40 Node division of counter-flow configuration of heat exchanger.	102
4.41 Top left: constant mass flow rates and input temperatures. Bottom left: simulation of counter-flow configuration of flat plate heat exchanger with 10 nodes. Top right: all node temperatures of hot stream. Bottom right: all node temperatures of cold stream.	103
4.42 Flat plate response under mass flow rate and input temperature variations. .	104
4.43 Input and internal temperatures of heat exchanger.	104
4.44 Comprison between MATLAB (M) and Apros (A) simulation results of the flat plat heat exchanger with counter-flow configuration.	105
4.45 Left: mass flow rates and input and output temperatures. Right: all node temperatures of shell and tube sides.	106
4.46 Counter-flow shell-and-tube heat exchanger response under mass flow rate and input temperature variations.	106
4.47 Input and internal temperatures of counter-flow shell-and-tube heat exchanger.	107
4.48 Comparison between MATLAB (M) and Apros (A) simulation results of the shell-and-tube heat exchanger with counter-flow configuration.	107
4.49 Simulation results of parallel and counter-flow configurations of shell-and-tube heat exchanger.	108
4.50 Schematic of TES configuration in DHCS.	109
4.51 Schematic of water tank and one layer.	110
4.52 Charging and discharging simulation results.	111
4.53 Comparison of layer temperatures and internal energy calculation between 5, 20 and 50 nodes division of TES.	112
4.54 Apros options to built the TES.	113

4.55 Simulation results of three models: MATLAB/Simulink, Apros option 1 (A1) and Apros option 2 (A2).	113
4.56 Specific heat and enthalpy of coda therm 53 PCM based on [12].	115
4.57 Normalized specific heat (top) and enthalpy (bottom) of PCM with hysteresis phenomenon.	116
4.58 Internal structure and containers of most common PCM based TES.	116
4.59 Internal structure and containers of most common PCM based TES.	117
4.60 Schematic of PCM based TES with tube configuration.	118
4.61 Control volumes and thermal resistance of single pipe of TES.	118
4.62 Sketch of the TES for heating application based on [15]	119
4.63 Specific heat curves for three experimental reported in [15]	121
4.64 Comparison of experimental data and 1-D dynamic model simulation results.	122
4.65 PCM temperature comparison between experimental data and simulation results of 1-D model during melting process at $\dot{m}_f = 1.02$ kg/sec.	123
4.66 PCM temperature comparison between experimental data and simulation results of 1-D model during solidification process at $\dot{m} = 1.02$ kg/sec.	123
4.67 Charging and discharging processes with different mass flow rates.	124
4.68 Specific heat and enthalpy curves of RigidexHD6070EA PCM including its Δh_f	125
4.69 Top: $T_P = 138^\circ\text{C}$ and SoC = 100%. Middle: $T_P = 126^\circ\text{C}$ and SoC = 56%. Bottom: $T_P = 115^\circ\text{C}$ and SoC = 20%.	126
4.70 Illustrative snapshot of the SoC of each pipe node.	127
4.71 Comparison between experimental data and simulation results of the output temperature of HTF ($T_{\text{out},f,s}$).	127
4.72 Simulation results of PCM temperature (average) (Top). Comparison between simulation results and experimental data of stored energy (middle) and SoC (bottom).	128
4.73 Sketch of the internal structure of the ice tank manufactured by CALMAC [®]	129
4.74 Top view of the horizontal levels of spiralled tubes inside the ice-based TES during discharging process.	130
4.75 Sequence of the ice growth in a ice-tank based TES level during charging process.	130
4.76 Imaginary bounds of the water-ice volume around the tubes.	131
4.77 Division of control volumes (nodes) in a single tube.	131
4.78 Water enthalpy curve.	132
4.79 Proposed specific heat and enthalpy curves of water.	132
4.80 Comparison between experimental and simulation results of discharging process.	133
4.81 Simulation results of the node temperatures of HTF and water ice during discharging process at $\dot{m}_f = 1.027$ kg/s.	134
4.82 Comparison between experimental and simulation results of power released during discharging process at $\dot{m}_f = 1.1306$ kg/s.	135
4.83 Comparison of the mean cooling power of the last three operating condition in Table 4.2.	135
4.84 Comparison between experimental and simulation results of charging process of ice based TES.	136
4.85 Top: $T_w = -5.7^\circ\text{C}$ and SoC = 100%. Middle: $T_w = -1.32^\circ\text{C}$ and SoC = 75%. Bottom: $T_w = -0.12^\circ\text{C}$ and SoC = 25%.	137

4.86	Simulated discharging process of ice-tank with $\dot{m} = 1$ kg/s.	138
4.87	Power contribution of the sensible and latent heat of the water to the released energy during discharging process.	138
4.88	Energy released during discharging process with constant and variable density.	139
4.89	Two SoCs of a discharging process of ice-tank.	140
4.90	Simulated charging process of ice-tank with $\dot{m} = 6$ kg/s.	140
4.91	Power contribution of the sensible and latent heat of the water to the absorbed energy during charging process.	141
4.92	Two SoCs of a charging process of ice-tank.	141
4.93	Top: Mass flow rate of HTF. Bottom: simulation results of the output temperature of HTF and water-ice in node number 20.	142
4.94	Simulation results of charging and discharging process in a row. Top: temperature of water ice in first and last node. Middle: total and latent heat energy. Bottom: SoC.	142
4.95	Schematics of house and insulated wall.	144
4.96	Electric circuit analogy of thermal model of house without insulator.	144
4.97	Electric circuit analogy of thermal model of insulated house.	146
4.98	Thermal response of house model for a winter day without heat supply.	147
4.99	(a) Thermal response of insulated house for a cold day. (b) Comparison between the internal temperatures of house without insulator (T_H) and insulated house (T_{IH}).. . . .	148
5.1	Block diagram of a feedback control system.	153
5.2	Block diagram for a differential pressure closed-loop system for the pipe network of a DHCS.	155
5.3	Schematic of the pipe network.	155
5.4	Block diagram for the differential pressure closed-loop system implemented in Apros.	157
5.5	(a) Open-loop Bode plots and (b) step responses of the $G_p(s)$ and $G_{p,so}(s)$	157
5.6	(a) Open-loop Bode plots of the equivalent second-order system and the loop-shaped obtained with $C_p(s)$. (b) Time step responses of the closed-loop system with $G_{p,so}(s)$ and $G_p(s)$	158
5.7	Differential pressure closed-loop system implemented in Apros.	159
5.8	Pipe network pressure closed-loop performance under valve opening changes.	160
5.9	Pipe network pressure closed-loop performance under under different set points.	161
5.10	Block diagram for a temperature closed-loop system for flat plate heat exchanger.	161
5.11	Step response of the valve.	165
5.12	(a) Open-loop Bode plots and (b) step responses of $G_v(s)$ $G_{HE}(s)$ and $G_{v,HE,so}(s)$	165
5.13	(a) Open-loop Bode plots of the equivalent second-order system and the loop-shaped obtained with $C_{HE}(s)$. (b) Time step responses of the closed-loop system with $G_{v,HE,so}(s)$ and $G_v(s)$ $G_{HE}(s)$	166
5.14	Temperature control of flat plate heat exchanger implemented in Apros.	167
5.15	Simulation results of the PI controller performance under disturbances.	168
5.16	Simulation results of the PI controller performance under different temperature set points.	168

5.17	Block diagram for a temperature closed-loop system for shell-and-tube heat exchanger.	169
5.18	(a) Open-loop Bode plots and (b) step time responses of the $G_v(s)G_{st}(s)$ and $G_{v,st,so}(s)$	171
5.19	(a) Open-loop Bode plots of the equivalent second-order system and the loop-shaped obtained with $C_{st}(s)$. (b) Time step responses of the closed-loop system with $G_{v,st,so}(s)$ and $G_v(s)G_{st}(s)$	172
5.20	Temperature control of shell-and-tube heat exchanger implemented in Apros	173
5.21	Simulation results of the PI controller performance under disturbances. . . .	174
5.22	Simulation results of the PI controller performance under different temperature set points.	174
5.23	Block diagram for a temperature closed-loop system for water tank-based TES.	175
5.24	Steady values used for the linearisation step of the TES tank model.	176
5.25	(a) Open-loop Bode plots and (b) step time responses of the original and equivalent linear systems.	177
5.26	Bode plots of $G_{T,so}$ and $C_T(s)G_{T,so}(s)$	178
5.27	Block diagram of the co-simulation between MATLAB/Simulink-Apros. . . .	178
5.28	Charging control of sensible TES implemented in Apros.	179
5.29	Simulation results of the charging control process of TES in 60 minutes. . . .	179
5.30	Simulation results or the charging control process of TES in 120 minutes. . .	180
5.31	Block diagram for a temperature closed-loop system for a single house. . . .	180
5.32	Open-loop Bode diagrams of the set of transfer function of the house model and their equivalent second-order system.	183
5.33	(a) Open-loop Bode plots of the equivalent second-order system and the loop-shaped obtained with $C_h(s)$. (b) Time step response of the closed-loop system with $G_{u,H,so}(s)$ and the set of transfer functions $G_H(s)$	184
5.34	Simulation result of closed-loop insulated house system.	185
6.1	Schematic diagram of the district heating pipe networks of the case study. . .	189
6.2	Schematic diagram of the hydraulic connections of the DHS to the header. . .	189
6.3	Schematic diagram of the water tank-based TES.	190
6.4	Schematic of the pipe network.	191
6.5	Schematic of substation.	193
6.6	Substation's temperature control scheme.	194
6.7	Comparison between the volumetric flow-head ($Q_v - h$) curves of the original and equivalent pumps.	194
6.8	Differential pressure control scheme of S8.	195
6.9	Charging process of sensible TES control scheme.	196
6.10	Thermal load of substation 1.	197
6.11	Thermal load of substation 1 given in temperature variations of $T_{c,in} = T_{S1}$. .	197
6.12	Illustrative scheme of the thermal load profile in a substation generated by variation of the input temperature $T_{c,in}$	198
6.13	Apros model of the energy centre.	199
6.14	Overview of the developed Apros model of the pipe network section.	200
6.15	Schematic of TES configuration with two uni-directional pumps.	201

6.16	Apros diagram of the substation.	201
6.17	PI controllers performances in substation 8: Temperature (top), differential pressure (middle) and mass flow rate of the primary circuit (bottom).	202
6.18	Top: daily temperature profile of the heat load. Bottom: comparison between the heat transferred and the heat load of substation 8.	203
6.19	Top: Differential pressure and hot water mass flow rate of <i>S8</i> . Bottom: pump's speed and total mass flow rate in the DHS.	204
6.20	Temperature profiles of the eight substation.	205
6.21	Comparison between the heat load and the heat transferred by the substation's heat exchangers.	206
6.22	Temperature controller responses of the eight substations.	207
6.23	Differential pressure of the eight substations.	208
6.24	Mass flow rate of hot water supplied to each substation of the DHS.	209
6.25	Snapshots of differential pressure and pressure head diagrams of the DHS at 5 hrs and 20 hrs.	210
6.26	Charging and discharging process of the sensible TES.	211
6.27	Charging process of the TES by means of a ramp function using a PI controller for the temperature in the fifth layer.	212
6.28	Inlet temperatures of the pipe network, substation 4 and 8.	213
6.29	Comparison between the heat supplied by the energy centre (Q_{ec}) and the total heat transferred in the substations Q_{sbus}	213
6.30	Top: Supplied energy by energy centre. Bottom: Transferred energy by substations.	214
6.31	Quantification of the thermal losses due to transportation of hot water through insulated pipe networks.	214
6.32	Schematic of the cooling energy centre.	216
6.33	Charging process of ice tank-based TES with a HTF conditions of $T_{in} = -6^{\circ}C$ and a $\dot{m}_f = 10$ kg/s.	217
6.34	Discharging process of ice tank-based TES with a HTF conditions of $T_{in} = 12^{\circ}C$ and a $\dot{m}_f = 5$ kg/s.	217
6.35	Schematic diagram of communication between Apros and MATLAB/Simulink platforms for co-simulation.	218
6.36	Configuration for MATLAB and Apros co-simulation.	218
6.37	Apros model of the cooling energy centre.	219
6.38	Thermal load of heat exchanger given in cooling power (top) and temperature (bottom) variations.	220
6.39	Output temperature of the secondary circuit of the heat exchanger (top) and thermal load injected and cooling power transferred by heat exchanger (bottom).	221
6.40	Input and output temperatures of TES tank 1 (top) and mass flow rates during charging and discharging modes (bottom).	221
6.41	Ice nodes temperatures (top) and SoC (bottom) of one ice tank-based TES model.	222
6.42	Absorbed and released cooling power of one TES tank during the operation of the cooling energy centre.	222

6.43	Output temperature of the secondary circuit (top), and the thermal load comparison with the heat transferred in the heat exchanger using the compressor chiller (bottom).	223
6.44	Input and output temperatures of TES tank 1 (top) and mass flow rates of the cooling energy centre (bottom).	224
6.45	Ice nodes temperatures (top) and SoC (bottom) of one TES tank.	224
6.46	Absorbed and released cooling power of one TES tank during the operation of the cooling energy centre.	225
A.1	Schematic of the continuous system.	237
E.1	Apros simulation of shell-and-tube with 10 nodes	253
E.2	Comparison simulation of the output temperatures of the built-in Apros system and the developed model using method 1 (M1) and 2 (M2) to compute the heat exchanged.	254
G.1	Steps of the proposed control design process.	258
G.2	(a) Open-loop Bode plots and (b) closed-loop step responses of the $G(s)$ and $G_{so}(s)$	262
G.3	(a) Open-loop Bode plots of $G_{so}(s)$ and $C(s)G_{so}(s)$. (b) Closed-loop step responses of the equivalent and original linear system.	263
G.4	Simulation results of the non-linear system controlled by the designed PI controller.	264
H.1	Schematic of the simplified pipe network.	265
H.2	(a) Open-loop Bode plots and (b) step responses of the $G_p(s)$ and $G_{p,so}(s)$	267
H.3	(a) Open-loop Bode plots of the equivalent second-order system and the loop-shaped obtained with $C_p(s)$. (b) Time step responses of the closed-loop system with $G_{p,so}(s)$ and $G_p(s)$	268
H.4	(a) Open-loop Bode plots and (b) step responses of the $G_{v,H}(s)$ and $G_{v,H,so}(s)$	270
H.5	(a) Open-loop Bode plots of the equivalent second-order system and the loop-shaped obtained with $C_H(s)$. (b) Time step responses of the closed-loop system with $G_{v,H,so}(s)$ and $G_{v,H}(s)$	270

List of Tables

2.1	Carbon intensity per unit of heating.	12
2.2	Carbon intensity per unit of cooling.	12
2.3	DHCS's control systems and their controlled variables.	30
3.1	Electric to heat transfer analogy.	57
3.2	Electric to hydraulic analogy.	63
4.1	Parameters of PCM's specific heat equation ($c_{p,P}$).	121
4.2	Operating conditions of discharging process.	134
4.3	Energy balance equation for insulate house elements.	146
4.4	Thermal capacitances of the house elements.	147
5.1	Steady-state values of pipe network system.	156
5.2	Steady-state values for flat plate heat exchanger linearisation.	163
5.3	Steady-state values for shell-and-tube heat exchanger linearisation.	170
5.4	Steady-state values for sensible TES tank.	176
5.5	Air hydraulic conditions and thermophysical properties.[5]	182
5.6	Coefficient values of transfer function set of insulated house model.	182
6.1	Water tank parameters.	190
6.2	Points of flow-head curve of pump and position-flow coefficient curve of valve.	191
6.3	Pipe parameters.	192
6.4	Flat plate heat exchanger parameters of S450+ model [1].	193
B.1	Conversion factors from English to International System.	241
C.1	Points of flow-head curve of pump and position-flow coefficient curve of valve.	243
C.2	Parameters of pipes, valves and pump.	244
C.3	Volumes of elements.	244
C.4	Flat plate heat exchanger parameters of S600+ model.	245
C.5	Shell and tubes heat exchanger parameters.	245
C.6	Water tank parameters.	246

C.7 Parameters of PCM based TES tank for heating application.	246
C.8 Parameters of single tube of ice tank model 1098C.	247
C.9 Thermophysical properties, thickness and area of house elements.	248
C.10 Equivalent resistances of house without insulator.	248
C.11 Equivalent resistances of house with insulator.	248
C.12 Shell and tubes heat exchanger parameters.	249
D.1 List of coefficient of matrix A and B	251
E.1 Mean square Errors of comparison between both methods and Apros simulation.	254
H.1 Pipe parameters of simplified pipe network.	265
H.2 Steady-state values for heat exchanger linearisation.	269

Nomenclature

Abbreviations

1-D	One-dimensional
CCHP	Combined cooling, heating and power
CHP	Combined heat and power
DHCS	District heating cooling system
DHS	District heating system
EU	European Union
HTF	Heat transfer fluid
ODE	Ordinary differential equation
OPC	Open platform communication
PCM	Phase change material
PDE	Partial differential equation
PDF	Probability density function
PI	proportional-integral
PID	Porportional-integral-derivative
Re	Reynodls number
SoC	State-of-charge
TES	Thermal energy storage

Subscripts

c	Cold
-----	------

h	Hot
A	Apros
in	Input
M	MATLAB/Simulink
out	Output
st	Stored energy

Variables and Parameters

Δp	Differential pressure (Pa and bar)
γ	Specific weight (N/m ³)
ϕ_m	Phase marging
ε	Absolute roughness (mm)
ζ	Damping ratio
D_h	Hydraulic diameter (m)
g	Gravitational acceleration (m/s ²)
k	Thermal conductivity (W/mK)
K_v	Valve's flow coefficient
o_s	Maximum overshoot (%)
t_s	Settling time (s)
U	Overall heat transfer coefficient (W/m ² K)
Δh_l	Latent heat value (J/kg)
Δh_s	Sensible heat value (J/Kg)
\dot{m}	Mass flow rate (kg/s)
η_h	Pump's hydraulic efficiency
η_m	Pump's mechanical efficiency
η_V	Pump's volumetric efficiency
\mathcal{V}	Voltage (V)
ν	Kinematic viscosity (m ² /s)
Ω	Arbitrary volume
ω	Pump speed (%)

Nomenclature

ω_{bw}	Bandwidth (rad/s)
ρ	Density (kg/m ³)
A	Area (m ²)
A_c	Cross-sectional area (m ²)
A_f	Flow area of shell-and-tube heat exchanger
C	Thermal capacitance (J/K)
c_p	Specific heat (J/kgK)
D	Diameter (m)
E	Energy (J)
f	Friction factor
g	Gravitational constant
G_f	Specific gravity
H	Enthalpy (J/kg)
h	Head (m)
i	Electric current (A)
k_i	Integral gain
K_L	Loss pressure coefficient
k_p	Proportional gain
μ	Viscosity (Ns/m ²)
o_v	valve opening
p	Pressure (Pa)
Q'	Heat flux
Q	Heat (J/s)
Q_v	Volumetric flow (m ³ /s)
R	Electric resistance
R_T	Thermal resistance
S	Closed surface
T	Temperature (°C)
U_{cd}	Conduction heat transfer coefficient (W/m ² K)

U_{cv}	Convection heat transfer coefficient (W/m ² K)
V	Volume (m ³)
v	mean velocity (m/s)
Nu	Nusselt number
Pr	Prandtl number

Chapter 1

Introduction

1.1 Motivation

Energy consumed by buildings is about 40% of the total consumption in the European Union (EU) and it is continuously increasing [1]. It constitutes a significant share of the world's total energy use. District heating and cooling systems (DHCSs) which are the energy supplier of the building sector, are also employed to supply energy to industrial processes or special use buildings, such as hospitals or supermarkets. For instance, the service and the industrial sector represents about 30% of the energy supplied by DHCS in some countries of the EU [2]. Then, strategies to reduce the greenhouse gas emissions of DHCSs become compulsory. Potential solutions have been proposed, such as using renewable energy technologies or changing old technology energy sources for more efficient devices. Nevertheless, the adoption of these solutions implies high investment that makes these options unaffordable for most of the cases [3, 4].

Alternative solutions have addressed the energy management within DHCS. For instance, forecast of energy consumption or implementation of more effective control strategies only requires installing more sensor devices to have enough information of the DHCS behaviour to be used for more effective controllers or for taking critical decisions of the energy supply process. These options seem to be accessible since significant modifications of the DHCS's infrastructure are not required. Nevertheless, for both options, a good understanding of the dynamic behaviour of the DHCS becomes essential and, arguably, control strategies cannot be designed without adequate dynamic models.

Models that accurately describe the behaviour of a DHCS are needed to analyse the current performance of the system and then evaluate the designed control strategies through simulations. The most common modelling approach used for DHCS is the energy hub based on steady-state values of the dispatched energy [5]. Analyses of DHCSs that only quantify the energy can be carried out using this approach. Nonetheless, DHCS's operation requires considering not only energy but also the fundamental variables that describe the generation, supply and consumption of energy: temperature, mass flow rate and pressure. Therefore, dynamic models capable of capturing the current system's operational conditions are compulsory; they will allow analysing in detail the most crucial physic phenomenon present in the DHCS: heat transfer. These phenomena are entirely neglected in steady-state modelling approaches and even in some dynamic analyses.

Although powerful commercial software are already available to dynamically simulate DHCS considering the heat transfer process, the complexity and the unavailability of the mathematical models restrict them to expert people. For instance, one of the most powerful software for energy system simulation, called Apros, uses models based on conservation laws of energy, mass and momentum, but it does not provide access to the mathematical description of the models [6]. Therefore, the availability of accurate dynamic models of a DHCS will facilitate that the users grasp the dynamic behaviour developed in simulation software and understand the actual system operation. Moreover, control strategies that aim to improve the DHCS's performance can be developed based on these mathematical models.

To contribute towards achieving such aims, the research work reported in this thesis uses energy balance, linear momentum and Newton's 2nd law of motion to describe the hydraulic and thermal behaviour of the main components of a DHCS. Moreover, the conductive and convection heat transfer phenomena are included in the thermal models. The developed modelling approaches are based on these physics principles to obtain dynamic models of the main components of DHCSs: pipe network (pumps, valves and pipes), heat exchangers, sensible and latent thermal energy storage (TES) tanks and buildings. The one-dimensional (1-D) dynamic models obtained are suitable for control system design and easy implementation in commercial software like MATLAB, allowing analysis and synthesis of classical control design by applying techniques based on Bode diagrams. Control design parameters may be given in time-domain and then translated to the frequency domain to tune proportional-integral (PI) controllers applying loop-shaping techniques on Bode plots. Thus, the performance of the designed controllers can be assessed by simulations.

The research work presented in this thesis is aimed at the global district heating and cooling service industry; it is a synergy of knowledge from various enabling backgrounds, namely heat transfer, fluid mechanics and control engineering. The overall contribution will be to improve the management of the supply energy process in DHCS, by implementing better control strategies based on accurate dynamic models.

1.2 Research objectives

This thesis's main objective is to develop accurate 1-D dynamic models based on first principles and suitable for control design purposes of DHCS's components. The two primary dynamic behaviours presented in a DHCS are considered: thermal and hydraulic. On the one hand, energy balance and heat transfer phenomena analyses are employed to develop a mathematical model capable of describing the temperature variations due to the heat transfer process during the supply of heat and cold within a DHCS. On the other hand, variations of pressure and mass flow rates are described by dynamic models of the hydraulic behaviour presented in the components of the DHCS. The models obtained are verified by comparison with powerful commercial software or experimental data available in the literature.

The suitability of differential equation representation of the model obtained allows to employ linearising methods to obtain transfer functions and then design PI controllers. The control design task may be carried out using time-domain or frequency-domain approaches.

More specifically, the main research objectives are the following:

- To develop dynamic modelling approaches that enable a clear understanding of the

thermal and hydraulic behaviours of a DHCS.

- To develop accurate dynamic models of DHCS's elements considering all variables and material properties involved in the supply, transport and consumption of heating-cooling energy.
- To design local controllers of critical variables for the operation of a DHCS using classical control theory (PI controllers) based on the developed mathematical models.

1.3 Challenges and research gaps

From the review of dynamic models and control design of DHCSs reported in Chapter 2 some challenges and research gaps have been identified and are addressed in this thesis:

1.3.1 Challenges

1. **The analysis of DHCS needs to expand from steady-state regime to a dynamic regime.**

Although thermal behaviour has been addressed in the literature, there is a lack of dynamic hydraulic behaviour models. To fully understand the dynamic interactions in a DHCS, it is essential to consider both dynamics simultaneously. Only by developing suitable models will it be possible to analyse and, therefore, fully comprehend how the dynamics propagate from one element of DHCS to another. For instance, the regulation of a control valve will affect the hydraulic conditions and the heat exchanged in a substation.

2. **Developing dynamic models for DHCS's is not a straightforward task.**

A good understanding of thermal and hydraulic behaviours is essential to develop a dynamic representation of a DHCS. However, by identifying the physics phenomena and describing them by a mathematical equation, it is possible to formulate accurate models that correctly feature each DHCS's element's dynamics. Thus, adequate analysis of DHCS can be carried out based on a reliable model.

3. **It is difficult to carry out efficient control design when an adequate model capturing the relevant dynamics of the system is unavailable.**

By defining adequate and accurate dynamic models describing the system's behaviour under study, it will be possible to design control systems capable of delivering high performance while meeting design specifications. The control design tasks could be carried out either using time-domain or frequency domain approaches.

1.3.2 Research gaps

1. **Development of thermal and hydraulic dynamic models of DHCS's elements based on 1-D analysis.**

Dynamic models capable of describing the thermal and hydraulic behaviours of the elements of DHCS should be based on the understanding of physics phenomena. System

parameters necessary to compute these phenomena should be identified to obtain accurate models. Typically, complex behaviours such as heat transfer or fluid friction are assumed constant and, in the worst case, completely ignored. In order to develop accurate dynamic models, the steps of 1-D modelling approach are described in Chapter 3 to develop dynamic models considering the physics phenomena presented in the system. Moreover, following the proposed modelling approach, detailed dynamic models of pipe network (pump, valve and pipe), sensible and latent TES tanks and houses (thermal loads) are developed in Chapter 4.

2. Suitable models for control design process

Dynamic models reported in the literature are commonly used for simulation. Therefore, iterative methods are used to solve the mathematical representation of the model. However, this representation is not suitable for control design. In order to address this issue, Appendix G presents a linearisation method to obtain the state-space and transfer function representations of the models presented in Chapter 4.

3. 1-D model of Latent TES tank.

Usually, the latent heat-based TES models are based on simple values of the latent heat value of the PCM used. Enthalpy and specific heat curves, which describe the behaviour of the PCM completely during its phase change transition, are not considered. Only three and two-dimensional models available in the literature accurately describe the enthalpy curve of the PCM. Chapter 4 presents 1-D dynamic models of latent TES tanks for heating and cooling applications. Both models are verified using experimental data found in the literature. Enthalpy curves of the PCM materials are proposed.

4. Design of classical controllers.

The implementation of classical controllers such as PI or PID has been studied in the literature. Nevertheless, their design is not shown or empirical procedure is used to obtain the controllers' gains. On the other hand, the most advanced control strategies studied do not consider dynamic variations of critical variables during changes in the operating conditions. In Chapter 5, classical PI controllers for the systems presented in Chapter 4 are designed using time and frequency domain approaches. The implementation of PI controllers for a DHS is presented in Chapter 6. The temperature controller for eight substations and the differential pressure controller for the farthest DHS's substation are designed. Their performances are assessed using a heat profile load for each substation.

1.4 Main contributions

The work presented in this thesis is focused on 1-D dynamic modelling of the main DHCS's components based on physics principles and the design of PI controllers to ensure the efficient heat and cold supply. The developed modelling and control design procedures performed in this thesis could be applied to other components of DHCSs. The following results can be considered an original contribution to knowledge:

- **Modelling approaches for thermal and hydraulic dynamics of DHCSs.** Modelling frameworks are established to develop dynamic models of the thermal and hydraulic

behaviour of the main components of DHCS. Thus, critical transient responses can be simulated under different operating conditions.

- **Dynamic models of DHCSs' elements.** The models are derived from first principles. The mathematical models' verification is carried out through comparison against simulation results obtained with a commercial process simulation software and real data available in the literature. Pipe network, flat plate and shell-and-tube heat exchangers, sensible and latent TES tanks, and house models have been developed following the 1-D modelling approaches.
- **Use of classical control design tools based on the frequency and time domain.** Non-linear dynamic models of DHCS's components are linearised around operating points and then used to design proportional-integral feedback controllers. The performance of the controller is evaluated under different set points and disturbances.
- **Use of a 1-D dynamic model of latent TES tank in co-simulation with commercial software.** The lack of adequate dynamic models of latent TES tank is bridged. Moreover, a computation method of the state-of-charge (SoC) of a latent TES tank is developed using the temperatures of the phase change materials located inside the TES tank. Co-simulation with commercial software is detailed explained.

1.5 Conference and journal publications

The following articles were published during the course of the present research work.

Journal article:

- **H. Bastida**, C. E. Ugalde-Loo, M. Abeysekera, and M. Qadrdan, "Modelling and control of district heating networks with reduced pump utilisation," *IET Energy Systems Integration*, vol. 3, no. 1, pp. 13–25, 2021, doi: <https://doi.org/10.1049/esi2.12001>.

Conference articles:

- **H. Bastida**, C. E. Ugalde-Loo, M. Abeysekera, and M. Qadrdan, "Dynamic modeling and control of a plate heat exchanger," in *2017 IEEE Conference on Energy Internet and Energy System Integration (EI2)*, Nov. 2017, pp. 1–6, doi: 10.1109/EI2.2017.8245736.
- **H. Bastida**, C. E. Ugalde-Loo, M. Abeysekera, M. Qadrdan, J. Wu, and N. Jenkins, "Dynamic Modelling and Control of Thermal Energy Storage," *Energy Procedia*, vol. 158, pp. 2890–2895, Feb. 2019, doi: 10.1016/j.egypro.2019.01.942.
- **H. Bastida**, C. E. Ugalde-Loo, M. Abeysekera, M. Qadrdan, and J. Wu, "Thermal Dynamic Modelling and Temperature Controller Design for a House," *Energy Procedia*, vol. 158, pp. 2800–2805, Feb. 2019, doi: 10.1016/j.egypro.2019.02.041.
- **H. Bastida**, C. E. Ugalde-Loo, M. Abeysekera, X. Xu, and M. Qadrdan, "Dynamic Modelling and Control of Counter-Flow Heat Exchangers for Heating and Cooling Systems," in *2019 54th International Universities Power Engineering Conference (UPEC)*, Sep. 2019, pp. 1–6, doi: 10.1109/UPEC.2019.8893634.

Collaborative articles:

- I. De La Cruz Loreda, **H. Bastida**, C. E. Ugalde-Loo, D. A. Morales Sandoval, and L. A. A. Brooks, “Dynamic Coupling Analysis and Control of an Integrated Thermal Energy Storage System,” in 2020 55th International Universities Power Engineering Conference (UPEC), Sep. 2020, pp. 1–6, doi: 10.1109/UPEC49904.2020.9209848.
- D. A. Morales Sandoval, I. De La Cruz Loreda, **H. Bastida**, J. J. R. Badman, and C. E. Ugalde-Loo, “Design and verification of an effective state-of-charge estimator for thermal energy storage,” IET Smart Grid, vol. 4, no. 2, pp. 202–214, 2021, doi: <https://doi.org/10.1049/stg2.12024>.

1.6 Thesis outline

The thesis is comprised of seven chapters and appendices. Its structure and the description of each chapter are discussed in this section. The structure of the thesis is shown in Figure 1.1

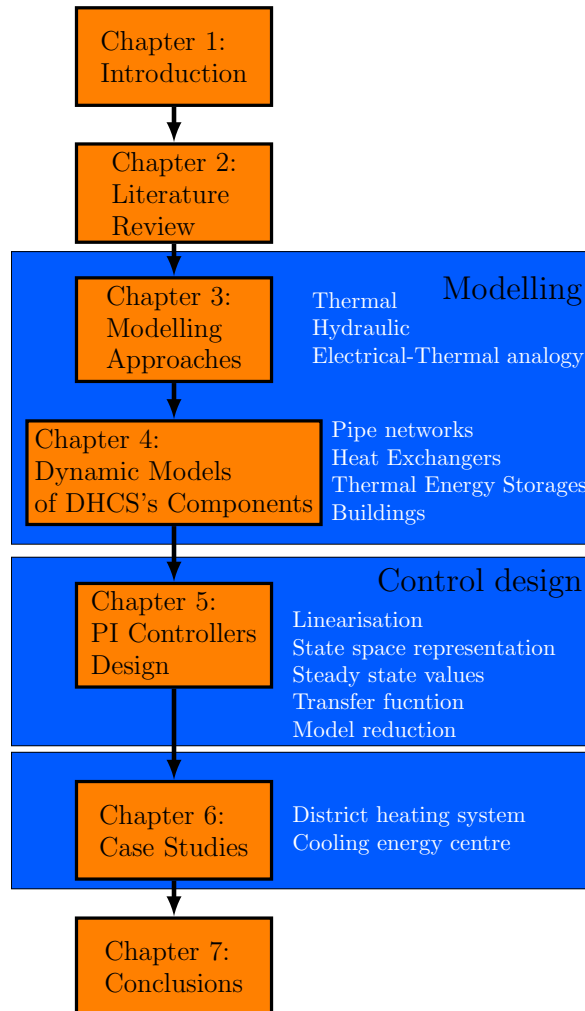


Figure 1.1: Structure of the thesis.

Chapter 2 gives an overview of DHCSs. The chapter discusses potential solutions to improve the performance of the DHCS, aiming to reduce greenhouse gas emissions. A description of the main components of DHCS is given. Furthermore, modelling approaches and control

1.6. Thesis outline

strategies of DHCS are reviewed. The chapter ends with the knowledge gaps found during the research process, which are addressed further in the thesis.

Chapter 3 presents the 1-D dynamic modelling approaches for hydraulic and thermal behaviour of DHCSs' elements. A detailed modelling procedure is presented to obtain the dynamic models. The modelling approach is based on linear momentum and Newton's second law of motion for hydraulic behaviour. The models are based on energy balance and heat transfer phenomena for the thermal side: conduction and convection. The building modelling approach is based on the electrical to thermal analogy.

Chapter 4 details the dynamic models of DHCSs' elements based on the modelling approaches developed in Chapter 3. The models are built up using MATLAB/Simulink software. The hydraulic behaviour of a pipe network is modelled and verified by comparing the library components of Apros software. The dynamic models of the thermal behaviour of flat plate and shell-and-tube heat exchangers are detailed described. The parallel and counter flow configuration of both heat exchangers are presented and verified through Apros simulations. Sensible and latent TES tanks are dynamically modelled. For the sensible case, a water tank-based TES is used and the model is verified using Apros software. For the latent case, two TES tanks (for heating and cooling) are modelled and verified with real data available in the literature. Finally, a single house's dynamic model is developed based on the electrical to thermal analogy presented in Chapter 3.

Chapter 5 details the control design process of classical PI controllers for district heating elements. Five PI controllers are developed for the following systems: differential pressure controller of a pipe network, temperature controllers of flat plate and shell-and-tube heat exchangers, charging process controller for sensible TES tank and the internal temperature controller for a single house. A linearising method is applied to obtain a system transfer function. Then, the Bode diagrams are employed to carry out a loop shaping process to obtain the PI controller gains. The design parameters are established in the time-domain and translated to the frequency domain. Simulations in MATLAB/Simulink and Apros software are carried out to assess the performance of the PI controllers under disturbances and changes of the operating point used for the control design

Chapter 6 addresses the analysis of two case studies. In case study one, temperature and differential pressure controllers for a district heating system (DHS) are designed based on the dynamic models presented in Chapter 4 and the control design procedure described in Appendix G. The controller performances under operational conditions are assessed. A one-day simulation with a time step of one second is carried out with the system's substations undergo heat load profiles. Sensible TES tank is used to support the energy source's heat supply. In case study two, the dynamic model of latent TES tank developed in Chapter 4 is used to analyse a cooling energy centre. The co-simulation between MATLAB/Simulink and Apros platforms is detailed described and the performance of two ice-tank-based TESs is conducted.

Chapter 7 presents the results obtained in this research and discusses potential directions to carry out further research.

1.7 References

- [1] EU., “Directive 2010/31/EU of the European Parliament and of the Council of 19 May 2010 on the energy performance of buildings,” *Official Journal of the European Union*, vol. L 153, pp. 13–15, June 2010.
- [2] K. Szabó, A. Mezősi, A. Tőroőcsik, *et al.*, “Renewable based district heating in europe - policy assessment of selected member states.,” 2015. Fraunhofer ISI.
- [3] M. A. Sayegh, J. Danielewicz, T. Nannou, M. Miniewicz, P. Jadwiszczak, K. Piekarska, and H. Jouhara, “Trends of European research and development in district heating technologies,” *Renewable and Sustainable Energy Reviews*, vol. 68, pp. 1183–1192, Feb. 2017.
- [4] D. Connolly, H. Lund, B. V. Mathiesen, S. Werner, B. Möller, U. Persson, T. Boermans, D. Trier, P. A. Østergaard, and S. Nielsen, “Heat Roadmap Europe: Combining district heating with heat savings to decarbonise the EU energy system,” *Energy Policy*, vol. 65, pp. 475–489, Feb. 2014.
- [5] M. Geidl and G. Andersson, “Optimal Power Flow of Multiple Energy Carriers,” *IEEE Transactions on Power Systems*, vol. 22, pp. 145–155, Feb. 2007.
- [6] Fortum and VTT Technical Research Centre of Finland, “Apros software, dynamic process simulation software for nuclear and thermal power plant applications..” <https://www.apros.fi/>. Accessed: 2021-02-02.

Chapter 2

Literature review

2.1 Introduction

The main purpose of this chapter is to provide the essential background of DHCSs. The current situation of DHCS regarding climate change is addressed. Potential solutions proposed in the literature to reduce the greenhouse gas emissions of DHCS during energy generation are presented. Emphasis is placed on the relevant role of the DHCS's dynamic models. A description of the DHCS and its main components is given to provide more detail about their operation. This chapter reviews the state-of-art of DHCS's modelling approaches and control strategies. Particular attention is paid to the needs for suitable models of DHCSs for the control design process.

2.2 District heating and cooling systems

DHCS comprises heat and cooling sources, a distribution pipe network, and thermal loads (*e.g.*, buildings). Thermal energy is distributed by circulating hot and chilled water through underground pipe networks. Several variables are involved in the operational performance of a DHCS. Therefore, adequate management and control of these variables play a significant role in the energy generation, distribution and consumption within DHCSs.

The popularity of DHCSs has increased in recent years [1]. Some of the latest reports mention that more than 6000 different DHCSs are installed in Europe [2]. Currently, European countries have well-established DHCSs. Three main sectors are covered by DHCSs and these are residential, service and industry. Figure 2.1 shows the percentage of each sector in some countries of the EU reported in 2015 [3], being residential sector the highest in all countries. It means that the primary consumers of DHCS's service are the 73% of the EU population that live in buildings located in high heat density areas [4]. Demand for heating and hot water in the residential sector is significant; it represents about 43% of the total EU final energy consumption.

Nearly 50% of the total energy demand in the UK is used to provide heat to different sectors [5]. For instance, the total annual demand for heating and cooling in buildings reported in 2010 was 483 TWh/year and 6 TWh/year, respectively. In 2012 the annual consumption of heat in the industry sector was 201 TWh [6]. Nevertheless, in 2013 only 2% of the domestic, commercial and public sectors were supplied with district heating systems. This accounted

for around 2,000 district heating systems supplying approximately 210,000 dwellings and 1,700 commercial and public buildings across the UK [7]. Recent estimations showed that the number of district heating rose to 5,500 in 2018, serving around 500,000 consumers [8].

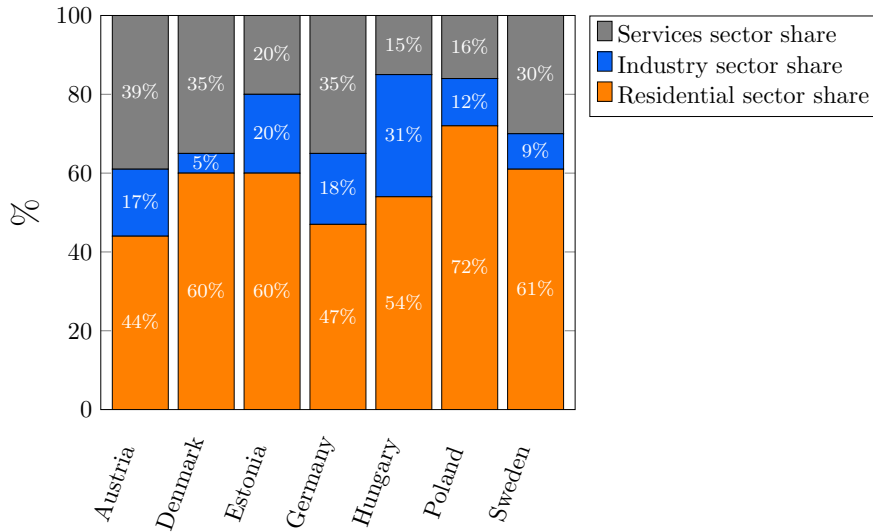


Figure 2.1: Percentages of residential, service and industry shares of district heating.

The scale of a DHCS varies in size as it is determined by the number of buildings covered by the supply energy service. The range varies from small areas with few buildings to huge city areas which encompass thousands of buildings [9, 10, 11]. The energy generation capacity of a DHCS is defined by the number and type of energy sources. A wide range of heating supply sources such as combined heat and power (CHP) units, gas boilers, geothermal and nuclear plants are currently available. For instance, the Russian city of Sosnovy Bor started to provide heat to an industrial park and all city customers through the nuclear plant *Leningrad II-1* in 2019. China’s Hiyang nuclear power plant in Shandong province provides heat to the surrounding area since November 2020 [12]. In the cooling case, a reduced number of cooling supply sources exists, with absorption and electric chillers being the most common. All these devices require a specific fuel to produce thermal energy.

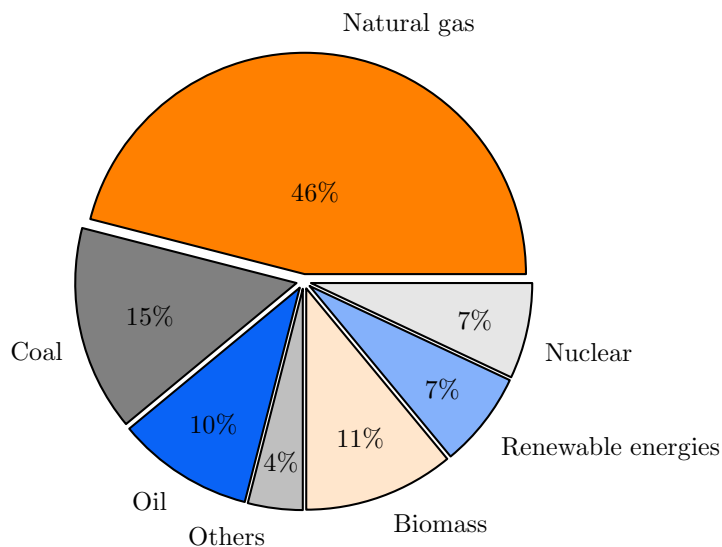


Figure 2.2: Fuels used for heating and cooling in EU .

2.2. District heating and cooling systems

Fossil fuels are the most common option for DHCS in Europe according to [13]. It means that the energy generation systems are the most important contributors to global greenhouse gas emissions [14]. Figure 2.2 shows the share of fuels used for heating and cooling in Europe.

2.2.1 District heating and cooling systems tackling climate change

The employment of technologies like CHP units that use waste heat to supply thermal energy during electricity generation contributes to sustainable energy production. The combustion of natural gas and the high use of solid fuels such as coal have a substantial environmental impact.

The total energy used for heating and cooling reported in 2015 is about 5123 TWh [15], which is more than half of the EU's consumption energy. In 1990, fuel combustion emissions, including all energy generation of DHCS and fugitive emissions from fuels, were responsible for 62% of European greenhouse gas emissions [16]. However, the integration of renewable energy technologies, the improvement of the efficiency of energy source devices and the increased use of natural gas instead of coal have contributed to a reduction from 62% to 53% within 28 years. Despite this reduction, the percentage of gas emission is still considerably high [17]. Figure 2.3 shows the comparison between 1990 and 2018 year's European greenhouse gas emissions divided into main source sectors.

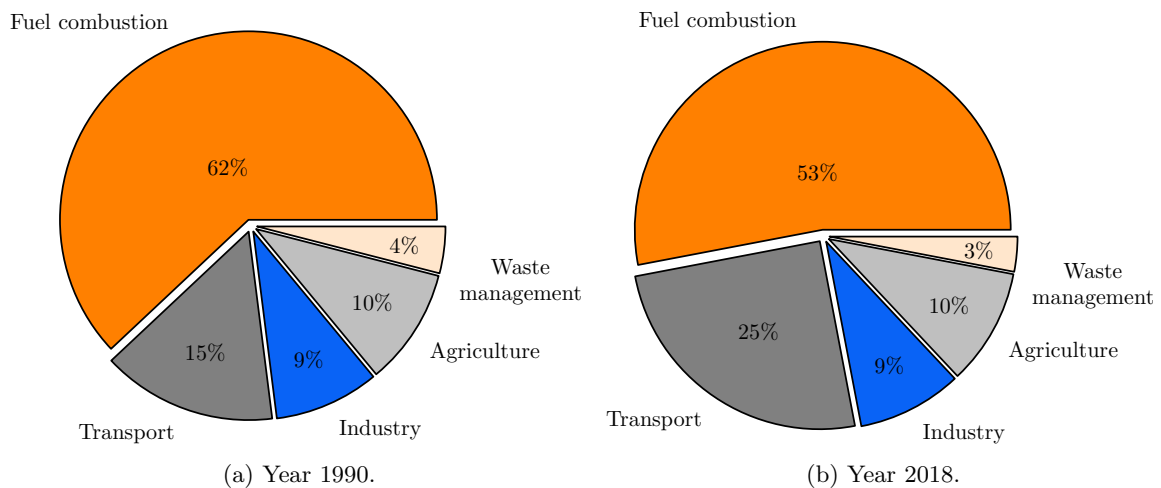


Figure 2.3: Greenhouse gas emissions by source sector [16].

The significant contribution of the energy generation systems to the greenhouse gas emissions is mostly attributed to coal. Carbon dioxide (CO_2) molecules are part of the greenhouse gas emissions which also include methane (CH_4), nitrous oxide (N_2O) and other components in smaller portions. Coal combustion generates an estimated amount of 1115 gCO_2/kWh . This value outstrips by more than two times the limit of 454 gCO_2/kWh established by the US environmental protection agency (EPA) [1]. Table 2.1 shows the carbon intensity of different district heating energy sources compared to other options available in local heating systems. Regarding cooling, the district cooling sources offer a lower carbon intensity than local cooling systems, as shown in Table 2.2 [18].

Thus, DHCS plays an essential role in the decarbonisation of the EU. Their potential contribution to the operation of low-carbon energy systems lies in their flexibility to incorporate different devices to generate energy, such as renewable technologies or co-generation units

[2]. Although the CO₂ emissions of district heating systems are lower than common heating systems, it is still important to improve their efficiency to decrease their greenhouse gas emissions. The low efficiency of some energy sources and the excessive waste heat due to ineffective energy management contribute to the greenhouse gas emissions of DHCS. Therefore, actions need to be taken to increase the performance of DHCS to reduce this contribution. Promising solutions have been addressed in the literature. They are reviewed in the following subsection.

Table 2.1: Carbon intensity per unit of heating.

District Heating	CO ₂ [g/kWh]	Building local heating	CO ₂ [g/kWh]
CHP gas	10	Gas boiler	260
CHP coal	270	Coal fired boiler	530
Biomass	30	Oil fired boiler	350
Waste incineration	20	Electric heating	850
Oil	360	Heat pump	300

Table 2.2: Carbon intensity per unit of cooling.

Cooling system	CO ₂ [g/kWh]
District cooling (free cooling)	25
District cooling (absorption)	1.3 · CO ₂ of Heat used
District cooling (heat pump)	270
Building specific compressor	340-680

2.2.2 Potential solutions

Reducing emissions is critical to cope with the climate change. Developing strategies to have more efficient and sustainable DHCSs has become a priority. There are different proposals in the literature, with some of them already being implemented. The main options are:

- Updating current energy technologies and/or integrating renewable energy technologies,
- Using DHCS of 4th generation,
- Modifying behaviour of end users.

Option one proposes modifying the energy technologies. Firstly, the efficiency of the energy technology has to increase, either improving, or renewing technologies. For instance, coal power plants offer an efficiency of 0.20 against 0.35-0.42 of gas turbine-based CHP units [1]. Gas-steam turbines, which have a heat recovery steam generator to supply heat, achieve up to 0.59 of electrical efficiency. Moreover, the reciprocating engine, which forms the base of several CHP units, has an electrical efficiency between 0.2 to 0.4. Thus, to have more sustainable

2.2. District heating and cooling systems

DHCSs it is of paramount importance to replace the low-efficiency energy generation methods to include devices of higher efficiency [19, 20]. Secondly, the use of renewable fuels such as hydrogen, biomass and geothermal may represent a promising option. For instance, there are CHP units able to combust biogas [21]. Nevertheless, they require building new networks or retrofitting the existing ones [2, 22, 23, 24, 25, 26]. Finally, integration of additional renewable energy technologies such as solar photovoltaic or wind turbines is also suggested [27, 28]. Some challenges must be met by the DHCS to integrate properly the fluctuating and intermittent renewable energy production to the operation of the system [29].

Option two suggests that the conversion of a DHCS into a low-temperature heating network with operating temperatures of 30-70°C (4th generation) looks like the most feasible option to increase the efficiency and sustainability of DHCSs as current pipe networks are still suitable [30, 31]. Heat pumps are key devices to achieve these temperatures [21]. Nevertheless, a thorough analysis is required to ensure that temperature conditions are suitable for the thermal load infrastructure (*e.g.*, heating devices of buildings). Thus, improvement of building installations may be required to suit the space heating and cooling systems to the new temperature levels or retrofit the buildings [32, 33]. Finally, changes in end-user behaviours have also been analysed [34, 35]. In these references, authors highlight that the DHCS operation conditions are affected by the consumer's habits. Nevertheless, further analyses should be undertaken due to the lack of an adequate monitoring infrastructure is still required for consumer behaviour understanding.

All these proposals that look for DHCS sustainability represent economic or social behaviour challenges that may take too much time to be implemented. Furthermore, the current conditions of the DHCS' infrastructure should be analysed to determine the viability of the proposed changes. Historically a low price of fossil fuel compared to the price of renewable energy sources suggests that sustainable DHCS would be an expensive option [3]. Economic investment in renewables would help to achieve the EU reduction emission targets. Nevertheless, the actions and the rate of investment depend on the economic capabilities of each country [4]. Therefore, less expensive and faster solutions should be applied while new higher efficiency technologies become affordable. That said, three main and most feasible solutions are proposed in the literature:

- Forecast of energy consumption,
- DHCS's flexibility,
- Implementation of more effective control strategies.

All these solutions are strongly related to the effectiveness of energy management within DHCSs. Forecasting plays an important role in the optimisation and planning of energy production. Forecasting can be divided according the time horizon: daily, weekly or monthly basis [36, 37, 38]. Different forecasting methods have been proposed in the literature, such as static approaches or artificial intelligence techniques [39]. The main requirement of the forecasting process is the availability of historical data of energy consumptions. Therefore, DHCS should have an adequate monitoring system that measures and records the energy consumption in each thermal load.

Flexibility is defined in [40] as the ability to modify the energy supply and generation rates into or from a system. Flexibility has been a subject of study for many years [41, 42, 43]

and now is also considered as a good solution for DHCS. For instance, TES tanks, thermal inertia of buildings and pipe networks are established as the cornerstones of flexibility within DHCSs [44, 45, 46, 47, 48].

The implementation of flexibility in DHCSs requires effective control strategies to improve the management of energy distribution, storage and consumption. According to [40], the design process of these control strategies presents three main challenging tasks:

- Size of thermal network,
- Prediction of uncertainties,
- Complex dynamics.

The implemented control strategy may determine the sampling time and the number of sensors. The size of a DHCS may range from a single street to an entire region. Therefore, several sensors are needed to monitor the system operation. This requires a large investment to deploy the controllers. Nevertheless, the design of suitable controllers and observers can reduce the number of sensors and thus mitigate the costs of monitoring the system. Different operating conditions should be considered during the design of a control strategy. For instance, the weather determines the heat and cold demand or variations in the domestic hot water temperature and this affects the heat supply process. These conditions may be defined through uncertainty ranges. Then, the performance of the controllers needs to be evaluated at the boundaries of these ranges. Therefore, adequate models of the DHCS capable of considering all critical operating conditions are required.

Finally, the design of control strategies must consider the thermal and hydraulic behaviours of the DHCS. Accurate mathematical models capable of describing the interaction between different components of the DHCS are necessary. Thus, temperature, mass flow rate and pressure controllers can be developed using dynamic models based on physic principles [40].

From a control theory point of view, these tasks represent the step sequence to design and test any controller: obtaining a dynamic model of the system (complex dynamics), defining the system parameters (size of the thermal network) and testing the robustness of the controller under disturbances (prediction of uncertainties). Many control strategies of DHCSs have been reported in the literature from classical control approaches such as rule-based or proportional-integral-derivative (PID) controllers to advanced control strategies, as model predictive control (MPC) [49]. Nevertheless, the main issue of all these proposals is the lack of accurate dynamic models. For instance, a classical PID controller is proposed in [50] to manage the differential pressure of a pipe network. The employed model does not consider the high non-linearity of the hydraulic and thermal behaviours of the pipes. On the other hand, MPC and artificial network control strategies have been analysed in [51, 40, 52, 53]. Once again, no dynamics are considered in the plug-flow models employed to develop the MPC. The use of simple models entails many assumptions that may neglect real operating conditions. For instance, the dynamic behaviour of important parameters such as pipe friction factor and heat transfer coefficients are entirely overlooked in most references.

2.3 District heating and cooling system operation description

The DHCS is a set of different devices working together to provide energy services; thus, local customer heat/cold demands are satisfied. Thermal energy is supplied by transporting heat or cold from available energy sources to end consumers [54]. The components of a DHCS can be clustered into three main sections [55]:

- heating and cooling sources,
- energy distribution network,
- thermal loads.

These three groupings are shown only for district heating in Figure 2.4.

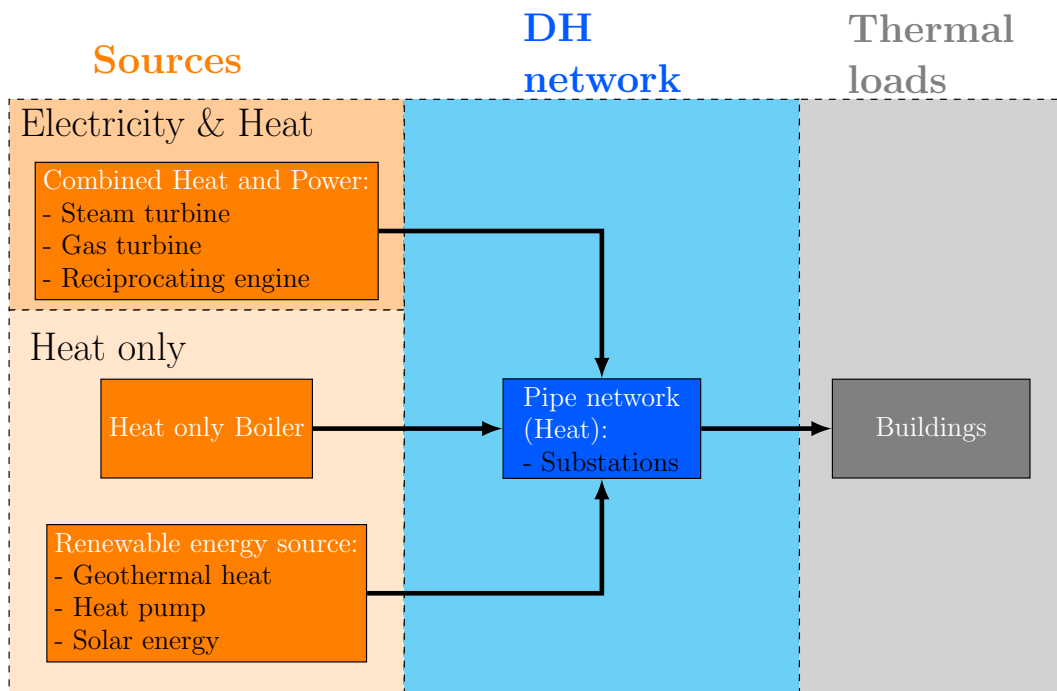


Figure 2.4: Scheme of district heating system components [4].

It is important to notice that the pipe network for cooling is independent of the district heating network. Figure 2.5 shows the schematic diagram of the cooling side components of a DHCS. Energy from district heating sources is typically used to produce chilled water using either heat (absorption chiller) or electricity (electric chiller).

Heating and cooling are centrally produced. They may be distributed to the consumer location or stored if the consumer's thermal demands are already achieved. Pipe networks are used to transport heat or cold energy by circulating hot or chilled water. Control valves and pumps are used to manage the hydraulic operating conditions of the DHCS. A critical component of DHCS, the TES medium, is used to store the overproduced energy during low heat demands.

Finally, the heat is supplied to the thermal loads through heat exchangers located in the substations. A DHCS's substation is a unit comprised of different devices (heat exchanger, control valves and pipes) in which the supplied thermal energy is transformed from a higher to a lower level, in terms of the characteristics of the energy supply medium; water for DHCS.

Like substations in electric power systems where voltage is transformed from high to low values, in DHCS's substations, heat exchangers reduce the temperature and pressure of the energy coming from the heat sources. A detailed description of a DHCS substation is given in subsection 2.3.2. Thus, the substation's heat exchanger's primary hydraulic circuit receives the energy from the distribution pipe network and the secondary hydraulic circuit of the heat exchanger supplies the exchanged energy for space heating/cooling use or domestic hot water. All these components should be operated adequately to ensure operation points while the thermal demands are met. Therefore, understanding the dynamics involved in the entire operation becomes a critical factor for the system's effective management.

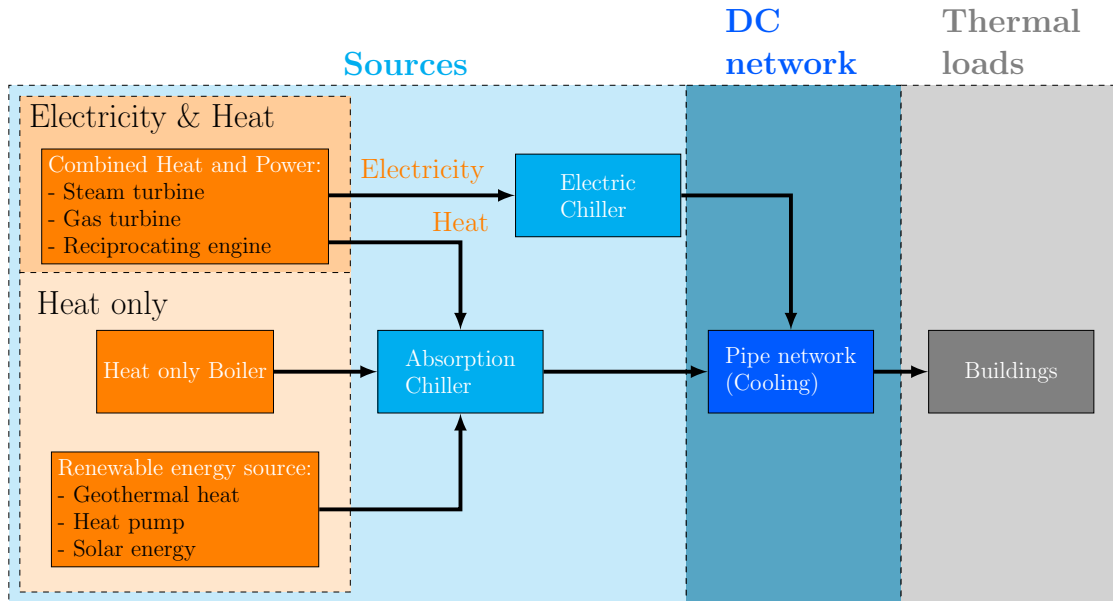


Figure 2.5: Scheme of district cooling system components [33].

Figure 2.6 shows a schematic diagram of a district heating system. A CHP unit based on a reciprocating engine burns natural gas to move the crankshaft linked to an electric alternator to produce electricity. The exhaust gases produced by the natural gas combustion and the engine's coolant jacket system are used to heat the return cold water of the pipe network employing heat exchangers. TES tank is used to save the heat during low heat demands to be later supplied if the heat demand increases.

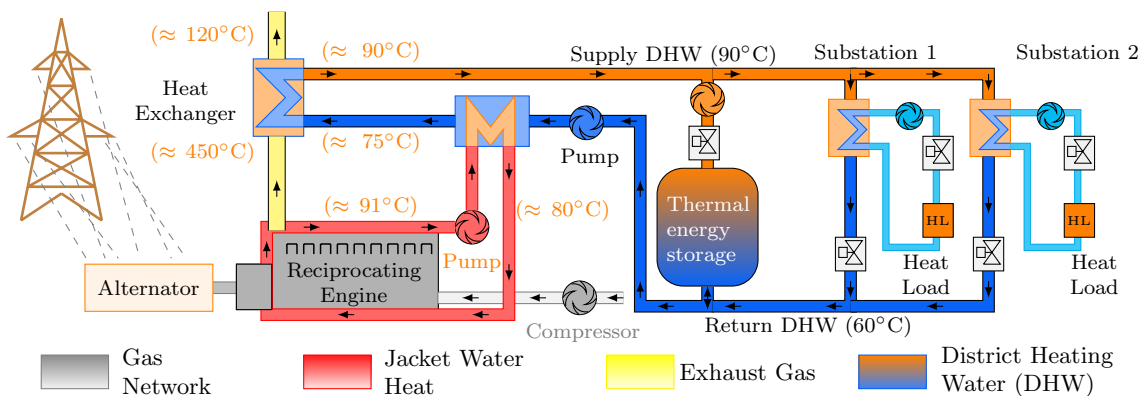


Figure 2.6: Schematic diagram of a district heating system.

2.3.1 Heating and cooling sources

The first generation of DHCS took place at the end of the 19th century and the beginning of the 20th century. Steam condensation and evaporator-condenser systems were used to provide heat and cold, respectively. In the 1930s, the second generation of DHCS incorporated CHP units. In the 1970s, the third generation of DHCS introduced coal, biomass or natural gas as a replacement for petrol oil. Renewable energy sources have been integrated to the fourth generation of DHCS [4, 54]. Nowadays, an extensive range of possible energy sources is available for district heating and cooling applications.

They are divided into two main categories [54, 1]:

- CHP systems
 - Gas and steam turbines
 - Reciprocating engines
- Heat-only systems
 - Boilers
 - Heat pumps
 - Renewable energy sources: geothermal.

Due to the late development of district cooling systems, a reduced number of cooling energy sources are available, being the most commonly used the absorption and electric chillers [56, 57, 58].

CHP systems

A CHP unit harnesses the excess heat generated by the combustion process. CHP is a term applied to any power generation systems which uses the by-product (heat) generated by fossil fuel's combustion process. An alternator uses the mechanical energy produced during combustion to generate electricity. The heat is generated as a by-product. It is obtained by the thermal energy transferred from circulating fluid into the engine jacket water or combustion exhaust gas conducts. CHP units offer higher energy efficiency than separate heat and electricity generation processes [4]. Its electrical efficiency approximately ($\eta_{el} = 0.3$) is added to the thermal efficiency, which in turn may reach values of $\eta_{th} = 0.45$, to produce a total efficiency of $\eta = 0.75$. This feature makes the CHP unit the most popular energy technology for DHCSs. Regarding the combined heating and cooling process, an advanced option of the CHP units is available; namely, combined cooling, heating and power (CCHP) [59].

A gas turbine is comprised of a combustion chamber, electricity generator and compressors connected with the same crankshaft. The power capacity of gas turbines ranges from 1 MW to 250 MW. Their electrical efficiency (η_{el}) rates between 0.35 to 0.42 [4]. Steam turbines use the thermal energy from pressurised steam to generate mechanical energy. Thus, electricity is generated by the motion of a crankshaft. Unlike gas turbines, steam turbines generate electricity as a by-product. Steam turbine implementation may include a heat recovery steam generator and a condenser to increase the efficiency of the electricity generation up to $\eta_{el} = 0.59$ [4]. A reciprocating engine-based CHP unit uses the mechanical energy produced

by the engine's pistons' movement to produce electricity. There are two types of reciprocating engines: spark, which used natural gas, and compress ignition, which uses diesel, respectively. The size of reciprocating engine ranges from 10 kW to 5 MW [59]. This option is trendy for medium size DHCS.

Heat-only systems

Heat-only boilers are the simplest heat technologies in DHCS. They can use solid fuel or natural gas as fuels. Nevertheless, modern boilers can burn biomass [4]. Their high thermal efficiencies, which ranges between $\eta_{th} = 0.85 - 0.97$, makes the boilers a good choice to produce heat compared to CHP units in terms of heat only generation. Heat pump units consist of a compressor and absorber. They uses high temperature heat (80 to 130 °C) and low temperature heat (0 to 30 °C) to produce medium-temperature heat (40 to 60 °C) [60]. Their efficiency is determined by a factor called coefficient of performance (COP). The COP of heat pump units rates from 3 to 6. It means that three or six units of useful thermal energy (medium temperature heat) are generated from each unit of driving energy consumed (low and high-temperature heats) [4]. Nevertheless, the use of heat pumps is limited due to their low effectiveness compared to a CHP unit [61]. Finally, geothermal and solar energy represent a renewable option; thermal energy located underneath the ground is used to provide heat to heat pump units or directly to heat exchangers in DHCS's substations. The temperature of geothermal plants ranges between 30 to 90 °C [62]. Despite their sustainable benefits, the use of these sources is still in initial stages because of their intermittent availability and the lack of policies to incentivise their implementation.

Absorption chillers

The absorption chiller uses a heat compressor, which comprises an absorber, pump and generator. Figure 2.7 shows the absorption chiller cycle's schematic diagram: low pressure and low-temperature refrigerant vapour from an evaporator supply high pressure and high-temperature refrigerant vapour to a condenser. In order to increase temperature and pressure, the refrigerant is boiled in a generator using thermal energy. The condenser converts the refrigerant into vapour liquid, then the absorbent of the condensation process is bonded with refrigerant vapour in the absorber to begin the process again [59]. The feature of recovering the thermal energy from CHP units or boilers makes the absorption technology the best option to produce fluid cooling within DHCS.

The choice of energy technology depends on factors such as electricity and heat capacity required and its cost-competitiveness. Nevertheless, CHP units and CCHP units are the most common options for typical DHCS applications due to its higher efficiencies than other options [63]. Nevertheless, one of the most important advantages of DHCS is the possibility of integrating different energy sources and coordinating their operation to increase the system's flexibility. A thorough analysis of the operating points under different scenarios has become imperative to achieve this effective coordination. Thus, limited availability or low effectiveness energy technologies can work together with those technologies with better performances.

2.3. District heating and cooling system operation description

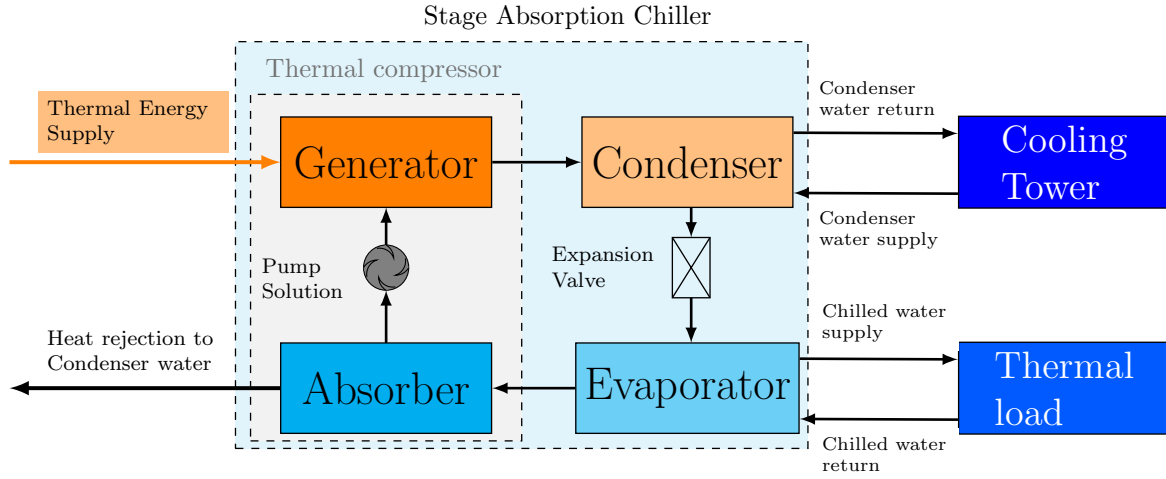


Figure 2.7: Stages of absorption chiller cycle.

2.3.2 Distribution network

The term *distribution network* stands for the set of components used to transport and distribute thermal energy. Heat and cold from the energy sources are transported to the customers through a fluid within supply pipes. Once the substations transfer the thermal energy, the fluid goes back to the energy technologies using return pipes. The terms distribution network and pipe network are used indistinctly in the literature. The DHCS's pipe networks consist of three main elements: pipes, pumps and valves. Steel pipes with insulation are buried to create the pipe network of typical DHCS configurations [54]. Polyurethane foam is the most common insulator used for pipes, with a thermal conductivity of about 0.025 W/mK. A pair of pipes is used for each branch of the pipe network. The water circulates back to the energy technology through the second pipe to be heated again. Thus, the line pipes are labelled as supply and return pipes. Different control valves are located through the whole network to regulate flows and pressure drops through the pipe network. Centrifugal pumps are the most typical turbomachine type used to circulate water to the pipes, adding mechanical energy. A schematic diagram of a small DHCS including pipe network elements is shown in Figure 2.8.

Appropriate hydraulic conditions in pipe networks, such as safe limits of pressure or enough mass flow rate in substations, are necessary. For this reason, effective controls should be implemented over the pumps and valves. Nevertheless, the lack of suitable models has restricted development and consequently the use of better controllers. Whilst models are being developed, simple look-up tables based on limited system characterisation [54] are commonly used.

Substations

Buildings are connected thermally to the DHCS's pipe network through substations that manage the energy consumption of the thermal loads. Figure 2.9 shows the schematic of a DHCS's substation, with four of its main elements: pumps, pipes, control valves and heat exchangers. The hot/cold water from the energy technologies circulates through the heat exchanger's primary circuit. The thermal energy is transferred to water in the second circuit and is sent to the thermal loads. Control valves regulate the amount of mass flow rate required to keep constant the water's output temperature in the secondary circuit. The heat exchanger

reduces the temperature from a high to a medium value to be manageable for the thermal load systems. Thus, the heat exchanger can be seen as a step-down transformer in an electric power system [54]: for the heat exchanger, temperature and pressure are reduced, whereas the voltage is reduced and the current is increased in the transformer. Different types of heat exchangers are available, with the flat plate heat exchanger being the most popular. The temperature of the second circuit output and the primary circuit's mass flow rate are the critical variables that guarantee an efficient energy supply process.

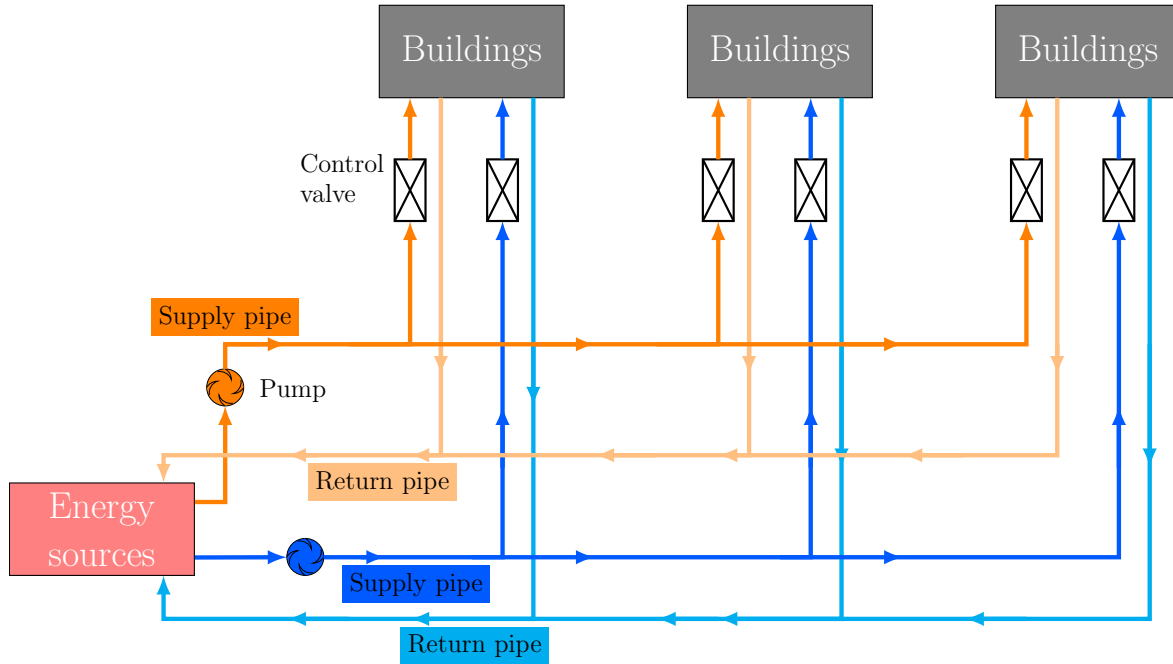


Figure 2.8: Scheme of a heating and cooling pipe network of a DHCS.

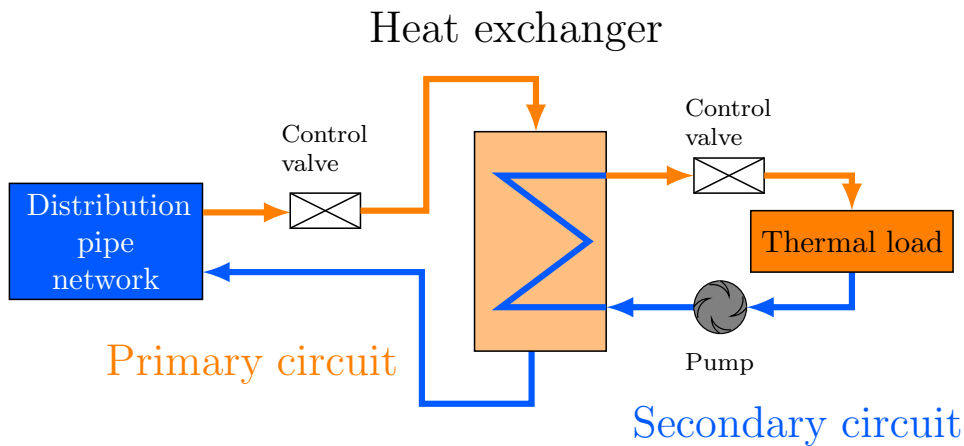


Figure 2.9: Schematic diagram of a DHCS's substation.

2.3.3 Thermal energy storage

The heat and cold produced by energy technologies can be stored through TES tanks to be supplied at a later time. The thermal energy may be produced during lower generating cost or low demand and used during peak demand. Thus, the heat/cold supply process is supported by TES. Figure 2.10 shows the classification of TES in two main categories: the method and

2.3. District heating and cooling system operation description

scale of storage. Another category is mentioned in the literature, namely thermochemical. Nevertheless, only a few analyses of the use of this kind of TES has been reported [64, 65]. Therefore, more assessments are to be done before considering thermochemical TES as an alternative for TES.

The storage method category includes two different types of matter heat. The sensible heat storage is given by the storage medium's internal thermal energy produced when its temperature is varied. The storage capacity depends on the specific heat (c_p) of the TES's medium and its volume density. For this type of TES the most popular storage medium is water. Water offers an economic and sustainable option for storing. Nevertheless, its low specific value requires large volumes of water, limiting its use to DHCS without space restrictions.

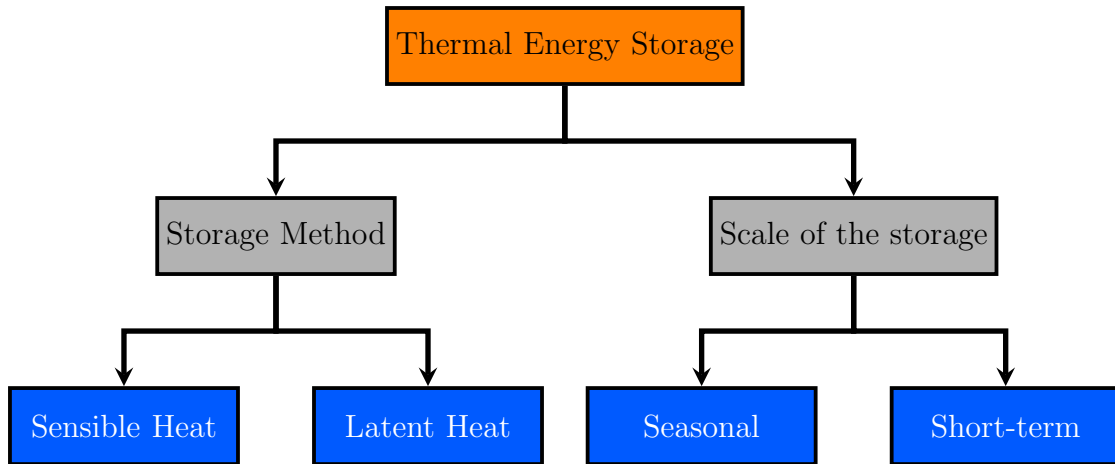


Figure 2.10: Classification of thermal energy storage [66].

On the other hand, latent heat storage uses the heat released or absorbed when there is a phase change of the storage medium. During this transition, the temperature remains constant. Phase change materials (PCMs) are used to store energy and the TES capacity is defined by its latent heat value. The most common phase change used in DHCS is liquid to solid for both heat and cold storage. A prevalent option of latent TES is ice storage for cooling. In contrast to sensible mediums, a PCM has an overly high specific heat that stores the same amount of energy within a smaller space. However, latent TES has four main drawbacks: a higher cost than sensible TES, the toxicity of some PCMs, low conductivity and subcooling phenomenon [66, 67].

The scale category is related to the storage periods—seasonal TES stores thermal energy for a long time. One typical option of seasonal TES is the underground aquifer where a considerable amount of water located beneath the soil provides a massive storage capacity [66]. The main constraints of this TES option are its availability and its geological conditions. Conversely, the short-term TES counterpart helps supplying heating/cooling loads that vary hourly or daily. Within this latter category, the water tank is reported to be a suitable option.

Water tank-based TESs are well insulated stainless or plastic tanks which contain hot water. The hot water from the energy source is injected at the top of the tank. A constant volume of water is required to maintain water temperature conditions and facilitate thermal energy extraction. Thus, during the discharging process, the return warm water from the DHCS's pipe network is pumped into at the top of the tank. The internally displaced volume

of water forces the hot water at the top to be released and, in turn, to be supplied to the substations. Figure 2.11 shows the water tank's schematic diagram. Temperature sensors are located along the wall of the tank so that the internal temperature distribution gives an estimated SoC. Heat exchanger coils or resistive heating elements can be incorporated into a water tank. Usually, this configuration is used for domestic energy storage or medium size TES tank located near thermal loads.

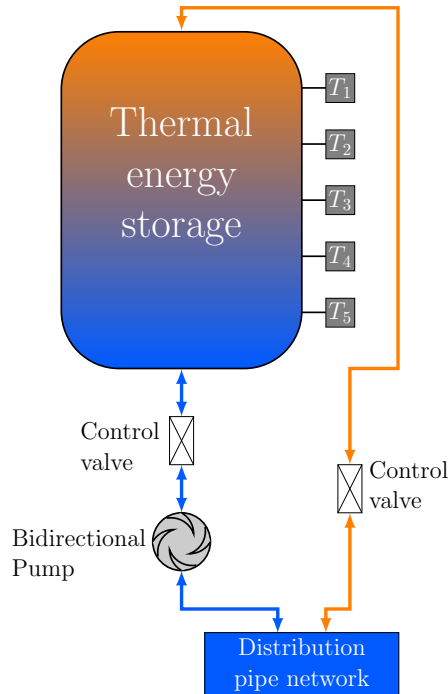


Figure 2.11: Water tank-based TES schematic diagram.

For the cooling side of a DHCS, latent TES tanks have become an effective and affordable option, particularly the ice tank-based TES, which offers low-cost maintenance [68]. A refrigerant is cooled down to a temperature below $0\text{ }^{\circ}\text{C}$ by the chiller and then pumped to the ice tank during the charging process. The refrigerant provides thermal energy to solidify the water into ice. For the discharging process, the warm refrigerant circulates through the tank to take out the cooling energy during the ice's melting process. Despite its popularity, one disadvantage of ice tank-based TES is that a high number of ice bank units is required for large size DHCSs due to its medium storage capacity, that ranges from 144 to 1710 kWh [69]. Therefore, series or parallel interconnections should be analysed to find the most effective configuration to be implemented in a DHCS. Accurate dynamic models of ice tank-based TES are necessary to carry out this type of analysis.

Thermal energy storage within DHCSs

TES tanks have demonstrated their important role in the energy supply management in DHCSs. TES tanks can decouple the generation and demand for thermal energy. They act as an energy buffer that shifts the energy loads for the peak to off-peak hours in thermal systems that use electricity. For instance, the heating generated by the CHP units that operate during high electricity demands can be stored in TES tanks to be used later during increments of heat demands. The buffer action of the TES tanks may also reduce the effect provoked by the fluctuating operation of intermittent renewable-based energy systems such as solar

thermal collectors. On the other hand, the cooling produced by chillers when heat recovery (absorption chiller) is available or there is low cost electricity (electric chiller), is stored by TES tanks to be used later to supply cooling thermal loads. Thus, with the implementation of TES tanks, the CHP units and chillers performance increase their effectiveness.

TES tanks also contribute to the improvement of DHCS's flexibility. Different TES tank configurations, such as centralised and distributed, are analysed to determine the best option to increment the system flexibility. Thus, the flexibility provided by a CHP unit coupled to a decentralised TES tank is less than the value obtained in a centralised setup. This decrement in the flexibility happens because of the CHP unit operation's weak coupling, which is commanded by the instantaneous heat demand [70].

The development of dynamic models or TES tanks is critical to operationally analyse DHCSs where different time scales, energy sources and storage capacities are involved. Furthermore, well-controlled charging and discharging process are critical to guarantee a stable and effective overall operation of the DHCS.

2.3.4 Thermal loads

The main end consumer of DHCS is the residential sector (see Figure 2.1). Three main heat loads are presented in buildings: space heating and cooling and domestic hot water. The largest cold demand supplied by DHCSs is space cooling, in which chilled water is provided to air conditioning systems. Another type of cold demand occurs when the moisture in the air has to be cooled to regulate indoor temperatures efficiently. Dry air requires less energy to increase or decrease its temperature [54]. They represent approximately 50% of the energy consumption worldwide [4]. Most of the buildings in Europe have been built before 1990. This means that inefficient systems may be currently used to supply cooling and heating energy [71]. Keeping in mind the United Nations's estimations about an increase in urban population [72], it is important to analyse potential energy savings. Adequate building models may therefore become very useful.

Detailed models of thermal loads are complex. Often, modelling of energy consumption is replaced in some studies for thermal loads profiles [45, 73]. Conversely, complex thermal models of buildings have been analysed in [74, 75, 76]. Resistance-capacitive (RC) models are used for dynamic modelling considering the thermal conductivity of the construction materials. Electrical to thermal analogies are implemented to obtain differential equations. Although detailed dynamic modelling of buildings is a mature subject, the effective temperature controllers in these models are absent in the literature. Thus, these models could be useful for improving the energy consumption of space heating and cooling systems.

2.4 Benefits and disadvantages of DHCSs

Different devices can generate heat and cold within a DHCS. This allows the integration of different energy sources using the same supply infrastructure. Moreover, the addition of TES tanks significantly improves the performance of the energy technologies. Thus, the heat and cold supply processes increase their reliability. In summary, the benefits of DHCS are [54]

- Reliable direct heat and cold delivery for a wide range of users,

- Enabling integration of different energy sources to meet heat and cold demands,
- Reducing the cost of energy generation.
- Saving space for the customer's heating and cooling equipment.
- Lower operation and maintenance costs compared to individual heating systems.
- Lower risks for fire due to no fuel combustion in buildings.

Despite the benefits, DHCS present the following drawbacks:

- High capital investment.
- Heat losses in pipe networks.
- Rigid contracts that do not allow the customers to negotiate prices and delivery conditions.
- Reliant on fossil fuels if not renewable sources are incorporated.

2.5 Modelling challenges

At the start of the design process or analysis of a system, a prediction of its performance is essential [77]. This prediction must be based on a mathematical description of physics phenomena present in the system's dynamics. This description allows obtaining a model. Factors such as knowledge of the system dynamics and some assumptions will compromise simplicity and accuracy levels. Thus, some models may neglect variables or phenomena to reduce their complexity. Therefore, the model's validation depends on the agreement between the model predictions and the real system behaviour. This section briefly describes the main dynamic behaviours involved in DHCSs and the attempts to model these dynamics.

Two main behaviours are presented in a DHCS: thermal and hydraulic. Four main physics variables are involved: temperature, energy, pressure and mass flow rate. The operational management of DHCS is based on continuing measurements of these variables. Thus, the behaviour of critical elements must be known at any moment. For this purpose, several sensors are installed to provide measurements. Furthermore, for effective controllers, continuous measurements are critical. Some studies assume as constant some critical dynamic behaviours, ignoring important operational conditions that affect the overall performance of the DHCS. Models capable of accurately describing the thermal and hydraulic dynamics will allow reliable analysis and proper control design processes. This section presents the challenges of modelling dynamic behaviours and how some references have faced them.

2.5.1 Thermal behaviour

Heat: temperature or energy

Heat is defined as "*the thermal energy in transit due to a spatial temperature difference*" [78]. Heat involves two physics variables: energy and temperature. For the sake of precision, it is important to establish which variable will describe the thermal behaviour of a system. Usually,

energy systems are studied considering only their energy capacities, ignoring the temperature conditions under which they are operating. Pioneering work was developed in [79], through the introduction of energy hub. In this modelling approach, a power flow model describes the coupling between different energy carriers, including heat and cooling. The conversion and transmission of energy are then modelled by a steady-state approach where power and efficiency of energy generators and converter elements are assumed constant or linear. This approach is enough for economic dispatch or energy estimation analysis, where no in-depth details of the system's performance are necessary [80, 81, 82].

Therefore, if only values of the energy transferred, consumed or generated are considered in the models, the system's real operational conditions, where dynamic temperature variations enable the energy changes, cannot be modelled. An accurate dynamic description of these energy changes requires the inclusion of temperature variations. Temperature is the fundamental variable used to quantify thermal energy. By definition, if a temperature difference is presented in a system, heat transfer is occurring. This flux of heat should be described by physics principles, including convection, conduction, and radiation heat transfer processes. Thus, the thermal energy E [J] in a system is computed by the temperature gradient T (quantified temperature change) and a function f capable of describing how the heat flux Q [J/s] is produced as

$$f : T \rightarrow Q. \quad (2.1)$$

Temperature is more intuitive than energy for understanding and describing the thermal dynamic of any systems. For instance, it is easier for human beings to notice energy changes using the system's temperature: when a cup of coffee is losing thermal energy, the temperature *measurement* makes noticeable the energy change. Thus, a cold coffee not only has a bad taste but also shows how fast a high-temperature liquid can lose energy in a cold environment. Temperature is the most direct and suitable variable to describe a system's thermal behaviour dynamically, likewise, to analyse the heating-cooling energy distribution, transfer, and consumption within a DHCS.

Modelling of DHCS's thermal behaviour

Several studies have presented dynamic models of heat transfer phenomenon within DHCS analysis. For instance, [83] dynamically computes the energy transferred by substation heat exchangers to analyse the optimal energy consumption of a distribution network. Reynolds and Nusselt numbers are used to define a general conductance which might be defined as heat transfer coefficient. Nevertheless, besides variations of thermophysical properties of the water, no mathematical model is presented. Regarding the DHCS's pipe network's thermal behaviour, a few works present dynamic and quasi-dynamic models. For instance, [84] uses the energy conservation equation to obtain a mathematical model of a single pipe divided into many nodes. The thermal behaviour is described dynamically, but the hydraulic behaviour is assumed constant. Ordinary differential equations (ODEs) of the node pipe temperatures are obtained; they are reduced to algebraic equations to be solved in an iterative method. The same method is applied in [85] where a distribution network of a DHS is modelled and non-linear algebraic equations are solved by a Newton-Raphson iterative method.

Similarly, a dynamic thermal model of a pipe is developed in [86] implementing the quasi-dynamic modelling approach. Energy balance is applied by spatial discretisation of the

pipe; the ODE is solved to define the output temperature of the pipe. The hydraulic behaviour model is not developed. The main restriction of this type of models is that each solution of the iterative method requires specific conditions which are not allowed to be modified during the solving time. Thus, different operational conditions have to be analysed in separate simulations. Furthermore, control design for thermal energy distribution is not affordable with algebraic equations.

2.5.2 Hydraulic behaviour

Conversely to the thermal dynamic, the hydraulic behaviour is defined by two variables: pressure p [Pa] and mass flow rate \dot{m} [kg/s]. Two more variables are commonly used for the flow of water within pipe networks: fluid mean velocity v [m/s] and volumetric flow Q_v [m³/s]. The basic description of a hydraulic system is a set of elements capable of producing a fluid movement. Three basic components are required for a hydraulic system: a pump to force a fluid to move through the system, pipes to build a hydraulic circuit where the fluid flows, and a valve to regulate the fluid's flow and pressure the circuit. Each element should be sized according to the amount of fluid to be moved. For instance, the main parameter of a pump is the head h [m], which determine its pumping capacity. On the other hand, loss pressure coefficients K_L are critical parameters of control valves that define their operating ranges.

Modelling of accurate dynamic models of hydraulic systems must consider phenomena like the laminar and the turbulent flow of the fluid and critical pipe parameters such as the internal roughness material. These factors affect the pressure drop through the pipe. Nevertheless, some complex characteristics of the fluids, such as compressibility or viscous effects, may be neglected.

Modelling of DHCS's hydraulic behaviour

The most common modelling approach for DHCS's pipe network has been presented in several studies. It consists of algebraic equations of the pressure losses and flow rates of water that are solved using iterative methods such as Newton-Raphson method. For instance, an empirical equation of the head losses of the pipes is used to define the model's matrix formulation and then solved by an iterative method in [87]. Although accurate equations of pipe's friction factor are used, its explicit solution is not defined properly, thus increasing the computing time to solve the model. Furthermore, valve openings (o_v) are not considered in the valve model equation limiting the use of the model to fixed values of o_v , which in turn clearly does not represent a real operating mode. A pipe network model is presented in [88, 89]. Simple algebraic equations of pipe's pressure are established and the friction factor value is assumed constant. An improvement model is presented in [90], where friction factor is iteratively computed. Nevertheless, control valves are not considered.

The simplicity of the steady-state pipe network models has limited the development of more accurate models. Critical parameters and elements which behave dynamically, for instance, friction factors of pipes and valves, are also not considered. The dynamic models reported in the literature are limited to the employment of commercial simulation software. For instance, *Modelica* libraries are used in [86, 91] to build a pipe network but no mathematical models of hydraulic elements are presented

2.5.3 Dynamic or steady-state models of DHCSs

The simplest way to describe a mathematical model is by using a set of mathematical operators and system parameters. Algebraic or differential operators can be used to generate the model outputs. Differential operators establish the time-dependant rate of changes of the output variables. Differential equations usually define these type of models. Whereas algebraic relationships compute the output variable in equilibrium, it means no variable changes through time. A simple block diagram of a mathematical model is shown in Figure 2.12a. The transient (dynamic) and steady-state scopes of the model output are illustrated in Figure 2.12b. As it can be observed, steady-state models are not able to capture the transient response. Conversely, differential equation representations can predict the transient response of the system when variations of its inputs are applied.

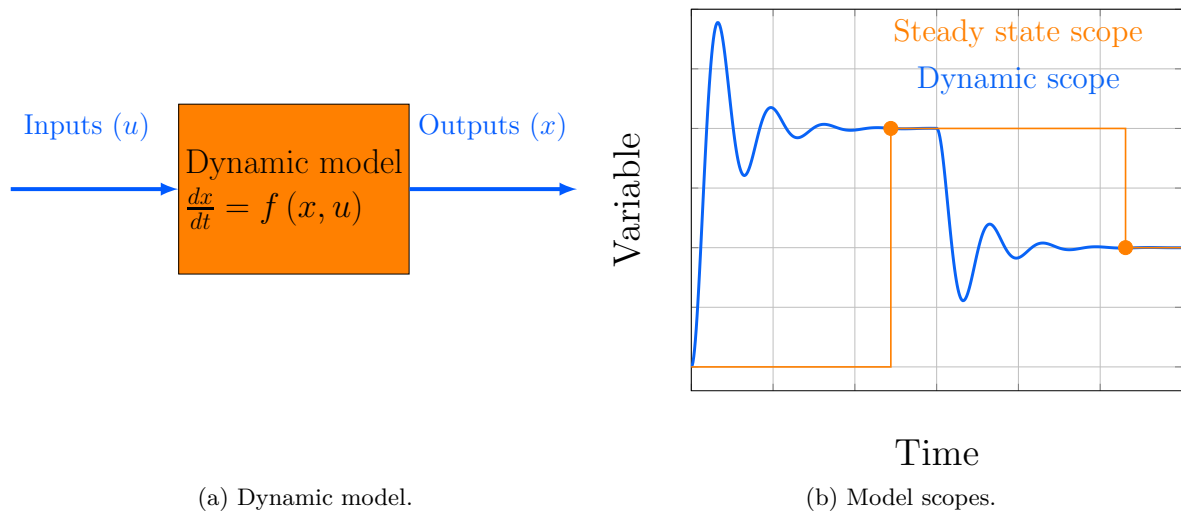


Figure 2.12: Left: Dynamic model block diagram. Right: comparison between scopes of dynamic and steady state models.

Within the dynamic framework, there are some modelling approaches with different levels of accuracy. Partial differential equations (PDE) have used to model DHCS’s elements. A PDE describes the change rates of a variable through two independent coordinates: space and time. Usually, numerical methods are implemented to solve the equations because of the complexity of an analytical solution. The most common methods are the finite difference, volume and element methods. In these methods, the volume of the system is split into several nodes and then PDEs are used to describe the dynamic behaviour through the three space dimensions. The solution of all these equations means a high computational cost. Some works in the literature have followed these methods to model DHCS’s elements. For instance, a flat plate heat exchanger is modelled in [92]. The model validation exhibits good agreement with respect to experimental data.

Nevertheless, a critical parameter used to compute the heat transfer coefficient, called the Nusselt number, is assumed constant and computed using an empirical equation with correlation coefficients. The authors concluded that empirical parameters might be lead to high errors if they are not estimated adequately. Similarly, two dimensional model of domestic TES tank is developed using the finite volume method in [93]. Although the model gives

enough information about the temperature distribution inside the tank, discharging and charging simulation results do not present the output temperature of the TES tank, which is necessary to analyse the TES tank's interaction with the whole system.

A complete DHCS's pipe network is modelled with the finite volumes method in [94]. Each site of the system is represented as a node: substations and energy technologies. The distribution network is discretised in smaller elements where energy balance is solved. Hydraulic behaviour is modelled using nodes at each location of the DHCS. Pressure drop is computed considering the mass flow rates and pipe's parameters. Nevertheless, valves and heat exchangers are not included. Due to the limited number of nodes, each pipe's temperature is assumed constant through its length. This assumption reduces the model's accuracy dramatically if DHCSs with long pipes are modelled as the temperature profile is not constant throughout the pipe length.

Regarding the TES tanks, [95] present a three dimensional model of a cylindrical storage tank where the finite volume method is used to solve energy and momentum equations. Internal temperatures and fluid velocities are modelled by applying a stratification method. Due to the number of nodes required to obtain an accurate model, a high computation time is necessary. Therefore, the model is impractical for a system where more elements are involved.

Water tank-based TES is modelled by PDEs in [96, 97]. The finite volume method is then used to solve the PDEs derived from an energy balance. Similarly, latent heat TES tank is modelled using a three-dimensional approach. A paraffin wax-based TES tank is modelled and simulated in [98] using PDEs. Average of the output temperature of fluid used to charge and discharge the storage is shown for different operating points. Two dimensional model of latent TES tank is presented in [99]. Well defined thermophysical characteristics of the PCM are presented. The enthalpy of the PCM is proposed and verified through a comparison between simulated and experimental data. Although the good agreement achieved against the experimental results, the high computational cost makes the use of this type of models unfeasible for simulations with more DHCS's elements.

The heat exchanger's thermal behaviour is modelled based on PDEs in [100, 101]. Energy balance is implemented to describe the temperature rates of the system. Spatial discretisation is implemented to reduce the model to ODEs, which describe the temperature rates in only one dimension. The models do not present a dynamic computation of the heat transfer coefficient. Likewise, the thermal pipe networks model is developed based on PDEs derived from the energy conservation law in [102]. A discretisation method is implemented to obtain a reduced model. Once again, the heat transfer coefficient between the pipe's internal fluid and the exterior temperature is not computed dynamically.

As it can be noticed, the main drawback of the use of PDEs is the complexity of their solution and the computing time required to be solved. Their use is ineffective for large DHCSs where several elements need to be simulated or for control design purposes. Usually, this modelling approach is used to obtain accurate models for design analysis where spatial (three dimensions) description helps to understand the internal behaviour. Hence, a detailed model of DHCS's elements is not necessary and the average value of the main variables (1-D) are enough to know the system's state. This is confirmed by the fact that real systems are monitored with punctual sensors which measure the average value of temperatures, pressures and mass flow rates to provide enough information to the energy management system.

Several studies have developed 1-D dynamic models of DHCS's elements. A heat exchanger

is described by ODEs in [103, 104]. Nevertheless, the heat transfer coefficient is not described dynamically and the finite difference numerical method used to solve the model is not suitable for control purposes. Regarding the pipe network, several studies have addressed the model of pipe networks with 1-D analysis mainly focused in thermal behaviour [85, 105]. The pipe network temperature is modelled by a time delay equation considering the fluid's velocity. The hydraulic behaviour is modelled using a steady-state approach.

The water tank-based TES have also been modelled following the 1-D approach. Due to its simplicity, well-described dynamic models are available in the literature. Stratification is the most popular approach to model water tanks. For instance, a stratified model is presented in [106]. ODEs describe the temperature profile through the height of the tank. The ODEs are converted into finite differences and an iterative method is used to solve it. Although the model is validated using experimental data and good agreement is obtained, the model is not suitable for the control design process. A dynamic reduced model of water tank-based TES is presented in [107]. The model needs to be tuned for the charging and discharging process. Some parameters are empirically identified to obtain the simplified model. This estimation requirement is also presented in [108]. A more complex model considers buoyancy effects, which causes less dense water in the tank bottom to rise to the top. Thus, the use of both models is limited to the availability of experimental data.

As mentioned previously in this chapter, dynamic models offer a better description of the system than steady-state counterparts. However, due to the complexity of some phenomena involved in the system's behaviour, this challenging task has not been overcome for DHCSs, at least in a complete way. On the one hand, thermal behaviour has been analysed dynamically, but suitable models for control design are lacking. On the other hand, reported hydraulic models usually assume no pressure and mass flow rate dynamics.

2.6 Classical control for DHCSs

The control in a DHCS's is performed over temperature, differential pressure and mass flow rate variables. The most straightforward option found in DHCS is the on/off controller. A simple temperature or pressure switch governs the supply of heat or mass flow rate, respectively. Although this option simplifies the implementation of a feedback controller and no complex models are required, the actuators that are commanded by the control signals could be damaged due to the switching frequency of on/off states during changes in the system's conditions. To avoid this, classical feedback controllers as PID controllers are very popular within DHCS. Due to each control action, the controller can adequately face the disturbances of reference changes to the system dynamics. These controllers may be tuned by trial and error or following a formal design process where the systems' dynamics are considered. The latter option is addressed in this work. Firstly, the basic control systems found in DHCSs are described. They are typically classified in four types according to [54]:

- Heat demand control,
- Flow control,
- Differential pressure control,
- Supply temperature control.

The heat demand and flow control locations are the consumer heating systems and DHCS's substations, respectively. Conversely, differential pressure and supply temperature controls are located in the energy centre. This classification helps understanding the function of each control scheme within the management of the heat supply process. Nevertheless, from a control theory point of view, heat demand and flow control are temperature controls. A brief explanation of each one is given to clarify this point.

Heat demand control ensures the temperature conditions of the customer devices, such as regulating the heat supply to the building radiators to cope with the space heating conditions. Thus, the temperature setup of the hot water supplied to the radiators may be changed according to weather conditions. It entails a decrement/increment of the supplied hot water's mass flow rate to achieve the temperature setup of the heated or cooled space. Thus, heat demand control is a temperature controller regulating the hot and cold water flow in the heat and cold consumer devices (*e.g.*, radiators, HVAC or tap water).

Flow control regulates the mass flow rate of the primary circuit of the substation's heat exchanger. The controller keeps the temperature of the secondary circuit constant. A control valve modifies its opening to increase/decrease the hot water's mass flow rate that comes from the energy centre. Mass flow rate and temperature changes in the secondary circuit should be managed by the controller to guarantee the heat demand achievement. Therefore the control variable is the temperature of the secondary circuit and the regulated variable is the mass flow rate of the primary circuit. This regulation may affect the differential pressure of the pipe network, forcing the energy centre to modify the whole network's hydraulic conditions through a differential pressure control. Thus, the differential pressure controller acts over the hydraulic conditions of the pipe network. This control aims to keep the differential pressure of the farthest substation constant. The pump speed is regulated to increase/decrease the mass flow rate supplied to the substations according to the differential pressure changes. Thus, the amount of hot water is guaranteed to accomplished the heat demands.

The supply temperature control acts over the energy technologies. For instance, in a DHCS with a CHP unit as an energy technology, its control variable is the hot water temperature supplied by the CHP unit. The temperature of warm water that returns from the DHCS's pipe network is increased through heat addition. The temperature controller regulates the CHP unit's internal exhaust gases' mass flow rate to exchange heat through the heat exchangers. Thus, the return water flows through the heat exchangers, increasing its temperature and achieving the supplied water's temperature set-point. Table 2.3 shows the control and regulated variable of each control and Figure 2.13 illustrates their implementation in a DHCS.

Table 2.3: DHCS's control systems and their controlled variables.

Control system	Control variable	Actuator
Heat demand	Mass flow rate Temperature	Control valve
Flow	Temperature	Control valve
Differential pressure	Pressure	Pump
Supply temperature	Temperature	Heat technology

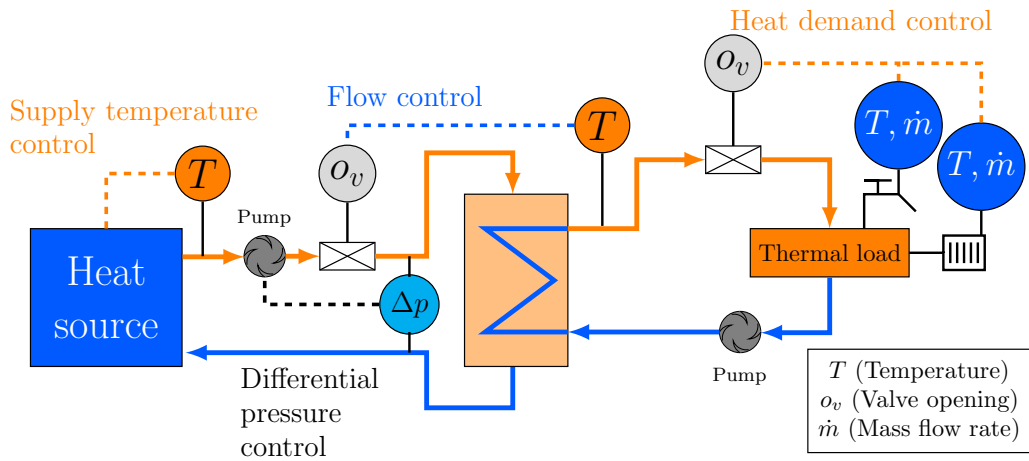


Figure 2.13: Overview of the four control systems in DHCS.

Several works have proposed different controllers for each DHCS's element. Temperature control of heat exchangers is presented in [109]. A 1-D dynamic model is developed and classical PID and state-space feedback controllers are presented. However, the dynamic computation of the heat transfer coefficient and the control design process are not presented. In [110], an accurate dynamic model of a heat exchanger and a robust state-space controller are presented. Both control schemes are unfeasible due to the need for internal temperature sensors to obtain the model's states. PID and fuzzy logic controllers for heat exchanger are presented in [111]. Nevertheless, the control design processes are not explained. PID controllers for charging and discharging process of water tank-based TES [112, 113]. Although the dynamic model of the TES tank is developed, the control design process is not presented. Similarly, an empirical tuning process of PID controller gains is used [114] to obtain certain desired performance parameters of a TES tank.

Regarding the controllers for DHCS's pipe networks, the main impediment to analysing the use of classical controllers is the lack of dynamic models. Because most of the models reported in the literature are based on steady or quasi-steady modelling approaches, the implementation of classical controllers is not possible. The use of classical P and PID controllers in hydraulic networks have been reported in [115, 116, 117]. Nevertheless, the process to obtain the control gains is not explained. In addition, the control structures are implemented in simple models, which do not consider important pipe parameters such as friction factor or absolute roughness.

2.7 Modelling tools for dynamic simulation of DHCSs

Detailed modelling of DHCS's tends to require powerful software capable of simulating thermal and hydraulic behaviours with a certain level of accuracy. Therefore, simulation tools are essential for the analysis of DHCSs. Different configurations of DHCS's elements can be simulated and element parameters modified to determine the best option for a specific design requirements. For instance, pipe sizes, heat exchanger dimensions may be simulated to predict the pressure and heat transferred under different conditions. Nowadays, different commercial software for DHCS simulations are available. One of the most widely used for engineering simulations is MATLAB/Simulink platform. Mathematical models described by ODEs can be solved in real-time or speed-up simulation through powerful algorithms already contained

in MATLAB. For instance, dynamic models of thermal behaviour of DHS are presented in [118, 119]. The Simscape toolbox of MATLAB/Simulink is used to build pipes and thermal losses are modelled dynamically. The results show a good agreement with experimental data. Although MATLAB/Simulink is a good option for the dynamic simulation of DHCS, its main drawback is that critical values such as friction factor of heat transfer coefficient remain constant during simulation time.

For the sake of accuracy, software capable of considering all the parameters involved in the thermal and hydraulic behaviour of a DHCS are necessary. Three software packages stand out among the current options: Dymola, TRNSYS and Apros. Dymola works based on Modelica language; several components are available in its libraries. The users also can modify the code to improve models. On the other hand, TRNSYS has a solving engine that allows the user to solve complex models and it also has a library of DHCS's components. Several studies have used them to simulate configurations of DHCSs [120, 121]. Finally, Apros, which started focusing on modelling nuclear power plants, uses a complex modelling approach based on conservation laws. Its solve engine is based on six PDEs, from which momentum, mass and energy conservations laws are solved. The PDEs are discretised by node stratification with respect to time and space then the resulting ODEs are solved by the matrix equation-solving system. As Dymola and TRNSYS, Apros already includes the thermophysical properties of some fluids.

Any of these software engines offers an accurate and vast library of elements to dynamically model DHCSs. Nevertheless, Apros has been chosen for this research due to its higher fidelity of the mathematical solution (six-equation). Another advantage of Apros is that it uses a popular communication protocol called OPC (open platform communication) that may be linked to other platforms in real-time. Thus, data are exchanged to carry out co-simulation. This characteristic is critical when control strategies need to be implemented in other software like MATLAB. For instance, designed controllers can be build in MATLAB/Simulink, then the feedback measurement from Apros and output controller from MATLAB can be read and written, respectively. Figure 2.14 shows the data exchange process between MATLAB and Apros.



Figure 2.14: Communication between MATLAB and Apros.

2.8 Summary

The literature review for the work presented in this thesis was made. First, an overview of the DHCSs and their contribution to greenhouse gas emissions were presented. An in-depth review of the relevant solutions for this issue was done. Emphasis was placed on forecasting, flexibility and effective control strategies as their implementation does not require significant investments or system modifications. Then, the DHCS's operation is explained with a detailed description of its main components. The modelling challenge of the DHCS's hydraulic and

thermal behaviours is described. The difference between steady-state and dynamic models of DHCS's components and the advantages of dynamic modelling to develop effective control strategies for the operational improvement of DHCS were presented. Finally, a review of the dynamic simulation software available for the analysis of DHCSs was made.

2.9 References

- [1] M. A. Sayegh, J. Danielewicz, T. Nannou, M. Miniewicz, P. Jadwiszczak, K. Piekarska, and H. Jouhara, "Trends of European research and development in district heating technologies," *Renewable and Sustainable Energy Reviews*, vol. 68, pp. 1183–1192, Feb. 2017.
- [2] D. Connolly, H. Lund, B. V. Mathiesen, S. Werner, B. Möller, U. Persson, T. Boermans, D. Trier, P. A. Østergaard, and S. Nielsen, "Heat Roadmap Europe: Combining district heating with heat savings to decarbonise the EU energy system," *Energy Policy*, vol. 65, pp. 475–489, Feb. 2014.
- [3] K. Szabó, A. Mezősi, A. Tőroőcsik, *et al.*, "Renewable based district heating in europe - policy assessment of selected member states.," 2015. Fraunhofer ISI.
- [4] M. A. Sayegh, P. Jadwiszczak, B. P. Axcell, E. Niemierka, K. Bryś, and H. Jouhara, "Heat pump placement, connection and operational modes in European district heating," *Energy and Buildings*, vol. 166, pp. 122–144, May 2018.
- [5] Z. Wang, "Heat pumps with district heating for the UK's domestic heating: individual versus district level," *Energy Procedia*, vol. 149, pp. 354–362, Sept. 2018.
- [6] D. Connolly, "Heat Roadmap Europe: Quantitative comparison between the electricity, heating, and cooling sectors for different European countries," *Energy*, vol. 139, pp. 580–593, Nov. 2017.
- [7] DECC, "The future of heating: meeting the challenge.," 2013. Department of Energy & Climate Change.
- [8] ade, "Bringing energy together.," 2018. The Association for Decentralised Energy.
- [9] J. Chen, W. Zheng, Y. Kong, X. Yang, Z. Liu, and J. Xia, "Case study on combined heat and water system for nuclear district heating in Jiaodong Peninsula," *Energy*, vol. 218, p. 119546, Mar. 2021.
- [10] I. K. Iliev, A. K. Terziev, H. I. Beloev, I. Nikolaev, and A. G. Georgiev, "Comparative analysis of the energy efficiency of different types co-generators at large scales CHPs," *Energy*, vol. 221, p. 119755, Apr. 2021.
- [11] T. Kurek, A. Bielecki, K. Świrski, K. Wojdan, *et al.*, "Heat demand forecasting algorithm for a Warsaw district heating network," *Energy*, vol. 217, p. 119347, Feb. 2021.
- [12] World nuclear news, "Nuclear plants." <https://www.world-nuclear-news.org/>. Accessed: 2021-06-20.

- [13] U. Persson and S. Werner, “District heating in sequential energy supply,” *Applied Energy*, vol. 95, pp. 123–131, July 2012.
- [14] European Commission, “Communication from the commission to the european parliament, the council, the european economic and social committee and the committee of the regions- an eu strategy on heating and cooling.,” 2016. European Commission.
- [15] K. Kavvadias, J. Jimenez Navarro, A. Zucker, and S. Quoilin, “Case study on the impact of cogeneration and thermal storage on the flexibility of the power system,” Feb. 2018.
- [16] European Environment Agency, “Greenhouse gas emission statistics - emission inventories,” 2020.
- [17] Eurostat, “Greenhouse gas emission statistics - emission inventories.,” 2016. European Commission.
- [18] Euroheat & Power, “Guidelines for assessing the efficiency of district heating and district cooling systems.,” 2006. Ecoheatcoo, a Europe & Power Initiative.
- [19] V. M. Soltero, R. Chacartegui, C. Ortiz, and R. Velázquez, “Evaluation of the potential of natural gas district heating cogeneration in Spain as a tool for decarbonisation of the economy,” *Energy*, vol. 115, pp. 1513–1532, Nov. 2016.
- [20] U. Fahl and A. Dobbins, “Chapter 29 - District Heating in Europe: Opportunities for Energy Savings, Business, and Jobs,” in *Europe’s Energy Transition* (M. Welsch, S. Pye, D. Keles, A. Faure-Schuyer, A. Dobbins, A. Shivakumar, P. Deane, and M. Howells, eds.), pp. 249–259, Academic Press, Jan. 2017.
- [21] M.-A. Millar, N. M. Burnside, and Z. Yu, “District Heating Challenges for the UK,” *Energies*, vol. 12, p. 310, Jan. 2019. Number: 2 Publisher: Multidisciplinary Digital Publishing Institute.
- [22] A. Pfeifer, D. F. Dominković, B. Čosić, and N. Duić, “Economic feasibility of CHP facilities fueled by biomass from unused agriculture land: Case of Croatia,” *Energy Conversion and Management*, vol. 125, pp. 222–229, Oct. 2016.
- [23] M. Huculak, W. Jarczewski, and M. Dej, “Economic aspects of the use of deep geothermal heat in district heating in Poland,” *Renewable and Sustainable Energy Reviews*, vol. 49, pp. 29–40, Sept. 2015.
- [24] D. Buoro, P. Pinamonti, and M. Reini, “Optimization of a Distributed Cogeneration System with solar district heating,” *Applied Energy*, vol. 124, pp. 298–308, July 2014.
- [25] F. Sun, L. Fu, J. Sun, and S. Zhang, “A new waste heat district heating system with combined heat and power (CHP) based on ejector heat exchangers and absorption heat pumps,” *Energy*, vol. 69, pp. 516–524, May 2014.
- [26] R. Chacartegui, M. Carvalho, R. Abrahão, and J. Becerra, “Analysis of a CHP plant in a municipal solid waste landfill in the South of Spain,” *Applied Thermal Engineering*, vol. 91, pp. 706–717, Dec. 2015.

- [27] Y. Wang, S. Zhang, D. Chow, and J. M. Kuckelkorn, "Evaluation and optimization of district energy network performance: Present and future," *Renewable and Sustainable Energy Reviews*, vol. 139, p. 110577, Apr. 2021.
- [28] H. Lund, B. Möller, B. V. Mathiesen, and A. Dyrelund, "The role of district heating in future renewable energy systems," *Energy*, vol. 35, pp. 1381–1390, Mar. 2010.
- [29] H. Lund, S. Werner, R. Wiltshire, S. Svendsen, J. E. Thorsen, F. Hvelplund, and B. V. Mathiesen, "4th Generation District Heating (4GDH): Integrating smart thermal grids into future sustainable energy systems," *Energy*, vol. 68, pp. 1–11, Apr. 2014.
- [30] P. Manz, K. Kermeli, U. Persson, M. Neuwirth, *et al.*, "Decarbonizing District Heating in EU-27 + UK: How Much Excess Heat Is Available from Industrial Sites?," *Sustainability*, vol. 13, p. 1439, Jan. 2021. Number: 3 Publisher: Multidisciplinary Digital Publishing Institute.
- [31] S. Nielsen and B. Möller, "GIS based analysis of future district heating potential in Denmark," *Energy*, vol. 57, pp. 458–468, Aug. 2013.
- [32] H. Lund, P. A. Østergaard, M. Chang, S. Werner, S. Svendsen, *et al.*, "The status of 4th generation district heating: Research and results," *Energy*, vol. 164, pp. 147–159, Dec. 2018.
- [33] V. Eveloy and D. S. Ayou, "Sustainable District Cooling Systems: Status, Challenges, and Future Opportunities, with Emphasis on Cooling-Dominated Regions," *Energies*, vol. 12, p. 235, Jan. 2019. Number: 2 Publisher: Multidisciplinary Digital Publishing Institute.
- [34] T. Hong, S. C. Taylor-Lange, S. D'Oca, D. Yan, and S. P. Corgnati, "Advances in research and applications of energy-related occupant behavior in buildings," *Energy and Buildings*, vol. 116, pp. 694–702, Mar. 2016.
- [35] M. Pothitou, A. J. Kolios, L. Varga, and S. Gu, "A framework for targeting household energy savings through habitual behavioural change," *International Journal of Sustainable Energy*, vol. 35, pp. 686–700, Aug. 2016. Publisher: Taylor & Francis _eprint: <https://doi.org/10.1080/14786451.2014.936867>.
- [36] P. Zymelka and M. Szega, "Short-term scheduling of gas-fired CHP plant with thermal storage using optimization algorithm and forecasting models," *Energy Conversion and Management*, vol. 231, p. 113860, Mar. 2021.
- [37] Y. Liu, X. Hu, X. Luo, Y. Zhou, D. Wang, and S. Farah, "Identifying the most significant input parameters for predicting district heating load using an association rule algorithm," *Journal of Cleaner Production*, vol. 275, p. 122984, Dec. 2020.
- [38] Z. Zhang, Y. Liu, L. Cao, and H. Si, "A Forecasting Method of District Heat Load Based on Improved Wavelet Neural Network," *Journal of Energy Resources Technology*, vol. 142, May 2020.

- [39] A. R. Choudhury, “Demand Forecasting in DHC-network using machine learning models,” in *Proceedings of the Eighth International Conference on Future Energy Systems, e-Energy '17*, (New York, NY, USA), pp. 367–372, Association for Computing Machinery, May 2017.
- [40] A. Vandermeulen, B. van der Heijde, and L. Helsen, “Controlling district heating and cooling networks to unlock flexibility: A review,” *Energy*, vol. 151, pp. 103–115, May 2018.
- [41] Z. Ma, A. Knotzer, J. D. Billanes, and B. N. Jorgensen, “A literature review of energy flexibility in district heating with a survey of the stakeholders’ participation,” *Renewable and Sustainable Energy Reviews*, vol. 123, p. 109750, May 2020.
- [42] R. G. Junker, A. G. Azar, R. A. Lopes, *et al.*, “Characterizing the energy flexibility of buildings and districts,” *Applied Energy*, vol. 225, pp. 175–182, Sept. 2018.
- [43] K. M. Luc, A. Heller, and C. Rode, “Energy demand flexibility in buildings and district heating systems – a literature review,” *Advances in Building Energy Research*, vol. 13, pp. 241–263, July 2019. Publisher: Taylor & Francis _eprint: <https://doi.org/10.1080/17512549.2018.1488615>.
- [44] W. Gu, J. Wang, S. Lu, Z. Luo, and C. Wu, “Optimal operation for integrated energy system considering thermal inertia of district heating network and buildings,” *Applied Energy*, vol. 199, pp. 234–246, Aug. 2017.
- [45] J. Vivian, D. Quaggiotto, and A. Zarrella, “Increasing the energy flexibility of existing district heating networks through flow rate variations,” *Applied Energy*, vol. 275, p. 115411, Oct. 2020.
- [46] J. M. Jebamalai, K. Marlein, and J. Laverge, “Influence of centralized and distributed thermal energy storage on district heating network design,” *Energy*, vol. 202, p. 117689, July 2020.
- [47] L. A. Hurtado, J. D. Rhodes, P. H. Nguyen, I. G. Kamphuis, and M. E. Webber, “Quantifying demand flexibility based on structural thermal storage and comfort management of non-residential buildings: A comparison between hot and cold climate zones,” *Applied Energy*, vol. 195, pp. 1047–1054, June 2017.
- [48] K. Klein, S. Herkel, H.-M. Henning, and C. Felsmann, “Load shifting using the heating and cooling system of an office building: Quantitative potential evaluation for different flexibility and storage options,” *Applied Energy*, vol. 203, pp. 917–937, Oct. 2017.
- [49] S. Buffa, M. H. Fouladfar, G. Franchini, *et al.*, “Advanced Control and Fault Detection Strategies for District Heating and Cooling Systems—A Review,” *Applied Sciences*, vol. 11, p. 455, Jan. 2021. Number: 1 Publisher: Multidisciplinary Digital Publishing Institute.
- [50] W. Birk, K. T. Atta, and F. Udén, “Improving District Heating System Operation through Control Configuration Selection and Adaptive Control,” in *2019 18th European Control Conference (ECC)*, pp. 2944–2949, June 2019.

2.9. References

- [51] G. Lennermo, P. Lauenburg, and S. Werner, “Control of decentralised solar district heating,” *Solar Energy*, vol. 179, pp. 307–315, Feb. 2019.
- [52] S. Buffa, M. Soppelsa, A. and Pipiciello, G. Henze, and R. Fedrizzi, “Fifth-Generation District Heating and Cooling Substations: Demand Response with Artificial Neural Network-Based Model Predictive Control,” *Energies*, vol. 13, p. 4339, Jan. 2020. Number: 17 Publisher: Multidisciplinary Digital Publishing Institute.
- [53] B. Leitner, E. Widl, W. Gawlik, and R. Hofmann, “Control assessment in coupled local district heating and electrical distribution grids: Model predictive control of electric booster heaters,” *Energy*, vol. 210, p. 118540, Nov. 2020.
- [54] S. Frederiksen and S. Werner, *District Heating and Cooling*. Studentlitteratur AB, 2013. Google-Books-ID: vH5zngEACAAJ.
- [55] S. Werner, “District heating and cooling,” in *Reference Module in Earth Systems and Environmental Sciences*, Elsevier, Jan. 2013.
- [56] M. Pellegrini and A. Bianchini, “The Innovative Concept of Cold District Heating Networks: A Literature Review,” *Energies*, vol. 11, p. 236, Jan. 2018. Number: 1 Publisher: Multidisciplinary Digital Publishing Institute.
- [57] S. Werner, “International review of district heating and cooling,” *Energy*, vol. 137, pp. 617–631, Oct. 2017.
- [58] A. Lake, B. Rezaie, and S. Beyerlein, “Review of district heating and cooling systems for a sustainable future,” *Renewable and Sustainable Energy Reviews*, vol. 67, pp. 417–425, Jan. 2017.
- [59] M. Liu, Y. Shi, and F. Fang, “Combined cooling, heating and power systems: A survey,” *Renewable and Sustainable Energy Reviews*, vol. 35, pp. 1–22, July 2014.
- [60] G. Chardon, N. Le Pierrés, and J. Ramousse, “On the opportunity to integrate absorption heat pumps in substations of district energy networks,” *Thermal Science and Engineering Progress*, vol. 20, p. 100666, Dec. 2020.
- [61] E. Popovski, A. Aydemir, T. Fleiter, D. Bellstädt, R. Büchele, and J. Steinbach, “The role and costs of large-scale heat pumps in decarbonising existing district heating networks – A case study for the city of Herten in Germany,” *Energy*, vol. 180, pp. 918–933, Aug. 2019.
- [62] L. Ozgener, A. Hepbasli, and I. Dincer, “A key review on performance improvement aspects of geothermal district heating systems and applications,” *Renewable and Sustainable Energy Reviews*, vol. 11, pp. 1675–1697, Oct. 2007.
- [63] D. W. Wu and R. Z. Wang, “Combined cooling, heating and power: A review,” *Progress in Energy and Combustion Science*, vol. 32, pp. 459–495, Sept. 2006.
- [64] M. Duquesne, J. Toutain, A. Sempey, S. Ginestet, and E. Palomo del Barrio, “Modeling of a nonlinear thermochemical energy storage by adsorption on zeolites,” *Applied Thermal Engineering*, vol. 71, pp. 469–480, Oct. 2014.

- [65] H. Böhm and J. Lindorfer, “Techno-economic assessment of seasonal heat storage in district heating with thermochemical materials,” *Energy*, vol. 179, pp. 1246–1264, July 2019.
- [66] I. Dincer and M. A. Rosen, *Thermal Energy Storage: Systems and Applications*. Chichester, England: Wiley & Sons, 2nd ed., Nov. 2010.
- [67] L. F. Cabeza, *Advances in thermal energy storage systems: Methods and applications*. Chichester, England: Elsevier, Nov. 2014.
- [68] A. López-Navarro, J. Biosca-Taronger, B. Torregrosa-Jaime, J. M. Corberán, J. L. Bote-García, and J. Payá, “Experimental investigations on the influence of ice floating in an internal melt ice-on-coil tank,” *Energy and Buildings*, vol. 57, pp. 20–25, Feb. 2013.
- [69] Calmac, “CALMAC global leader in energy storage.”
- [70] T. Nuytten, B. Claessens, K. Paredis, J. Van Bael, and D. Six, “Flexibility of a combined heat and power system with thermal energy storage for district heating,” *Applied Energy*, vol. 104, pp. 583–591, Apr. 2013.
- [71] M. Economidou, B. Atanasiu, D. Staniaszek, J. Maio, *et al.*, “Europe’s buildings under the microscope BPIE - Buildings Performance Institute Europe.”
- [72] United Nations, “Department of Economic and Social Affairs.” Publisher: United Nations.
- [73] P. Pylysy, K. Lylykangas, and J. Kurnitski, “Buildings’ energy efficiency measures effect on CO2 emissions in combined heating, cooling and electricity production,” *Renewable and Sustainable Energy Reviews*, vol. 134, p. 110299, Dec. 2020.
- [74] M. Martin, A. Afshari, P. R. Armstrong, and L. K. Norford, “Estimation of urban temperature and humidity using a lumped parameter model coupled with an EnergyPlus model,” *Energy and Buildings*, vol. 96, pp. 221–235, June 2015.
- [75] A. Zarrella, E. Pratavia, P. Romano, L. Carnieletto, and J. Vivian, “Analysis and application of a lumped-capacitance model for urban building energy modelling,” *Sustainable Cities and Society*, vol. 63, p. 102450, Dec. 2020.
- [76] N. Aoun, R. Baviere, M. Vallée, A. Aourousseau, and G. Sandou, “Modelling and flexible predictive control of buildings space-heating demand in district heating systems,” *Energy*, vol. 188, p. 116042, Dec. 2019.
- [77] K. Ogata, *System Dynamics*. Upper Saddle River, NJ: Wiley & Sons, 4th ed., 2003.
- [78] F. P. Incropera, D. P. Dewitt, T. L. Bergman, and A. S. Lavine, *Principles of Heat and Mass Transfer*. New York: Wiley & Sons, 7th ed., 2013.
- [79] M. Geidl and G. Andersson, “Optimal Power Flow of Multiple Energy Carriers,” *IEEE Transactions on Power Systems*, vol. 22, pp. 145–155, Feb. 2007. Conference Name: IEEE Transactions on Power Systems.

2.9. References

- [80] Z. Li, W. Wu, M. Shahidehpour, J. Wang, and B. Zhang, “Combined Heat and Power Dispatch Considering Pipeline Energy Storage of District Heating Network,” *IEEE Transactions on Sustainable Energy*, vol. 7, pp. 12–22, Jan. 2016. Conference Name: IEEE Transactions on Sustainable Energy.
- [81] R. Li, L. Chen, B. Zhao, W. Wei, F. Liu, X. Xue, *et al.*, “Economic Dispatch of an Integrated Heat-Power Energy Distribution System with a Concentrating Solar Power Energy Hub,” *Journal of Energy Engineering*, vol. 143, p. 04017046, Oct. 2017. Publisher: American Society of Civil Engineers.
- [82] Y. Wang, K. Hou, H. Jia, Y. Mu, L. Zhu, *et al.*, “Decoupled Optimization of Integrated Energy System Considering CHP Plant Based on Energy Hub Model,” *Energy Procedia*, vol. 142, pp. 2683–2688, Dec. 2017.
- [83] T. Laajalehto, M. Kuosa, T. Mäkilä, M. Lampinen, and R. Lahdelma, “Energy efficiency improvements utilising mass flow control and a ring topology in a district heating network,” *Applied Thermal Engineering*, vol. 69, pp. 86–95, Aug. 2014.
- [84] Y. Wang, S. You, H. Zhang, X. Zheng, W. Zheng, Q. Miao, and G. Lu, “Thermal transient prediction of district heating pipeline: Optimal selection of the time and spatial steps for fast and accurate calculation,” *Applied Energy*, vol. 206, pp. 900–910, Nov. 2017.
- [85] X. Qin, H. Sun, X. Shen, Y. Guo, Q. Guo, and T. Xia, “A generalized quasi-dynamic model for electric-heat coupling integrated energy system with distributed energy resources,” *Applied Energy*, vol. 251, p. 113270, Oct. 2019.
- [86] B. van der Heijde, M. Fuchs, C. Ribas Tugores, G. Schweiger, K. Sartor, D. Basciotti, D. Müller, C. Nytsch-Geusen, M. Wetter, and L. Helsen, “Dynamic equation-based thermo-hydraulic pipe model for district heating and cooling systems,” *Energy Conversion and Management*, vol. 151, pp. 158–169, Nov. 2017.
- [87] S. Ateş, “Hydraulic modelling of closed pipes in loop equations of water distribution networks,” *Applied Mathematical Modelling*, vol. 40, pp. 966–983, Jan. 2016.
- [88] I. Ben Hassine and U. Eicker, “Impact of load structure variation and solar thermal energy integration on an existing district heating network,” *Applied Thermal Engineering*, vol. 50, pp. 1437–1446, Feb. 2013.
- [89] Y.-F. Wang and Q. Chen, “A direct optimal control strategy of variable speed pumps in heat exchanger networks and experimental validations,” *Energy*, vol. 85, pp. 609–619, June 2015.
- [90] H. Wang, H. Wang, Z. Haijian, and T. Zhu, “Optimization modeling for smart operation of multi-source district heating with distributed variable-speed pumps,” *Energy*, vol. 138, pp. 1247–1262, Nov. 2017.
- [91] A. Fabre, R. Thomas, B. Duplessis, C.-T. Tran, and P. Stabat, “Dynamic modeling for evaluation of triple-pipe configuration potential in geothermal district heating networks,” *Energy Conversion and Management*, vol. 173, pp. 461–469, Oct. 2018.

- [92] A. Michel and A. Kugi, “Accurate low-order dynamic model of a compact plate heat exchanger,” *International Journal of Heat and Mass Transfer*, vol. 61, pp. 323–331, June 2013.
- [93] A. A. Dehghan and A. Barzegar, “Thermal performance behavior of a domestic hot water solar storage tank during consumption operation,” *Energy Conversion and Management*, vol. 52, pp. 468–476, Jan. 2011.
- [94] A. Menapace, W. Boscheri, M. Baratieri, and M. Righetti, “An efficient numerical scheme for the thermo-hydraulic simulations of thermal grids,” *International Journal of Heat and Mass Transfer*, vol. 161, p. 120304, Nov. 2020.
- [95] D. L. Savicki, H. A. Vielmo, and A. Krenzinger, “Three-dimensional analysis and investigation of the thermal and hydrodynamic behaviors of cylindrical storage tanks,” *Renewable Energy*, vol. 36, pp. 1364–1373, May 2011.
- [96] D. Taler, P. Dzierwa, M. Trojan, J. Sacharczuk, K. Kaczmarski, and J. Taler, “Mathematical modeling of heat storage unit for air heating of the building,” *Renewable Energy*, vol. 141, pp. 988–1004, Oct. 2019.
- [97] D. Taler, P. Dzierwa, M. Trojan, J. Sacharczuk, K. Kaczmarski, and J. Taler, “Numerical modeling of transient heat transfer in heat storage unit with channel structure,” *Applied Thermal Engineering*, vol. 149, pp. 841–853, Feb. 2019.
- [98] B. Akhmetov, M. E. Navarro, A. Seitov, A. Kaltayev, Z. Bakenov, and Y. Ding, “Numerical study of integrated latent heat thermal energy storage devices using nanoparticle-enhanced phase change materials,” *Solar Energy*, vol. 194, pp. 724–741, Dec. 2019.
- [99] T. Barz, C. Zauner, D. Lager, D. C. López Cárdenas, F. Hengstberger, M. N. Cruz Bournazou, and K. Marx, “Experimental Analysis and Numerical Modeling of a Shell and Tube Heat Storage Unit with Phase Change Materials,” *Industrial & Engineering Chemistry Research*, vol. 55, pp. 8154–8164, July 2016. Publisher: American Chemical Society.
- [100] J. Dostal and V. Havlena, “Convection oriented heat exchanger model,” in *2016 12th IEEE International Conference on Control and Automation (ICCA)*, pp. 347–352, June 2016.
- [101] S. Heo, S. S. Jogwar, and P. Daoutidis, “Dynamics and control of high duty counter-current heat exchangers,” in *2011 19th Mediterranean Conference on Control Automation (MED)*, pp. 1034–1039, June 2011.
- [102] L. Hao, F. Xu, Q. Chen, M. Wei, L. Chen, and Y. Min, “A thermal-electrical analogy transient model of district heating pipelines for integrated analysis of thermal and power systems,” *Applied Thermal Engineering*, vol. 139, pp. 213–221, July 2018.
- [103] T. Gao, B. Sammakia, and J. Geer, “Dynamic response and control analysis of cross flow heat exchangers under variable temperature and flow rate conditions,” *International Journal of Heat and Mass Transfer*, vol. 81, pp. 542–553, Feb. 2015.

2.9. References

- [104] A. Korzeń and D. Taler, “Modeling of transient response of a plate fin and tube heat exchanger,” *International Journal of Thermal Sciences*, vol. 92, pp. 188–198, June 2015.
- [105] Z. Pan, Q. Guo, and H. Sun, “Interactions of district electricity and heating systems considering time-scale characteristics based on quasi-steady multi-energy flow,” *Applied Energy*, vol. 167, pp. 230–243, Apr. 2016.
- [106] K. M. Powell and T. F. Edgar, “An adaptive-grid model for dynamic simulation of thermocline thermal energy storage systems,” *Energy Conversion and Management*, vol. 76, pp. 865–873, Dec. 2013.
- [107] A. L. Nash, A. Badithela, and N. Jain, “Dynamic modeling of a sensible thermal energy storage tank with an immersed coil heat exchanger under three operation modes,” *Applied Energy*, vol. 195, pp. 877–889, June 2017.
- [108] J. Lago, F. De Ridder, W. Mazairac, and B. De Schutter, “A 1-dimensional continuous and smooth model for thermally stratified storage tanks including mixing and buoyancy,” *Applied Energy*, vol. 248, pp. 640–655, Aug. 2019.
- [109] K.-L. He, Q. Chen, Y.-T. Liu, J.-H. Hao, Y.-F. Wang, and Y. Yuan, “A transient heat current model for dynamic performance analysis and optimal control of heat transfer system,” *International Journal of Heat and Mass Transfer*, vol. 145, p. 118767, Dec. 2019.
- [110] Y. Wang, S. You, W. Zheng, H. Zhang, X. Zheng, and Q. Miao, “State space model and robust control of plate heat exchanger for dynamic performance improvement,” *Applied Thermal Engineering*, vol. 128, pp. 1588–1604, Jan. 2018.
- [111] S. K. Al-Dawery, A. M. Alrahawi, and K. M. Al-Zobai, “Dynamic modeling and control of plate heat exchanger,” *International Journal of Heat and Mass Transfer*, vol. 55, pp. 6873–6880, Nov. 2012.
- [112] K. M. Powell and T. F. Edgar, “Modeling and control of a solar thermal power plant with thermal energy storage,” *Chemical Engineering Science*, vol. 71, pp. 138–145, Mar. 2012.
- [113] X. Li, Z. Wang, E. Xu, L. Ma, L. Xu, and D. Zhao, “Dynamically Coupled Operation of Two-Tank Indirect TES and Steam Generation System,” *Energies*, vol. 12, p. 1720, Jan. 2019. Number: 9 Publisher: Multidisciplinary Digital Publishing Institute.
- [114] A. Mawire and M. McPherson, “Experimental characterisation of a thermal energy storage system using temperature and power controlled charging,” *Renewable Energy*, vol. 33, pp. 682–693, Apr. 2008.
- [115] S. L. Prescott and B. Ulanicki, “Improved Control of Pressure Reducing Valves in Water Distribution Networks,” *Journal of Hydraulic Engineering*, vol. 134, pp. 56–65, Jan. 2008. Publisher: American Society of Civil Engineers.
- [116] P. R. Page, A. M. Abu-Mahfouz, and S. Yoyo, “Real-time Adjustment of Pressure to Demand in Water Distribution Systems: Parameter-less P-controller Algorithm,” *Procedia Engineering*, vol. 154, pp. 391–397, Jan. 2016.

- [117] T. C. Mosetlhe, Y. Hamam, S. Du, and E. Monacelli, “A Survey of Pressure Control Approaches in Water Supply Systems,” *Water*, vol. 12, p. 1732, June 2020. Number: 6 Publisher: Multidisciplinary Digital Publishing Institute.
- [118] Y. Li, Y. Rezgui, and H. Zhu, “Dynamic simulation of heat losses in a district heating system: A case study in Wales,” in *2016 IEEE Smart Energy Grid Engineering (SEGE)*, pp. 273–277, Aug. 2016.
- [119] A. Dahash, S. Mieck, F. Ochs, and H. J. Krautz, “A comparative study of two simulation tools for the technical feasibility in terms of modeling district heating systems: An optimization case study,” *Simulation Modelling Practice and Theory*, vol. 91, pp. 48–68, Feb. 2019.
- [120] H. Li and N. Nord, “Operation strategies to achieve low supply and return temperature in district heating system,” *E3S Web of Conferences*, vol. 111, p. 05022, 2019. Publisher: EDP Sciences.
- [121] H. Braas, U. Jordan, I. Best, J. Orozaliev, and K. Vajen, “District heating load profiles for domestic hot water preparation with realistic simultaneity using DHWcalc and TRNSYS,” *Energy*, vol. 201, p. 117552, June 2020.

Hydraulic and thermal dynamic modelling approaches for district heating and cooling systems

3.1 Introduction

The most common approach used to analyse DHCSs is through steady or quasi-steady models. Nevertheless, the transient responses during the change of operating conditions are neglected. Moreover, some analyses only include the energy dispatch process based on percentages without considering the generation, supply and consumption energy processes in detail. These approaches are not enough if a DHCS needs to be analysed in detail, including the fundamental variables involved in its operation: temperature, pressure and mass flow rate.

This chapter presents the modelling approaches developed for the study of the operation of a DHCS. The DHCS's behaviour is described by considering its two interrelated dynamics: thermal and hydraulic. Since models capable of including all variables necessary to capture both dynamics are essential for accurate analyses, for this purpose physics principles are used to establish ODEs to obtain a high-fidelity description of the phenomena presented in the DHCS's dynamics. Energy balance, heat transfer and linear momentum concepts are employed to develop the modelling framework for thermal and hydraulic dynamic models. Some assumptions were made on the fluids used to transfer energy within DHCSs. For simplicity, their potential and kinetic energy are neglected. Moreover, the fluids are considered incompressible and their motion frictionless to conduct energy balance. The developed modelling frameworks enable simplicity since they are based on a 1-D modelling approach. Additionally, suitability for the control design process is obtained.

3.2 Thermal dynamic modelling

The aim of modelling the thermal dynamics of a system is to obtain a mathematical description of its temperature change due to energy transfer. The main concept used for this objective is the energy conservation law. Heat transfer theory is also employed to describe in detail the conduction and convection heat transfer phenomena presented in the DHCS's thermal behaviour.

As defined in Chapter 2, if a temperature difference is presented in a system, heat transfer occurs. Although heat or cold are forms of energy flux and their quantification is critical for energy systems analysis, the use of temperature allows to know in detail the thermal dynamic behaviour of energy systems. Besides, it provides an accurate computation of the total system energy, which will be explained in this chapter.

To outline the modelling approach developed in this Section, Figure 3.1 shows the steps to obtain the thermal dynamic models. This framework can be implemented in different systems where their internal structure and the matter or fluids involved in the heat transfer are well known.

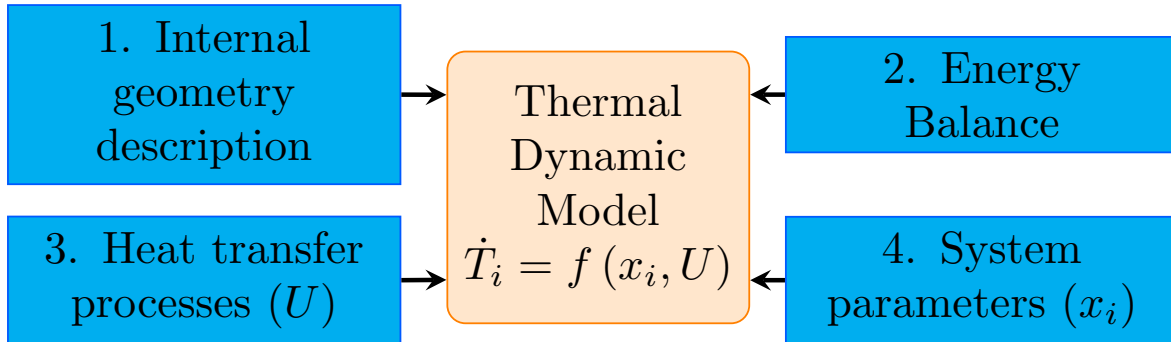


Figure 3.1: Framework of the thermal dynamic modelling approach.

The first step is the basis of heat transfer analysis. The internal geometry description means knowing how the energy is introduced to the system. Here, it is important to notice that for DHCS's components, the transportation of energy is done by a fluid. It may be water for heating or refrigerant for cooling. Therefore, the internal structure description is necessary to know the shape and dimensions of the channel by which the fluid is crossing the system to define how the energy is transferred, transported or stored. The next step is to apply an energy balance where internal and external energy sources should be included. Then, the transferred energy is described mathematically through an overall coefficient. Finally, the system parameters (*e.g.*, the dimensions of channels and thermophysical properties) are fed up to the model.

3.2.1 Energy balance

General form of conservation law

The energy transferred in a thermal system is described by the energy conservation law, which is derived from the general form of the conservation law. The general conservation law analyses the evolution over time of a measurable system property when a system undergoes some process. The general form of the conservation law establishes the foundations to describe how a system variable changes under different conditions. Not all physical variables obey a conservation law. From the fluid mechanics theory, the dynamic of a fluid can be described by applying the conservation law for three fundamental physical quantities:

- Energy.
- Momentum.
- Mass.

3.2. Thermal dynamic modelling

Figure 3.2 illustrates the conservation law statement: "The variation of the total amount of a quantity \mathbf{U} inside a given domain is equal to the balance between the amount of the quantity entering and leaving the considered domain, plus the contributions from eventual sources generating that quantity" [1], where an arbitrary volume Ω called *control volume* is bounded by a closed surface S .

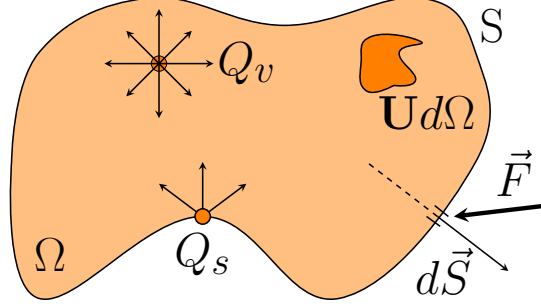


Figure 3.2: General form of conservation law in a control volume.

The amount of \mathbf{U} is affected by the contributions coming from the surroundings of Ω . The term *flux* is used in thermodynamic and fluid mechanics to name the amount of \mathbf{U} crossing the unit of surface S per unit of time. The flux variations are dependent on time and space. Therefore, a flux variation has a direction and a magnitude and is expressed as a vector: \vec{F} . The contribution of this flux to the variation of \mathbf{U} within Ω is defined mathematically by the scalar product of the flux and the unit of surface as [1]

$$F_n dS = \vec{F} \cdot d\vec{S}. \quad (3.1)$$

The total contribution of external fluxes is defined by considering the whole surface of the control volume, and is given by the general form of the conservation law for the quantity \mathbf{U} as

$$\frac{\partial \mathbf{U}}{\partial t} = -\vec{\nabla} \cdot \vec{F} + Q_V + \vec{\nabla} \cdot \vec{Q}_S, \quad (3.2)$$

where $\vec{\nabla}$ is the gradient operator, which implies differentiation in the three-dimensional space of the flux F . The Q_V and Q_S are related to sources located inside the volume and the surface of the control volume, respectively.

Flux F may be generated in two ways: fluid in movement or molecular agitation. The first one is called convective flux and is associated with the fluid velocity (v), which describes its movement. It quantifies the amount of \mathbf{U} that is injected into or carried away from Ω and is defined by

$$\vec{F}_C = \mathbf{U}\vec{v}. \quad (3.3)$$

The second one is called diffusive flux and is provoked by the macroscopic effect of a material's molecular motion. It is associated with the movement of these molecules toward different directions. Therefore, a gradient is necessary to describe its behaviour through the three-dimensional space as

$$\vec{F}_D = -\kappa \vec{\nabla} \mathbf{U}, \quad (3.4)$$

where κ is the diffusivity coefficient, which depends on the material properties. Replacing

equations (3.3) and (3.4) into (3.2) leads to

$$\frac{\partial \rho \mathbf{U}}{\partial t} = -\vec{\nabla} \cdot (\vec{F}_C + \vec{F}_D) + Q_V + \vec{\nabla} \cdot Q_S. \quad (3.5)$$

The presented description of the conservation law allows understanding how a system's quantified variable is analysed. Its variation through time is captured applying the law, which requires a well-defined control volume and knowledge of its surroundings (fluxes and sources). Thus, the sources and fluxes should be described mathematically to obtain a model capable of describing a system's thermal behaviour. This way, the energy is defined as the quantified physical variable.

Energy conservation equation

The thermal behaviour of a system can be described by applying the general conservation law for energy. For the sake of clarity, it is important to establish the *internal energy* and *heat* concepts. A clear understanding of these terms will avoid any confusion of its use throughout this work. Recall that

- *Heat* is defined as "the form of energy that is transferred between two systems (or a system and its surroundings) by virtue of a *temperature* difference" [2].

Therefore, the use of the term *Heat* (Q) is limited to when the energy is flowing. In the field of thermodynamics, this physical phenomenon is called *heat transfer* and its units are J/s. Conversely, the total energy E of a system is defined by three parameters; its *kinetic energy*, associated with the motion of the system, its *potential energy*, associated with the position of the system, and the rest of contributions usually encompassed in its total *internal energy*. This last term may include thermal, chemical or nuclear energy. A more specific definition of internal energy includes the terms; sensible energy, which describes the molecules' motion comprising the mass within the control volume, and latent energy, which is related to intermolecular forces provoked by phase change of the matter.

For the purposes of this work, the internal energy considered in the analysis is referred only to sensible and latent components, (*i.e.*, internal *thermal energy*), and is defined by the enthalpy per unit of mass, with units [J/kg], as

$$h_m = e + p\nu, \quad (3.6)$$

where p [Pa] is the pressure and ν [m³/kg] is the specific volume of the fluid. The term $p\nu$ is related to the pressure energy [3]. An alternative expression for enthalpy uses the inverse variable of ν , which is the matter density ρ [kg/m³], and is defined by

$$h_m = e + \frac{p}{\rho}. \quad (3.7)$$

The pressure energy term is also known as flow work. It includes the contribution of the pressure forces acting over the fluid motion [4]. Thermodynamically, h_m is defined by pressure and temperature as $h_m(p, T)$. Nevertheless, a common practice to reduce complexity is to approximate the fluid as an ideal gas and consider it as incompressible liquid. Therefore, its specific heat at constant pressure c_p [J/kgK] and volume c_V are equal, and the flow work term

3.2. Thermal dynamic modelling

is neglected since significant changes in pressure are not presented in components of DHCSs. Thus, the internal thermal energy per unit of mass can be defined in terms of temperature only as [1, 4]

$$e(T) = c_p(T) \Delta T, \quad (3.8)$$

where ΔT is the change of temperature caused by the variation of the thermal energy. To quantify the total internal energy for a specific amount of mass contained in a control volume, equation (3.8) can be expressed as

$$E_{st} = \rho V c_p \Delta T, \quad (3.9)$$

where st subscript means stored energy and V [m³] is the total volume of the medium.

Now that the terminology has been defined, it is necessary to explain the relation of thermodynamics with the energy conservation law. The first law of thermodynamic establishes that:

- "The increase in the amount of energy stored in a control volume must be equal the amount of energy that enters the control volume, minus the amount of energy that leaves the control volume" [4].

which basically is the same statement of the general form of conservation law and can be expressed mathematically as

$$\frac{dE_{st}}{dt} = \dot{E}_{in} - \dot{E}_{out} \quad (3.10)$$

where the energy stored (E_{st}) in the control volume is expressed as a rate basis, the input (E_{in}) and the output energy (E_{out}) are described as a time rate of change with a dot above them. As it can be observed, (3.10) is a simplification of (3.2), where it depends on the direction of the fluxes, and the sources contributions are included in the input and output energy terms of the equation (see Figure 3.3).

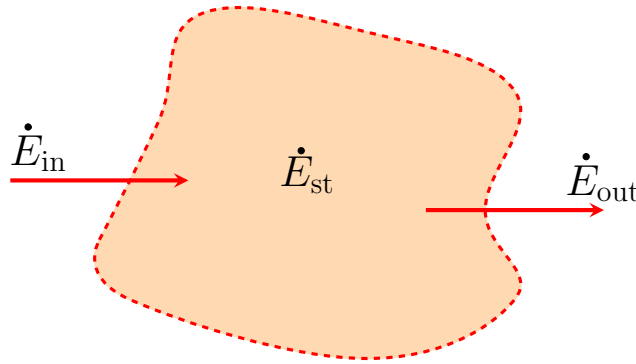


Figure 3.3: Conservation of energy within a control volume.

Convection and diffusion fluxes quantities in (3.5) should be defined in terms of the total energy. The formal definition of these terms is done using the energy per unit of volume (ρE) and considering its kinetic and potential energy, which is defined by

$$E = e + \frac{\vec{v}^2}{2} + gz, \quad (3.11)$$

where g [m/s²] is the gravitational constant and z [m] its vertical position. Thus, using (3.3)

for the quantity ρE , the convective flux of energy is defined by

$$\vec{F}_C = \rho E \vec{v} = \rho \vec{v} \left(e + \frac{\vec{v}^2}{2} + gz \right). \quad (3.12)$$

For diffusive flux, there is no motion. Therefore, kinetic and potential energy are not considered. Thus, diffusive flux is defined considering (3.4) as

$$\vec{F}_D = -\rho \kappa \nabla e, \quad (3.13)$$

Then (3.5) becomes

$$\frac{\partial \rho e}{\partial t} = \vec{\nabla} \cdot \left(-\rho \vec{v} E + \kappa \rho \vec{\nabla} e \right) + Q_V + \vec{\nabla} \cdot \vec{Q}_S. \quad (3.14)$$

1-D analysis

In practice, sensors commonly located within a DHCS measure the temperature, pressure and mass flow rate in a specific location. No spatial variations are considered and these measurements are enough to have an accurate value of the physical variable. A 1-D approach where only one coordinate is considered to model the thermal behaviour of components of DHCS can reproduce the same condition of an actual sensor. This modelling approach reduces the complexity of the dynamic analysis without loss of accuracy. The term 1-D implies that the temperature variations and fluid velocities occur through a single coordinate and then the energy fluxes have only one direction.

Mathematical operator $\vec{\nabla}$ presented in (3.14) defines the energy contribution of the fluxes to each spatial coordinate as

$$\vec{\nabla} = \left(\mathbf{i} \frac{\partial}{\partial x} + \mathbf{j} \frac{\partial}{\partial y} + \mathbf{k} \frac{\partial}{\partial z} \right). \quad (3.15)$$

Let Q be the energy flow provided by any flux and its contribution to each coordinate defined as Q_x , Q_y and Q_z . Figure 3.4(a) illustrates this energy flux in a defined differential control volume. The contribution of Q over coordinate x is defined by

$$\frac{\partial Q}{\partial x} = Q_x - Q_{x-dx}. \quad (3.16)$$

Therefore, restricting the energy balance to a single dimension, for instance in the x direction, and considering only thermal energy and neither flow work, kinetic nor potential energies, equation (3.14) is reduced to

$$\frac{d\rho e}{dt} = -\rho v_x \frac{de}{dx} + \kappa \rho \frac{d}{dx} \left(\frac{de}{dx} \right) + Q_V + \frac{de}{dx} Q_S. \quad (3.17)$$

For illustrative purposes of the application of energy balance, a simple control volume with a surface energy input (inflow and outflow of a fluid) is shown in Figure 3.5. A fluid with a constant velocity (v) is flowing into the control volume with a temperature of $T_{f,\text{in}}$ and is leaving it with a temperature of $T_{f,\text{out}}$. The average velocity is considered in one direction and input and output temperatures are punctually measured.

3.2. Thermal dynamic modelling

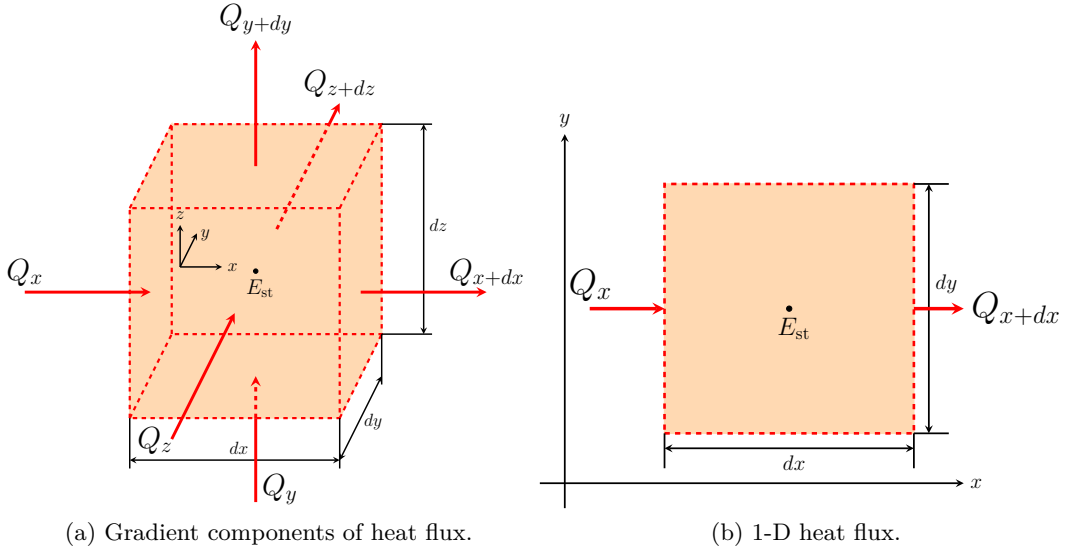


Figure 3.4: Control volume reduction from three to 1-D analysis.

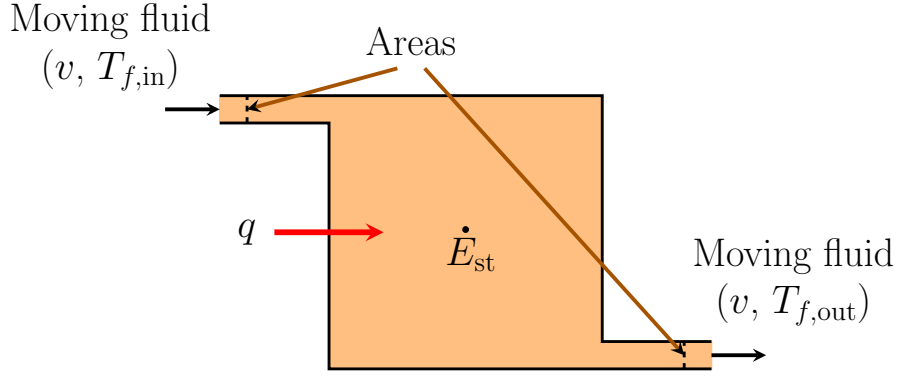


Figure 3.5: Convective flux contribution to internal energy of a control volume.

To apply the energy balance equations is necessary to obtain the integral of the area and the volume to eliminate operator ∇ as:

$$\int_S dS = A. \quad (3.18)$$

where A [m^2] is the orifice area through which the fluid flows to the volume, and

$$\int_{\Omega} d\Omega = V. \quad (3.19)$$

Thus, the energy balance of the system without internal sources of energy is defined by

$$\frac{dE_{st}}{dt} = A\rho v c_p \Delta T = \dot{m} c_p (T_{f,out} - T_{f,in}), \quad (3.20)$$

where the mass flow rate of the fluid is defined by $\dot{m} = A\rho v$ [kg/s]. Finally, the energy contribution given by the fluid is defined as:

$$\rho V c_p \frac{dT}{dt} = \dot{m} c_p (T_{f,out} - T_{f,in}). \quad (3.21)$$

3.2.2 Heat transfer: conduction and convection

Energy balance allows describing the variation of a system's internal energy bounded by a surface, knowing the fluxes' characteristics and external sources (surroundings). Nevertheless, it is necessary to have a mathematical description of the physical phenomena occurring in this energy exchanged. For this purpose heat transfer theory is employed.

There are three different heat transfer types when a difference of temperature exists: convection, conduction and thermal radiation [4]. This research is focused only on the first two heat transfer modes. Since radiation is a weak energy flux for the analysis presented in this work, it is neglected. In this section, the mathematical equations required to quantify the heat transferred are presented.

Convection

In the convection heat transfer, the flow of energy is given by the interaction between a solid surface and a moving fluid. Figure 3.6 shows this interaction, where the surface and the fluid are defined by the temperature between them. The fluid description also includes its velocity. This implies molecular motion (diffusion) and bulk fluid motion (advection). Figure 3.7 shows the boundary layer development due to the velocity and the temperature profile of the fluid.

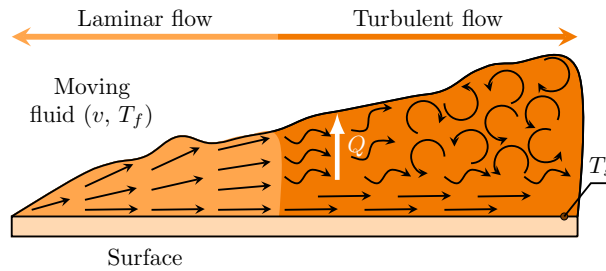


Figure 3.6: Convection from a surface to a moving fluid

Hydraulic phenomena, such as shear stress, affect the fluid's velocity through the perpendicular distance of the surface of the plane (see Figure 3.7). Thus, the contribution of the diffusion mechanism is limited to the region near the surface where the velocity is zero (micro scale effects of particles colliding are neglected). On the other hand, the heat transfer due to the bulk fluid motion starts when there is a fluid movement. Convection heat transfer contributions are quantified using Newton's law of cooling [4], which is defined by

$$Q = \int_S U_{cv} (T_s - T_\infty), \quad (3.22)$$

where U_{cv} is named *convection heat transfer coefficient* and its units are $[\text{W}/\text{m}^2\text{K}]$. This coefficient is computed based on the boundary layer conditions (velocity magnitude of the fluid) which, in turn, are affected by the nature of the fluid motion (laminar or turbulent), surface geometry and the fluid's thermophysical properties.

It is important to point out that the analysis developed in this work is mainly focused to internal flows. This means that a defined surface, such as the area of a circular pipe or an irregular geometry channel, confines the fluid. This condition defines the computation of U_{cv} to specific channel forms presented in DHCS's components such as heat exchangers or pipe networks. This way, the boundary layers have particular profiles given by the conditions of

3.2. Thermal dynamic modelling

channel's internal fluid. Let the fluid be enclosed in a circular pipe. Figure 3.8.(a) and 3.8.(b) show the hydraulic and the thermal boundary layers presented inside the pipe. The hydraulic conditions modify the velocity of the fluid through the radius of the pipe and the temperature profile of the fluid.

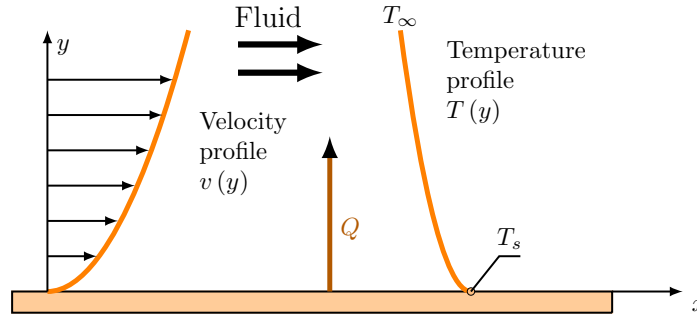


Figure 3.7: Boundary layer development in convection heat transfer.

The computation of U_{cv} enables defining the hydraulic conditions of the flow that provoke the convection heat transfer process. Within the fluid conditions, three different regions are defined. The closest one to the surface area is denominated viscous surface. Here, the heat transfer is given mainly by diffusion and the velocity profile may be considered as linear. The next region is called the buffer layer, where diffusion and turbulent conditions are presented simultaneously. Finally, in the turbulent zone, the heat transfer is provoked by turbulent mixing of the fluid.

Laminar and turbulent fluid present different behaviours. Laminar fluid has a highly ordered flow where streamlines can be identified. On the other hand, turbulent fluid has random particle motions, modifying the fluid's velocity profile and making it difficult to determine the fluid's speed with respect to the surface distance, unlike laminar fluid conditions. Therefore, it is important to use a defined criteria to establish whether the heat transfer is given by the fluid's laminar or turbulent conditions. A dimensionless parameter is used in fluid mechanics to define the fluid conditions based on its direction and its thermophysical properties. This is the Reynolds number, which represents the ratio of the inertia to viscous force [4], and is defined by

$$\text{Re}_x = \frac{\rho v x}{\mu} \quad (3.23)$$

where x [m] is the length of the channel and μ is the viscosity of the fluid [Ns/m^2]. Thus, a small Reynolds number means the inertial forces are so small in comparison to viscous forces that no disturbances are present and the flow remains laminar. Conversely, a large Reynolds number indicates that inertial forces increase the disturbances and a turbulent flow is present. Equation (3.29) can be used for a circular pipe (see Figure 3.8) as:

$$\text{Re} = \frac{\rho v_m D}{\mu} = \frac{v_m D}{\nu} \quad (3.24)$$

where v_m [m/s] is the mean velocity of the fluid, D [m] is the internal hydraulic diameter of the pipe and ν [m^2/s] is the kinematic viscosity. The value of D is defined according to the shape of the channel.

For hydraulic and thermal analysis, knowing whether the fluid is turbulent or laminar is not sufficient. Two more conditions are presented in internal flows: entrance and fully

developed regions. The conditions that generate disturbances capable of modifying the flow conditions are related to fluid movement. As the Reynolds number is defined, these conditions evolve according to the location of the fluid. Thus, at the channel entrance, the viscous effects given by the contact of the fluid with the channel surface start to increase as the fluids flow through the length of the channel. Then the boundary layer is created and there is a specific region called the hydrodynamic entrance region. Once the velocity profile has been affected through the length of the cross-sectional area of the channel, it will not present more changes (see Figure 3.8a). Similarly, the fluid temperature presents a thermal entrance region during the convection heat transfer, as Figure 3.8b shows.

Computation of the velocity and temperature profile of the fluid during the entrance regions requires a detailed analysis. Usually, this issue is addressed by using the mean velocity of the fluid. It simplifies heat transfer analysis and considers the average fluid velocity without compromising accuracy [4]. Such an assumption is justified in this work due to the length of the entrance regions, usually about ten times the channel's diameter, which for DHCS's elements is insignificant. Although laminar fluid may facilitate the computation of the velocity profile due to its high ordered streamlines, and parabolic profile for the fully developed region for circular tubes (see. Figure 3.8.a), only fully developed regions are considered in this work. Thus, a flatter velocity profile is considered through the system's whole length analysed in this work (see Figure 3.8.(c)). A general equation to compute the mean velocity can be used for laminar and turbulent flows as

$$v_m = \frac{\dot{m}}{\rho A_c} \quad (3.25)$$

where A_c [m²] is the cross-sectional area of the channel. For mean velocity computation, it is assumed that small variations through the radial position ($T(r)$) are negligible.

The use of mean velocity values simplifies not only the hydraulic profile of the fluid, but also its thermal conditions. This velocity average is also considered for thermal behaviour. Thus, the temperature is just affected by the axial movement of the fluid. This assumption is in agreement with a 1-D modelling approach.

Finally, considering the fluid conditions (either laminar or turbulent), the fluid's thermo-physical properties (*e.g.*, thermal conductivity k , specific heat c_p , dynamic viscosity μ and density ρ), and the channel's geometry, a dimensionless parameter is established by heat transfer theory, called Nusselt number [4]. This number provides the amount of the convection heat transfer occurring at the surface of the channel and is defined by

$$\text{Nu} = f(\text{Re}, \text{Pr}) = \frac{U_{cv}L}{k_f} \quad (3.26)$$

where L [m] is the length where the coefficient is calculated, k_f [W/mK] is the thermal conductivity of the fluid and Pr is the Prandtl number, which is the ratio of momentum diffusivity to thermal diffusivity of a fluid and is dimensionless [4].

The calculation of the Nusselt number for circular channels such as pipes is defined for each type of flow. For laminar flow, assuming an incompressible fluid within the fully developed region in a circular pipe, the Nusselt number is constant and is given by [4]

$$\text{Nu} = \frac{U_{cv}D}{k_f} = 4.36 \quad (3.27)$$

3.2. Thermal dynamic modelling

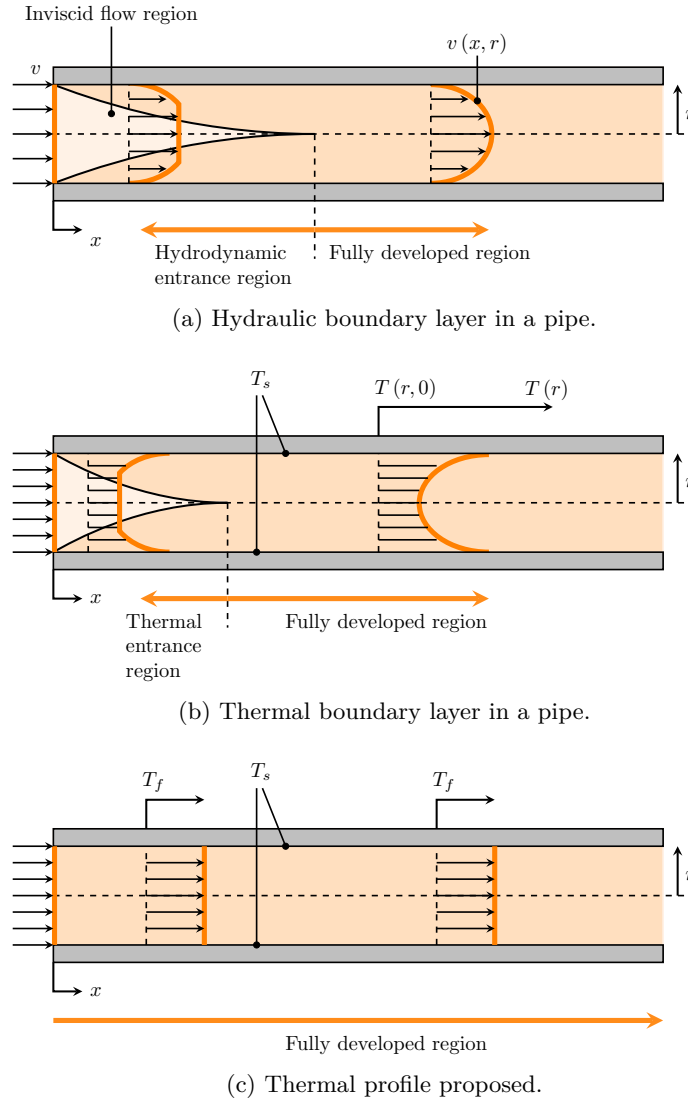


Figure 3.8: Temperature profiles with and without boundary layers.

Furthermore, if there is no change in the temperature of the surface, which means a constant value of T_s , the Nusselt number is defined by

$$\text{Nu} = 3.66 \quad (3.28)$$

More complex analysis is required to compute Nu for turbulent flow. Nevertheless, empirical correlations are done to get an equation based on hydraulic conditions [4]. For fully developed turbulent flow in a smooth circular tube, the local value of Nu may be obtained from the Dittus-Boelter equation [4]. For heating, this is given as:

$$\text{Nu} = 0.023\text{Re}^{4/5}\text{Pr}^{0.4}, \quad (3.29)$$

whereas for cooling:

$$\text{Nu} = 0.023\text{Re}^{4/5}\text{Pr}^{0.3}. \quad (3.30)$$

Finally, the convection heat transfer coefficient is defined as

$$U_{cv} = \frac{\text{Nu}k_f}{D}, \quad (3.31)$$

whose units are $[\text{W}/\text{m}^2\text{K}]$. Then, equation (3.29) can be re-written as

$$Q = U_{cv}A(T_s - T_\infty) = \frac{\text{Nuk}_f}{D}(T_s - T_f). \quad (3.32)$$

where T_f is the average temperature of the fluid.

Conduction

Conduction is the heat transfer due to the movement of particles in a medium (random translation and vibrational motion). Its direction is defined from the particles with more energy to the low energetic ones. The high-temperature zones are associated with the larger energy value of their particles. Their movement, which implies particle collisions, allows to transfer of energy to the less energetic molecules located in a zone with lower temperature. Therefore, if there is a temperature difference between two zones in a medium (*i.e.*, a temperature gradient), energy transfer by conduction must occur.

Figure 3.9 illustrates the heat transfer by conduction for a plane wall and a circular pipe. Both elements exhibit convective heat transfer: the right and left surfaces of the wall and inner and outer surfaces of the pipe are in contact with two fluids at different temperatures. High energetic molecules presented in the hot side, which temperature is more significant than the cold ones ($T_1 > T_2$), crosses the middle line that divides the medium between high and low temperature, establishing the direction of the heat transferred (Q) from the right to the left surface in the wall, and for the inner to the outer surface in the pipe. The temperature profile is defined axially through the x direction for the wall and radially through the radius r direction of the pipe. This diffusive flow of energy can be quantified in a similar manner as for convective flow by defining a coefficient called the conduction heat transfer coefficient U_{cd} .

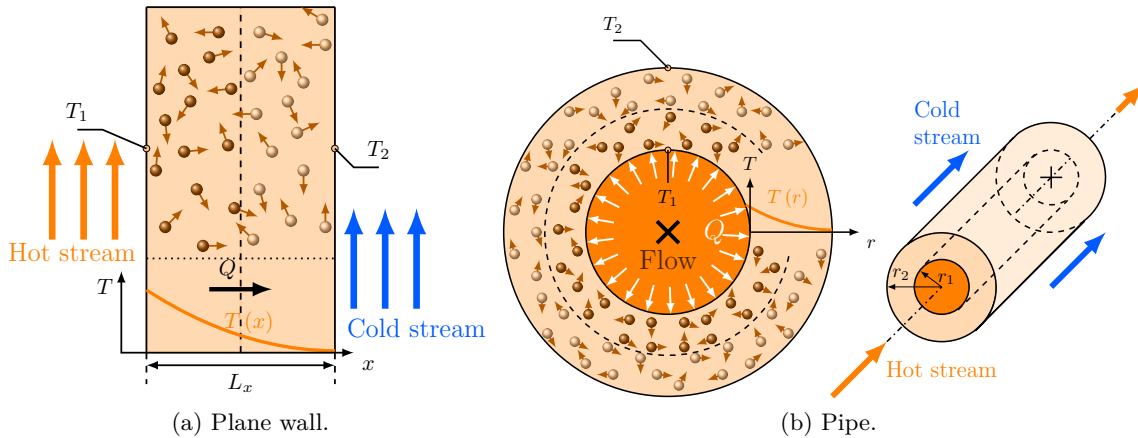


Figure 3.9: Association of conduction heat transfer with diffusion of energy due to molecular activity.

A main assumption is made to simplify the conduction heat transfer analysis: all the internal temperature gradients within the medium are neglected. This approach is called the lumped capacitance method [4] and allows quantifying the rate of energy change through time due to conduction, reducing the complexity of its calculation. The conduction heat flux is defined by the diffusive flux in equation (3.13) and in equation (3.14) as

$$Q' = \vec{\nabla} \left(k \vec{\nabla} T \right), \quad (3.33)$$

3.2. Thermal dynamic modelling

where $k = \rho\kappa c_p$ [W/mK] is the coefficient of thermal conductivity. It is important to notice that the apostrophe on Q variable stands for heat flux, not heat. Following the 1-D analysis, the only heat flux component in the wall is given by axis x . Then, using Fourier's law, the conductive heat flux is determine by

$$Q' = -\frac{d}{dx} \left(k \frac{dT}{dx} \right). \quad (3.34)$$

Equation (3.40) is integrated twice and the limit conditions are defined as the surface temperatures (T_1 and T_2) to obtain the value of the heat flux due to conduction through the wall by

$$Q' = -\frac{k(T_2 - T_1)}{L_x}, \quad (3.35)$$

where L_x [m] is the wall thickness. Finally, the conduction heat is obtained by solving the integral of the surface to eliminate the gradient operator as

$$Q = -\int_S q' ds = \frac{Ak(T_2 - T_1)}{L_x}, \quad (3.36)$$

where A [m²] is the area of the wall which is normal to the direction of the heat flux; therefore, the negative sign is eliminated.

For the conduction heat transfer through the pipe walls, a similar analysis is done. The temperature profile is defined radially. Therefore, the conductive heat flux is defined by expressing the Fourier's law in cylindrical coordinates as

$$Q' = \frac{1}{r} \left(kr \frac{dT}{dr} \right). \quad (3.37)$$

Equation (3.37) is solved by integrating twice respect to r . The boundary conditions are the temperature of the internal T_1 and external surface (T_2) of the pipe as it is illustrated in Figure 3.9. Then, the conductive heat flux is defined as:

$$Q' = -k \frac{T_1 - T_2}{\ln(r_1/r_2) r_2}. \quad (3.38)$$

Finally, the conduction heat transfer is obtained by solving the integral of the transfer area as

$$Q = \int_S q' ds = Ak \frac{(T_1 - T_2)}{\ln(r_1/r_2) r} = \frac{2\pi r_2 Lk (T_1 - T_2)}{\ln(r_1/r_2) r_2}, \quad (3.39)$$

where L is the length of the pipe. The variable r_2 might be eliminated by simplifying equation (3.39). However, it is kept in the equation to establish separately U_{cd} and the transfer area in the heat conduction equation. Similar to heat transfer by convection, a conduction heat transfer coefficient may be defined from equation (3.39). As for U_{cv} , the units of U_{cd} are [W/m²K]. Thus, for a plane wall, the heat transfer coefficient of conduction is defined by

$$U_{cd} = \frac{k}{L}, \quad (3.40)$$

and for a pipe as:

$$U_{cd} = \frac{k}{\ln(r_1/r_2) r}. \quad (3.41)$$

Dynamic calculation of the overall heat transfer coefficient

The energy balance is a rate of change; therefore, the energy variations through the time will imply temperature changes in the materials involved in the heat transfer process. The thermophysical properties of matter are temperature dependent. Thus, variations of matter temperature imply changes in its thermophysical properties. The impact of these variations depends on the type of material. Some properties can be considered constant at certain temperature ranges.

For the sake of accuracy, these variations are considered in the thermal models. Critical properties define the whole thermal behaviour of a fluid or solid such as the specific heat for PCMs or for water steam presented in DHCSs. Therefore, the equation to compute the heat transfer should capture these variations. The equations of the heat transfer coefficient for convection and conduction presented in the previous section are re-written, including the dependence of temperature of the thermophysical properties:

$$\text{Re}(T) = \frac{\rho(T) v_m D}{\mu(T)} \quad (3.42)$$

$$\text{Nu}(T) = f(\text{Re}(T), \text{Pr}(T)) \quad (3.43)$$

$$U_{\text{cv}}(T) = \frac{\text{Nu}(T) k_f(T)}{D} \quad (3.44)$$

$$U_{\text{cd}}(T) = \frac{k(T)}{L} \quad (3.45)$$

To visualize the magnitude of the variations of the thermophysical properties with respect to temperature, the graphs of the saturated water properties [4] are shown in Figure 3.10. These values are used to compute the heat transfer coefficient in this work when water is involved in the heat transfer process.

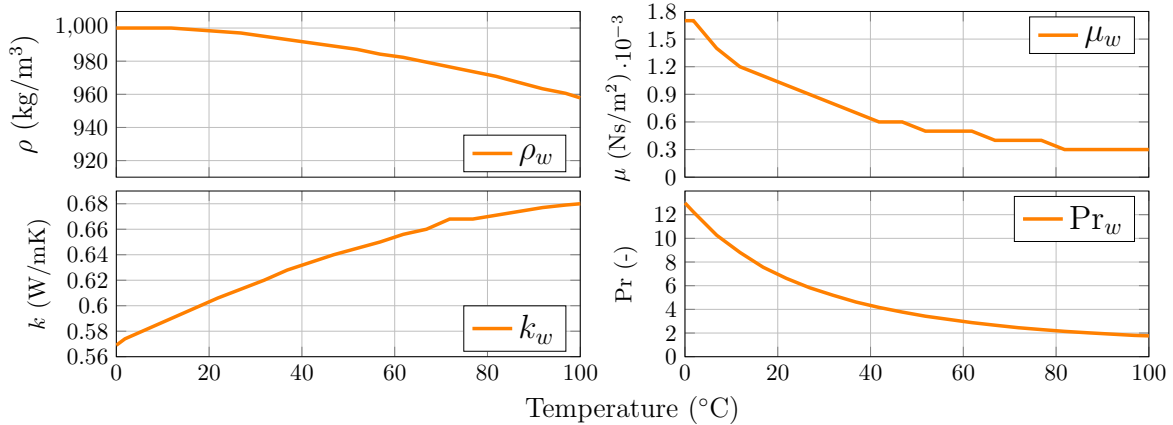


Figure 3.10: Thermophysical properties of saturated water. Left from top to bottom: density, thermal conductivity. Right from top to bottom: viscosity, Prandtl number

Overall heat transfer coefficient

The equation for convection and conduction heat transfer given by (3.39) and (3.43) look similar to the electrical relation linking potential difference, electrical flow (current) and

3.2. Thermal dynamic modelling

resistance, namely, Ohm's law:

$$(\mathcal{V}_1 - \mathcal{V}_2) = Ri, \quad (3.46)$$

where \mathcal{V} [V] is the potential difference, i [A] is the current and R [Ω] is the electric resistance. Thus, the heat flow equation with a general value of U can be re-arranged as

$$(T_1 - T_2) = \frac{Q}{UA}, \quad (3.47)$$

Thus, an electric to heat transfer analogy is established (see Table.3.1). Thus, the electric current flow is analogue to the heat flow. The electric potential difference able to produce current is analogue to the temperature difference that produces a flow of heat. A restriction of the current given by the electric resistance is analogue to the thermal resistance.

Table 3.1: Electric to heat transfer analogy.

Variable	Electric	Heat
Flow variable	Current (i)	Heat flow (Q)
Potential variable	Voltage ($\mathcal{V}_1 - \mathcal{V}_2$)	Temperature ($T_1 - T_2$)
Resistance	Electric resistance (R)	Thermal resistance ($1/UA$)

The thermal resistance is defined by

$$R_T = \frac{1}{UA} [\text{K/W}]. \quad (3.48)$$

This term is very useful in treating more complex systems with more than one heat transfer process occurring, such as heat exchangers or TES tanks. Those heat transfer processes can be represented as many series or parallel thermal resistances and they can be added following the rules for electric resistances. The total resistance obtained from this addition is called the overall heat transfer coefficient (U).

To exemplify the computation of U , a system with two fluids (convection) and four walls (conduction) is presented in Figure 3.11. The 1-D analysis of the heat flux between the temperature of the outermost walls (T_1, T_2) is given by

$$Q = UA(T_1 - T_2) = \frac{T_1 - T_2}{R_T}. \quad (3.49)$$

The thermal resistance is located in each layer and specified by subscripts 'cd' and 'cv', which stand for conduction and convection heat transfer, respectively. The resistances are linked in series. Therefore, the total resistance is computed by

$$R_T = R_{cd1} + R_{cv2} + R_{cd3} + R_{cd4} + R_{cv5} + R_{cd6}. \quad (3.50)$$

Using equation (3.50), the overall heat transfer coefficient is calculated by

$$U = \frac{1}{R_T A} = \frac{1}{\frac{1}{U_{cd1}} + \frac{1}{U_{cv2}} + \frac{1}{U_{cd3}} + \frac{1}{U_{cd4}} + \frac{1}{U_{cv5}} + \frac{1}{U_{cd6}}}. \quad (3.51)$$

Using equations (3.31) and (3.40) to specify the values of each heat transfer coefficient, equation (3.51) is re-written as

$$U = \frac{1}{(L_1/k_1) + (D/Nu k_h) + (L_2/k_1) + (L_3/k_2) + (D/Nu k_c) + (L_4/k_2)}. \quad (3.52)$$

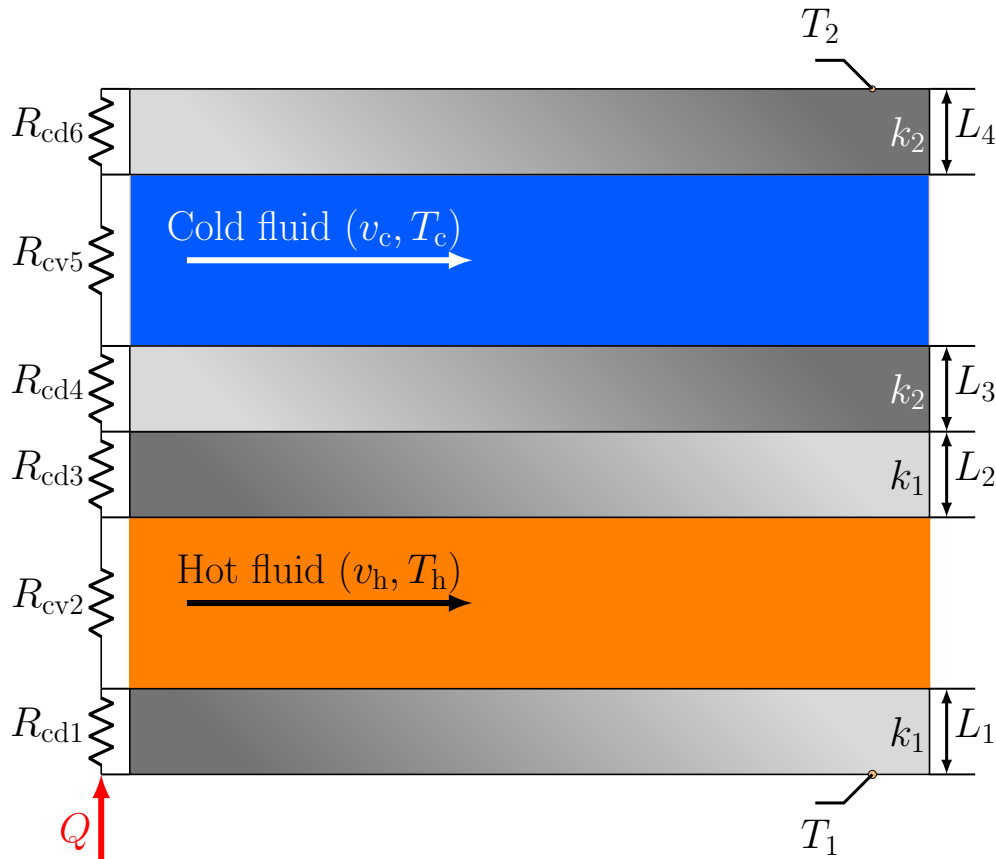


Figure 3.11: Equivalent thermal circuit for a series heat transfer composite.

3.2.3 Discretisation/stratification method

Once the tools necessary to analyse a system's thermal behaviour have been explained (*i.e.*, energy balance and the overall heat transfer coefficient), the next step is to describe their implementation. The main aim of the thermal modelling approach is to obtain differential equations capable of describing a system's temperature based on balance energy and heat transfer theory. Nevertheless, implementing the energy balance directly to a system is not sufficient because the system's size affects the accuracy of the modelling process. The heat flow effects due to the temperature gradients given in the system require a discretisation method.

The discretisation method consists of splitting the system analysed into several nodes (N_i) linked thermally through the heat flowing through the system. The energy balance is applied to these nodes; thus, each node contains a control volume for each fluid. To illustrate the method, a simple system with two parallel flows crossing two joined square channels is shown in Figure 3.12. Cold and hot water streams have associated temperature input $T_{x,in}$ and constant velocity v_x . Subscripts 'c' and 'h' stand for cold and hot fluids, respectively.

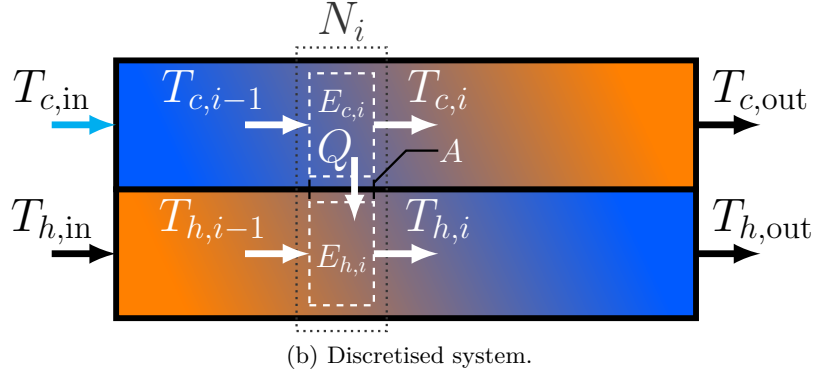
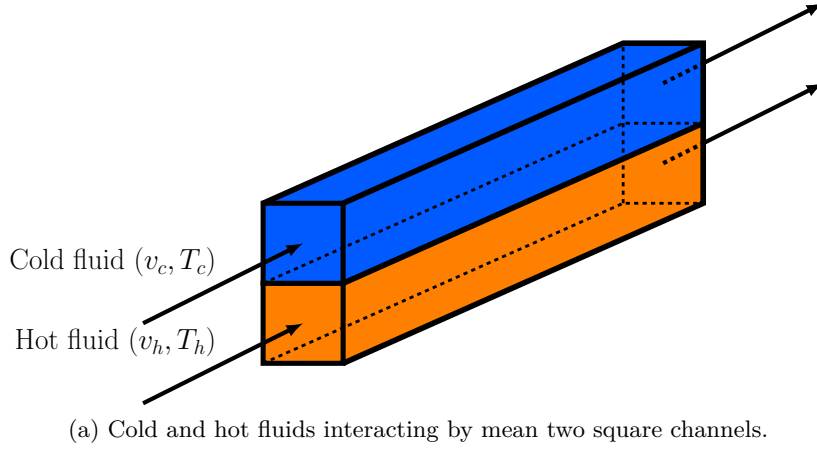


Figure 3.12: Control volume of two fluids flowing in square channels.

To apply energy balance to both fluids, it is necessary to establish a control volume. Figure 3.12 shows the lateral area of the control volume covering both streams and the wall of the channels through which the heat is transferred. The total thermal energy transferred to a specific element is given by the sum of the heat fluxes from the system's energy sources. This transit of energy is dynamically described by equation (3.10). Its use for the control volume of node N_i is defined by

$$\dot{E}_{c,i-1} = \dot{E}_{c,in} - \dot{E}_{c,out}. \quad (3.53)$$

The input of energy is given by the input conditions of the fluid before entering into the control volume and it is given by equation (3.21), which can be defined in terms of the control volume conditions as (*e.g.*, for cold stream):

$$\dot{E}_{c,in} = \dot{m}_{f,c} c_{p,c} (T_{c,i-1} - T_{c,i}) \quad (3.54)$$

The other source of heat for the control volume is the heat transferred Q by conduction due to the channel's wall and by convection due to the fluids flow. For the cold stream with a lower temperature, this amount is positive and for the hot stream negative. The whole heat transfer process can be captured by the overall heat transfer coefficient (U) and the internal energy of the control volume as defined by equation (3.9). The energy balance of the cold stream is established as

$$\rho_c V c_{p,c} \frac{dT_{c,i}}{dt} = \dot{m}_c c_{p,c} (T_{c,i-1} - T_{c,i}) + UA (T_{h,i} - T_{c,i}), \quad (3.55)$$

where A [m²] is the heat transfer area of the control volume. For the hot stream, the energy

balance is given by

$$\rho_h V c_{p,h} \frac{dT_{h,i}}{dt} = \dot{m}_h c_{p,h} (T_{h,i-1} - T_{h,i}) + UA (T_{c,i} - T_{h,i}), \quad (3.56)$$

For equations (3.55) and (3.56), U is defined using equation (3.51) as

$$U = \frac{1}{\frac{1}{U_{cv,c}} + \frac{1}{U_{cd}} + \frac{1}{U_{cv,h}}}, \quad (3.57)$$

where the convection heat transfer coefficient due to the flow of cold water is given by

$$U_{cv,c} = \frac{\text{Nu}(T_{c,i}) k_w (T_{c,i})}{D_h}, \quad (3.58)$$

where D_h [m] is the hydraulic diameter for a square channel. The heat transfer coefficient due to conduction occurs in the wall of the square channel. It is defined as:

$$U_{cd} = \frac{k_{ch}}{L_{ch}}, \quad (3.59)$$

and the heat transfer coefficient due to the hot stream of water is calculated by

$$U_{cv,h} = \frac{\text{Nu}(T_{h,i}) k_w (T_{h,i})}{D_h}. \quad (3.60)$$

By applying the discretisation method to the system, a set of non-linear differential equations for energy balance are obtained, with two equations per control volume. Thus, the thermal model of a system divided in N number of control volumes is defined by

$$\begin{aligned} \rho_c V c_{p,c} \frac{dT_{c,1}}{dt} &= \dot{m}_c c_{p,c} (T_{c,\text{in}} - T_{c,1}) + UA (T_{h,1} - T_{c,1}), \\ \rho_h V c_{p,h} \frac{dT_{h,1}}{dt} &= \dot{m}_h c_{p,h} (T_{h,\text{in}} - T_{h,1}) + UA (T_{c,1} - T_{h,1}), \\ &\vdots \\ \rho_c V c_{p,c} \frac{dT_{c,i}}{dt} &= \dot{m}_c c_{p,c} (T_{c,i-1} - T_{c,i}) + UA (T_{h,i} - T_{c,i}), \\ \rho_h V c_{p,h} \frac{dT_{h,i}}{dt} &= \dot{m}_h c_{p,h} (T_{h,i-1} - T_{h,i}) + UA (T_{c,i} - T_{h,i}), \\ &\vdots \\ \rho_c V c_{p,c} \frac{dT_{c,N}}{dt} &= \dot{m}_c c_{p,c} (T_{c,N-1} - T_{c,N}) + UA (T_{h,N} - T_{c,N}), \\ \rho_h V c_{p,h} \frac{dT_{h,N}}{dt} &= \dot{m}_h c_{p,h} (T_{h,N-1} - T_{h,N}) + UA (T_{c,N} - T_{h,N}). \end{aligned} \quad (3.61)$$

The steps defined in Figure 3.1 guided the modelling process. Equation (3.61) completely defines the thermal behaviour of the system shown in Figure 3.12. The number of control volumes may affect the level of accuracy and this will be studied in the next chapter. Thus, the discretised thermal dynamic model of a system based on energy balance provides the temperature values through time of each node. The model considers the mass flow rate \dot{m} of the fluids, the input temperatures and the dynamic computation of U .

3.3 Hydraulic dynamic modelling

The core of energy transportation within DHCSs are the pipe networks. A fluid with low or high temperature flows inside the pipes to carry the heat or cold to substations or TES. The movement of the fluid is generated and managed by pumps and valves. The fluid is pumped due to the head (h) produced by the pump at an specific volumetric flow (Q_v)¹. An adequate approach enables developing dynamic models of pipe networks based on physics principles of fluid mechanics. For instance, the changes in magnitude and direction of the fluid velocities may result from the applied forces to the fluid according to the Newton's second law of motion. The model should also consider the parameters of the fluid and elements of the pipe networks such as pumps and valves. The main aim of developing dynamic models is to compute the velocities generated within the pipe networks knowing the hydraulic behaviour of the components. Thus, a pressure drop equation for each element should be established and an appropriate dynamic solution of the hydraulic circuit is obtained considering all the operating conditions of the network.

The framework of the hydraulic modelling approach is illustrated in Figure 3.13. The steps necessary to obtain the dynamic model of the DHCS's pipe network are explained in the following paragraphs.

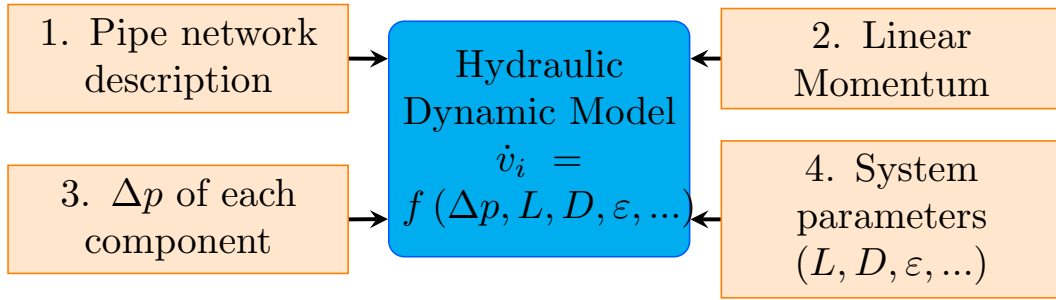


Figure 3.13: Framework of the dynamic hydraulic modelling approach.

The dynamics of the fluid inside a pipe can be described by the continuity equation, which is obtained from the general form of the conservative law given by equation (3.2) where the quantity \mathbf{U} is the specific mass: ρ [kg/m³]. The mass is only transported by convection [1]. Therefore, there is neither diffusive flux nor volume or surface mass sources. The convective flux (3.3) is defined by

$$\vec{F}_C = \rho \vec{v}, \quad (3.62)$$

where v [m/s] is the fluid velocity. The mass conservation law, also called the continuity equation, is given by

$$\frac{\partial \rho}{\partial t} + \vec{\nabla} \cdot (\rho \vec{v}) = 0. \quad (3.63)$$

As with the energy conservation law, it is necessary to define a control volume (Ω) and a surface S to implement equation (3.63). Figure 3.14 illustrates a cylindrical control volume and an amount of fluid crossing it, which is called system. The fluid has a velocity profile which is constant since the flow is assumed fully developed in a long, straight and constant diameter control volume [3]. This assumption simplifies the use of equation (3.63), because v

¹Pump's head is related to pressure by $p = hG_{SG}$, where G_f is the fluid specific gravity. Q_v can be converted to mass flow rate using the fluid density: $\dot{m} = Q_v \rho$

is considered uniformly distributed, which means 1-D flow is presented over the cross-sectional area of the control volume. Thus, using equation (3.63) over the control volume and the system results in

$$\frac{d}{dt} \int_{\Omega} \rho d\Omega + \int_S \rho v dS = 0. \quad (3.64)$$

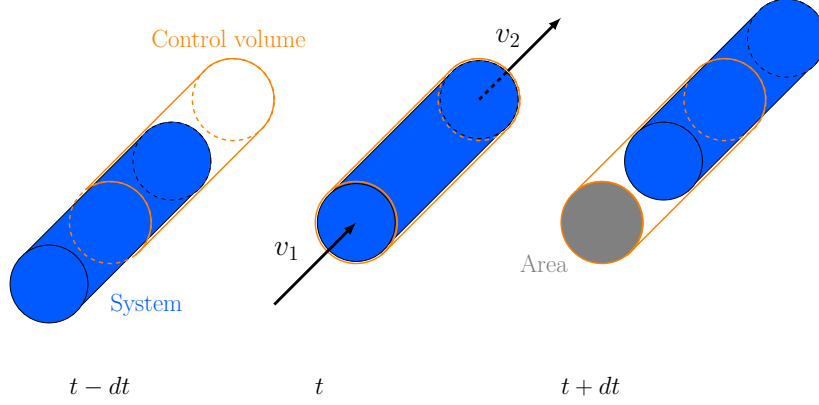


Figure 3.14: Control volume and system at three different moments.

To link the velocities (v) and the forces F presented in the DHCS's pipe network, the Newton's second law of motion is used:

$$\frac{\partial}{\partial t} \int_{sys} v \rho dV = \sum F_{sys} \quad (3.65)$$

The first term of equation (3.65) is called linear momentum [3]. Employing this equation for the control volume and the system shown in Figure 3.14. The rate of change of the linear momentum with respect to time is equal to the rate of change of the linear momentum of the control volume plus the net rate of the flow of linear momentum through the control surface. Similar to the continuity equation, the linear momentum equation is given by

$$\frac{d}{dt} \int_{\Omega} v \rho dV + \int_S v \rho v dA = \sum F. \quad (3.66)$$

The total linear momentum of the system is comprised of the linear momentum of the contents of the control volume and the sources going into and out to the control volume. It is defined as:

$$\frac{d}{dt} \int_{sys} v \rho dV = \frac{d}{dt} \int_{\Omega} v \rho dV + \int_S v \rho v dS, \quad (3.67)$$

By defining the forces in a cylindrical control volume in terms of the pressure and surface area as $F = pA$, as it is shown in Figure 3.15, the linear momentum in a fixed control volume is given by

$$\frac{d}{dt} v \rho dV = p_2 A_2 - p_1 A_1, \quad (3.68)$$

where p [Pa] is the pressure over the surface area.

Then, solving the integral in equation (3.67) yields

$$m \frac{dv}{dt} = \Delta p A, \quad (3.69)$$

where m [kg] is the mass contained in the control volume and $A = A_1 = A_2$.

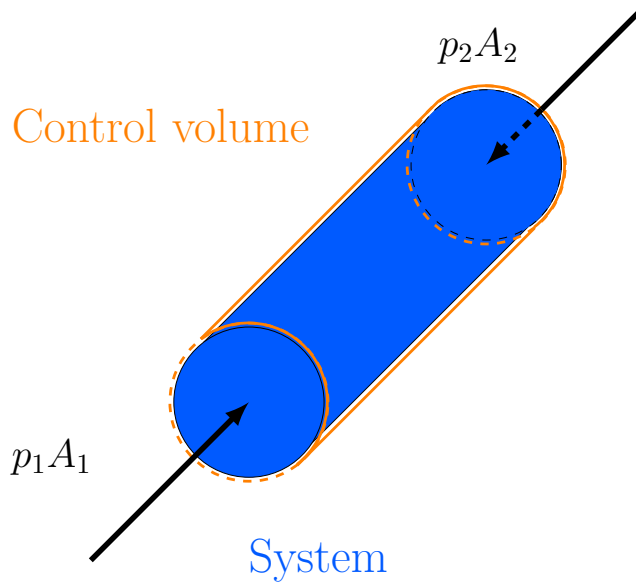


Figure 3.15: External forces over cylindrical control volume.

Thus, the dynamic relationship between the fundamental hydraulic variables of the pipe networks are given by equation (3.68). The next step of the modelling approach consists in employing the electric to hydraulic analogy to use the Kirchhoff's laws to solve the velocities in the branches of a pipe network. This analogy is summarised in Table 3.2.

Table 3.2: Electric to hydraulic analogy.

Variable	Electric	Hydraulic
Flow variable	Current (i)	Volumetric flow (\dot{V})
Potential variable	Voltage ($\mathcal{V}_1 - \mathcal{V}_2$)	Pressure ($p_1 - p_2 = \Delta p$)
Resistance	Electric resistance (R)	Fluid resistance (R_f)

To simplify the implementation of the linear momentum equation, the current analogue variable is the velocity of the fluid instead of the volumetric flow \dot{V} . To exemplify the use of the analogy for solving the hydraulic behaviour of a pipe network, a simple pipe branch with a pump, a valve and three pipes is used. Figure 3.16 shows the schematic of the pipe network and its analogue electric circuit.

The total force in the branch is obtained using the pressure boost/drop and the flow area of each element. The total force should produce a specific acceleration for the total fluid's mass in the branch. Thus, the velocity of the pipe network shown in Figure 3.16 is calculated by solving the following equation.

$$m_{t,1} \frac{dv_1}{dt} = A_{pu} \Delta p_{pu} - A_{k1} \Delta p_{k1} - A_{k2} \Delta p_{k2} - A_{cv} \Delta p_{cv} - A_{k3} \Delta p_{k3}, \quad (3.70)$$

The dynamic modelling of the pressure boost/drop of the pump, valve and pipe are defined in terms of the fluid velocity and include the specific characteristics of each element. These dynamic models are presented in Chapter 4 and a more complex pipe network model is solved and verified.

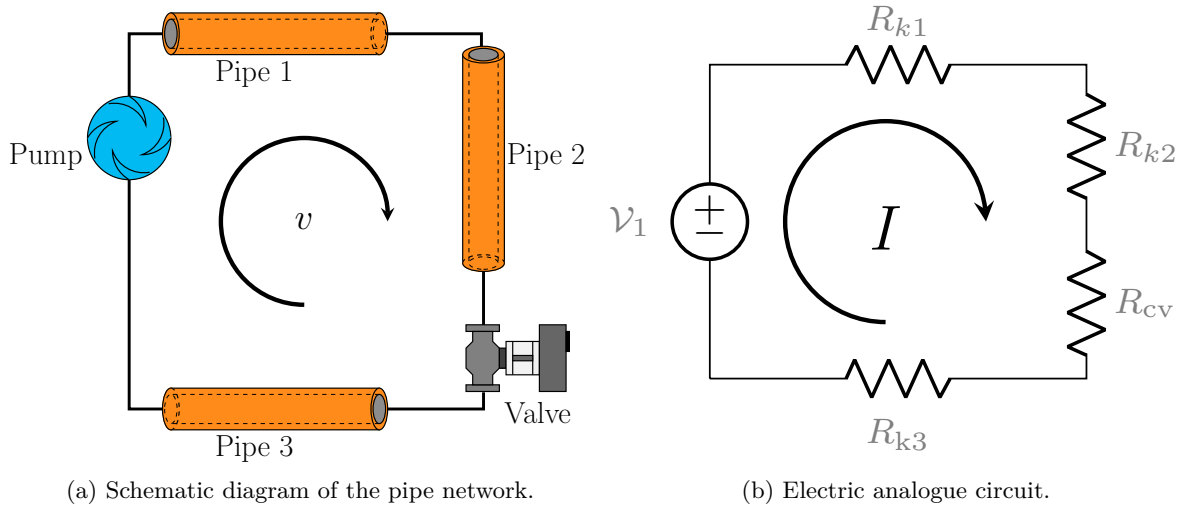


Figure 3.16: Simple pipe network comprises of a pump, a heat exchanger and three pipes connected in series.

3.4 Electric-thermal analogy for thermal dynamic building models

A thermal dynamic model of a building describes the interaction of all possible energy sources presented in the building. The main aim of developing this model is to estimate the energy consumption under different ambient conditions and design effective temperature controllers for interior temperatures. The modelling approach to derive this model is based on the work presented in [5]. Heat transfer theory and an electrical to thermal analogy are employed to describe the thermal behaviour of a building considering ambient temperature and wind speed, thermophysical properties of the building materials, and internal energy sources.

The modelling approach for a building is in accordance with the modelling framework shown in Figure 3.1. It means that the building should be described in terms of its shape, for instance, the type of walls and roof, the number of windows and the insulator material type. The energy balance for each element is developed. An ODE describes the temperature of each building element. Convection and conduction heat transfer process are considered. Although radiation plays an important role in the thermal behaviour of a building, its analysis falls beyond the scope of this research. Instead, the radiation contribution is modelled as a system disturbance.

At this modelling stage, the electric to thermal analogy shown in Table 3.1 is implemented to simplify the solution of the system. Then, similar to the hydraulic dynamic modelling approach, an electric circuit is built to obtain the energy balance of each building's component by applying Kirchhoff's laws over each grid. An extra variable is added to the analogy, the thermal capacitance (C) [J/K], defined as

$$C = mc_p \quad (3.71)$$

where m [kg] is the mass of the element and c_p [J/kgK] is the specific heat of the element

3.4. Electric-thermal analogy for thermal dynamic building models

material. Therefore, equation (3.49) is re-written as:

$$Q = mc_p \frac{dT}{dt} = C \frac{dT}{dt} = \frac{T_1 - T_2}{R_T} \quad (3.72)$$

To exemplify the use of the electric to thermal analogy in the energy balance implementation, the thermal dynamic model of a simple wall is obtained. The left surface of the wall is exposed to ambient conditions, and the right side is the interior of the building. Figure 3.17a shows the schematic of a wall and the electric representation of the convection and conduction heat transfers. Its electric representation is shown in Figure 3.17b, where the ambient temperature is modelled as a voltage source (T_a), and the thermal capacitances of the wall C_W and the interior air C_H as electrical capacitors. Latter values are defined by the wall and the interior air masses, respectively.

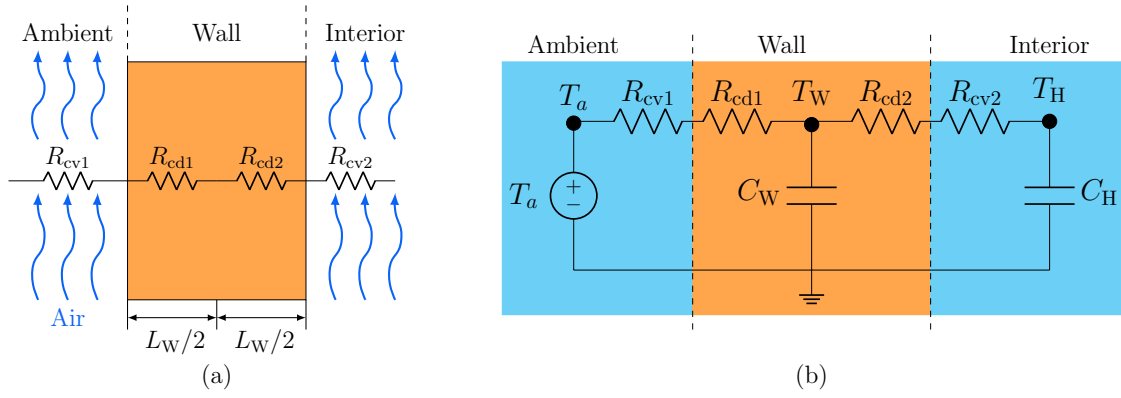


Figure 3.17: Electric circuit analogy of convection and conduction heat transfers presented in a wall.

The convection heat transfer resistance is defined by equation (3.48) as

$$R_{cv} = \frac{1}{U_{cv}A} \quad (3.73)$$

where A [m^2] is the wall area and U_{cv} is computed by equation (3.26)

$$U_{cv} = \frac{\text{Nu}k}{L}, \quad (3.74)$$

where k [W/mK] is the thermal conductivity of the air, L [m] is the horizontal length of the wall, and Nu is the Nusselt number which is calculated for an open channel as [4]:

$$\text{Nu} = 0.664\text{Re}^{0.5}\text{Pr}^{0.333}, \quad (3.75)$$

where Pr is the Prandtl number of the air, and Re is the Reynolds number, computed with equation (3.24) as:

$$\text{Re} = \frac{vL}{\nu}, \quad (3.76)$$

where ν [m^2/s] and v [m/s] is the kinematic viscosity and the velocity of the air, respectively.

On the other hand, the conduction thermal resistance is given by

$$R_{cd} = \frac{L_W}{kA} = \frac{1}{U_{cd}A}, \quad (3.77)$$

where k [W/mK] is the thermal conductivity of the wall material and L_W [m] is the wall thickness.

It is important to point out that equations (3.75) and (3.76) are defined for heat transfer to or from a surface in external flow [4]. The external flow does not present constraints as the ambient and internal air flow in a building.

Employing the Kirchhoff's laws over each grid node. The energy balance for the wall is given by

$$C_W \dot{T}_W = \frac{T_a - T_W}{R_{cv1} + R_{cd1}} + \frac{T_H - T_W}{R_{cd2} + R_{cv2}}. \quad (3.78)$$

For the interior side, the energy balance is defined by

$$C_H \dot{T}_H = \frac{T_W - T_H}{R_{cv2} + R_{cd2}}. \quad (3.79)$$

An insulator layer is added to the wall to show the development of a model considering the wall insulation effect. Figure 3.18 shows the schematic of the insulator-wall system and its electric circuit representation.

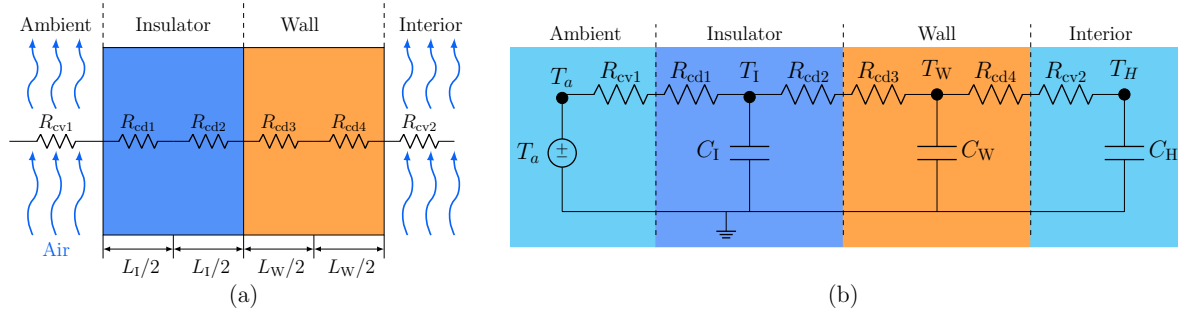


Figure 3.18: Electric circuit analogy of convection and conduction heat transfer presented in an insulator-wall.

The energy balance for the insulator, wall and interior are defined by

$$C_1 \dot{T}_1 = \frac{T_a - T_1}{R_{cv1} + R_{cd1}} + \frac{T_W - T_1}{R_{cd2} + R_{cd3}}, \quad (3.80)$$

$$C_W \dot{T}_W = \frac{T_1 - T_W}{R_{cd2} + R_{cd3}} + \frac{T_H - T_W}{R_{cd4} + R_{cv2}}, \quad (3.81)$$

$$C_H \dot{T}_H = \frac{T_W - T_H}{R_{cd4} + R_{cv2}}. \quad (3.82)$$

Finally, the thermophysical properties of the insulator, wall and air should be fed to the model. Thus, the system can be solved to describe the dynamic behaviour of each system component. Chapter 4 presents the thermal dynamic model of an insulated single house using the equations presented in this section.

3.5 Summary

Thermal and hydraulic 1-D modelling approaches for DHCS's components were presented. Physics principles are used to develop dynamic models capable of accurately describing a system's thermal and hydraulic behaviour. Modelling steps are established to define the modelling procedure necessary to obtain the mathematical model of the system. These steps are presented as a framework to facilitate the use of the modelling approaches. Both modelling approaches are based on the general conservation law. This is used for the thermal behaviour and mass and momentum for the hydraulic behaviour. For the thermal side, the heat transfer theory is used to obtain the mathematical equations to compute the overall heat transfer coefficient dynamically. Two important modelling analogies are employed to simplify the modelling process: electric to thermal and electric to hydraulic. Thus, electric circuits are developed to make simpler the understanding and the calculation of heat transfer, linear momentum and energy balance implementations.

Simple systems are used to exemplify the modelling processes. These are helpful in understanding the modelling approaches and to enable modelling more complex systems. These modelling approaches are employed in the next chapter to obtain the 1-D dynamic models of the main components of a DHCS.

The main advantages of the developed modelling approaches are simplicity and accuracy. 1-D analysis allows describing complex processes using ODEs, which can be solved in any programming language or software featuring an ODE solver. On the other hand, there is no accuracy loss because the models are based on physics principles such as energy balance, heat transfer and linear momentum. Nevertheless, the models require several critical parameters which may not be always available from manufacturers. This is the main drawback of the presented modelling approaches.

The presented mathematical models cover a wide range of applications, such as system level analysis of energy systems or control system design. Complex energy systems can be simulated by implementing the developed models on simulation software to study different operating points or system configurations. On the other hand, as the models are described by ODEs a number of different control design tools can be used to design control strategies, which in turn can be easily assessed.

3.6 References

- [1] C. Hirsch, *Numerical Computation of Internal and External Flows*. Elsevier, 2007.
- [2] Y. A. Çengel, *Thermodynamics : an engineering approach*. Sixth edition. Boston : McGraw-Hill Higher Education, [2008] ©2008, 2008.
- [3] B. R. Munson, A. P. Rothmayer, and T. H. Okiishi, *Fundamentals of Fluid Mechanics, 7th Edition*. Wiley, Apr. 2012. Google-Books-ID: GQMcAAAAQBAJ.
- [4] F. P. Incropera, D. P. DeWitt, T. L. Bergman, and A. S. Lavine, *Fundamentals of Heat and Mass Transfer*. Wiley, 6th edition ed., June 2020.
- [5] Z. T. Taylor, K. Gowri, and S. Katipamula, "GridLAB-D Technical Support Document:

Residential End-Use Module Version 1.0,” Tech. Rep. PNNL-17694, Pacific Northwest National Lab. (PNNL), Richland, WA (United States), July 2008.

Dynamic models of district heating and cooling system's elements

4.1 Introduction

In this chapter, the dynamic models of the core components of a DHCS are elaborated further. The models are based on the modelling approaches presented in Chapter 3. ODEs describe the thermal and hydraulic behaviours of the components. On the one hand, the models of heat exchangers, TES tanks and a house consider the conduction and convection heat transfer phenomena. The models of the heat exchanger and TES systems assume perfect insulation from the environment. Therefore, losses are not included in the energy balance. As established in Chapter 3, the radiation heat transfer is neglected due to its low contribution and, for the house model, it is considered as an input. The heat sources of the house model are restricted to environment temperature, solar irradiation through the windows and air conditioning systems.

On the other hand, a pipe network comprised of pumps, valves and pipes is modelled using the relationship between linear momentum and Newton's second law of motion. As in the thermal models, simplifications and assumptions are made. All pipes are considered horizontal. Therefore, the pressure drop due to bends or tee connections is lumped in a single loss coefficient term. The flow through the pipes is assumed steady and incompressible.

The parameters of each model are obtained from manufacturer data sheets or publications with experimental results of real systems. All models are implemented in MATLAB/Simulink. Results obtained with the pipe network, flat plate and shell-and-tube heat exchangers, and sensible TES models are compared to those available in the Apros software. Latent TES models for heating and cooling applications are verified using experimental data available in the literature. The models' suitability allows designing PI controllers, which are developed in Chapter 5.

4.2 Pipe networks

Increments and reduction of thermal demands cause continuous changes in operating conditions upon heat and cold transportation in DHCSs. The variations of mass flow rates and differential pressures affect the whole pipe network performance. Therefore, the development of accurate

models capable of capturing these variations and their effects is critical. This section presents the hydraulic dynamic models of the essential elements of a pipe network: pump, pipe, and valve. Critical parameters such as the volumetric-head relationship of the pumps, loss coefficient of valves and friction factor of pipes are well described.

The model of a three branches' pipe network is developed following the modelling approach for hydraulic behaviour presented in Chapter 3. Each branch's mean velocity is calculated, and different operating conditions are established, modifying the valve openings. The simulation results obtained with models in MATLAB/Simulink are compared to those obtained with Apros.

4.2.1 Pump

A pump is a mechanical device (*i.e.*, turbomachine) that transfers energy to a fluid through a rotor and blades. The fluid enters the pump and is accelerated by the blades, which are moved by an electric motor. The blade shape determines the fluid direction and the rotor's axis; thus, pumps may be classified as axial-flow, mixed-flow, or radial flow. The centrifugal pump (axial flow) is one of the most popular turbomachine used in DHCSs (see Figure 4.1). It mainly comprises an impeller (curved blades) attached to the rotating shaft and the housing that encloses the impeller.

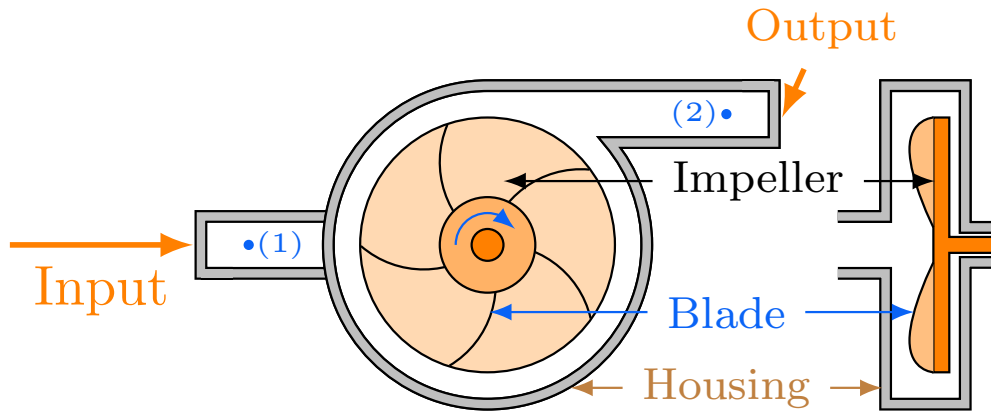


Figure 4.1: Schematic diagram of a centrifugal pump.

The pressure and velocity of the fluid are increased as the fluid passes through the pump. The analytical description of these variables requires complex equations such as the Euler turbomachine equation, which considers the fluid velocity, the shaft torque and the pump speed. This analysis becomes a challenging task due to the complexity of the pump's flow since unsteady behaviour and three-dimensional variation of velocity are presented. Nevertheless, the fluid's average flow may be sufficient to describe the hydraulic dynamics of the centrifugal pump. Analytically, the head¹ (h) and volumetric flow (Q_v) produced by the pump are related by a function considering the angular velocity of the blades w , the height b , the radial distance from the rotor's axis (r_1 and r_2) and the exit angle (β) of the impeller's blade as

$$h = \frac{(r_2 w)^2}{g} - \frac{(r_2 w)^2 \cot \beta_2}{2\pi r_2 b_2 g} Q_v, \quad (4.1)$$

¹ h is the height of a column of fluid of specific weight γ required to give a pressure difference ($p_1 - p_2$).

4.2. Pipe networks

where g [m/s²] is the gravitational acceleration. Figure 4.2 shows the linear variation of h respect to Q_v for an specific pump's blade parameters and angular velocity ω .

For the sake of simplicity, equation (4.1) assumes zero losses. Therefore, the actual value of a pump's head h_a shows a non-linear variation with respect to Q_v (see Figure 4.2). This difference might be caused by several sources such as friction, leaks in the pump housing, and three-dimensional flow effects [1]. Therefore, an analytical solution does not represent the actual value of the head for a real pump. Rather, experimental tests are used to determine the performance of the pump. The outcomes of these tests are a set of curves called pump performance curves, which the manufacturers provide. The head curves define the actual value of h at different pump speed in rpm or rad/s. These curves are shown in Figure 4.3.

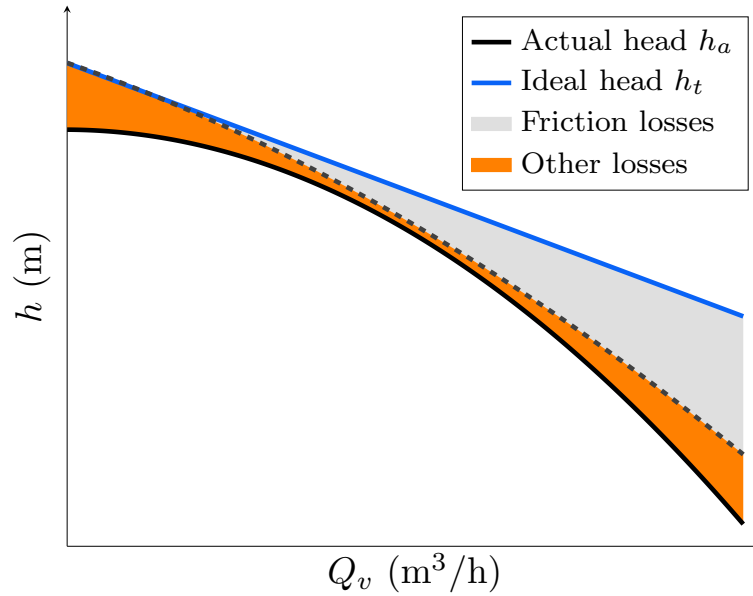


Figure 4.2: Losses of the head-flow rate curve of the pump.

Special laws that rule the pump behaviour, so-called pump affinity laws, are used to determine the pump performance under different conditions. Only knowing the nominal head curve is required, which may be the head curve at maximum pump speed. These laws relate the speed of the pump ω_{sp} to the head h , volumetric flow Q_v and power gained by the fluid P as [1]

$$\frac{Q_{v1}}{Q_{v2}} = \frac{\omega_{sp,1}}{\omega_{sp,2}}, \quad (4.2)$$

$$\frac{h_1}{h_2} = \frac{\omega_{sp,1}^2}{\omega_{sp,2}^2}. \quad (4.3)$$

and

$$\frac{P_1}{P_2} = \frac{\omega_{sp,1}^3}{\omega_{sp,2}^3}. \quad (4.4)$$

From the previous equations, the head in the operating point 2 at $\omega_{sp,2}$ can be determined by knowing the head h_1 and $\omega_{sp,1}$.

Pump performance curves of a commercial pump are used to exemplify the use of affinity laws. Performance curves of impeller model C2145WRT1 manufactured by WARMAN[®] are shown in Figure 4.3a [2]. To simplify the computation of h , speed set-points are scaled from 0

to 1, being 1 the maximum pump speed in rpm. Thus, 2800 rpm (100%) becomes 1. Equation (4.3) is rewritten as

$$\frac{h_1}{h_2} = \frac{\omega_{sp,1}^2}{\omega_{sp,2}^2} = \frac{(\omega_{sp=100\%}/\omega_{sp=100\%})^2}{(\omega_{sp=x\%}/\omega_{sp=100\%})^2}, \quad (4.5)$$

where $\omega_{sp=x\%}/\omega_{sp=100\%}$ takes values between 0 to 1. The polynomial equation that represents the head curve at $\omega_{sp} = 100\%$ is calculated via linear regression from Figure 4.3a. This is described by

$$h_1 = P_1 Q_{v,1}^2 + P_2 Q_{v,1} + P_3, \quad (4.6)$$

where $P_1 = -0.0011$, $P_2 = 0.0245$, $P_3 = 70.6820$ are the coefficients of the polynomial equation. To express h_2 in terms of h_1 , first consider $\omega_{sp,1} = 1$ in equation (4.2). Q_{v1} is expressed in terms of Q_{v2} as

$$\frac{Q_{v1}}{Q_{v2}} = \frac{\omega_{sp,1}}{\omega_{sp,2}} = \frac{1}{\omega_{sp,2}} \Rightarrow Q_{v1} = \frac{Q_{v2}}{\omega_{sp,2}}. \quad (4.7)$$

From equation (4.5), h_2 is defined in terms of h_1 as

$$\frac{h_1}{h_2} = \frac{\omega_{sp,1}^2}{\omega_{sp,2}^2} = \frac{1}{\omega_{sp,2}^2} \Rightarrow h_2 = h_1 \omega_{sp,2}^2. \quad (4.8)$$

Substituting the expressions for h_1 from equations (4.6), (4.7) and (4.8), yields

$$h_2 = \left(P_1 Q_{v1}^2 + P_2 Q_{v1} + P_3 \right) \omega_{sp,2}^2 = \left[P_1 \left(\frac{Q_{v2}}{\omega_{sp,2}} \right)^2 + P_2 \left(\frac{Q_{v2}}{\omega_{sp,2}} \right) + P_3 \right] \omega_{sp,2}^2, \quad (4.9)$$

which is simplified to

$$h_2 = P_1 Q_{v2}^2 + P_2 Q_{v2} \omega_{sp,2} + P_3 \omega_{sp,2}^2. \quad (4.10)$$

By having a polynomial representation of the volumetric flow-head curve at maximum speed, it is possible to obtain the head produced by the pump at any speed employing the affinity laws. Figure 4.3b shows the volumetric flow-head curves computed at different speeds through the whole range of Q_v using equation (4.10). The 'test' and 'mod' legends in the Figure 4.3b stand for experimental and calculated curves, respectively.

On the other hand, the power gained by the fluid flowing through the pump is given by

$$P = \frac{\rho g Q h}{\eta}, \quad (4.11)$$

where η is the overall efficiency of the pump, which incorporates the contribution of three different efficiencies that affect the pump's performance: mechanical (η_m), hydraulic (η_h) and volumetric (η_V). Figure 4.4 shows the non-linear behaviour of η . This curve is determined experimentally and is provided by the manufacturer. Equation (4.4) is used to determine the curves at the same efficiency but different speeds, shown with grey traces in Figure 4.3b. Efficiency curves are helpful to select the adequate pump required for a specific operating point defined by Q_v and h .

4.2. Pipe networks

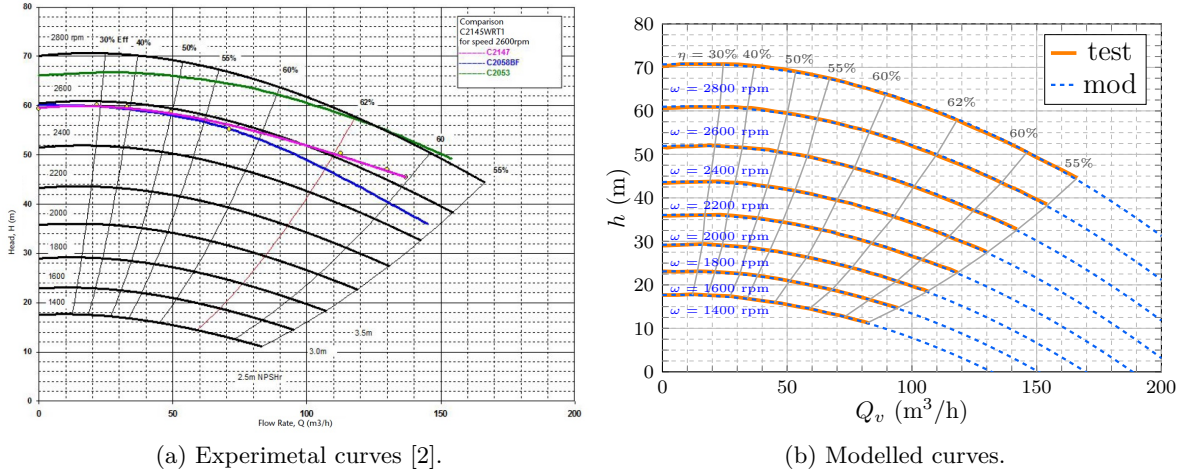


Figure 4.3: Experimental (right) and computed (left) volumetric flow-head curves of real impeller.

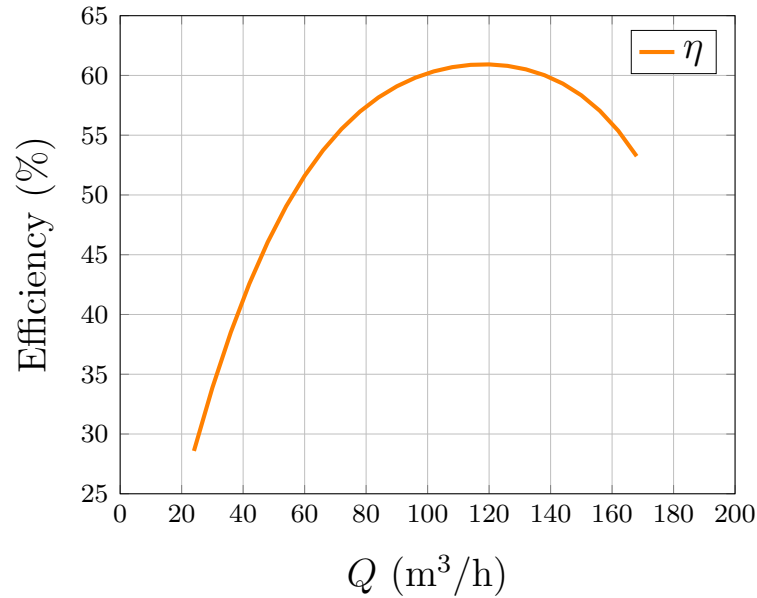


Figure 4.4: Efficiency curve of the pump's impeller model C2145WRT1 [2]

The next step in the pump's modelling process is to obtain the relationship between the head and the pressure boost of the pump. The head rise (h) developed by a fluid flowing through the pump is given by

$$h = h_2 - h_1. \quad (4.12)$$

where h_1 and h_2 are the head at points (1) and (2) shown in Figure 4.1. Assuming a steady and incompressible flow and neglecting friction effects, Bernoulli's equation is applied along the streamline through the pump as

$$h = \frac{p_2 - p_1}{\gamma} + \frac{v_2^2 - v_1^2}{2g} + (z_2 - z_1), \quad (4.13)$$

where p [Pa]² is the pressure at a chosen point, v the fluid velocity at that point, z the

²Pressure expressed in Pascals requires large numbers, thus, bar units become a more suitable unit to define the pressure. A bar is equal to 10^5 Pa.

elevation of the point above a reference plane, and γ the specific weight of the fluid which is defined as $\gamma = \rho g$. By assuming the difference of elevations and velocities between the inlet and outlet of the pump is small [1], the head rise in a pump is simplified to

$$h \approx \frac{p_2 - p_1}{\rho g}. \quad (4.14)$$

Then, the pressure boost of a pump is obtained as

$$\Delta p_p = p_2 - p_1 = \rho g h. \quad (4.15)$$

4.2.2 Valve model

The mass flow rate in a pipe network needs to be regulated to operate under different operating conditions such as heat/cold demands or pressure drops. For this purpose, pump speed variations are not enough. Therefore, control valves are implemented to aid pipe networks in mass flow rate regulation. A special mechanism (*e.g.*, ball, stem, disc) allows modifying the flow area inside the valve and, thus, the flow is reduced or incremented (see Figure 4.5). These flow variations imply pressure changes between the input and output of the valve. Like the pump model, the theoretical analysis to calculate the pressure drop for a valve is a rather challenging task. To relieve this issue, the valve performance is experimentally characterised using a parameter called flow coefficient, which may be defined in English (C_v) or International System (K_v) of units. The units are (gpm,psi) and ($\text{m}^3/\text{h},\text{bar}$), respectively. The relation between the flow and the pressure drop in a valve is defined by

$$Q_v = K_v \sqrt{\frac{\Delta p}{G_f}}, \quad (4.16)$$

where G_f is a dimensionless parameter called specific gravity of the fluid. For water, this is assumed as 1. K_v can be obtained from C_v by means of a conversion factor (see Appendix B) as

$$K_v = 0.8651 C_v. \quad (4.17)$$

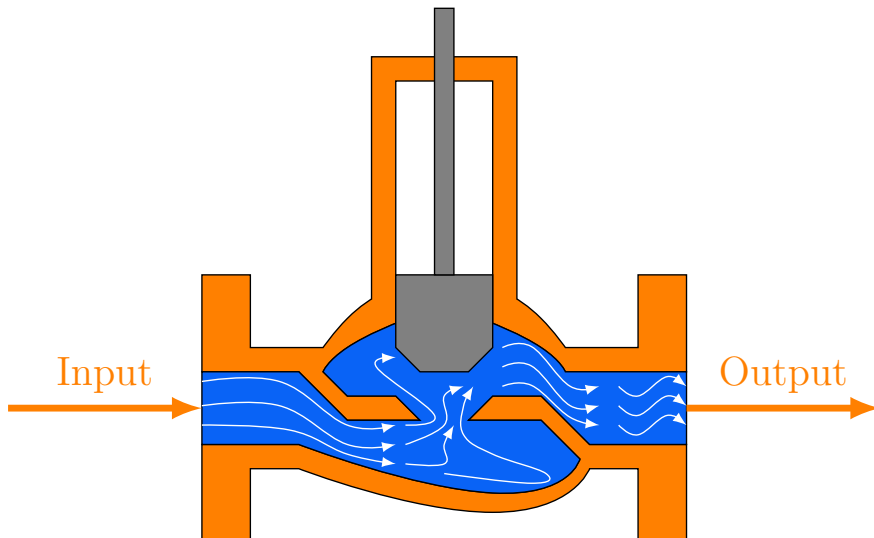


Figure 4.5: Schematic of the flow through a valve.

4.2. Pipe networks

The flow coefficient is a function of the valve opening (o_v). This function depends on the mechanism and the internal geometry of the valve. The flow coefficient curve is given by the manufacturer. Figure 4.6 shows different types of valve performances which are determined by its particular flow coefficient curve.

Therefore, the hydraulic valve model can be defined by equation (4.16) and its flow coefficient curve as

$$\Delta p_v = \frac{Q_v^2}{K_v (o_v)^2}. \quad (4.18)$$

Due to the units of K_v , the pressure drop of the valve is given in [bar] instead of [Pa]. Therefore, a conversion factor of 1×10^5 should be included to express it in [Pa]:

$$\Delta p_v = \frac{(1 \times 10^5) Q_v^2}{K_v (o_v)^2}. \quad (4.19)$$

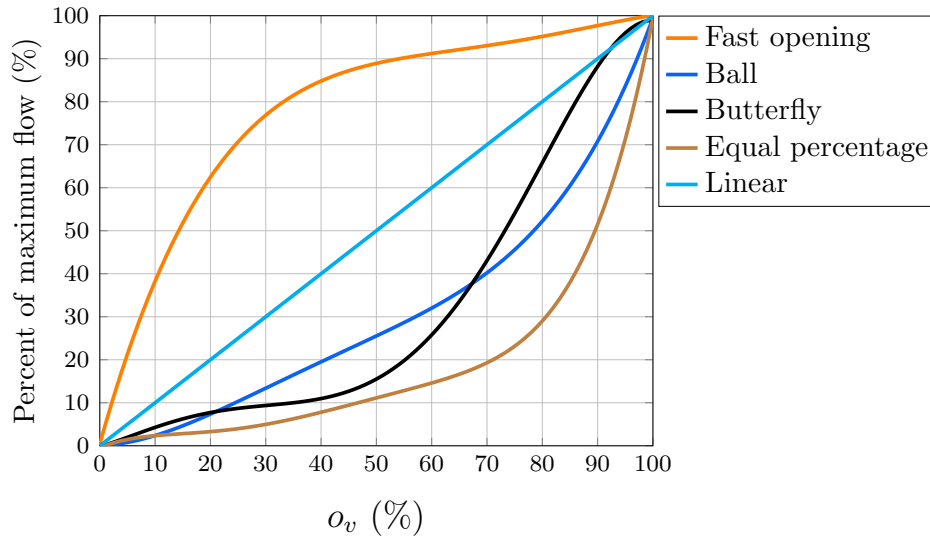


Figure 4.6: Flow-valve opening curves of different type of valves.

4.2.3 Pipe

Different sizes of circular pipes, both in terms of length and diameter, are used in DHCS's pipe networks. The heat/cold transportation utilising a fluid requires to accomplish specific hydraulic operating conditions. Thus, the knowledge of the developed pressure drop and flow (*i.e.*, mean velocity, volumetric flow or mass flow rate) within the pipes is critical to understanding their effect over other network hydraulic elements. For this purpose, a model capable of describing the pipe's hydraulic behaviour considering the pipe's size and the dynamic change of the friction factor becomes essential to have an accurate dynamic model of a pipe network. Assuming a steady incompressible flow, the energy equation between section (1) and (2) (see Figure 4.7) of the pipe is given by [1]

$$\frac{p_1}{\gamma} + \alpha_1 \frac{v_1^2}{2g} + z_1 = \frac{p_2}{\gamma} + \alpha_2 \frac{v_2^2}{2g} + z_1 + h_k, \quad (4.20)$$

where h_k^3 is the head loss between sections (1) and (2) and is associated with viscous effects, α_1 and α_2 are the kinetic energy coefficients, v is the mean velocity of the fluid and z is the elevation of the point respect to a reference. There are no variations in the velocities for a pipe with a constant diameter ($v_1 = v_2$). A horizontal pipe ($z_1 = z_2$) and a fully developed fluid, which implies no kinetic energy variations ($\alpha_1 = \alpha_2$), are assumed. Equation (4.20) is rewritten as

$$p_1 - p_2 = \Delta p = \gamma h_k = \rho g h_k. \quad (4.21)$$

As it can be observed, equation (4.21) is equal to (4.15). Nevertheless, the head loss in a pipe is defined by more complex phenomena such as viscous effects (major loss, h_{major}) and the head losses due to bends, elbows, reducers and tees connections that may exist in a pipe (minor loss, h_{minor}).

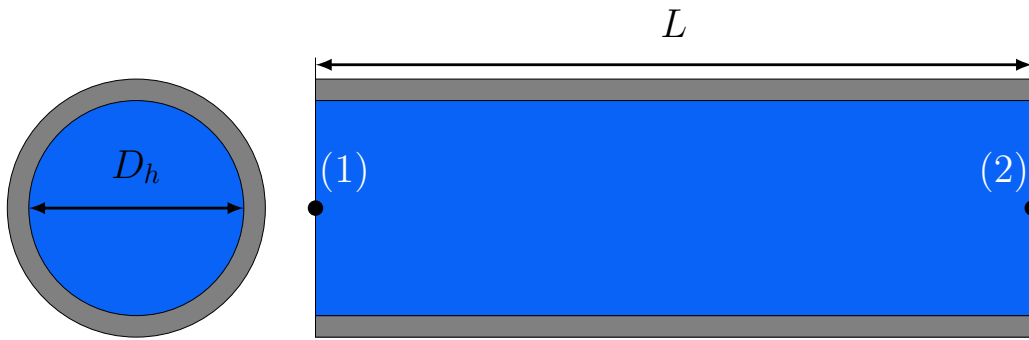


Figure 4.7: Schematic of circular pipe.

The pressure loss in a pipe is dependent on the wall shear stress (τ) between the pipe surface and the fluid flowing through it [1, 3]. For laminar flow, the shear stress is defined by

$$\tau_{\text{lam}} = \frac{\mu}{u}, \quad (4.22)$$

where μ is the dynamic viscosity and u is the velocity of the fluid. On the other hand, shear stress for turbulent flow involves components of fluid velocity in three dimensions, the density (ρ) due to momentum transfer of the fluid within turbulences and the rate of mass transfer of the fluid (v_m). This is described by

$$\tau_{\text{turb}} = \rho \overline{uv_m}, \quad (4.23)$$

where the over-bar denotes a mean value [1]. Thus, the pressure drop Δp in a pipe is strongly related to the viscosity μ and the density of the fluid ρ . Figure 4.8 shows how the turbulent flow is affected by the roughness (ε) of the pipe due to a viscous sublayer formed in the fluid. If the wall roughness element sticks out sufficiently to be part of this sublayer, the viscous effects have a different effect than the smooth wall.

Therefore, ε should be included in the computation of Δp . On the other hand, no viscous sublayers are presented in laminar flow [1, 3]. Thus, small values of ε are neglected on laminar pipe flow: $0 \geq \varepsilon/D_k \geq 0.05$, where D_k is the hydraulic diameter of the pipe. To include this phenomenon in the pipe loss head computation, a parameter called friction factor is used.

³To avoid confusion with the head loss of the pump a subscript k is adopted for the head loss of the pipe.

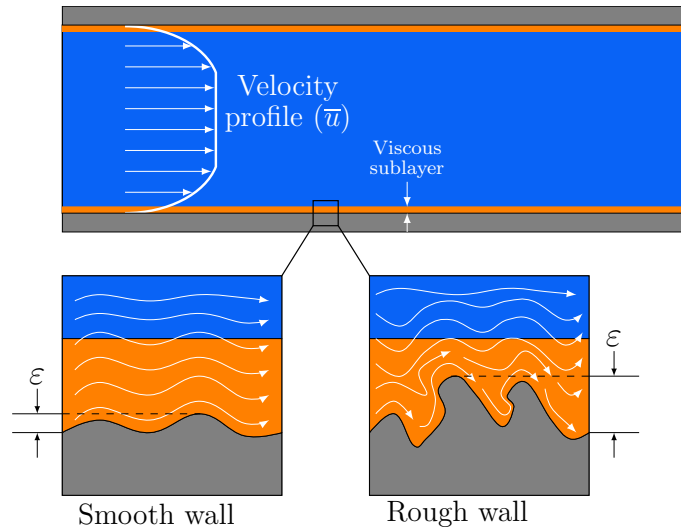


Figure 4.8: Viscous sublayer on rough and smooth wall of a pipe.

It is defined in terms of the type of flow using the Reynolds number (Re) and the relative roughness of the pipe (ϵ/D_k) as

$$f = \phi \left(Re, \frac{\epsilon}{D_k} \right). \quad (4.24)$$

For a laminar flow independent of the roughness of a pipe, the friction factor is defined by

$$f = \frac{64}{Re}. \quad (4.25)$$

For turbulent flow, there is not an analytical solution available in the literature. Experimental pipe pressure-flow data are used instead. Figure 4.9 shows graphically the behaviour of equation (4.24). This is called a Moody chart. Usually, ϵ/D_k value is given for new and clean pipes. Therefore, these values should increase due to the pipe's duty.

Although a Moody chart is built by experimental data, a useful empirical equation has been defined for the turbulent flow, called Colebrook-White equation [1, 3]:

$$\frac{1}{\sqrt{f}} = -2 \log \left(\frac{\epsilon/D}{3.7} + \frac{2.51}{Re\sqrt{f}} \right). \quad (4.26)$$

The difficulty to use equation (4.26) lies in its dependence of f , only iterative methods could be applied to solve it. Nevertheless, several equations have been proposed to solve f without requiring iterative schemes. For instance, [4] proposed the following explicit solution:

$$f = \frac{0.25}{\left[\log \left(\frac{\epsilon/D_k}{3.71} + \frac{5.74}{Re^{0.9}} \right) \right]^2}. \quad (4.27)$$

It is important to notice that the accuracy level of these empirical equations is about 10% [1].

Even though the computation of friction factor for laminar and turbulent flow have a well-defined equation, there is no equation for the transient region due to its complex behaviour.

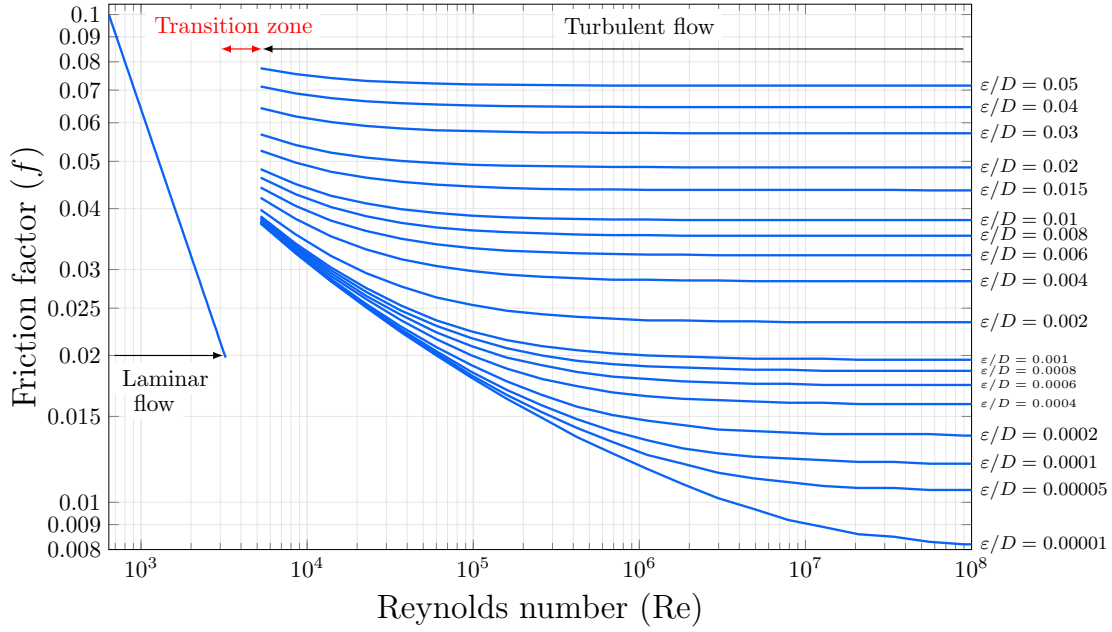


Figure 4.9: Friction factor computed by equation (4.27) which is defined in terms of Re and relative roughness or circular pipes.

This issue might be neglected in the analysis of DHCS as the region of operation does not imply operating under this zone. Nevertheless, the model should be able to compute f because the transition zone may be present temporarily during variations of hydraulic conditions. Being a dynamic model, an incomplete definition of f may produce numerical issues during simulations. To address this, a method implemented within Apros to compute f is used [5]. A slight different version of equation (4.26), simply called Colebrook equation, is adopted. It is defined as

$$\frac{1}{\sqrt{f}} = 1.74 - 2 \log \left(\frac{1}{\sqrt{f}} \frac{18.7}{\text{Re}} + 2 \frac{\varepsilon}{D_k} \right). \quad (4.28)$$

For the fully developed turbulent flow the friction factor is computed assuming that Re is infinity as

$$f_{\text{turb}} = \frac{1}{\left[1.74 - 2 \log \left(\frac{2\varepsilon}{D_k} \right) \right]^2}. \quad (4.29)$$

The corresponding Re, called critical Reynolds number, is calculated by the following equation [5] as

$$\text{Re}_{\text{cr}} = 0.355 \left[\frac{378.3}{f_{\text{turb}}} \left(\frac{2\varepsilon}{D_k} \right)^{-0.9} \right]. \quad (4.30)$$

For the laminar flow ($\text{Re} < 4000$ for Apros) the corresponding f is obtained from the maximum value between equation (4.25) and the Blasius equation, which is defined by

$$f_B = \frac{0.316}{\text{Re}^{0.25}}. \quad (4.31)$$

⁴This equation in [5] is miswritten. The limit: $\text{Re} \rightarrow \infty$ in equation (4.28) is properly applied here.

4.2. Pipe networks

If Re is greater than Re_{cr} , f is equal to f_{turb} . If Re is between 4000 and Re_{cr} , an interpolation is applied between f_B for $Re = 4000$ and the f_{turb} . Finally, f is determined by

$$f = \begin{cases} \max\left(\frac{64}{Re}, \frac{0.316}{Re^{0.25}}\right), & \text{if } Re \leq 4000 \\ \frac{0.316}{4000^{0.25}} + \frac{\min\left(f_{turb}, \frac{0.316}{4000^{0.25}}\right) - \frac{0.316}{4000^{0.25}}}{1 - \left(\frac{4000}{Re_{cr}}\right)^{0.25}} & \text{if } 4000 < Re < Re_{cr} \\ \left[1 - \left(\frac{4000}{\min(Re, Re_{cr})}\right)^{0.25}\right] \cdot f_{turb} & \text{if } Re > Re_{cr} \end{cases} \quad (4.32)$$

For ε/D greater than 0.05, the maximum value between f_{turb} and f_B for $Re = 4000$ should be used instead of the minimum as it is expressed in equation (4.32)⁵. Figure 4.10 shows the computation of f based on the Apros's method in terms of Re and ε/D . As it can be observed, the value of f in the transition zone is well defined. Nevertheless, a slight difference with respect to the original Moody chart during turbulent flow is presented. This mismatch may be due to the interpolation during the transition zone.

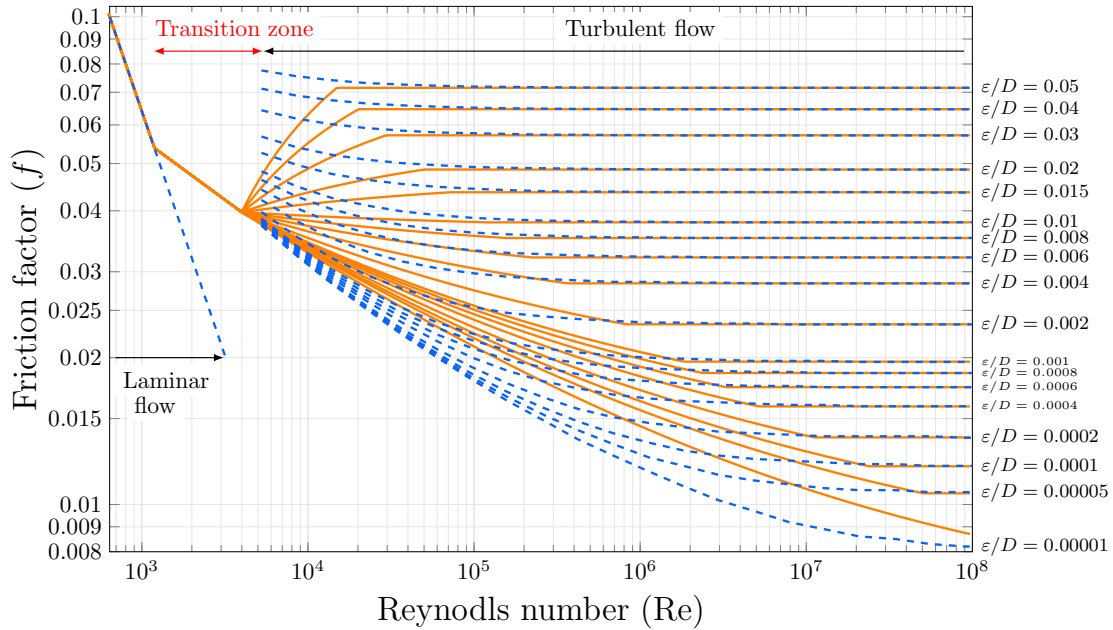


Figure 4.10: Comparison between original Moody chart (blue dashed traces) and the friction factor computed by Apros's method (orange traces).

Thus, the head loss due to the friction factor in a pipe is computed using the Darcy-Weisbach equation [1] as

$$h_k = f \frac{Lv^2}{2gD_k} \quad (4.33)$$

where v [m/s] is the mean velocity of the fluid. Additional to h_k , there are head losses due to pipe's components such as bends, and tee connections. These contributions to the overall head loss of the pipe (h_k) are estimated by a loss coefficient (K_L). Thus, the overall head loss

⁵This variation is not explained in [5] and was found during the computation of f with Apros' method to build Figure 4.10.

in a horizontal pipe is defined by

$$h_k = f \frac{Lv^2}{2gD_k} + K_L \frac{v^2}{2g}. \quad (4.34)$$

Replacing h_k in equation (4.21), the pressure drop in a circular pipe is given by

$$\Delta p_k = f \frac{\rho Lv^2}{2D_k} + K_L \frac{\rho v^2}{2}. \quad (4.35)$$

where Δp_k is given in [Pa].

4.2.4 Verification of pipe network element models

The presented hydraulic models are verified using Apros. This verification shows that the hydraulic models can determine the pressure boost/drop of the hydraulic elements and the mean velocity in each branch accurately. For this purpose, a simple hydraulic line is built-in in Apros. It comprises a pump, a valve and a pipe (see Figure 4.11). Thus, volumetric flows Q_v and the fluid velocities v for different operating conditions are obtained from Apros' simulations and then applied to equations (4.15), (4.18) and (4.35). The results are compared to the Apros' simulation results of the pressure boosts/drops.

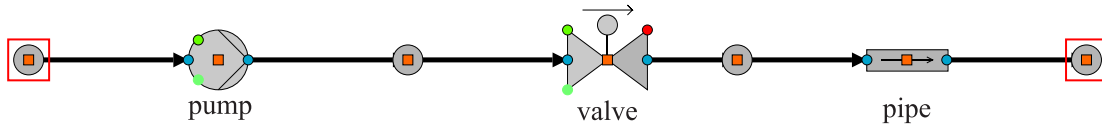


Figure 4.11: Simple hydraulic line built-up in Apros.

The parameters of each element are established in Apros. Firstly, the pump element requires the volumetric flow-head curve, usually at maximum speed, which is established in a table by pair of numbers: Q_v in [m³/s] and h in [m]. It is defined from equation (4.10) with the inclusion of conversion factor for Q_v as

$$h_M = P_1 (3600Q_v)^2 + P_2 (3600Q_v) \omega_{sp} + P_3 \omega_{sp}. \quad (4.36)$$

The values of P_1 , P_2 and P_3 are similar as those for the impaler model C2145WRT1 [2]. Nine points of this curve are presented in Appendix C. Apros allows up to 22 points.

For the valve element, the model *Type 2671* manufactured by Burkert[®] (butterfly valve) is used [6]. The opening of this valve type is determined by the position of the mechanism, with a range defined between 0° to 90°. Nevertheless, the range of the o_v - K_v curve requires to be established between 0 to 1 rather than degrees (0°-90°). Table C.1 in Appendix C shows the values of C_v - o_v in degrees given by the manufacturer and their conversion to K_v - o_v in percentage. A 150 m long pipe with $\varepsilon = 1.1283 \times 10^{-6}$ and $D_h = 0.11283$ m is defined. The flow area of all elements is $A_f = 0.01$ m².

The simulation is carried out modifying the valve opening (o_v) from 0.1 to 1 and keeping constant the pump speed at $w_{sp} = 0.6$. Thus, the volumetric flow varies due to the increments of o_v . Figure 4.12 shows the simulation's operating conditions, the variations of pump's head h_A and the volumetric flow through the whole line Q_{vA} (subscript A stands for Apros's results). Figure 4.12b shows the comparison between the pump's curve (Q_v - h) of the simulation results

4.2. Pipe networks

h_A and h_M computed for $\omega_{sp} = 0.6$. As it can be observed, the results are very close. In fact, if h_M is multiplied by a factor of 0.98 as $h_{M'} = 0.98h_M$, the curve is equal to h_A . It can be concluded that the Apros' pump element resembles the pump's behaviour described by h_M .

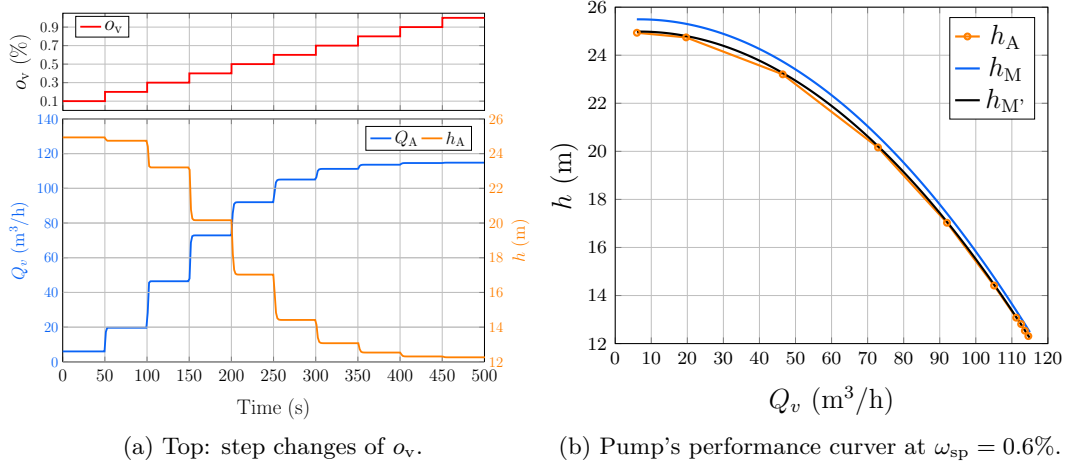


Figure 4.12: Left: Operating conditions of Apros' simulation of hydraulic line. Right: Comparison of the pump's performance curve between Apros' simulation and pump's model equation.

The pressure boost of the pump ($\Delta p_{p,A}$), the pressure drop of the valve ($\Delta p_{v,A}$) and the pipe ($\Delta p_{k,A}$) from Apros' simulation are compared to the results obtained with the models for each step change of α_v , using v_A (see Figure 4.13). The Apros environment expresses the pressure in bars. Nevertheless, the simulation data are stored in MPa. Thus, the values are converted to bar multiplying the pressure data by 10. The comparison of the pump, valve and pipe pressure drops shows a very good agreement through the whole range of the fluid velocity. Although this verification is done with a simple hydraulic line and in steady-state regimes (fixed values), it provides confidence in the element models to be used for more complex pipe networks and implemented in dynamic simulations, as it is shown in the next subsection.

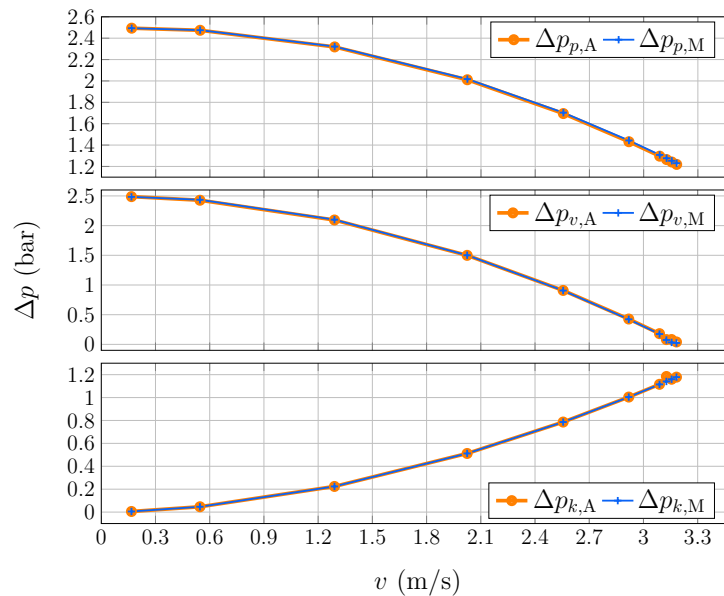


Figure 4.13: Comparison between Apros' simulation and model equations results of Δp of pump (top), valve (middle) and pipe (bottom).

4.2.5 Dynamic modelling of pipe network

A simple pipe network, shown in Figure 4.14, is modelled using the dynamic modelling approach presented in Chapter 3. It is comprised of four valves, nine pipes and a pump. The valve's loss coefficient curve and pump's volumetric-flow curve shown in Table C.1 are used for all valves and the pump. The pipe lengths and additional parameters are presented in Appendix C.

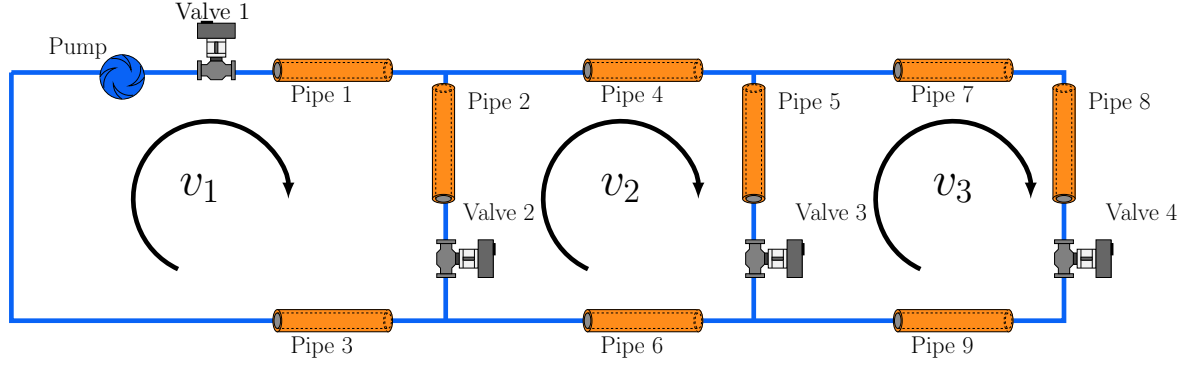


Figure 4.14: Schematic of the pipe network.

Before obtaining the system's dynamic hydraulic model, it is necessary to include the conversion factor to define pressure boost/drops in terms of velocity instead of volumetric flow. Similar to the pressure variable units where the use of Pa requires large values to express small pressures, the volumetric flow Q_v is usually expressed in small amounts. Therefore, the mean velocity of the fluid (v) is chosen to calculate the pressure boost/drops of the elements. Thus, equation (4.15) and (4.19) need to include this conversion factor from Q_v to v , which is defined by

$$Q_v = 3600A,$$

where A [m^2] is the flow area of the element. Thus, the pump's boost pressure is rewritten as

$$\Delta p_p = \rho g \left[P_1 (3600A_p v)^2 + P_2 (3600A_p v) \omega_{sp} + P_3 \omega_{sp}^2 \right] \quad (4.37)$$

where v is the mean velocity of the fluid through the pump and A_p is the pump's flow area. The valve's pressure drop is defined in terms of v as

$$\Delta p_v = \frac{(1 \times 10^5) (3600A_v v)^2}{K_v (o_v)^2}, \quad (4.38)$$

where A_v is the flow area of the valve. Regarding the pressure drop of the pipe, it is already defined in terms of v . However, it is important to highlight the parameters and variables involved in the friction factor calculation. Thus, equation (4.35) is rewritten expressing f as a function:

$$\Delta p_k = f(v, \varepsilon, D_k, \rho, \mu) \frac{\rho L_k v^2}{2D_k} + K_L \frac{\rho v^2}{2}. \quad (4.39)$$

According to the modelling steps shown in Figure 3.13, the flow velocity in the branches is obtained by applying Kirchhoff's laws to the analogue electric representation of the hydraulic circuit shown in Figure 4.15.

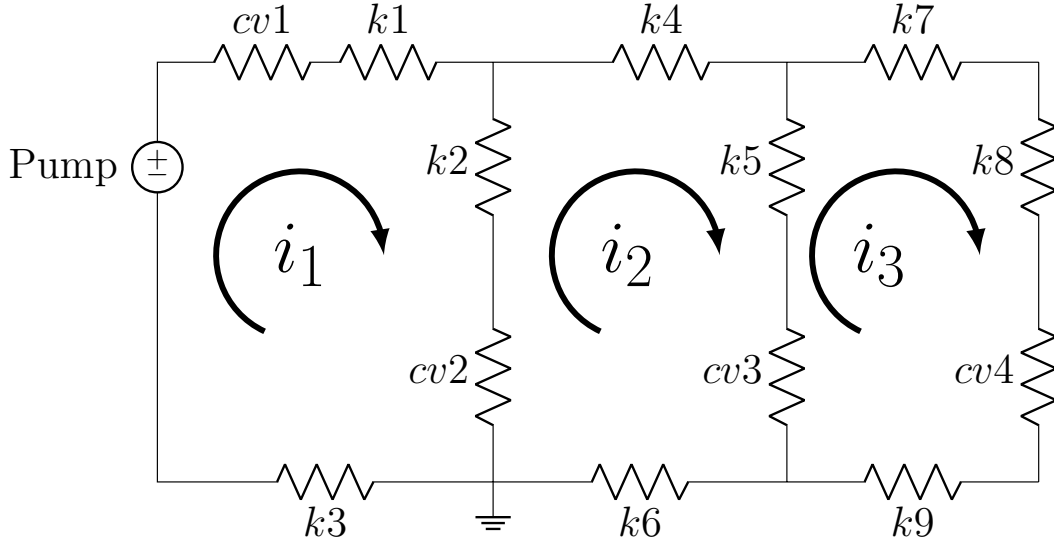


Figure 4.15: Analogue electric circuit of the pipe network system.

Using equations (3.69) and (4.37)-(4.39) expressed as a function of v , the electric circuit is solved as

$$m_{T1} \frac{dv_1}{dt} = A_p \Delta p_p(\omega_{sp}, v_1) - A_{cv1} \Delta p_{cv1}(v_1) - A_{k1} \Delta p_{k1}(v_1) - A_{k2} \Delta p_{k2}(v_1 - v_2) - A_{cv2} \Delta p_{cv2}(v_1 - v_2) - A_{k3} \Delta p_{k3}(v_1), \quad (4.40)$$

$$m_{T2} \frac{dv_2}{dt} = -A_{k4} \Delta p_{k4}(v_2) - A_{k5} \Delta p_{k5}(v_2 - v_3) - A_{cv3} \Delta p_{cv3}(v_2 - v_3) - A_{k6} \Delta p_{k6}(v_2) - A_{cv2} \Delta p_{cv2}(v_2 - v_1) - A_{k2} \Delta p_{k2}(v_2 - v_1), \quad (4.41)$$

$$m_{T3} \frac{dv_3}{dt} = -A_{k7} \Delta p_{k7}(v_3) - A_{k8} \Delta p_{k8}(v_3) - A_{cv4} \Delta p_{cv4}(v_3) - A_{k9} \Delta p_{k9}(v_3) - A_{cv3} \Delta p_{cv3}(v_3 - v_2) - A_{k5} \Delta p_{k5}(v_3 - v_2), \quad (4.42)$$

where m_{T1} , m_{T2} and m_{T3} [kg] are the total masses of the water in each branch. The values are presented in Appendix C.

The system described by equations (4.40), (4.41) and (4.42) is implemented in MATLAB/Simulink using s-functions (See Appedix A). To provide confidence in the modelling approach, a verification is carried out using Apros. A screenshot of the implemented system in Apros is shown in Figure 4.16. The fluid used for this simulation is water at 25 °C.

Different operating conditions are simulated through variation of the pump speed ω_{sp} and valve openings o_v . Figures 4.17 and 4.18 show the simulation results from both software platforms, where subscripts 'M' and 'A' are adopted for MATLAB and Apros, respectively. Different initial conditions for v_1 , v_2 and v_3 are set in the simulation. As it can be observed in the bottom graphs, the velocities agree well in both cases.

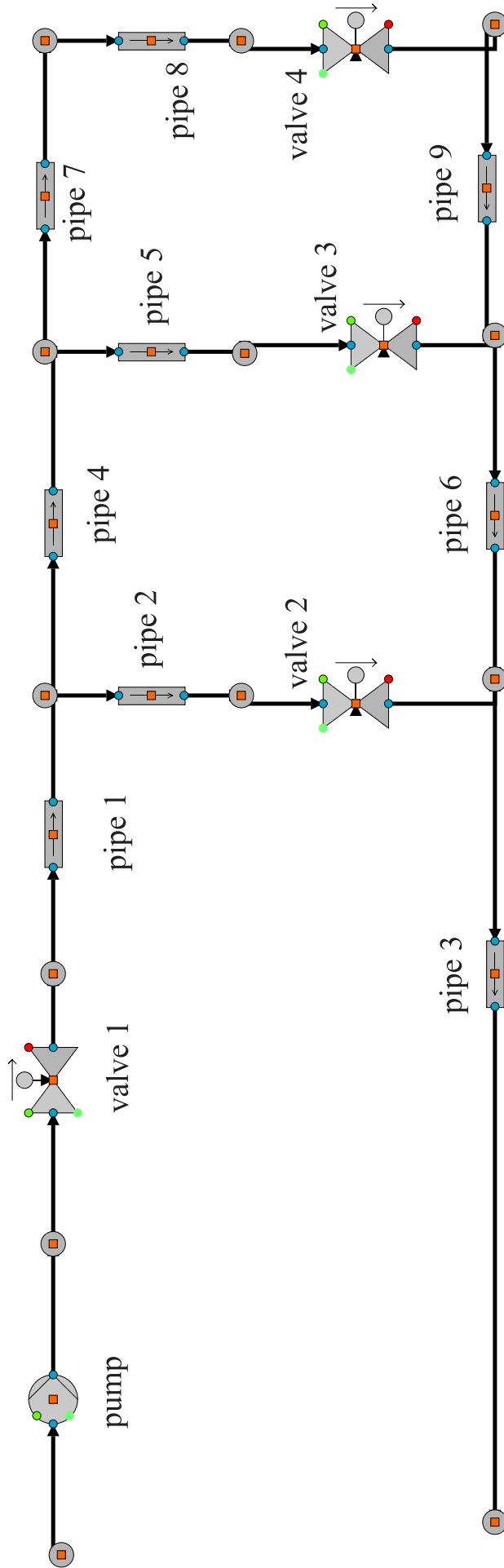


Figure 4.16: Overview of the developed Aprosim model of the pipe network.

4.2. Pipe networks

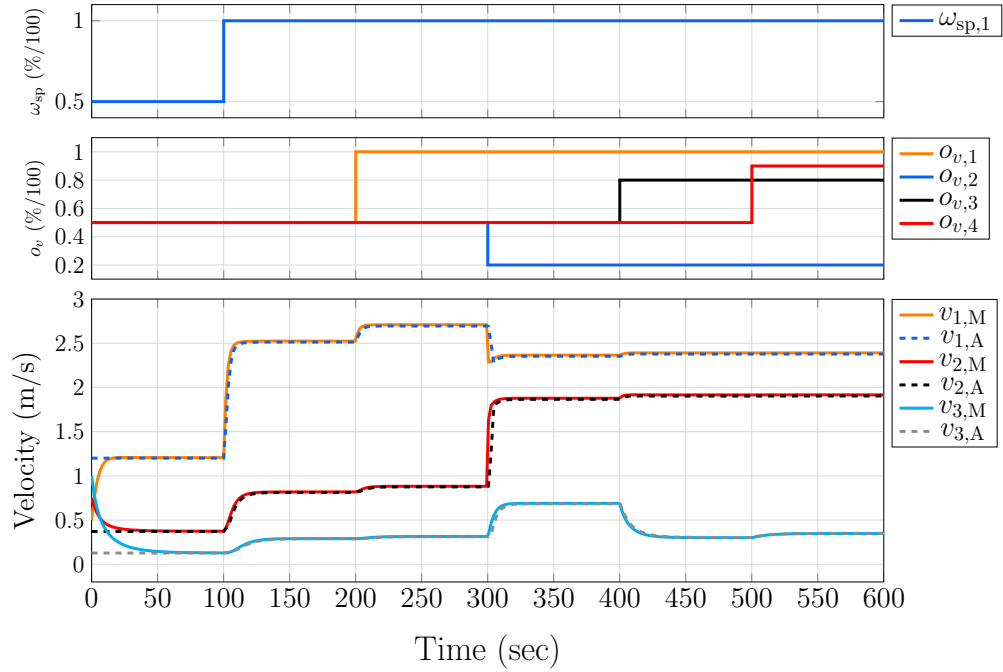


Figure 4.17: Comparison of simulation results of the pipe network. Changes in flow velocities (bottom) due to pump's speed (top) and valve openings (middle)

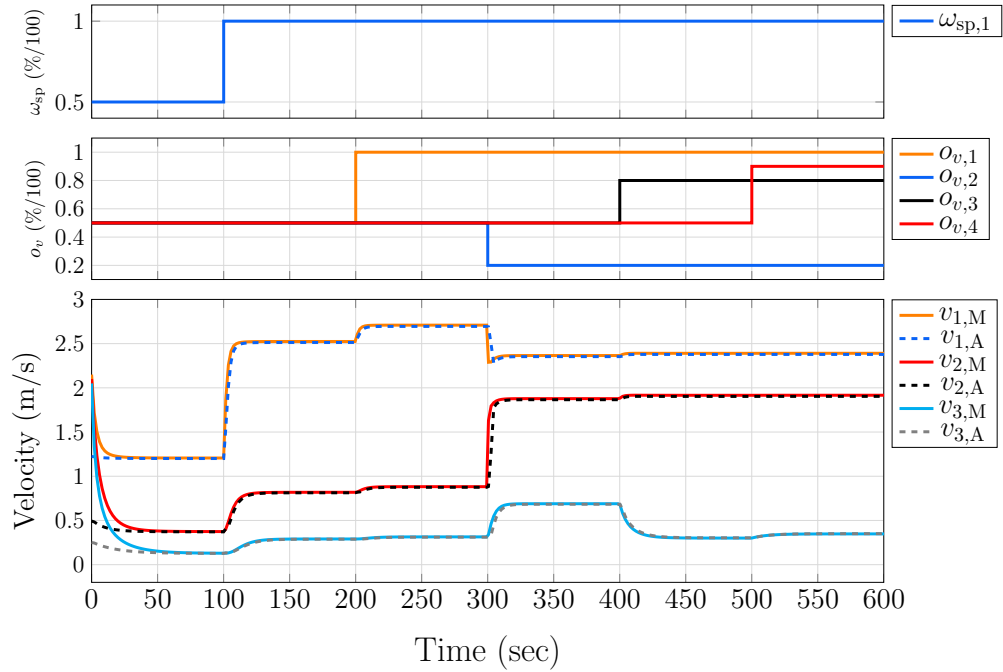


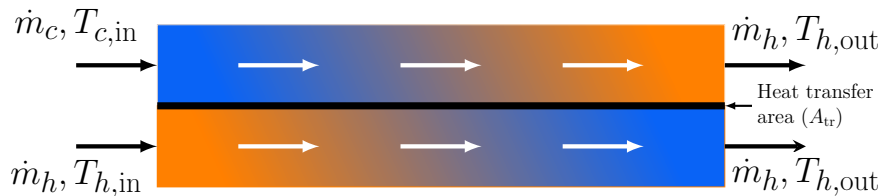
Figure 4.18: Simulation results with different initial conditions of the flow velocities (bottom) under the same variations of pump's speed (top) and valve openings (middle).

4.3 Heat exchangers

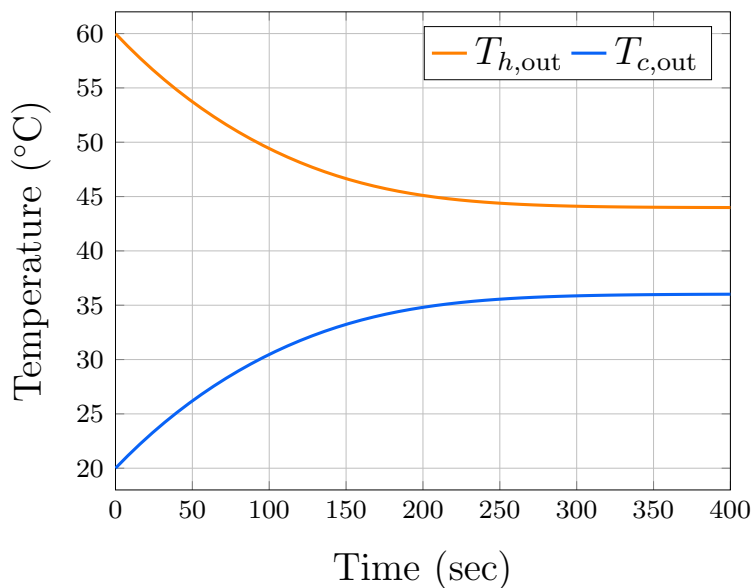
The core of the heat transfer within DHCS's are heat exchangers. The basic description of a heat exchanger is two fluids at different temperatures crossing a common wall. Thus, heat is exchanged as convection (flow) and conduction (wall) exist. The output temperature of the fluid in the secondary circuit is modified by regulating the mass flow rate in the primary circuit. There are different flow configurations and types of construction of heat exchangers. The modelling work presented in this chapter is limited to the most common flow arrangement and types used in DHCSs. In this section, parallel and counter-flow configurations are discussed and their version for flat plate and shell-and-tube heat exchangers are modelled and simulated.

4.3.1 Parallel-flow heat exchanger

The parallel-flow configuration is described in Figure 4.19a, the cold and hot streams flow in the same direction and their inputs and outputs are at the same end of the heat exchanger. The fluids are described by their temperatures (T_x) and mass flow rates (\dot{m}_x), where the subscripts 'c' and 'h' stand for the cold and the hot stream, respectively, and 'in' and 'out' stand for input and output temperatures. The outlet temperature of both streams ($T_{h,out}$ and $T_{c,out}$) are shown in Figure 4.19b. A parallel-flow configuration guarantees that the cold stream's output temperature will never be higher than the output temperature of the hot one [7]. This characteristic is helpful where high temperatures might cause damage to the system, but it reduces the heat transfer process's efficiency.



(a) Parallel-flow configuration of heat exchangers.



(b) Output temperatures

Figure 4.19: Stream directions and typical output temperature of Parallel-flow heat exchanger.

4.3. Heat exchangers

The dynamic thermal model of the heat exchanger is obtained following the steps shown in Figure 3.1. Firstly, it is necessary to know the internal geometry of the heat exchanger, then apply the energy balance and define the equation of the overall heat transfer coefficient. Finally, the dimensions of the heat exchanger, the material of the internal walls and the type of fluids should be defined. For these purposes, the following subsections present the development of the dynamic thermal model of a flat plate and shell-and-tube heat exchangers and their verification through comparison to Apros heat exchanger elements.

Flat plate heat exchanger (parallel-flow)

The most common heat exchanger used in a DHCS is the flat plate type [8]. There are many manufacturers and a wide range of sizes for the different heat-cooling supply capacities found within DHCSs. A schematic diagram of parallel-flow flat plate heat exchanger is shown in Figure 4.20. Several plates are located in a row. The mass flow rate (\dot{m}) of hot and cold fluids are spread out through the space between them. The main advantage of this type of heat exchanger is its large heat transfer area provided by each plate's flat sides.

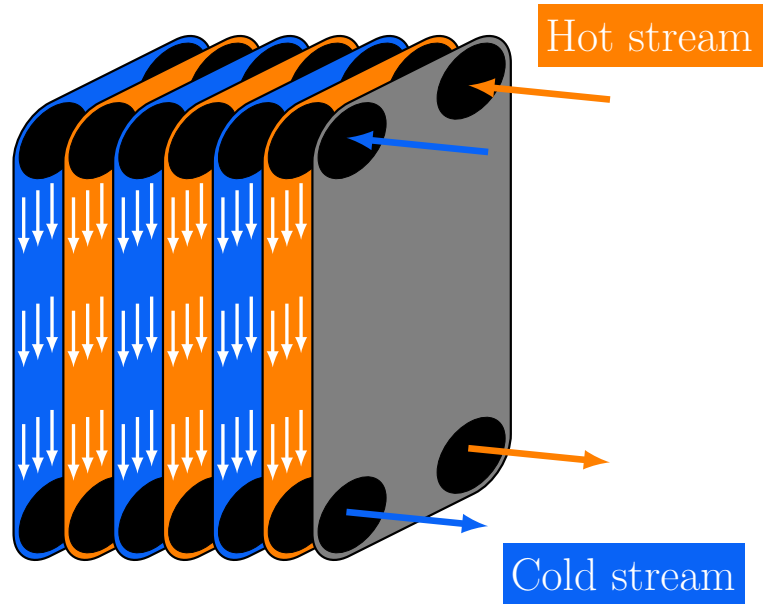


Figure 4.20: Schematic of flat plates heat exchanger.

The developed model assumes that the heat exchanger is insulated from its surroundings. Therefore, energy losses are neglected and only heat exchange between the fluids is considered for the energy balances. As it is established in Chapter 3, the potential and kinetic energy of the matter in the fluids are negligible. To illustrate the energy balance implementation, a schematic of the internal geometry of the heat exchanger is shown in Figure 4.21. The space between plates forms rectangular channels. The discretization is done by dividing the heat exchanger in nodes through the same direction in which fluid flows. The control volumes created by the division include each plate's portion.

Each node contains the volume of cold and hot stream, which are located alternatively. Hence, the energy balance is applied for cold and hot separately within the same node:

$$\dot{E}_{st,i} = \dot{E}_{in,i} - \dot{E}_{out,i}, \quad (4.43)$$

where the input energy and output energy result from the contribution of the mass flow rate moving through the plates and the heat exchange by the plate's wall (Q). The storage energy (E_{st}) is defined based on the total mass (m) [kg], which is related to the volumetric capacity of the heat exchanger by $m = \rho V$. Figure 4.22 shows separately the cold (V_c) and hot (V_h) volume alongside the wall of one plate.

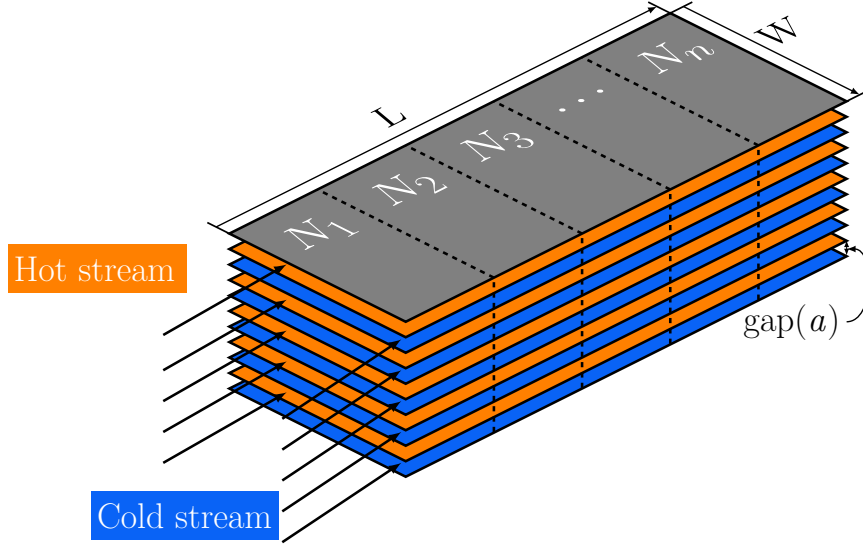


Figure 4.21: Schematic of the discretization of the flat plate heat exchanger.

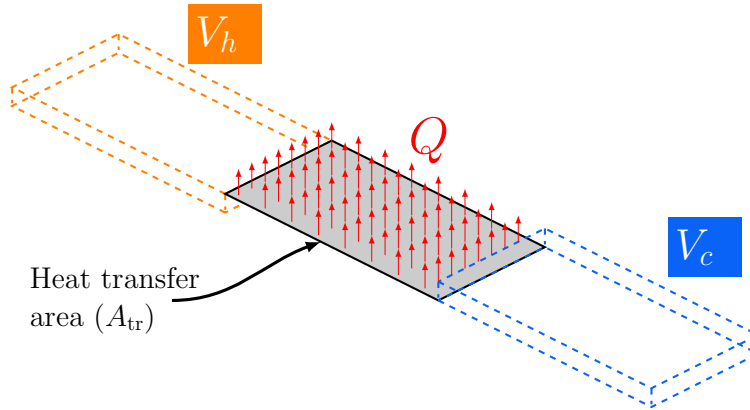


Figure 4.22: Heat transferred (Q) and the cold and hot volumes next to a plate in a node.

The energy balance equation for each node ($i = 1, 2, \dots, n$) is given as

$$m_{c,i} c_{p,ci} \dot{T}_{c,i} = \dot{m}_c c_{p,ci} (T_{c,(i-1)} - T_{c,i}) + U_i A_{tr} (T_{h,i} - T_{c,i}), \quad (4.44)$$

$$m_{h,i} c_{p,hi} \dot{T}_{h,i} = \dot{m}_h c_{p,hi} (T_{h,(i-1)} - T_{h,i}) + U_i A_{tr} (T_{c,i} - T_{h,i}), \quad (4.45)$$

where T [$^{\circ}\text{C}$] is the temperature, c_p [J/kg K] is the specific heat, U [W/m²K] is the overall heat transfer coefficient and A_{tr} [m²] is the heat transfer area. It is important to point out the convention used for the inlet and outlet temperatures. The inlet temperatures has the subscript '0' ($i - 1$), that is $T_{c,0} = T_{c,in}$ and $T_{h,0} = T_{h,in}$. On the other hand, as beyond node n there is no more fluid within the heat exchanger, the temperature of the last nodes is considered the outlet temperature of the streams, as $T_{c,n} = T_{c,out}$ and $T_{h,n} = T_{h,out}$. For the sake of clarity, a simpler schematic of the parallel-flow configuration is shown in Figure 4.23.

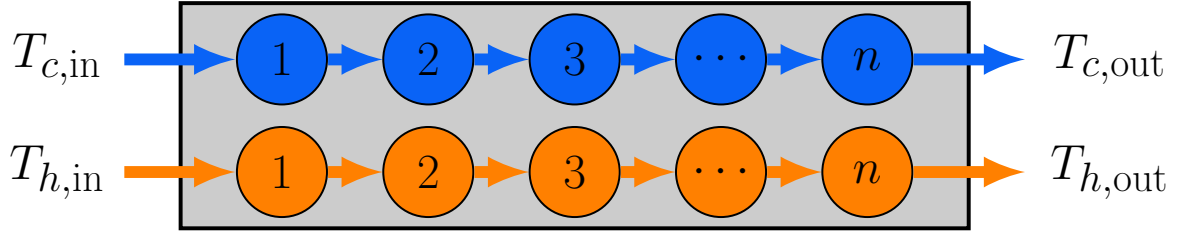


Figure 4.23: Node division modelling approach.

The mass of each node is defined by the total mass of each stream divided by the total number of nodes (n) as

$$m_{x,i} = \frac{\rho V}{n}, \quad (4.46)$$

where V is the total volumetric capacity of the heat exchanger divided by 2 (considering cold and hot sides) and it is defined as

$$V = \frac{aWLN_p}{2}, \quad (4.47)$$

where a [m] is distance between plates, commonly called gap, L [m] and W [m] are the length and width of the plates and N_p is the number of plates. According to Figure. 4.21, the heat transfer area is the sum of all plate areas divided by the number of nodes (n). It is defined by

$$A_{tr} = \frac{LWN_p}{n}. \quad (4.48)$$

The next step in the modelling approach is to define the equation to compute U . The heat transfer processes presented are convection due to the fluid and conduction by the wall plate. For the convective heat transferred according to Chapter 3, the first step is to compute the stream's mean velocity through the heat exchanger. The fluid is spread out through the channel formed by the spaces between the plates. Then, the cross-sectional area (A_c) of this channel is the sum of all spaces. Thus, the mean velocity of the cold fluid is defined by

$$v_{m,c} = \frac{\dot{m}_c}{\rho A_{c,c}} = \frac{\dot{m}}{\rho (Wa (N_p/2))}. \quad (4.49)$$

For the hot fluid, this is instead

$$v_{m,h} = \frac{\dot{m}_h}{\rho A_{c,h}} = \frac{\dot{m}}{\rho (Wa (N_p/2))}. \quad (4.50)$$

The next value that needs to be defined is the Reynolds number (Re). According with equation (3.24), for the cold stream it is given by

$$Re_c = \frac{\rho v_{m,c} D_h}{\mu}, \quad (4.51)$$

and for hot stream as:

$$Re_h = \frac{\rho v_{m,h} D_h}{\mu}, \quad (4.52)$$

where D_h [m] is the hydraulic diameter, which depends of the shape of the channel. For a very wide rectangular channel, where $W \gg a$, it is defined as $D_h = 2a$ [7]. The Nusselt number for the hot stream (Nu_h) is defined using equation (3.29) and for cold stream (Nu_c) with equation (3.30). Thus, the convection heat transfer coefficient for the cold stream is

defined by

$$U_{cv,c} = \frac{Nu_c k_c}{D_h}, \quad (4.53)$$

and for hot stream as:

$$U_{cv,h} = \frac{Nu_h k_h}{D_h}, \quad (4.54)$$

where k [W/mK] is the thermal conductivity of the fluid.

The conduction heat transfer that occurs in the plate is defined by equation (3.40) as

$$U_{cd} = \frac{k_p}{w_p}, \quad (4.55)$$

where k_p [W/mK] is the thermal conductivity of the plate material and w_p [m] is the thickness of the plates. Finally, using the electric to heat transfer analogy, U is obtained adding the analogue resistances connected in series as

$$U = \frac{1}{\frac{1}{U_{cv,c}} + \frac{1}{U_{cd}} + \frac{1}{U_{cv,h}}}, \quad (4.56)$$

The definition of the heat exchanger parameters is the last step in the modelling process. The detailed parameters for the dynamic thermal model defined by equations (4.44) and (4.45) are usually not provided by manufacturers of industrial heat exchangers. Nevertheless, some data sheets offer some values such as the size, maximum flow rate, and plate material type. This information is helpful to estimate the required parameters. Using the data sheet of a gasketed plate heat exchanger manufactured by HRS® [9], the details of the model S600+ are used to define the parameters of the dynamic thermal model (see Appendix C). The plate material is stainless steel and both streams are water.

The dynamic thermal model described by equations (4.44) and (4.45) has been implemented in MATLAB/Simulink using s-functions. All thermophysical characteristics are temperature dependent. Therefore, a look up table with their values at different temperatures are defined. These values are provided in [7]. The system is solved for constant temperature and mass flow rate inputs. The simulation results are shown in Figure 4.24. The cold and hot mass flow rates are defined as $\dot{m}_h = 40$ kg/s and $\dot{m}_c = 30$ kg/s, the input temperatures as $T_{h,in} = 90^\circ\text{C}$ and $T_{c,in} = 25^\circ\text{C}$. The number of nodes for this simulation is 10. The temperature nodes' initial conditions are 90°C and 25°C for the hot and cold streams, respectively. The cold stream achieves an output temperature of 58°C and the hot stream decreases to 65°C . Figure 4.24b shows the temperature of all nodes.

The model can capture the temperature variations of both streams. To this end input temperatures and mass flow rates are modified at different moments. Figure 4.25 shows the response of the system under these variations. Similar initial conditions are established for both streams. The node temperatures of the hot stream are presented in Figure 4.26a. As it can be observed, the fluid temperature is gradually changing from the value of $T_{h,in}$ to the temperature of the last node, which represents the output temperature of the stream. A similar behaviour is exhibited by the cold stream (see Figure 4.26b).

4.3. Heat exchangers

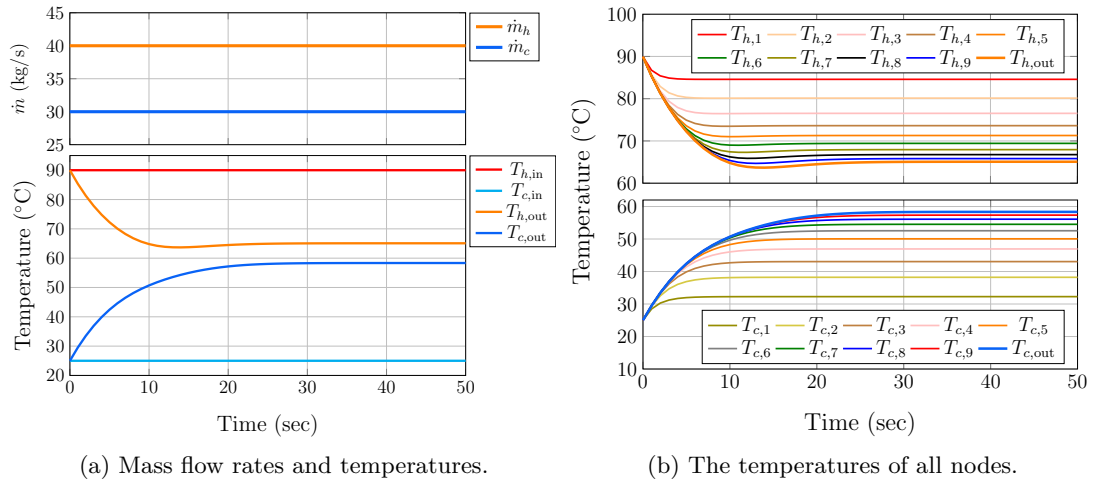


Figure 4.24: Simulation results of the parallel-flow configuration of flat plate heat exchanger with $n = 10$.

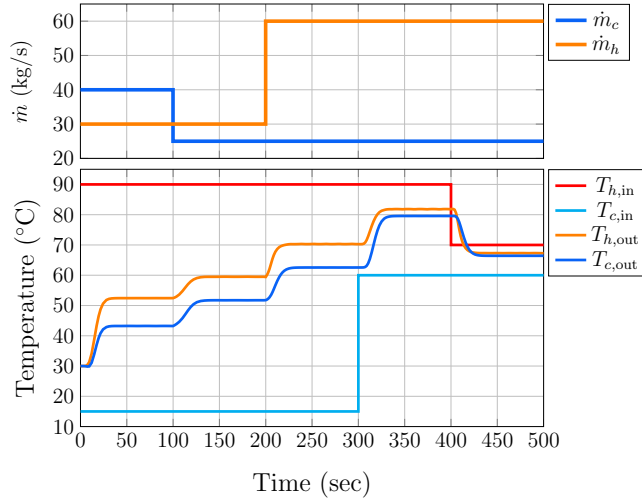


Figure 4.25: Flat plate heat exchanger response under mass flow rate and input temperature variations.

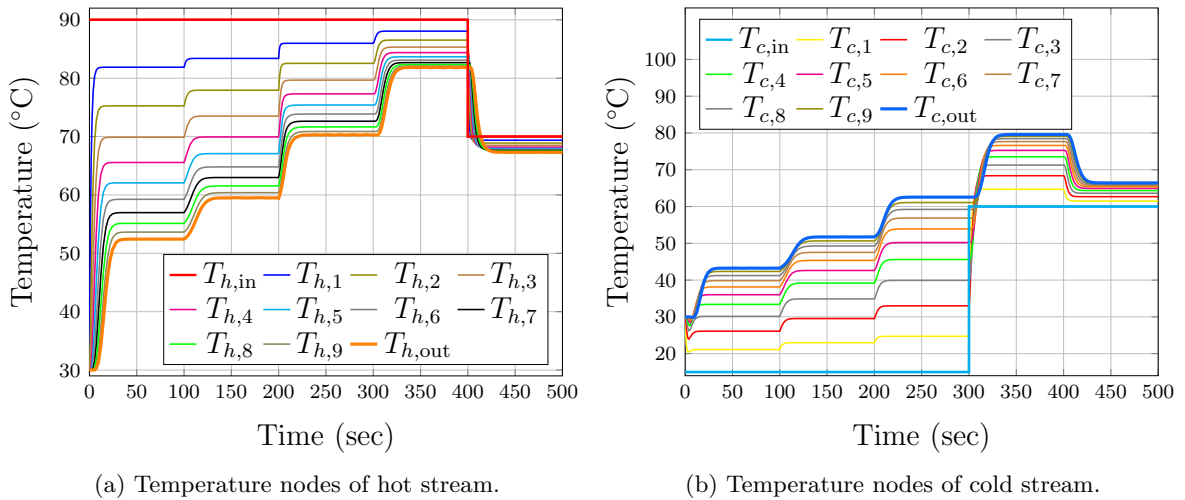


Figure 4.26: Input and internal temperatures of heat exchanger under mass flow rate variations.

The selection of the number of nodes depends on a trade-off between accuracy and the computation time. There is no rule of thumb to select this number. The type of analysis and the computing resources may determine the number of nodes required. For instance, a simulation with high accuracy requires at least 30 nodes. This value is suggested based on the comparison between model simulations with a different number of nodes under the same conditions. Figure 4.27 shows the simulation of the heat exchanger with three different number of nodes: 30, 50 and 100. As it can be observed, there is a difference less than 0.3°C between the simulation result of the last node of the two systems 30 and 100 nodes. This discrepancy may be considered within the tolerance of a temperature sensor measurement. It means that a division of 30 nodes offers the same accuracy of real system instrumentation. Figure 4.27 presents the output temperatures of the flat plate heat exchanger, the subscript of the plots stand for the stream (cold or hot) and the number of nodes.

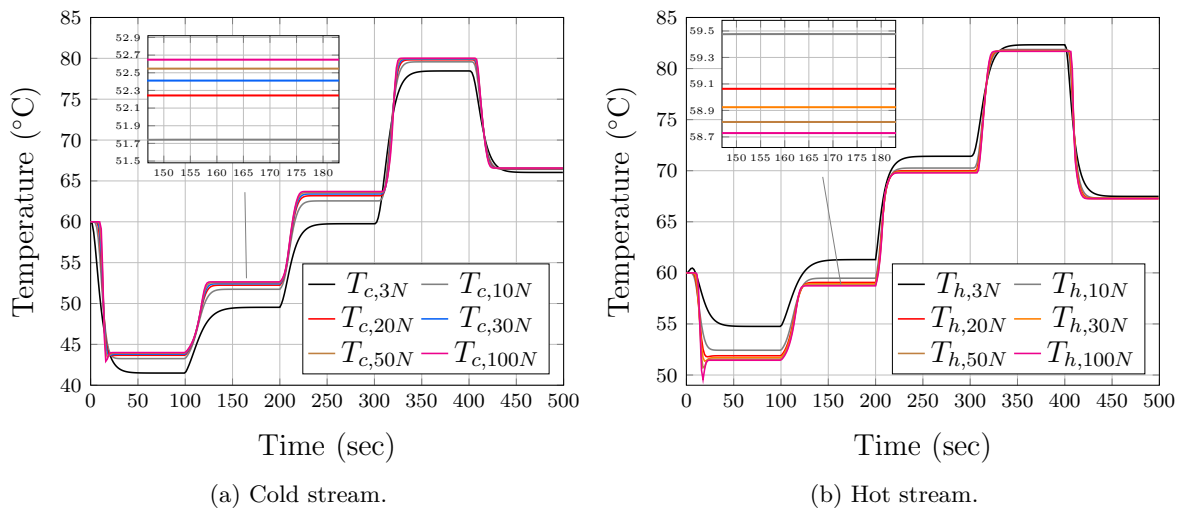


Figure 4.27: Output temperatures (T_c and T_h) of flat plate heat exchanger divided into 3, 10, 20, 30, 50 and 100 nodes.

Verification

The non-linear model defined by equations (4.44) and (4.45) is verified through comparison with Apros. A flat plate heat exchanger with the same parameters (see Appendix C) is built-in in Apros. Figure 4.28 shows the model already available in the Apros' library. The name of this element is *plate_heat_exchanger*.

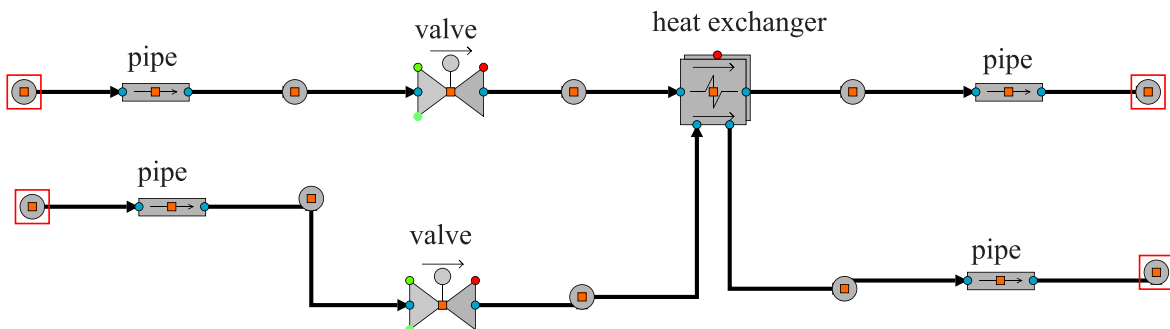


Figure 4.28: Flat plate heat exchanger implementation in Apros.

4.3. Heat exchangers

Simulations under the same operating conditions are carried out to verify the accuracy of the model. Similarly, as with the model implemented in MATLAB/Simulink, the flat plate heat exchanger element of Apros has the functionality to define the number of calculation nodes. This characteristic allows making comparisons with the same number of nodes in both software engines. A comparison is addressed with $n = 3$, $n = 10$ and $n = 30$. This way, the models defined by equations (4.44) and (4.45) are described by 6, 20 and 60 ODEs, respectively. Figure 4.29 shows simulation results for both platforms under the same conditions of mass flow rates and input temperatures. Subscripts 'M' and 'A' stand for Apros and MATLAB results, respectively.

The three models (3, 10 and 30 nodes) show a slight difference during the transient response when the conditions are modified. Nevertheless, once steady-state is achieved, a good agreement irrespective of the number of nodes is obtained. The model with three nodes shows the best agreement between MATLAB and Apros simulations during the transient response. This is mainly noticeable in the hot stream (orange trace). When the nodes are increased to 10 and 30 (see Figures 4.29c and 4.29d), the response becomes faster, provoking slight differences during the transient response. On the other hand, Figure 4.29d shows the comparison between MATLAB and Apros simulations of the 30 nodes model which presents the best agreement in steady-state when there are no changes in the system inputs. The differences in the steady-state regime for the three model comparisons vary with the operating conditions. Nevertheless, the most consistent behaviour is shown by the model of 30 nodes.

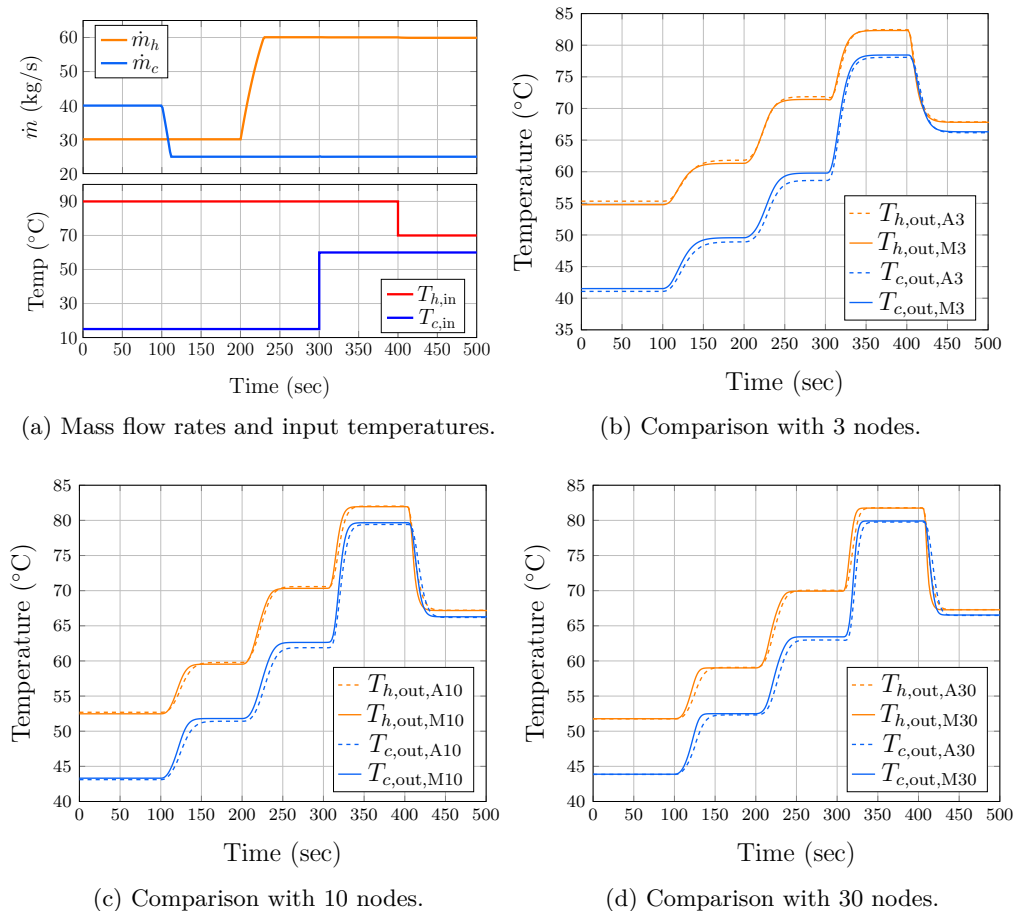


Figure 4.29: Comparison between MATLAB (M) and Apros (A) simulation results of the flat plate heat exchanger with different number of nodes.

Shell-and-tube heat exchanger (parallel-flow)

A shell-and-tube heat exchanger contains a large number of tubes located inside a shell. Usually, the cold stream flows through the tubes and the hot stream through the shell. The fluid in the tube side is spread out through several tubes. Thus, the heat transfer process occurs through the tube walls. A simple scheme of the heat exchanger is shown in Figure 4.30. Inlets and outlets locations indicate a parallel flow configuration. Baffles are located to support the tubes and they also contribute to increasing the turbulence in the shell side flow. There could be heat exchangers with more than one shell-and-tube pass, which means a more considerable amount of heat is being transferred. For the sake of clarity, the most straightforward configuration with only one shell pass is considered.

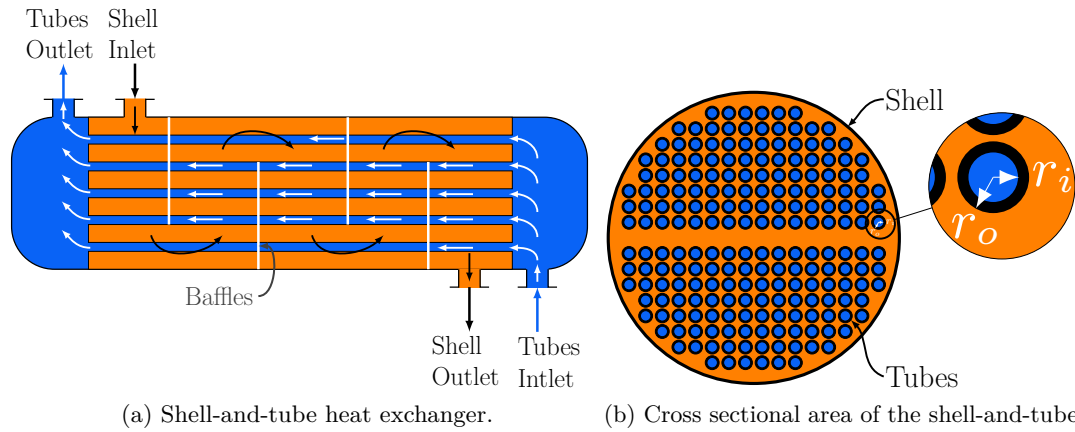


Figure 4.30: Shell-and-tube heat exchanger with one shell pass.

Similar to the analysis done for the flat plate heat exchanger in the previous subsection, the steps of the modelling approach are followed to obtain the dynamic thermal model of the shell-and-tube heat exchanger. Energy balance is applied. The same assumptions are made: there are no energy losses and the potential and kinetic energy of the fluids are neglected. The subscripts 't' and 's' stand for tubes and shell side, respectively. Being a parallel flow configuration, the energy stored in each node is defined by

$$m_{t,i}c_{p,ti}\dot{T}_{t,i} = \dot{m}_t c_{p,ti} (T_{t,(i-1)} - T_{t,i}) + U_{st}A_{tr} (T_{s,i} - T_{t,i}), \quad (4.57)$$

$$m_{s,i}c_{p,si}\dot{T}_{s,i} = \dot{m}_s c_{p,si} (T_{s,(i-1)} - T_{s,i}) + U_{st}A_{tr} (T_{t,i} - T_{s,i}), \quad (4.58)$$

where T [°C] is the temperature, m [kg] the mass, c_p [J/kg K] the specific heat for each fluid, U_{st} [W/m²K] is the overall heat transfer coefficient and A_{tr} [m²] is the transfer area. There are two different transfer areas: internal and external fluid. These heat exchange surfaces are illustrated in Figure 4.31. The internal area A_{itr} is related to the convection heat transfer coefficient due to the fluid inside the tubes. Additionally, the shell fluid transfers heat through the external surface of the tubes A_{etr} . The internal area for each node is defined by

$$A_{itr} = \frac{2\pi r_i N_t L_t}{n}, \quad (4.59)$$

where r_i [m] is the internal radius, N_t is the number of tubes and L_t [m] is the length of tubes,

4.3. Heat exchangers

and n the number of the nodes. Similarly, the external surface is given by

$$A_{\text{etr}} = \frac{2\pi r_o N_t L_t}{n}, \quad (4.60)$$

where r_o [m] is the external radius of the tubes.

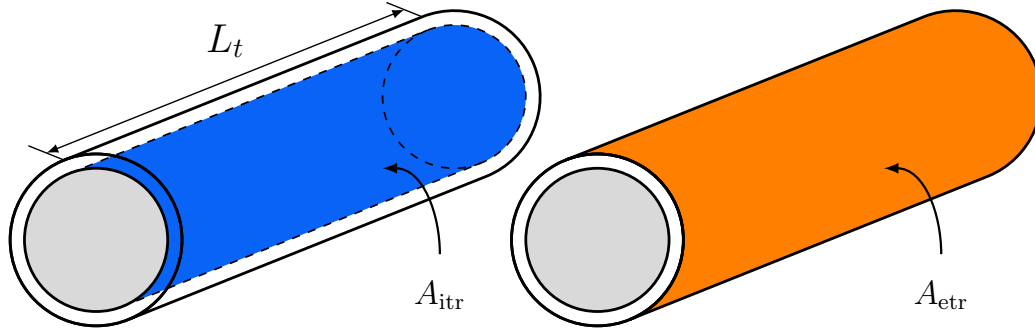


Figure 4.31: Internal and external heat transfer areas of the tubes.

The mass of fluid inside the tubes is defined by the sum of all tube's volume times the fluid density and divided by the number of nodes as

$$m_{t,i} = \frac{\rho V_t}{n} = \frac{\rho \pi r_i^2 l_t N_t}{n}, \quad (4.61)$$

Similarly, the mass of the fluid in the shell is defined by

$$m_{s,i} = \frac{\rho A_f L_s}{n}, \quad (4.62)$$

where L_s [m] is the length of the shell and A_f [m²] is the flow area of the shell side.

The next step is to compute U_{st} analysing the internal geometry of the shell-and-tube heat exchanger. Mean velocities should be calculated by determining the channel's cross-sectional area through which the fluid is flowing. On the tube side, the fluid is spread out through each tube. Therefore, the mean velocity is calculated using the sum of the tube cross-sectional areas as

$$v_{m,t} = \frac{\dot{m}_t}{\rho \pi r_i^2 N_t}, \quad (4.63)$$

where \dot{m}_t [kg/s] is the mass flow rate of the tubes side.

The mean velocity for the shell side considers the area through which the fluid is getting into the heat exchanger, which depends on the shell's shape. Due to the irregular shape of the shell and how the tubes are settled, this calculation is complex. Nevertheless, its value usually is provided by manufacturers, as the flow area (A_f). This parameter simplifies the calculation of the mean velocity and is helpful to obtain the hydraulic diameter used for the Reynolds number computation.

Two of the most common tube arrangements, namely square and triangular, are presented in Figure 4.32. As it can be seen, a geometry analysis should be done and distances of the tubes' arrangement are necessary. Thus, the value of A_f facilitates the computation of U_{st} .

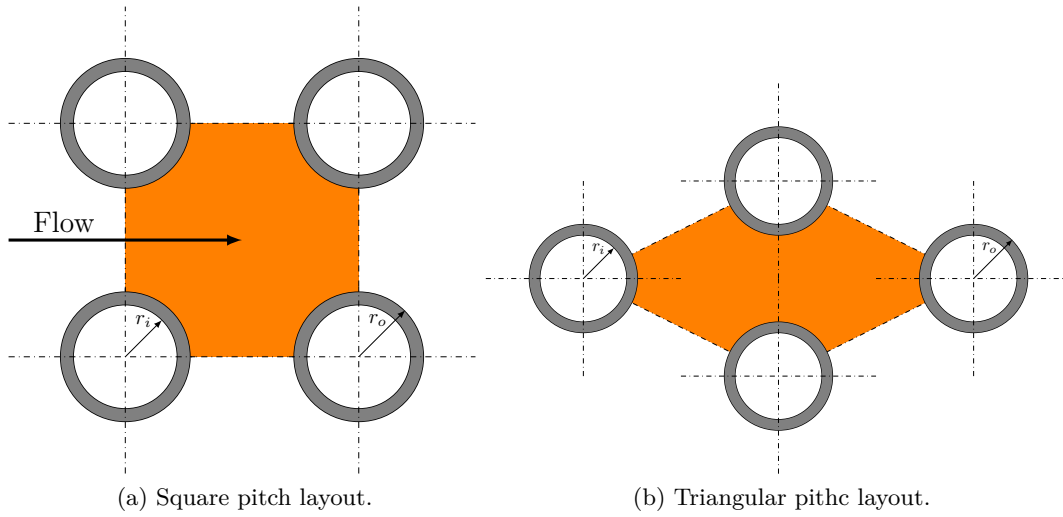


Figure 4.32: Types of tubes arrangement of shell-and-tube heat exchanger.

The mean velocity for the shell side is defined by

$$v_{m,s} = \frac{\dot{m}}{\rho A_f}, \quad (4.64)$$

where \dot{m}_s [kg/s] is the mass flow rate in the shell.

The Reynolds number for each fluid, is calculated using the hydraulic diameter D_h according to equation (3.24). This value is determined from the shape of the channel as

$$D_h = \frac{4A_c}{P_w}, \quad (4.65)$$

where A_c [m²] is the cross-sectional area and P_w [m] is the wetted perimeter of the cross-section. The latter term means the perimeter of the cross-sectional area of a channel in contact with the fluid (see Figure 4.33). For the tube side, D_h for a single tube is defined by

$$D_{t,h} = \frac{4\pi r_i^2}{2\pi r_i} = 2r_i. \quad (4.66)$$

For the shell side, it is necessary to compute the shell radius, which is related to A_f . Since neither the cross flow area nor the diameter are appropriately defined, a fair approximation of the hydraulic radius can be obtained by considering the total flow area for both sides as

$$A_{f,s+t} = A_t + A_s, \quad (4.67)$$

where A_t [m²] is the sum of all cross-sectional area of the tubes given by

$$A_t = \pi r_o^2 N_t. \quad (4.68)$$

Assuming a circular shape of the shell, the radius is computed by

$$r_{h,s} = \sqrt{\frac{A_{f,s+t}}{\pi}}. \quad (4.69)$$

Wetted perimeter (P_w) for the flow area of the shell is defined by the sum of shell and

4.3. Heat exchangers

external tubes perimeters, which are the surfaces in contact with the shell fluid (see Figure 4.33), by

$$D_{h,s} = \frac{2A_f}{P_{w,s}} = \frac{4A_f}{2\pi(2r_o N_t + 2r_{h,s})}. \quad (4.70)$$

The Reynolds number is calculated using equation (3.31). For the fluid inside the tubes: this is

$$\text{Re}_t = \frac{\rho v_t D_{h,t}}{\mu}, \quad (4.71)$$

and for the fluid in the shell: it is

$$\text{Re}_s = \frac{\rho v_t D_{h,s}}{\mu}. \quad (4.72)$$

The tube side usually is used for the cold stream that is heated by the hot stream. Thus, the Nusselt number is calculated using equation (3.29).

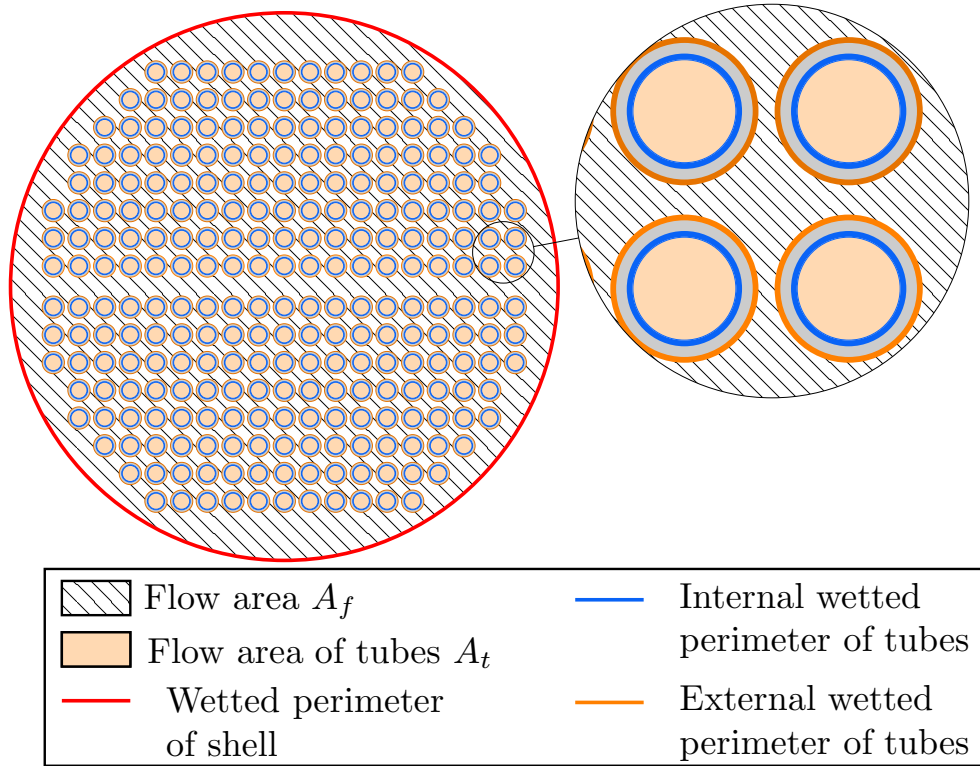


Figure 4.33: Flow areas and wetted perimeters of shell-and-tube heat exchanger.

The convection heat transfer that occurs in the tubes is given by

$$U_{cv,t} = \frac{\text{Nu}_t k_t}{D_{h,t}}, \quad (4.73)$$

where k_t [W/mK] is the thermal conductivity of the fluid. For the hot stream inside the shell, its Nusselt number is computed by equation (3.30) and its convection heat transfer coefficient is defined by

$$U_{cv,s} = \frac{\text{Nu}_s k_s}{D_{h,s}}, \quad (4.74)$$

where k_s [W/mK] is the thermal conductivity of the fluid. The conduction heat transfer

coefficient in the wall of the tubes is defined by equation (3.41) as

$$U_{cd} = \frac{k_m}{\ln\left(\frac{r_o}{r_i}\right) r_o}, \quad (4.75)$$

where k_m [W/mK] is the thermal conductivity of the tube material. Then, the overall heat transfer coefficient for the shell-and-tube heat exchanger U_{st} is obtained by

$$U_{st} = \frac{1}{\frac{1}{U_{cv,t}} + \frac{1}{U_{cd}} + \frac{1}{U_{cv,s}}}. \quad (4.76)$$

However, each heat transfer coefficient affects different surface areas of the tubes. The total resistance is calculated multiplying each coefficient by its transfer area using the thermal resistance concept presented in Chapter 3. Figure 4.34 shows the heat transfer process for the surface conditions between the shell and tube fluids. Each thermal resistance is defined according to equation (3.51). Thus, the total resistance is given by

$$R_T = \frac{1}{A_{itr}U_{cv,t}} + \frac{1}{A_{etr}U_{cd}} + \frac{1}{A_{etr}U_{cv,s}}.{}^6 \quad (4.77)$$

Hence, equation (3.49), which defines the heat transferred, is used to re-write the system equations (4.57) and (4.58) as

$$m_{t,i}c_{p,ti}\dot{T}_{t,i} = \dot{m}_t c_{p,ti} (T_{t,(i-1)} - T_{t,i}) + \frac{(T_{s,i} - T_{t,i})}{R_{T,i}}, \quad (4.78)$$

$$m_{s,i}c_{p,si}\dot{T}_{s,i} = \dot{m}_s c_{p,si} (T_{s,(i-1)} - T_{s,i}) + \frac{(T_{t,i} - T_{s,i})}{R_{T,i}}. \quad (4.79)$$

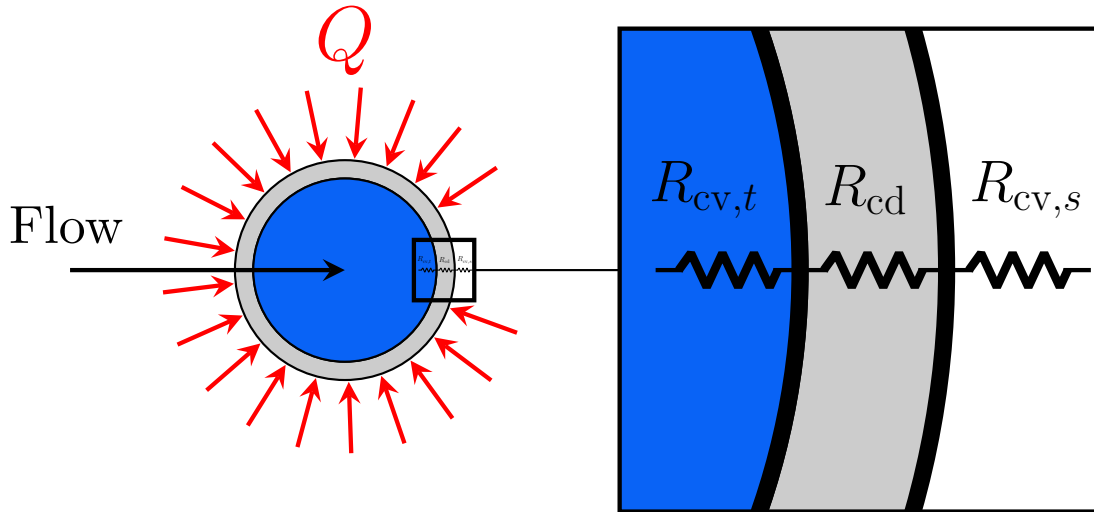


Figure 4.34: Thermal resistances of heat transfer coefficient of shell-and-tube heat exchanger.

⁶An alternative equation is discussed in Appendix E

4.3. Heat exchangers

The definition of the heat exchanger parameters is the last step in the modelling process. The shell-and-tube heat exchanger parameters used for simulations are taken from [10]. The model *G 270* manufactured by HRS[®] is chosen (see Appendix C). The main use of this shell-and-tube type of heat exchanger is to transfer heat from hot gases to cold fluid; for instance, the exhaust gas of a CHP unit or condensing vapour stream. The latter cases might present phase change of the gas due to the condensation, which means latent heat is transferred. For this operation mode, the gas flows through the tubes (hot stream) and the shell tube is used for the cold fluid. Nevertheless, the shell-and-tube heat exchanger may also be used for applications where no change in phase is presented and just sensible heat is transferred. When only liquids are considered, the hot and cold streams flow through shell-and-tube, respectively. This case is addressed in this work and both streams consider water.

Similarly to the flat plate heat exchanger, the shell-and tube heat exchanger model is implemented in MATLAB/Simulink by means of s-functions (see Appendix A). The simulation results with constant input temperatures and mass flow rates are presented in Figures 4.35. The cold stream is flowing through the tubes with $\dot{m}_t = 50$ kg/s and $T_{t,in} = 5^\circ\text{C}$. The hot stream through the shell has a $\dot{m}_s = 30$ kg/s and $T_{s,in} = 75^\circ\text{C}$. The number of nodes (N_t) for these simulations is 10. The initial conditions of all nodes within the same side are the inlet temperature of the stream.

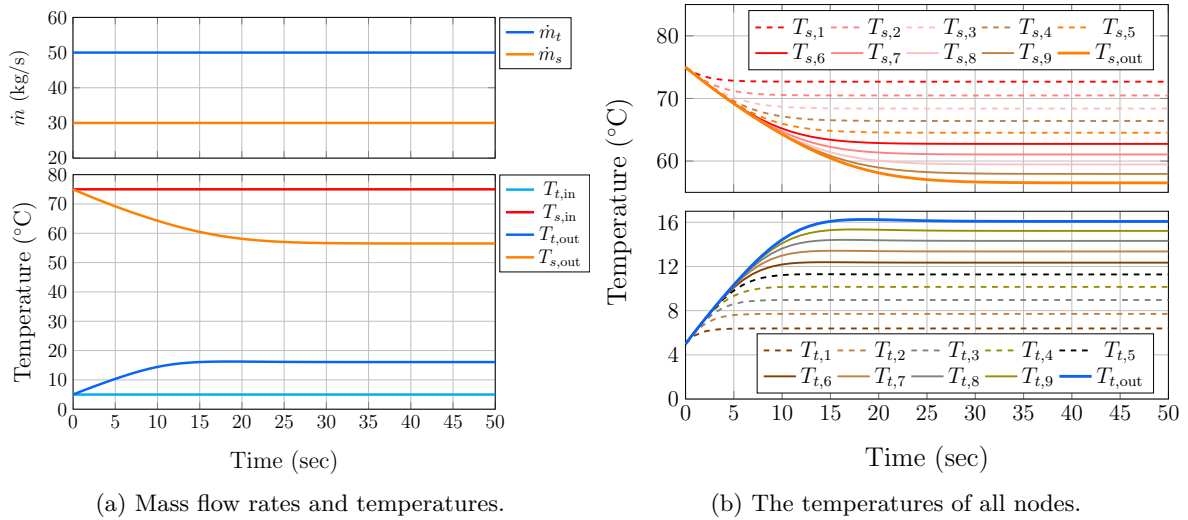


Figure 4.35: Simulation results of shell and tube heat exchanger with $n = 10$.

Variations of input temperatures and mass flow rates are implemented in the model. The transient response due to these variations is shown in Figure 4.36. The same initial conditions are established for both streams, which resembles the real situation where the streams achieve a thermal equilibrium during the out of service period. Figure 4.37 shows the solution of all ODEs defined by the model system.

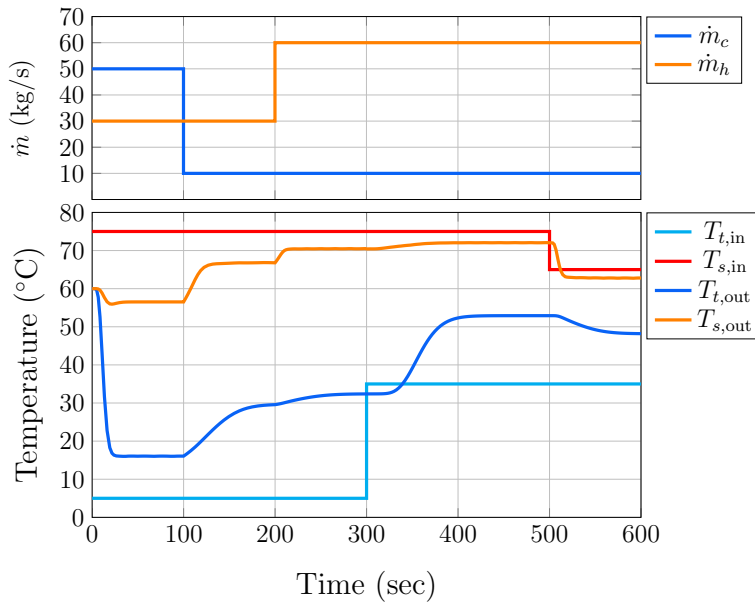
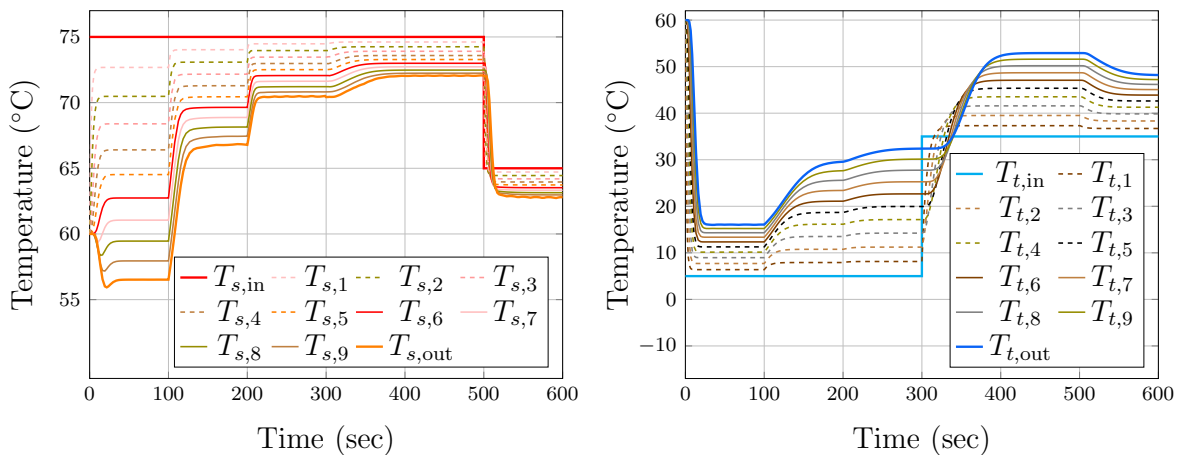


Figure 4.36: Top: mass flow rate variations. Bottom: Simulation results of the shell-and-tube heat exchanger under variations of input temperature and mass flow rates.



(a) Temperature nodes of fluid in tube side.

(b) Temperature nodes of fluid in shell side.

Figure 4.37: Input and internal temperatures of heat exchanger.

Verification

The verification of the shell-and-tube heat exchanger model is carried out using the Apros' element called *tube_heat_exchanger_1*. Like the flat plate heat exchanger, the number of nodes for this comparison is set to 3, 10 and 30. The models in both platforms are subjected to the same conditions. Input temperatures and mass flow rates are modified during the simulations. Figure 4.38 shows these comparisons. Subscripts 'A' and 'M' stand for Apros and MATLAB results, respectively. Subscripts 3, 10 and 30 are the number of nodes of the system.

The results present very slight differences between the MATLAB/Simulink and Apros simulation results. Nevertheless, the developed model has a faster response during changes in conditions, creating a small mismatch during these periods. This can be observed in Figure 4.38 (d) in the simulation periods of 300 to 350 secs and 700 to 750 secs. Conversely, the

4.3. Heat exchangers

model with 3 nodes shows a smaller error since its slow response during the same conditions. Nevertheless, during steady-state, the response of the system with 30 nodes is equal for both models.

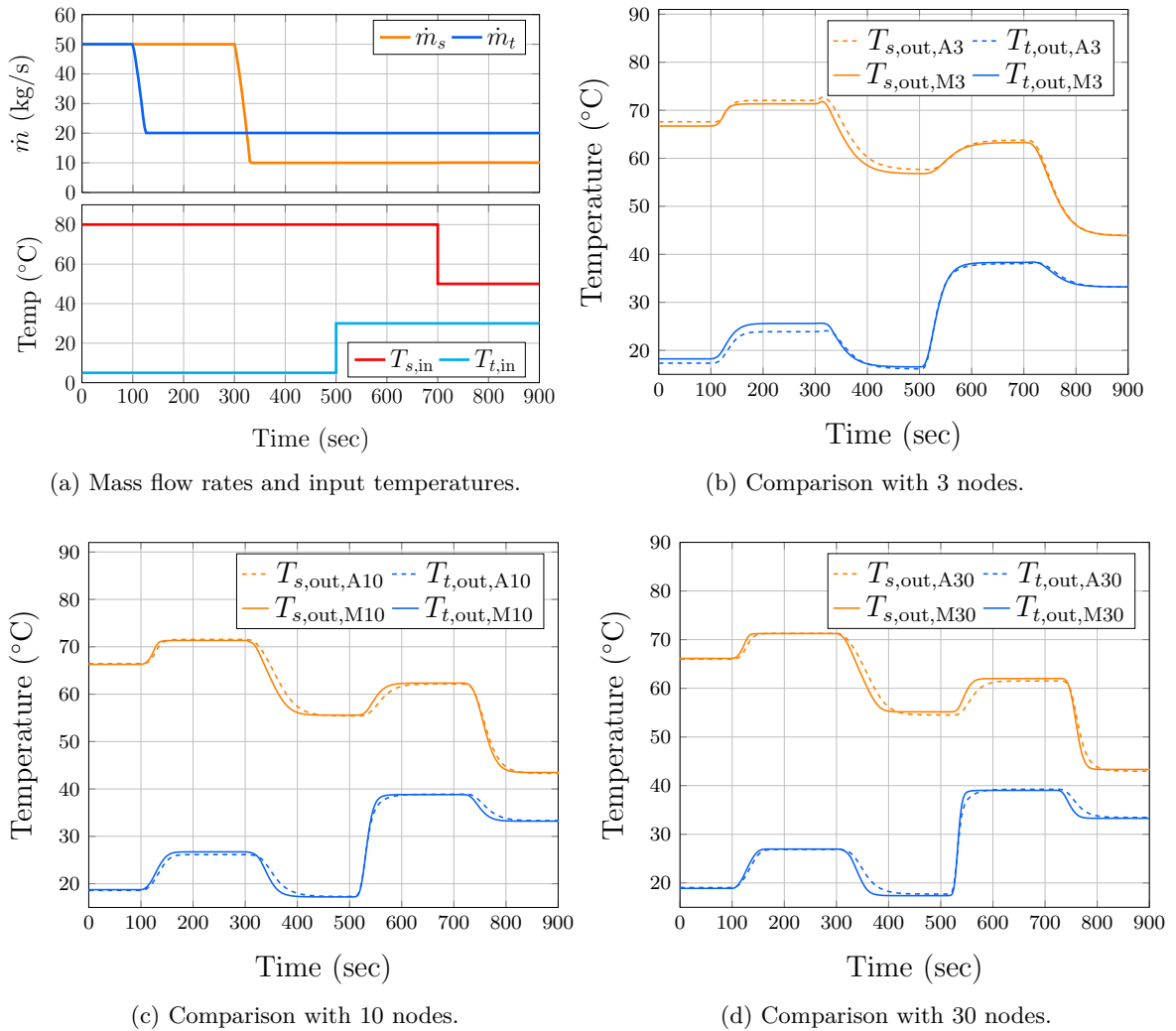


Figure 4.38: Comparison between MATLAB (M) and Apros (A) simulation results of the shell-and-tube heat exchanger with different number of nodes.

4.3.2 Counter-flow heat exchanger

In the counter-flow heat exchanger configuration, the inputs of the streams are at opposite ends and thus have opposite directions. The hot stream transfers energy input to the cold stream outlet at the same node of the model as illustrated in Figure 4.39a. Typical output temperatures of a counter flow heat exchanger are shown in Figure 4.39b. Unlike the parallel flow configuration, the cold stream's outlet temperature may be higher than the outlet temperature of the hot stream.

For the modelling purpose, the switch of one stream's direction must be implemented in the energy balance equations compared to a parallel configuration. Therefore, a different arrangement of the stream nodes needs to be applied. Figure 4.23 shows the node division with an inverted numeration for the hot stream nodes. The energy balance implementation considers this new order to develop the set of equations describing the heat exchanger. The

switch of hot stream direction implies that the output temperature of this stream is in the same node where the input of the cold stream is. Thus, the solution of the first node provides the output temperature of the hot stream as $T_{h,1} = T_{h,out}$. Conversely, the cold stream directions remains equal. Its output is defined by the last node as $T_{c,n} = T_{c,out}$.

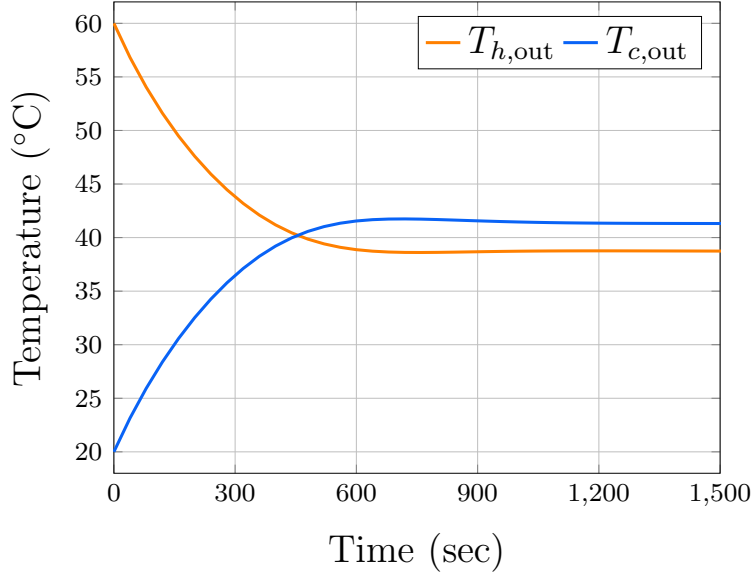
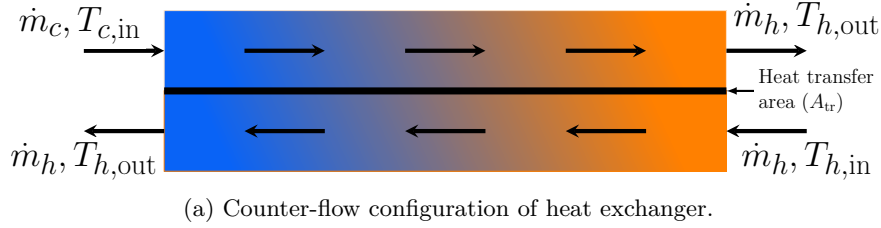


Figure 4.39: Stream directions and output temperature of counter-flow heat exchanger.

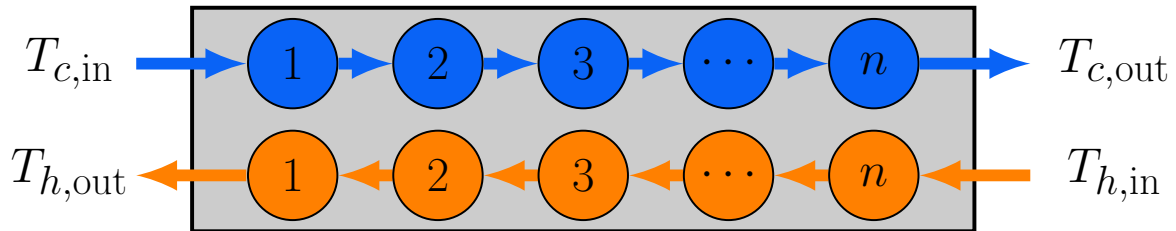


Figure 4.40: Node division of counter-flow configuration of heat exchanger.

The energy balance of the counter-flow heat exchanger for each node ($i = 1, 2, \dots, n$) is described by two general equations as

$$\dot{m}_{c,i} c_{p,ci} \dot{T}_{c,i} = \dot{m}_c c_{p,ci} (T_{c,(i-1)} - T_{c,i}) + U_i A_{tr} (T_{h,i} - T_{c,i}), \quad (4.80)$$

$$\dot{m}_{h,i} c_{p,hi} \dot{T}_{h,i} = \dot{m}_h c_{p,hi} (T_{h,(i+1)} - T_{h,i}) + U_i A_{tr} (T_{c,i} - T_{h,i}). \quad (4.81)$$

The difference regarding the parallel flow configuration defined by equations (4.44) and (4.45) is the sequence of the input temperatures on each node of the hot stream. As the next node contributes to the heat flow instead of the previous one, the input temperature's subscript in the first term of the ODE is $i + 1$.

4.3. Heat exchangers

For the sake of clarity, the energy balance of the first and last nodes are developed:

$$m_{c,1}c_{p,c1}\dot{T}_{c,1} = \dot{m}_c c_{p,c1} (T_{c,\text{in}} - T_{c,1}) + U_1 A_{\text{tr}} (T_{h,n} - T_{c,1}),$$

$$m_{h,1}c_{p,h1}\dot{T}_{h,1} = \dot{m}_c c_{p,h1} (T_{h,2} - T_{h,1}) + U_1 A_{\text{tr}} (T_{c,1} - T_{h,1}),$$

$$m_{c,n}c_{p,cn}\dot{T}_{c,n} = \dot{m}_c c_{p,cn} (T_{c,(n-1)} - T_{c,n}) + U_n A_{\text{tr}} (T_{h,n} - T_{c,n}),$$

$$m_{h,n}c_{p,hn}\dot{T}_{h,n} = \dot{m}_c c_{p,hn} (T_{h,\text{in}} - T_{h,n}) + U_n A_{\text{tr}} (T_{c,n} - T_{h,n}).$$

Flat plate heat exchanger (counter-flow)

The model of the counter-flow configuration of the flat plate heat exchanger is implemented in MATLAB/Simulink. The set of ODEs defined by equations (4.80) and (4.81) is coded through s-functions. The heat exchanger parameters are the same used for the parallel flow option (see Appendix C). Figure 4.41 shows the simulation results under the same conditions of the parallel flow configuration.

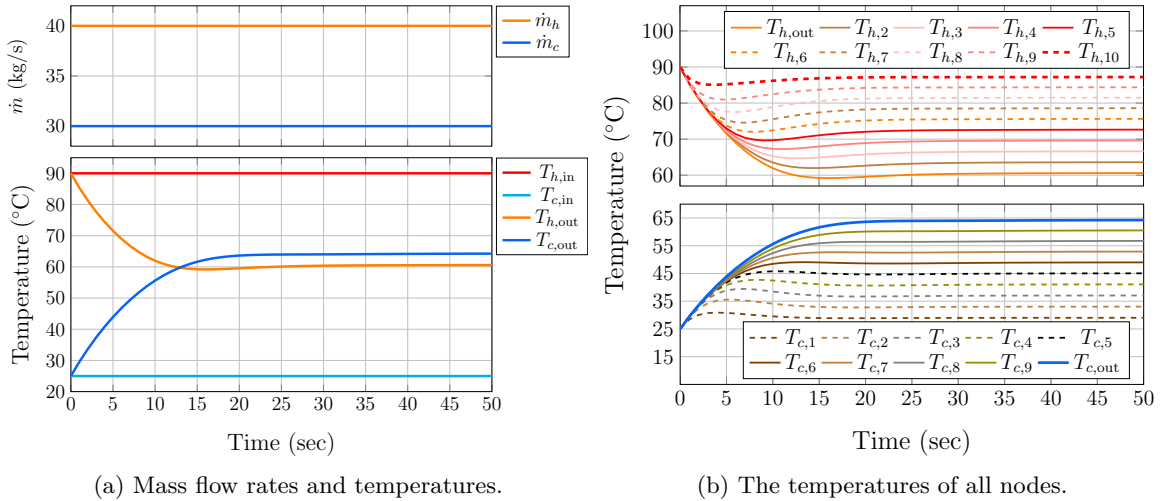


Figure 4.41: Top left: constant mass flow rates and input temperatures. Bottom left: simulation of counter-flow configuration of flat plate heat exchanger with 10 nodes. Top right: all node temperatures of hot stream. Bottom right: all node temperatures of cold stream.

To assess the model's response following modifications of its operating conditions, the cold and hot stream's mass flow rate and input temperatures are modified through time. Figure 4.42 shows the system inputs' changes and the output temperatures of the streams. The solution of all ODEs of the model are shown in Figure 4.43. All temperatures are included to show how the internal thermal behaviour dynamically responds to the changes in the mass flow rate and temperature conditions.

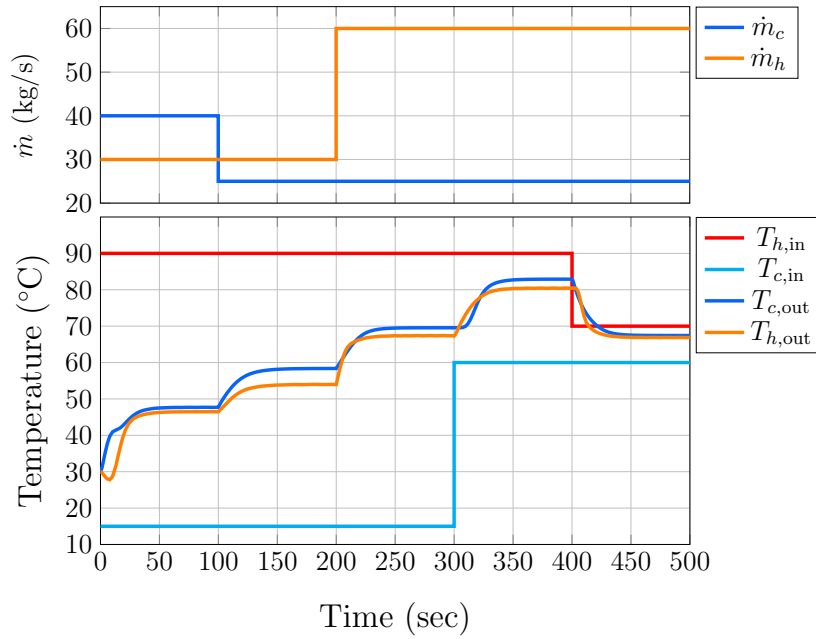
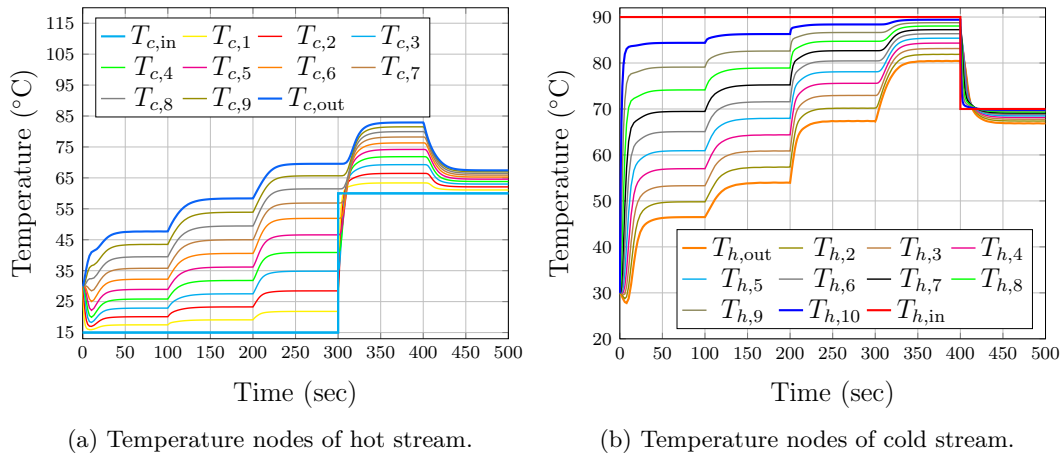


Figure 4.42: Flat plate response under mass flow rate and input temperature variations.



(a) Temperature nodes of hot stream.

(b) Temperature nodes of cold stream.

Figure 4.43: Input and internal temperatures of heat exchanger.

Verification

The counter-flow flat plate heat exchanger model is compared to a model built in Apros. The library element used for this validation is the same one used for the parallel flow, but the option *type counter- or co-current* in its properties is modified for a counter-flow configuration. Thus, no changes are implemented in the built-in model regarding the pipe and control valve connections. Different mass flow rates and input temperatures are defined for 3, 10 and 30 nodes simulations. The results are presented in Figure 4.44. Subscripts 'M' and 'A' stand for Apros and MATLAB results, respectively. As it can be seen, a better agreement is obtained with $n = 30$.

4.3. Heat exchangers

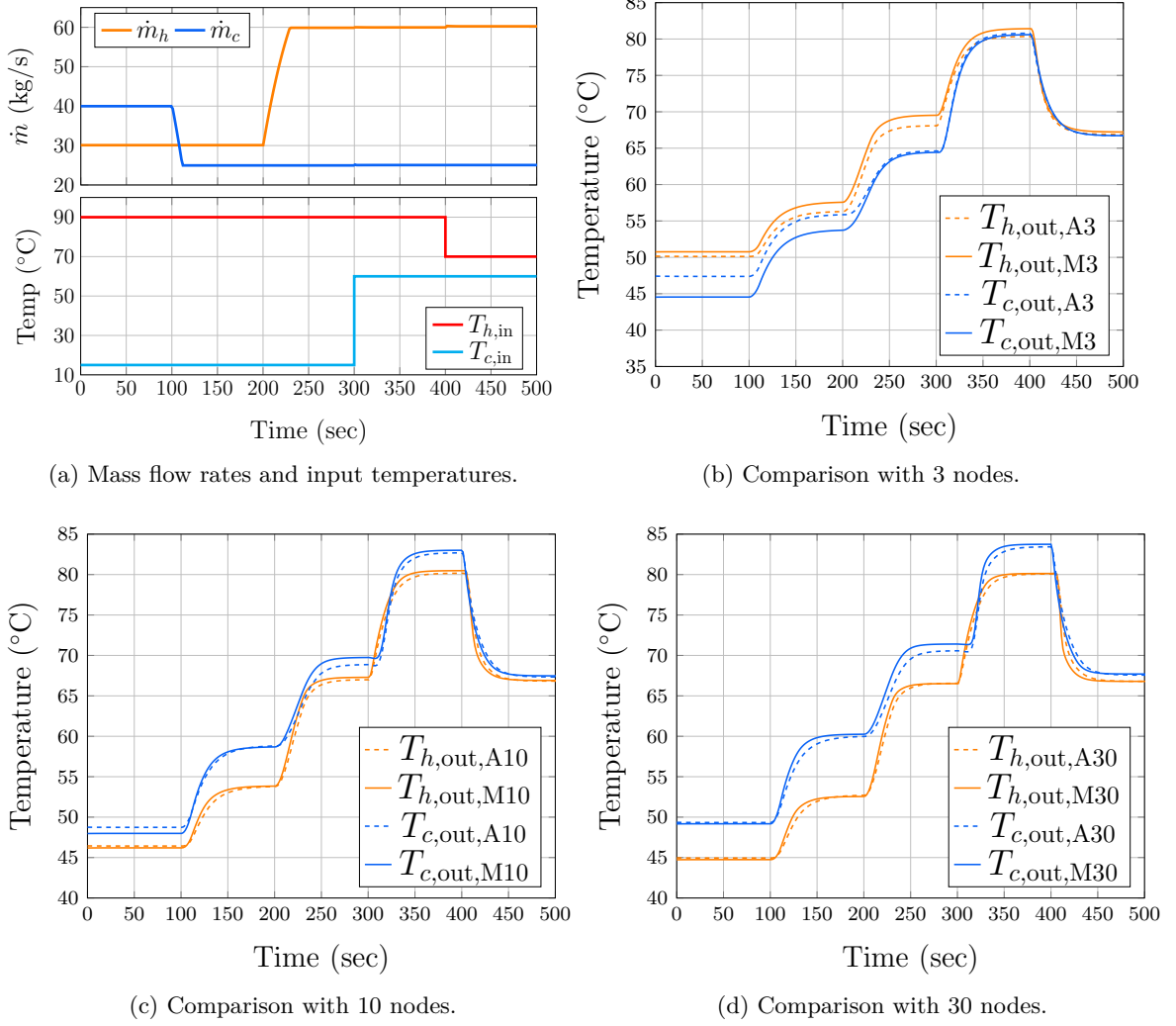


Figure 4.44: Comprison between MATLAB (M) and Apros (A) simulation results of the flat plat heat exchanger with counter-flow configuration.

Shell-and-tube heat exchanger (counter-flow)

Following the counter-flow configuration defined in Figure 4.40, the energy balance of the shell-and-tube heat exchanger is described by

$$m_{t,i}c_{p,ti}\dot{T}_{t,i} = \dot{m}_t c_{p,ti} (T_{t,(i-1)} - T_{t,i}) + U_{st}A_{tr} (T_{s,i} - T_{t,i}), \quad (4.82)$$

$$m_{s,i}c_{p,si}\dot{T}_{s,i} = \dot{m}_s c_{p,si} (T_{s,(i+1)} - T_{s,i}) + U_{st}A_{tr} (T_{t,i} - T_{s,i}), \quad (4.83)$$

where temperatures $T_{t,i}$ and $T_{s,i}$ are the inputs of the tube and shell sides, respectively. Similar to the counter-flow flat plate case, the output temperature of the hot stream, which flows through the shell side, is defined by the first node as $T_{s,1} = T_{s,out}$.

The model is implemented through s-function in MATLAB/Simulink. The parameters defined in Appendix C are used to carry out the simulations. Figure 4.45 shows the system's response under constant mass flow rates and input temperatures. These values are the same used for the parallel flow configuration. To illustrate the system's response with few nodes, the model is simulated with only 3 nodes. Figure 4.45 shows each node's temperature. As it can be observed, for the shell fluid (hot stream), the coldest node is the first ($T_{s,out}$).

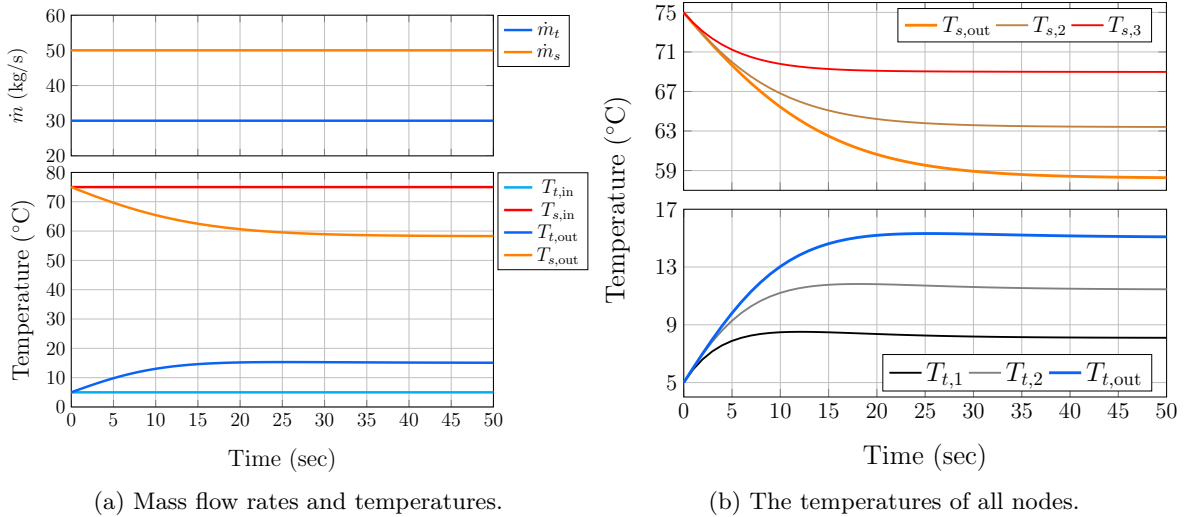


Figure 4.45: Left: mass flow rates and input and output temperatures. Right: all node temperatures of shell and tube sides.

The system is subjected to mass flow rate and input temperature variations. The simulation conditions and output temperatures are presented in Figure 4.46. A reduction in the cold mass flow rate is presented at 100 seconds, which produces an increment in both output temperatures. An increment of the mass flow rate at 200 seconds causes an increment in the output temperatures. At 300 seconds, an increment in the cold stream's input temperature causes a new increment in the outputs system. Finally, a decrement of the hot stream's input temperature produces a decrement in both output temperatures. The temperature of the six nodes of the system are shown in Figure 4.47.

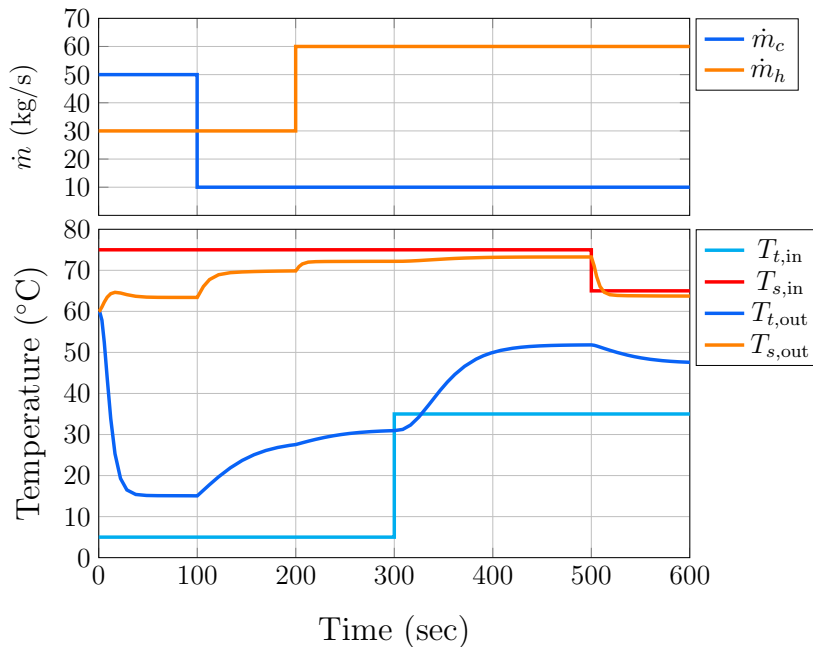


Figure 4.46: Counter-flow shell-and-tube heat exchanger response under mass flow rate and input temperature variations.

4.3. Heat exchangers

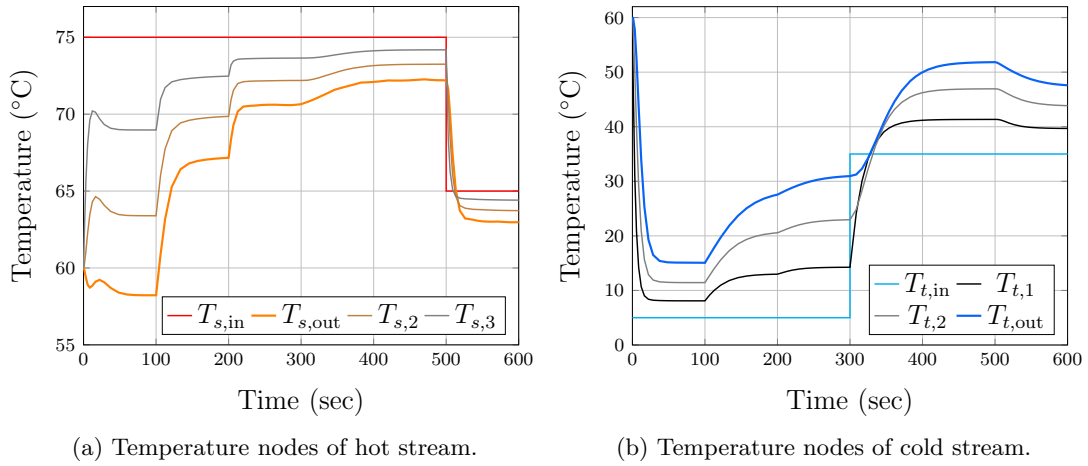


Figure 4.47: Input and internal temperatures of counter-flow shell-and-tube heat exchanger.

Verification

Finally, as it has been done for the previous heat exchangers, a comparison between the developed model and its Apros counterpart are presented in Figure 4.48. In both platforms, the number of nodes is set to 3, 10 and 30. A slightly better agreement between both simulation results is given when the system is divided into 30 nodes.

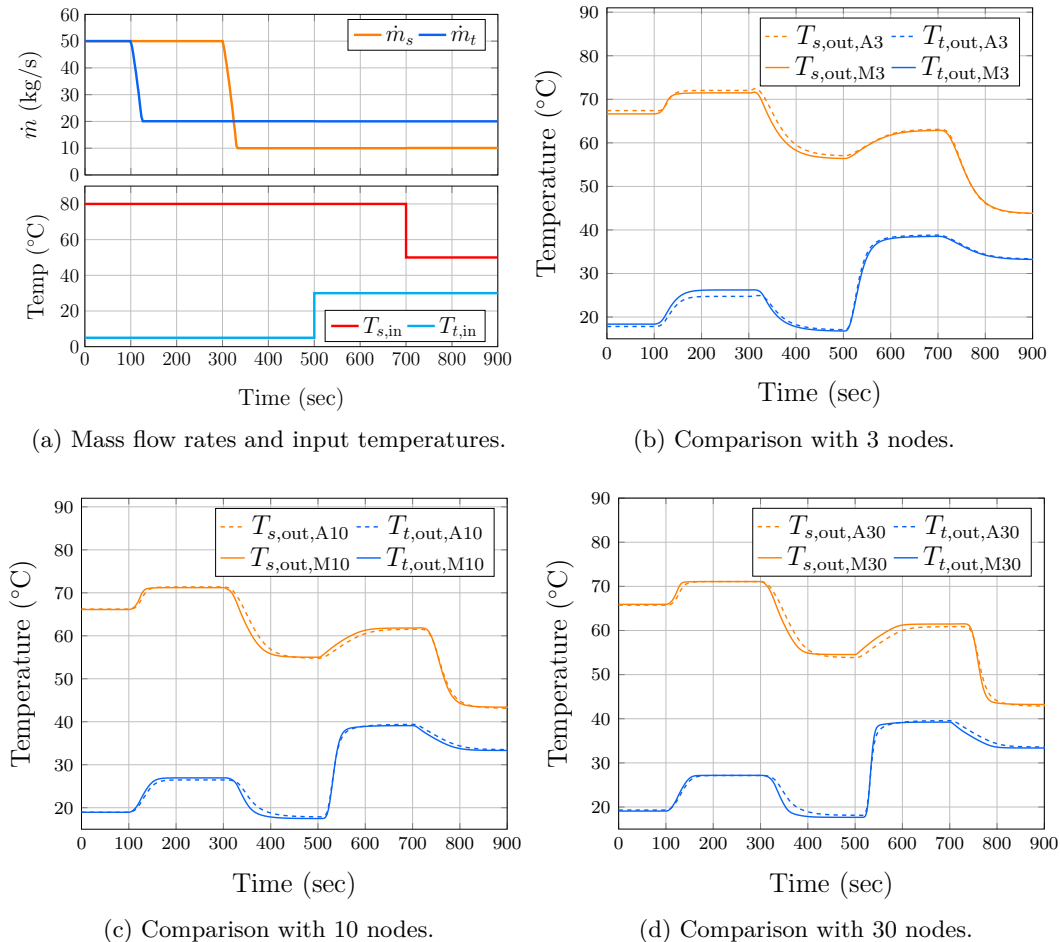


Figure 4.48: Comparison between MATLAB (M) and Apros (A) simulation results of the shell-and-tube heat exchanger with counter-flow configuration.

Counter or Parallel configuration

The counter-flow configuration of the heat exchanger, irrespective of having a flat plate or shell-and-tube arrangement, has the advantage of a higher efficiency over its parallel counterpart. This means that under the same operating conditions, a more significant amount of heat is exchanged. The counter-flow configuration allows transferring heat from the hotter node of the hot stream to the last node of the cold fluid. Thus, a higher temperature difference results in a higher rate of the transferred heat.

The dynamic model of the shell-and-tube heat exchanger is used to analyse this observation. Nevertheless, the industrial example used to validate the model has a short length (3 m), which implies a short surface area, but this offers a similar performance for both configurations. Therefore, it is necessary to increment the length of the shell-and-tube up to 15 m to illustrate the effect of adopting counter-flow configuration. This modification provides a longer distance where the fluids interact, obtaining a higher heat transfer.

Simulation of parallel and counter-flow configurations under the same conditions with $n = 30$ of the shell-and-tube heat exchanger are carried out. The mass flow rate for both water fluids is $\dot{m} = 50$ kg/s (see Figure 4.49). The heat flow Q given by the transfer process is computed using equation (3.20) and the temperatures of the fluid in the tube side as

$$Q = \dot{m}_t c_{p,t} (T_{t,\text{out}} - T_{t,\text{in}}). \quad (4.84)$$

The response of both configurations is shown in Figure 4.49a. Subscripts 'pf' and 'cf' stand for parallel and counter-flow, respectively. As it can be observed, the difference between the output temperature of the shell and tube sides in the parallel flow is about 6°C and the cold stream temperature (52.36°C) is below the hot stream temperature (57.75°C). Figure 4.49b presents the heat transferred, which is 6.8 MW for the parallel flow configuration. On the other hand, the counterflow configuration can increment the cold fluid's temperature up to 59.26°C and reduce the hot stream temperature 50.84°C . Thus, the cold stream is 6.9°C above its parallel flow counterpart. This evidences that 1.45 MW of additional heat is transferred.

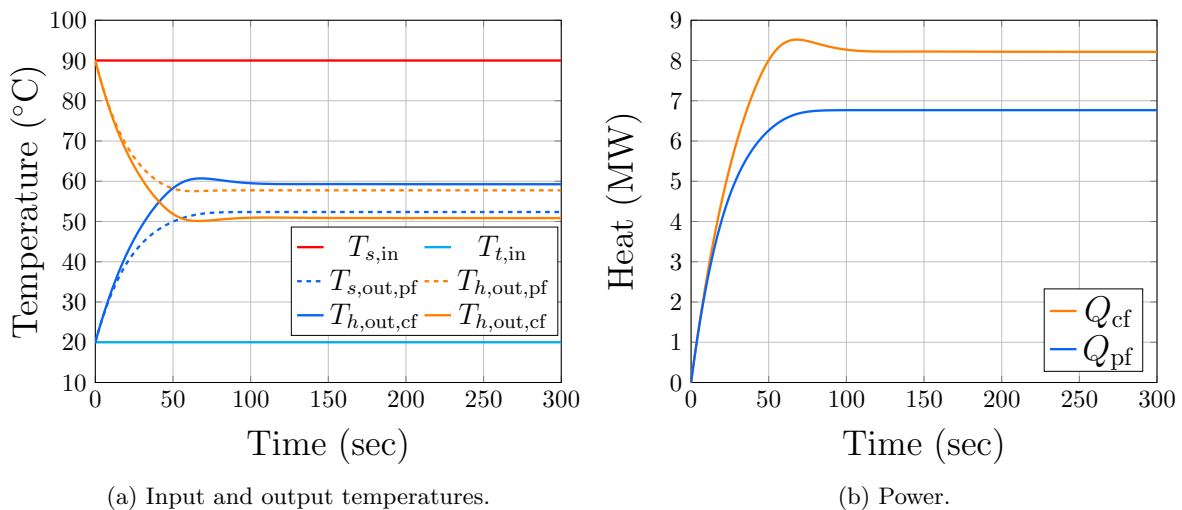


Figure 4.49: Simulation results of parallel and counter-flow configurations of shell-and-tube heat exchanger.

4.4 Thermal energy storage tanks

Dynamic thermal models of sensible and latent heat short-term TES are developed in this section. A water tank-based TES is modelled following the modelling approach presented in Chapter 3. Similar to the heat exchanger models, this is verified with a TES model in Apros. On the other hand, two latent TES tanks are modelled for heating and cooling applications. Experimental data available in the literature are used to verify the developed models. Enthalpy-specific heat curve of PCMs and a method to compute the SoC are proposed and verified.

4.4.1 Sensible heat-TES

The water tank-based TES is the most commonly used type of sensible storage in DHCSs. Heat is stored using hot water. Thus, hot water is injected and extracted during the charging and discharging processes, respectively, at the top of the tank. Operation of the TES requires that the volume remains constant to avoid energy losses. Thus, the same amount of water is injected/extracted at/from the bottom of the tank. Figure 4.50 shows a schematic of a water tank-based TES connected to an energy centre and a heating load. Usually, the tank's temperature is monitored by temperature sensors located through the height of the tank.

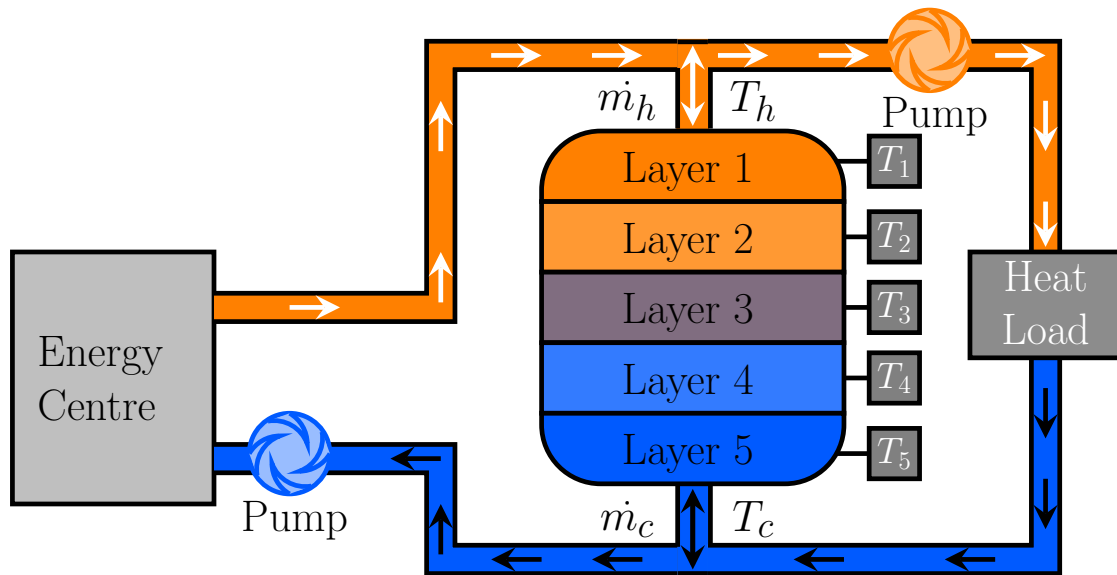


Figure 4.50: Schematic of TES configuration in DHCS.

The dynamic thermal model of the tank is developed following the modelling approach described by Figure 3.1. The water tank's internal geometry is simply a large volume bounded by a circular tank as it is shown in Figure 4.51a. The control volumes are obtained by a division of the tank through its height. Energy balance is applied to the stratified system using 1-D analysis (see Figure 4.51b). The main heat flux contribution to each layer comes from the fluid flow when the tank is charged or discharged. For instance, during the charging process, the hot fluid gets into and leaves the layer with a certain velocity and temperature (T_{in}) to continue its path towards the bottom of the tank. There is a heat flux between the water and the external environment through the tank's wall. This is described by the conduction heat transfer coefficient U_{cd} .

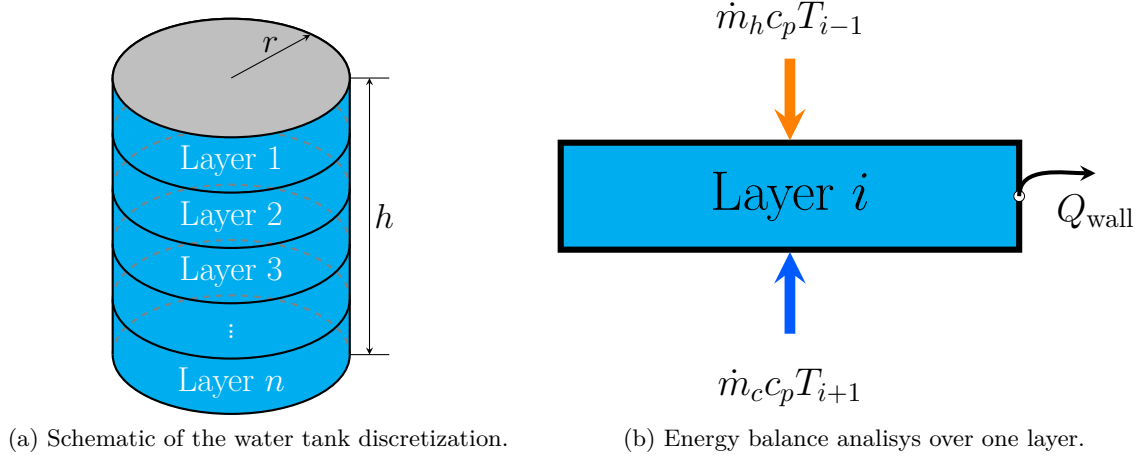


Figure 4.51: Schematic of water tank and one layer.

The first step of the modelling is to apply energy balance to the stratified tank. Thus, each layer's temperatures are described considering the heat flux's contribution due to the mass flow rate of the hot and cold water during the charging and discharging processes, plus the heat transferred through the walls of the tank. Thus, the dynamic thermal model of the tank is described by

$$\rho c_{p,1} A \Delta h \dot{T}_1 = \dot{m}_h c_{p,1} (T_{h,\text{in}} - T_1) + \dot{m}_c c_{p,1} (T_{i+1} - T_1) + U_{\text{cd}} A_{\text{tr}} (T_{\text{ext}} - T_1), \quad (4.85)$$

$$\rho c_{p,i} A \Delta h \dot{T}_i = \dot{m}_h c_{p,i} (T_{i-1} - T_i) + \dot{m}_c c_{p,i} (T_{i+1} - T_i) + U_{\text{cd}} A_{\text{tr}} (T_{\text{ext}} - T_i), \quad (4.86)$$

$$\rho c_{p,n} A \Delta h \dot{T}_n = \dot{m}_h c_{p,n} (T_{n-1} - T_n) + \dot{m}_c c_{p,n} (T_{c,\text{in}} - T_n) + U_{\text{cd}} A_{\text{tr}} (T_{\text{ext}} - T_n), \quad (4.87)$$

where A [m^2] is the cross-sectional area of the circular tank, \dot{m}_h and \dot{m}_c [kg/s] are the hot and cold mass flow rates of the fluid, A_{tr} [m^2] is the area defined by the tank wall (lateral area), given by $2\pi r \Delta h$, and h [m] is the height of the tank. Δh [m] is given by the number of chosen layers (n) as

$$\Delta h = \frac{h}{n}. \quad (4.88)$$

It is important to notice that the operation of the TES does not allow both mass flow rates (hot and cold) simultaneously. Therefore, when the TES is being charged, only \dot{m}_h is presented and $\dot{m}_c = 0$. Conversely, for discharging operating mode the $\dot{m}_h = 0$. For this simulation, a well-insulated tank is assumed. Therefore, the energy losses through the wall of the tank are neglected. Thus, the term of heat transfer by conduction is removed from equations (4.85)-(4.87). The thermal dynamic model equations (4.85)-(4.87) are rewritten for the charging process as

$$\rho c_{p,1} A \Delta h \dot{T}_1 = \dot{m}_h c_{p,1} (T_{h,\text{in}} - T_1), \quad (4.89)$$

$$\rho c_{p,i} A \Delta h \dot{T}_i = \dot{m}_h c_{p,i} (T_{i-1} - T_i), \quad (4.90)$$

$$\rho c_{p,n} A \Delta h \dot{T}_n = \dot{m}_h c_{p,n} (T_{n-1} - T_n). \quad (4.91)$$

For discharging, these are given as

$$\rho c_{p,1} A \Delta h \dot{T}_1 = \dot{m}_c c_{p,1} (T_{i+1} - T_1), \quad (4.92)$$

4.4. Thermal energy storage tanks

$$\rho c_{p,i} A \Delta h \dot{T}_i = \dot{m}_c c_{p,i} (T_{i+1} - T_i), \quad (4.93)$$

$$\rho c_{p,n} A \Delta h \dot{T}_n = \dot{m}_c c_{p,n} (T_{c,in} - T_n). \quad (4.94)$$

The model is implemented in MATLAB/Simulink using s-functions (see Appendix A). The water tank parameters are shown in Appendix C. Simulations are carried out for charging and discharging processes with constant mass flow rates of 100 kg/s and 50 kg/s, respectively. The tank is divided into 5 layers resembling a real implemented TES, for which internal temperature is monitored by few temperature sensors [8].

The layer temperatures are used to calculate the internal energy E of the tank. The coldest input temperature is defined as the reference of the internal energy computation. For instance, if all layer temperatures reach the same temperature of T_c , the total internal energy is 0 Wh. On the contrary, the TES is completely charged when all internal temperatures have being raised to T_h . Then, the internal energy of each layer is computed by

$$E_i = \frac{(V_T/n) \rho c_p (T_i - T_c)}{3600}. \quad (4.95)$$

The total water's mass in the tank and the average of all internal temperatures are used to compute the total energy of the TES as

$$E_T = \frac{V_T \rho c_p \left(\frac{1}{n} \sum_{i=1}^n (T_i - T_c) \right)}{3600}. \quad (4.96)$$

As it can be observed, solving equations (4.89)-(4.94), the temperature variation of each layer is obtained. Figure 4.52a shows how the duration of charging and discharging processes are affected by the mass flow rate. For instance, the time required to achieve the complete charging from an empty TES tank is 56 minutes, whereas a reduction of 50% of the mass flow rate for a discharging process implies a longer time, equal to 106 minutes. Figure 4.52b shows each layer's internal energy and the total TES energy during charging and discharging processes. This energy state can be used to determine the available internal energy for consumption or the necessary energy to fulfil the total charge.

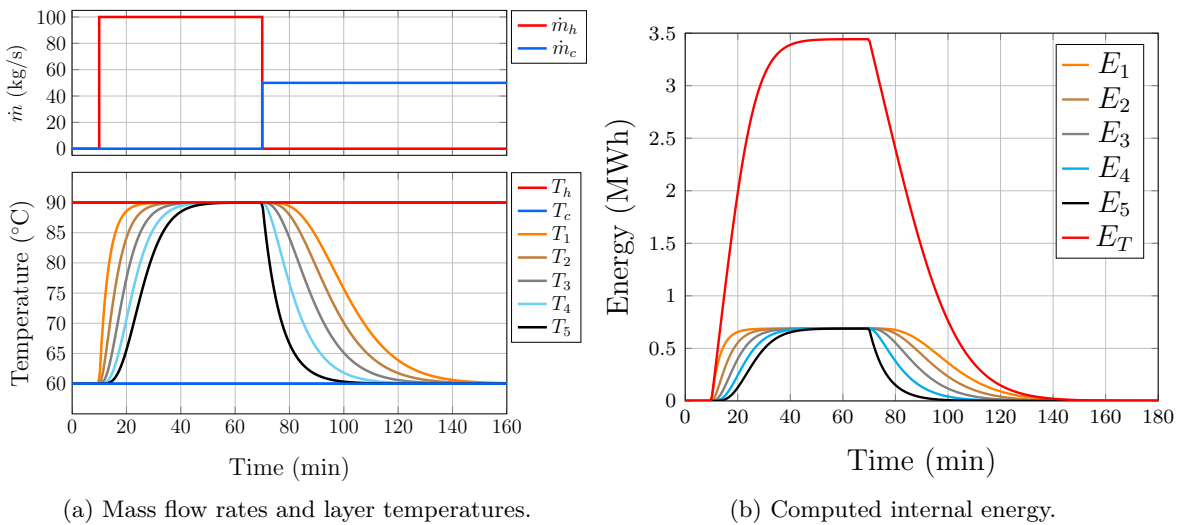


Figure 4.52: Charging and discharging simulation results.

The criteria to choose the number of nodes is a compromise between the simulation's accuracy and computation time. The accuracy offered by five layers might be sufficient to simulate a practical TES tank. To illustrate the system response with a larger number of nodes, a ten layers TES is simulated under the same conditions and its layer temperatures (grey lines) are compared with the 5 layers TES (see Figure 4.53a). As it is expected, with a more significant number of nodes, a higher accuracy is achieved by the model. Nevertheless, the SoC (internal energy) value does not present a significant difference if the number of nodes is incremented and, for some applications, few nodes might be enough to represent a real monitoring TES system (see Figure 4.53b) [8].

As it can be expected, the computation of the internal energy of the TES presents slight differences between the 5, 20 and 50 layers division during the last part of the charging and discharging processes (see Figure 4.53b). The compromise between accuracy and time computing may determine the number of layers used for simulations.

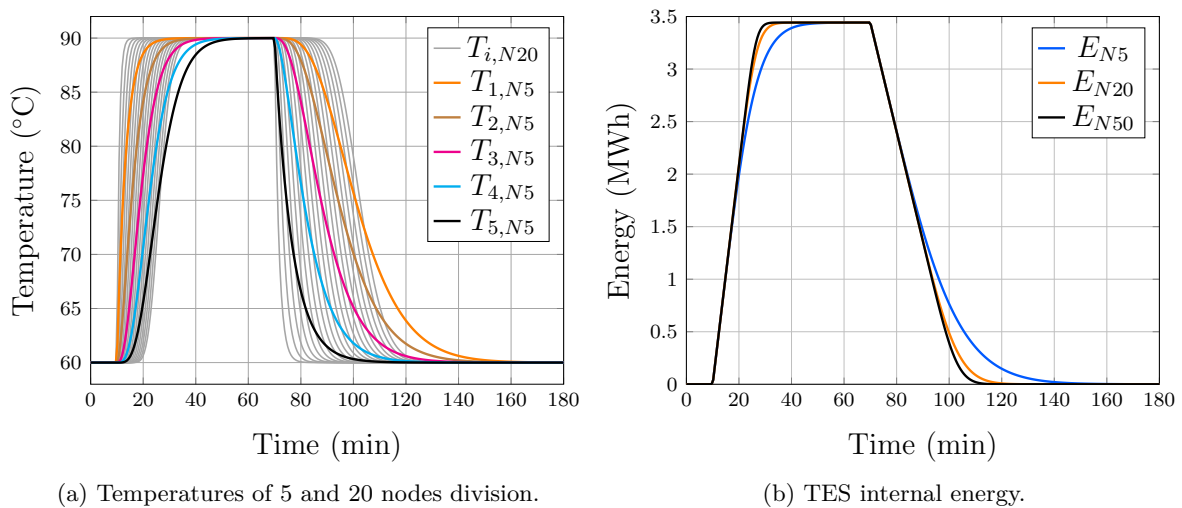


Figure 4.53: Comparison of layer temperatures and internal energy calculation between 5, 20 and 50 nodes division of TES.

Verification

A water tank-based TES can be built in Apros. There are two alternatives to achieve this, but different building approaches. Firstly, the TES can be programmed using the Apros' elements called *NODE* and *PIPE*. The link between these components defines each layer. The tank's size is defined through the radius and the height of the pipe. Additionally, the same parameters inputted in the node element. The structure of the tank is formulated by joining pipes with large radius linked to node elements (see Figure 4.54a). Apros has another option to create a TES using the *TANK* element, which is effectively a tank that can store different kind of fluids (liquid or gas). The number of nodes to be solved for this element can be established according to the layer division of the TES. Internal nodes are displayed in Figure 4.54b.

A comparison between simulations of the developed model and the Apros modelling options is presented in Figure 4.55. A sequence of discharging and charging processes are carried out at different conditions of mass flow rate and input temperatures. The tank is divided into five

4.4. Thermal energy storage tanks

layers and it is assumed as well insulated. Therefore, heat losses are neglected. The subscripts 'A1' and 'A2' stand for the Apros options, namely, node-pipes and tank element, respectively. No subscripts are used for the simulation results of the developed model implemented in MATLAB/Simulink.

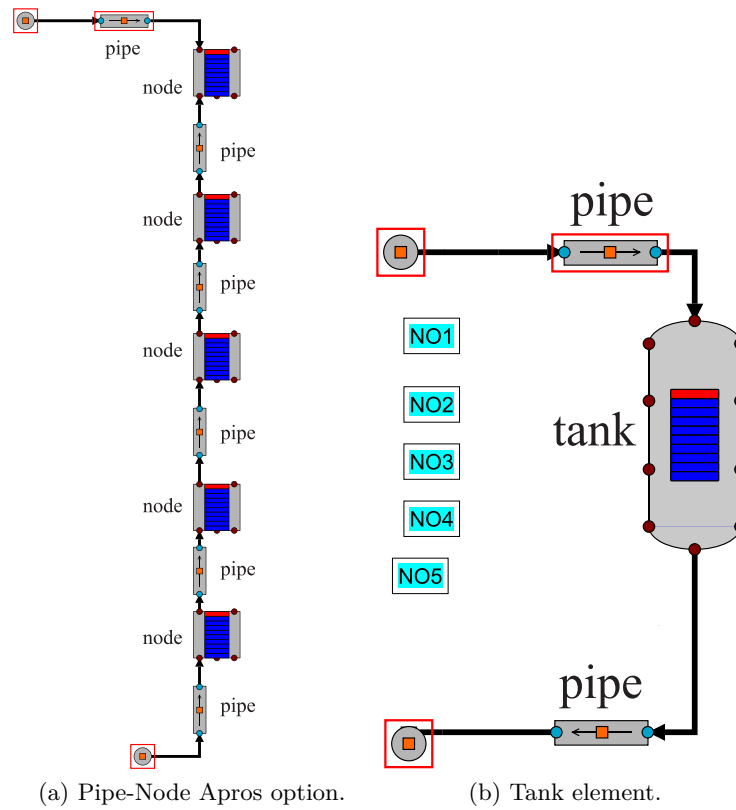


Figure 4.54: Apros options to build the TES.

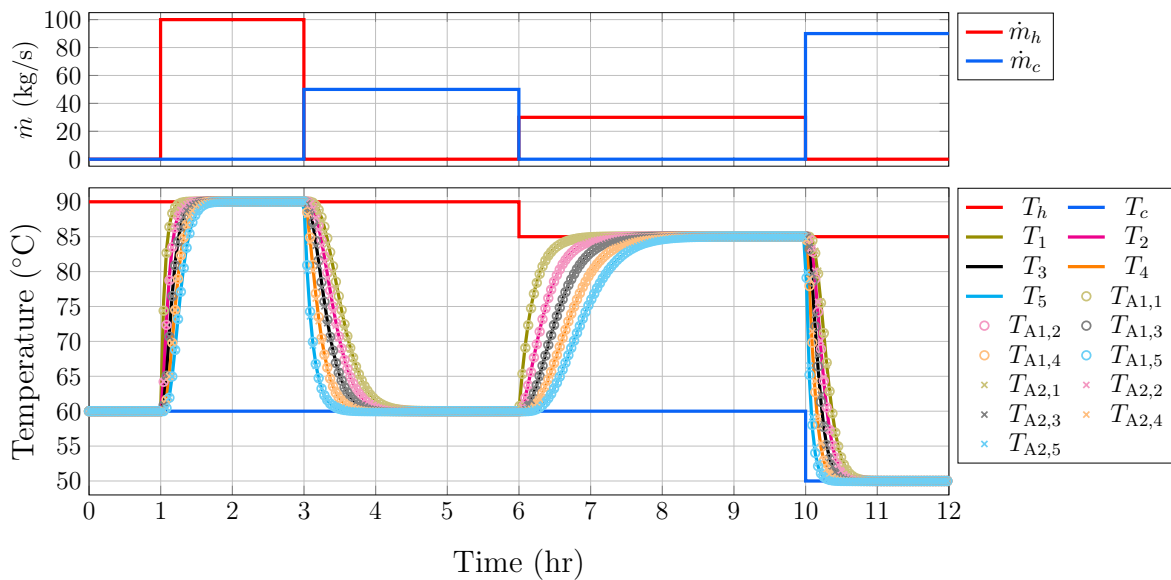


Figure 4.55: Simulation results of three models: MATLAB/Simulink, Apros option 1 (A1) and Apros option 2 (A2).

Because there is no control for the operating point, the system is left with a constant mass flow rate, irrespective of the TES tank being charged or discharged. A control design is developed in Chapter 5 to regulate the operating modes of the TES. The controller should

vary the mass flow rate in order to achieve any internal energy reference. Once the reference is achieved, the controller should reduce the mass flow rate to zero.

As it can be observed, the simulation results show an excellent agreement between the proposed model and the two Apros' models. Transient and steady-state responses are equal for the three different models. Regarding the number of nodes, it can be concluded that five nodes are sufficient to give an accurate prediction of the total energy of the TES tank. Nevertheless, if high accuracy is required for the analysis, this number should be incremented.

4.4.2 Latent heat-thermal energy storage

The advantage offered by PCM with regards to the energy released during the phase change period has made the latent TES an essential element within DHCSs. In this section, the dynamic thermal models of two latent TES for heating and cooling applications are developed using the modelling approach presented in Chapter 3. They are verified using experimental data available in the literature. The enthalpy -specific heat curve, a critical thermophysical property of PCM, is defined mathematically. Furthermore, a calculation method of the TES's SoC, which uses the temperatures predicted by the model, is presented.

Latent heat value and specific heat relationship

The enthalpy (H) [J/kg] is another indicator of the internal energy per unit mass of a substance and it is limited to the thermal energy for an incompressible liquid, where flow work contribution is neglected. The change of this value is defined by equation (3.8) and can be re-written in an integral form as

$$H = \int_{T_1}^{T_2} c_p(T) dT. \quad (4.97)$$

This relationship between H and c_p allows computing the specific heat within a range of temperatures through the enthalpy's derivative. Thus, knowing either of them, it is possible to compute the other one. This relationship is very useful for the modelling approach of latent heat TES.

The main characteristic of a PCM is that they exhibit a dramatic increment of internal thermal energy during its phase change (liquid, solid or gas). This energy is released or absorbed at a specific temperature. In other words, the substance keeps a nearly constant temperature during the phase change. The total storage capacity of a PCM is defined by the property called latent heat value Δh_l . It is defined in terms of its enthalpy. Therefore its units are J/kg. The latent heat value can be seen as the heat required to convert a certain amount of liquid substance to solid or, conversely, the cold required to change a solid substance to liquid at the same temperature and pressure. The most common phase change transition used for TES is liquid to solid and vice-versa. Vapour and gases are avoided due to their lower volumetric storage density and storage requirements [11].

To illustrate the relationship between specific heat and enthalpy, information from a commercial PCM is used. CrodaTherm[®] offers a wide range of PCM with different melting and solidification temperatures [12]. The data sheet of the high-temperature PCM CrodaThermTM 53 provides the Δh_l of melting and solidification. Besides, the graph of its specific heat is included (see Figure 4.56a). The area below the specific heat curve is the Δh_l of the material.

4.4. Thermal energy storage tanks

Thus, the computation of its enthalpy or latent heat value during solidification is defined by

$$\Delta h_{l,\text{pcm53}} = \int_{44}^{59} c_{p,\text{pcm53}}(T) dT = 218.05 \text{kJ/kg.}$$

As it can be observed, the total Δh_l is not released precisely at the solidification temperature (52°C). A transition zone encompassing a range of temperatures is distributed in this zone. Thus, melting and solidification temperatures are also named peak temperatures. The result of the specific heat curve integral with respect to the temperature is approximately the value reported in the data sheet: 220 kJ/kg. The slight difference might be due to the limits of the plot, which do not match with the temperature range of the reported latent heat value (40°C to 60°C). Thus, enthalpy H can be plotted in terms of temperature as it is shown in Figure 4.56b.

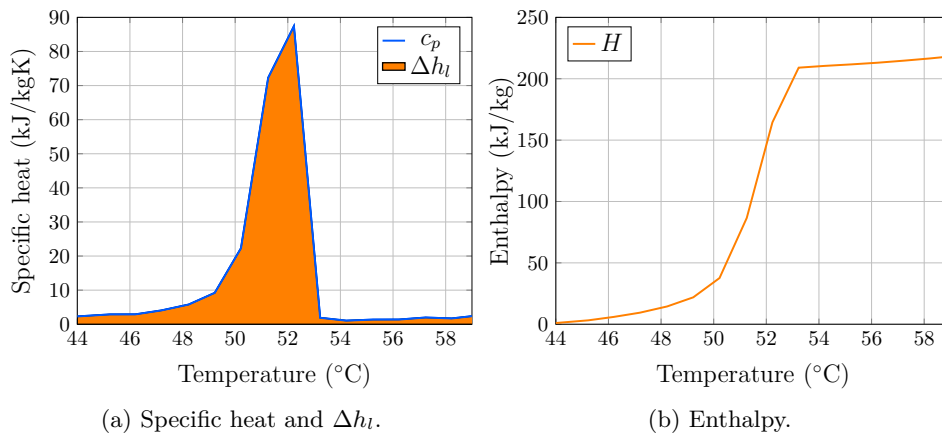


Figure 4.56: Specific heat and enthalpy of coda therm 53 PCM based on [12].

The latent heat value of a PCM may be sufficient for a simple analysis where only the total storage capacity of a TES tank is calculated. Nevertheless, for dynamic analysis, a precise definition of the enthalpy or specific heat during the transition zone for melting and solidification processes is critical. Energy balance requires knowing the specific heat and its temperature dependency. Therefore, this thermophysical property is more suitable for dynamic modelling instead of enthalpy. Two industry-standard analysis are used to determine the heat capacity of a substance: differential scanning calorimetry (DSC) and three-layer calorimetry (3LC) [13, 14]. Unfortunately, a detailed description of specific heat for some PCMs are not provided by the manufacturer. Hence, experimental results are used to fit the specific heat curve by means of parameter estimation [15].

Moreover, some PCMs present a special characteristic: melting and solidification occur at different temperatures. Even a PCM may have a different latent heat value for each phase change. Therefore, having two peak temperatures implies considering two curves of specific heat or enthalpy separately for melting and solidification processes. This phenomenon is called hysteresis of enthalpy. For the sake of clarity, normalized specific heat curves of fictional PCM, whose values have been exaggerated, are used to illustrate this phenomenon. Let $c_{p,l}$ and $c_{p,s}$ denote the specific heat for melting and solidification, respectively. If the solid PCM is brought to the liquid phase by increasing its temperature employing heat, the thermal behaviour during the transition phase change is governed by $c_{p,l}$. On the other hand, if cold is provided for a liquid PCM to bring it to the solid phase, the transition zone is determined

by $c_{p,s}$. As it can be observed, although the peak of $c_{p,l}$ occurs at 23°C and this is higher than the $c_{p,s}$, its latent heat value is lower due to its narrower transition zone.

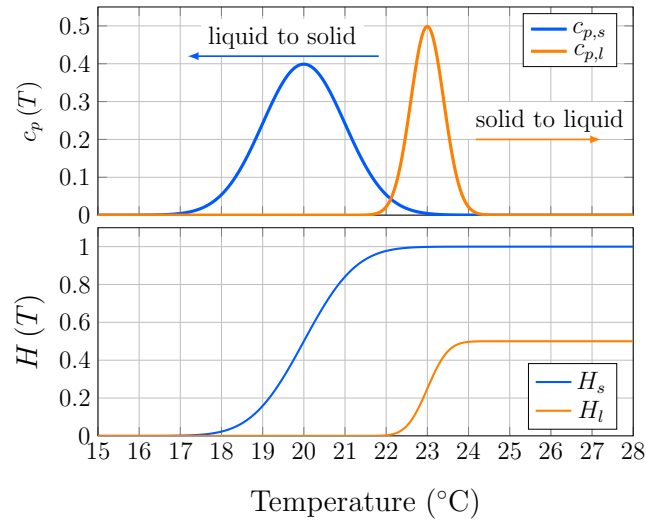


Figure 4.57: Normalized specific heat (top) and enthalpy (bottom) of PCM with hysteresis phenomenon.

Dynamic model

A heat transfer fluid (HTF) is used in PCM based TES. It crosses the tank at a specific temperature (T_f) and mass flow rate (\dot{m}_f) to transfer the heat from/to the PCM during discharging/charging processes. There are different forms of the internal structure of the PCM based TES. They are related to the shape of the container where the PCM is encapsulated. There are three main types of PCM capsules: spheres, slabs and cylinders [11]. A TES tank with spherical containers has several spheres made of plastic and filled with PCM located in its interior. The HTF flows through the space formed between the spheres. The heat transfer occur through the sphere walls (see Figure 4.58a). On the other hand, PCM also may be encapsulated in rectangular containers. The internal structure is given by stacked slab containers with a gap between them, where the HTF flows through, as in, a flat plate heat exchanger (see Figure 4.58b).

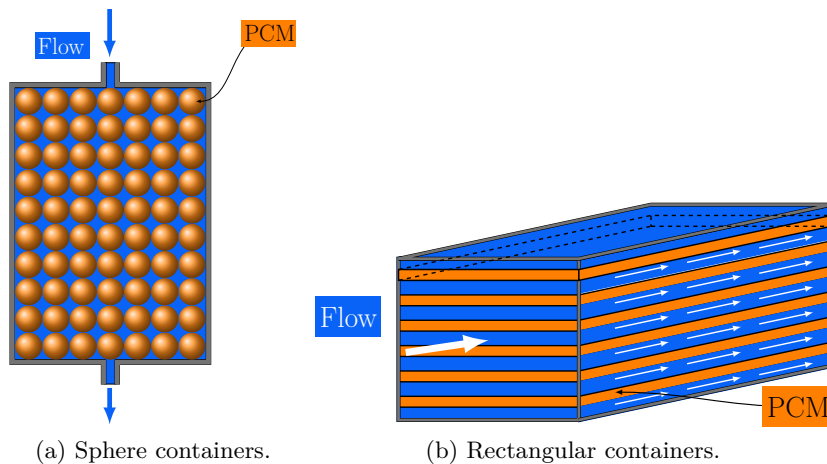


Figure 4.58: Internal structure and containers of most common PCM based TES.

The third option involves a cylindrical PCM container with an annular channel for the

4.4. Thermal energy storage tanks

HTF flow or a tube option through which the HTF flows and is surrounded by PCM (see Figure 4.59). This option is very similar to the shell-and-tube heat exchanger configuration. For instance, the tubes for the cylindrical container are replaced by the PCM capsules and the HTF flows through the shell (see Figure 4.59a). Conversely, the shell is filled up by PCM and the HTF is spread through small tubes (see Figure 4.59b). This configuration is the most popular form used within DHCSs [11].

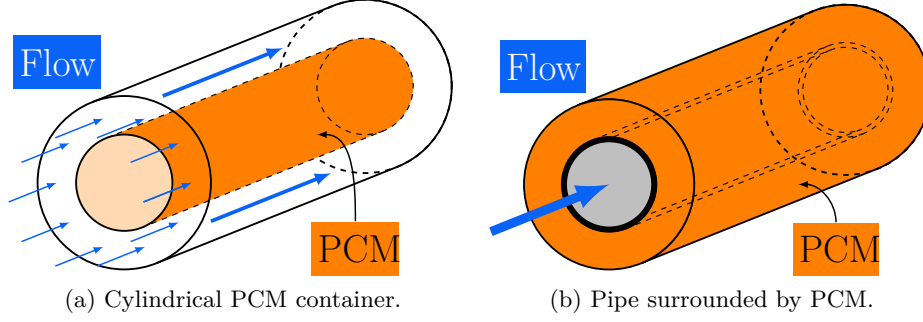


Figure 4.59: Internal structure and containers of most common PCM based TES.

The latent TES's dynamic thermal model is explained using the latter option of the internal structure of PCM based TES. Nevertheless, by the modelling approach can be similarly implemented for the rectangular and cylindrical capsules, which present a well-defined channel for the HTF. Use of PCM spheres present a complex computation of the heat transfer area. Moreover, the shape of the formed space between the spheres makes the calculation of the HTF hydraulic conditions (mean velocity, Reynolds number and Nusselt number) a challenging task. Therefore, a more complex analysis such as finite element may be required to model the heat transfer process in a TES with PCM spheres.

The internal structure of a TES with pipes is the same as in the shell-and-tube heat exchanger. Hence, the same energy balance can be applied, with the only difference in that the shell is filled with PCM instead of having fluid flowing. The equation for the tube side (4.57) can be rewritten for the pipe side just by changing subscript 't' (tube) for 'f' (heat transfer fluid) as

$$m_{f,i}c_{p,f,i}\dot{T}_{f,i} = \dot{m}_f c_{p,f,i} (T_{f,(i-1)} - T_{f,i}) + U_P A_{tr} (T_{P,i} - T_{f,i}), \quad (4.98)$$

where m_f [kg] and T_f [$^{\circ}$ C] is the mass and the temperature of the HTF, respectively, T_P is the PCM temperature, A_{tr} [m^2] is the heat transfer area and U_P [W/m^2K] is the overall heat transfer coefficient between the HTF, the pipe wall and the PCM. On the other hand, the PCM keeps stagnant with no movement. Therefore, it does not receive energy other than the transferred one from the HTF, and only heat transfer by conduction is presented in the shell side. Thus, the PCM energy balance is defined by

$$m_{P,i}c_{p,P,i}\dot{T}_{P,i} = U_P A_{tr} (T_{f,i} - T_{P,i}), \quad (4.99)$$

where m_P [kg] is the mass of the PCM. Typically, the pipes are submerged in the PCM with a not-well defined bound for the PCM mass around the pipes. Therefore, the definition of imaginary bounds is necessary to know the PCM volume involved in the energy transfer process. Figure 4.60 shows a special configuration as proposed in [15], where the cross-sectional area is

divided in hexagons for each pipe. A circle perimeter is used to establish the cross-sectional area of the control volume, which is defined by the radius r_p .

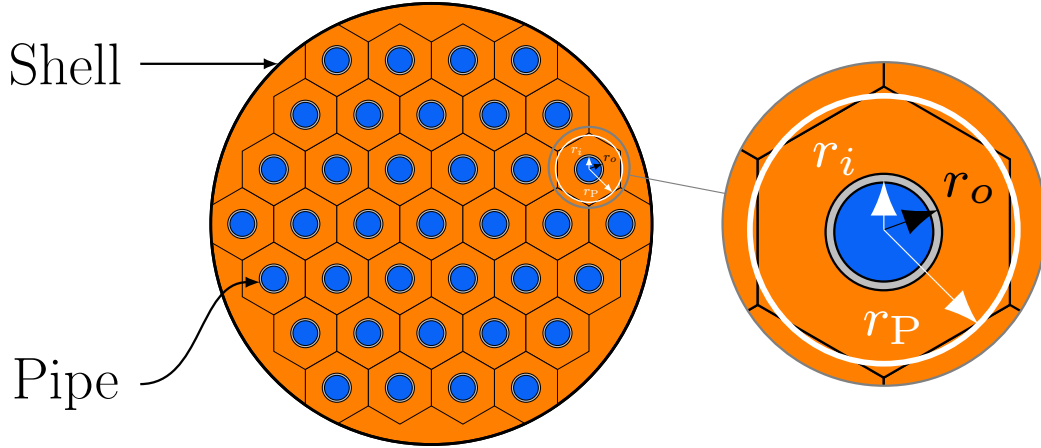


Figure 4.60: Schematic of PCM based TES with tube configuration.

The node division is defined for a single pipe as shown in Figure 4.61a. The radial direction of the heat flux is illustrated by the white arrows in Figure 4.61b. Heat flux from the HTF to the PCM means that a higher HTF temperature causes the PCM to melt. Conversely, a higher temperature of PCM causes a heat flux towards the HTF, increasing the HTF temperature during the solidification process of the PCM.

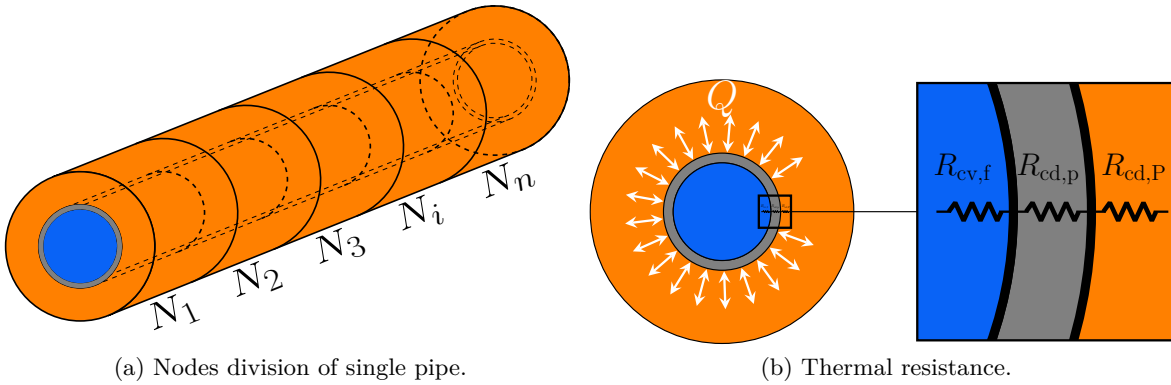


Figure 4.61: Control volumes and thermal resistance of single pipe of TES.

The next step is to define the equations to compute U_p . Similarly to the heat transfer coefficient by convection in the shell-and-tube heat exchanger, $U_{cv,f}$ due to the HTF is computed by equations (4.63), (4.72), (4.74). Equation (3.41) is used to compute the conduction heat transfer coefficient of the wall as

$$U_{cd,p} = \frac{k_p}{\ln \left(\frac{r_o}{r_i} \right)}, \quad (4.100)$$

4.4. Thermal energy storage tanks

where k_p [W/mK] is the thermal conductivity of the pipe material and, r_i [m] and r_o [m] the internal and external radius of the pipe, respectively. The heat transfer presented by the PCM is caused by conduction exclusively. Thus, the heat transfer coefficient is calculated with

$$U_{cd,P} = \frac{k_P}{\ln\left(\frac{r_P}{r_o}\right) r_i}, \quad (4.101)$$

where k_P [W/mK] is the thermal conductivity of the PCM and r_P [m] is the radius defined by the imaginary bounds, as previously discussed.

Finally, adding the thermal resistances shown in Figure 4.61b, which are defined by the heat transfer coefficients, the total thermal resistance is defined by

$$R_T = \frac{1}{A_{tr}U_{cv,f}} + \frac{1}{A_{tr}U_{cd,p}} + \frac{1}{A_{tr}U_{cd,P}}. \quad (4.102)$$

Model verification for a heating application

PCMs cover a wide range of peak temperatures, allowing PCM-based TES either for heating or cooling applications. Validation for both applications becomes necessary to show the accuracy of the model under different temperatures and PCM types. In this section a PCM based TES for a heating application is modelled and the simulation results are compared with the experimental data reported in [15], where a shell-and-tube internal configuration of a PCM based TES is presented. Figure 4.62 shows the sketch of the tank. It has 72 steel tubes with a length of 2.5 m. The type of PCM is a special polyethene manufactured by INEOS Polyolefins. The parameters of the TES are shown in Appendix C.

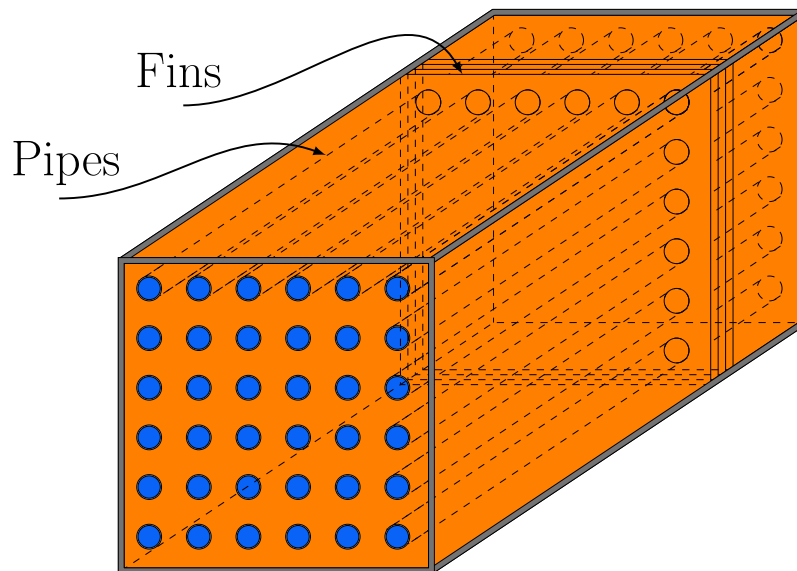


Figure 4.62: Sketch of the TES for heating application based on [15]

Unlike the model developed for the shell-and-tube heat exchanger, the modelling of the TES can be simplified by defining two important assumptions: an equal internal flow for all pipes exits and an equal temperature distribution of HTF and PCM are present through

the whole tank. Since every pipe has the same hydraulic and thermal conditions, the energy balance can be applied for a single pipe that represents all pipes' behaviour.

As with the modelling of heat exchangers, boundary effects such as small variations of fluid velocity and energy losses are neglected. The control volumes required to apply the energy balance are defined by the single pipe's node division. Thus, the thermal behaviour of the single pipe is described by a set of equations. The temperature dependency of U_P and the thermophysical properties of the PCM and the HTF are included in equations (4.103) and (4.104). The energy balance is defined by

$$m_{f,i}c_p(T_{f,i})\dot{T}_{f,i} = \dot{m}_f c_{p,f,i}(T_{f,(i-1)} - T_{f,i}) + U_P(\rho_f, k_f, \nu_f, Pr_f, \rho_P, k_P) A_{tr}(T_{P,i} - T_{f,i}), \quad (4.103)$$

$$m_{P,i}c_p(T_{P,i})\dot{T}_{P,i} = U_P(\rho_f, k_f, \nu_f, Pr_f, \rho_P, k_P) A_{tr}(T_{f,i} - T_{P,i}), \quad (4.104)$$

where ρ [kg/m³], k [W/mK], ν [Ns/m²] and Pr are the density, thermal conductivity, kinematic viscosity and Prandtl number, respectively. These temperature dependent properties are defined by polynomial equations which are obtained from [15].

Regarding the specific heat curve of a PCM, it usually is defined through a probability density function (PDF) [15] which independent variable is the temperature. This analytic form allows adjusting the parameters of the PDF to fit the model using experimental data. The general equation of specific heat curve proposed in [15] is defined as

$$c_{p,P}(T_P) = 1000 [(a_0 + a_1 T_P) + a_2 \phi(T_P)], \quad (4.105)$$

where coefficients a_0 , a_1 and a_2 are defined by means of parameter estimation, and ϕ is the PDF. Four different PDFs are considered in [15] to generate the specific heat curve. Firstly, the Gumbel minimum distribution is defined by

$$\phi_1(T, \mu, \beta) = \left(\frac{1}{\beta}\right) \exp\left(\frac{T - \mu}{\beta}\right) \exp\left(-\exp\left(\frac{T - \mu}{\beta}\right)\right), \quad (4.106)$$

where μ and β are the location (locp) and scale (scap) parameters, respectively. Secondly, an adaptation of the Weibull distribution is defined by

$$\phi_2(T, \gamma, \mu, \alpha) = \begin{cases} \frac{\gamma}{\alpha} \left(-\frac{T - \mu}{\alpha}\right)^{\gamma-1} \exp\left(\left(\frac{T - \mu}{\alpha}\right)^\gamma\right) & T < \mu \\ 0, & T \geq \mu \end{cases} \quad (4.107)$$

where γ , μ and α are the shape (shap), location (locp) and scale (scap) parameters, respectively. Finally, an adaptation of the log-normal distribution is defined by

$$\phi_3(T, \sigma, \mu, m) = \begin{cases} \frac{\exp\left[-\left(\frac{\ln[-(T - \sigma)/m]}{\sigma}\right)^2 / (2\sigma^2)\right]}{-(T - \mu)\sigma\sqrt{2\pi}} & T < \mu \\ 0, & T \geq \mu \end{cases} \quad (4.108)$$

where σ , μ and m are the shape (shap), location (locp) and scale (scap) parameters, respectively.

The work presented in [15] consists of fitting a two-dimensional (2-D) dynamic model of PCM based TES to experimental data from melting and solidification experiments. The 2-D

4.4. Thermal energy storage tanks

model uses energy balance, but it considers axial and radial direction of the heat transfer. This modelling approach requires 450 ODEs to describe the thermal behaviour of the TES. The fitting process is done by means of parameter estimation of the thermal conductivity (k_P) and specific heat ($c_{p,P}$) of the PCM. Three different experiments are carried out: individual melting, individual solidification and simultaneous melting-solidification. For each experiment, four different sets of estimated parameters are obtained.

For the verification process of the 1-D model described by equations (4.103) and (4.104), one set of estimated parameters is used to compare each experiment. Table 4.1 shows the estimated parameters for the thermal conductivity and specific heat curves. For equation (4.105), the coefficients c_1 and c_4 remain constant for all fitted models and their values are 0.41857 and 0.036647, respectively. Likewise, coefficient $a_1 = 6.5655 \times 10^{-3}$ is constant for all models.

Table 4.1: Parameters of PCM's specific heat equation ($c_{p,P}$).

Experiment	$c_{p,P}$						k_P	
	a_0	a_2	ϕ	locp	scap	shap	c_2	c_3
Melting (M)	3.5016	167.1719	ϕ_2	138.7	7.3249	2.944	153.7	1.4914
Solidification (S)	1.1372	283.5574	ϕ_3	125.6	4.7951	2.118	126.453	1.3505
Simultaneous (SM)	0.8405	261.55	ϕ_1	126.5	9.3897		265.599	0.542

The curves for the specific heat are shown in Figure 4.63. As it can be observed, the PCM (Rigidex HD6070EA) presents hysteresis of its enthalpy. The temperature peak of melting and solidification occur at 132.4°C and 125.5°C, respectively. For melting and solidification experiments, the specific heat curve presents a temperature peak at 126.6°C.

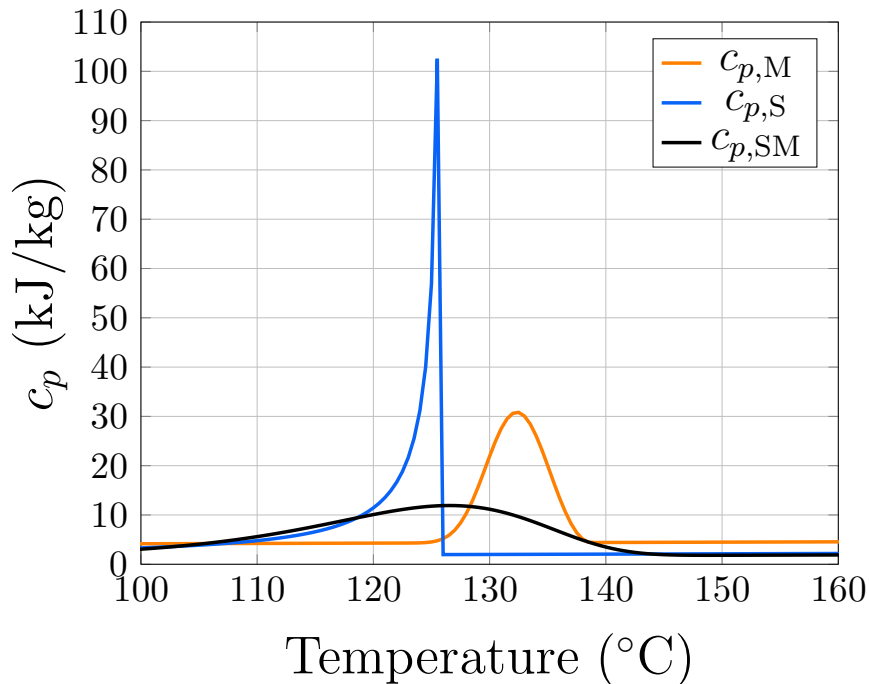


Figure 4.63: Specific heat curves for three experimental reported in [15]

The system defined by equations (4.103) and (4.104) is implemented in MATLAB/Simulink using s-functions. The modelled single pipe is divided into 50 nodes, which means that only 50 ODEs are required to model the TES instead of 450 ODEs. The 2-D model requires two corrective coefficients. Firstly, a correction factor of 2.88 is applied to the computation of the overall heat transfer coefficient. Secondly, the energy stored in the pipe is amplified by a factor of 2.13. This correction is introduced to consider additions of thermal capacity of the tube plate and the headers of the external wall of the TES. The 1-D model only requires the correction factor of U_P , which has been defined empirically, with a value of 4.5.

Comparisons between simulation and experimental data are shown in Figure 4.64. Subscripts 'e' and 's' stand for experimental data and simulation results (1-D model), respectively. The input ($T_{in,f,e}$) and output ($T_{out,f,e}$) temperatures of the HTF of the individual melting experiment is shown in Figure 4.64a. The mass flow rate of the HTF remains constant during the whole process and its value is 1.02 kg/s. The initial temperature of the HTF and of the PCM is 153.4°C. As it can be observed, the output temperature of the HTF ($T_{out,f,s}$) given by the simulation results is very close to the experimental data.

On the other hand, the solidification process is compared in Figure 4.64b, with operation conditions of $\dot{m}_f = 1.02$ kg/s and initial conditions of 104°C for the HTF and the PCM. Similarly, $T_{out,f,e}$ and $T_{out,f,s}$ show a very good agreement during the whole solidification process.

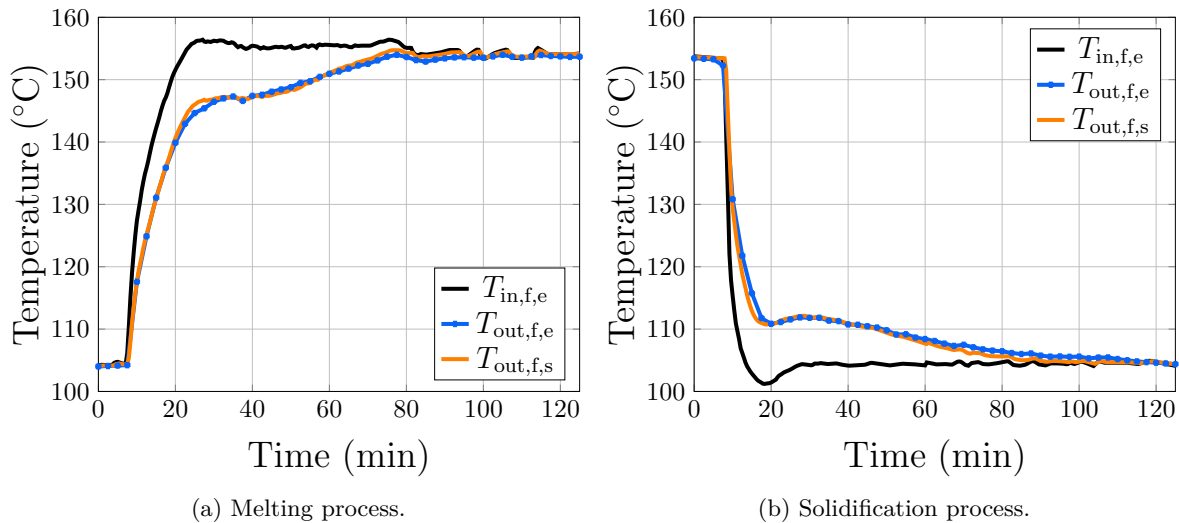


Figure 4.64: Comparison of experimental data and 1-D dynamic model simulation results.

Despite the good results in the HTF output temperatures, the PCM's internal temperatures present considerable deviations with respect to the experimental results. They can be explained from the fact that no radial heat transfer is considered in the developed model, unlike the 2-D model that splits the PCM's radial distance into nine nodes. Figures 4.65 and 4.66 show the measurements from four temperature sensors. They are located in the PCM inside the tank. Their positions are located axially through the length of the TES at 0.1 m, 0.87 m, 1.64 m, and 2.4 m. The comparison with the extremes (first and last) and middle nodes of the 1-D model show a large difference. However, the HTF output temperature, which is the key variable, matches with the experimental data in all the addressed operating modes.

4.4. Thermal energy storage tanks

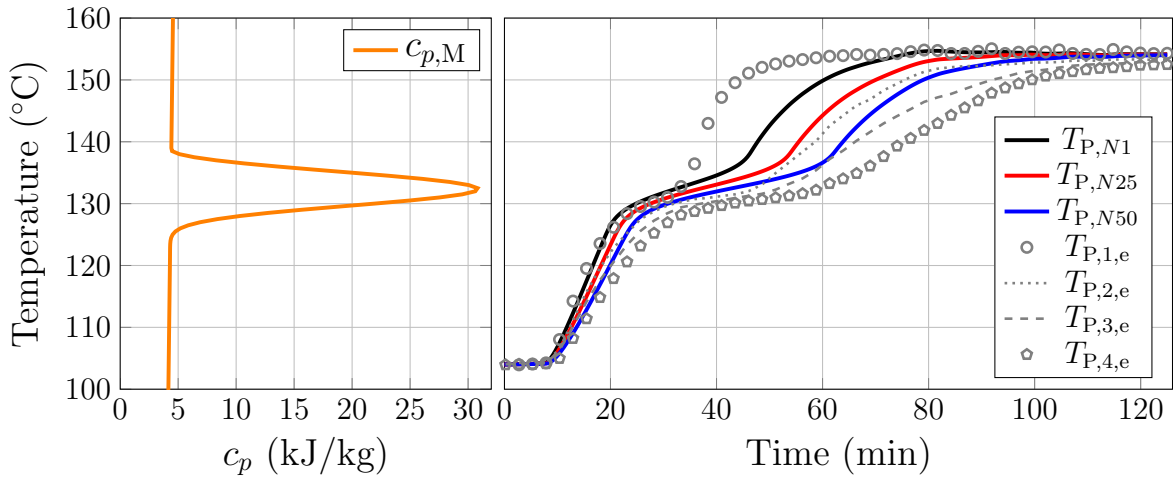


Figure 4.65: PCM temperature comparison between experimental data and simulation results of 1-D model during melting process at $\dot{m}_f = 1.02$ kg/sec.

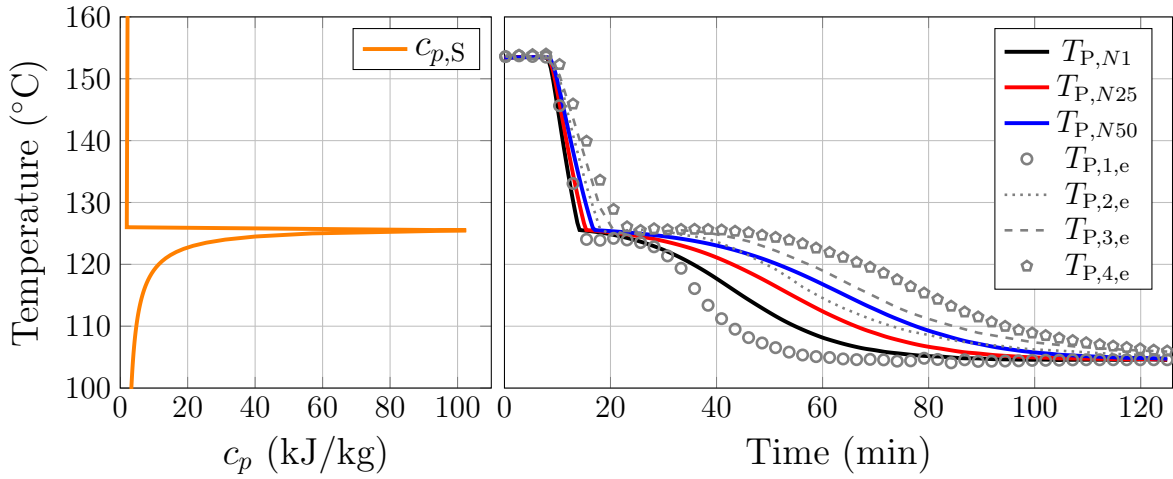


Figure 4.66: PCM temperature comparison between experimental data and simulation results of 1-D model during solidification process at $\dot{m} = 1.02$ kg/sec.

Based on the previous observations, the simultaneous melting and solidification comparison does not include the temperature of the PCM. Melting and solidification process are carried out at different values of mass flow rate of HTF: 0.415 kg/s, 0.6 kg/s, 1.03 kg/s and 1.98 kg/s. The thermal conductivity and specific heat curve are set with the estimated parameters of SM model shown in Table 4.1. The simulation results and the experimental data are shown in Figure 4.67. As it can be observed, slight differences are presented in the melting processes. These differences are expected due to having a PCM with a hysteresis of enthalpy. Here, its specific heat has been fitted with only one curve, which is not enough for a good agreement of the simulated with the experimental HTF temperature during the melting process.

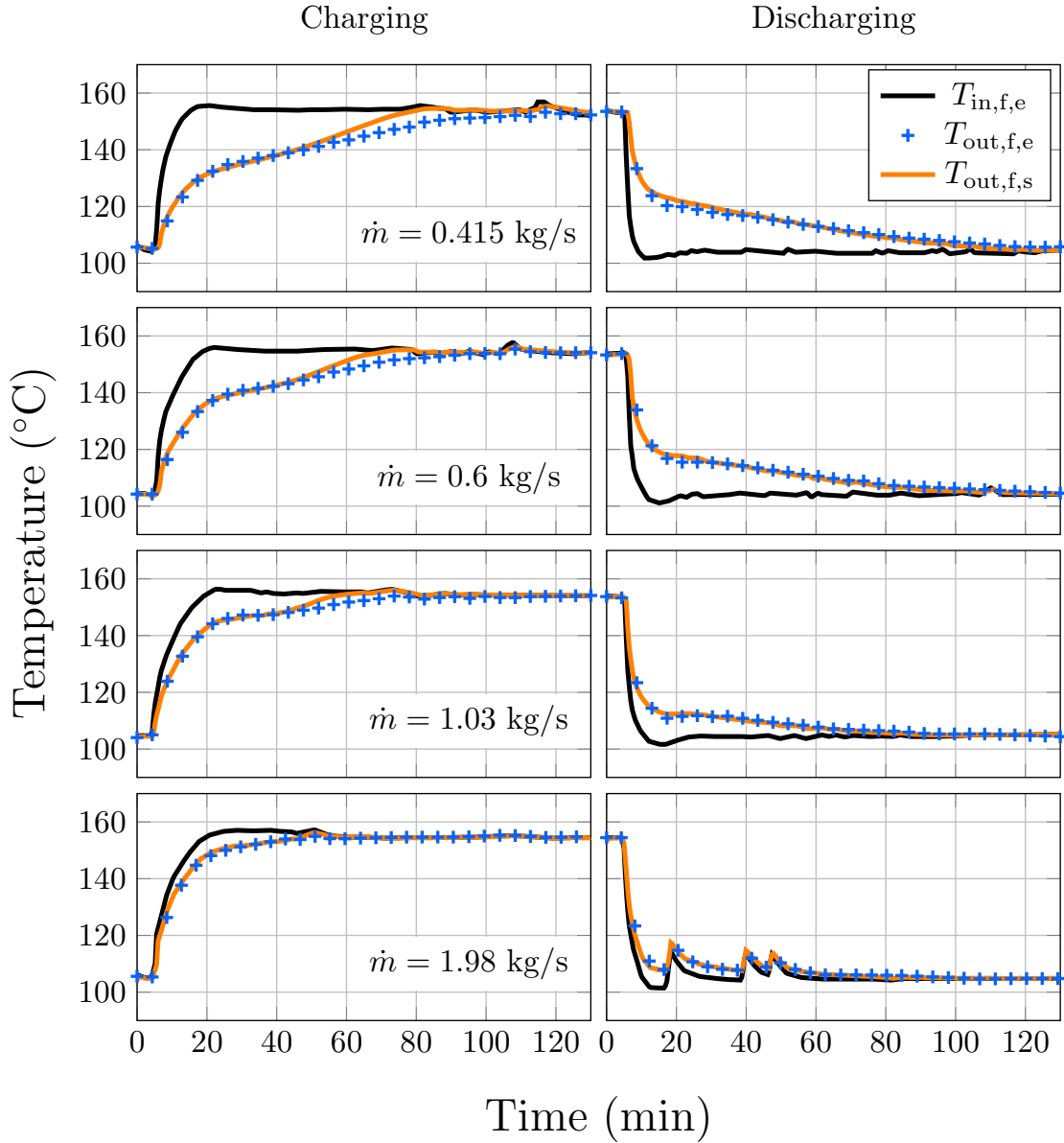


Figure 4.67: Charging and discharging processes with different mass flow rates.

State of charge

The energy storage capacity of a TES is given by the amount of PCM and its latent heat value (Δh_l). The total energy stored (E_e) may be computed exclusively using the latent heat value. When the TES is completely charged E_e is defined by

$$E_e = \Delta h_l m_P. \quad (4.109)$$

However, these measurements are not enough to know how the TES has been charged or discharged regarding the latent heat that can be stored. Thus, SoC is a key value to know whether the TES tank has been fully charged or how much energy remains during the discharging process at any specific time. For this purpose, the temperature of the PCM in each node defined by equation (4.104) is used to compute the latent heat value released or absorbed using its enthalpy-specific heat relationship. Let the temperature of the PCM in a node (T_P) and its specific heat curve be defined by $c_{p,SM}$, its storage capacity is given by

4.4. Thermal energy storage tanks

the latent heat value Δh_l , which is the area below the specific heat curve $c_{p,SM}$ (see Figure 4.68a). Assuming that the $\Delta h_l = 260 \text{ kJ/kg}$ [15], the area is computed using equation (4.97) and establishing the temperature limits as

$$\Delta h_l = \int_{T_1=109.4}^{T_2=138} c_{p,SM}(T) dT.$$

Thus, the latent heat value can be defined in terms of enthalpy solving equation (4.97) through the whole range of temperature for which the specific heat curve has been defined (see Figure 4.68b).

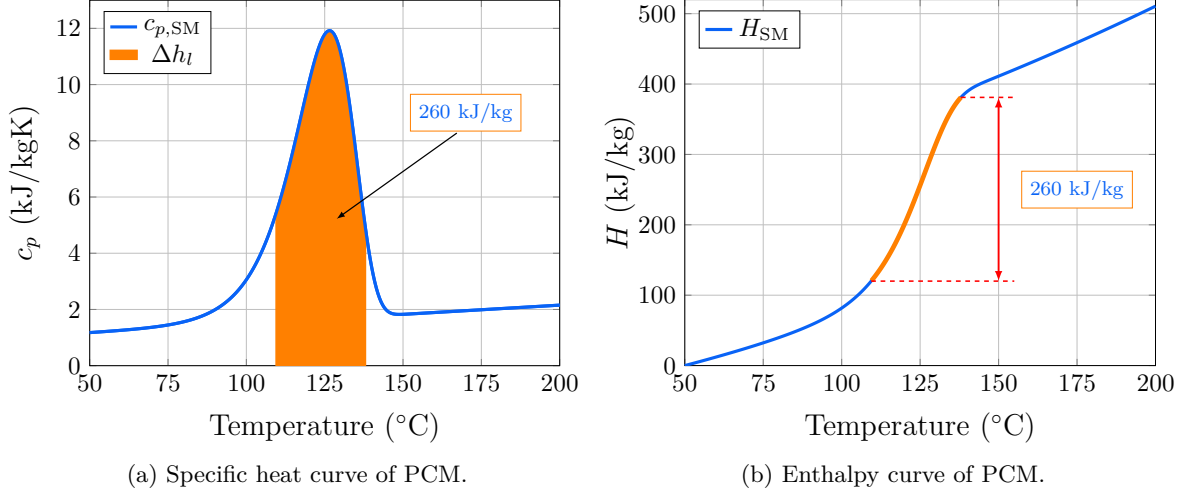


Figure 4.68: Specific heat and enthalpy curves of RigidexHD6070EA PCM including its Δh_l .

The PCM-based TES for a heating application needs to increase the PCM's temperature to store the heat released during the discharging process. Thus, the PCM absorbs (charging) its total latent heat value when its temperature is higher than T_1 . Conversely, the PCM releases (discharging) its latent heat value when its temperature is below T_2 . Then, the PCM's SoC is easily computed knowing T_1 and its current temperature. Let T_1 be renamed as T_{empty} and T_2 as T_{full} . Then, the SoC of the PCM can be defined by

$$\text{SoC}(T) = \begin{cases} 1, & T_P > T_{\text{full}} \\ \frac{\int_{T_{\text{empty}}}^{T_P} c_{p,SM}(T) dT}{\Delta h_l} \times 100, & T_{\text{empty}} < T_P < T_{\text{full}} \\ 0, & T_P < T_{\text{empty}}. \end{cases} \quad (4.110)$$

Therefore, the SoC of the TES when the PCM temperature is outside the transition zone is 0 or 1, which means that it is either empty or full. This computation method of the SoC does not require knowing the initial conditions of charging or discharging processes, unlike methods proposed in the literature, where the SoC is a simple addition of the energy stored or released by the PCM and the energy is quantified since the beginning of the processes. It is important to bear in mind that the calculation of SoC only considers the latent heat value. Nevertheless, the PCM keeps transferring or absorbing energy from its sensible heat value (Δh_s) when it is liquid or solid.

The SoC of three different PCM temperatures is shown in Figure 4.69. At the top, the full charged PCM which temperature $T_P = 138^\circ\text{C}$ is shown, in the middle $T_P = 126^\circ\text{C}$ and at

the bottom $T_P = 115^\circ\text{C}$.

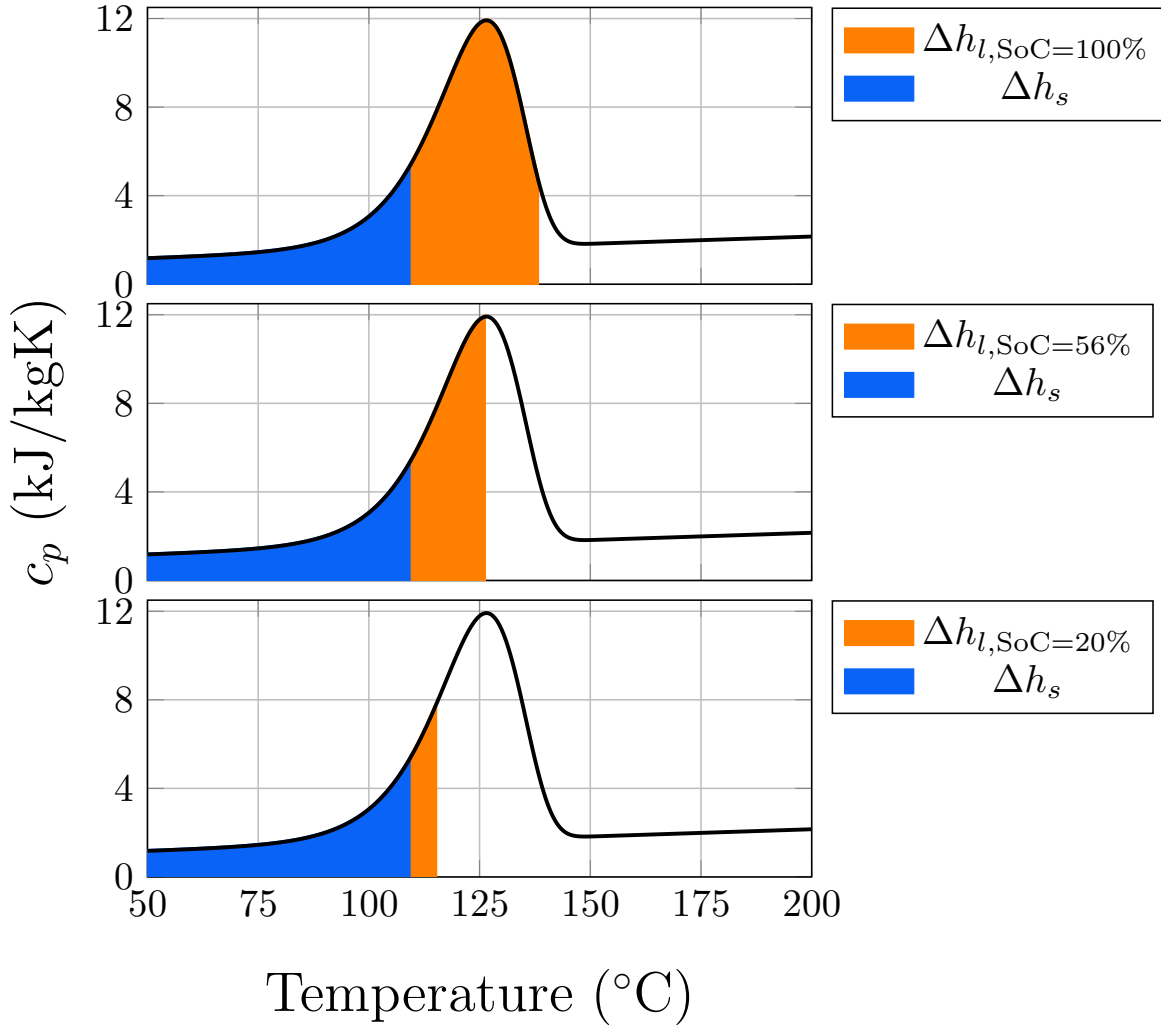


Figure 4.69: Top: $T_P = 138^\circ\text{C}$ and $\text{SoC} = 100\%$. Middle: $T_P = 126^\circ\text{C}$ and $\text{SoC} = 56\%$. Bottom: $T_P = 115^\circ\text{C}$ and $\text{SoC} = 20\%$.

To quantify the SoC of the TES dynamically, it is necessary to use the PCM temperature in the control volumes and solve equation (4.110) for each one. Then the total SoC is given by the average of all these SoCs as

$$\text{SoC}_T = \frac{\sum_{i=1}^N \text{SoC}(T_{P,i})}{N}. \quad (4.111)$$

Figure 4.70 illustrates a snapshot of the SoC calculation for each pipe node at specific moment. The PCM temperatures in the nodes have different values according to the heat transfer process during charging or discharging, resulting in different values of the absorbed or released latent heat.

The SoC calculation is also presented in [15]. As the thermal behaviour of the PCM is modelled through the axial and radial directions, a more complex equation compared to (4.110)-(4.111) is required. The summation of all SoC has to be quantified not only through the length of the pipe as in equation (4.111), but also through the radius of the control volume, requiring more computation time.

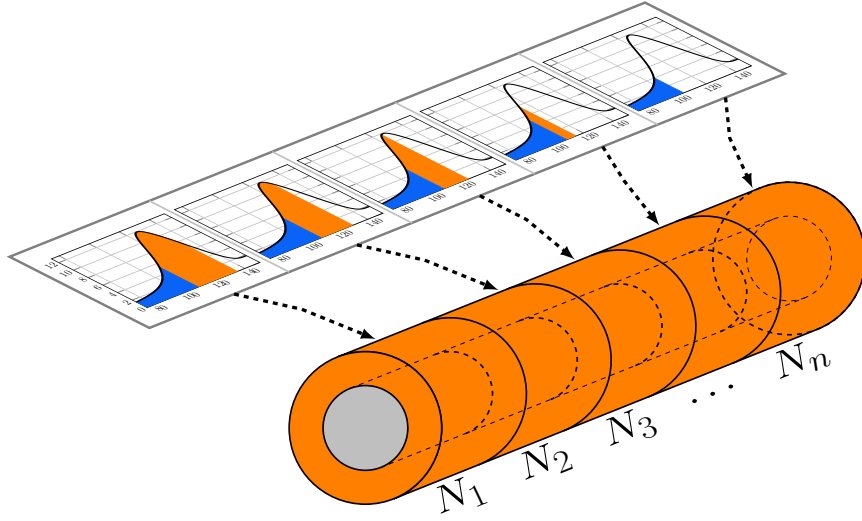


Figure 4.70: Illustrative snapshot of the SoC of each pipe node.

One more experiment is used to verified the proposed method. Charging and discharging processes are carried out varying the input temperature of the HTF ($T_{in,f,e}$) with a constant mass flow rate of 1.09 kg/s. These experimental results are used to make a comparison with the method presented in this work. The same input temperature is injected into the model implemented in MATLAB/Simulink. The output temperature of the HTF is the temperature of the HTF in the last node ($N = 50$) of the pipe. The comparison between simulated and experimental temperatures is shown in Figure 4.71, where subscripts 'e' and 's' stand for experimental and simulated results, respectively. As it can be observed, the simulation result of the HTF output temperature is in good agreement with the experimental data.

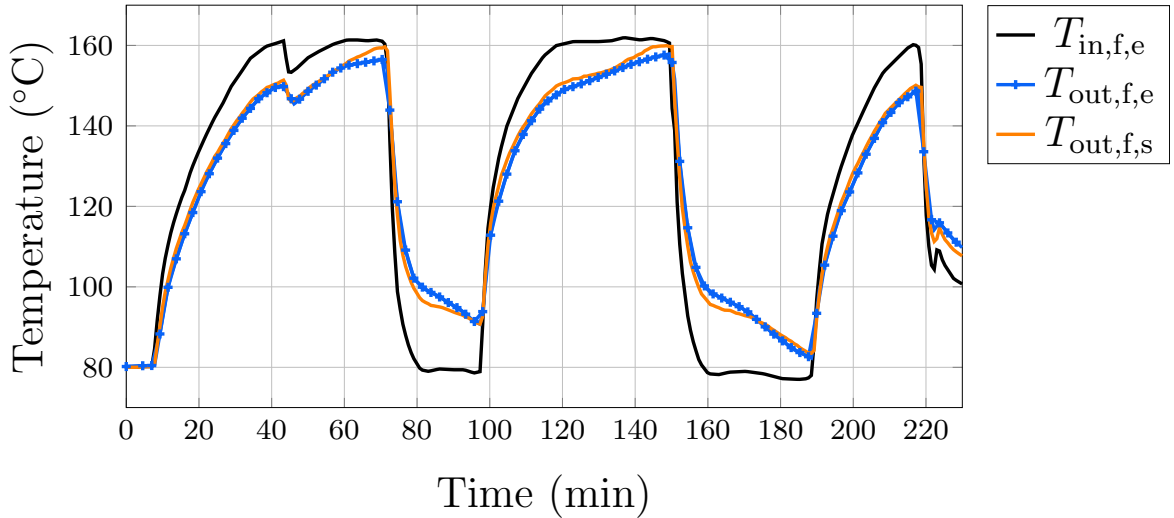


Figure 4.71: Comparison between experimental data and simulation results of the output temperature of HTF ($T_{out,f,s}$).

The energy absorbed or released by the TES (E_e) is obtained by solving equation (3.20) for the HTF through the length of the pipe. It is important to notice that the HTF energy includes latent and sensible heat of the PCM and it is not related with equation (4.109), which only consider the latent heat. As energy is plotted in Watts per hour (Wh) instead of Joules (J), a factor of 3600^{-1} is required. Thus, the energy supplied or removed by the HTF

is given by

$$E_s = \frac{1}{3600} \dot{m}_f c_{p,f} (T_{in,f,s} - T_{out,f,s}). \quad (4.112)$$

Figure 4.72 shows a comparison of the energy transferred by the HTF (middle) and the SoCs (bottom). The HTF energy comparison shows a small offset, which may be caused by the initial conditions of the HTF used to compute E_e . Additionally, the energy transferred by the PCM exclusively due to its latent heat value is plotted ($E_{\Delta h_l}$). On the other hand, the SoC's comparison presents a slight mismatch which is caused by two main factors. Firstly, SoC_s is computed considering only the latent heat value area, which is defined by the proposed temperatures T_{full} and T_{empty} . Conversely, SoC_e is computed in [15] using function ϕ of equation (4.105), which does not represent the total latent heat value because the contributions of coefficients a_0 and a_1 to the specific heat curve are ignored. This increases the region of the phase change, including a bigger amount of energy from the considered latent heat value. Secondly, the accuracy of the PCM temperature is higher in the model presented in [15] as it has been discussed above. However, the trends for both SoCs are similar.

Regarding the simulation results, the average temperature of the PCM ($T_{P,ave}$) is shown at the top of Figure 4.72. To illustrate the relation between the PCM temperature and the latent heat transferred, horizontal dashed lines are added to highlight the phase change zone of the PCM limited by T_{empty} and T_{full} , and vertical dashed lines indicate the moment when those temperatures are reached. These vertical lines are extended to the middle and bottom graphs. As it can be observed, the beginning and the end of the phase change match the $E_{\Delta h_l}$ release or absorbing, and the full and empty SoCs. For the sake of clarity, the charging and discharging process are pointed out with 'ch' (charging) and 'dch' (discharging) labels.

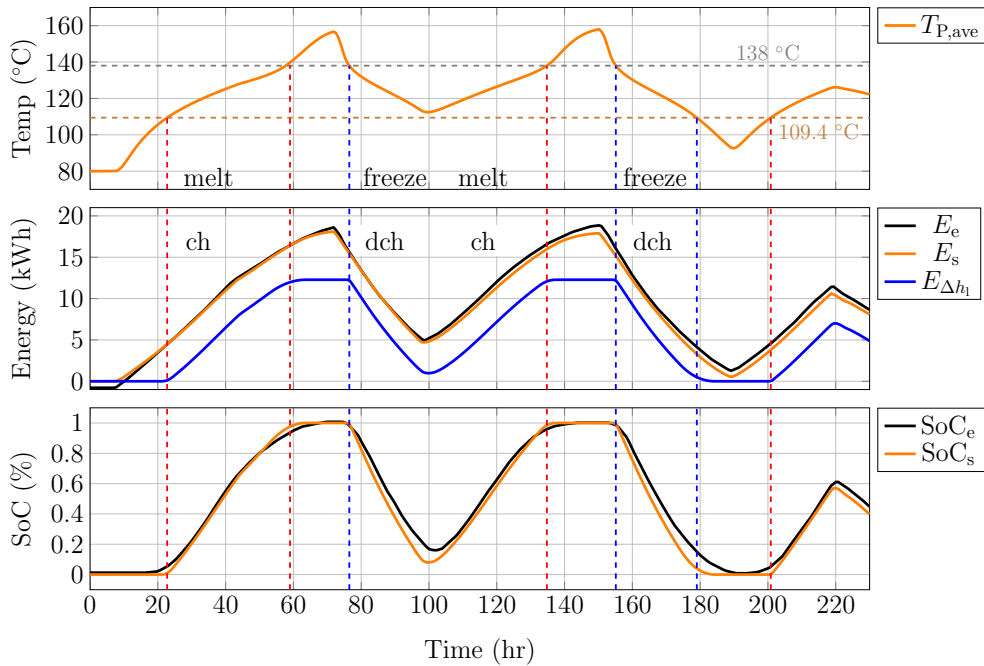


Figure 4.72: Simulation results of PCM temperature (average) (Top). Comparison between simulation results and experimental data of stored energy (middle) and SoC (bottom).

Verification of latent heat TES for a cooling application

Cooling energy can be stored employing PCM with low peak temperatures on its specific heat curve. Many PCM options are available, even with peak temperatures below 0°C . Nevertheless, ice is one of the most common choices for cooling applications due to its high energy density, low cost and accessible melting temperature. To verify the validity of the PCM-based TES model for cooling applications, simulation results are compared against experimental results reported in [16, 17], where a commercial ice tank manufactured by CALMAC[®] is characterised. The specific model used is the ICEBANK 1098C, which has a nominal storage capacity of 350 kWh [18].

Figure 4.73 shows a schematic for the interior of the tank. The arrangement consists of 34 spiralled pairs of polyethylene tubes (i.e. 68 tubes in total) submerged in water. Each pair of tubes is enrolled in a spiral shape and placed in a horizontal plane throughout the tank's height, as shown in Figure 4.74. HTF at a suitable temperature is pumped inside the tubes to solidify water into ice (for charging) or melt the ice built around the tubes (for discharging).

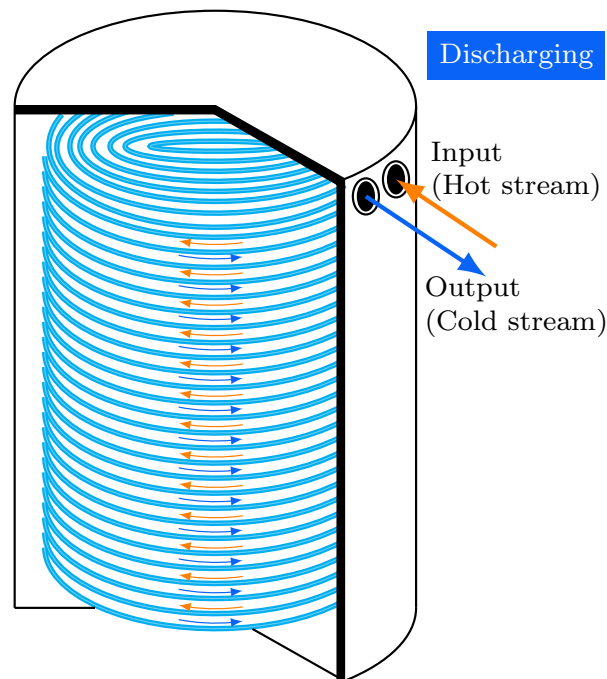


Figure 4.73: Sketch of the internal structure of the ice tank manufactured by CALMAC[®]

As shown in Figure 4.74, there are four tube headers for each horizontal level. Each level is connected to the other levels by two separate supply and return manifolds, namely the HTF inlet and outlet headers, respectively. This arrangement enables the HTF inside the pair of tubes for any horizontal level to flow in a counter-current direction to, in turn, facilitate a homogenous ice growth and melting process throughout the tank. In addition, the split of the flow through the 68 tubes (34 horizontal levels \times 2 pair of tubes) reduces the pressure drop through the tank related to the HTF. Figure 4.74 also shows a top view for a single horizontal level during charging and discharging modes. For a charging process, ice builds in a cylindrical form around each tube when the HTF cooled down to low temperatures (*e.g.*, -4°C) circulates inside the tubes. During a discharging process, a warm HTF (*e.g.*, 12 to 15°C) flows through the tubes so that the cooling energy stored in the ice is transferred to the HTF by melting the ice. The sequence of the charging process is illustrated in Figure 4.75.

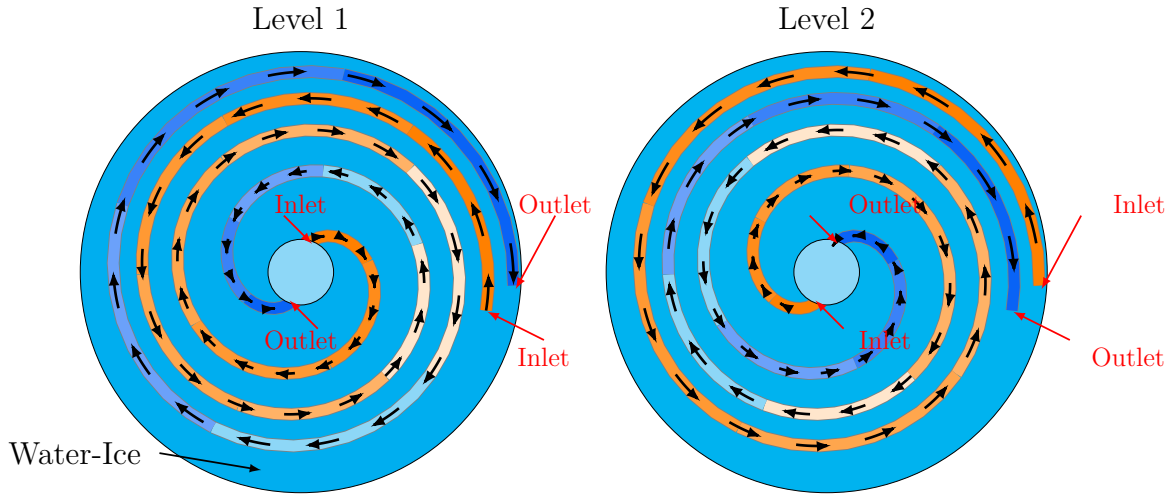


Figure 4.74: Top view of the horizontal levels of spiralled tubes inside the ice-based TES during discharging process.

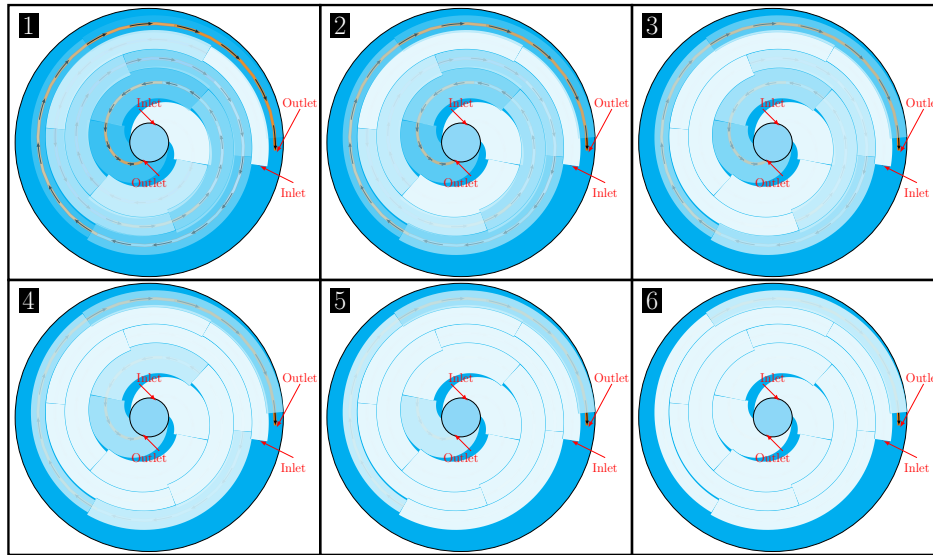


Figure 4.75: Sequence of the ice growth in a ice-tank based TES level during charging process.

Figure 4.76 provides further detail on the ice formation for adjacent tubes during the charging process. The value of r_{ice} defines the specific size of the water/ice cylindrical shape around the tubes. This assumption helps to establish a control volume for the HTF, tube and water/ice. This volume is used to apply energy balance to determine the average temperature of the HTF and of water/ice. Tube dimension is defined by its internal (r_i) and external (r_o) radius.

The ice-tank based TES dynamic thermal model is obtained applying the same steps established for the PCM based TES for heating applications, which are based on Figure 3.1. Firstly, the tank is considered well insulated as it is reported in [18]. Similarly, equal internal flow for all spiralled tubes and equal temperature distribution of the HTF and the water-ice through the whole tank are assumed. Thus, a single tube energy balance represents the same conditions for all 68 tubes in the tank. Figure 4.77 shows a single spiralled tube divided into nodes to define the energy balance's control volumes.

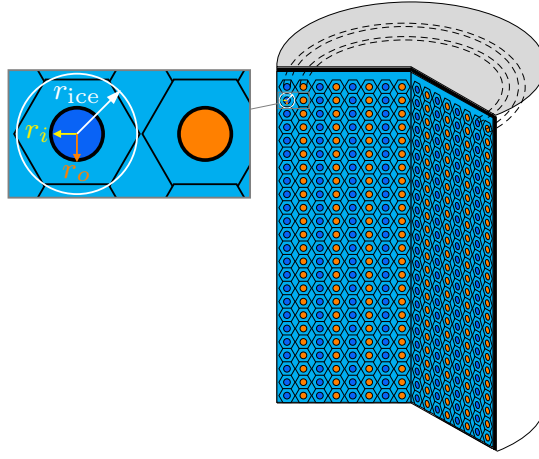


Figure 4.76: Imaginary bounds of the water-ice volume around the tubes.

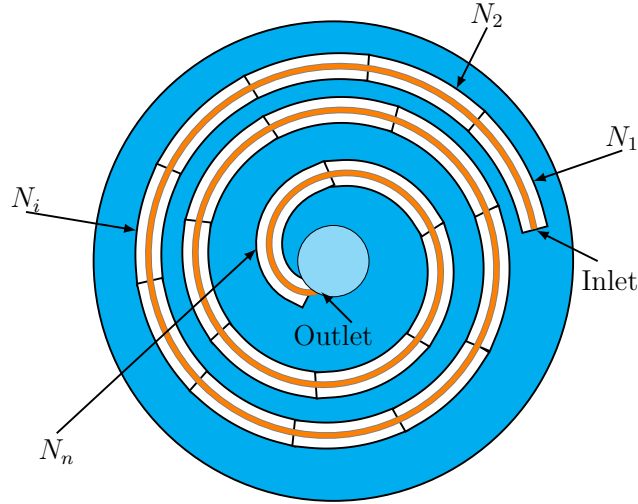


Figure 4.77: Division of control volumes (nodes) in a single tube.

Applying the energy balance to the split tube, a set of non-linear differential equations is obtained. The model equations are similar to equations (4.103) and (4.104). Substituting subscript 'P' by 'w' for the water-ice and keeping f for the HTF yields

$$m_{f,i}c_p(T_{f,i})\dot{T}_{f,i} = \dot{m}_f c_{p,f,i}(T_{f,(i-1)} - T_{f,i}) + U_{f-w}(\rho_f, k_f, \nu_f, Pr_f, \rho_w, k_w) A_{tr}(T_{P,i} - T_{f,i}), \quad (4.113)$$

$$m_{w,i}c_p(T_{w,i})\dot{T}_{w,i} = U_{f-w}(\rho_f, k_f, \nu_f, Pr_f, \rho_w, k_w) A_{tr}(T_{f,i} - T_{w,i}), \quad (4.114)$$

where $T_{f,(i-1)}$ when $i = 1$ is the input temperature of the HTF ($T_{f,in}$) and m_w [kg] is the mass of the water.

Having circular tubes, the heat transfer process occurs in the same way as it is shown in Figure 4.61. Thus, conduction heat transfer coefficients through the tube $U_{cd,t}$ and through the water $U_{cd,w}$ are computed by equations (4.100) and (4.101), respectively.

The next step of the modelling process is to define the thermophysical properties of the PCM and the HTF. The HTF used in the experiments reported in [16, 17] is a mixture of water and glycol at 32%. Due to the lack of information about its properties, a mixture of 34% is used in the simulations, whose thermophysical properties are defined by polynomial

equations included in Appendix F. The latent heat values of solidification-melting (Δh_l) and melting-evaporation (Δh_v) and the well-known enthalpy curve of water are shown in Figure 4.78. As it is observed, Δh_l and Δh_v are released or absorbed around 0°C and 100°C , respectively.

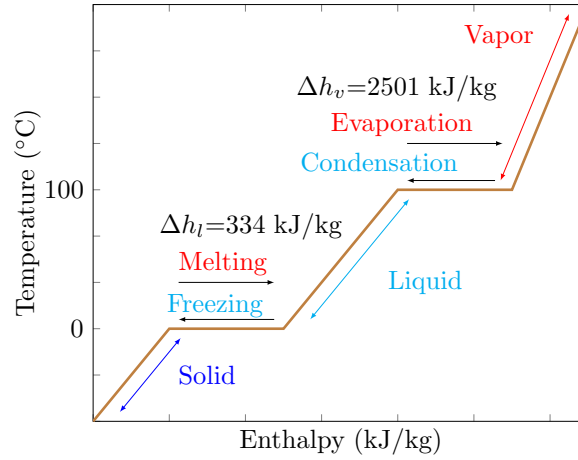


Figure 4.78: Water enthalpy curve.

A detailed curve of the enthalpy or the specific heat of the transition zone during phase changes is not available in the literature. Therefore, following the same approach to determine the specific heat of the PCM for heating applications, a PDF is used to estimate the water-ice's specific heat curve. The transition zone of the solidification-melting phase change is defined by equation (4.108). The parameters of this equation are $\sigma = 2.118$, $\mu = 0$, $m = 0.65$. A slight variation on equation (4.105) is necessary to include specific heat values of the liquid and solid phase of the water, which are approximated by 4.18 kJ/kgK and 2.1 kJ/kgK , respectively. Then, the specific heat curve of the water-ice is described by

$$c_{p,w}(T_w) = 1000 [4.18 + a_0 (\phi(T_w) - a_1)], \quad (4.115)$$

where, $a_0 = 406.12$, $a_1 = 0.0128$ and ϕ is the log-normal distribution defined by equation (4.108) (see Figure 4.79).

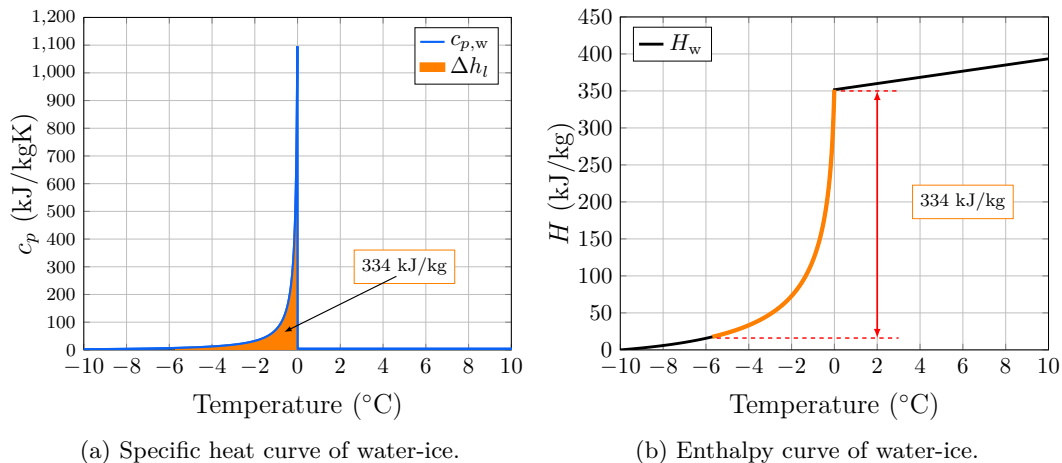


Figure 4.79: Proposed specific heat and enthalpy curves of water.

4.4. Thermal energy storage tanks

The detailed parameters of a single tube provided in [19, 20] are shown in Appendix C. The model described by equations (4.113) and (4.114) is build in MATLAB/Simulink using s-functions. The single tube is divided into 20 nodes. A special setup is used for these experiments [16]: the top 16 levels of spiralled tubes are blocked. The HTF only circulates through the bottom 18 levels (36 single tubes) submerged in water. Then, the storage capacity is approximately reduced to 172 kWh.

The same operation conditions of the experiments reported in [16] are used for the first simulation: HTF's mass flow rate of $\dot{m}_f = 3698$ kg/h, which is converted to the international system as $\dot{m}_f = 1.027$ kg/s and, input temperature of $T_{f,in} = 12.8^\circ\text{C}$. Initial conditions of the HTF and water-ice temperature are set to -5°C . Typically, during the discharging process, the output temperature of the fluid $T_{f,out}$ in a TES tank reaches the value of $T_{f,in}$ when the storage is depleted. It makes sense because no more cooling energy exits that might decrease the HTF's temperature. Nevertheless, the data reported has a discrepancy of 1.28°C . This difference may be due to several factors, such as an incomplete discharging process or sensor error measurement. This difference provokes a mismatch between simulation and experimental results. Therefore, a -1.28°C offset is applied to the experimental input temperature. The temperature of the HTF in the last node ($T_{f,20}$) is considered as the output temperature $T_{f,out,s}$. Subscripts 'e' and 's' stand for experimental and simulation results in Figure 4.80.

The cooling power produced during the discharging process is compared as well. This value is computed using the \dot{m}_f , $T_{f,in,s}$ and $T_{f,out,s}$ in equation (3.20). There is a mismatch between the simulated power released (P_s) and the power graph provided (P_{e1a}). Nevertheless, having the experimental data of the input ($T_{f,in,e}$) and output ($T_{f,o,e}$) of the HTF, it is possible to compute the power using equation (3.20) as

$$\frac{dE_e}{dt} = P_{e,1b} = \dot{m}_f c_{p,f} (T_{f,o,e} - T_{f,in,e}).$$

This calculations show a better agreement with P_s , as it is shown in Figure 4.80b.

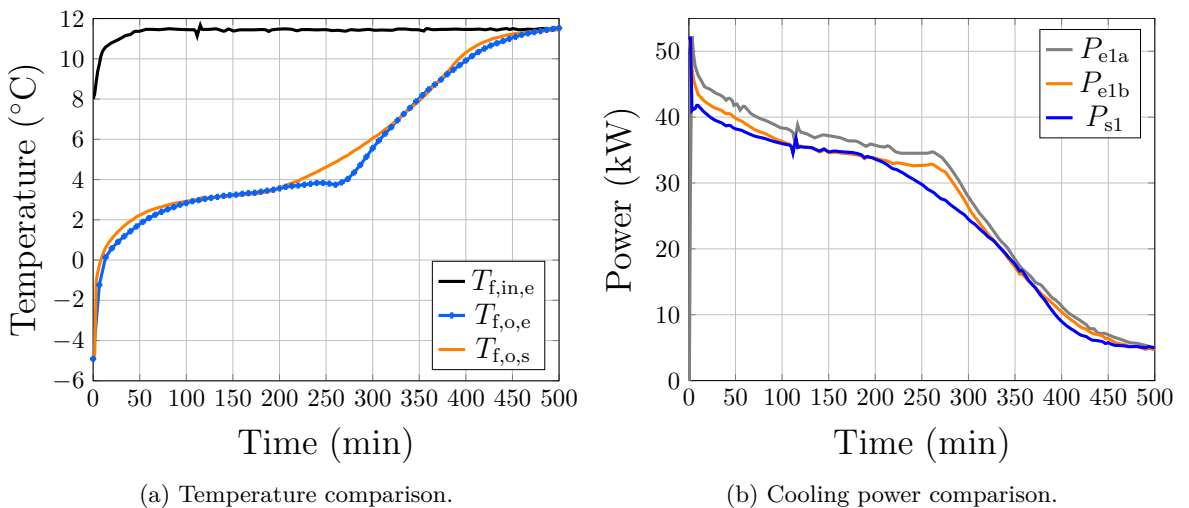


Figure 4.80: Comparison between experimental and simulation results of discharging process.

The ice melting process inside the TES is shown in Figure 4.81. Water-ice temperatures of some nodes (1,10 and 20) are plotted. Their corresponding HTF temperatures are also presented.

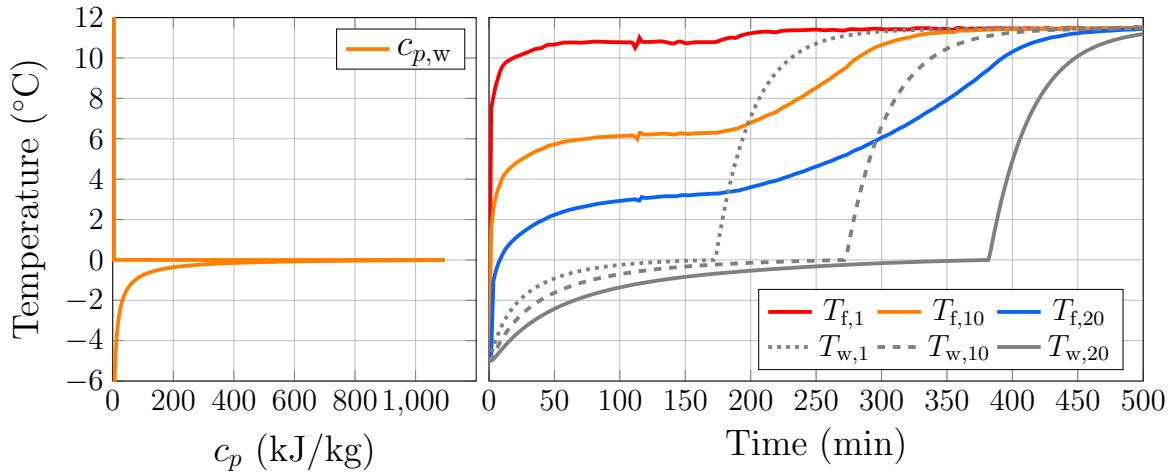


Figure 4.81: Simulation results of the node temperatures of HTF and water ice during discharging process at $\dot{m}_f = 1.027$ kg/s.

Only one experiment is reported with input and output temperatures of HTF. However, the cooling power graphs of four more different experiments are reported. These operating conditions are used to carry out further comparisons. Since $T_{f,in,e}$ is not provided, the same profile used before is adjusted. For instance, for the second comparison, the reported $T_{f,i,e}$ is equal to 14.4°C . Thus, a factor of 1.6°C ($14.4-12.8$) is added to the temperature profile besides the offset applied in simulation 1 as $T_{f,in,e} + 1.6 - 1.28$. The operating conditions for all simulations are shown in Table 4.2.

Table 4.2: Operating conditions of discharging process.

Simulation	\dot{m}_f (kg/s)	$T_{f,in,e}$ ($^\circ\text{C}$) (Original)	$T_{f,in,e}$ ($^\circ\text{C}$) (Adjusted)
1	1.027	12.8	11.52
2	1.1306	14.6	13.32
3	0.9775	14.4	13.12
4	0.9683	10.6	9.32
5	0.7761	14.1	12.82

The comparison of the cooling power released for the second experiment and simulation 2 is shown in Figure 4.82b. The input and output temperatures of HTF and output of water-ice are presented in Figure 4.82b. As it can be observed, the P_e and P_f present a good agreement that might be improved if the experimental input and output temperatures of HTF were provided as done in simulation 1.

Three more simulations are carried out under different operating conditions (see Table 4.2). The results are compared against the cooling power graphs of discharged tests reported in [16] (see Figure 4.83). Although there are small mismatches due to the lack of temperature measurements, simulated and experimental plots are very similar. It can be concluded that the proposed model can simulate a real system's energy transfer process with an acceptable level of accuracy.

4.4. Thermal energy storage tanks

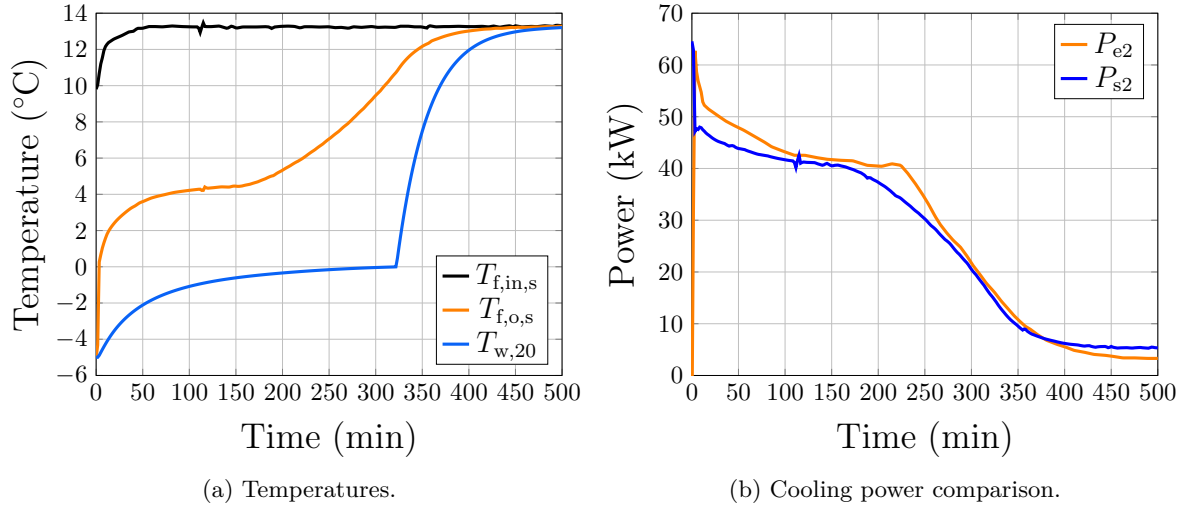


Figure 4.82: Comparison between experimental and simulation results of power released during discharging process at $\dot{m}_f = 1.1306$ kg/s.

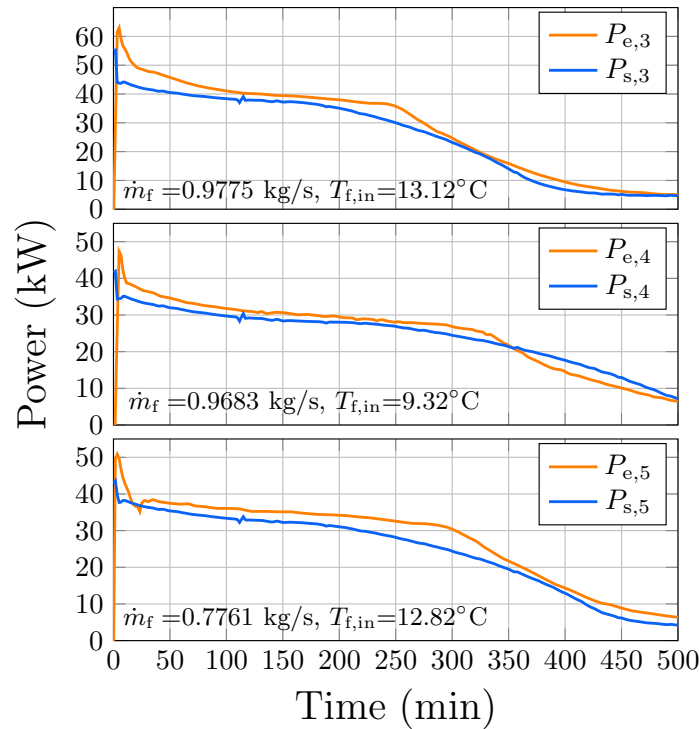


Figure 4.83: Comparison of the mean cooling power of the last three operating condition in Table 4.2.

Finally, a charging test is carried out with the same tank's setup as in [17] where only temperature profiles are provided. A chiller system is used to supply cold HTF with temperature below 0°C . No constant input temperature is injected thoroughly during the charging test. A large decrement of the input temperature is presented at 200 mins, which might be due to chiller conditions or a subcooling phenomenon [11]. The time required to charge the ice tank is significantly long (nearly 25 hours), which implies the operating conditions ($\dot{m}_f = 0.6817$ kg/s and $T_{f,in,e} = -3.7^\circ\text{C}$) do not represent typical values of real operating points in a cooling centre where the TES should be charged at night. These charging conditions are used to run a simulation with initial conditions of HTF and water-ice equal to 10.5°C .

The comparison depicted in Figure 4.84a between the experimental ($T_{f,o,e}$) and the simulated ($T_{f,o,s}$) output temperature of HTF shows a very good agreement. Temperature of nodes 1, 10 and 20 are presented in Figure 4.84b.

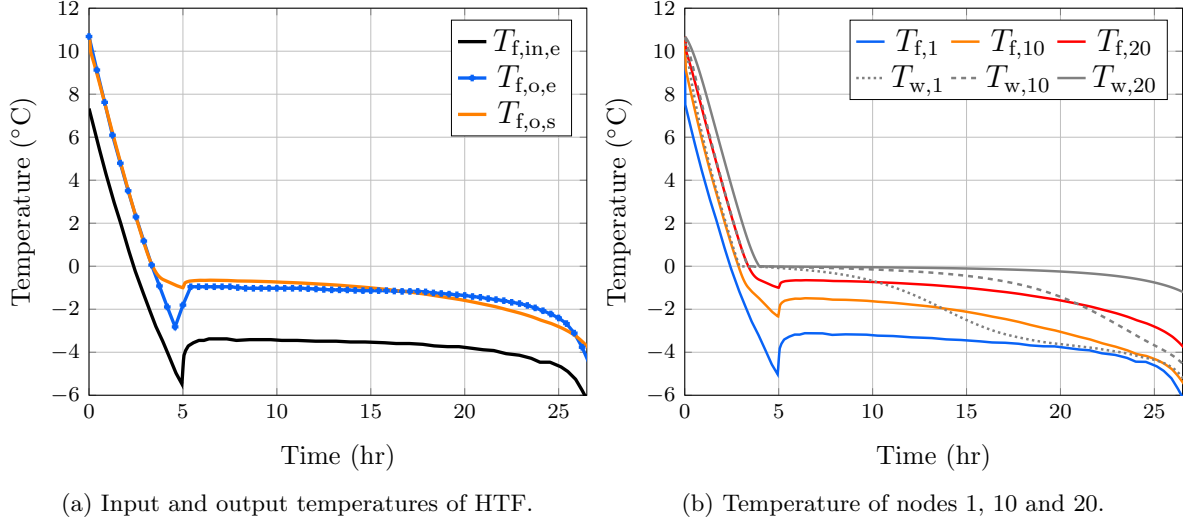


Figure 4.84: Comparison between experimental and simulation results of charging process of ice based TES.

State of charge

The tank's energy storage capacity given by the manufacturer is 350 kWh, which has been reduced to 172 kWh due to the tank's special setup in [16]. This value is verified using equation (4.109) to compute the energy released or absorbed by the mass of the water-ice inside the tank. The mass of the water (m_w) is obtained by means of the volumetric capacity of the tank ($V_{\text{tank}} = 3710$ L) reduced by half [18]. Thus, the storage capacity is obtained as

$$E = \frac{1}{3600} \Delta h_l m_w = \frac{1}{3600} \Delta h_l (V_{\text{tank}}/2) \rho_w = 171.69 \text{ kWh},$$

where ρ_w at 25°C is equal to 997.37 kg/m³. Nevertheless, the fitting of simulated to experimental results implied the reduction of the volume of water as no match was achieved using the exactly half the value of V_{tank} . The total volume used for the simulations is defined by $V_w \times N_p$, where $N_p = 36$ is the number of single tubes. Then, the storage capacity of the ice tank with a total volume of 1702 L is given by

$$E = \frac{1}{3600} \Delta h_l m_w = \frac{1}{3600} \Delta h_l (1702 \text{ L}) \rho_w = 158 \text{ kWh},$$

The proposed method to compute the SoC is assessed by simulations of charging and discharging processes with the same tank configuration reported in [16]. SoC is obtained using $c_{p,w}$ and equations (4.110) and (4.111). For water-ice, the total discharge SoC = 0 occurs when the ice is completely depleted at $T_{\text{empty}} = 0$ °C, according to $c_{p,w}$. Conversely, the full charge SoC = 100% is presented when the solid phase is achieved at $T_{\text{full}} = -5.7$ °C. Therefore, the limits of SoC equation (4.110) have to be swapped: the low and upper limits mean full and empty charge, respectively, and the integral of c_p from lower limit to T_w is subtracted

4.4. Thermal energy storage tanks

from 1 as

$$\text{SoC}(T) = \begin{cases} 0, & T_w > T_{\text{empty}} \\ \left[1 - \frac{\int_{T_{\text{full}}}^{T_w} c_{p,w}(T) dT}{\Delta h_l} \right] \times 100, & T_{\text{full}} \leq T_w \leq T_{\text{empty}} \\ 100, & T_w < T_{\text{full}} \end{cases} \quad (4.116)$$

Figure 4.85 shows the SoC at three different temperatures of the water-ice. For instance, if $T_w = -5.7^\circ\text{C}$, the phase change is completed and the water is totally frozen; *i.e.*, all latent heat has been absorbed. Hence, the TES tank is considered charged. On the other hand, as T_w increases, the latent heat value is released and the charge is reduced. Emptiness is achieved when no more latent heat is available and T_w is bigger than 0°C .

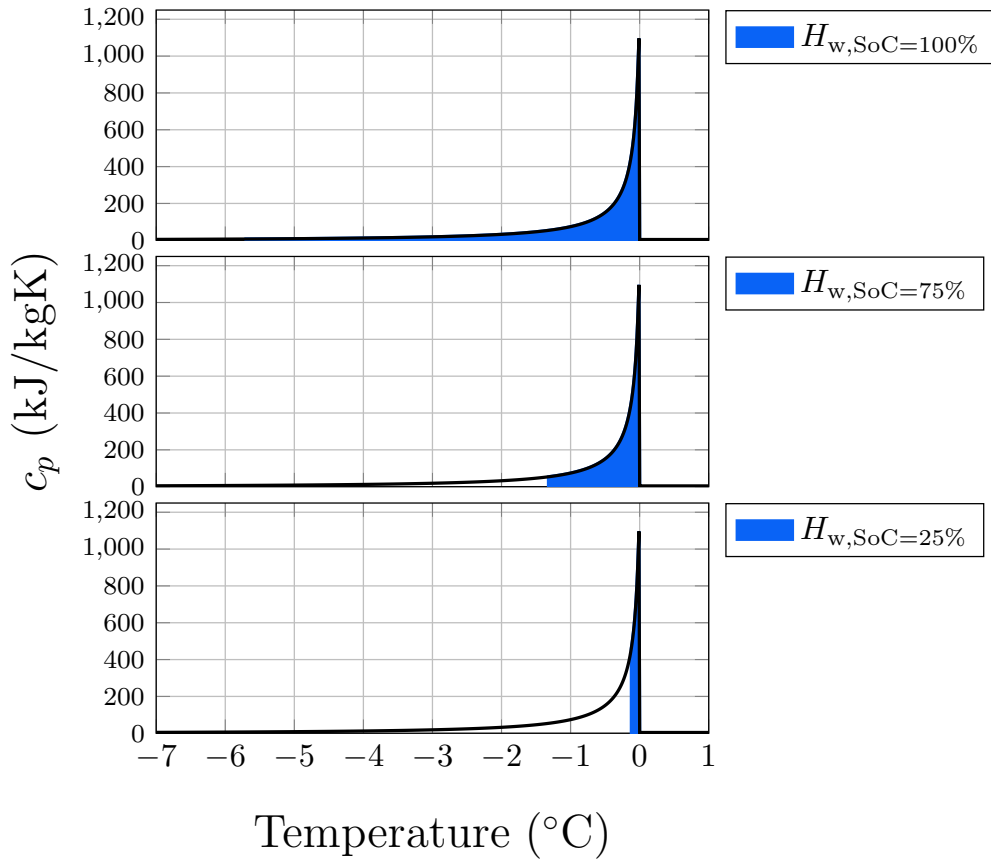
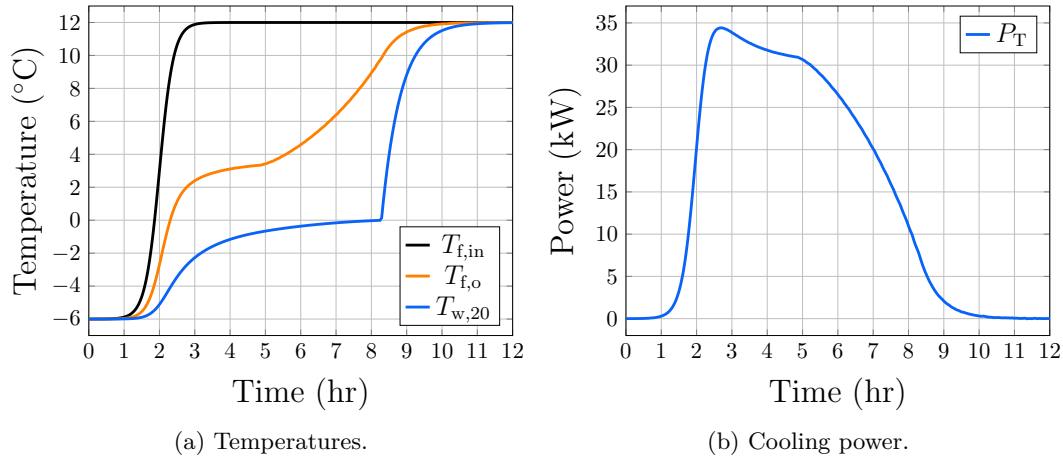


Figure 4.85: Top: $T_w = -5.7^\circ\text{C}$ and SoC = 100%. Middle: $T_w = -1.32^\circ\text{C}$ and SoC = 75%. Bottom: $T_w = -0.12^\circ\text{C}$ and SoC = 25%.

The total SoC of the ice tank is obtained applying equation (4.111) as

$$\text{SoC}_T = \frac{\sum_{i=1}^N \text{SoC}(T_{w,i})}{N}. \quad (4.117)$$

A discharging process is simulated to address the contribution of the sensible (Δh_s) and latent (Δh_l) heat of the water to the energy provided by the tank. The operation conditions are a mass flow rate of 1.0 kg/s and an input temperature of 12°C . The initial conditions of water-ice and of the HTF are set to -6°C . The number of nodes to solve equations (4.113) and (4.114) is 20. Figure 4.86 shows the simulation results.


 Figure 4.86: Simulated discharging process of ice-tank with $\dot{m} = 1$ kg/s.

The total energy released during the discharging process is the contribution of sensible plus latent heat of the water-ice. Having a dynamic model of the thermal behaviour, it is possible to know the amount of these contributions. Figure 4.87 shows the simulation results of a discharging process. Horizontal dashed lines are used to identify when the water-ice temperature of the first, middle and last nodes ($T_{w,1}$, $T_{w,10}$ and $T_{w,20}$) reach T_{full} and T_{empty} . These moments indicate the beginning and the end of the phase change. During this period, all latent heat is released. As it can be observed, the power due to sensible heat ($P_{\Delta h_s}$) starts to decrease when the first node reaches T_{full} . On the other hand, the power due to latent heat ($P_{\Delta h_l}$) begins at the same time and lasts up to the last node reaching T_{empty} . Afterwards, only released energy by sensible heat (liquid phase) contributes to the total power.

The sharp shape of the power curve is caused by the melting process of the nodes occurring at different moments, showing a sudden rise in $P_{\Delta h_s}$ and drop in $P_{\Delta h_l}$ due to its fast change of temperature being liquid (constant c_p).

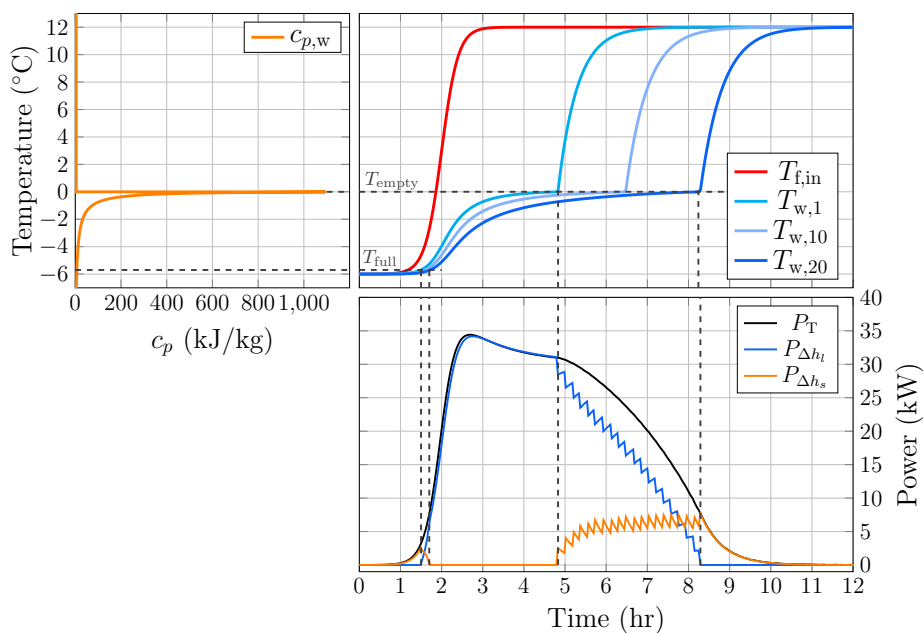


Figure 4.87: Power contribution of the sensible and latent heat of the water to the released energy during discharging process.

4.4. Thermal energy storage tanks

The integral of power curve yields the energy released or absorbed by the PCM. Nevertheless, analytically, the PCM's mass defined by the energy balance's control volume is changing due to the temperature dependence of the density. This causes a slight variation between the simulation results and the calculated released energy with a constant density (158 kWh). To verify this effect, two simulations are carried out: with variable ($\rho_w(T)$) and constant ($\rho_w = 1000 \text{ kg/m}^3$) density, denoted with subscripts 'a' and 'b', respectively. Total energy (E_T), energy contribution of latent ($E_{\Delta h_l}$) and sensible heat ($E_{\Delta h_s}$) of both simulations are presented in Figure 4.88. As it is expected, the $E_{T,b}$ matches the calculated value (158 kWh). It means that an accurate computation of the storage capacity requires considering the variation of the PCM's density, which implies a variable mass of PCM during charging and discharging processes. A variable density is considered for the next simulations.

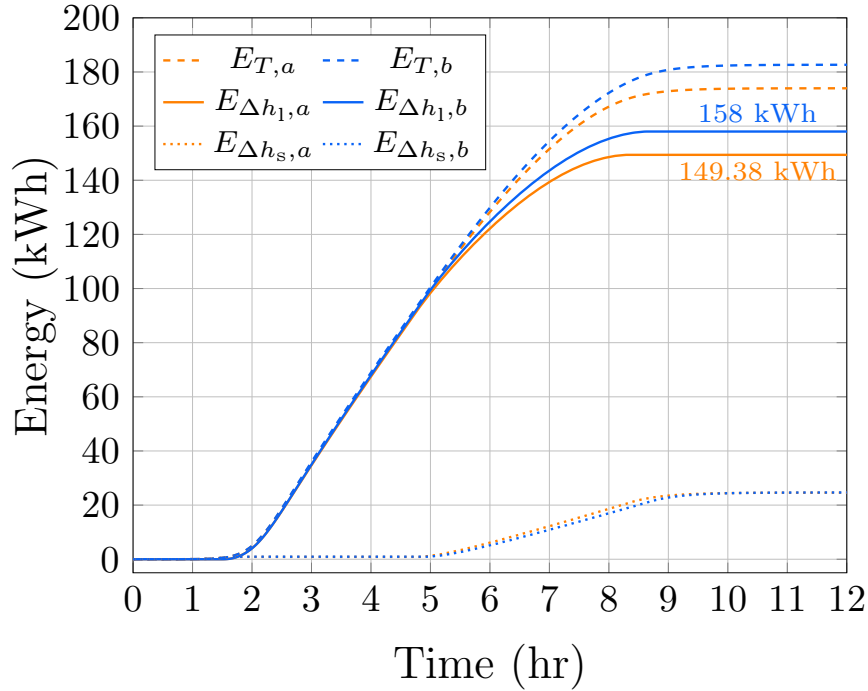


Figure 4.88: Energy released during discharging process with constant and variable density.

Whether the charge of the ice-tank is expressed in power or energy, the SoC computation method shows a good agreement for both. Figure 4.89a shows the SoC at two different hours after the process begins. The power plot (top) highlights the contribution of the latent heat in terms of energy (area below the curve), and the dashed line points out the SoC. This value is verified through the energy curve (bottom), showing the amount of energy released (34.16 kWh) and the percentage of remaining energy (76.14%). An additional SoC is presented in Figure 4.89b, when the storage is almost depleted at six and a half hours after the beginning of the discharging process.

The computation of the SoC is addressed for a charging process. The operation conditions are $\dot{m}_f = 6 \text{ kg/sec}$, $T_{f,i} = -6^\circ\text{C}$ and the initial conditions of the water-ice and HTF are 12°C . Figure 4.90a presents the input, output temperatures of the HTF, and the water-ice temperature in the last node. Since the energy is absorbed by water-ice, its value is negative. For the sake of clarity, powers are multiplied by -1 (see Figure 4.90b).

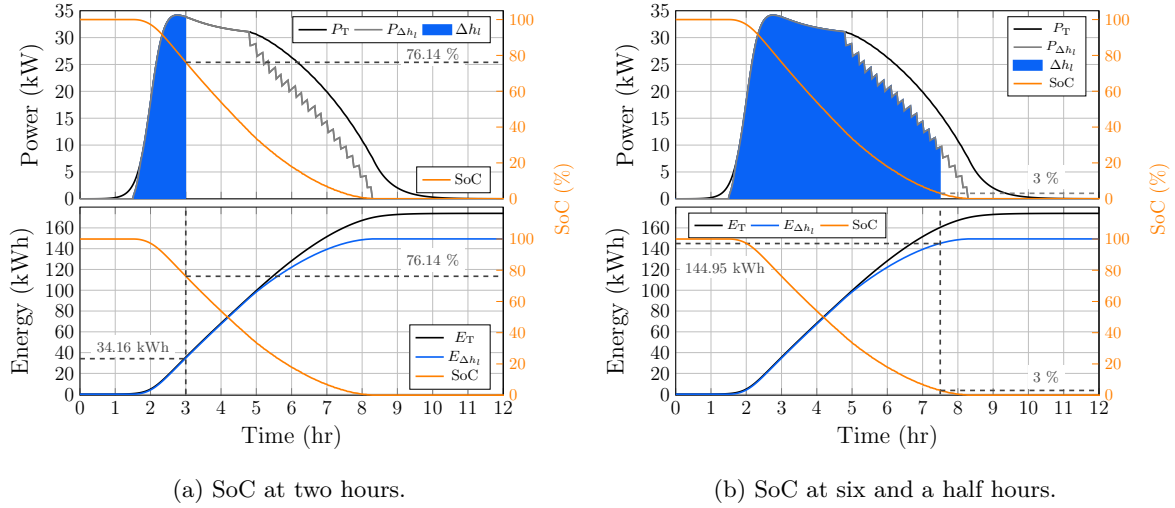


Figure 4.89: Two SoCs of a discharging process of ice-tank.

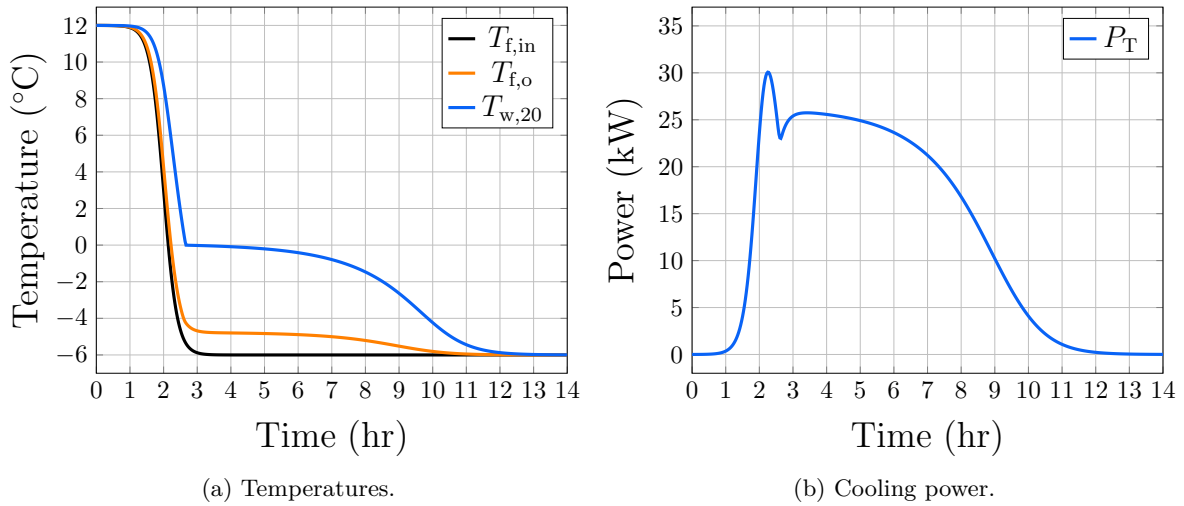

 Figure 4.90: Simulated charging process of ice-tank with $\dot{m} = 6$ kg/s.

Figure 4.91 shows the contribution of latent and sensible heat to the power absorbed during the charging process. The specific heat curve of water is used to specify the beginning and end of the latent heat being absorbed. Dashed lines are used to identify T_{full} and T_{empty} . When $T_{w,1}$ reaches 0°C , $P_{\Delta h_i}$ begins, and $P_{\Delta h_s}$ suddenly drops as the water starts to solidify into ice. At the end of the process, when $T_{w,1}$ reaches -5.7°C , the power due to sensible heat starts to increase since transition phase change is finishing and only ice is present. No more $P_{\Delta h_i}$ is available when the last node temperature decreases to -5.7°C .

Two SoC are assessed for the charging process. Figure 4.92a shows the power (top) absorbed. It includes the SoC, which indicates the percentage of energy charged at four hours after the beginning of the process (at 1 hour). Dashed lines show the amount of energy absorbed in an energy plot (bottom). Similarly, the SoC is obtained at eight and a half hours after $T_{f,i}$ starts to rise (see Figure 4.92b).

4.4. Thermal energy storage tanks

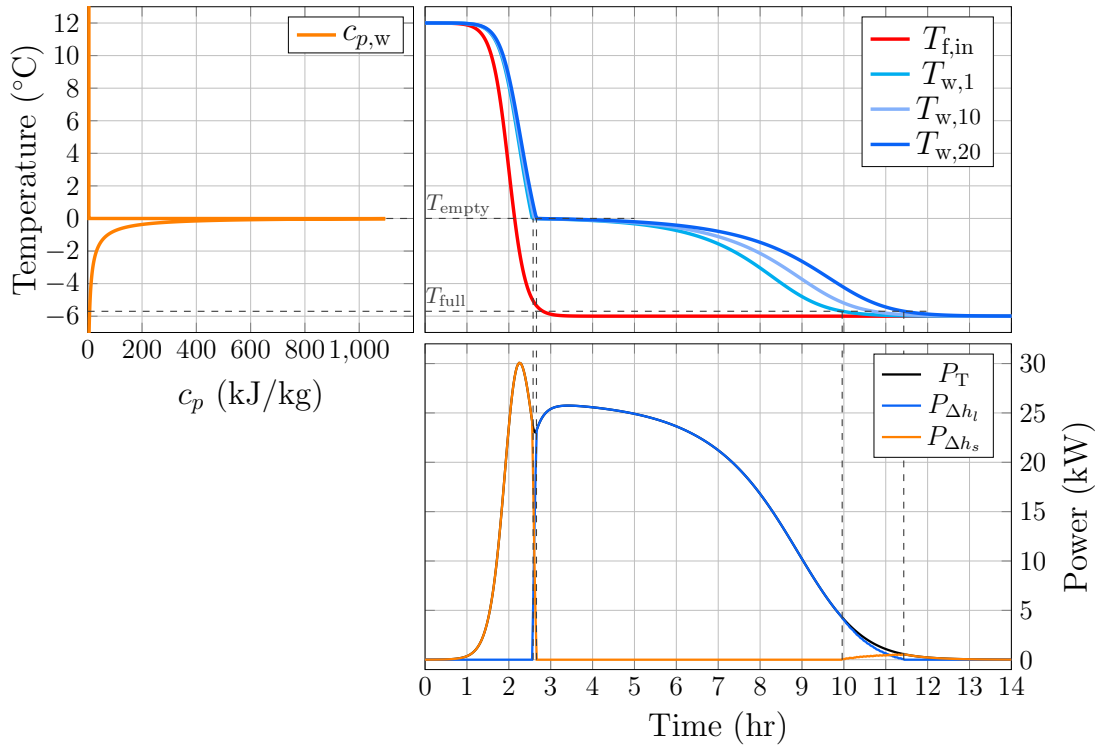


Figure 4.91: Power contribution of the sensible and latent heat of the water to the absorbed energy during charging process.

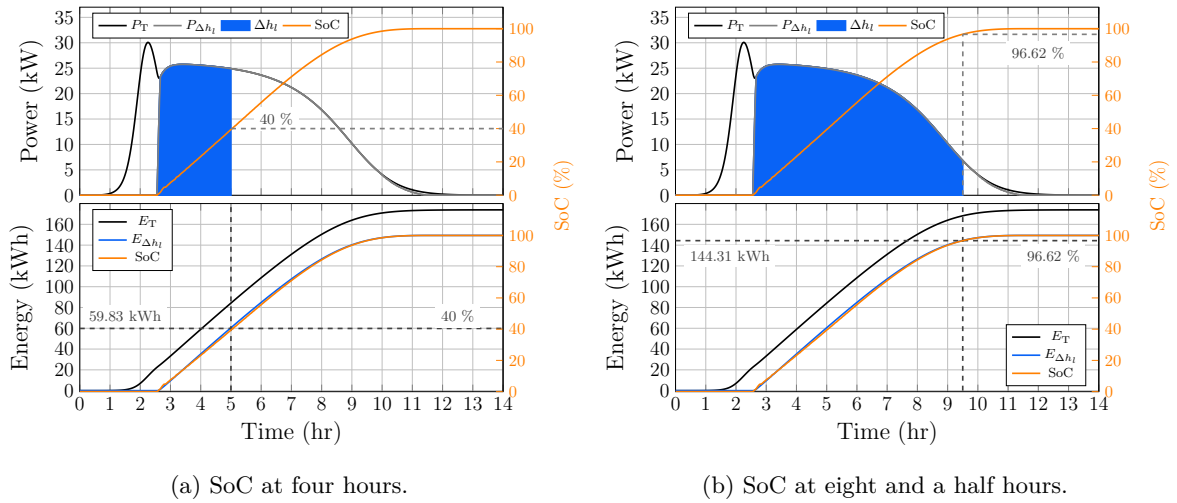


Figure 4.92: Two SoCs of a charging process of ice-tank.

Finally, charging and discharging processes are simulated throughout the same simulation. Different mass flow rates are used: $\dot{m}_f = 1.5$ kg/sec and $\dot{m}_f = 6$ kg/sec for discharging and charging, respectively (see top of Figure 4.93). The ice-tank is discharged at 12°C and 14°C in the first and second charging processes, respectively. The $T_{f,i}$ for both charging processes is -6°C. The HTF and the water-ice temperature in the last node are also included to indicate when the ice is completely built or depleted.

Figure 4.94 shows the water-ice temperature in the first and last node (top). The total energy provided and absorbed by the water-ice (E_T) and the energy due to sensible heat are also included. Dashed lines are used to highlight how the SoC represents the released and absorbed latent heat.

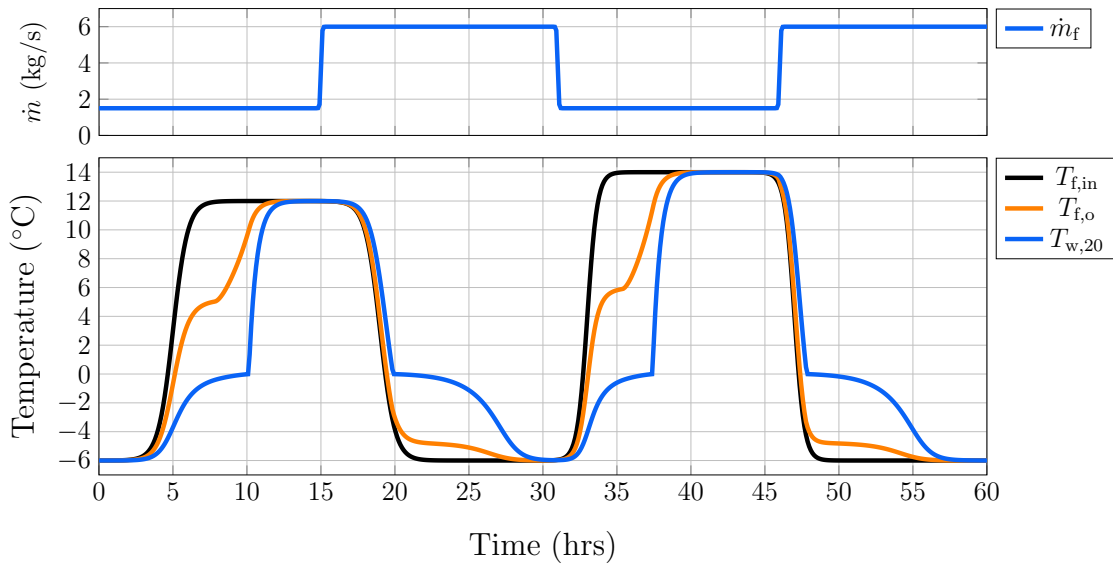


Figure 4.93: Top: Mass flow rate of HTF. Bottom: simulation results of the output temperature of HTF and water-ice in node number 20.

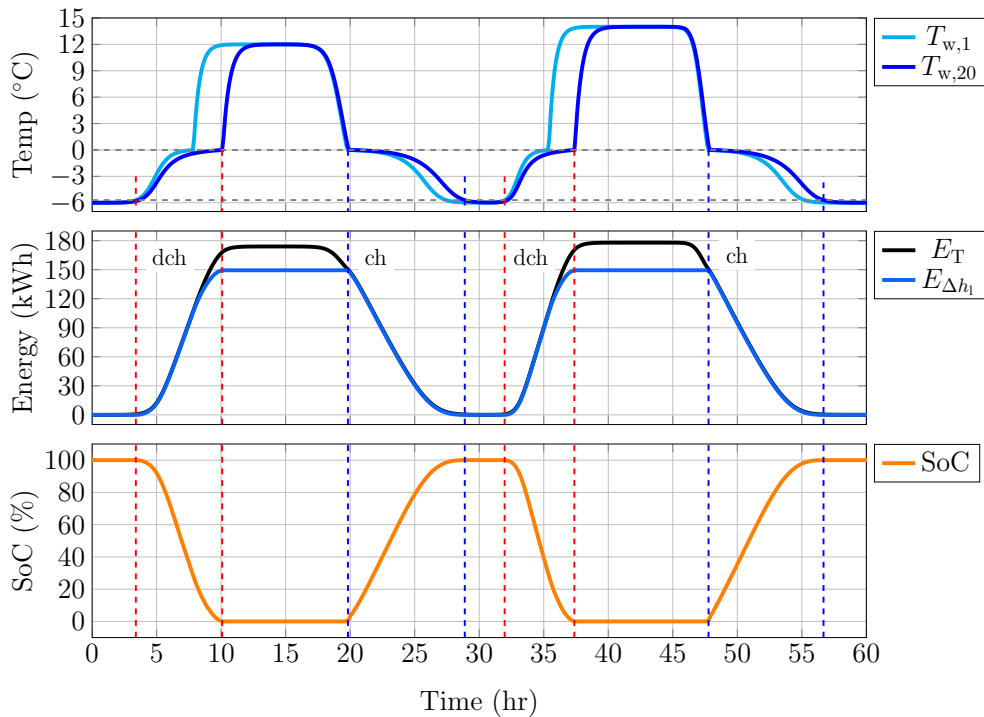


Figure 4.94: Simulation results of charging and discharging process in a row. Top: temperature of water ice in first and last node. Middle: total and latent heat energy. Bottom: SoC.

As it can be observed, the dynamic thermal behaviour of a TES tank for a cooling application can be predicted with the developed model. The SoC can be calculated at any moment with the proposed method. The specific heat curve of the PCM is required to obtain an accurate value. Different operating conditions can be simulated. Thus, more complex analyses of the TES tank performance within a DHCS can be carried out.

4.5 Buildings

An indoor temperature mainly describes the thermal behaviour of a building. This is affected by the heat sources presented in the surroundings, such as air conditioning (AC) systems, ambient temperature, or people transit. The properties of the construction materials also have a significant effect on the internal temperature of a building. For instance, the use of a wall insulator mitigates the impact of the ambient temperature. The dynamic model presented in this section can describe the internal temperature of a building, considering its dimensions and materials' properties and how the heat from different sources is transferred. The model is based on the electrical to thermal behaviour analogy and the dynamic calculation of conduction and convection heat transfer. Although radiation heat transfer also has an important effect due to solar radiation through windows, its analysis is out of the scope of this research. Therefore, it is simply considered as a heat profile.

A set of linear ODEs defines the rate of change with respect to time of the temperature of walls, roof, windows, and building interior. The heat supplied to regulate the building's indoor temperature, such as that from radiators or AC systems, is defined as the model input. The ambient temperature and any other heat source presented in the building, such as people transit and radiation from windows, are considered. The computation of the convection heat transfer coefficient U_{cv} between the building and the exterior requires the weather conditions (air mean velocity and ambient temperature). These variations are established as uncertainty ranges. Thus, U_{cv} is computed dynamically using equation (3.74). On the other hand, the conduction heat transfer coefficient is calculated using equation (3.77), which includes the thickness and thermal conductivity of the construction materials (wall, roof, window and insulator).

The modelling procedure presented in this chapter is focused on a single house with and without insulation. Nevertheless, this approach can be extended to larger residential and commercial buildings with several rooms. The thermal capacitance of the rooms can be connected to each other through the thermal resistance of the walls shared by the rooms. This might increase the complexity of the model. Nevertheless, lumping the thermal capacitances of rooms may simplify the model if detailed modelling is not required while providing acceptable results [21].

4.5.1 Dynamic model of a single house

The main heat sources and losses presented in a single house are the ambient conditions (temperature and speed wind), internal heating system, people transit, solar radiation and heat loss due to air infiltration through windows or door openings. The thermal mass of the house interior is defined as the mass of air inside the house. The material of the walls is a concrete block and the roof is made of asbestos tiles⁷. Figure 4.95a shows the dimension of the house. Firstly a model of the single house without insulation is developed, then insulation is added. The schematic of an insulated wall is shown in Figure 4.95b. The total surface of the house, including the roof, is considered insulated. The insulator material used in the model is cellulose [22, 23].

⁷Although asbestos tiles are no longer permitted in the UK, they were used in this model due to the availability of its thermophysical properties.

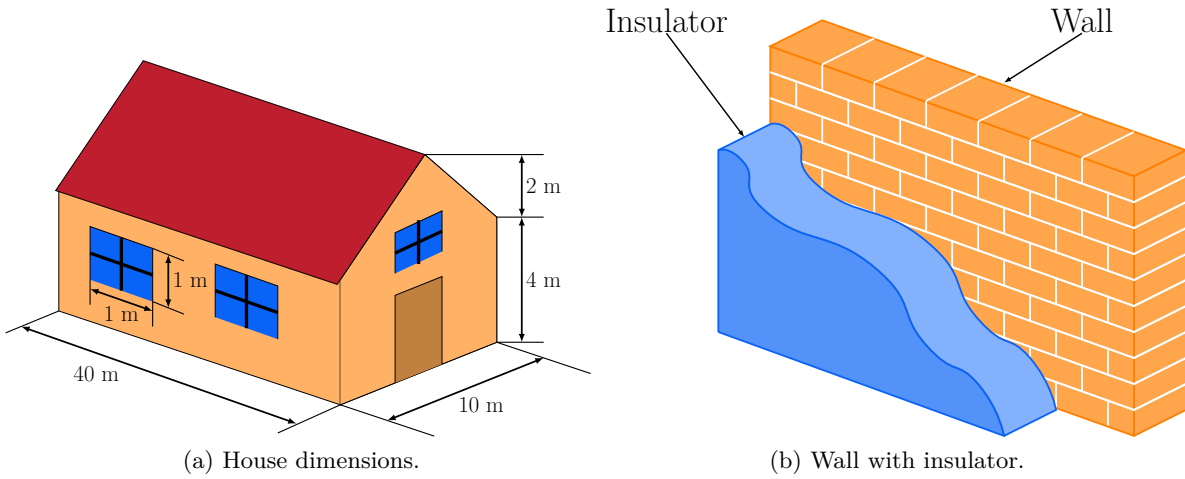


Figure 4.95: Schematics of house and insulated wall.

House without insulation

Following the modelling approach presented in Section 3.4, the energy balance equation for each house element is obtained and described by its electric analogy. The electric circuit analogy of the heat transfer analysis is shown in Figure 4.96. The energy balance for each energy storage element (thermal capacitance) is described by the circuit branches, where subscripts 'cd' and 'cv' stand for conduction and convection, respectively. For instance, the circuit branch of the roof includes the heat flow through its surface caused by the outdoor wind, which is computed by equation (3.74) and is defined by R_{cv7} (convection). Then, the conduction heat transfer inside the roof is determined by equation (3.77) and called R_{cd8} . The convection heat transfer between the interior house and the roof is computed by R_{cv9} . The same analysis is implemented to the thermal capacitance of the windows and walls.

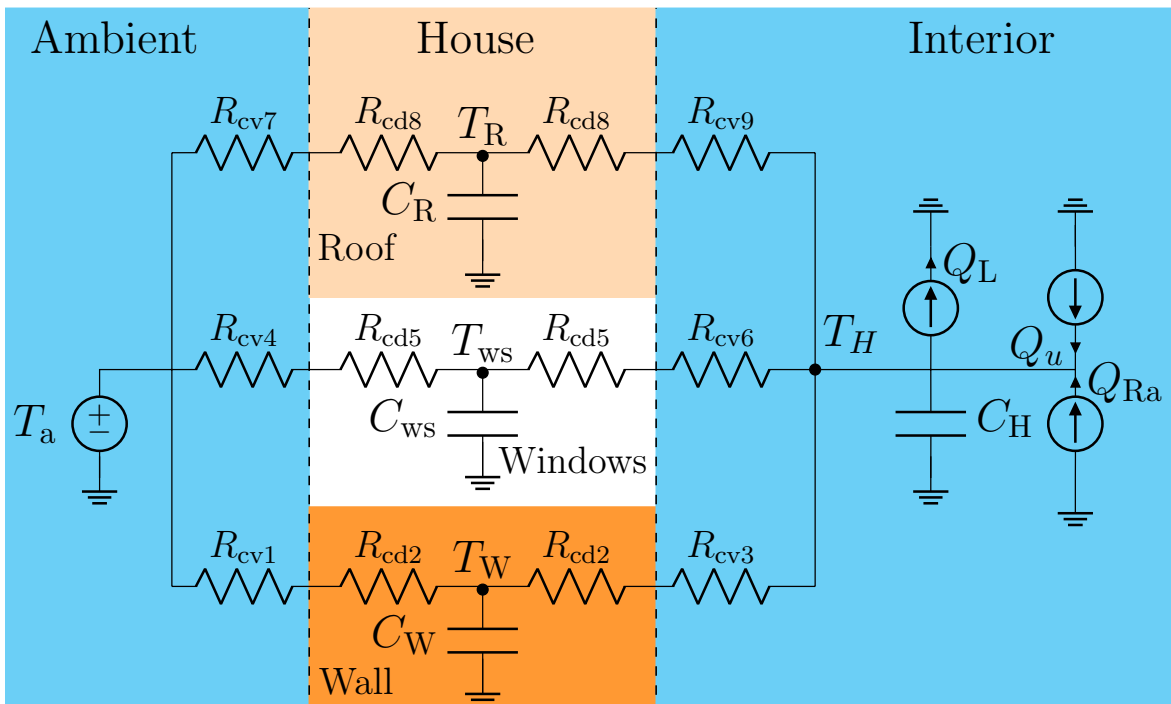


Figure 4.96: Electric circuit analogy of thermal model of house without insulator.

4.5. Buildings

The house's energy balance equation is directly obtained by applying Kirchoff's on the electric circuit analogy representation of the heat transfer in the house. Thus, the energy balance equation for the roof is defined by

$$C_R \dot{T}_R = [(T_a - T_R) / (R_{cv7} + R_{cd8})] + [(T_H - T_R) / (R_{cd8} + R_{cv9})], \quad (4.118)$$

where T_a , T_R and T_H are the ambient, roof and house interior temperatures, respectively. C_R is the thermal capacitance of the roof, which is calculated using its mass and specific heat according to equation (3.71). The energy balance for the windows is computed as

$$C_{ws} \dot{T}_{ws} = [(T_a - T_{ws}) / (R_{cv4} + R_{cd5})] + [(T_H - T_{ws}) / (R_{cd5} + R_{cv6})], \quad (4.119)$$

where T_{ws} is the lumped windows temperature. For the walls, the energy balance is defined by

$$C_W \dot{T}_W = [(T_a - T_W) / (R_{cv1} + R_{cd2})] + [(T_H - T_W) / (R_{cd2} + R_{cv3})], \quad (4.120)$$

where T_W is the wall temperature. The energy balance equation of the thermal mass of the interior house is defined by the contributions of the convection heat transfer due to ambient conditions over the roof, windows and walls plus the heat flow given by the heating system, solar radiation and heat losses denoted by Q_u , Q_{Ra} , Q_L , respectively. All these heat sources are represented as current sources in the electric circuit. Then the energy balance equation for the house interior is given by

$$\begin{aligned} C_H \dot{T}_H = & [(T_R - T_H) / (R_{cd8} + R_{cv9})] + [(T_W - T_H) / (R_{cd2} + R_{cv3})] \\ & + [(T_{ws} - T_H) / (R_{cd5} + R_{cv6})] + Q_{Ra} + Q_L + Q_u \end{aligned} \quad (4.121)$$

House with insulation

The thermal model of an insulated house is presented in this section. The roof and walls are covered with cellulose. The insulator externally covers the walls (see Figure 4.95b) and it is also placed below the roof. This insulation adds two extra elements to the house model, which requires two additional energy balance equations. Thus, two extra thermal masses are incorporated into the system: the masses of the insulators located in the roof (C_{RI}) and in the walls (C_{WI}). The electric circuit analogy of the thermal model is shown in Figure 4.97. As it can be observed, the heat transfer between the insulator and the wall or roof is given by conduction, as it is explained in Section 3.4.

The six energy balance equations are shown in Table 4.3. For the sake of simplicity, the equivalent resistances have been renamed as

$$\begin{aligned} R_{cv1} + R_{cd2} = R_1, \quad R_{cd2} + R_{cv3} = R_2, \quad R_{cv4} + R_{cd5} = R_3, \\ R_{cd5} + R_{cv6} = R_4, \quad R_{cv7} + R_{cd8} = R_5, \quad R_{cd8} + R_{cv9} = R_6. \end{aligned}$$

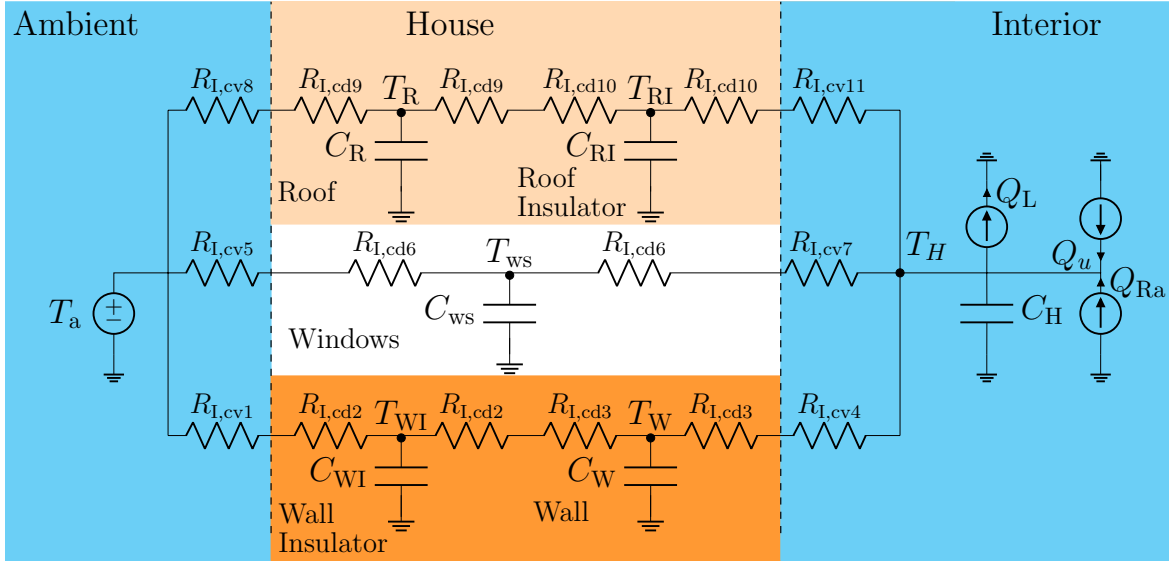


Figure 4.97: Electric circuit analogy of thermal model of insulated house.

Table 4.3: Energy balance equation for insulate house elements.

Element	Energy balance / Simplified equation
Wall Insulator	$C_{WI}\dot{T}_{WI} = [(T_a - T_{WI}) / (R_{I,cv1} + R_{I,cd2})] + [(T_W - T_{WI}) / (R_{I,cd2} + R_{I,cd3})], \quad (4.122)$ $C_{WI}\dot{T}_{WI} = [(T_a - T_{WI}) / R_{I,1}] + [(T_W - T_{WI}) / R_{I,2}],$
Wall	$C_W\dot{T}_W = [(T_{WI} - T_W) / (R_{I,cd3} + R_{I,cd2})] + [(T_H - T_W) / (R_{I,cd3} + R_{I,cv4})], \quad (4.123)$ $C_W\dot{T}_W = [(T_{WI} - T_W) / R_{I,2}] + [(T_H - T_W) / R_{I,3}],$
Windows	$C_{ws}\dot{T}_{ws} = [(T_a - T_{ws}) / (R_{I,cv5} + R_{I,cd6})] + [(T_H - T_{ws}) / (R_{I,cd6} + R_{I,cv7})], \quad (4.124)$ $C_{ws}\dot{T}_{ws} = [(T_a - T_{ws}) / R_{I,4}] + [(T_H - T_{ws}) / R_{I,5}],$
Roof	$C_R\dot{T}_R = [(T_a - T_R) / (R_{I,cv8} + R_{I,cd9})] + [(T_{RI} - T_R) / (R_{I,cd9} + R_{I,cd10})], \quad (4.125)$ $C_R\dot{T}_R = [(T_a - T_R) / R_{I,6}] + [(T_{RI} - T_R) / R_{I,7}],$
Roof insulator	$C_{RI}\dot{T}_{RI} = [(T_R - T_{RI}) / (R_{I,cd9} + R_{I,cd10})] + [(T_H - T_{RI}) / (R_{I,cd10} + R_{I,cv11})], \quad (4.126)$ $C_{RI}\dot{T}_{RI} = [(T_R - T_{RI}) / R_{I,7}] + [(T_H - T_{RI}) / R_{I,8}],$
House interior	$C_H\dot{T}_H = [(T_W - T_H) / (R_{I,cd3} + R_{I,cv4})] + [(T_{ws} - T_H) / (R_{I,cd6} + R_{I,cv7})] \quad (4.127)$ $+ [(T_{RI} - T_H) / (R_{I,cd10} + R_{I,cv11})] + Q_R - Q_L + Q_u,$ $C_H\dot{T}_H = [(T_W - T_H) / R_{I,3}] + [(T_{ws} - T_H) / R_{I,5}] + [(T_{RI} - T_H) / R_{I,8}] + Q_R - Q_L + Q_u,$

4.5.2 Simulations

The systems defined by equations (4.119)-(4.121) and (4.122)-(4.127) are implemented in MATLAB/Simulink. The thermophysical properties, area (A) and thickness (d) values of the house elements are shown in Appendix C. Electric resistances for conduction heat transfer are computed using equation (3.77), thermal conductivity, and the elements' thickness. The computation of electric resistance for convection requires the air's wind speed and thermophysical properties. The thermal capacitance of each house element is calculated using equation (3.71) and the values shown in Table 4.4.

4.5. Buildings

Table 4.4: Thermal capacitances of the house elements.

C	Value [J/K]	C	Value [J/K]	C	Value [J/K]
C_W	6.5393×10^7	C_R	1.6608×10^7	C_{ws}	125550
C_{WI}	5.7797×10^6	C_{RI}	8.741×10^5	C_H	1.9706×10^6

The electrical resistances by conduction and convection are calculated by equations (3.74) and (3.77), respectively. Air conditions are required to compute the Reynolds number and, thus, the value of U_{cv} . Therefore, the equivalent resistance value shown in Appendix C is given in ranges, depending on the variations to the air thermodynamics properties according to the ambient temperature and the wind speed. Three ranges are established to compute the maximum and minimum values of the resistances by convection for all possible combinations of internal wind speed: [0.1 0.3] m/s, outdoor wind speed range: [3.65 5.7] m/s and ambient temperature between 10°C to 30°C. The equivalent resistances values of house model with and without insulation are shown in Appendix C.

An ambient temperature reported in [24] of a winter day of 2018 in London is used to simulate the behaviour of both house models. The initial condition of all elements is 20°C. For the sake of simplicity, neither heat input nor disturbances such as radiation or people transit are considered yet. Figure 4.98 shows the temperature response of all house elements through the whole day of the house model without insulation.

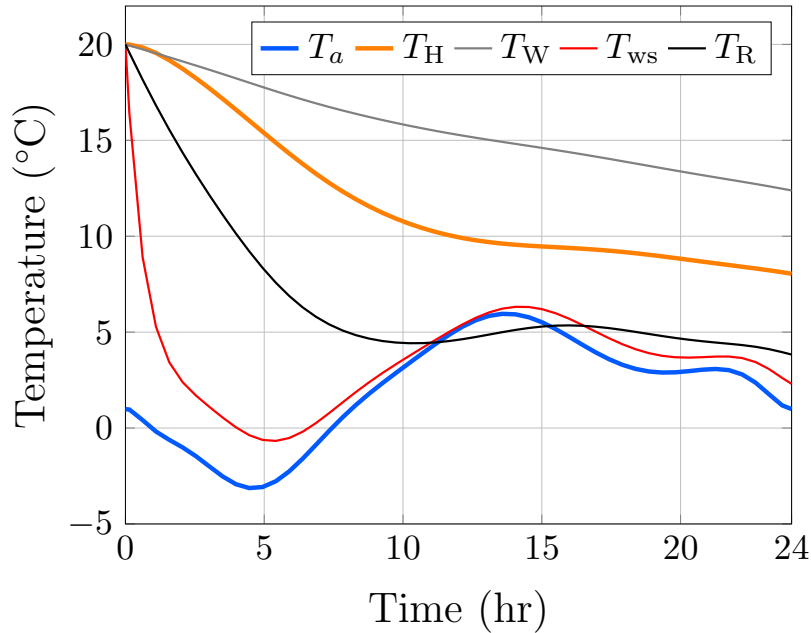


Figure 4.98: Thermal response of house model for a winter day without heat supply.

As it can be observed, the materials with higher thermal conductivity reduce their temperature faster than those with small values. For instance, the roof and windows temperatures decrease dramatically due to the cold ambient temperature. On the other hand, the wall temperature does not present fast changes despite its large exposed area.

The insulated house model is subjected to the same cold ambient temperature. Figure 4.99a shows the thermal behaviour of each element. It can be seen, the exterior materials (wall-

insulator and asbestos tiles of the roof) present a faster response than the wall and internal roof-insulator due to the ambient temperature effect. For instance, the wall temperature decreases less than 2°C . It is important to notice that the wall-insulator temperature (T_{WI}) has a faster response than the wall temperature when it is not insulated T_W . Although it has a lower thermal conductivity, the thermal capacitance C_{WI} is almost ten times less than C_W , which implies that a lower amount of energy is required to modify its temperature. Nevertheless, the internal temperature of the insulated house decreases more slowly than the internal temperature of the house without insulation (see Figure 4.99b).

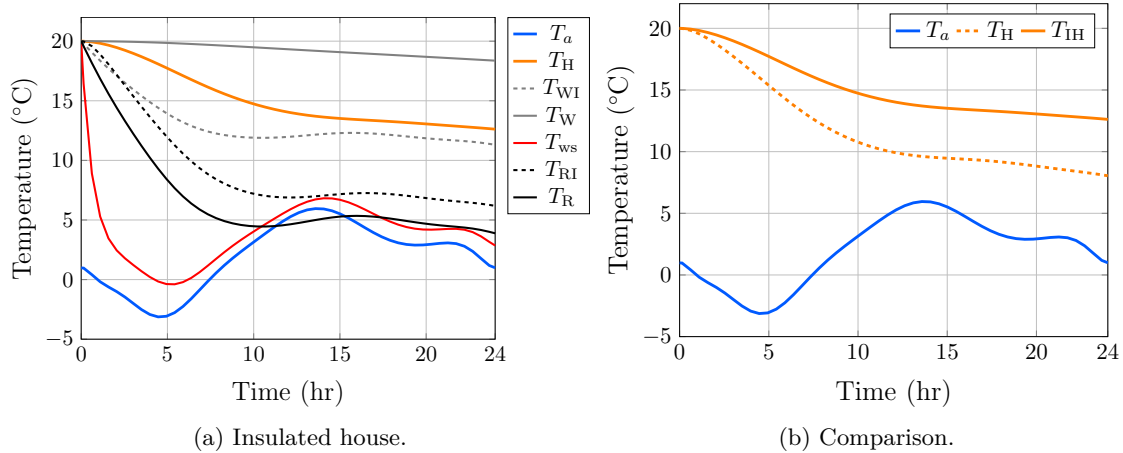


Figure 4.99: (a) Thermal response of insulated house for a cold day. (b) Comparison between the internal temperatures of house without insulator (T_H) and insulated house (T_{IH}).

4.6 Summary

In this chapter, the 1-D dynamic models of a pipe network, heat exchangers, TES tanks and of a single house were developed using the dynamic modelling approaches developed in Chapter 3. ODEs describe the hydraulic or thermal behaviour of these DHCS's components. The mathematical models were implemented in MATLAB/Simulink and solved using s-functions. The models were verified through simulation results compared against Apros or experimental data reported in the literature. These verifications provide confidence in the 1-D dynamic models of each element.

The dynamic hydraulic model of a pipe network was obtained using the well-described mathematical models of its main components: pump, valve and pipe. Critical parameters of each component were used to set up the dynamic models. These parameters were taken from commercial pumps and valves. Fundamental factors such as friction factor and loss coefficients were computed dynamically. The verification was carried out by comparison with the pipe network's model built-in Apros using its high-fidelity components. Different operating points were assessed with fair agreements between both simulations.

The 1-D dynamic thermal models of flat plate and shell-and-tube heat exchangers were developed. The parallel and counter-flow configuration of both heat exchangers were modelled dynamically. Energy balance was implemented to describe the interaction between the hot and cold stream of each heat exchanger. The overall heat transfer coefficient calculation was described considering the internal structure of the heat exchanger. The four models were

4.7. References

verified against the high-fidelity heat exchanger models available in Apros. Different operating conditions were assessed with a good agreement between the simulation results. The division of 30 nodes was defined as the most accurate setup of the stratified system. This value was obtained by comparing models with a different number of nodes. Moreover, the comparison between the parallel and the counter-flow configuration of the shell-and-tube was presented.

The 1-D dynamic thermal models of sensible and latent TES tanks were developed. The water tank-based TES thermal model and the computation of its SoC were described. Energy balance was implemented in a stratified water tank model. Its verification was done through simulation results of its Apros model counterpart. A good agreement for discharging and charging simulations were achieved.

Dynamic thermal models of latent TES for heating and cooling were developed. The energy balance of the heat transfer fluid and the PCM were used to describe the TES tanks thermal behaviour during charging and discharging operating modes. The overall heat transfer coefficient is computed dynamically. The relationship between the enthalpy and specific heat of the PCM located inside the TES tanks was also explained. A computation method of the SoC was developed. The verification of both latent TES tanks were carried out using experimental data available in the literature. A good agreement between the developed models and the reported data was achieved.

Finally, the dynamic thermal model of a single insulated house was developed. Energy balance and electrical to thermal analogy were implemented to describe the thermal behaviour of the house. The properties of the house's materials are considered for computing the convection, and conduction heat transfer processes during a cold day. The temperature of each house component is solved. The comparison between a house with and without insulation was shown.

The implementation of the 1-D dynamic modelling approaches for the DHCS's components showed that some critical system parameters are essential to achieve an accurate model. The mathematical models are obtained using energy balance, heat transfer, and linear momentum principles, offering sufficient accuracy compared to experimental data or even commercial software models using energy, mass, and momentum conservation laws. Despite their accuracy, the main disadvantage is that detailed system parameters are not always available.

The successful integration and coordination of all components of a DHCS are critical for managing the energy supply. Analyses of potential improvements to increase the efficiency of DHCS are of great importance for services (*e.g.*, hospitals, supermarkets), industry and residential sectors where DHCS are implemented to provide energy. For instance, space heating and space cooling systems, either in houses or in industrial premises, are supplied by similar system configurations where only the size of components varies. Therefore, the detailed understanding afforded by the developed dynamic models of the main DHCS's components will positively contribute to these analyses. Dynamic simulations of complex DHCSs and effective control designs are enabled using the models presented in this chapter.

4.7 References

- [1] B. R. Munson, *Fundamentals of Fluid Mechanics*. Hoboken, N.J: John Wiley & Sons, 7th ed. edition ed., Sept. 2014.

- [2] “Slurry Pumps - Warman.” <https://www.global.weir/brands/warman/>. Accessed: 2021-03-06.
- [3] P. K. Kundu, I. M. Cohen, and D. R. D. Ph.D, *Fluid Mechanics*. Amsterdam ; Boston: Academic Press, June 2015.
- [4] P. K. Swamee and A. K. Jain, “Explicit Equations for Pipe-Flow Problems,” *Journal of the Hydraulics Division*, vol. 102, no. 5, pp. 657–664, 1976. Publisher: ASCE.
- [5] J. Kurki, J. Ylijoki, and J. Leskinen, “The constitutive equations of the two-fluid model,” report, VTT Technical Research Centre of Finland, 05 2019.
- [6] “Burkert - fluid control systems.” <https://www.burkert.com/en>. Accessed: 2021-03-06.
- [7] F. P. Incropera, D. P. DeWitt, T. L. Bergman, and A. S. Lavine, *Fundamentals of Heat and Mass Transfer*. Wiley, 6th edition ed., June 2020.
- [8] S. Frederiksen and S. Werner, *District Heating and Cooling*. Studentlitteratur AB, 2013. Google-Books-ID: vH5zngEACAAJ.
- [9] “HRS Hevac Gasketed Plate Heat Exchangers.” <https://www.hrshevac.co.uk/?products=hrs-hevac-gasketed-plate-heat-exchanger>. Accessed: 2021-03-10.
- [10] HRS Heat Exchangers, “Gas Cooling Heat Exchangers.” <https://www.hrs-heatexchangers.com>. Accessed: 2021-01-10.
- [11] I. Dincer and M. A. Rosen, *Thermal Energy Storage: Systems and Applications*. Chichester, England: John Wiley & Sons, Nov. 2010.
- [12] “CrodaTherm™ Bio-based Phase Change Materials | Croda Phase Change Materials.”
- [13] C. Barreneche, A. Solé, L. Miró, I. Martorell, A. I. Fernández, and L. F. Cabeza, “New methodology developed for the differential scanning calorimetry analysis of polymeric matrixes incorporating phase change materials,” *Measurement Science and Technology*, vol. 23, p. 085606, July 2012. Publisher: IOP Publishing.
- [14] F. Bruno, M. Belusko, M. Liu, and N. H. S. Tay, “9 - Using solid-liquid phase change materials (PCMs) in thermal energy storage systems,” in *Advances in Thermal Energy Storage Systems* (L. F. Cabeza, ed.), Woodhead Publishing Series in Energy, pp. 201–246, Woodhead Publishing, Jan. 2015.
- [15] T. Barz, C. Zauner, D. Lager, D. C. López Cárdenas, F. Hengstberger, M. N. Cruz Bournazou, and K. Marx, “Experimental analysis and numerical modeling of a shell and tube heat storage unit with phase change materials,” *Industrial & Engineering Chemistry Research*, vol. 55, no. 29, pp. 8154–8164, 2016.
- [16] A. López-Navarro, J. Biosca-Taronger, B. Torregrosa-Jaime, I. Martínez-Galván, J. M. Corberán, J. C. Esteban-Matías, and J. Payá, “Experimental investigation of the temperatures and performance of a commercial ice-storage tank,” *International Journal of Refrigeration*, vol. 36, pp. 1310–1318, June 2013.

4.7. References

- [17] A. López-Navarro, J. Biosca-Taronger, B. Torregrosa-Jaime, J. M. Corberán, J. L. Bote-García, and J. Payá, “Experimental investigations on the influence of ice floating in an internal melt ice-on-coil tank,” *Energy and Buildings*, vol. 57, pp. 20–25, Feb. 2013.
- [18] Calmac, “Thermal storage.” <http://www.calmac.com/>. Accessed: 2021-03-10.
- [19] K. H. Drees and J. E. Braun, “Modeling of Area-Constrained Ice Storage Tanks,” *HVAC&R Research*, vol. 1, pp. 143–158, Apr. 1995. Publisher: Taylor & Francis _eprint: <https://www.tandfonline.com/doi/pdf/10.1080/10789669.1995.10391315>.
- [20] J. West and J. E. Braun, “Modeling Partial Charging and Discharging of Area-Constrained Ice Storage Tanks,” *HVAC&R Research*, vol. 5, pp. 209–228, July 1999. Publisher: Taylor & Francis _eprint: <https://www.tandfonline.com/doi/pdf/10.1080/10789669.1999.10391234>.
- [21] Z. T. Taylor, K. Gowri, and S. Katipamula, “GridLAB-D Technical Support Document: Residential End-Use Module Version 1.0,” Tech. Rep. PNNL-17694, Pacific Northwest National Lab. (PNNL), Richland, WA (United States), July 2008.
- [22] C. Hill, A. Norton, and J. Dibdiakova, “A comparison of the environmental impacts of different categories of insulation materials,” *Energy and Buildings*, vol. 162, pp. 12–20, Mar. 2018.
- [23] C. Colli, A. Bataille, and E. Antczak, “Investigating eco-efficiency procedure to compare refurbishment scenarios with different insulating materials,” *Procedia CIRP*, vol. 90, pp. 322–327, Jan. 2020.
- [24] “Time and date.” <https://www.timeanddate.com/weather/uk/london/historic?month=2year=2018>. Accessed: 2021-02-05.

Design and implementation of local controllers for district heating and cooling systems.

5.1 Introduction

The efficient operation and even the safety of a DHCS rely on the proper functioning of several feedback controllers implemented through the whole system [1]. Figure 5.1 shows the basic schematic of a feedback control system. Measurement of the controlled variable is used to compute the error with respect to a reference, which in turn a controller uses to generate an output. This output regulates the system input to ensure the controlled variable follows the reference. The system response under the control action should reach the reference value x_r .

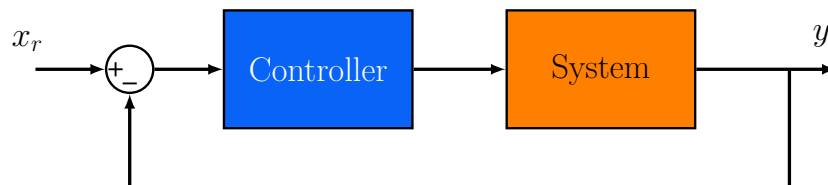


Figure 5.1: Block diagram of a feedback control system.

Feedback control systems are designed and implemented to perform specific tasks within the operation of a system. In DHCSs, these tasks may be to ensure operation under a certain range and to avoid sudden changes of critical variables, such as total pressure of the pipe network or substation temperatures. The system's operation is at risk of failures, and damage to the infrastructure might occur if those conditions cannot be achieved. Therefore, well-designed control strategies for these variables become imperative for the DHCS's performance. In connection with the classification of control systems presented in Chapter 2 and using the dynamic models of DHCS's elements developed in Chapter 4, feedback controllers of pressure and temperature are presented in this chapter.

Complex control strategies and optimisation methods of DHCS have been presented in the literature [2]. Nevertheless, important assumptions such as constant pump speed, valve openings, or supply temperatures do not represent the real system's operating conditions. Moreover, the practical implementation of these schemes requires having the system variables

controlled locally. Therefore, it is necessary to develop basic controllers capable of guaranteeing hydraulic and thermal operating conditions within the established control references. Following this line, a control design method is used to develop classical controllers over pressure and temperature variables. This method is explained in Appendix G.

PID controllers are the most popular control structures for industrial processes including energy services [1]. PID controllers can reject disturbances and deal with the non-linearities caused by different operating points. Furthermore, PID controllers are frequently tuned through empirical methods (*i.e.*, 'trial and error'), increasing their popularity [3]. Nevertheless, implementing a PID controller without previous design or simulation requires specialists experienced in control theory and with knowledge of DHCSs [3, 4]. Besides, many systems do not allow to carry out control tests for different operating conditions for controller validation. These drawbacks may be overcome by the PID controller's design based on accurate dynamic models of the system and previous test by software simulations.

This chapter aims to bridge this gap by designing and analysing the performance achieved by PI controllers over critical variables of DHCSs. As the derivative gain is mainly helpful to prevent sudden changes in the variables and fast responses in the actuator [3], the present work is limited to PI controllers. MATLAB software is used for the control design process. The PI controller's performance is assessed through simulation conducted in Apros. The controllers presented in this chapter are:

- Differential pressure control of a pipe network,
- Temperature output of the secondary circuit of a flat plate heat exchanger,
- Temperature output of the secondary circuit of a shell-and-tube heat exchanger,
- Charging process of a TES tank and
- Internal temperature of a single insulated house.

5.2 Design and implementation of local controllers

The method presented in Appendix G is implemented for elements of a DHCS: a pipe network, heat exchangers, TES tank and a single house. MATLAB/Simulink is used for the loop-shaping process and the controller test step is implemented in Apros. The PI controller component is available in the Apros component's library. The gains obtained from the controller design are set up in Apros to assess the performance of the PI controller. The models and the parameters presented in Chapter 4 are adopted to develop their PI controllers.

5.2.1 Differential pressure controller for a pipe network

The design of a differential pressure controller is presented in this subsection. A schematic of the feedback control scheme is shown in Figure 5.2. The control scheme aims to keep a constant differential pressure in the pipe 8 and valve 4 of the pipe network, shown in Figure 5.3.

5.2. Design and implementation of local controllers

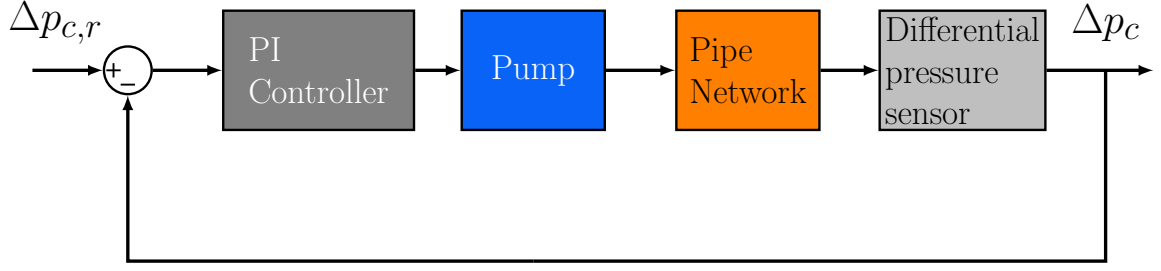


Figure 5.2: Block diagram for a differential pressure closed-loop system for the pipe network of a DHCS.

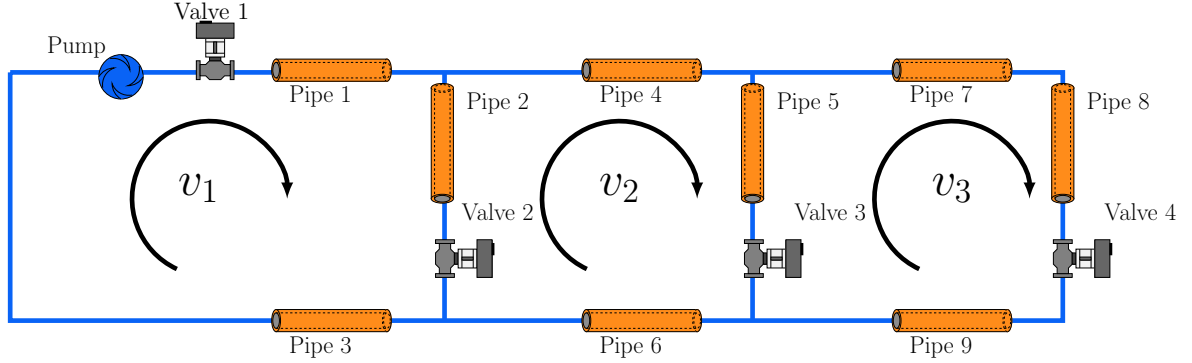


Figure 5.3: Schematic of the pipe network.

The controller output modifies the pump's speed to achieve the differential pressure set point. The system is described by equations (4.40)-(4.42) and its parameters are shown in Appendix C. The variable states are the velocities (v_1 , v_2 , v_3) in each branch. An extra state variable is added to the system: the pressure drop in pipe 8 ($'k_8'$) and valve 4 ($'cv_4'$), which in turn are the farthest elements of the pipe network. The sum of both pressure drops is named Δp_c . Using the pressure drop equations for a pipe (4.35) and a valve (4.38) and the velocity in branch number 3, v_3 , Δp_c is obtained as

$$\Delta p_c = f \frac{\rho L_{k8} v_3^2}{2D_{k8}} + K_{L8} \frac{\rho v_3^2}{2} + \frac{(1 \times 10^5) (3600 A_{cv4} v_3)^2}{K_{v4} (o_{v4})^2}. \quad (5.1)$$

Differentiating equation (5.1) with respect to time gives:

$$\Delta \dot{p}_c = \left[f \frac{\rho L_{k8} v_3}{D_{k8}} + K_{L8} \rho v_3 + \frac{2(1 \times 10^5) (3600 A_{cv4})^2 v_3}{K_{cv4} (o_{v4})^2} \right] \dot{v}_3, \quad (5.2)$$

which enables incorporating Δp_c as a state variable into the state-space representation.

The system's state variables are established as the velocities in each branch and the sum of the pressure drops in pipe 8 and valve 4. The system variables are renamed using the state space notation as: $x_1 = v_1$, $x_2 = v_2$, $x_3 = v_3$ and $x_4 = \Delta p_c$. The system equations are re-written as

$$\begin{aligned} \dot{x}_1 = & [A_p \Delta p_p (\omega_{sp}, x_1) - A_{cv1} \Delta p_{cv1} (x_1) - A_{k1} \Delta p_{k1} (x_1) - A_{k2} \Delta p_{k2} (x_1 - x_2) \\ & - A_{cv2} \Delta p_{cv2} (x_1 - x_2) - A_{k3} \Delta p_{k3} (x_1)] / m_{T1}, \end{aligned} \quad (5.3)$$

$$\begin{aligned} \dot{x}_2 = & [-A_{k4}\Delta p_{k4}(x_2) - A_{k5}\Delta p_{k5}(x_2 - x_3) - A_{cv3}\Delta p_{cv3}(x_2 - x_3) \\ & - A_{k6}\Delta p_{k6}(x_2) - A_{cv2}\Delta p_{cv2}(x_2 - x_1) - A_{k2}\Delta p_{k2}(x_2 - x_1)] / m_{T2}, \end{aligned} \quad (5.4)$$

$$\begin{aligned} \dot{x}_3 = & [-A_{k7}\Delta p_{k7}(x_3) - A_{k8}\Delta p_{k8}(x_3) - A_{cv4}\Delta p_{cv4}(x_3) \\ & - A_{k9}\Delta p_{k9}(x_3) - A_{cv3}\Delta p_{cv3}(x_3 - x_2) - A_{k5}\Delta p_{k5}(x_3 - x_2)] / m_{T3}. \end{aligned} \quad (5.5)$$

For the derivative of the state variable x_4 (Δp_c), a special arrangement is done. The derivative of x_3 that appears in equation (5.2) is replaced by the expression of \dot{x}_3 in equation (5.5). In addition, the sum of pressure drops of pipe 8 and valve 4 included in equation (5.5) and being highlighted for clarity is replaced by x_4 according to equation (5.1) (also highlighted in equation (5.6)). Thus, the added state variable can be defined as

$$\begin{aligned} \dot{x}_4 = & \left[f \frac{\rho L_{k8} x_3}{D_{k8}} + K_{L8} \rho x_3 + \frac{2(1 \times 10^5)(3600 A_{cv4})^2 x_3}{K_{cv4} (o_{v4})^2} \right] [A_{k7} \Delta p_{k7}(x_3) \\ & - x_4 - A_{k9} \Delta p_{k9}(x_3) - A_{cv3} \Delta p_{cv3}(x_3 - x_2) - A_{k5} \Delta p_{k5}(x_3 - x_2)] / m_{T3} \end{aligned} \quad (5.6)$$

This procedure allows representing the new state variable in a simple form suitable for system linearisation.

Following the proposed control design process, the next step is to obtain the steady-state values of the system's variable for specific operating conditions. The system built in Apros for Chapter 4 is used for this purpose (see Figure 4.14). Firstly, the setup of the system is established for the following values of valve openings: $o_{v1} = 100\%$, $o_{v2} = 30\%$, $o_{v3} = 30\%$ and $o_{v4} = 30\%$. The desired value for Δp_c is 0.4 bars = 40000 Pa. The pump's speed is adjusted to $\omega_{sp} = 90\%$ to achieve the desired value of Δp_c . The steady-state values are shown in Table 5.1.

Table 5.1: Steady-state values of pipe network system.

x_1 (m/s)	x_2 (m/s)	x_3 (m/s)	x_4 (Pa)
2.196	1.197	0.5667	-40000

Following the Kirchhoff's law's sign convention, state variable x_4 is defined as negative. Due to the size of the system equations (5.3)-(5.6), differentiating each equation becomes a cumbersome task. Symbolic variables are implemented in MATLAB to obtain the Taylor series expansion defined by equation (G.2). Using symbolic substitution, the steady-state values of Table 5.1 are evaluated. The linear state-space representation of the system (5.3)-(5.6) is given by

$$\begin{aligned} \dot{\mathbf{x}} = & \begin{bmatrix} -0.6553 & 0.2529 & 0 & 0 \\ 0.4177 & -0.8913 & 0.2644 & 0 \\ 0 & 0.5219 & -1.1030 & 0 \\ 0 & 24.2973 & 1051.1 & -0.0152 \end{bmatrix} [\mathbf{x}] + \begin{bmatrix} 1.2623 \\ 0 \\ 0 \\ 0 \end{bmatrix} u, \\ y = & \begin{bmatrix} 0 & 0 & 0 & 1 \end{bmatrix} [\mathbf{x}]. \end{aligned} \quad (5.7)$$

5.2. Design and implementation of local controllers

Implementation of equation (G.5) into the linearised system (5.7) yields

$$G_p(s) = \frac{12.8104s + 303.4}{s^4 + 2.6647s^3 + 2.0864s^2 + 0.4683s + 0.0066} \quad (5.8)$$

It is important to notice that the units of pressure are given in bar instead of Pa in Apros. Figure 5.4 shows a block diagram to illustrate how the feedback control should consider this factor.

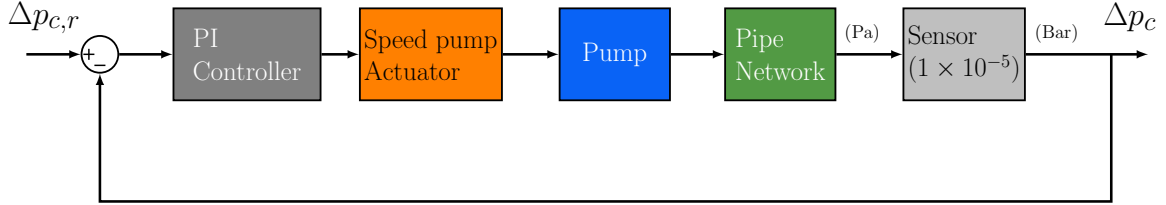


Figure 5.4: Block diagram for the differential pressure closed-loop system implemented in Apros.

Then, the system transfer function (5.8) multiplied by the conversion factor 1×10^{-5} is defined by

$$G_p(s) = \frac{1.281 \times 10^{-4}s + 3.034 \times 10^{-3}}{s^4 + 2.665s^3 + 2.086s^2 + 0.4683s + 0.006627}. \quad (5.9)$$

An equivalent second-order system of G_p is obtained employing equation (G.13) and its parameters values: $A_1 = 0.58 \times 10^3$, $\omega_n = 0.035$ rad/s and $\zeta = 0.9$, as

$$G_{p,so}(s) = \frac{5.574 \times 10^{-4}}{s^2 + 0.063s + 0.001225}. \quad (5.10)$$

Figure 5.5 shows the frequency and step time responses of G_p and $G_{p,so}$.

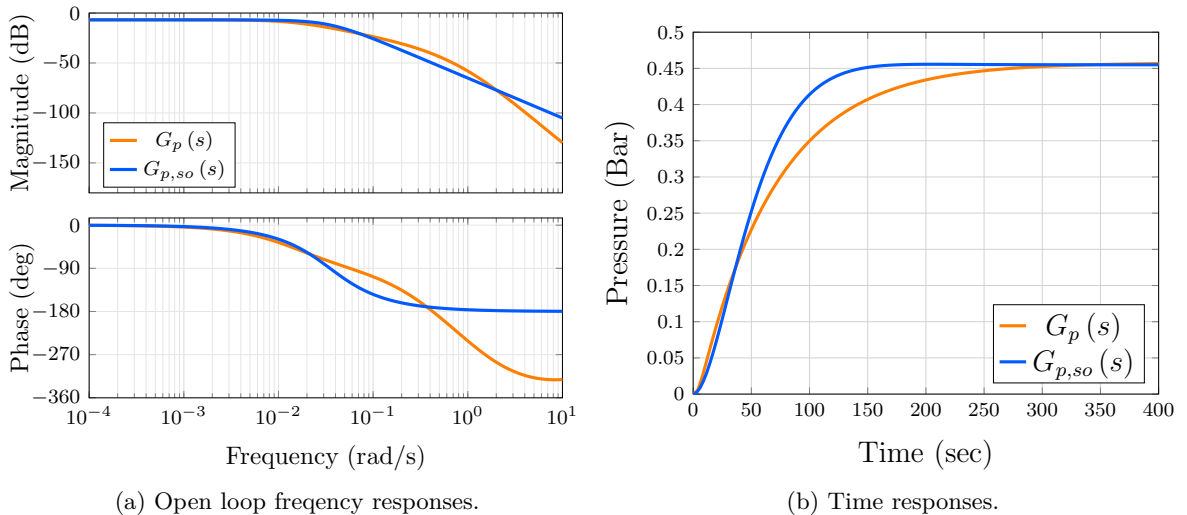


Figure 5.5: (a) Open-loop Bode plots and (b) step responses of the $G_p(s)$ and $G_{p,so}(s)$.

PI controller design

The performance specifications are defined as 1% overshoot and a settling time of $t_s = 320$ s. This small overshoot value is adopted to avoid severe pressure drop variations, which may

cause damage to the pipe network. The design specifications are translated to the frequency domain as a $\zeta = 0.8261$, a minimum phase margin $\phi_m = 70.9048^\circ$ and a minimum bandwidth $\omega_{bw} \approx 0.0095$ rad/s. These requirements are met with

$$C_p(s) = \frac{0.108s + 0.0152}{s}, \quad (5.11)$$

where the proportional k_p and integral k_i gains are 0.108 and 0.0152, respectively.

Figure 5.6 shows the open-loop frequency response of the system controlled by (5.11) (*i.e.*, $C_p(s)G_{p,so}(s)$). It can be observed that the frequency response specifications are achieved: the system with controller $C_p(s)$ exhibits a phase margin of 72.9° and a bandwidth of $\omega_{bw} \approx 0.00935$ rad/s. Figure shows the closed-loop step response of the equivalent and original linear system, showing that the time-domain specifications are satisfactorily met. Although the condition of $t_s = 320$ s is achieved, there is a small overshoot of 3%, which is still adequate for the system performance.

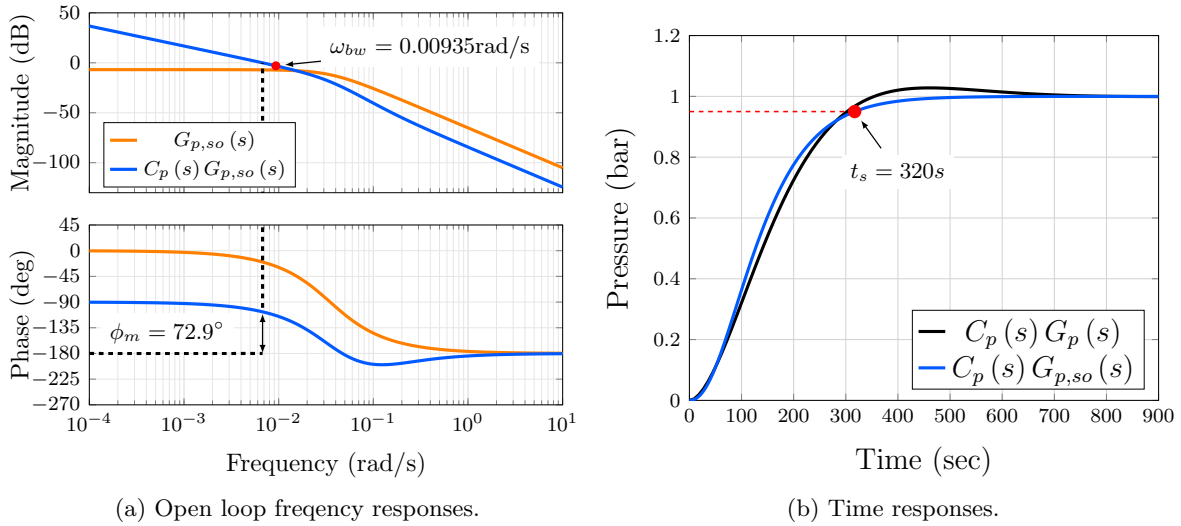


Figure 5.6: (a) Open-loop Bode plots of the equivalent second-order system and the loop-shaped obtained with $C_p(s)$. (b) Time step responses of the closed-loop system with $G_{p,so}(s)$ and $G_p(s)$.

Controller verification

The instrumentation required to implement a real system is resembled in Apros by employing sensors and drivers elements. On the one hand, system variables are measured using temperature and pressure sensors. On the other hand, valve openings and pump's speed are modified through driver elements. Therefore, these elements are added to the system shown in Figure 4.16. A PI controller receives the signal from pressure sensors, then the controller output is sent to the speed pump actuator (driver) to modify ω_{sp} . This control scheme is shown in Figure 5.7.

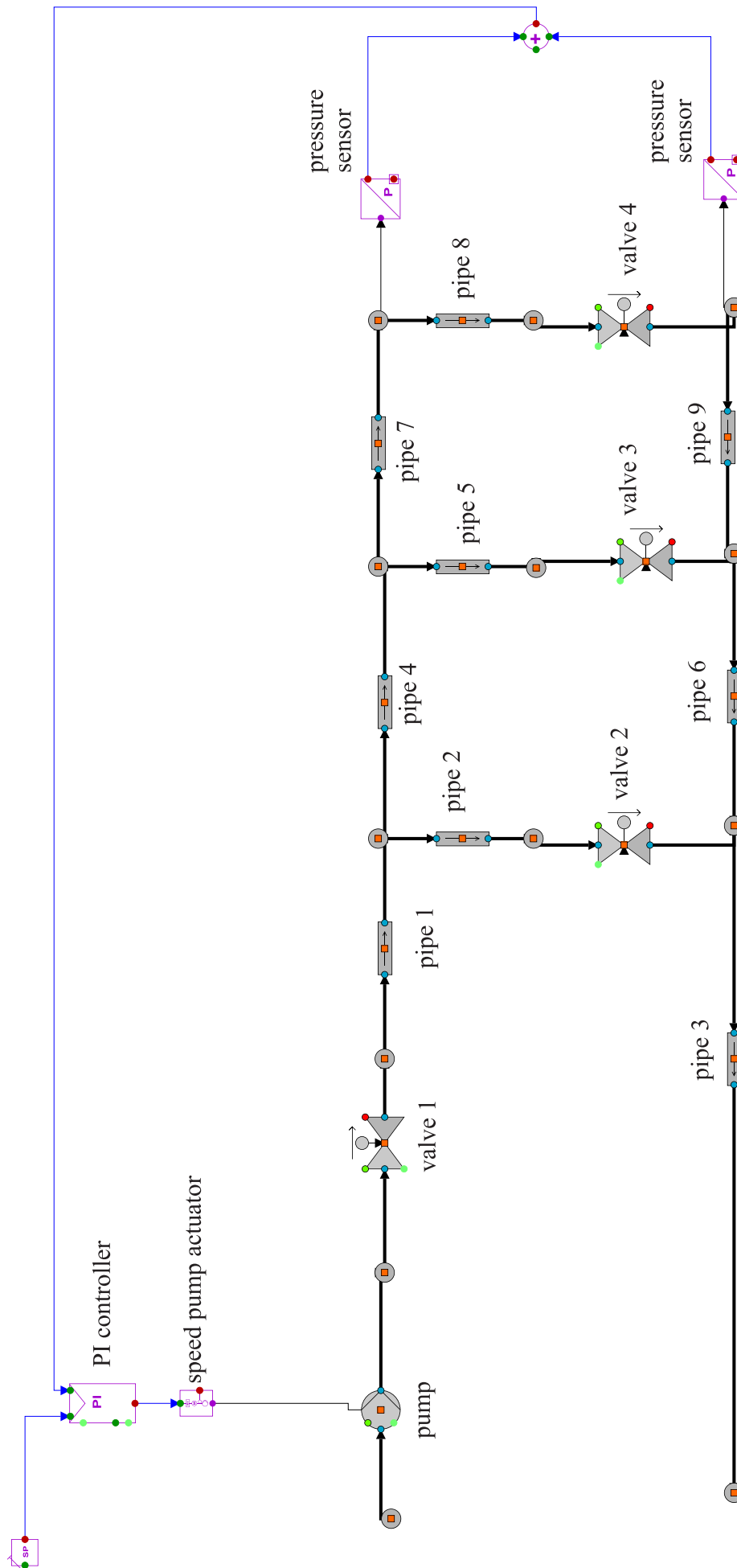


Figure 5.7: Differential pressure closed-loop system implemented in Apros.

Similar to the example presented in the Appendix G, the system's performance under different operating conditions is assessed. Figure 5.8 shows the response of the system when valve openings o_{v2} , o_{v3} and o_{v4} are modified. As it can be observed, the PI controller can offer a good performance despite these changes in the system conditions. The reference value is reached again after the adjustment of ω_{sp} by the controller output. The pump's speed and pressures drops in other branches are also shown in Figure 5.8. The pressure drop in branch 1 and 2 is defined as $\Delta p_1 = \Delta p_{k2} + \Delta p_{cv2}$ and $\Delta p_2 = \Delta p_{k5} + \Delta p_{cv3}$.

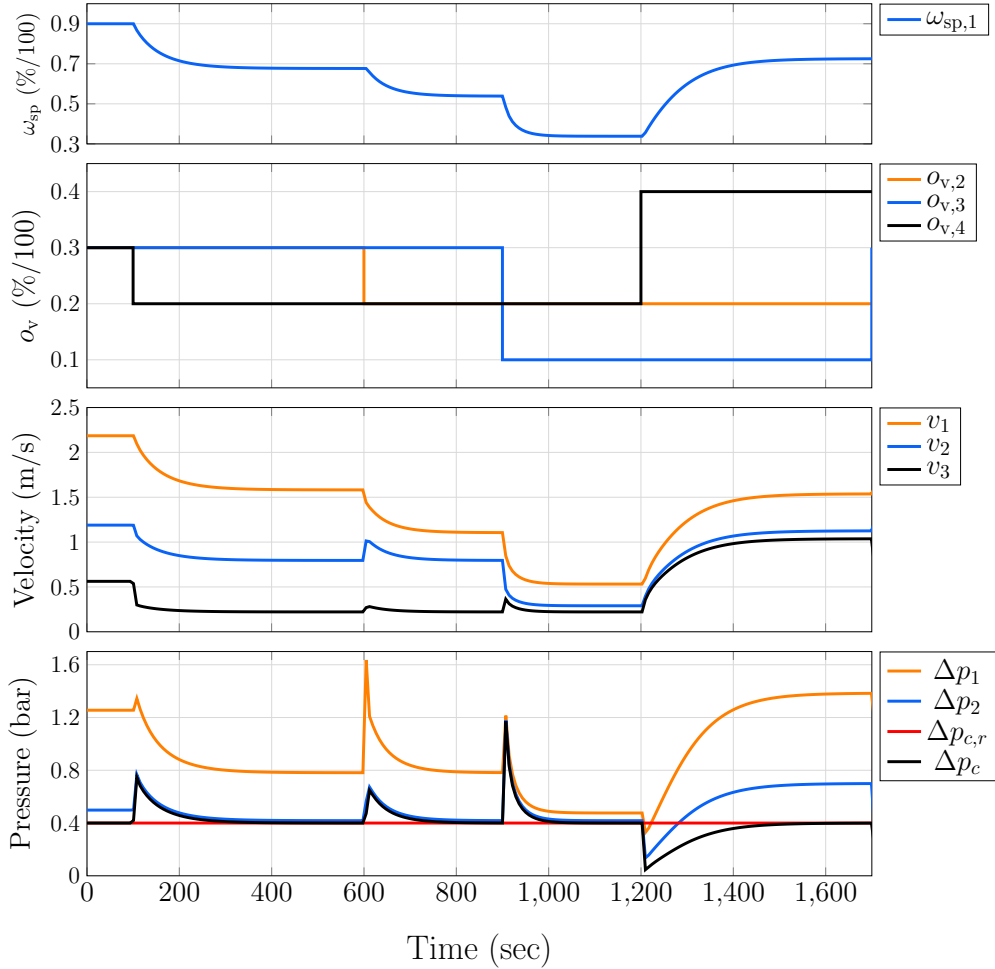


Figure 5.8: Pipe network pressure closed-loop performance under valve opening changes.

The PI controller's response for different references of Δp_c is shown in Figure 5.9. As it can be seen, the PI controller successfully reaches the different reference values within the desired performance parameters, even when it was designed for a specific operating point.

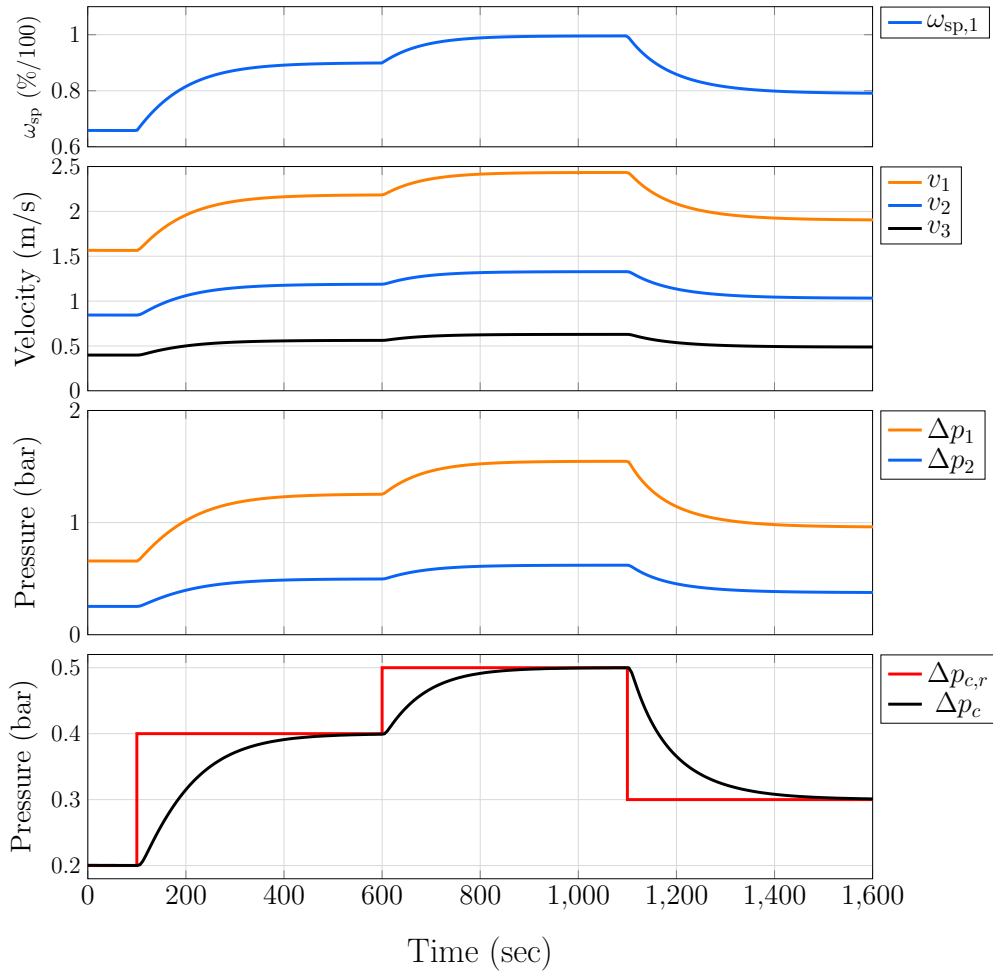


Figure 5.9: Pipe network pressure closed-loop performance under under different set points.

5.2.2 Temperature controller for a flat plate heat exchanger

Heat exchangers manage the heat demand in DHCS's substations. The hot water temperature in the secondary circuit must be kept constant to achieve the customer side's heat demands. For this purpose, a feedback controller is necessary. The mass flow rate in the primary circuit is regulated to increase or decrease the heat transferred to maintain the temperature reference, albeit with changes in the secondary circuit's fluid temperature and mass flow rate. The control scheme should reject disturbances such as changes in the inlet temperatures and variations in the secondary circuit's mass flow rate. This closed-loop control is illustrated in Figure 2.13. For the sake of clarity, a block diagram of the temperature feedback control for a flat plate heat exchanger is shown in Figure 5.10.

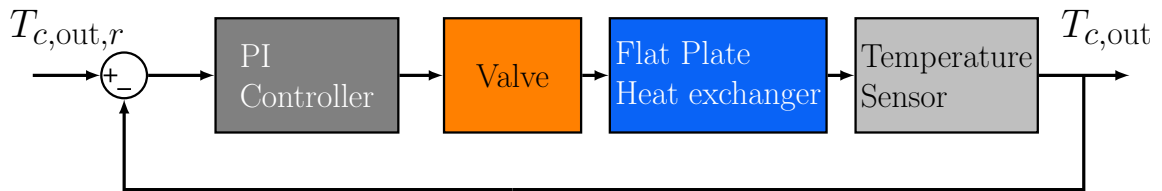


Figure 5.10: Block diagram for a temperature closed-loop system for flat plate heat exchanger.

The dynamic model of the counter flow configuration of a flat plate heat exchanger is defined by equations (4.80) and (4.81) and its parameters are shown in Appendix C. PI

controller is designed for a heat exchanger divided into 10 nodes and assessed for a heat exchanger with 30 nodes in Apros. For clarity, the system equations are grouped per each node as

$$\begin{aligned} m_{c,1}c_{p,c1}\dot{T}_{c,1} &= \dot{m}_c c_{p,c1} (T_{c,in} - T_{c,1}) + U_1 A_{tr} (T_{h,1} - T_{c,1}), \\ m_{h,1}c_{p,h1}\dot{T}_{h,1} &= \dot{m}_h c_{p,h1} (T_{h,2} - T_{h,1}) + U_1 A_{tr} (T_{h,1} - T_{c,1}), \end{aligned} \quad (5.12)$$

$$\begin{aligned} &\vdots \\ m_{c,i}c_{p,ci}\dot{T}_{c,i} &= \dot{m}_c c_{p,ci} (T_{c,i-1} - T_{c,i}) + U_i A_{tr} (T_{h,i} - T_{c,i}), \\ m_{h,i}c_{p,hi}\dot{T}_{h,i} &= \dot{m}_h c_{p,hi} (T_{h,i+1} - T_{h,i}) + U_i A_{tr} (T_{c,i} - T_{h,i}), \end{aligned} \quad (5.13)$$

$$\begin{aligned} &\vdots \\ m_{c,10}c_{p,c10}\dot{T}_{c,10} &= \dot{m}_c c_{p,c10} (T_{c,9} - T_{c,10}) + U_{10} A_{tr} (T_{h,10} - T_{c,10}), \\ m_{h,10}c_{p,h10}\dot{T}_{h,10} &= \dot{m}_h c_{p,h10} (T_{h,in} - T_{h,10}) + U_{10} A_{tr} (T_{c,10} - T_{h,10}). \end{aligned} \quad (5.14)$$

where U is the overall heat transfer coefficient, A_{tr} is the heat transfer area, \dot{m}_c and \dot{m}_h are the mass flow rate of the cold and hot stream, respectively, and $T_{c,x}$ and $T_{h,x}$ are the cold and hot stream temperatures in the system nodes, respectively.

The system state variables are the temperature in each node, using the state space notation, the odd state variables are the cold temperature of the nodes as

$$x_1, x_3, \dots, x_{19} = T_{c,1}, T_{c,2}, \dots, T_{c,10}$$

and the even state variables are the hot temperature of the nodes as

$$x_2, x_4, \dots, x_{20} = T_{h,1}, T_{h,2}, \dots, T_{h,10}.$$

Then, replacing the state variables notation and re-arranging the system equations yields

$$\dot{x}_1 = [\dot{m}_c c_{p,x_1} (T_{c,in} - x_1) + U_1 A_{tr} (x_2 - x_1)] / (m_{c,1}c_{p,x_1}), \quad (5.15)$$

$$\dot{x}_2 = [\dot{m}_h c_{p,x_2} (x_4 - x_2) + U_1 A_{tr} (x_2 - x_1)] / (m_{h,1}c_{p,x_2}), \quad (5.16)$$

$$\dot{x}_3 = [\dot{m}_c c_{p,x_3} (x_1 - x_3) + U_2 A_{tr} (x_4 - x_3)] / (m_{c,2}c_{p,x_3}), \quad (5.17)$$

$$\dot{x}_4 = [\dot{m}_h c_{p,x_4} (x_6 - x_4) + U_2 A_{tr} (x_3 - x_4)] / (m_{h,2}c_{p,x_4}), \quad (5.18)$$

$$\dot{x}_5 = [\dot{m}_c c_{p,x_5} (x_3 - x_5) + U_3 A_{tr} (x_6 - x_5)] / (m_{c,3}c_{p,x_5}), \quad (5.19)$$

$$\dot{x}_6 = [\dot{m}_h c_{p,x_6} (x_8 - x_6) + U_3 A_{tr} (x_5 - x_6)] / (m_{h,3}c_{p,x_6}), \quad (5.20)$$

$$\dot{x}_7 = [\dot{m}_c c_{p,x_7} (x_5 - x_7) + U_4 A_{tr} (x_8 - x_7)] / (m_{c,4}c_{p,x_7}), \quad (5.21)$$

$$\dot{x}_8 = [\dot{m}_h c_{p,x_8} (x_{10} - x_8) + U_4 A_{tr} (x_7 - x_8)] / (m_{h,4}c_{p,x_8}), \quad (5.22)$$

$$\dot{x}_9 = [\dot{m}_c c_{p,x_9} (x_7 - x_9) + U_5 A_{tr} (x_{10} - x_9)] / (m_{c,5}c_{p,x_9}), \quad (5.23)$$

$$\dot{x}_{10} = [\dot{m}_h c_{p,x_{10}} (x_{12} - x_{10}) + U_5 A_{tr} (x_9 - x_{10})] / (m_{h,5}c_{p,x_{10}}), \quad (5.24)$$

$$\dot{x}_{11} = [\dot{m}_c c_{p,x_{11}} (x_9 - x_{11}) + U_6 A_{tr} (x_{12} - x_{11})] / (m_{c,6}c_{p,x_{11}}), \quad (5.25)$$

5.2. Design and implementation of local controllers

$$\dot{x}_{12} = [\dot{m}_h c_{p,x_{12}} (x_{14} - x_{12}) + U_6 A_{tr} (x_{11} - x_{12})] / (m_{h,6} c_{p,x_{12}}), \quad (5.26)$$

$$\dot{x}_{13} = [\dot{m}_c c_{p,x_{13}} (x_{11} - x_{13}) + U_7 A_{tr} (x_{14} - x_{13})] / (m_{c,7} c_{p,x_{13}}), \quad (5.27)$$

$$\dot{x}_{14} = [\dot{m}_h c_{p,x_{14}} (x_{16} - x_{14}) + U_7 A_{tr} (x_{13} - x_{14})] / (m_{h,7} c_{p,x_{14}}), \quad (5.28)$$

$$\dot{x}_{15} = [\dot{m}_c c_{p,x_{15}} (x_{13} - x_{15}) + U_8 A_{tr} (x_{16} - x_{15})] / (m_{c,8} c_{p,x_{15}}), \quad (5.29)$$

$$\dot{x}_{16} = [\dot{m}_h c_{p,x_{16}} (x_{18} - x_{16}) + U_8 A_{tr} (x_{15} - x_{16})] / (m_{h,8} c_{p,x_{16}}), \quad (5.30)$$

$$\dot{x}_{17} = [\dot{m}_c c_{p,x_{17}} (x_{15} - x_{17}) + U_9 A_{tr} (x_{18} - x_{17})] / (m_{c,9} c_{p,x_{17}}), \quad (5.31)$$

$$\dot{x}_{18} = [\dot{m}_h c_{p,x_{18}} (x_{20} - x_{18}) + U_9 A_{tr} (x_{17} - x_{18})] / (m_{h,9} c_{p,x_{18}}), \quad (5.32)$$

$$\dot{x}_{19} = [\dot{m}_c c_{p,x_{19}} (x_{17} - x_{19}) + U_{10} A_{tr} (x_{20} - x_{19})] / (m_{c,10} c_{p,x_{19}}), \quad (5.33)$$

$$\dot{x}_{20} = [\dot{m}_h c_{p,x_{20}} (T_{h,in} - x_{20}) + U_{10} A_{tr} (x_{19} - x_{20})] / (m_{h,10} c_{p,x_{20}}). \quad (5.34)$$

The steady-state values are obtained using the model of the flat plate heat exchanger in a counter flow configuration developed in Chapter 4 and implemented in MATLAB/Simulink. The operating point is defined as $T_{c,out} = 50^\circ\text{C}$, $T_{c,in} = 25^\circ\text{C}$, $T_{h,in} = 90^\circ\text{C}$ and $\dot{m}_c = 40$ kg/s. The hot stream's mass flow rate is adjusted until the operating condition is achieved, with $\dot{m}_h = 23.1$ kg/s. The steady-state values are shown in Table 5.2. The transfer area is the same value for all equations: $A_{tr} = 35.55$ m² (see Appendix C). The mass in each node is calculated with equation (4.46). For simplicity, only the value of the denominator in equations (5.15)-(5.34) is shown in Table 5.2.

Table 5.2: Steady-state values for flat plate heat exchanger linearisation.

Node	Cold stream ($^\circ\text{C}$)	Hot stream ($^\circ\text{C}$)	U (W/m ² K)	$m_c c_{p,T_c}/n$	$m_h c_{p,T_h}/n$
1	$x_1 = 26.6970$	$x_2 = 47.2389$	$U_1 = 387.8725$	2.2959×10^5	2.2780×10^5
2	$x_3 = 28.5246$	$x_4 = 50.1269$	$U_2 = 396.6814$	2.2941×10^5	2.2760×10^5
3	$x_5 = 30.4972$	$x_6 = 53.2387$	$U_3 = 406.2368$	2.2921×10^5	2.2733×10^5
4	$x_7 = 32.63$	$x_8 = 56.5994$	$U_4 = 416.3403$	2.29×10^5	2.2695×10^5
5	$x_9 = 34.9398$	$x_{10} = 60.2359$	$U_5 = 427.0009$	2.2879×10^5	$2.2669e \times 10^5$
6	$x_{11} = 37.4490$	$x_{12} = 64.1778$	$U_6 = 438.8305$	2.2857×10^5	2.2632×10^5
7	$x_{13} = 40.1857$	$x_{14} = 68.4639$	$U_7 = 452.3521$	2.2835×10^5	2.2586×10^5
8	$x_{15} = 43.18$	$x_{16} = 73.1428$	$U_8 = 467.18$	2.2811×10^5	2.2541×10^5
9	$x_{17} = 46.4492$	$x_{18} = 78.2660$	$U_9 = 480.4599$	2.2785×10^5	2.2495×10^5
10	$x_{19} = 50.0331$	$x_{20} = 83.8619$	$U_{10} = 495.6999$	2.2761×10^5	2.2437×10^5

A heat exchanger is a multivariable system since \dot{m}_h , \dot{m}_c , $T_{h,in}$ or $T_{c,in}$ may be considered as system inputs. Nevertheless, the practical implementation in heating substations of a DHCS is limited to control $T_{c,out}$ through \dot{m}_h . Therefore, the heat exchanger is modelled as a single-input single-output system where its input and output are defined as $y = T_{c,out} = x_{19}$ and $u = \dot{m}_h$, respectively. Applying symbolic analysis in MATLAB, the state-space representation defined by equation (G.4) is obtained. Matrices **A**, **B** and **C** are defined by equations (5.35), (5.36) and (5.37), respectively.

$$\mathbf{A} = \begin{bmatrix}
 a_1 & a_2 & 0 & 0 & 0 & 0 & 0 & 0 & 0 & 0 & 0 & 0 & 0 & 0 & 0 & 0 & 0 & 0 & 0 \\
 a_3 & a_4 & 0 & a_5 & 0 & 0 & 0 & 0 & 0 & 0 & 0 & 0 & 0 & 0 & 0 & 0 & 0 & 0 & 0 \\
 a_6 & 0 & a_7 & a_8 & 0 & 0 & 0 & 0 & 0 & 0 & 0 & 0 & 0 & 0 & 0 & 0 & 0 & 0 & 0 \\
 0 & 0 & a_9 & a_{10} & 0 & a_{11} & 0 & 0 & 0 & 0 & 0 & 0 & 0 & 0 & 0 & 0 & 0 & 0 & 0 \\
 0 & 0 & a_{12} & 0 & a_{13} & a_{14} & 0 & 0 & 0 & 0 & 0 & 0 & 0 & 0 & 0 & 0 & 0 & 0 & 0 \\
 0 & 0 & 0 & 0 & a_{15} & a_{16} & 0 & a_{17} & 0 & 0 & 0 & 0 & 0 & 0 & 0 & 0 & 0 & 0 & 0 \\
 0 & 0 & 0 & 0 & a_{18} & 0 & a_{19} & a_{20} & 0 & 0 & 0 & 0 & 0 & 0 & 0 & 0 & 0 & 0 & 0 \\
 0 & 0 & 0 & 0 & 0 & 0 & a_{21} & a_{22} & 0 & a_{23} & 0 & 0 & 0 & 0 & 0 & 0 & 0 & 0 & 0 \\
 0 & 0 & 0 & 0 & 0 & 0 & a_{24} & 0 & a_{25} & a_{26} & 0 & 0 & 0 & 0 & 0 & 0 & 0 & 0 & 0 \\
 0 & 0 & 0 & 0 & 0 & 0 & 0 & 0 & a_{27} & a_{28} & 0 & a_{29} & 0 & 0 & 0 & 0 & 0 & 0 & 0 \\
 0 & 0 & 0 & 0 & 0 & 0 & 0 & 0 & a_{30} & 0 & a_{31} & a_{32} & 0 & 0 & 0 & 0 & 0 & 0 & 0 \\
 0 & 0 & 0 & 0 & 0 & 0 & 0 & 0 & 0 & 0 & a_{33} & a_{34} & 0 & a_{35} & 0 & 0 & 0 & 0 & 0 \\
 0 & 0 & 0 & 0 & 0 & 0 & 0 & 0 & 0 & 0 & a_{36} & 0 & a_{37} & a_{38} & 0 & 0 & 0 & 0 & 0 \\
 0 & 0 & 0 & 0 & 0 & 0 & 0 & 0 & 0 & 0 & 0 & 0 & a_{39} & a_{40} & 0 & a_{41} & 0 & 0 & 0 \\
 0 & 0 & 0 & 0 & 0 & 0 & 0 & 0 & 0 & 0 & 0 & 0 & a_{42} & 0 & a_{43} & a_{44} & 0 & 0 & 0 \\
 0 & 0 & 0 & 0 & 0 & 0 & 0 & 0 & 0 & 0 & 0 & 0 & 0 & 0 & a_{45} & a_{46} & 0 & a_{47} & 0 \\
 0 & 0 & 0 & 0 & 0 & 0 & 0 & 0 & 0 & 0 & 0 & 0 & 0 & 0 & a_{48} & 0 & a_{49} & a_{50} & 0 \\
 0 & 0 & 0 & 0 & 0 & 0 & 0 & 0 & 0 & 0 & 0 & 0 & 0 & 0 & 0 & 0 & a_{51} & a_{52} & 0 \\
 0 & 0 & 0 & 0 & 0 & 0 & 0 & 0 & 0 & 0 & 0 & 0 & 0 & 0 & 0 & 0 & a_{54} & 0 & a_{55} \\
 0 & 0 & 0 & 0 & 0 & 0 & 0 & 0 & 0 & 0 & 0 & 0 & 0 & 0 & 0 & 0 & 0 & 0 & a_{57} & a_{58}
 \end{bmatrix}. \quad (5.35)$$

$$\mathbf{B} = \begin{bmatrix}
 0 & b_1 & 0 & b_2 & 0 & b_3 & 0 & b_4 & 0 & b_5 & 0 & b_6 & 0 & b_7 & 0 & b_8 & 0 & b_9 & 0 & b_{10}
 \end{bmatrix} \quad (5.36)$$

$$\mathbf{C} = \begin{bmatrix}
 0 & 0 & 0 & 0 & 0 & 0 & 0 & 0 & 0 & 0 & 0 & 0 & 0 & 0 & 0 & 0 & 0 & 0 & 0 & 1 & 0
 \end{bmatrix} \quad (5.37)$$

The coefficients of matrices \mathbf{A} and \mathbf{B} are shown in Appendix D. The next step is to obtain the transfer function representation of the linearised system. Due to the number of state variables, the implementation of equation (G.5) yields a 20th order transfer function defined by

$$G_{HE}(s) = \frac{0.008897s^{18} + 0.1092s^{17} + 0.6345s^{16} + 2.32s^{15} + 5.98s^{14} + 11.55s^{13} + 17.33s^{12} + 20.66s^{11} + 19.86s^{10} + 15.52s^9 + 9.907s^8 + 5.158s^7 + 2.179s^6 + 3434s^{13} + 3522s^{12} + 2952s^{11} + 2032s^{10} + 1151s^9 + 535.4s^8 + 203.2s^7 + 0.7395s^5 + 0.1978s^4 + 0.04046s^3 + 0.006007s^2 + 0.0005856s + 2.916 \times 10^{-5} + 62.28s^6 + 15.16s^5 + 2.86s^4 + 0.4014s^3 + 0.03927s^2 + 0.002361s + 6.369 \times 10^{-5}}{s^{20} + 12.95s^{19} + 79.39s^{18} + 306.3s^{17} + 834.1s^{16} + 1704s^{15} + 2710s^{14}} \quad (5.38)$$

As it is shown in Figure 5.10, the system input \dot{m}_h is regulated by a valve. Its dynamic behaviour should be considered in the transfer function of the system. Thus, a linear model is proposed based on the characteristic of the Apros elements: *control valve* and *actuator valve* with a time response of 30 sec and a gain of 100 is proposed. The transfer function of this model is defined by

$$G_v(s) = \frac{100}{5s + 1}. \quad (5.39)$$

The step response of $G_v(s)$ is shown in Figure 5.11.

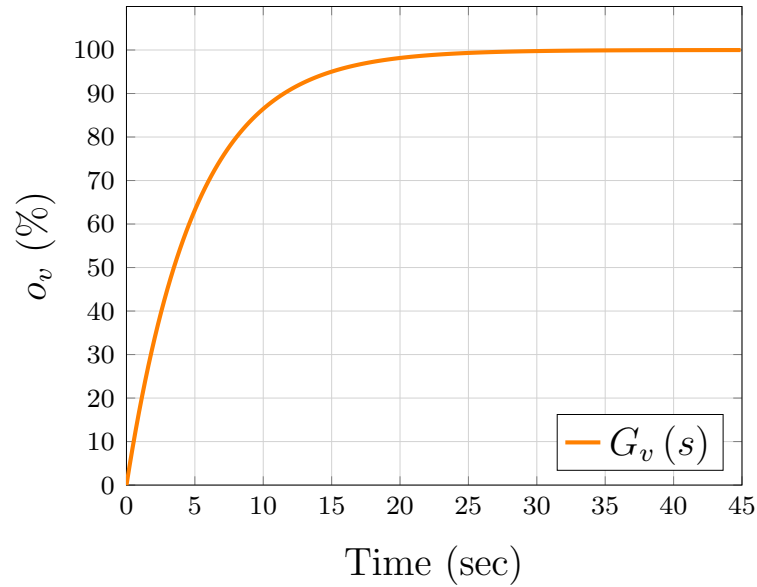
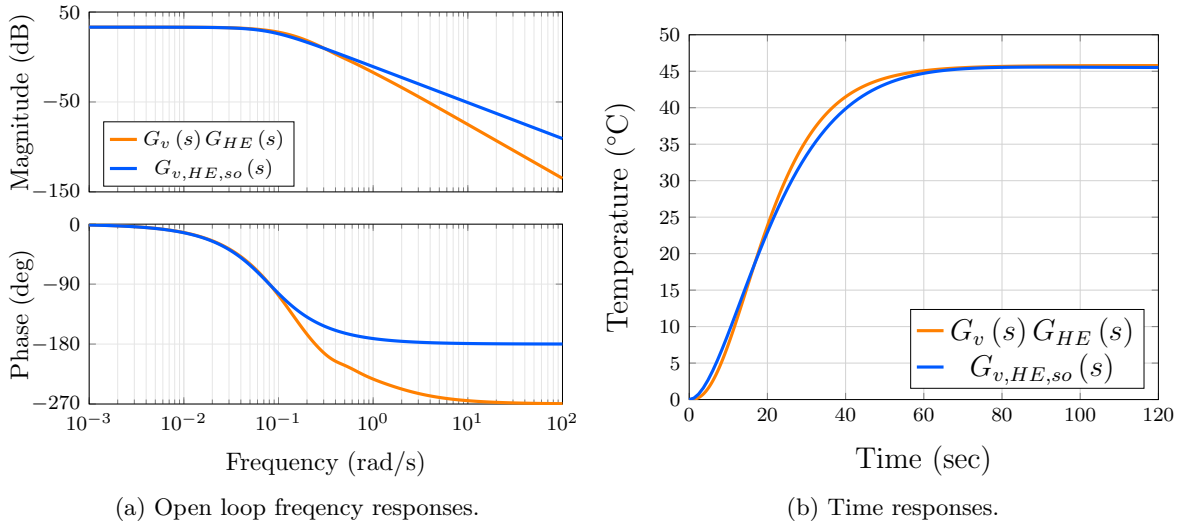


Figure 5.11: Step response of the valve.

Thus, the transfer function of the system including the valve is defined by $G_v(s)G_{HE}(s)$. An equivalent second-order system is obtained by defining the parameters of equation (G.13) as $A_1 = 45.5$, $\omega_n = 0.08$ rad/s and $\zeta = 0.9$. The transfer function of the equivalent system is defined by

$$G_{v,HE,so} = \frac{0.2912}{s^2 + 0.144s + 0.0064} \quad (5.40)$$

Figure 5.12 shows the open-loop frequency response and the closed-loop step time response of $G_v(s)G_{HE}(s)$ and $G_{v,HE,so}(s)$.



(a) Open loop frequency responses.

(b) Time responses.

 Figure 5.12: (a) Open-loop Bode plots and (b) step responses of $G_v(s)G_{HE}(s)$ and $G_{v,HE,so}(s)$.

PI controller design

Like the differential pressure controller, the desired performance specifications should consider a slow response and no overshoot to avoid a sudden high demand of mass flow rate \dot{m}_h during

disturbances or changes in the operating point. A large mass flow rate may cause not only damage due to overpressure of the pipe, but also affect the performance of the rest of the substation. Therefore, a settling time of $t_s = 360$ s and a maximum overshoot of $o_s = 1\%$ are defined as desired performance parameters. These are translated to the frequency domain as a $\zeta = 0.8261$, a phase margin of at least $\phi_m = 70.9^\circ$, and a minimum bandwidth $\omega_{bw} = 0.0084$ rad/s.

Applying the loop shaping process through Bode diagrams, the gains of a PI controller (C_{HE}) capable of meeting the desired performance are obtained, with $k_p = 0.0042$ and $k_i = 0.00018$. The transfer function of C_{HE} is defined by

$$C_{HE} = \frac{0.0042s + 0.00018}{s}. \quad (5.41)$$

The open-loop frequency responses of the equivalent system alone and with controller's action C_{HE} are shown in Figure 5.13a. The frequency domain desired specifications are met, a $\phi_m = 91.2$ rad/s and a $\omega_{bw} = 0.0122$ rad/s. The closed-loop step responses in Figure 5.13b confirm the PI controller successful performance over both systems: linearised ($G_v(s) G_{HE}(s)$) and equivalent ($G_{v,HE,so}(s)$). A settling time of 360 and no overshoot are achieved.

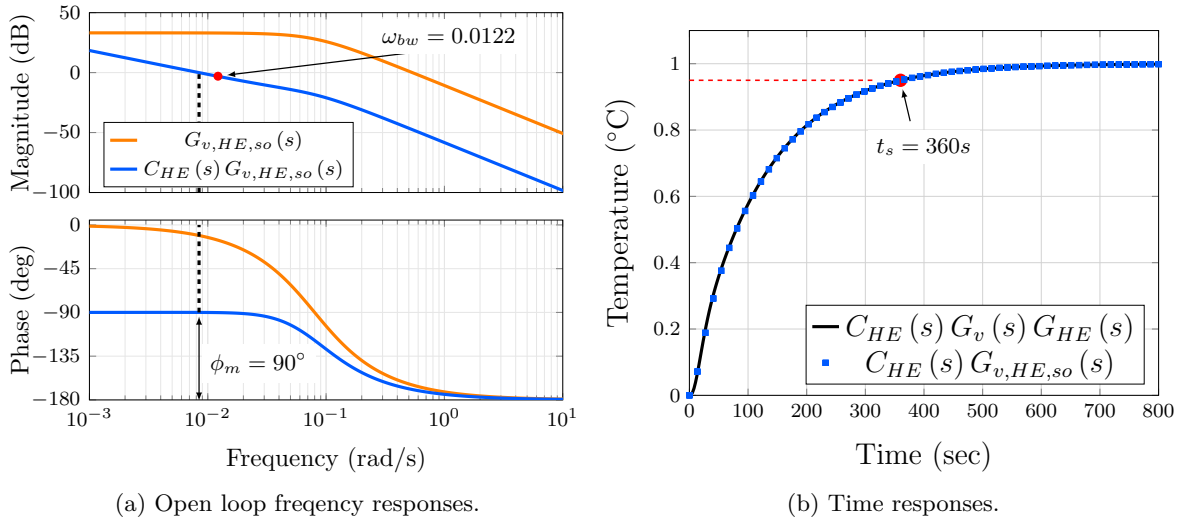


Figure 5.13: (a) Open-loop Bode plots of the equivalent second-order system and the loop-shaped obtained with $C_{HE}(s)$. (b) Time step responses of the closed-loop system with $G_{v,HE,so}(s)$ and $G_v(s) G_{HE}(s)$.

Controller verification

The performance of the control system is assessed in Apros. The parameters of the flat plate heat exchanger used Chapter 4 are adopted. A temperature sensor, valve driver and PI controller elements are added, as shown in Figure 5.14. The Apros's PI controller is set with the gains of $C_{HE}(s)$. Two simulations are carried out to assess the performance of the PI controller under disturbances and changes in the temperature set point of $T_{c,out}$. Although the PI controller has been designed using the linearisation of a heat exchanger model divided into 10 nodes, the PI controller is assessed in Apros for both 10 and 30 nodes. Results are labelled thus with subscripts '10' and '30'.

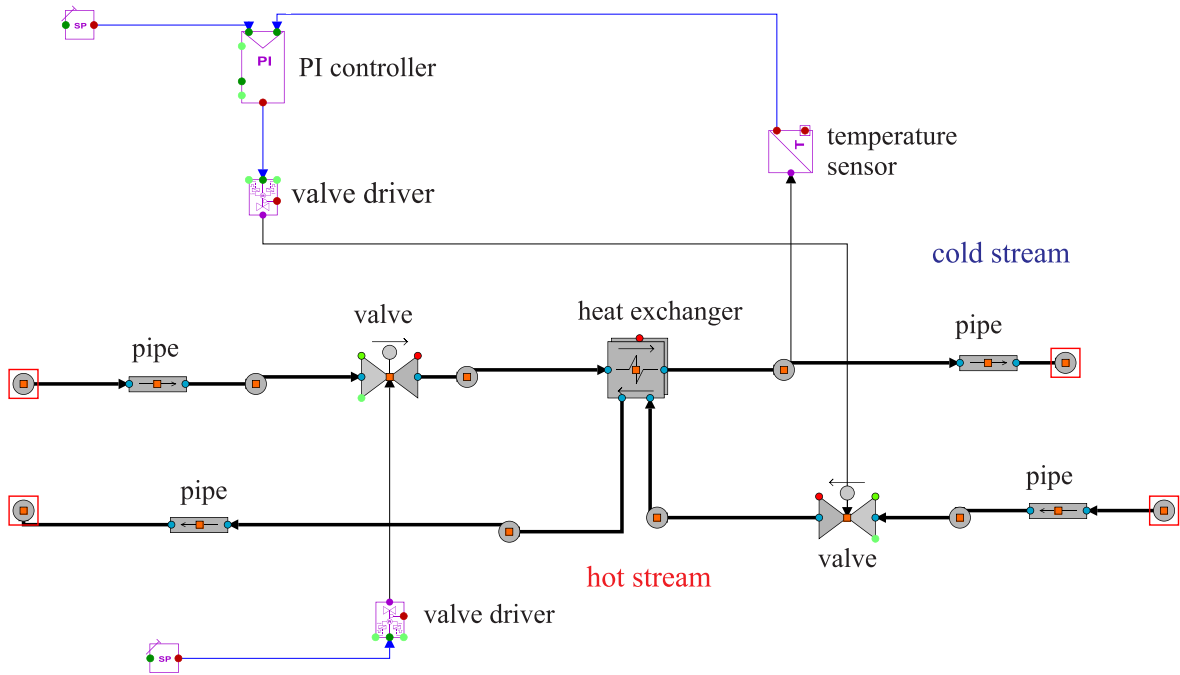


Figure 5.14: Temperature control of flat plate heat exchanger implemented in Apros.

The operating point used for the linearisation process is set as $T_{c,in} = 25^{\circ}\text{C}$, $T_{h,in} = 90^{\circ}\text{C}$ and $\dot{m}_c = 40 \text{ kg/s}$. Changes in these variables are present at different moments through the simulation. These disturbances resemble potential scenarios of real systems. The cold stream's mass flow rate (\dot{m}_c) varies 5 kg/s below and above its operating value. Similarly, the input temperatures are varied. As it can be observed, in Figure 5.15, the reference temperature is kept constant by the PI controller, albeit with variations in the system conditions. The simulation results for both 10 and 30 nodes show the same behaviour for output temperatures. A slight difference in the \dot{m}_h is present at 850 seconds, when there is a decrement of $T_{h,in}$ and an increment of \dot{m}_c . This condition requires a high amount of \dot{m}_h to transfer more heat to keep the temperature reference. Since the heat transferred in the heat exchanger model with several nodes is higher than those with a lower number of nodes, a smaller amount of hot mass flow rate is required.

The performance of the PI controller under changes in the reference are shown in Figure 5.16. The initial value of $T_{c,out}$ is 49°C . Set points of 50°C , 55°C and 45°C also established. In all cases there is no overshoot present and the settling time is about 200 seconds. There is a difference of 160 seconds between the desired and the resulted settling times. This discrepancy may be related to the system's non-linearities when the PI controller is acting on a different operating point rather than the one it was designed for. Although the desired t_s parameter is not achieved, the controller system's performance is still considered adequate. Both heat exchangers (10 and 30 nodes division) present similar behaviour. As it is expected, a slightly less amount of \dot{m}_h is required for a heat exchanger with 30 nodes compared with one with 10 nodes during high demand of heat (high-temperature reference).

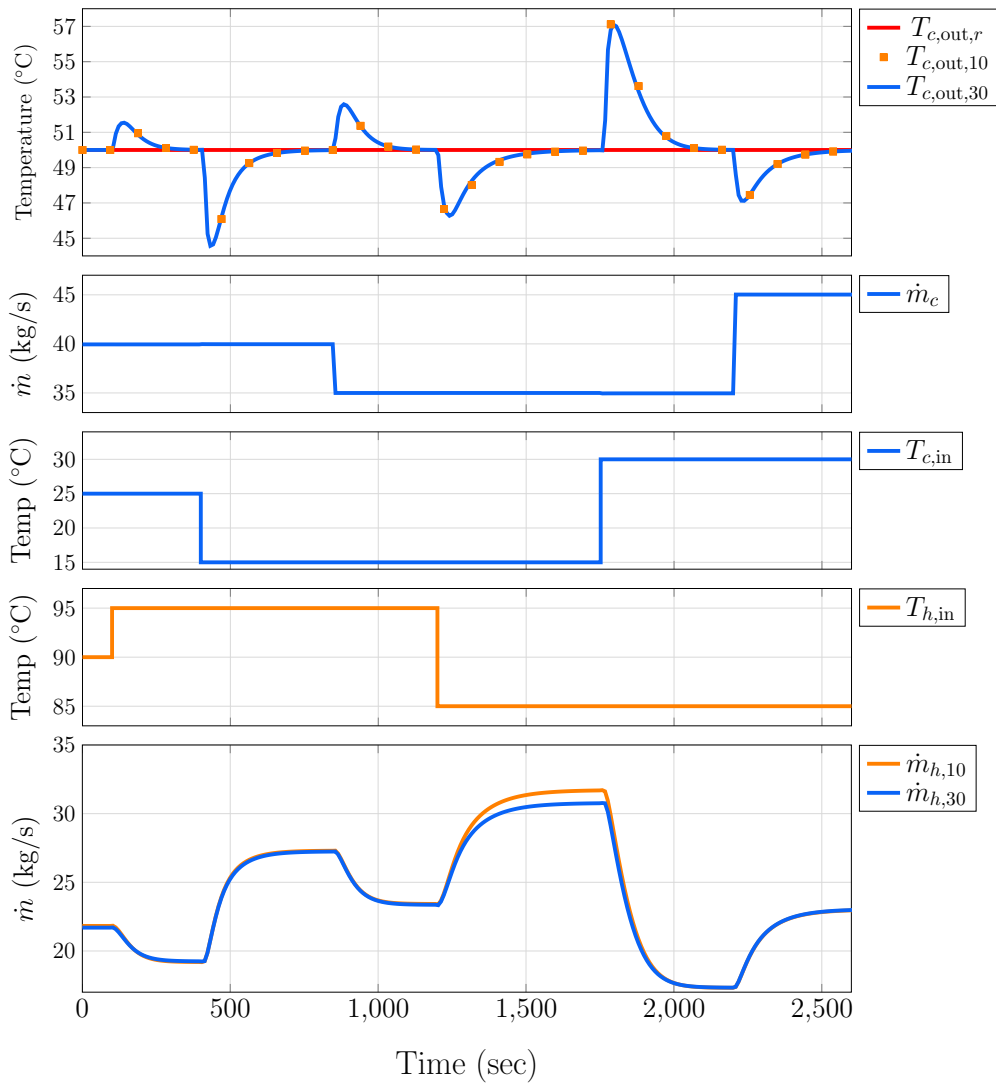


Figure 5.15: Simulation results of the PI controller performance under disturbances.

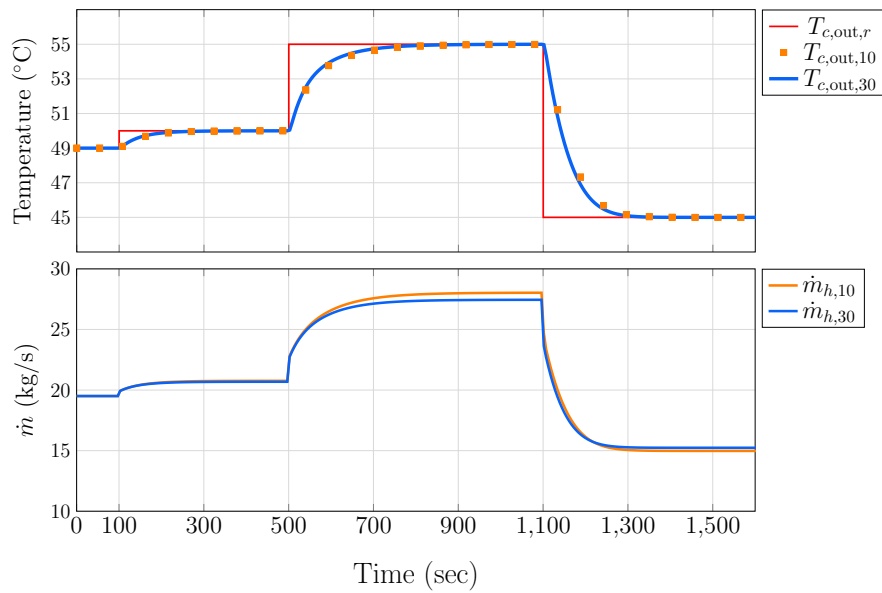


Figure 5.16: Simulation results of the PI controller performance under different temperature set points.

5.2.3 Temperature controller for a shell-and-tube heat exchanger

The cooling energy produced in a DHCS needs to be transferred to the customer cooling systems employing heat exchangers. The cold stream provided by the energy technologies is supplied to the primary circuit of a heat exchanger. The secondary circuit stream should be chilled by the heat transfer process inside the heat exchanger. Temperature set points are established in the secondary circuit outlet to guarantee a constant supply temperature of cold water in cooling systems. In this section, a PI controller of a shell-and-tube heat exchanger for cooling applications is designed. The parameters of the shell-and-tube heat exchanger are shown in Appendix C. Similar to the flat plate heat exchanger, the system should include the dynamics of a valve. The block diagram of the closed-loop system is shown in Figure 5.17.

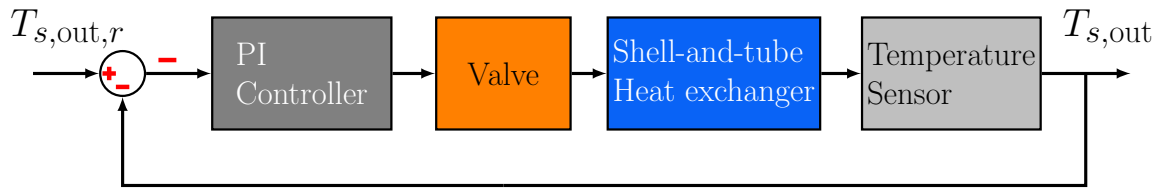


Figure 5.17: Block diagram for a temperature closed-loop system for shell-and-tube heat exchanger.

In a shell-and-tube heat exchanger, the hot and cold stream flow through the shell and tube sides, respectively. Using the model defined by equations (4.82) and (4.83), the shell stream outlet is considered the system's output $T_{s,out}$. Then, the heat transferred is regulated through cold stream's flow variation (\dot{m}_t).

Figure 5.17 highlights with red colour the error calculation signs in the closed-loop diagram to notice that a special computation of the error is required. The control system's aim in a heat exchanger is to reduce the error between the reference $T_{s,o,r}$ and the system output $T_{s,o}$ regulating the cold stream's injection \dot{m}_t . The PI controller's action in a standard configuration is to increase its output when a positive error is present. Conversely, when a negative error occurs, the output should be reduced. For instance, in the previous subsection, when the PI controller of the flat plate heat exchanger receives a positive error for a set point change at 500 seconds (see Figure 5.16), with $T_{c,out,r} - T_{c,out} = (55 - 50^\circ\text{C} = 5^\circ\text{C})$, the output increases the amount of hot mass flow rate. Conversely, if the error is negative at 1100 seconds: $(45 - 55^\circ\text{C} = -10^\circ\text{C})$, the effect PI controller's action reduces the amount of hot mass flow rate.

Nevertheless, for a cooling application the PI controller should achieve an opposite effect. Otherwise, the hot stream would not be cooled. Thus, when a positive error is present, the hot stream is colder than the reference and the PI controller should reduce its output. Conversely, when the hot stream is hotter than the reference thereby producing a negative error, the PI controller should increase the cold mass flow rate to deliver more cold to the heat exchanger. Therefore, a negative sign is added to the closed-loop configuration.

Unlike the linearisation method presented in the previous subsection where the heat exchanger models is divided in 10 nodes, the shell-and-tube heat exchanger is divided in only 3 nodes. This adopted simplification demonstrates that a simpler model could be used for the

control design process. Grouping the node equations of the shell and tube model yields

$$\begin{aligned} m_{t,1}c_{p,t1}\dot{T}_{t,1} &= \dot{m}_t c_{p,t1} (T_{t,\text{in}} - T_{t,1}) + U_1 A_{tr} (T_{s,1} - T_{t,1}), \\ m_{s,1}c_{p,s1}\dot{T}_{s,1} &= \dot{m}_s c_{p,s1} (T_{s,2} - T_{s,1}) + U_1 A_{tr} (T_{s,1} - T_{t,1}). \end{aligned} \quad (5.42)$$

$$\begin{aligned} m_{t,2}c_{p,t2}\dot{T}_{t,2} &= \dot{m}_t c_{p,t2} (T_{t,1} - T_{t,2}) + U_2 A_{tr} (T_{s,2} - T_{t,2}), \\ m_{s,2}c_{p,s2}\dot{T}_{s,2} &= \dot{m}_s c_{p,s2} (T_{s,3} - T_{s,2}) + U_2 A_{tr} (T_{s,2} - T_{t,2}). \end{aligned} \quad (5.43)$$

$$\begin{aligned} m_{t,3}c_{p,t3}\dot{T}_{t,3} &= \dot{m}_t c_{p,t3} (T_{t,2} - T_{t,3}) + U_3 A_{tr} (T_{s,3} - T_{t,3}), \\ m_{s,3}c_{p,s3}\dot{T}_{s,3} &= \dot{m}_s c_{p,s3} (T_{s,\text{in}} - T_{s,3}) + U_3 A_{tr} (T_{s,3} - T_{t,3}). \end{aligned} \quad (5.44)$$

where U is the overall heat transfer coefficient, A_{tr} is the heat transfer area and \dot{m}_t and \dot{m}_s are the mass flow rates of the tube and shell sides, respectively. The temperature of the tube and shell side in each node are defined by $T_{t,x}$ and $T_{s,x}$, respectively. The state variables are defined as $x_1 = T_{t,1}$, $x_2 = T_{s,1}$, $x_3 = T_{t,2}$, $x_4 = T_{s,2}$, $x_5 = T_{t,3}$ and $x_6 = T_{s,3}$. The system equations (5.42)-(5.44) are re-arranged and the state variables are replaced as

$$\dot{x}_1 = [\dot{m}_t c_{p,x1} (T_{t,\text{in}} - x_1) + U_1 A_{tr} (x_2 - x_1)] / (m_{t,1} c_{p,x1}), \quad (5.45)$$

$$\dot{x}_2 = [\dot{m}_s c_{p,x2} (x_4 - x_2) + U_1 A_{tr} (x_2 - x_1)] / (m_{s,1} c_{p,x2}), \quad (5.46)$$

$$\dot{x}_3 = [\dot{m}_t c_{p,x3} (x_1 - x_3) + U_2 A_{tr} (x_4 - x_3)] / (m_{t,2} c_{p,x3}), \quad (5.47)$$

$$\dot{x}_4 = [\dot{m}_s c_{p,x4} (x_6 - x_4) + U_2 A_{tr} (x_3 - x_4)] / (m_{s,2} c_{p,x4}), \quad (5.48)$$

$$\dot{x}_5 = [\dot{m}_t c_{p,x5} (x_3 - x_5) + U_3 A_{tr} (x_6 - x_5)] / (m_{t,3} c_{p,x5}), \quad (5.49)$$

$$\dot{x}_6 = [\dot{m}_s c_{p,x6} (T_{s,\text{in}} - x_6) + U_3 A_{tr} (x_5 - x_6)] / (m_{s,3} c_{p,x6}). \quad (5.50)$$

The shell-and-tube heat exchanger model (5.42-5.44) is implemented in MATLAB/Simulink to simulate the operating point and obtain its steady-state values. The linearisation method is applied for the next conditions $T_{t,\text{in}} = 5^\circ\text{C}$, $T_{s,\text{in}} = 25^\circ\text{C}$ and $\dot{m}_s = 20$ kg/s and a desired hot stream temperature outlet of $T_{s,\text{out}} = 15^\circ\text{C}$. These conditions are achieved by modifying \dot{m}_t to 22.9 kg/s. The steady-state values are shown in Table 5.3. The value of the heat transfer area is the same for all equations: $A_{tr} = 1.2566$ m² (see Appendix C).

Table 5.3: Steady-state values for shell-and-tube heat exchanger linearisation.

Node	Tube stream ($^\circ\text{C}$)	Shell stream ($^\circ\text{C}$)	U (W/m ² K)	$m_c c_{p,T_c}/n$	$m_h c_{p,T_h}/n$
1	$x_1 = 7.7061$	$x_2 = 15.0039$	$U_1 = 149.6545$	4.1965×10^6	4.1832×10^6
2	$x_3 = 10.6070$	$x_4 = 18.1103$	$U_2 = 155.8267$	4.1912×10^6	4.1780×10^6
3	$x_5 = 13.7134$	$x_6 = 21.4381$	$U_3 = 161.9273$	4.1856×10^6	4.1732×10^6

Applying the Taylor series linearisation method for equations (5.45)-(5.50) and using the

5.2. Design and implementation of local controllers

steady-state values, the linearised system is given by

$$\dot{\mathbf{x}} = \begin{bmatrix} -0.0270 & 0.0071 & 0 & 0 & 0 & 0 \\ 0.0337 & -0.1088 & 0 & 0.0750 & 0 & 0 \\ 0.0199 & 0 & -0.0273 & 0.0074 & 0 & 0 \\ 0 & 0 & 0.0352 & -0.1102 & 0 & 0.0751 \\ 0 & 0 & 0.0199 & 0 & -0.0276 & 0.0077 \\ 0 & 0 & 0 & 0 & 0.0366 & -0.1117 \end{bmatrix} [\mathbf{x}] + \begin{bmatrix} 0.0022 \\ 0 \\ 0.0023 \\ 0 \\ 0.0025 \\ 0 \end{bmatrix} [u], \quad (5.51)$$

$$y = \begin{bmatrix} 0 & 1 & 0 & 0 & 0 & 0 \end{bmatrix} [\mathbf{x}].$$

where $u = \dot{m}_t$ and $y = x_2 = T_{s,2}$.

The transfer function of the linearised system is obtained implementing equation (G.5) into (5.51) yielding

$$G_{st} = \frac{7.261 \times 10^{-5} s^4 + 2.62 \times 10^{-5} s^3 + 3.431 \times 10^{-6} s^2 + 1.488 \times 10^{-7} s + 2.118 \times 10^{-9}}{s^6 + 0.4127 s^5 + 0.06503 s^4 + 0.004875 s^3 + 0.0001781 s^2 + 3.017 \times 10^{-6} s + 1.81 \times 10^{-8}}. \quad (5.52)$$

Similar to the flat plate heat exchanger, the valve's behaviour that regulates \dot{m}_t should be considered for the PI controller design. The dynamics defined by (5.39) is used here. The transfer function of the system including the valve is given by

$$G_{v,st}(s) = G_v(s) G_{st}(s). \quad (5.53)$$

The parameters of equation (G.13) are defined as $A_1 = 11.68$, $\omega_n = 0.019$ rad/s and $\zeta = 0.9$. The equivalent second-order system of (5.53) is given as

$$G_{v,st,so} = \frac{0.004216}{s^2 + 0.0342s + 0.000361}. \quad (5.54)$$

Figure 5.18 shows the frequency and step time response of $G_{v,st}$ and $G_{v,st,so}$.

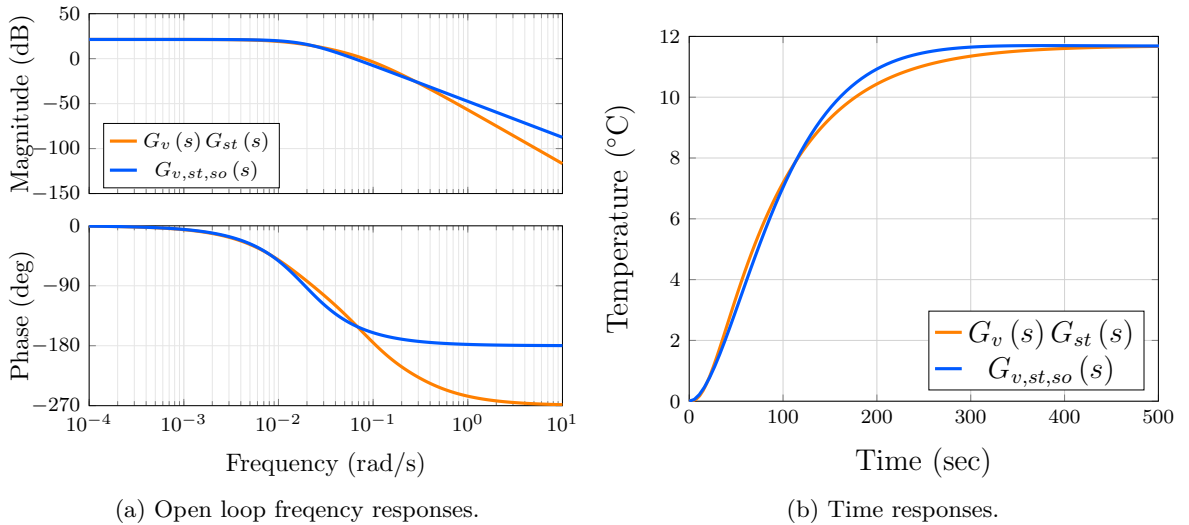


Figure 5.18: (a) Open-loop Bode plots and (b) step time responses of the $G_v(s)G_{st}(s)$ and $G_{v,st,so}(s)$.

PI controller design

The desired performance specifications for the temperature control should consider a slow response to avoid high amounts of mass flow rate during disturbances to the operating point. Therefore, a $t_s = 700$ seconds and a maximum overshoot of $o_s = 1\%$ are considered for the PI control design. These parameters in the frequency domain are defined as $\zeta = 0.9$, a ϕ_m of at least 70.9° and a minimum bandwidth of $\omega_{bw} = 0.0058$ rad/s. Similar to the previous designs, loop-shaping of the system's frequency response is done to obtain the PI controller gains meeting the design specifications. These gains are given as $k_p = 0.0195$ and $k_i = 0.00033$, resulting in the PI controller

$$C_{st} = \frac{0.0195s + 0.00033}{s}. \quad (5.55)$$

The open-loop frequency responses of the $G_{v,st,so}$ and $C_{st}G_{v,st,so}$ are shown in Figure 5.19a. As it can be observed in Figure 5.19a, design specifications are met. Although ω_{bw} is slightly lower than the desired one no overshoot and a settling time of 700 seconds are achieved for linearised system ($G_{v,st}(s)$).

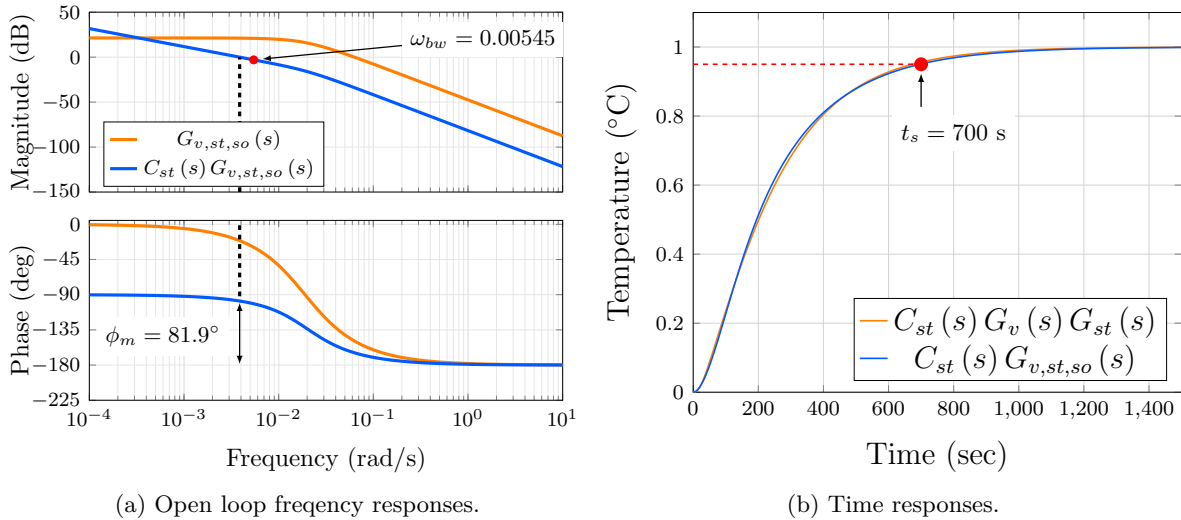


Figure 5.19: (a) Open-loop Bode plots of the equivalent second-order system and the loop-shaped obtained with $C_{st}(s)$. (b) Time step responses of the closed-loop system with $G_{v,st,so}(s)$ and $G_v(s)G_{st}(s)$.

Controller verification

The performance of the PI controller (C_{st}) is assessed in Apros. The parameters shown in Appendix C are adopted in the *tube heat exchanger* element of Apros. A temperature sensor, valve driver and PI controller elements are included in the system, as shown in Figure 5.20. Like for the flat plate heat exchanger control, two simulations are carried out to verify the designed controller's performance under disturbances and different operating points. For this assessment, the Apros element is divided in 30 nodes. The special computation of the error is obtained by defining the PI controller's proportional gain in Apros with a negative value.

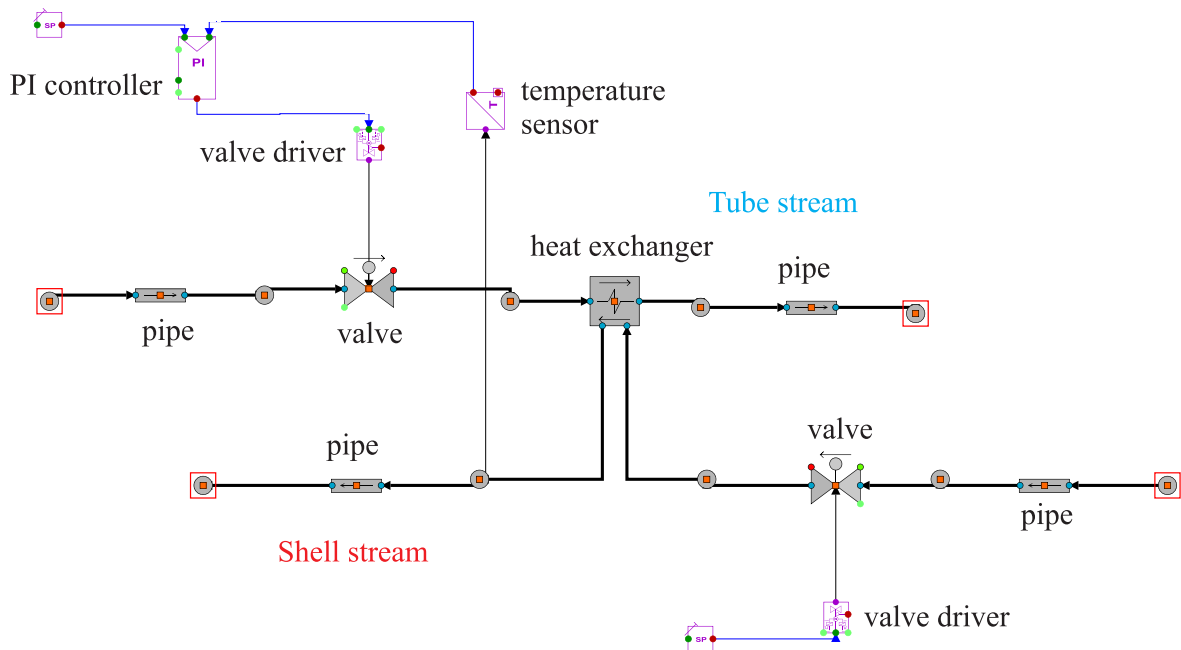


Figure 5.20: Temperature control of shell-and-tube heat exchanger implemented in Apros

Firstly, the operating conditions are set as $T_{t,in} = 5^\circ\text{C}$, $T_{s,in} = 25^\circ\text{C}$ and $\dot{m}_s = 20 \text{ kg/s}$. Variations of 5 kg/s below and above operating point value of the shell mass flow rate are present at 26 minutes and 200 minutes, respectively. Temperature changes in the input of tube and shell streams are carried out as well. $T_{t,in}$ and $T_{s,in}$ vary from 3°C to 7°C and from 22°C to 28°C , respectively. Simulation results are shown in Figure 5.21. As it can be seen, the PI controller works successfully under disturbances as it is able to force the heat exchanger to follow the reference after any change of the operating point. Due to the long settling time specified during the control design process, the time required to achieve the references again is about 20 minutes. This slow response is acceptable because the PI controller reduces and increments the tube side's mass flow rate slowly, avoiding overshoots that might damage the heat exchanger or the pipe network.

Step changes in the reference temperature are implemented as well, with results shown in Figure 5.22. Three different temperature set points including the value for which it is designed are set. The PI exhibits a successful performance. As it can be observed, all references are achieved with a settling time of about 600 seconds, as defined during the design process. No overshoot is present for 15°C and 13°C temperature set points. Nevertheless, a slight overshoot occurs for the set point of 17° , which is still considered acceptable as the PI controller has been designed for a different set point.

It is important to notice how the PI controller acts when a negative sign is introduced to the closed-loop control. Figure 5.22 shows how the mass flow rate of the tubes is reduced when a positive error is present at 100 seconds and 1100 seconds ($e_t = 15 - 14 = 1$, $e_t = 17 - 15 = 2$). Conversely, when a negative error is present at 2400 seconds ($e_t = 13 - 17 = -4$), the amount of cold mass flow rate is increased. As it is shown in the simulation results, a dynamic model of heat exchanger divided into only 3 nodes is sufficient to design a PI controller whose performance under different operating points is successful.

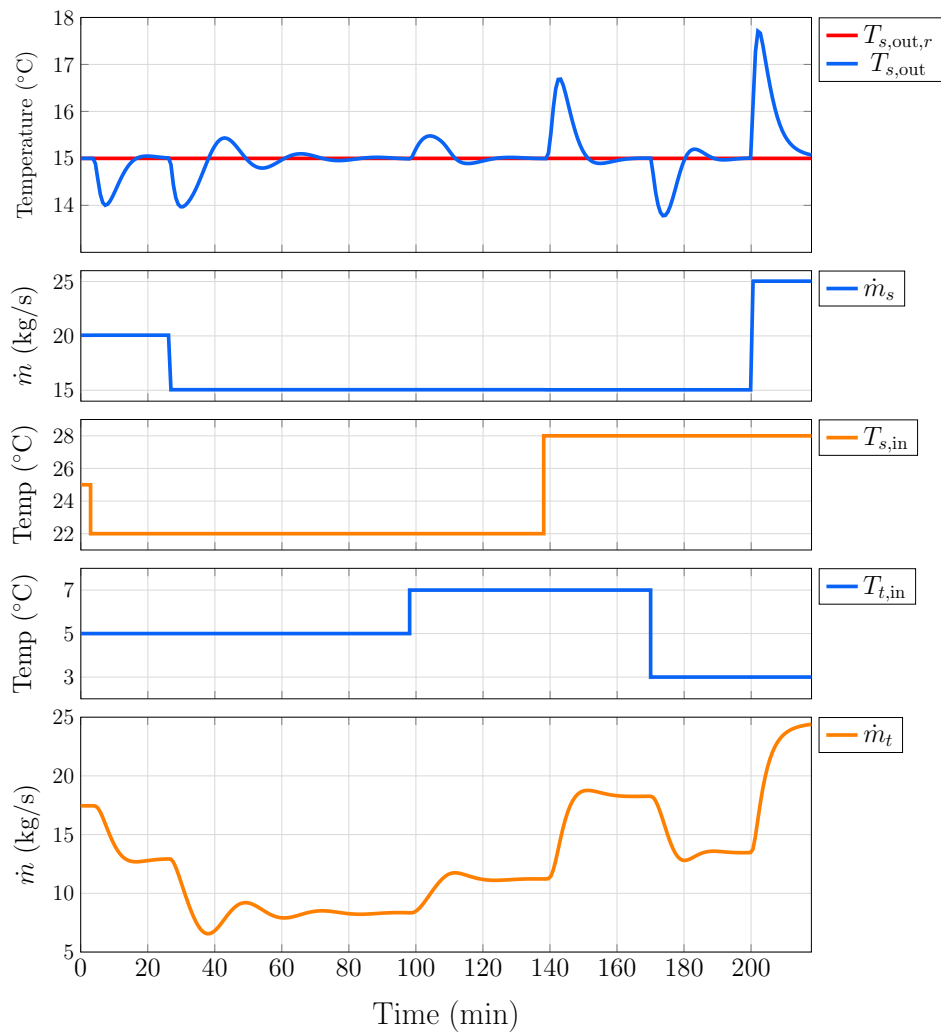


Figure 5.21: Simulation results of the PI controller performance under disturbances.

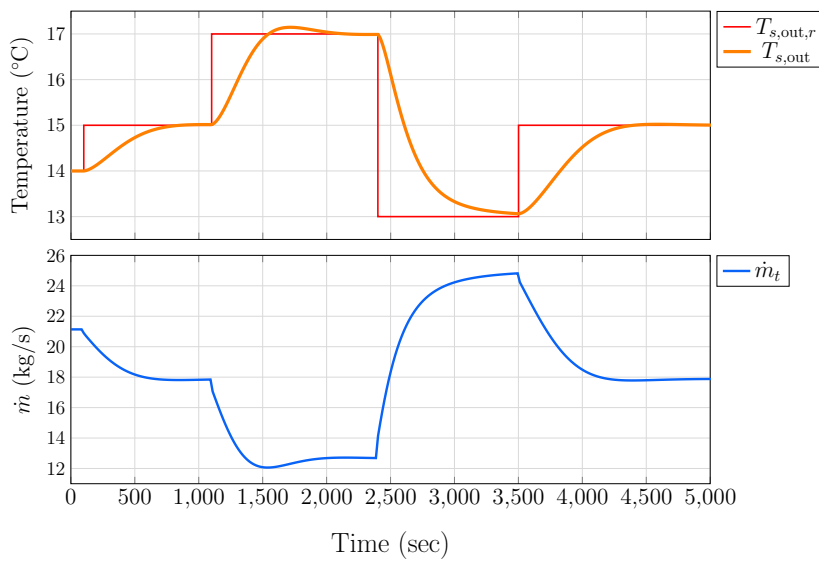


Figure 5.22: Simulation results of the PI controller performance under different temperature set points.

5.2.4 Charging process controller for a sensible TES

Charging and discharging processes define the operating points of TES tanks. The behaviour during discharging process directly depends on the heat demands of the consumers. Conversely, the energy centre manages the charging process when operational conditions, such as empty TES, and low heat demand, are present. The TES may be filled within a defined period to guarantee conditions to face later high heat demands. In this section, a PI controller is designed for the charging process of a water tank-based TES. A well-insulated tank is assumed. Therefore, there are no energy losses. The model used for the control design process is defined by equations (4.89)-(4.91). The tank is stratified into five layers. According to Figure 4.50, the charging process is carried out by injecting hot water at the tank's top. Therefore, the tank is considered full when the temperature of layer 5 reaches the input temperature of the hot mass flow rate \dot{m}_h . A block diagram of the closed-loop control is shown in Figure 5.23.

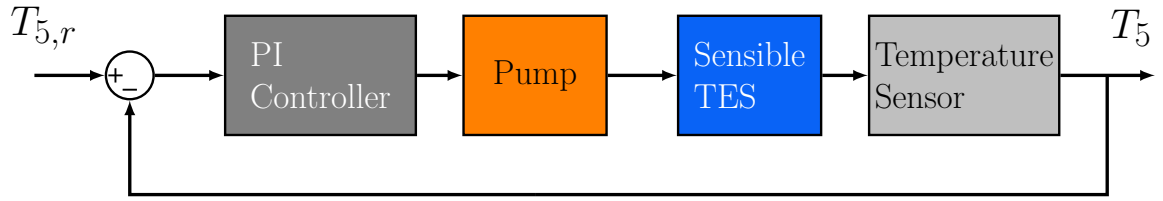


Figure 5.23: Block diagram for a temperature closed-loop system for water tank-based TES.

The dynamic model for the charging process of a five layers stratified TES is expressed using equations (4.89)-(4.91) as

$$\rho c_{p,1} A \Delta h \dot{T}_1 = \dot{m}_h c_{p,1} (T_{h,\text{in}} - T_1), \quad (5.56)$$

$$\rho c_{p,2} A \Delta h \dot{T}_2 = \dot{m}_h c_{p,2} (T_1 - T_2), \quad (5.57)$$

$$\rho c_{p,3} A \Delta h \dot{T}_3 = \dot{m}_h c_{p,3} (T_2 - T_3), \quad (5.58)$$

$$\rho c_{p,4} A \Delta h \dot{T}_4 = \dot{m}_h c_{p,4} (T_3 - T_4), \quad (5.59)$$

$$\rho c_{p,5} A \Delta h \dot{T}_5 = \dot{m}_h c_{p,5} (T_4 - T_5), \quad (5.60)$$

The state-space variables of the system are the temperature in each layer. These are defined as $x_1 = T_1$, $x_2 = T_2$, $x_3 = T_3$, $x_4 = T_4$ and $x_5 = T_5$. By re-ordering equations (5.56-5.60) and using a state-space notation, yields

$$\dot{x}_1 = [\dot{m}_h c_{p,1} (T_{h,\text{in}} - x_1)] / (\rho c_{p,1} A \Delta h), \quad (5.61)$$

$$\dot{x}_2 = [\dot{m}_h c_{p,2} (x_1 - x_2)] / (\rho c_{p,2} A \Delta h), \quad (5.62)$$

$$\dot{x}_3 = [\dot{m}_h c_{p,3} (x_2 - x_3)] / (\rho c_{p,3} A \Delta h), \quad (5.63)$$

$$\dot{x}_4 = [\dot{m}_h c_{p,4} (x_3 - x_4)] / (\rho c_{p,4} A \Delta h), \quad (5.64)$$

$$\dot{x}_5 = [\dot{m}_h c_{p,5} (x_4 - x_5)] / (\rho c_{p,5} A \Delta h), \quad (5.65)$$

The parameters of the model are shown in Appendix C. The sensible TES tank model is implemented in MATLAB/Simulink to obtain the steady-state values required for the linearisation method. To do this an intermediate point of the charging process is selected.

If the operating point is chosen when all temperatures are equal, equation (G.5) yields zero as all elements of \mathbf{B} are zero. Figure 5.24 highlights the temperatures of each layer at 1250 seconds during a charging process with a \dot{m}_h of 100 kg/s. The steady-values and the term $\rho c_{p,i} A \Delta h$ are shown in Table 5.4.

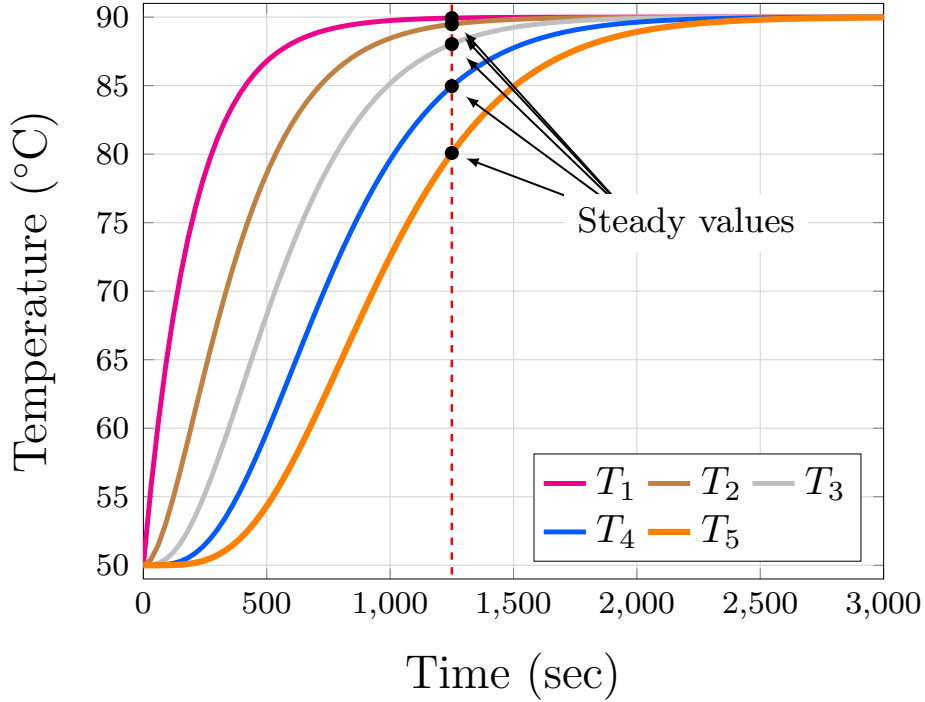


Figure 5.24: Steady values used for the linearisation step of the TES tank model.

Table 5.4: Steady-state values for sensible TES tank.

Layer	Temperature (°C)	$\rho c_{p,i} A \Delta h$ (J/K)
1	$T_1 = 89.9292$	8.2625×10^7
2	$T_2 = 89.4770$	8.2644×10^7
3	$T_3 = 88.0323$	8.2702×10^7
4	$T_4 = 84.9606$	8.2841×10^7
5	$T_5 = 80.0822$	8.3049×10^7

The state space representation of the linearised model is given by

$$\dot{\mathbf{x}} = \begin{bmatrix} -0.0051 & 0 & 0 & 0 & 0 \\ 0.0051 & -0.0051 & 0 & 0 & 0 \\ 0 & 0.0051 & -0.0051 & 0 & 0 \\ 0 & 0 & 0.0051 & -0.0051 & 0 \\ 0 & 0 & 0 & 0 & 0.0051 & -0.0051 \end{bmatrix} [\mathbf{x}] + \begin{bmatrix} 0.0036 \times 10^{-3} \\ 0.0230 \times 10^{-3} \\ 0.0734 \times 10^{-3} \\ 0.1558 \times 10^{-3} \\ 0.2466 \times 10^{-3} \end{bmatrix} [u], \quad (5.66)$$

$$y = \begin{bmatrix} 0 & 0 & 0 & 0 & 1 \end{bmatrix} [\mathbf{x}].$$

where $u = \dot{m}_h$ and $y = T_5$. Applying equation (G.5) to (5.66), the transfer function of the

5.2. Design and implementation of local controllers

linearised model of the TES tank is defined by

$$G_T = \frac{0.0002466s^4 + 5.802e - 06s^3 + 5.214e - 08s^2 + 2.129e - 10s + 3.349e - 13}{s^5 + 0.02539s^4 + 0.0002579s^3 + 1.31 \times 10^{-06}s^2 + 3.325 \times 10^{-09}s + 3.377 \times 10^{-12}}. \quad (5.67)$$

The next step of the design process is to find the equivalent second-order system. Parameters of equation (G.13) are defined as $A_1 = 0.099$, $\zeta = 0.9$, $\omega_n = 0.005$ rad/s. Then, the transfer function of $G_{T,so}$ is given by

$$G_{T,so} = \frac{2.475 \times 10^{-6}}{s^2 + 0.009s + 2.5 \times 10^{-5}}. \quad (5.68)$$

For simplicity, a proportional relation between the pump's speed and volumetric flow generated is assumed. Therefore, the dynamics of the pump are not included in the model of the TES tank. Figure 5.25 shows the open-loop frequency and step time responses of $G_T(s)$ and $G_{T,so}(s)$.

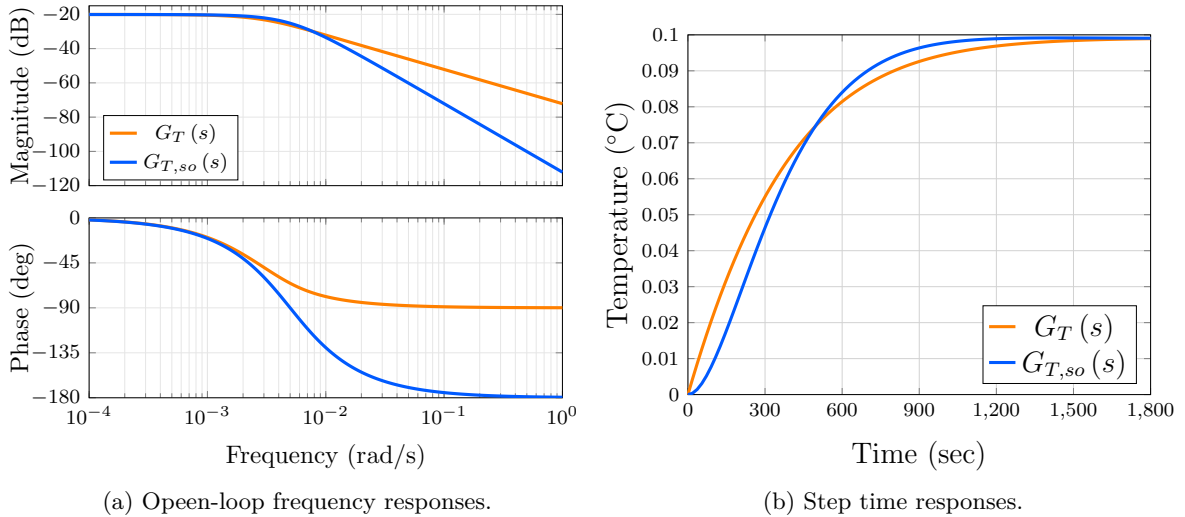


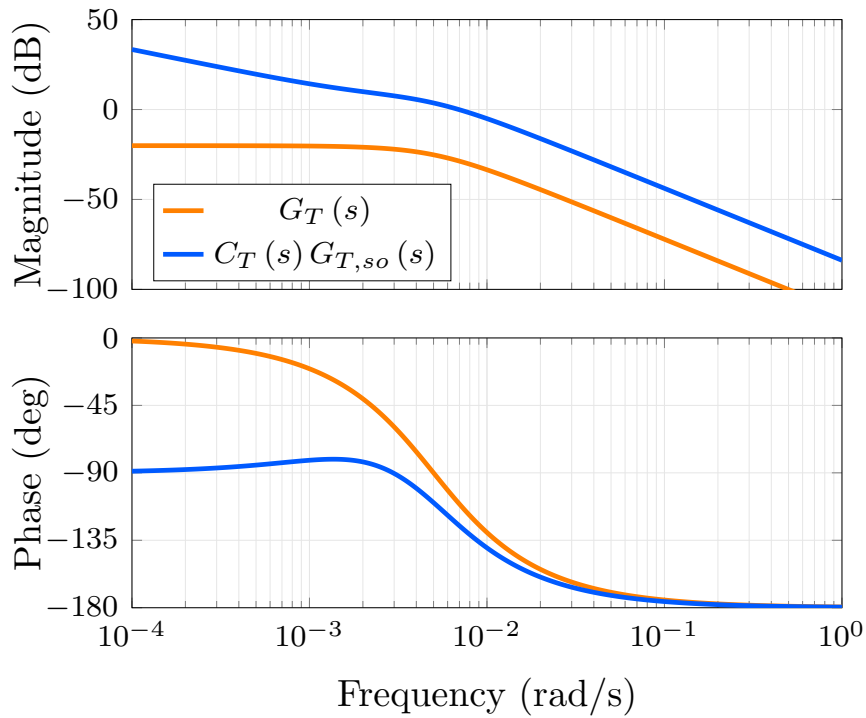
Figure 5.25: (a) Open-loop Bode plots and (b) step time responses of the original and equivalent linear systems.

PI controller design

The temperature of the bottom layer is used as the feedback variable. Thus, a complete charge is guaranteed with all layers reaching the input temperature of the hot water. In this case, a tracking controller is designed instead of a regulating one. The only control design parameter is of a ten times bandwidth of $G_{T,so}$ to achieve a fast response. This way, the system should be capable of following ramp inputs without errors. The following PI controller meets this desired performance

$$C_T = \frac{26s + 0.047}{s}, \quad (5.69)$$

where $k_p = 26$ and $k_i = 0.047$. Figure 5.26 shows the achievement of this design specification.


 Figure 5.26: Bode plots of $G_{T,so}$ and $C_T(s)G_{T,so}(s)$

Controller test

The PI controller performance is assessed in Apros. However, in this case a co-simulation is carried out with MATLAB. The ramp reference signal is generated in MATLAB/Simulink and sent to the PI controller in Apros. Figure 5.27 illustrates the configuration of the co-simulation using OPC communication protocol. The water tank-based TES and its PI controller implementation in Apros are shown in Figure 5.28. A sensor measures the temperature in the last node (layer) of the tank's five nodes. A pump regulates the mass flow rate of the system. The controller shows a good performance, albeit the pump's dynamics are not considered in the model since a proportional relation between the \dot{m}_h and the PI controller output has been assumed.

MATLAB/Simulink



Figure 5.27: Block diagram of the co-simulation between MATLAB/Simulink-Apros.

Two simulations are carried out. A ramp input with a slope of 0.0111 and 0.0056 are used to fill the TES tank in 60 and 120 minutes, respectively. For both cases, the initial conditions of the TES tank is a complete discharge condition at 50°C in all layers. Figure 5.29a shows the closed-loop system's response for the first ramp input. As it can be observed,

5.2. Design and implementation of local controllers

the temperature in the bottom layer is achieved approximately 60 minutes after the beginning of the ramp, which occurs at 10 minutes. It is important to notice that once the TES is full, the PI controller's action is disabled by reducing the ramp to the value of the initial conditions. Thus, the TES tank is ready to provide heating. Figure 5.29b shows the behaviour of the internal energy during the charging process. Individual and total energy are computed using equations (4.95) and (4.96), respectively. These are shown in Figure 5.29b.

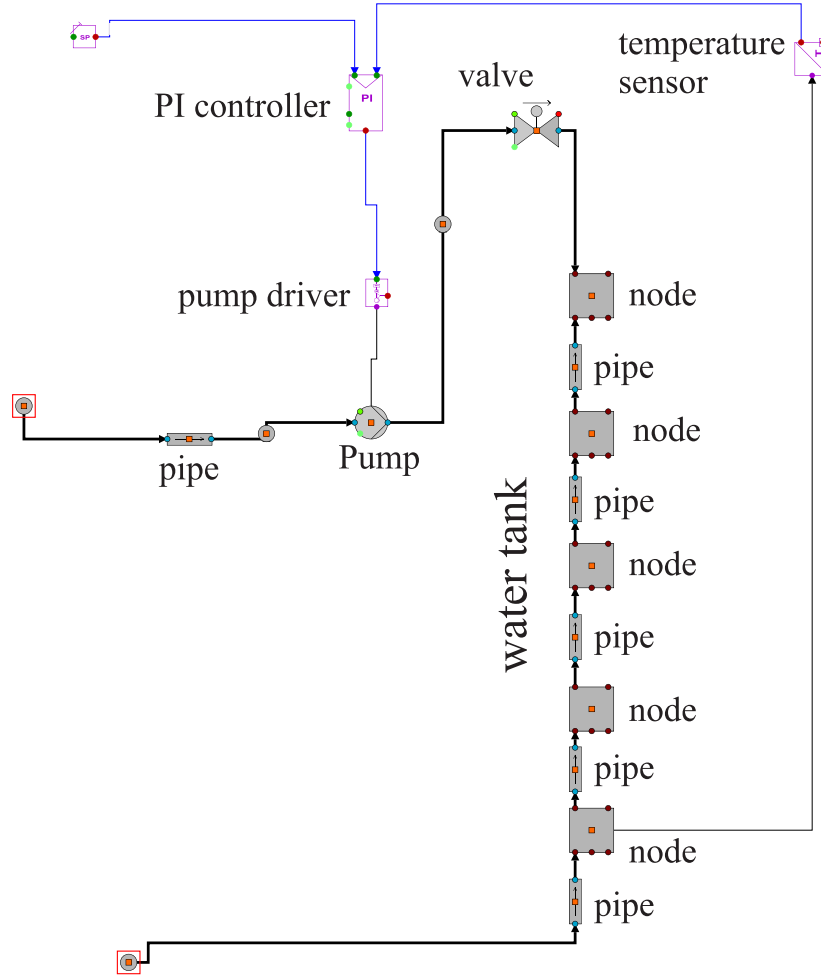


Figure 5.28: Charging control of sensible TES implemented in Apros.

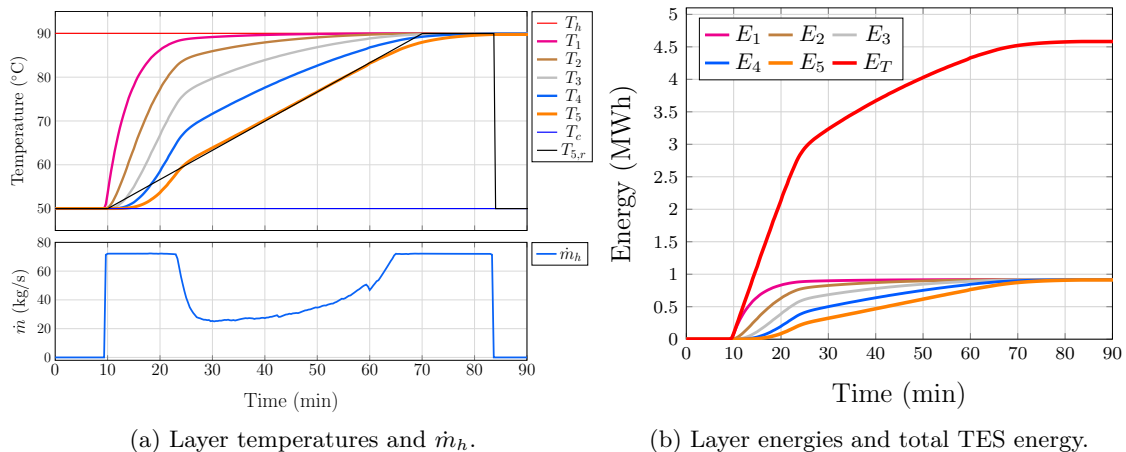


Figure 5.29: Simulation results of the charging control process of TES in 60 minutes.

A second assessment of the PI controller is carried out by simulating a slower charging process of two hours, shown in Figure 5.30. As it can be observed, the PI controller meets the desired performance successfully. It is important to notice that the control of the charging process aims to track the reference until the TES tank is full. Therefore, no regulation is expected after the reference is achieved. Thus, the TES is discharged according to the heat demands. Due to these conditions of TES tank operation, no disturbances and regulation tests are carried out.

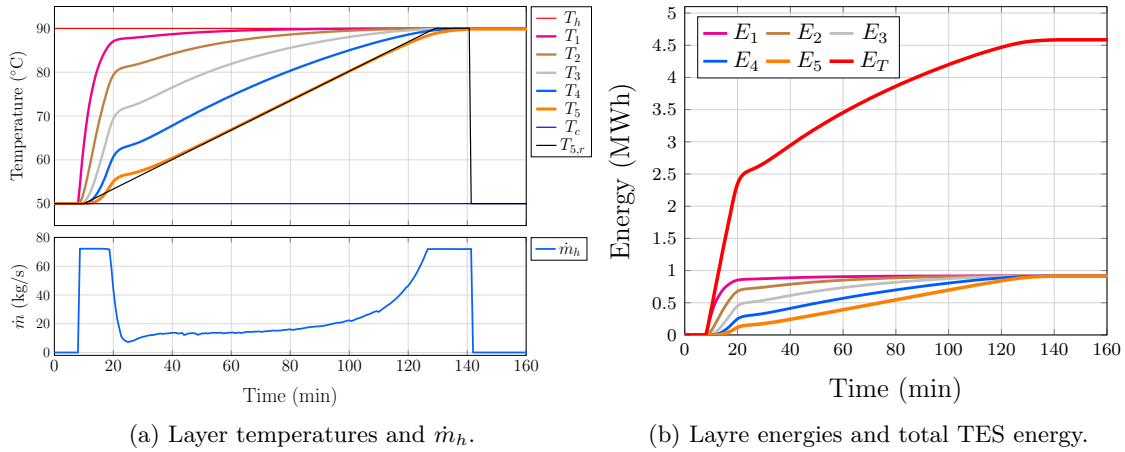


Figure 5.30: Simulation results of the charging control process of TES in 120 minutes.

5.2.5 Single house temperature controller

Usually, the indoor temperature of buildings is controlled by different types of heating/cooling systems. For instance, HVAC or radiators are implemented to keep the internal temperature within comfortable ranges. In this section, a PI controller is designed for a heating system of a single house. Figure 5.31 shows the block diagram of the temperature feedback control for the internal temperature of a house.

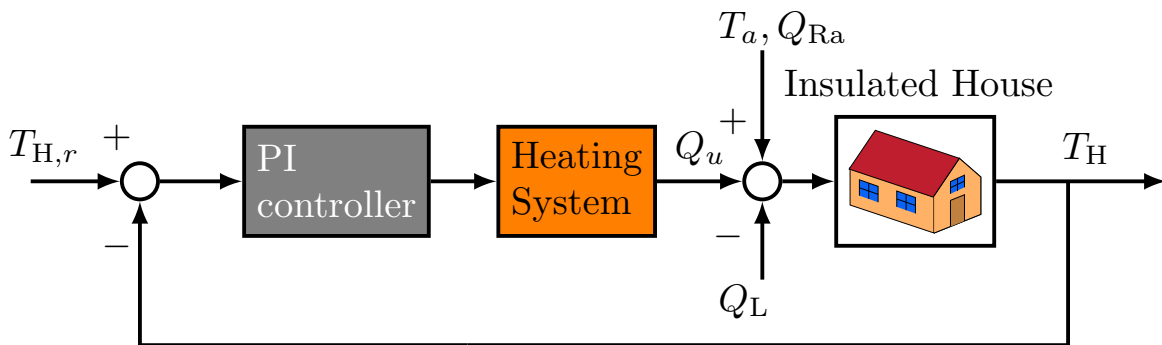


Figure 5.31: Block diagram for a temperature closed-loop system for a single house.

The dynamic thermal model of an insulated house defined by equations (4.122)-(4.127) is used to obtain a PI controller capable of keeping a temperature reference during winter days. The first step of the control design process is to define the state variables of the system. The temperature of each component of the single house is defined as a state variable: $T_{WI} = x_1$, $T_W = x_2$, $T_{ws} = x_3$, $T_R = x_4$, $T_{RI} = x_5$ and $T_H = x_6$. Thus, the system equations (4.122)-(4.127) are rewritten as

$$C_{WI}\dot{x}_1 = [(T_a - x_1)/R_{I,1}] + [(x_2 - x_1)/R_{I,2}], \quad (5.70)$$

$$C_W\dot{x}_2 = [(x_1 - x_2)/R_{I,2}] + [(x_6 - x_2)/R_{I,3}], \quad (5.71)$$

$$C_{ws}\dot{x}_3 = [(T_a - x_3)/R_{I,4}] + [(x_6 - x_3)/R_{I,5}], \quad (5.72)$$

$$C_R\dot{x}_4 = [(T_a - x_4)/R_{I,6}] + [(x_5 - x_4)/R_{I,7}], \quad (5.73)$$

$$C_{RI}\dot{x}_5 = [(x_4 - x_5)/R_{I,7}] + [(x_6 - x_5)/R_{I,8}], \quad (5.74)$$

$$C_H\dot{x}_6 = [(x_2 - x_6)/R_{I,3}] + [(x_3 - x_6)/R_{I,5}] + [(x_5 - x_6)/R_{I,8}] + Q_R - Q_L + Q_u, \quad (5.75)$$

Equations (5.70)-(5.75) are re-arranged and a further renaming of the equivalent resistance is implemented as

$$\begin{aligned} a_1 &= 1/R_{I,1}, & a_2 &= 1/R_{I,2}, & a_3 &= 1/R_{I,3}, & a_4 &= 1/R_{I,4}, \\ a_5 &= 1/R_{I,5}, & a_6 &= 1/R_{I,6}, & a_7 &= 1/R_{I,7}, & a_8 &= 1/R_{I,8}. \end{aligned} \quad (5.76)$$

The thermal model of the insulated house represented in the state-space form is given as

$$\begin{aligned} \dot{\mathbf{x}} &= \mathbf{A}_H \mathbf{x} + \begin{bmatrix} 0 \\ 0 \\ 0 \\ 0 \\ 0 \\ 1/C_H \end{bmatrix} [u] + \begin{bmatrix} a_1/C_{WI} \\ 0 \\ a_4/C_{ws} \\ a_6/C_R \\ 0 \\ 0 \end{bmatrix} T_a + \begin{bmatrix} 0 \\ 0 \\ 0 \\ 0 \\ 0 \\ (Q_{Ra} - Q_L)/C_H \end{bmatrix}, \\ y &= \begin{bmatrix} 0 & 0 & 0 & 0 & 0 & 1 \end{bmatrix} [\mathbf{x}]. \end{aligned} \quad (5.77)$$

where \mathbf{A}_H is defined by equation (5.78) and the system input is the heat supplied exclusively by the heating system ($u = Q_u$). Therefore, T_a , Q_{Ra} and Q_L are included in the model as disturbances. The system output is the temperature of the house interior (x_6).

$$\mathbf{A}_H = \begin{bmatrix} -\frac{a_1}{C_{WI}} - \frac{a_2}{C_{WI}} & \frac{a_2}{C_{WI}} & 0 & 0 & 0 & 0 \\ \frac{a_2}{C_W} & -\frac{a_2}{C_W} - \frac{a_3}{C_W} & 0 & 0 & 0 & \frac{a_3}{C_W} \\ 0 & 0 & -\frac{a_4}{C_{ws}} - \frac{a_5}{C_{ws}} & 0 & 0 & \frac{a_5}{C_{ws}} \\ 0 & 0 & 0 & -\frac{a_6}{C_R} - \frac{a_7}{C_R} & \frac{a_7}{C_R} & 0 \\ 0 & 0 & 0 & \frac{a_7}{C_{RI}} & -\frac{a_7}{C_{RI}} - \frac{a_8}{C_{RI}} & \frac{a_8}{C_{RI}} \\ 0 & \frac{a_3}{C_H} & \frac{a_5}{C_H} & 0 & \frac{a_8}{C_H} & -\frac{a_3}{C_H} - \frac{a_5}{C_H} - \frac{a_8}{C_H} \end{bmatrix} \quad (5.78)$$

As it can be observed, the effect of T_a is considered as a disturbance. This makes sense as the only variable in the house model that can be regulated and then used as an input is the heating system's output. Moreover, under this consideration, the system defined by (5.77)

and (5.78) may be linear for all ambient conditions. This implies that a linearisation method is not required because the value of T_a is not included in the control design process. Thus, the state space representation of the insulated house model without disturbances is defined by

$$\begin{aligned}\dot{\mathbf{x}} &= \mathbf{A}_H \mathbf{x} + \mathbf{B}u \\ y &= \begin{bmatrix} 0 & 0 & 0 & 0 & 0 & 1 \end{bmatrix} [\mathbf{x}]\end{aligned}\quad (5.79)$$

All resistances defined by equations (5.76) are computed within a range of the ambient temperature between -10°C to 30°C . Table 5.5 shows the values of the thermophysical properties of the air required for this computation.

Table 5.5: Air hydraulic conditions and thermophysical properties.[5]

Variable	Min Value	Max Value	Unit
External wind speed	3.65	5.7	m/s
Internal wind speed	0.1	0.2	m/s
Kinematic viscosity	2.43×10^{-6}	15.98×10^{-6}	m^2/s
Prandtl number	0.720	0.721	-
Thermal conductivity	0.020	0.028	W/mK

Applying equation (G.5) to all possible combination of the values given by the calculation of (5.76), a set of transfer functions is obtained. These are defined in terms of coefficients with a range of values provided in Table 5.6.

$$G_H(s) = \frac{a_1 s^5 + a_2 s^4 + a_3 s^3 + a_4 s^2 + a_5 s + a_6}{s^6 + b_1 s^5 + b_2 s^4 + b_3 s^3 + b_4 s^2 + b_5 s + b_6}, \quad (5.80)$$

Table 5.6: Coefficient values of transfer function set of insulated house model.

Coefficient	Value	Coefficient	Value
a_1	5.075×10^7	a_2	$[3.979 \times 10^{-10} \quad 5.431 \times 10^{-10}]$
a_3	$[9.298 \times 10^{-14} \quad 1.666 \times 10^{-13}]$	a_4	$[5.9 \times 10^{-18} \quad 1.34 \times 10^{-17}]$
a_5	$[1.47 \times 10^{-22} \quad 3.318 \times 10^{-22}]$	a_6	$[2.12 \times 10^{-28} \quad 9.092 \times 10^{-28}]$
b_1	$[8.566 \times 10^{-4} \quad 0.0012]$	b_2	$[2.374 \times 10^{-7} \quad 4.62 \times 10^{-7}]$
b_3	$[2.37 \times 10^{-11} \quad 6.466 \times 10^{-11}]$	b_4	$[9.664 \times 10^{-16} \quad 3.595 \times 10^{-15}]$
b_5	$[1.413 \times 10^{-20} \quad 7.089 \times 10^{-20}]$	b_6	$[1.832 \times 10^{-26} \quad 1.118 \times 10^{-25}]$

The closed-loop system shown in Figure 5.31 includes a heating system that can regulate the heat injection to the house. It could be an air conditioner or a radiator. The modelling of such an actuator is out of the scope of this research. Instead, a transfer function of a HVAC is used [6]:

$$G_u(s) = \frac{T_{hs} m_a c_p}{0.5s + 1}, \quad (5.81)$$

where T_{hs} is the heater temperature, m_a is the mass flow rate and c_p the specific heat of the

5.2. Design and implementation of local controllers

air. For the control design process, these values are assumed constant as $T_{hs} = 50^\circ \text{C}$, $m_a = 1 \text{ kg/s}$ and $c_p = 1005.4 \text{ J/kgK}$. The complete system, including the heating system, is defined by

$$G_{u,H}(s) = G_u(s) G_H(s). \quad (5.82)$$

The equivalent second-order system of $G_{u,H}$ is obtained by defining the following parameters of equation (G.13): $A_1 = 600$, $\zeta = 10$ and $\omega_n = 1 \times 10^{-4}$ as

$$G_{u,H,so}(s) = \frac{0.0006}{s^2 + 0.02s + 1 \times 10^{-6}}. \quad (5.83)$$

Figure 5.32 shows the frequency responses of $G_{u,H}$ and $G_{u,H,so}$.

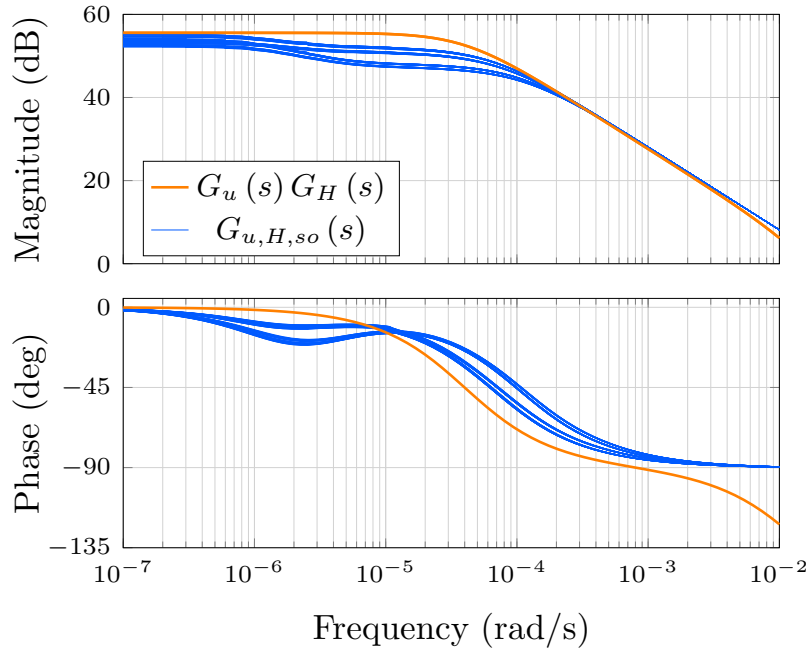


Figure 5.32: Open-loop Bode diagrams of the set of transfer function of the house model and their equivalent second-order system.

PI controller design

The desired closed-loop performance requirements are defined in the time domain as a settling time of 1500 s and a maximum overshoot of 1%. In the frequency domain these are defined by a damping ratio of $\zeta = 0.8261$, a phase margin of at least $\phi_m = 70.9^\circ$ and a minimum bandwidth of $\omega_{bw} = 0.0027 \text{ rad/s}$. These specifications are met with the PI controller defined by

$$C_h(s) = \frac{0.0765s + 3.0604 \times 10^{-6}}{s}, \quad (5.84)$$

where $k_p = 0.0765$ and $k_i = 3.0604 \times 10^{-6}$.

The open loop frequency responses of $G_{u,H,so}(s)$ and $C_h(s)G_{u,H,so}(s)$ are shown in Figure 5.33a. A ϕ_m much larger than 70.9° is obtaining, which means no overshoot is present. A bandwidth $\omega_{bw} = 0.00257 \text{ rad/s}$, which is achieved, and the settling time in the closed-loop step response is met: $t_s = 1500$ seconds or 25 mins (see Figure 5.33b). Even though there is a slight steady-state error about 3% when the PI controller is assessed over the transfer

function set, it shows a successful performance under disturbances, as shown in next section.

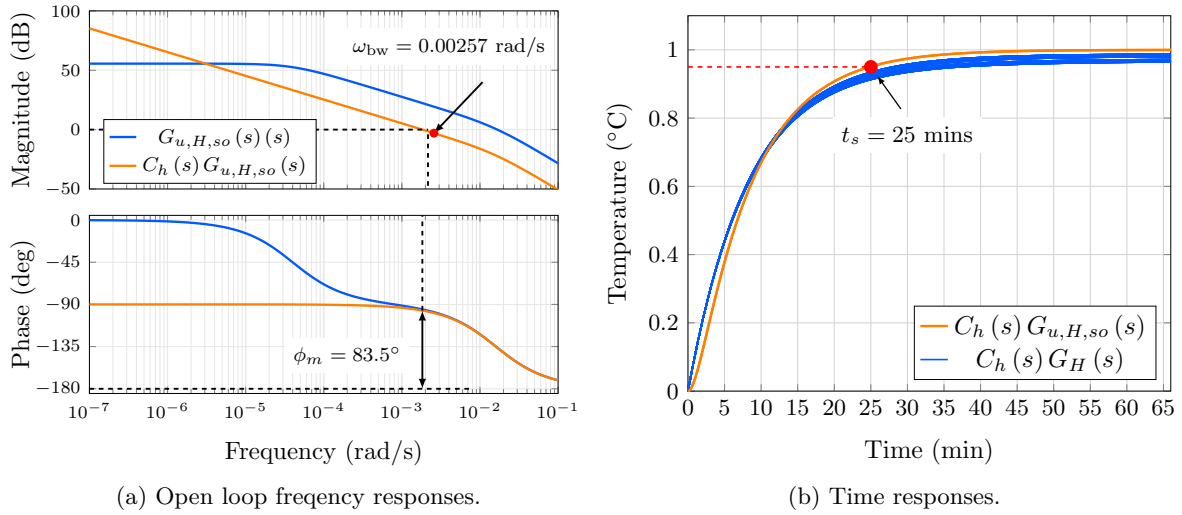


Figure 5.33: (a) Open-loop Bode plots of the equivalent second-order system and the loop-shaped obtained with $C_h(s)$. (b) Time step response of the closed-loop system with $G_{u,H,so}(s)$ and the set of transfer functions $G_H(s)$.

Controller verification

The closed-loop system shown in Figure 5.31 is simulated in MATLAB/Simulink using the designed PI controller. A simulation with a convectional on/off controller is also carried out to compare both performances. Disturbances are applied to the house. Firstly, the heat contribution of the solar radiation regards the position of the windows with respect to the North is considered and this is defined by [7]

$$Q_{RA} = \alpha_s A_{ws} I_s, \quad (5.85)$$

where I_s is the solar flux incidence to the windows area A_{ws} and α_s is the solar absorptivity of the windows frame.

The value of I_s determines the amount of radiation supplied. In order to consider the worst disturbance to the system, all windows are considered to receive the maximum value of I_s . The value of α_s is established as 0.2 [7], the daily profile of I_s is obtained from [8] and is shown in Figure 5.34a. Disturbances due to appliances, house occupants and heat losses are also included. A maximum value of wind speed (5.7 m/s) is used to have more challenging conditions for the control system. The temperature reference is set up to 22°C during the whole day. The performances of PI and on/off controllers are shown in Figure 5.34b

As it can be observed, the PI controller's interior temperature clearly has a better regulation than the on/off controller. Moreover, the system consumes 17.93 kWh when the PI controller is used and 19.36 kWh with the on/off controller. An energy saving of 7.9% is achieved when a PI controller is implemented.

The main drawback of the proposed control scheme is having a regulated output of the heating system that may be modified by the PI controller, unlike convectional heating actuators with only two states (on and off), which makes these devices unsuitable for PI controller regulation.

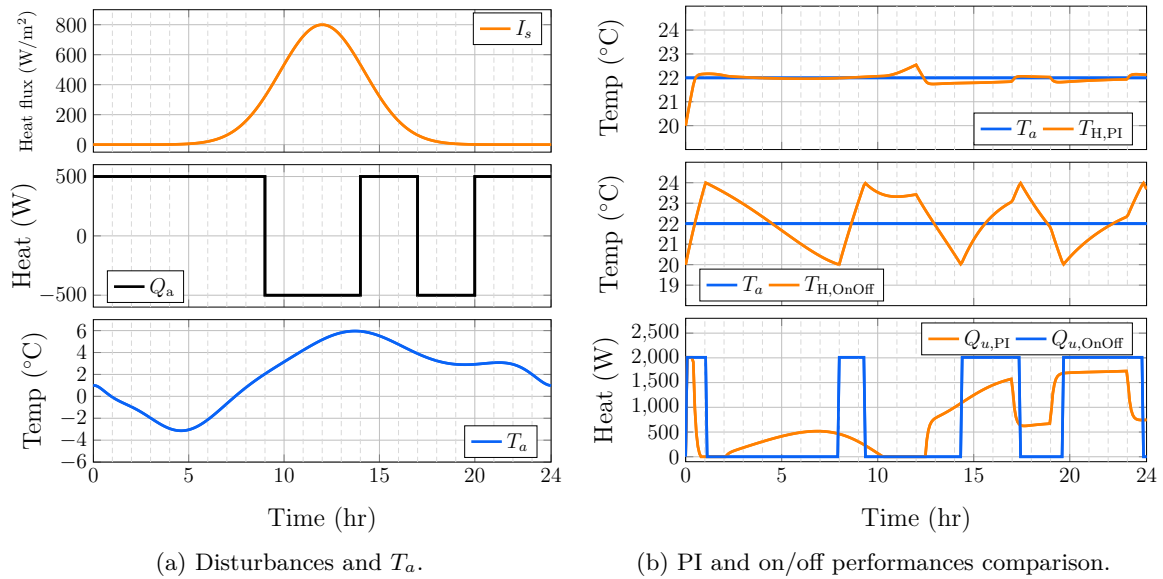


Figure 5.34: Simulation result of closed-loop insulated house system.

5.3 Summary

PI controllers for a pipe network, heat exchangers, sensible TES and a single insulated house were designed and tested. The control design process was described using a non-linear system as an example. A sequence of steps were proposed to guide the control design process. The Bode diagram was employed to carry out a loop-shaping method to define the controller's proportional and integral gains. Transfer functions of the non-linear systems are obtained by implementing a linearisation method. Then, an equivalent second-order system is used for the PI controller tuning method. The closed-loop system's desired performance is defined in the time-domain according to the system's capabilities. The desired parameters were translated to the frequency domain for the loop-shaping of the closed-loop system response.

The differential pressure controller of a pipe network, the temperature controllers for flat plate and shell-and-tube heat exchangers were directly implemented in Apros. For the charging process control system, a co-simulation between MATLAB and Apros platforms was carried out. Finally, the interior temperature control of the house was implemented in MATLAB/Simulink. The performance of all designed PI controllers was assessed under different operating conditions and disturbances with successful results.

5.4 References

- [1] S. Frederiksen and S. Werner, *District Heating and Cooling*. Studentlitteratur AB, 2013. Google-Books-ID: vH5zngEACAAJ.
- [2] S. Buffa, M. H. Fouladfar, G. Franchini, I. Lozano Gabarre, and M. Andrés Chicote, "Advanced Control and Fault Detection Strategies for District Heating and Cooling Systems—A Review," *Applied Sciences*, vol. 11, p. 455, Jan. 2021. Number: 1 Publisher: Multidisciplinary Digital Publishing Institute.
- [3] K. Ogata, *Modern Control Engineering*. Boston: Prentice Hall, 2009.

- [4] C. H. Houpis, S. N. Sheldon, and J. J. D'Azzo, *Linear Control System Analysis and Design: Fifth Edition, Revised and Expanded*. New York: CRC Press, 5th edition ed., Aug. 2003.
- [5] "Dry air properties." https://www.engineeringtoolbox.com/dry-air-properties-d_973.html. Accessed: 2018-04-18.
- [6] "Thermal Model of a House - MATLAB & Simulink - MathWorks United Kingdom." <https://uk.mathworks.com/help/simulink/slref/thermal-model-of-a-house.html;jsessionid=bd0160f5fb6cb0d1dab8790fd9e3>.
- [7] J. Wright and A. G. McGowan, "Calculating the Solar Heat Gain of Window Frames," 1999.
- [8] M. Van Belleghem, M. Steeman, A. Janssens, and M. De Paepe, "Heat, air and moisture transport modelling in ventilated cavity walls," *Journal of Building Physics*, vol. 38, pp. 317-349, Jan. 2015. Publisher: SAGE Publications Ltd STM.

Case studies of district heating and cooling systems

6.1 Introduction

Dynamic models and local controllers for elements within a DHCS have been developed in Chapters 4 and 5, respectively. On the one hand, mathematical models were verified against commercial software or experimental data. On the other hand, the designed controllers based on the developed mathematical models were assessed to demonstrate their effectiveness. Nevertheless, the interaction between the DHCS's elements may exhibit operating conditions not presented when elements are analysed independently. Two fictional case studies are presented in this chapter. Although they are not based on any practical system, they may resemble the basic configuration of a district heating system (DHS) and a cooling energy centre. Firstly, the capabilities of the local controllers are assessed under typical operating conditions of a DHS. The controllers should guarantee a suitable hydraulic performance while heat demands are met. Secondly, a cooling energy centre that includes latent TES tanks is analysed using a co-simulation between MATLAB/Simulink and Apros.

The test systems under study are relatively simple, yet realistic. For instance, the DHS is comprised of one energy centre, which includes sensible TES and eight substations. The study of larger and more complex configurations may include several additional elements similar to those already included. Therefore, a reduced DHS with the elements modelled in Chapter 4 is better placed for carrying out detailed analysis than a DHS with several elements that might require a huge number of variables due to repeated elements. However, the analysis presented throughout this chapter can be applied to a larger and more complex DHS. Regarding the second case study, the energy centre is comprised of a chiller system and latent TES tank, which provides cold water to the consumer through a heat exchanger.

The simulations are carried out using MATLAB/Simulink and Apros platforms. Apros' libraries encompass the dynamic model of most of the DHCS's elements. However, models of PCMs required for latent TES tank are not available. Thus, it is necessary to generate this model in MATLAB/Simulink according to Section 4.5.1 and then link it to Apros using the OPC communication protocol. Regarding the PI controllers, they are designed locally for each component considering the test system's parameters. The set points for the closed-loop references are proposed according to the operating points established for the daily operation

of the DHCS.

The two main aims of this chapter are to analyse the local controllers' response under different operating conditions and to assess how the interaction with other elements might affect their performance. For instance, the increment of heat demand implies an increment of the fluid's mass flow rate in the pipe network, which in turn means a variation of the differential pressure of the system. These types of changes represent challenging conditions for the proposed feedback control schemes. The thermal and hydraulic behaviours of the DHS are assessed by regulating the temperature in all substations and the differential pressure only in the farthest substation. Co-simulation between MATLAB/Simulink and Apros of a cooling energy centre is used to demonstrate the applications of the developed 1-D dynamic model of latent TES tanks for the analysis of district cooling systems.

6.2 Case study 1

This section presents the performance assessment of the temperature and differential pressure controllers in a DHS. The controllers are designed following the design process presented in Appendix G and implemented in Apros. The complete DHS is built in this platform using the device elements included in its libraries. For the analysis of the temperature controller, different heat demand profiles are used for each substation. A temperature reference is established to be followed by the controller at 50°C. On the other hand, a set point of 0.5 bar is defined for the differential pressure controller in the farthest substation. Thermal and hydraulic conditions of the DHS are analysed through simulations.

6.2.1 Description

In order to assess the performance of local controllers of a DHS during real operating conditions, the configuration of the system shown in Figure 6.1 is used. It consists of an energy centre that includes energy technologies and a sensible TES tank, a pipe network and eight substations (S_x) that manage the consumer's heat supply. The maximum heat consumed by each substation is about 0.8 MW. Therefore, the maximum heat supplied by the energy centre is 6.4 MW. The energy technologies might include CHP units or gas boilers able to provide this heat. It is important to notice that these device models are out of the scope of this research. Therefore, constant hot water generated at 90°C is assumed for the heat produced in the energy centre.

Energy centre

As discussed, the energy centre of the DHS is comprised of energy sources and a water tank-based TES. The hydraulic integration between the energy centre's components and the pipe network is achieved with a hydraulic header, as shown in Figure 6.2. The water's mass flow rate of each component's loop is circulated through the header. Thus, the energy technologies' hot water can be distributed either to the pipe network or to the TES. This distribution is governed by the pressure generated for each loop and an arrangement of control valves. The header allows having different loops connected with no need for loop's synchronisation. For instance, the hot water from the energy technologies flowing to the header may be re-circulating through its loop until a larger head from another loop is presented to take out the hot water.

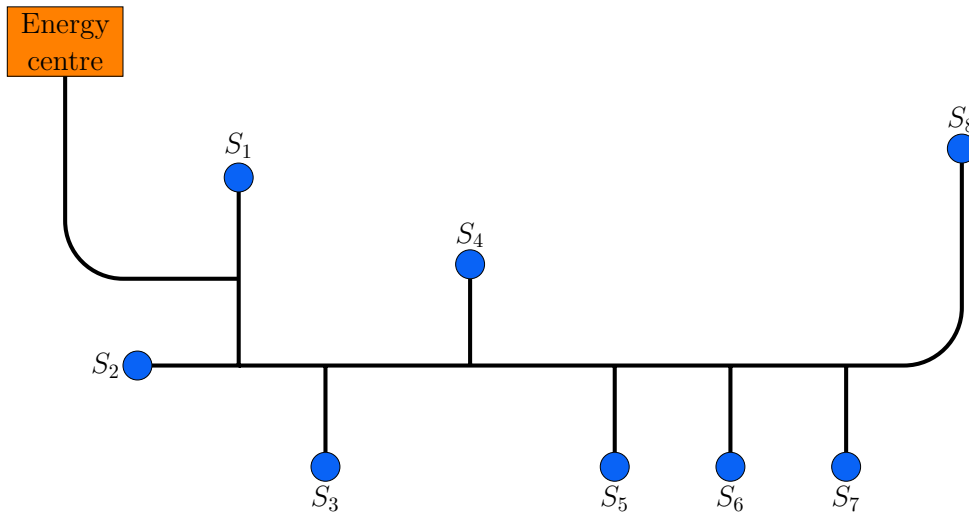


Figure 6.1: Schematic diagram of the district heating pipe networks of the case study.

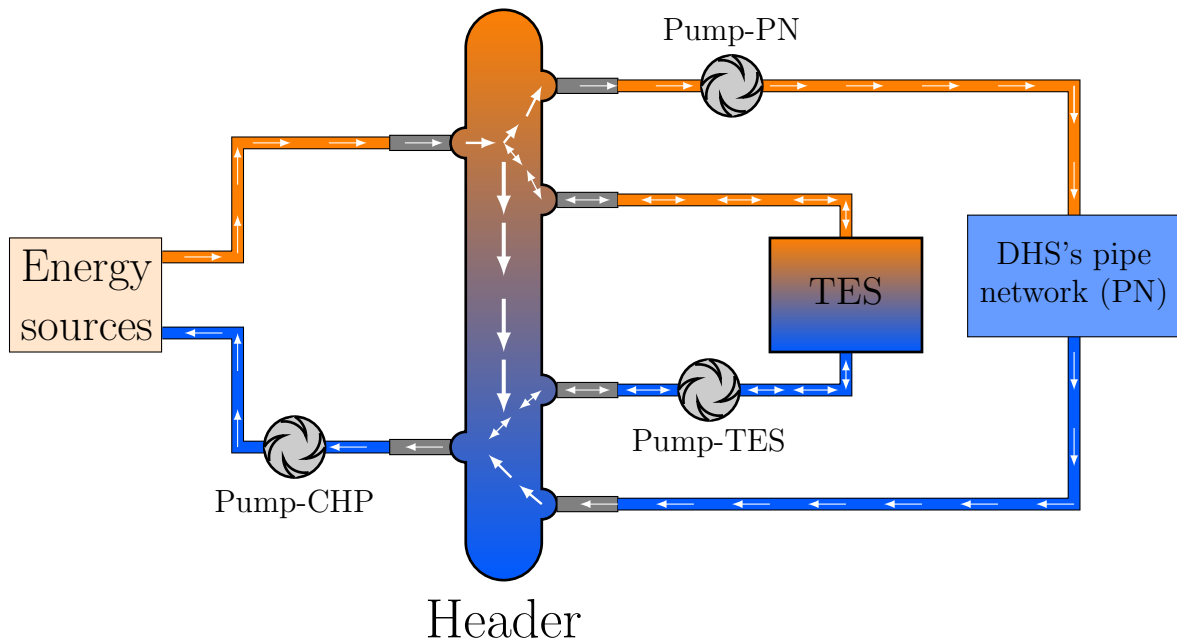


Figure 6.2: Schematic diagram of the hydraulic connections of the DHS to the header.

Thermal energy storage tank

A well-insulated large water tank is used to store/supply heat. The volumetric capacity of the tank is 100,000 L (100 m^3). A bidirectional pump and an arrangement of control valves is used to fill or empty the tank as is explained in section 4.4.1. Figure 6.3 shows the connection of the TES's loop to the header. Control valves 1 and 2 are opened when the TES tank is either charging or discharging. The bidirectional pump's setup is established according to operating point (*i.e.*, upward direction for charging and downward direction for discharging). Five sensors are located through the tank's height to measure the temperature and then estimate the tank's current energy, as described in Section 6.3. The parameters of the water tank and of the pump and valves in the loop are given in Tables 6.1 and 6.2, respectively.

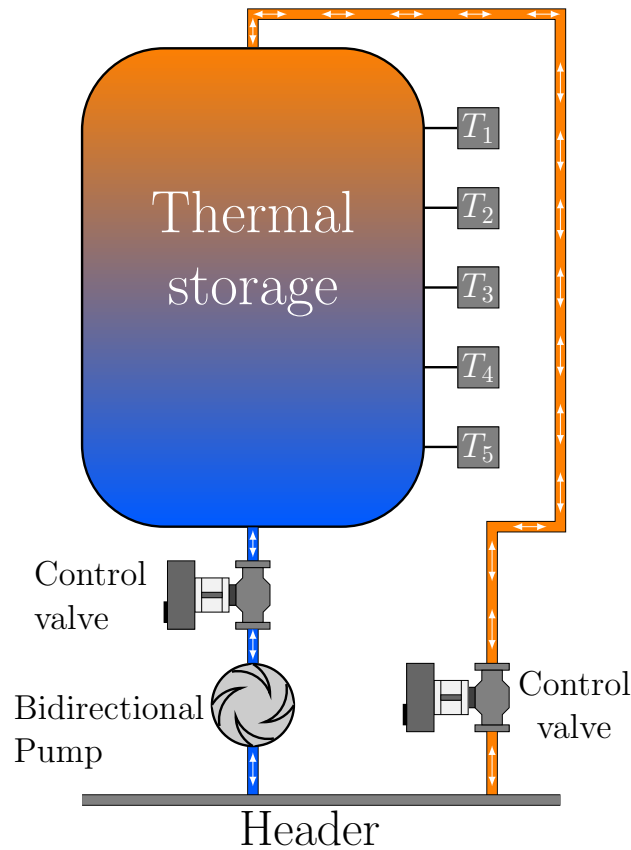


Figure 6.3: Schematic diagram of the water tank-based TES.

Table 6.1: Water tank parameters.

Variable	Value	Units
Radius r	1.8	m
Height h	10	m
Volumetric capacity V_T	101.78	m ³
Cross sectional area A	10.1788	m ²
Total lateral area $A_{tr,T}$	113.0973	m ²

Pipe network

The pipe network is comprised of two pumps, an arrangement of pipes and valves. The characteristics of the pumps and the valves are the same used in the thermal energy storage tank (see Table 6.2). Figure 6.1 shows the pipe network, which is broken down into single pipes as in Figure 6.4 to specify suitable identifying labels. A looped network implies two pipes for each branch. Label k is included to name each pipe and subscripts 's' and 'r' stand for supply pipe and return pipe, respectively. All pipes are insulated and located 1 meter below the ground. Neither bends in pipes nor elevations are considered for simplicity. This implies all pipes are straight. The insulator characteristics and the pipe's parameters, such as internal and external diameters, length and relative roughness are given in Table 6.3. The thermal loss model is beyond the scope of this research work. Therefore, the heat losses due to the ambient temperature are monitored using temperature sensors at each substation's inlet.

6.2. Case study 1

Table 6.2: Points of flow-head curve of pump and position-flow coefficient curve of valve.

Pump			Valve			
Q_v (m ³ /h)	Q_v (m ³ /s)	h (m)	o_v (°)	C_v	o_v (%)	K_v
0	0	70.6820	10	4.4	0.1111	3.8064
25	0.0069	70.6022	20	17.1	0.2222	14.7932
50	0.0139	69.1369	30	45.6	0.3333	39.4486
75	0.0208	66.2861	40	84.2	0.4444	72.8414
100	0.0278	62.0498	50	139.2	0.5556	120.4219
125	0.0347	56.4279	60	258.6	0.6667	223.7149
150	0.0417	49.4205	70	422.4	0.7778	365.4182
175	0.0486	41.0276	80	709	0.8889	613.3559
200	0.0556	31.2491	90	845.9	1	731.7881

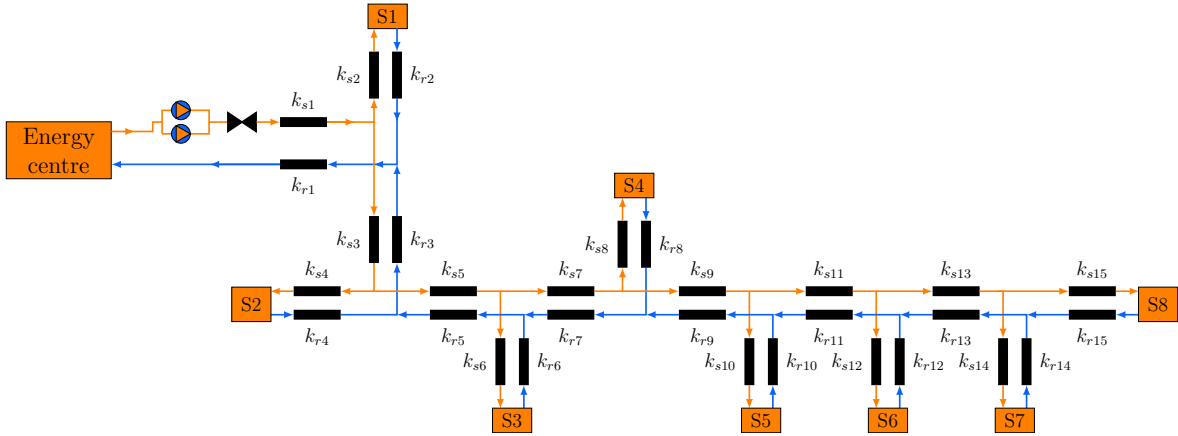


Figure 6.4: Schematic of the pipe network.

The hydraulic conditions of the system are monitored by differential pressure sensors located in each substation. Particularly, the measurement of the differential pressure in substation eight ($S8$) is used for the differential pressure control scheme that regulates the pump's speed to deal with the variations of differential pressure in $S8$.

Substation

The configuration of each substation is depicted in Figure 6.5. The heat exchanger for each substation is the commercial model S450+ manufactured by HRS[®] [1], with parameters shown in Table 6.4. As described in Section 5.2.3, the hot water's mass flow rate \dot{m}_h supplies the heat produced by the energy centre. The heat is transferred to the secondary circuit to increase its temperature to provide hot water to the consumer heating devices or water taps. Different thermal loads, such as building radiators or air conditioning systems, may be included after the substation. However, these model devices are beyond the scope of this work. Instead, a profile of each substation's heat demand is used. This is shown in Figure 6.5.

Table 6.3: Pipe parameters.

Pipe label	Length [m]	D_i [m]	D_o [m]	ε/D_i
k_{s1}, k_{r1}	1000	0.148	0.168	1×10^{-7}
k_{s2}, k_{r2}	400	0.148	0.168	1×10^{-6}
k_{s3}, k_{r3}	200	0.148	0.168	1×10^{-7}
k_{s4}, k_{r4}	500	0.148	0.168	1×10^{-6}
k_{s5}, k_{r5}	300	0.148	0.168	1×10^{-7}
k_{s6}, k_{r6}	100	0.148	0.168	1×10^{-6}
k_{s7}, k_{r7}	400	0.148	0.168	1×10^{-7}
k_{s8}, k_{r8}	400	0.148	0.168	1×10^{-6}
k_{s9}, k_{r9}	300	0.148	0.168	1×10^{-7}
k_{s10}, k_{r10}	150	0.148	0.168	1×10^{-6}
k_{s11}, k_{r11}	300	0.148	0.168	1×10^{-7}
k_{s12}, k_{r12}	300	0.148	0.168	1×10^{-6}
k_{s13}, k_{r13}	300	0.148	0.168	1×10^{-7}
k_{s14}, k_{r14}	400	0.148	0.168	1×10^{-6}
k_{s15}, k_{r15}	1000	0.148	0.168	1×10^{-7}

Note: D_i is the internal diameter of the pipe, D_o is the external diameter of the insulation layer, ε/D_i is the relative roughness of the pipe. The thermal conductivity of the the insulator is $k_{\text{ins}} = 0.027$ W/mK.

Regarding the substation's hydraulic conditions, hot mass flow rate of water is produced by the head of the centrifugal pump in the pipe network. The differential pressure Δp in the substation is regulated through the pump's speed variations. This amount of hot mass flow rate is critical to meet the heat demands. A differential pressure feedback controller modifies the pump's speed to keep the differential pressure constant and thus, sufficient heat is supplied to the substation. The hydraulic conditions of the secondary circuit depend on the devices connected to the substations, which are not included in this analysis. Therefore, the secondary circuit's mass flow rate (\dot{m}_c) is assumed constant and only variations of $T_{c,\text{in}}$ are considered.

6.2.2 PI controllers

Three controllers are assessed:

- Temperature control of substations,
- Differential pressure control in substation eight (S8), and
- Charging process of sensible TES tank.

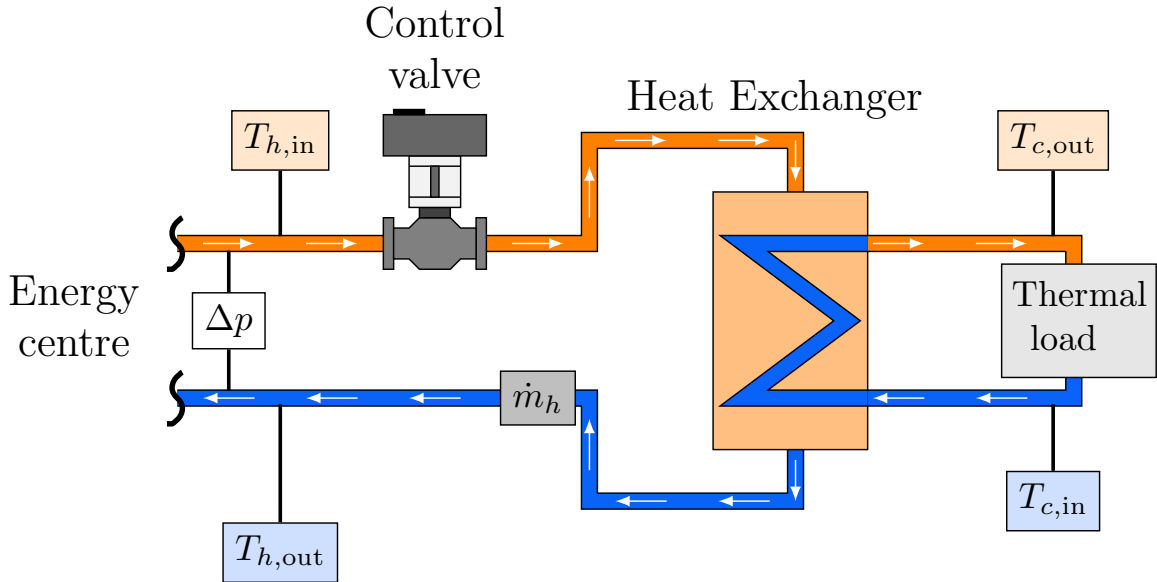


Figure 6.5: Schematic of substation.

Table 6.4: Flat plate heat exchanger parameters of S450+ model [1].

Variable	Value	Units
gap g	3.1	mm
length plate l	1.1	m
Width plate W	0.53	m
Number of plates N_p	108	-
Cold volumetric capacity V_c	0.0976	m ³
Hot volumetric capacity V_h	0.0976	m ³
Transfer area A_{tf}	125.3	m ²
Hydraulic diameter D_h	6.2	mm
Cross sectional area A_c	0.0887	m ²
Plate thickness w_p	1	mm
Plate thermal conductivity k_p	16	W/m K

Substation's temperature control

The temperature control scheme is based on the control diagram described in Figure 5.10. For clarity, this scheme is included in Figure 6.5 and shown in Figure 6.6. The design process of the PI controller for temperature is presented in Appendix H. The obtained controller is given as

$$C_{T,s}(s) = \frac{0.0066s + 0.00057}{s}, \quad (6.1)$$

where $k_p = 0.0085$ and $k_i = 0.00069$. The temperature reference is set as 50°C. Thus, hot water is guaranteed to achieve the heat demands of the consumers.

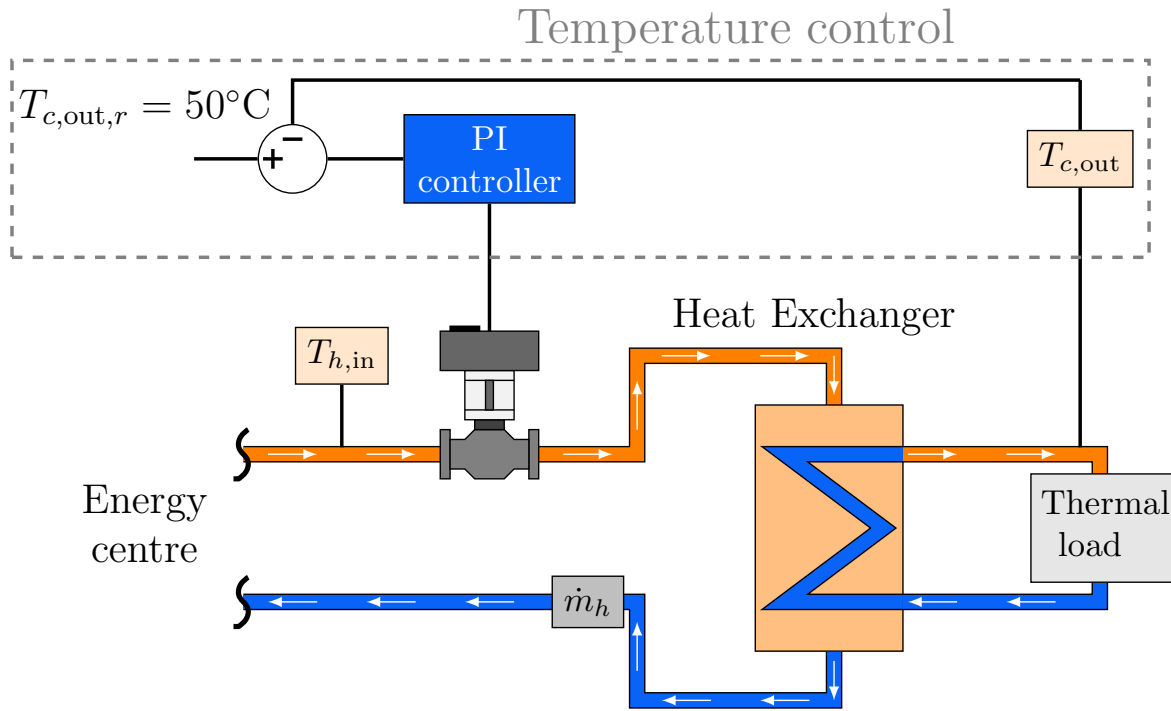
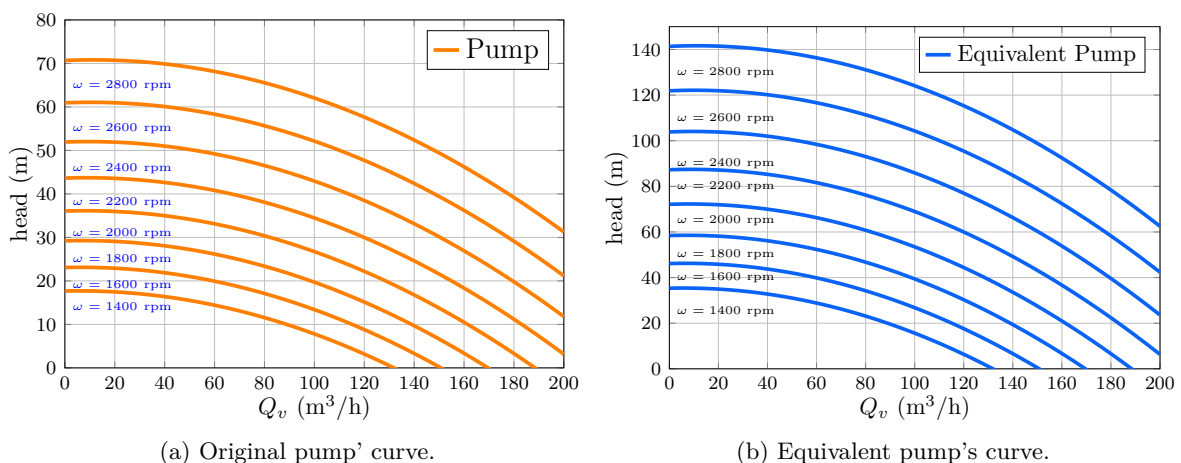


Figure 6.6: Substation's temperature control scheme.

Differential pressure control of DHS

The pipe network considers 2 pumps, 30 pipes, and 9 valves, which makes the linearisation process for the differential pressure controller a challenging task. Therefore, two simplifications are considered to address this issue. Firstly, an equivalent pump is defined by doubling the original pump's head. Figure 6.7 shows the comparison volumetric flow-head curves for both pumps. The equivalent pump only requires one driver and one PI controller, which reduces the control design process and the implementation of the differential pressure control of the pipe network in Apros.

Figure 6.7: Comparison between the volumetric flow-head ($Q_v - h$) curves of the original and equivalent pumps.

6.2. Case study 1

Secondly, a simplification of the pipe network for the control design process only is proposed. This simplification is shown in Figure 6.8, only two pipes are included and the effects of other substations are considered as disturbances. The total length of the equivalent supply pipe ($k_{s,a}$) is defined as the sum of the length of the pipes $k_{s,1}$, $k_{s,3}$, $k_{s,5}$, $k_{s,7}$, $k_{s,9}$, $k_{s,11}$, $k_{s,13}$ and $k_{s,15}$. In a similar vein, the length of the equivalent return pipe ($k_{r,a}$) is obtained by adding the length of the return pipes. Following these simplifications, the design of the differential pressure based-PI controller is presented in Appendix H and reproduced below as

$$C_{\Delta p, S8}(s) = \frac{23.95 + 0.057s}{s} \quad (6.2)$$

where $k_p = 23.95$ and $k_i = 0.057$. The set point for this case study is based on [2]. A minimum differential pressure of the 0.5 bar is required for the farthest substation to guarantee the hydraulic conditions of the whole system.

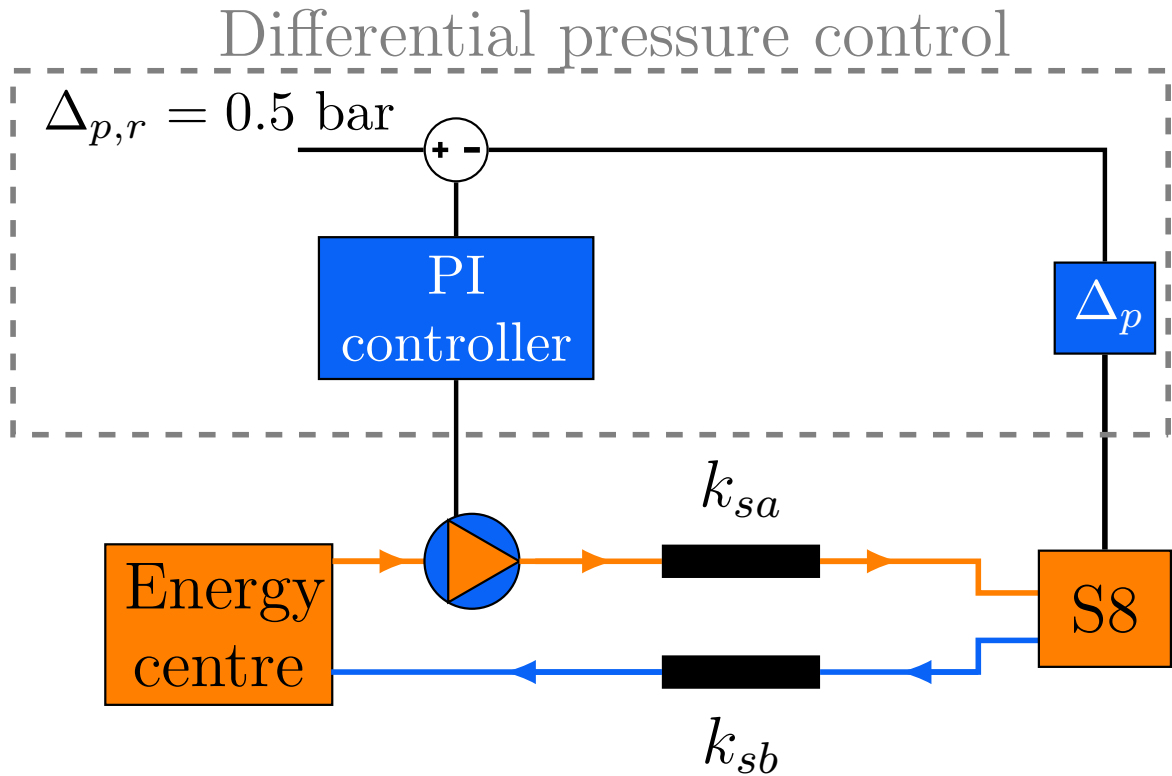


Figure 6.8: Differential pressure control scheme of S8.

Charging process of TES tank

The sensible TES tank is charged using the PI controller designed in Section 5.2.4. During the charging process, the hot water is supplied to the tank using its pump. A ramp input is used to achieve a full charge. The control scheme is shown in Figure 6.9. For this case study, the charging process period is set to 1 hr. The PI controller used in the simulations is defined by equation (5.69):

$$C_T = \frac{26s + 0.047}{s}.$$

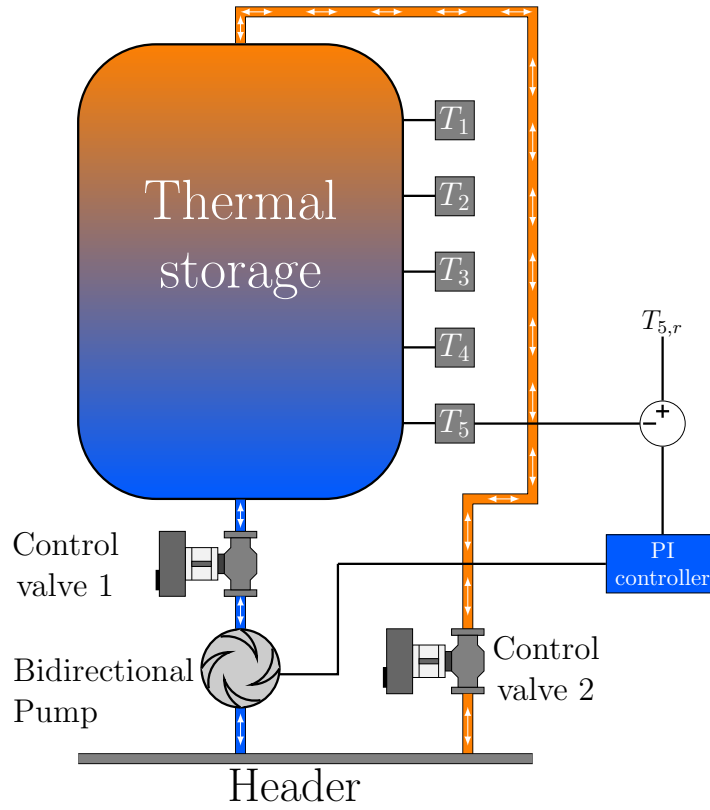


Figure 6.9: Charging process of sensible TES control scheme.

6.2.3 Assessment methodology of the designed controllers

The main aim of a DHS is to supply the thermal loads in its substations. The management of the heat supply implies the use of effective temperature controllers in those substations. They have to meet varying heat demands while keeping the temperature of the supplied hot water constant. A thermal load profile is used to resemble the heat demands in each substation. A Temperature profile is more suitable to be used for simulation than a heat profile. Therefore, the thermal load profile (Q) is converted to temperature T using equation (3.20):

$$Q = \dot{m}c_p(T_2 - T_1). \quad (6.3)$$

where c_p is the specific heat of the water.

Since it is desired that the output temperature ($T_{c,out}$) of the secondary circuit remains constant at 50°C (T_2), and a constant mass flow rate (\dot{m}) of 8 kg/s is assumed, equation (6.3) is used to compute T_1 as

$$T_1 = 50 - \left(\frac{Q}{8 \cdot 4180} \right). \quad (6.4)$$

The assumption of a constant mass flow rate in the secondary circuit of the heat exchanger of the substation is adopted because the model of the hydraulic behaviour of the heat load devices, such as heating space of tap hot water, are out of the scope of this work. Therefore, only temperature variations are considered for the secondary circuit of the substations. Thus, considering $T_1 = T_{c,in}$ and $\dot{m} = 8 \text{ kg/s}$ in the secondary circuit, the thermal load profile can be simulated. For completeness, Figure 6.10 shows the thermal load of substation 1 (given by Q_{S1}).

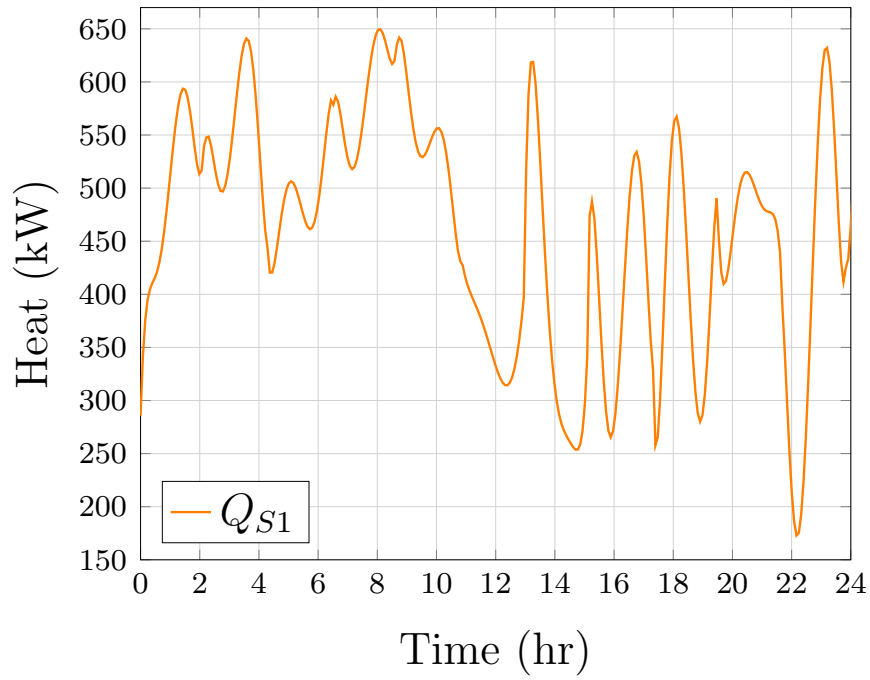
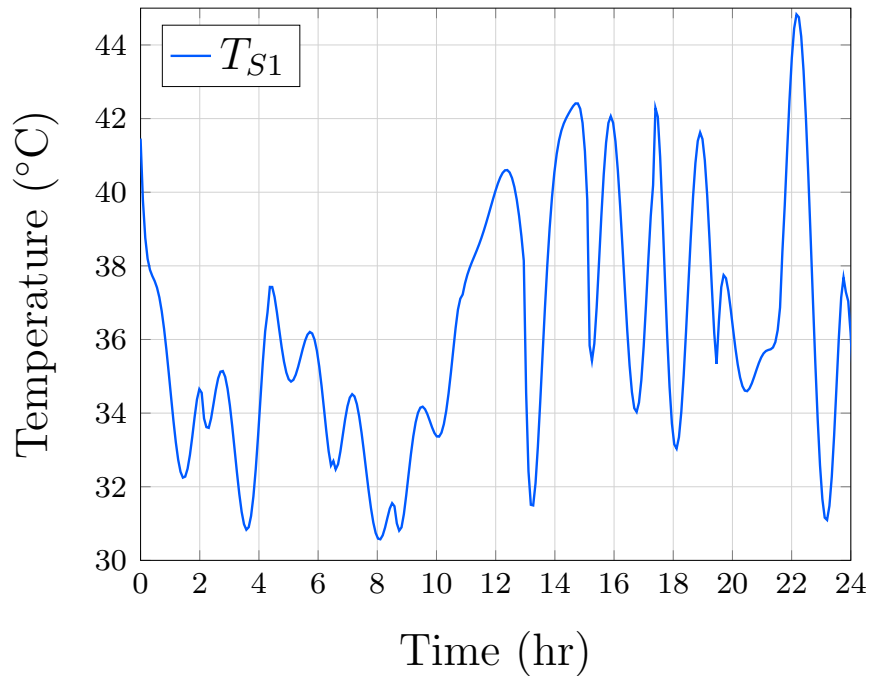


Figure 6.10: Thermal load of substation 1.

Figure 6.11 shows the temperature profile obtained after applying equation (6.3) to Q_{S1} and defining $\dot{m} = 8 \text{ kg/s}$. In order to simulate the thermal load, the input temperature of the secondary circuit ($T_{c,in}$) in substation 1 should be equal to T_{S1} . Figure 6.12 illustrates the implementation of the thermal load profiles of the substations.

Figure 6.11: Thermal load of substation 1 given in temperature variations of $T_{c,in} = T_{S1}$.

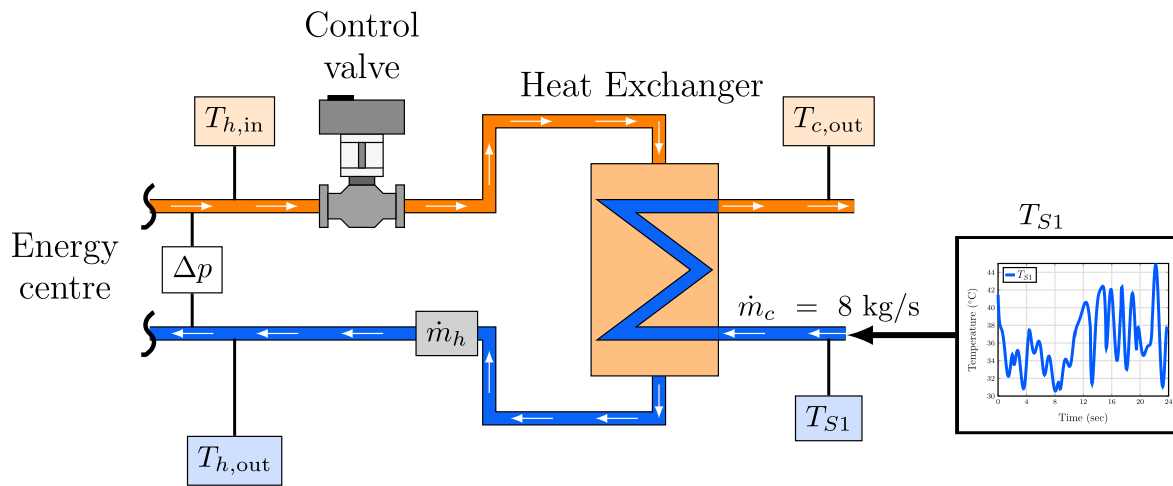


Figure 6.12: Illustrative scheme of the thermal load profile in a substation generated by variation of the input temperature $T_{c,in}$

6.2.4 Apros model

The developed Apros model of the DHS is divided in three main sections:

- Energy centre,
- Pipe network, and
- Substations.

Energy centre

The energy centre diagram is depicted in Figure 6.13. The TES tank is built using the same approach presented in Section 4.4.1. A single pipe is used as a header with node elements connecting each loop. The energy technologies' output is simulated using two nodes with temperature and pressure being defined to generate the mass flow required by the system. Apros does not include bi-directional pumps. Therefore, separate configurations are required to simulate charging and discharging processes. Thus, two pumps and a control valve arrangement are considered to allow the water's circulation upwards and downwards. This new configuration is schematically presented in Figure 6.15.

Pipe network

The pipe network diagram is shown in Figure 6.14. It is built using the *district heating pipe* element, which consists of two parallel pipes with separate inlet and outlet connections. Thus, supply and return pipes are included in the same element. The heat supplied is taken from the header using a *centrifugal pump*. A *control valve* is included as a safety element in case of system overpressure.

Substations

Eight substation diagrams are developed. Figure 6.16 shows the components of each. The *flat plate heat exchanger* element is used for the heat exchanger. The primary circuit includes a control valve which is the actuator used to regulate the mass flow rate during the PI controller action.

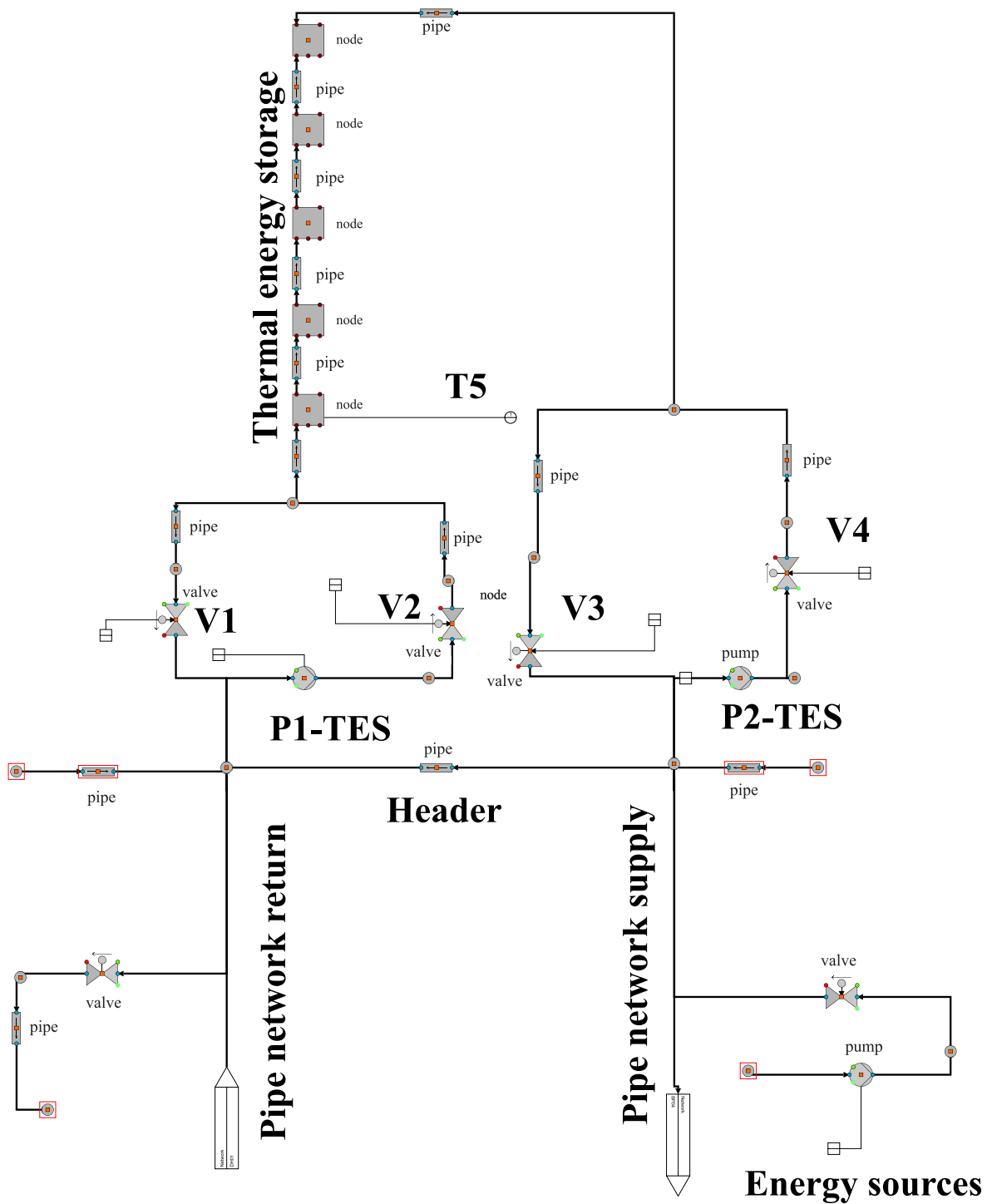


Figure 6.13: Apros model of the energy centre.

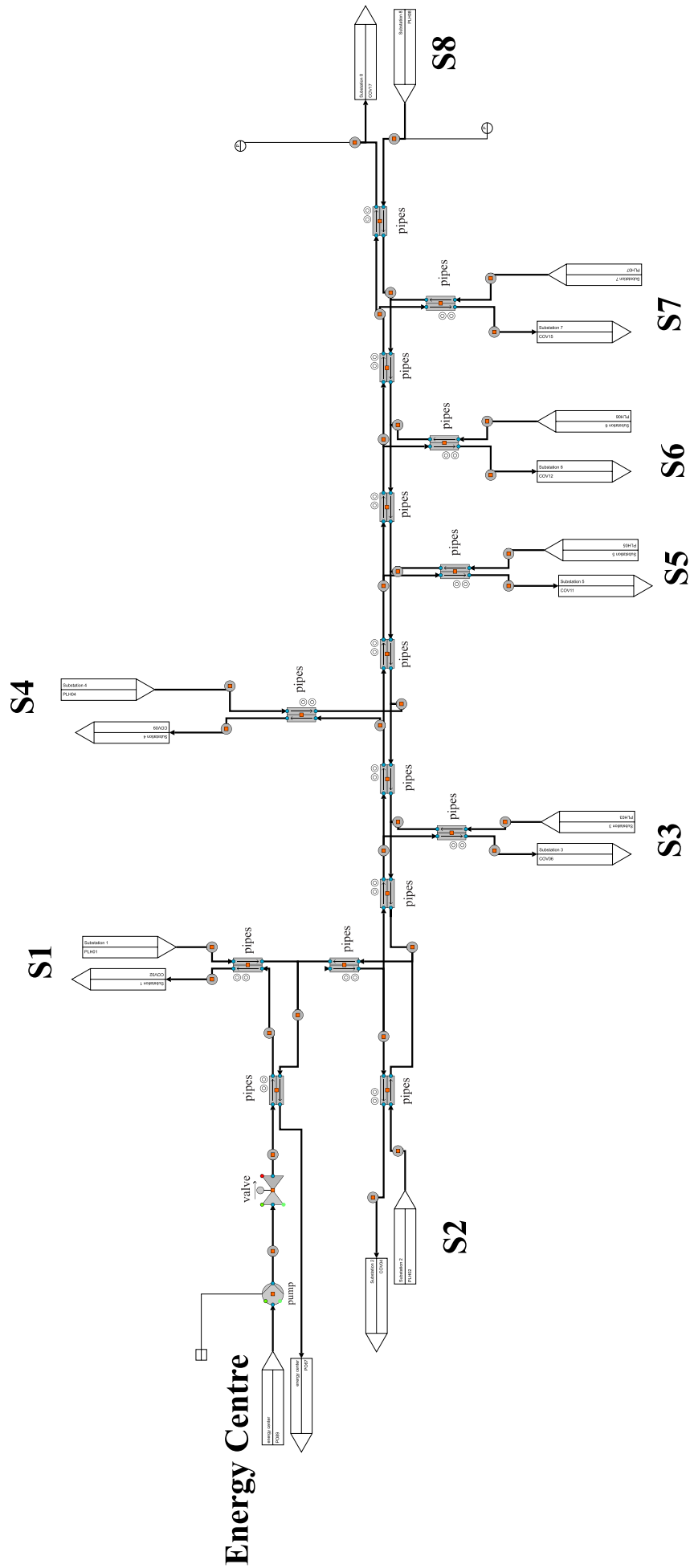


Figure 6.14: Overview of the developed Apropos model of the pipe network section.

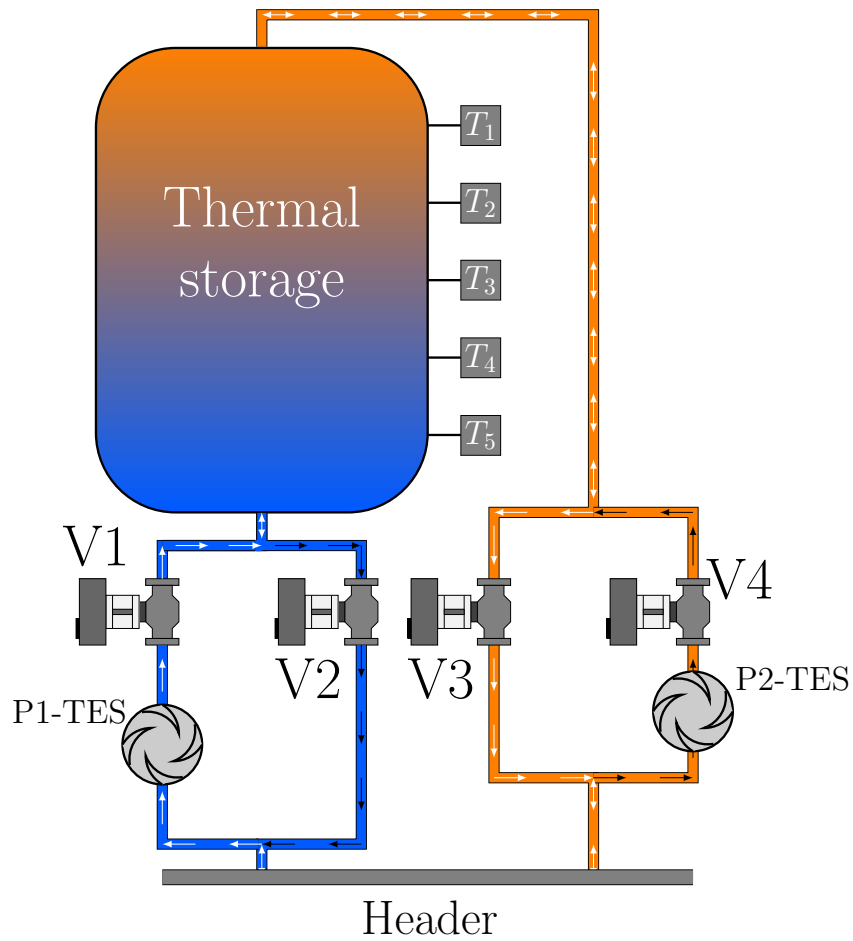


Figure 6.15: Schematic of TES configuration with two uni-directional pumps.

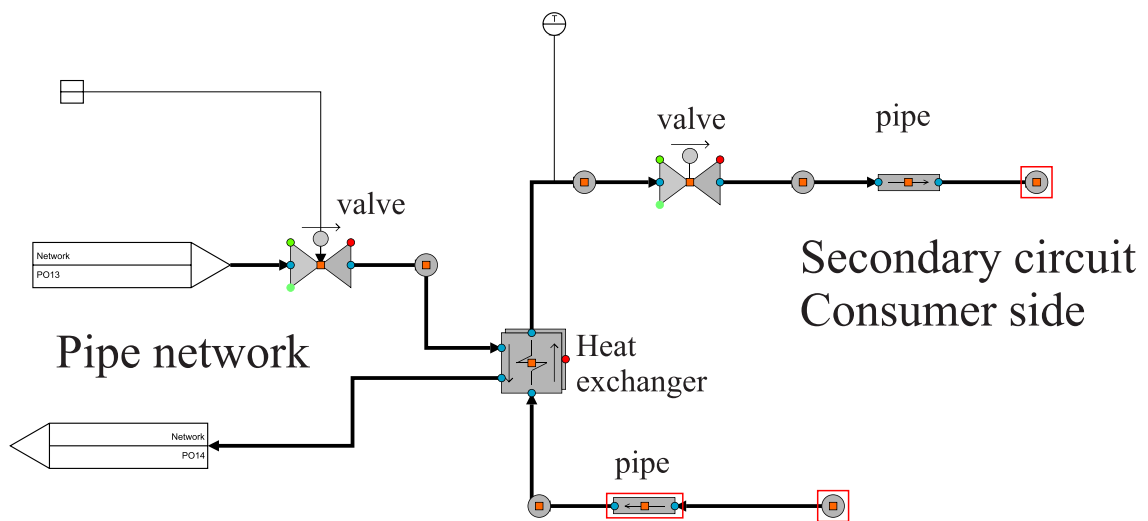


Figure 6.16: Apron diagram of the substation.

6.2.5 Simulation results

The heat loads in each substation define the operating conditions of the DHS. The ambient temperature is set at 10°C during the whole day. The water tank-based TES starts charging at 10 am and the discharging process starts at 3 pm. For clarity, results are presented first for substation $S8$. The responses of the temperature and differential pressure controllers are analysed. Afterwards, a comparison between the heat load demand and the heat transferred through the heat exchangers is carried out to assess the system's effectiveness for meeting the heat demands. The system's general response is analysed by the end showing the performance of the eight substations and of the energy centre.

Performance of substation 8

In terms of hydraulic behaviour, the farthest substation in a DHS is the most critical. Due to the pressure drop presented in long pipes, enough pressure in this location becomes a critical variable for the adequate operating of this substation. Regulation of the hydraulic conditions should guarantee meeting the thermal loads. Figure 6.17 shows the performance of the temperature and differential pressure controllers implemented in the substation $S8$. Subscript ' r ' stands for the control reference of the temperature and differential pressure controllers.

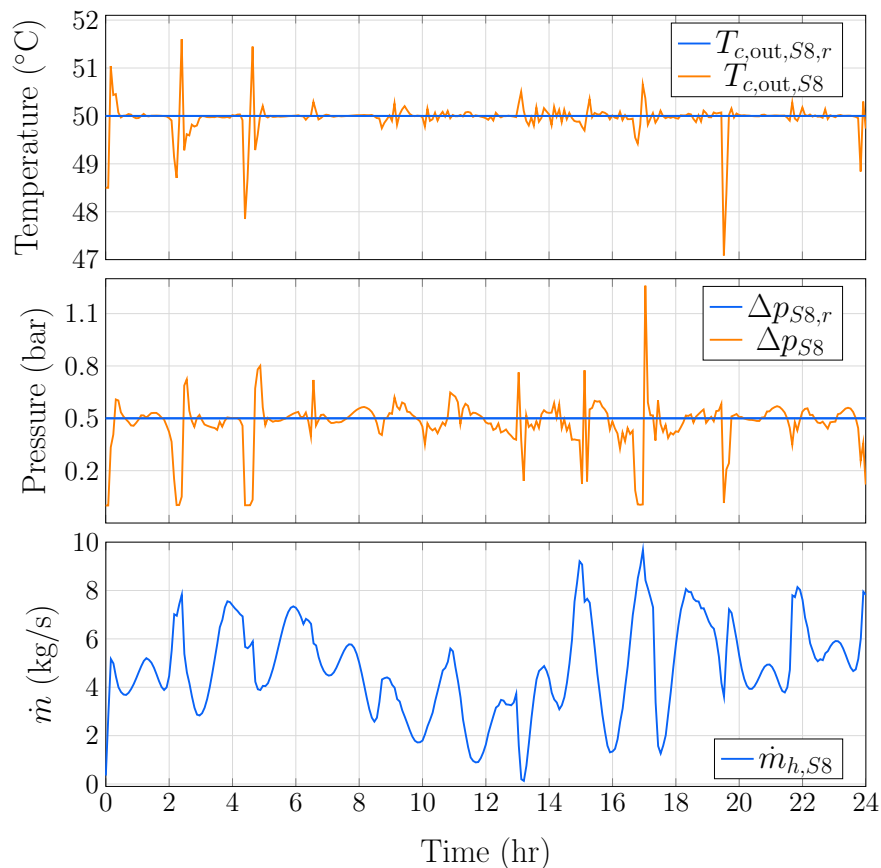


Figure 6.17: PI controllers performances in substation 8: Temperature (top), differential pressure (middle) and mass flow rate of the primary circuit (bottom).

The amount of heat transferred in the heat exchanger is compared to the heat load profile (Q_{S8}). Figure 6.18 shows the temperature profile of the consumer circuit and the comparison

6.2. Case study 1

between Q_{S8} and the heat transferred $Q_{A,S8}$ during the simulation, where subscript 'A' stands for Apros's simulation results ¹.

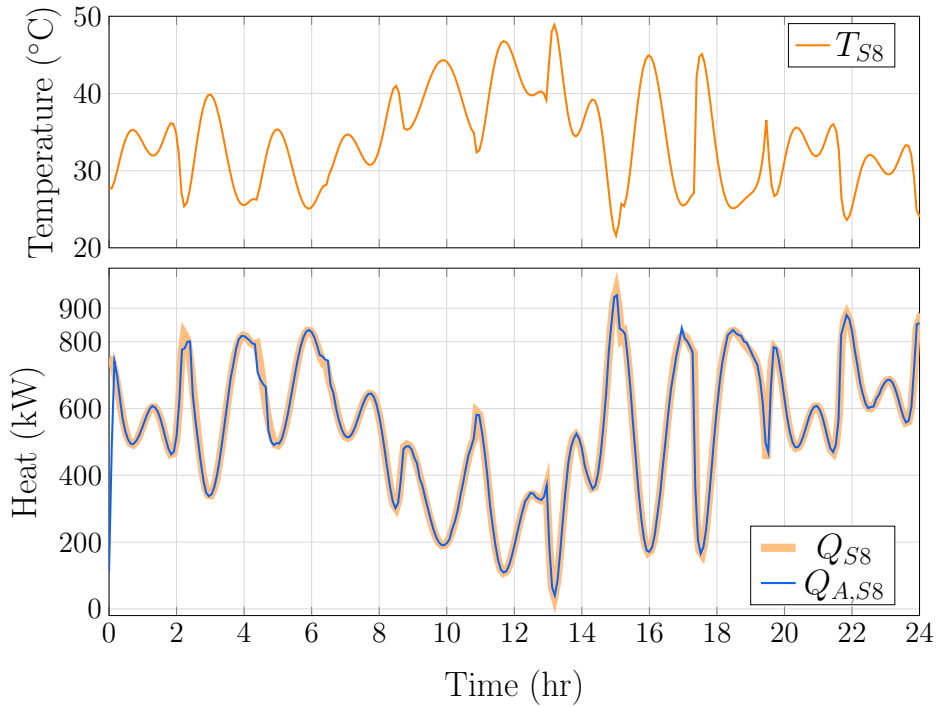


Figure 6.18: Top: daily temperature profile of the heat load. Bottom: comparison between the heat transferred and the heat load of substation 8.

As it can be observed, the heat load profile is satisfactorily met. The temperature controller is capable to maintain $T_{c,out,8}$ at 50°C most of the time. The controller is able to reject disturbances caused by the changes in the input temperature of the secondary circuit.

The most challenging scenario for the temperature controller is when the differential pressure drops below 0.2°C (see Figure 6.17). This means a reduction of $\dot{m}_{h,S8}$, which implies less hot water is available to maintain the temperature reference. Nevertheless, the temperature controller can follow the reference during this condition. Although the time of this transient disturbance is about 1 hr, the heat demand is met. The errors of the controlled variable are less than 3°C, which is considered a good tolerance.

For the differential pressure controller, it is necessary to consider the behaviour of the total mass flow rate provided to the pipe network by the equivalent pump. Figure 6.19 shows the hydraulic conditions of $S8$ (Δp_{S8} and $\dot{m}_{h,S8}$), the pump's speed (ω_{sp}) and the total mass flow rate of the DHS's pipe network \dot{m}_{DHS} . As it can be observed, increments and decrements of the system's total mass flow are related to variations of Δp_{S8} . The differential pressure controller tries to regulate the mass flow rate variations ($\dot{m}_{h,S8}$) due to the heat exchanger demands to follow the temperature references in each substation. Although the differential pressure reference in $S8$ is not met accurately, the maximum error is less than 0.8 bar, which is considered acceptable. This behaviour is expected, due to the fast response of the hydraulic behaviour of the DHS. Thus, continuous variations of the mass flow rates in each substation render challenging conditions for the differential pressure controller. Arguably, a stronger control action could be included, but this would imply higher variations in the pump's speed and instability of the system due to sudden significant changes in the total mass flow rate.

¹This subscript is only used for the heat transferred to avoid confusion with the thermal load profile.

Therefore, the designed PI controller (6.2) which keeps the differential pressure in $S8$ at 0.5 bar is considered satisfactory for the overall DHS operation.

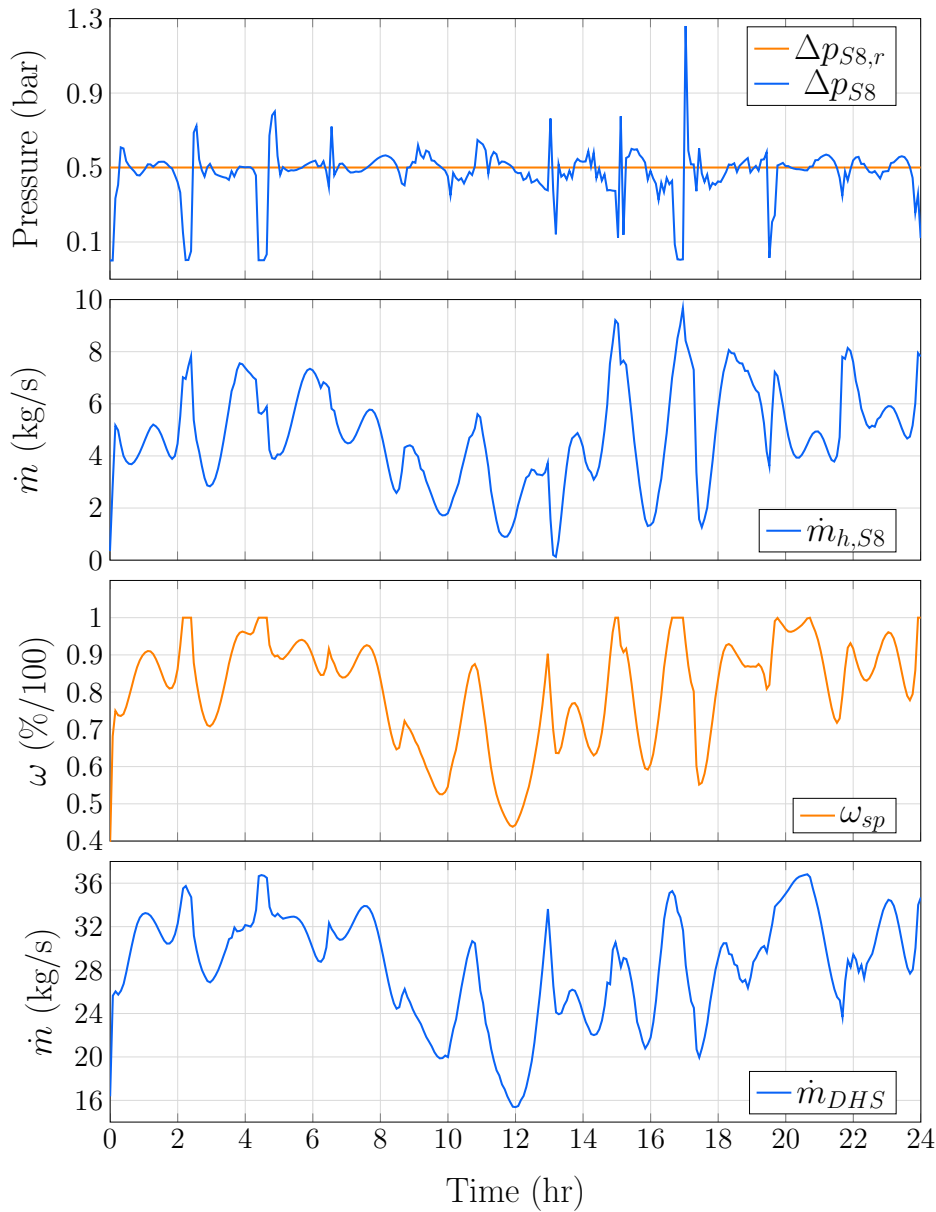


Figure 6.19: Top: Differential pressure and hot water mass flow rate of $S8$. Bottom: pump's speed and total mass flow rate in the DHS.

Overall performance of the district heating system

Representative results of the eight substations' conditions are plotted. Firstly, the temperatures injected into the secondary circuit in the substations are shown in Figure 6.20. These temperature profiles represent the heat loads that the heat supply should meet. Figure 6.21 shows the comparison between the heat load profiles (thick orange traces) and the heat transferred by the heat exchanger (blue traces). As it can be seen, all substations meet their heat loads. The temperature controllers are capable of following the temperature references and, thus, enough amount of heat is supplied to increase the temperature of the secondary circuit to 50°C at any moment.

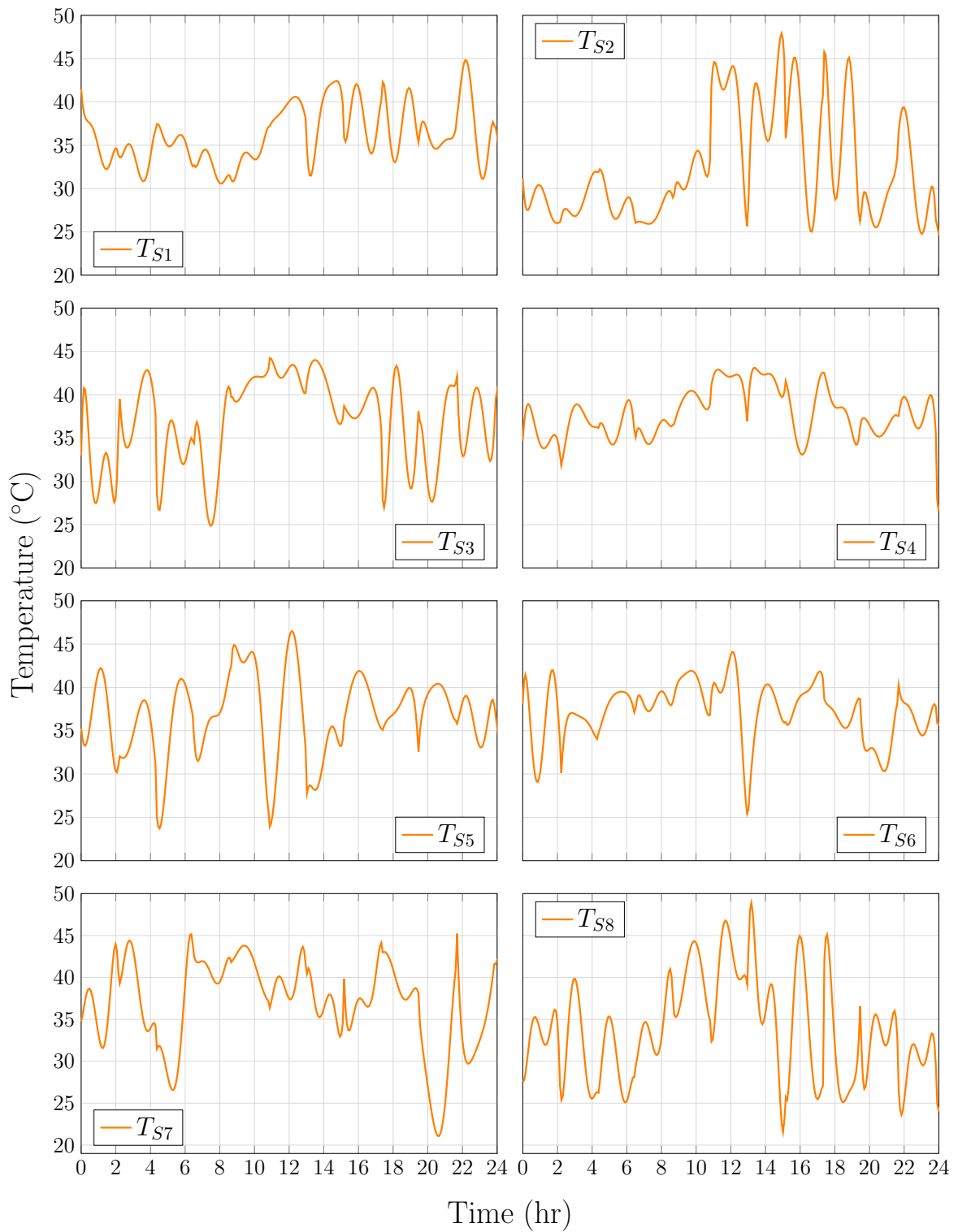


Figure 6.20: Temperature profiles of the eight substations.

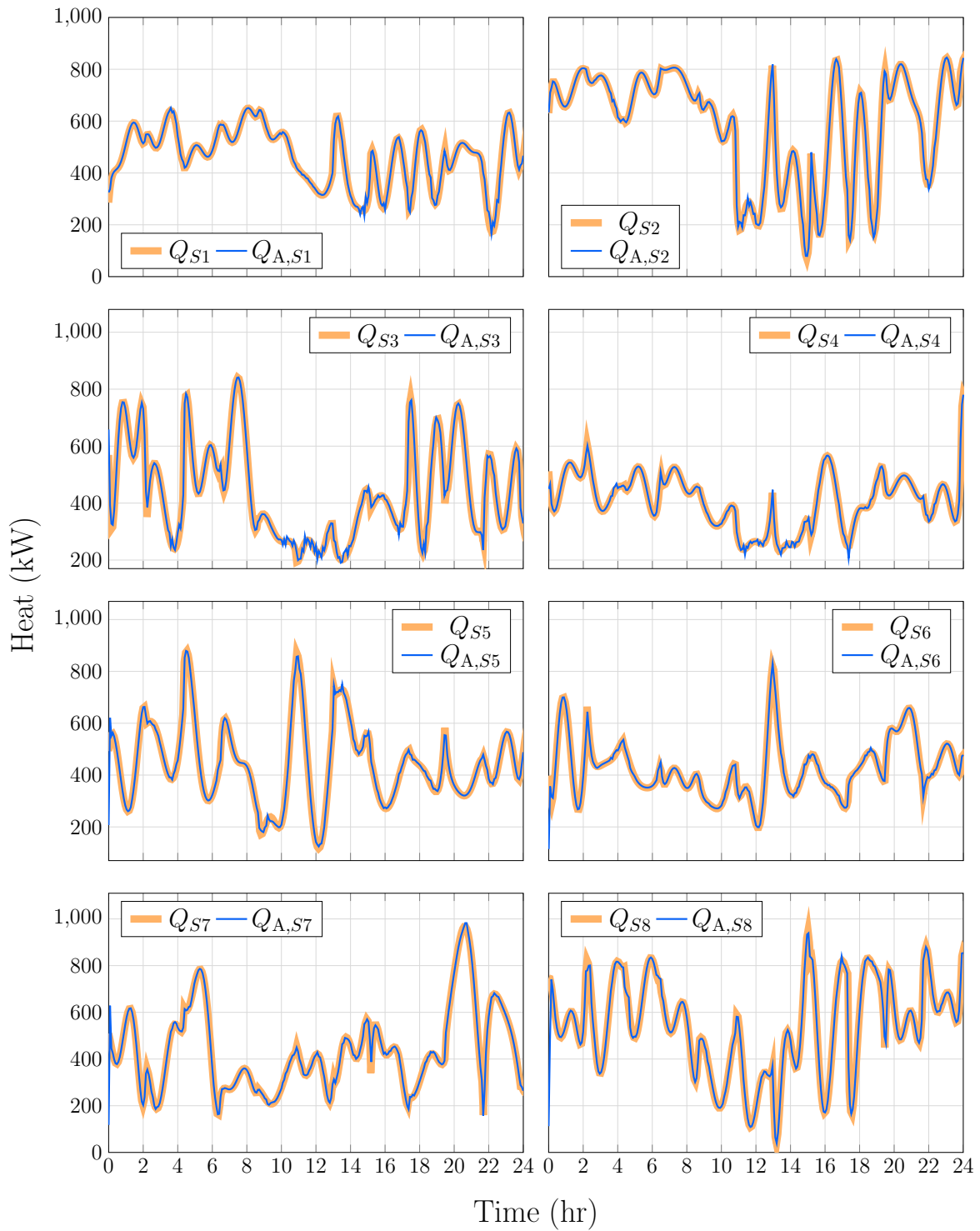


Figure 6.21: Comparison between the heat load and the heat transferred by the substation's heat exchangers.

6.2. Case study 1

The output temperature of each secondary circuit is shown in Figure 6.22. The temperature reference is followed by the PI controllers for most of the time. Even though some errors are present throughout the day, these are less than 1°C . As it is expected, the farthest substations (*S7*, *S8*) exhibit the most challenging conditions. Thus, errors greater than 1°C occur in these locations. Nevertheless, the control scheme is capable of reducing these errors and guarantee that the heat loads are met.

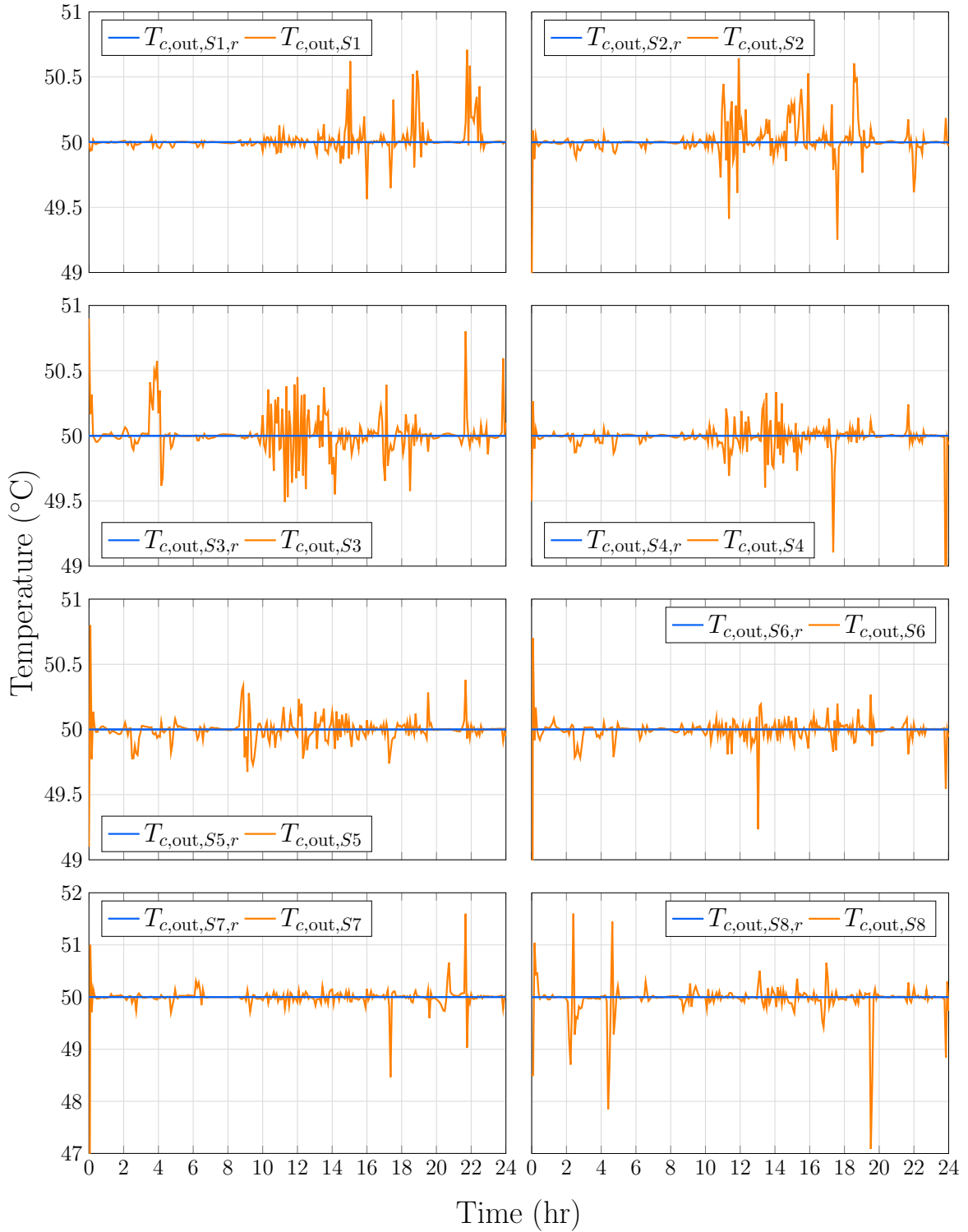


Figure 6.22: Temperature controller responses of the eight substations.

Figure 6.23 shows the behaviour of the differential pressure of each substation. Since no controller has been implemented in the first seven substations, the values of Δp vary from 0 up to 10 bars. Substation $S1$ and $S2$ present the higher values of differential pressure as they are the substations closest to the pump. The variation range gradually decreases as the distance from the pump increases. Thus, substation $S7$ presents the smallest range of the differential pressure variation for the uncontrolled substations.

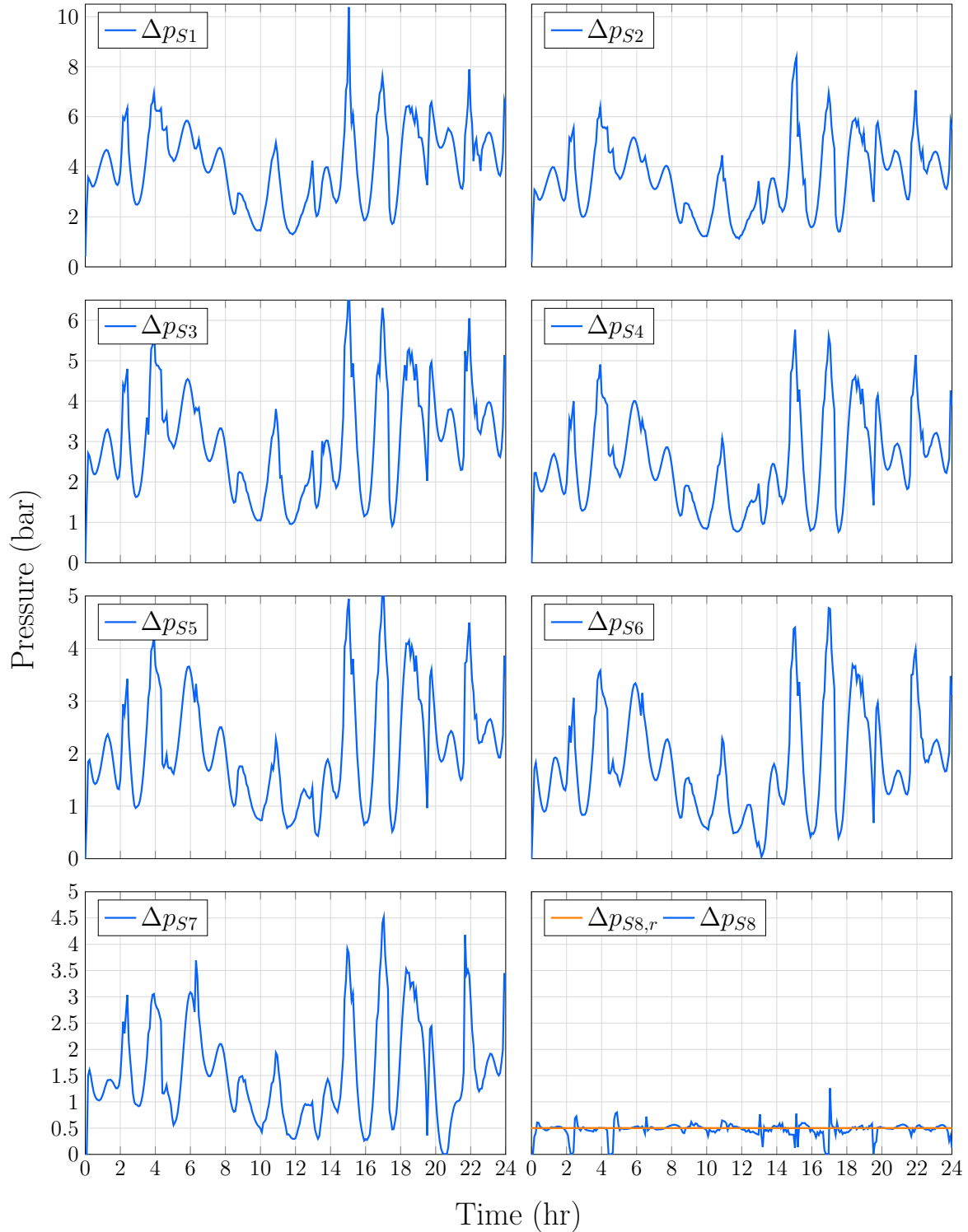


Figure 6.23: Differential pressure of the eight substations.

6.2. Case study 1

Finally, the hot water's mass flow rate required of each substation to supply heat to the consumer is shown in Figure 6.24. Mass flow rate \dot{m}_h is related to the amount of heat load. For instance, the largest amount of hot mass flow rate is required by $S2$, which is the substation with the highest heat load. Conversely, the smallest amount of hot mass flow rate is required by $S4$, which presents the least heat load of the DHS. Other factors like heat losses, which means a reduction of the substations' input temperature, will affect the amount required to meet the heat loads. Thus, the mass flow rate of $S8$ present peaks up to 8 kg/s, although its heat load is not so high. This high demand is because of the pipe's thermal losses, which are analysed in the last part of this subsection.

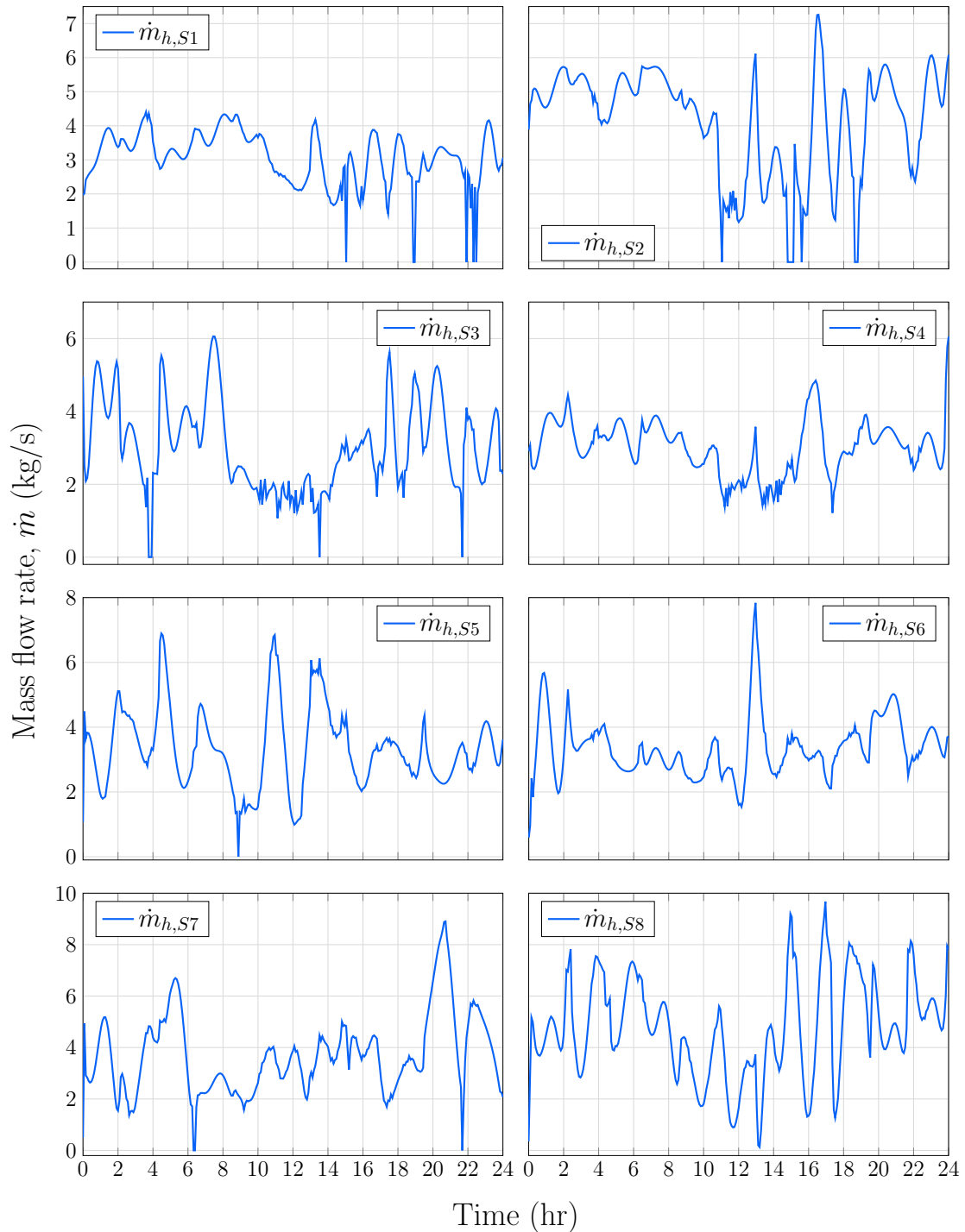


Figure 6.24: Mass flow rate of hot water supplied to each substation of the DHS.

The thermal performance of the DHS has been analysed by comparing the heat transferred by the heat exchangers to the heat loads. The hydraulic dynamic has been studied through the differential pressures and mass flow rates developed in each substations. Nevertheless, the pressure management in a DHCS can be described by pressure head diagrams [2]. This type of diagram shows the pressure head in each substation against its distance from the pump. Pressure heads continuously vary according to the operational conditions. Two instants of the DHS behaviour are presented in Figure 6.25: at 5 hrs and 20 hrs. For clarity, the y -axis variable is converted to pressure instead of head in Figure 6.25a. As it is expected, the shape of the diagram changes as the hydraulic conditions are modified. Nevertheless, the value of the most peripheral substation (*i.e.*, substation $S8$) remains nearly constant (0.5 bar) which is a result of the differential pressure controller. For completeness, Figure 6.25b shows the same instants but with the conversion of pressure to head. It is important to notice that the latter diagram is obtained using absolute pressure instead of gauge pressure.

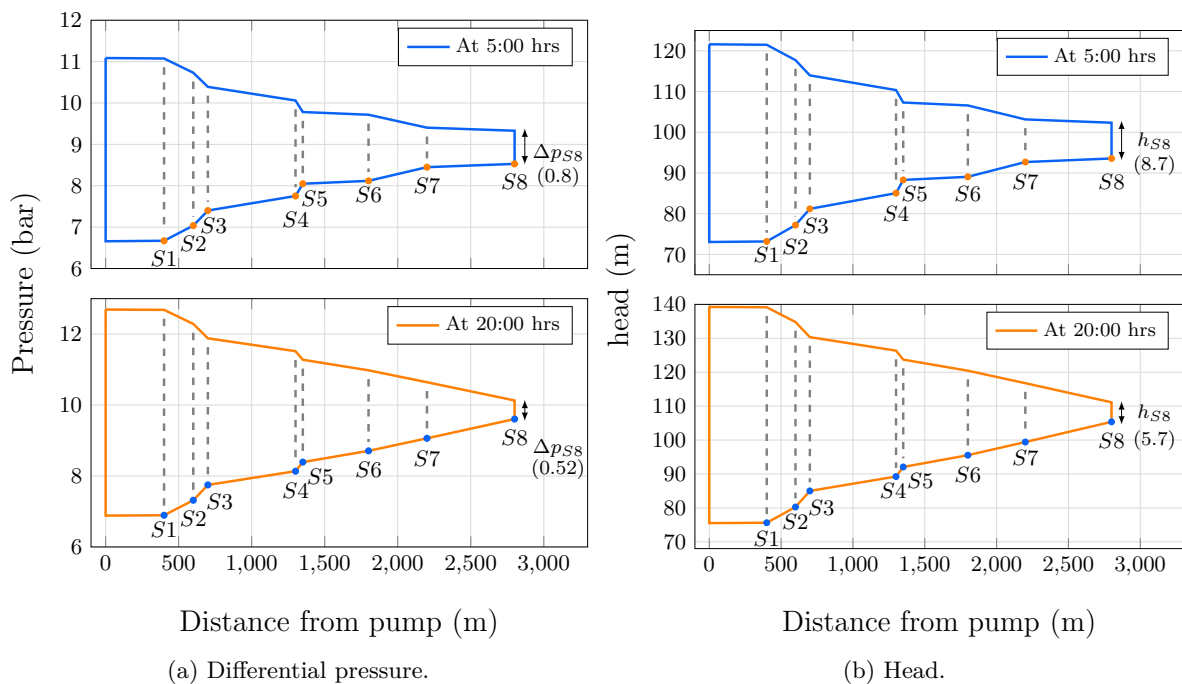


Figure 6.25: Snapshots of differential pressure and pressure head diagrams of the DHS at 5 hrs and 20 hrs.

Thermal energy storage performance

Figure 6.26 shows the use of the sensible TES tank in the DHS operation. The charging and discharging processes are set at 10:00 hrs and 15:00 hrs, respectively. The energy technologies' supply heat is stopped at 15:00 and the energy supplied to the substations is exclusively taken from the TES tank until 16:21 hrs. During the discharging process, the mass flow rate is constant (28 kg/s) to ensure that the hydraulic header in the energy centre has enough water to be taken by the pipe network's pump. It is important to notice that the TES tank is not completely discharged. As water is supplied at a temperature below 70°C, this forces the system to demand more mass flow rate. Thus, a control system able to mix the warm water of the TES tank with hot water from energy technologies is necessary. Such a system is out of the scope of this research work. Therefore, the discharging process is cut off when the top

6.2. Case study 1

layer's temperature is 70°C, as shown in Figure 6.26.

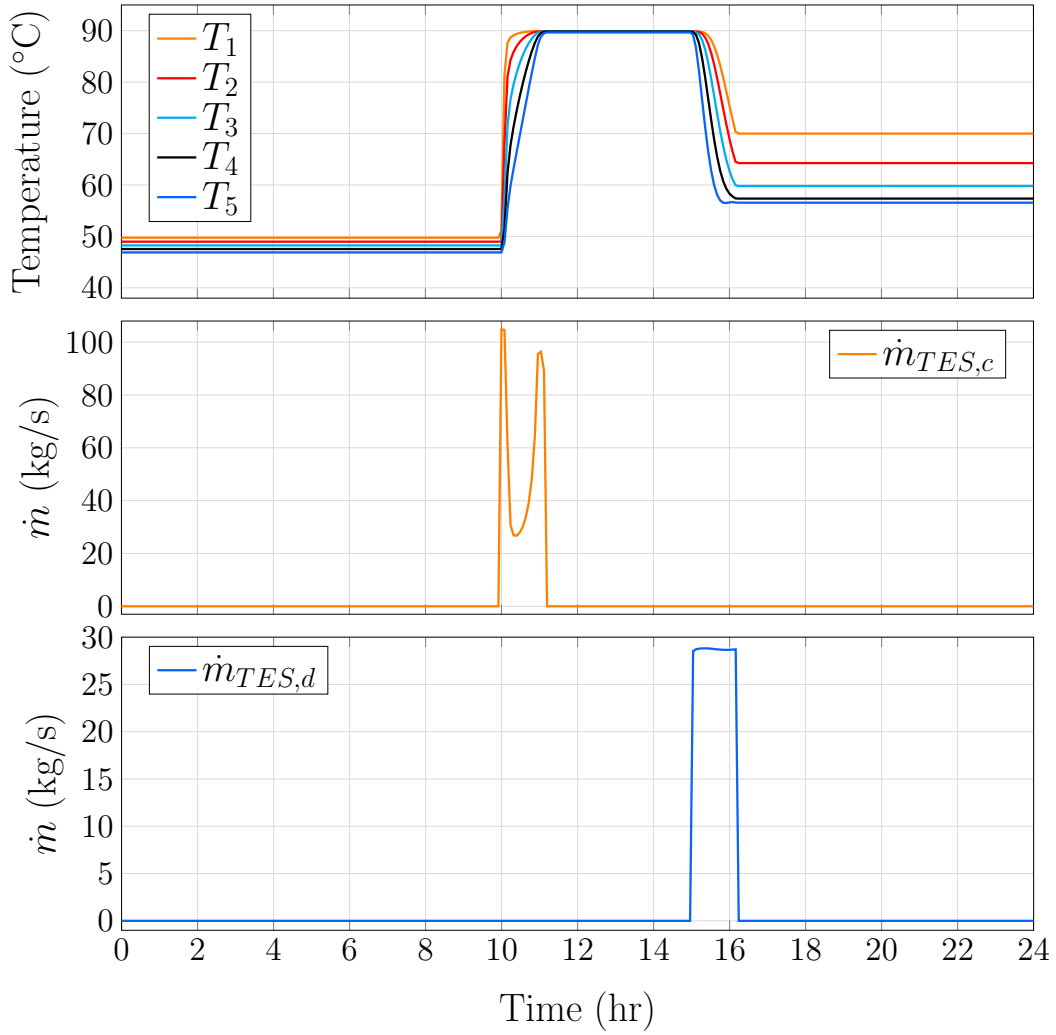


Figure 6.26: Charging and discharging process of the sensible TES.

The performance of the PI controller for the charging process is shown in Figure 6.27a. A charging period of 1hr is defined by a ramp function (as in Section 5.2.4). As it can be observed, the reference is followed by the temperature of layer 5 and the full energy stage is achieved in approximately 1 hr. The mass flow rate required is shown in Figure 6.26 (middle). Although a high demand of hot water is presented (up to 100 kg/s), the heat supply to the DHS is not jeopardised because the energy technologies produce sufficient heat to keep the thermal conditions of the DHS.

Figure 6.27b shows the energy stored during the charging process. This value is obtained using equation (4.95). The TES tank is considered empty when the layers' temperatures are 50°C. Thus, this value is considered to calculate stored energy in each layer as

$$E_{\text{layer}} = \frac{V \rho c_p (T_{\text{layer}} - 50)}{3600}, \quad (6.5)$$

where the volume of the layer (V) is 20.357 m³ (see Table 6.1). The total energy stored during the charging process is $E_{\text{tes}} = 4.685$ MWh.

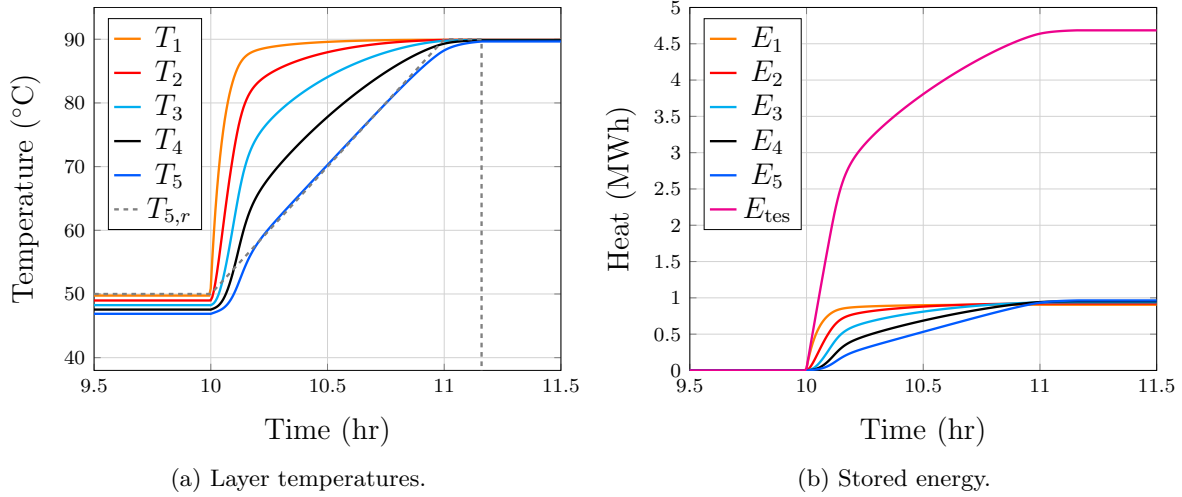


Figure 6.27: Charging process of the TES by means of a ramp function using a PI controller for the temperature in the fifth layer.

Thermal losses and energy supply quantification

The transportation of heat through insulated pipes reduces the thermal losses caused by the external temperature. Nevertheless, these losses are unavoidable in long district heating pipes. The modelling of the thermal behaviour of long pipes within a DHCS is beyond the scope of this work. However, the ambient temperature (T_a), the depth of the pipe centre below the ground (d_g), the thermal conductivity (k_{ins}) and the insulator's thickness (th_i) can be defined in the *district heating pipe* element of Apros. For the case study simulation, these parameters are set as $T_a = 10^\circ\text{C}$, $d_g = 1$ m, $k_{\text{ins}} = 0.027$ W/mK and $th_i = 0.02$ m. Apros can simulate these thermal losses within the pipe network. Although a detailed analysis of the thermal behaviour of the hot water flowing through the pipes is highly desirable, it is out of the scope of this thesis. Only the effect of these thermal losses is explained in terms of the effective heat transferred in the substation and the total heat supplied in the pipe network.

Figure 6.28 shows the hot water temperature at the right extreme of pipe k_{s1} (see Figure 6.4) and, the hot water inlet temperature in substations $S4$ and $S8$ (labelled as $T_{\text{in},DHS}$, $T_{\text{in},S4}$ and $T_{\text{in},S8}$, respectively). As it can be observed, temperature drops down to 12°C and 8°C at $S4$ and $S8$, respectively. This implies that part of energy centre's heat is lost due to the temperature reduction of the hot water flowing through the pipe network.

In order to determine the amount of heat lost due to the hot water transportation, the total heat supplied by the energy centre (Q_{ec}) is calculated using the total mass flow rate generated by the pipe network pump (\dot{m}_{DHS}), the output temperature in pipe k_{s1} (supply temperature $T_{DHS,s}$), the input temperature of pipe k_{r1} (return temperature $T_{DHS,r}$) and equation (3.20) as

$$Q_{\text{ec}} = \dot{m}_{DHS} c_p (T_{DHS,s} - T_{DHS,r}). \quad (6.6)$$

Then, all heat transferred in each substation is added as

$$Q_{\text{subs}} = Q_{S1} + Q_{S2} + Q_{S3} + Q_{S4} + Q_{S5} + Q_{S6} + Q_{S7} + Q_{S8}. \quad (6.7)$$

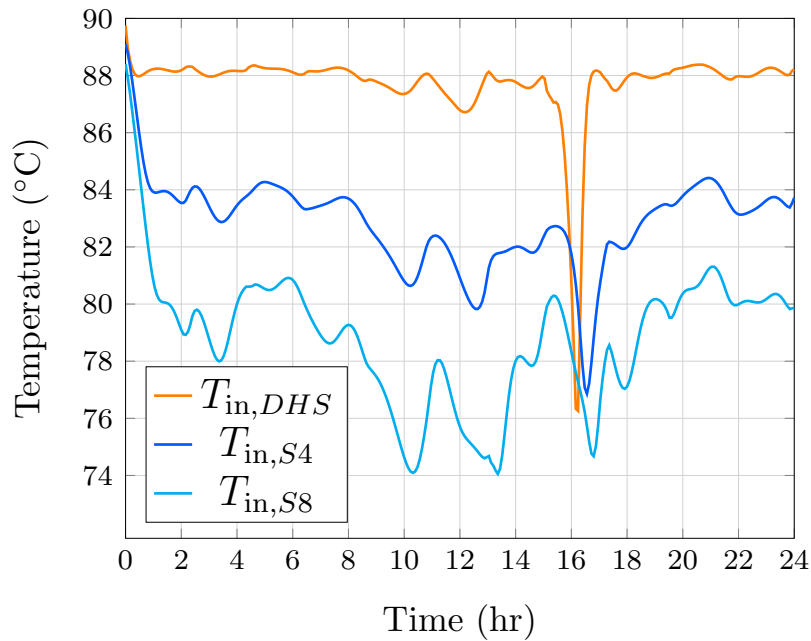


Figure 6.28: Inlet temperatures of the pipe network, substation 4 and 8.

Results of equations (6.6) and (6.7) are presented in Figure 6.29. As it can be observed, there is a considerable difference between both calculations. To quantify the thermal losses, the total energy supplied by the energy centre (E_{ec}) and the energy transferred in the substations E_{subs} are obtained.

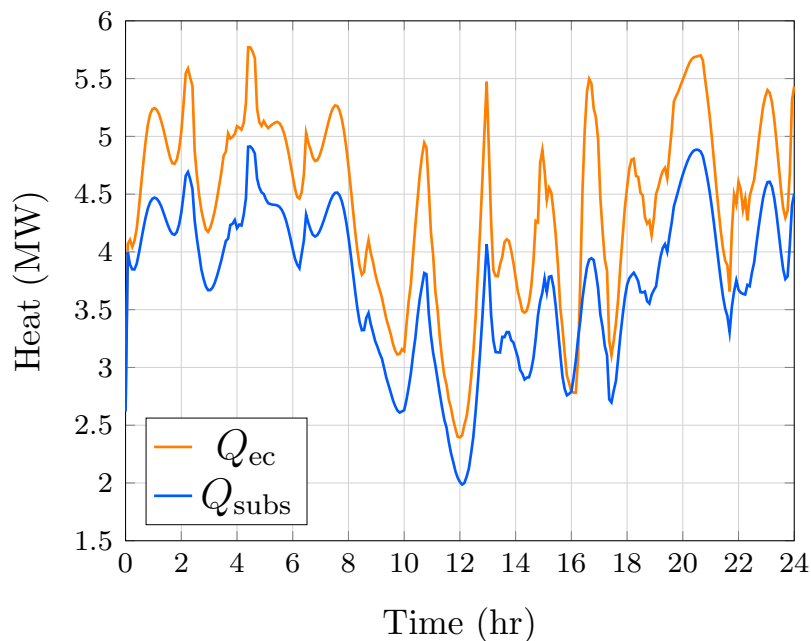


Figure 6.29: Comparison between the heat supplied by the energy centre (Q_{ec}) and the total heat transferred in the substations Q_{sbus} .

The area below the heat supplied to a system is the total energy absorbed during the heat transfer phenomenon. For the energy centre and substations of the DHS, these areas are shown in Figure 6.30. The total energy supplied to the pipe network is $E_{ec} = 383.6359$ GJ = 106.6 MWh. The TES gives a total energy released by the TES of $E_{tes} = 15.85$ GJ =

4.4 MWh. It means that 0.285 MWh remains after the end of the discharging process. The value of the energy transferred in the substations is $E_{\text{subs}} = 323.94 \text{ GJ} = 89.98 \text{ MWh}$. This implies an energy loss $E_{\text{losses}} = 59.6865 \text{ GJ} = 16.58 \text{ MWh}$, which is shown in Figure 6.31. This value may change due to the variation of ambient conditions. For the case study, the ambient temperature is kept constant at 10°C .

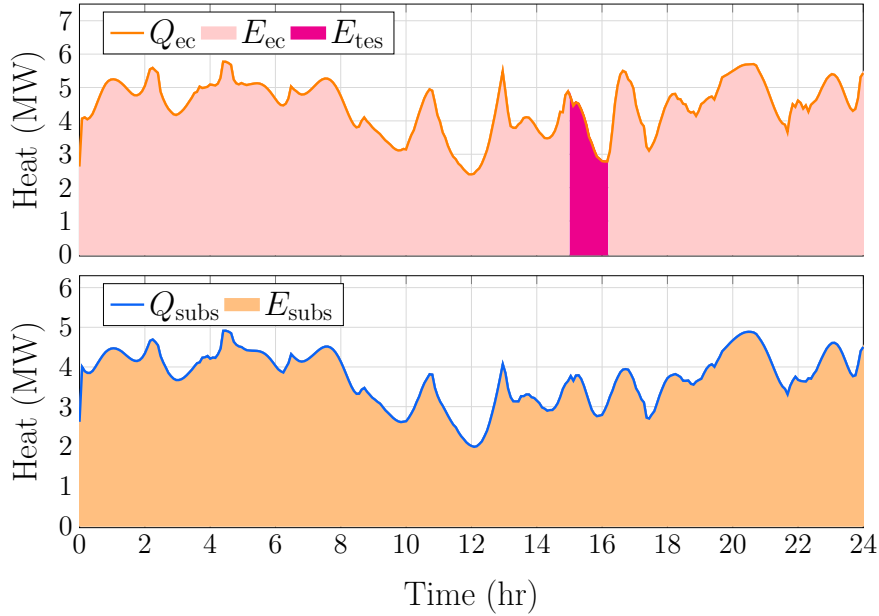


Figure 6.30: Top: Supplied energy by energy centre. Bottom: Transferred energy by substations.

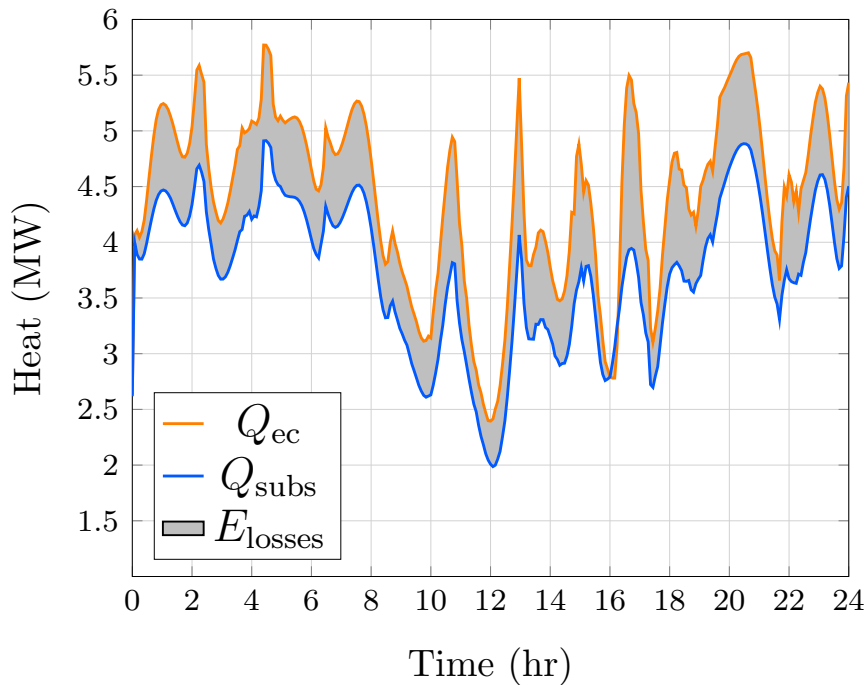


Figure 6.31: Quantification of the thermal losses due to transportation of hot water through insulated pipe networks.

6.3 Case study 2

This section presents the use of the 1-D dynamic model of the ice tank-based TES in a cooling energy centre. Simulations are carried out as co-simulation using two software platforms, with the 1-D dynamic model of the TES tank being implemented in MATLAB/Simulink and the rest of the energy cooling centre components implemented in Apros. The link between the two software platforms is achieved with the OPC communication protocol [3]. Two ice tank-based TESs support the cooling energy centre in the daytime, and they are charged during the night. A compressor chiller supplies the cooling energy to charge the TES tanks. The maximum cooling consumed is about 350 kW. The model of the energy technology is out of the scope of this work. Thus, the compressor chiller is replaced by a constant source of cold fluid. Two scenarios are analysed. Firstly, the cold fluid is only supplied by the TES tanks. Secondly, the supply process is shared with the compressor chiller.

6.3.1 Description

The configuration of the cooling energy centre is depicted in Figure 6.32 and includes the dynamic model of the latent TES tank developed in Section 4.4.2. It is comprised of two ice-based TES tanks connected in parallel. A mixture of glycol-water at 34% is used as HTF to supply the customer's cooling energy. This fluid can be chilled to temperatures below 0°C. The polynomial functions that define the thermophysical properties of HTF are shown in Appendix F. A heat exchanger transfers the cooling energy from the HTF to the district cooling network. A valve arrangement is set up to switch between different operating modes. During the charging process, the HTF is cooled down to temperatures below 0°C by the compressor chiller and is pumped to the ice tanks. To achieve this, valve 4 is opened and valves 1, 2 and 3 are closed to allow the cold HTF to pass through the ice tanks. Conversely, the chiller is turned off for a discharging process, where valves 2 and 4 are closed and valves 1 and 3 are opened. If the ice is completely depleted following a discharging process, a third operating mode to continue supplying cooling services without using the ice tanks is also possible. In this case, the chiller is turned on, valve 1 remains open, valves 3 and 4 are closed, and valve 2 is opened.

A fourth operation mode is enabled when valve 4 is closed, valve 1 is open and valve 2 and 3 are partially open to split the HTF to the TES tanks and to by-pass of valve 2. In this scenario, the compressor chiller supplies HTF at 3°C, increasing the mass flow rate of the HTF to meet the thermal loads.

6.3.2 Setup of thermal energy storage model

The commercial ice tank considered in this case study is a Calmac ICEBANK 1098C model with a nominal storage capacity of 350 kWh [4]. The model of this tank was developed and verified in Section 4.4.2. Charging and discharging processes are simulated to verify the total energy absorbed and released by the TES. Firstly, a HTF' mass flow rate of 10 kg/s at -6°C is supplied to the discharged TES at 12°C. Figure 6.33 shows temperatures, power, energy and SoC during the charging process. The model is divided into 20 nodes. The last node of the fluid side is considered the output temperature of the HTF (T_{out}), the temperature of the last node of the internal ice is also plotted ($T_{w,20}$). The total power absorbed (P_T) and the

total energy stored by the tank are shown in the middle of the Figure 6.33. The total value of energy is $E_T = 337.3$ kWh.

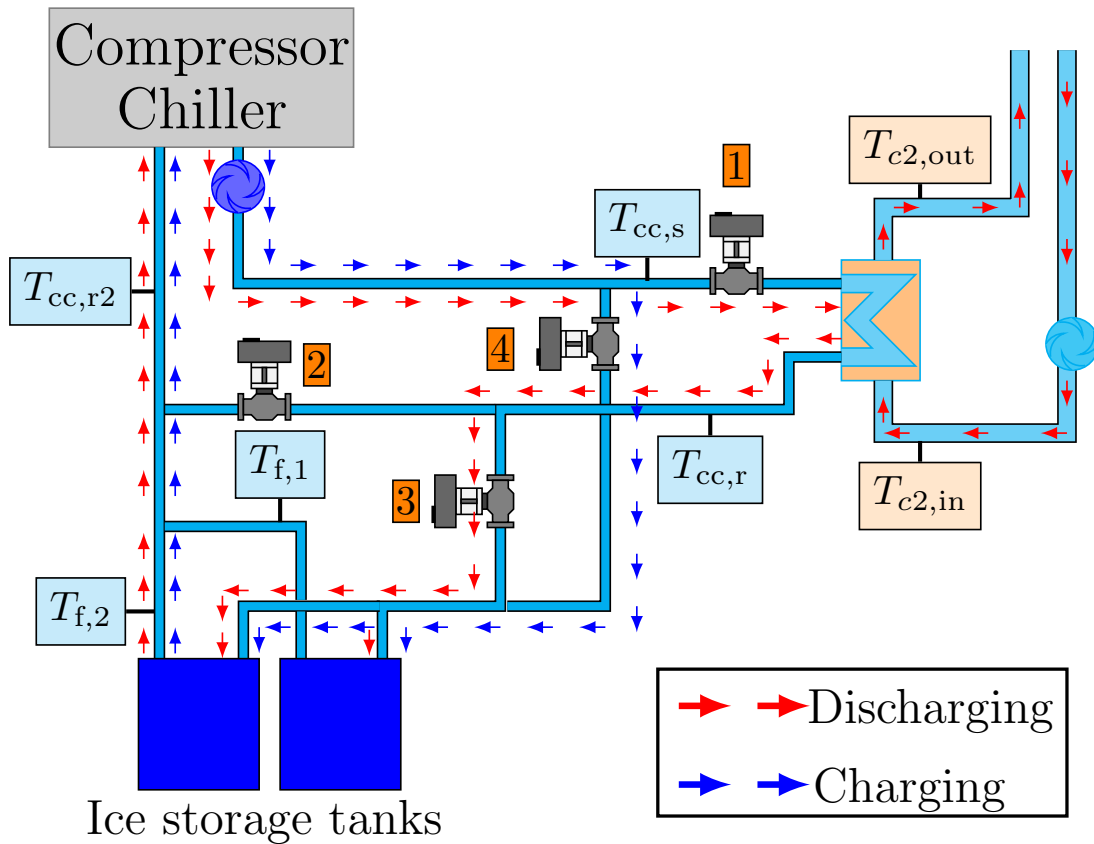


Figure 6.32: Schematic of the cooling energy centre.

Finally, the SoC is computed using the method developed in Section 4.4.2. It is important to notice that the energy and the SoC computation only consider the latent energy absorbed during the water's solidification. There is a discrepancy of 16.7 kWh with respect to the storage capacity reported by the manufacturer. As it was explained in Section 4.4.2, the variations of the water density during the process and the fixed value of the control volume produces this slight difference. Nevertheless, as it shown during the model's verification, the most critical variable, which is the fluid temperature, is not affected.

The discharging process is simulated with a HTF' mass flow rate of 5 kg/s at 12°C injected into a charged TES at -6°C . Figure 6.34 shows HTF temperatures and the last node of the ice. The total energy released during the process is $E_T = 337.7$ kWh.

6.3. Case study 2

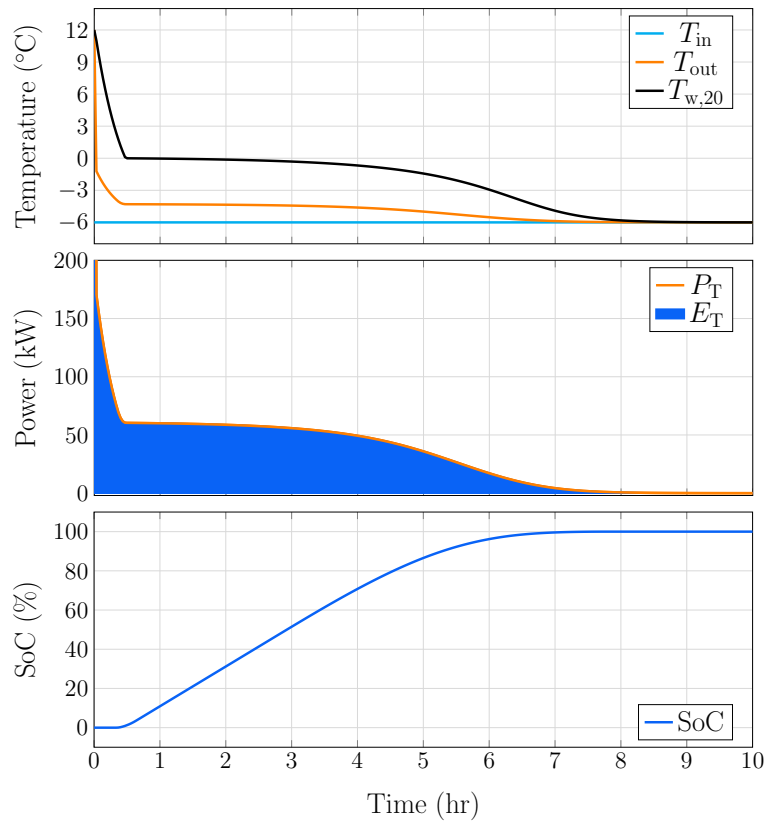


Figure 6.33: Charging process of ice tank-based TES with a HTF conditions of $T_{in} = -6^{\circ}\text{C}$ and a $\dot{m}_f = 10 \text{ kg/s}$.

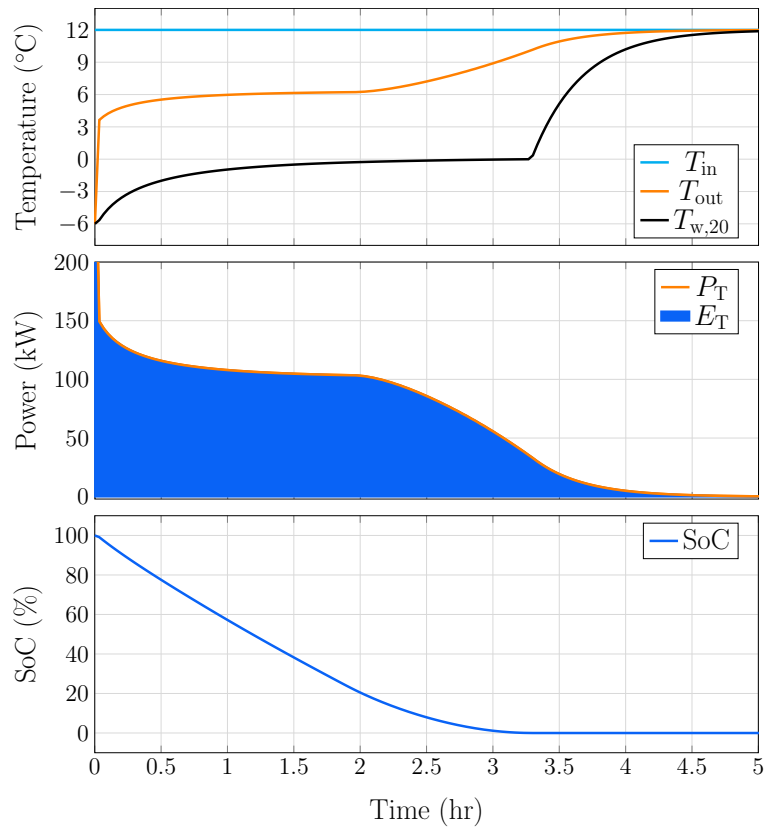


Figure 6.34: Discharging process of ice tank-based TES with a HTF conditions of $T_{in} = 12^{\circ}\text{C}$ and a $\dot{m}_f = 5 \text{ kg/s}$.

6.3.3 Co-simulation between MATLAB/Simulink and Apros software

The OPC communication protocol is used to establish the interface between clients and servers. Thus, the data generated during simulation time is available in real-time [3]. The configuration of the data exchange between MATLAB and Apros is shown in Figure 6.35. The OPC server is created when Apros is launched. MATLAB/Simulink has access to the variables generated during simulation time in Apros by via the OPC toolbox. Thus, reading and writing of Apros's variable is enabled.

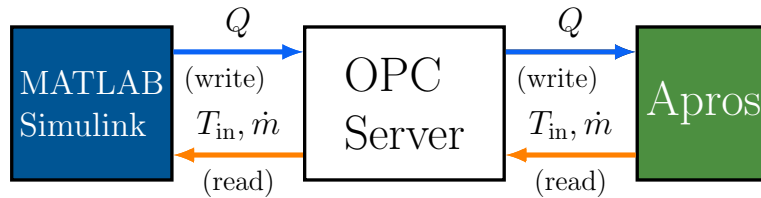


Figure 6.35: Schematic diagram of communication between Apros and MATLAB/Simulink platforms for co-simulation.

For each ice tank implemented in MATLAB/Simulink, and equivalent pipe that resembles its pressure drop is defined in Apros. The temperature and mass flow rate of the fluid crossing the pipe are read. These readings are used as inputs for the TES tank model. The heat transferred to the TES is written in a special Apros's component called *NO2_node*, as shown in Figure 6.36. This value will reduce or increase the temperature according to the thermophysical properties of the fluid crossing the node. The total heat transferred during the charging and discharging processes of the TES tank model is computed by equation (3.20):

$$Q = \dot{m}c_p (T_{\text{out}} - T_{\text{in}}), \quad (6.8)$$

where c_p is the specific heat of the glycol-water at 34%. This fluid was defined in Apros using the characteristics of water-glycol at 34% shown in Appendix F.

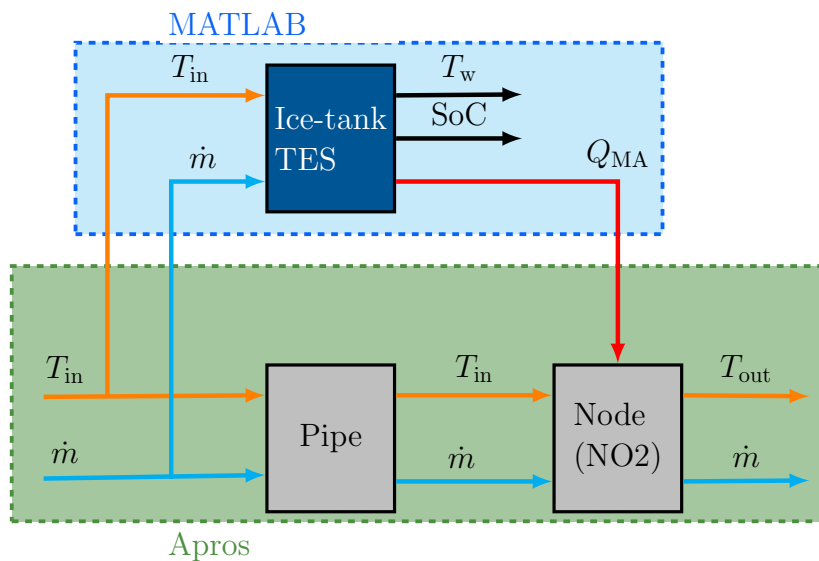


Figure 6.36: Configuration for MATLAB and Apros co-simulation.

6.3.4 Apros model

The diagram of the cooling energy centre is shown in Figure 6.37. The two TES tanks are defined as two equivalent pipes and two *NO2_nodes* are connected in parallel. A heat exchanger is defined to transfer the cold produced by the compressor chiller to the consumer. The arrangement of valves that govern the different operating modes is build using the *contro_valve* component. A pump is included to supply the mass flow rate to the heat exchanger and the TES tanks. The pump and heat exchanger are the same used in case study 1 and their parameters are shown Tables 6.2 and 6.4, respectively.

The two TES tanks are connected to the compressor chiller to support the energy supply process during peak demands. The main use of chilled water is for air conditioning systems or tap water. Therefore, the compressor chiller's output is simulated as a mass flow rate source of cold water, whose temperature is modified according to the operation modes (*i.e.*, -6°C for charging of TESs mode and 3°C for supplying cooling to the consumer mode). The chilled water consumption is simulated using a load thermal profile at the secondary circuit of the heat exchanger.

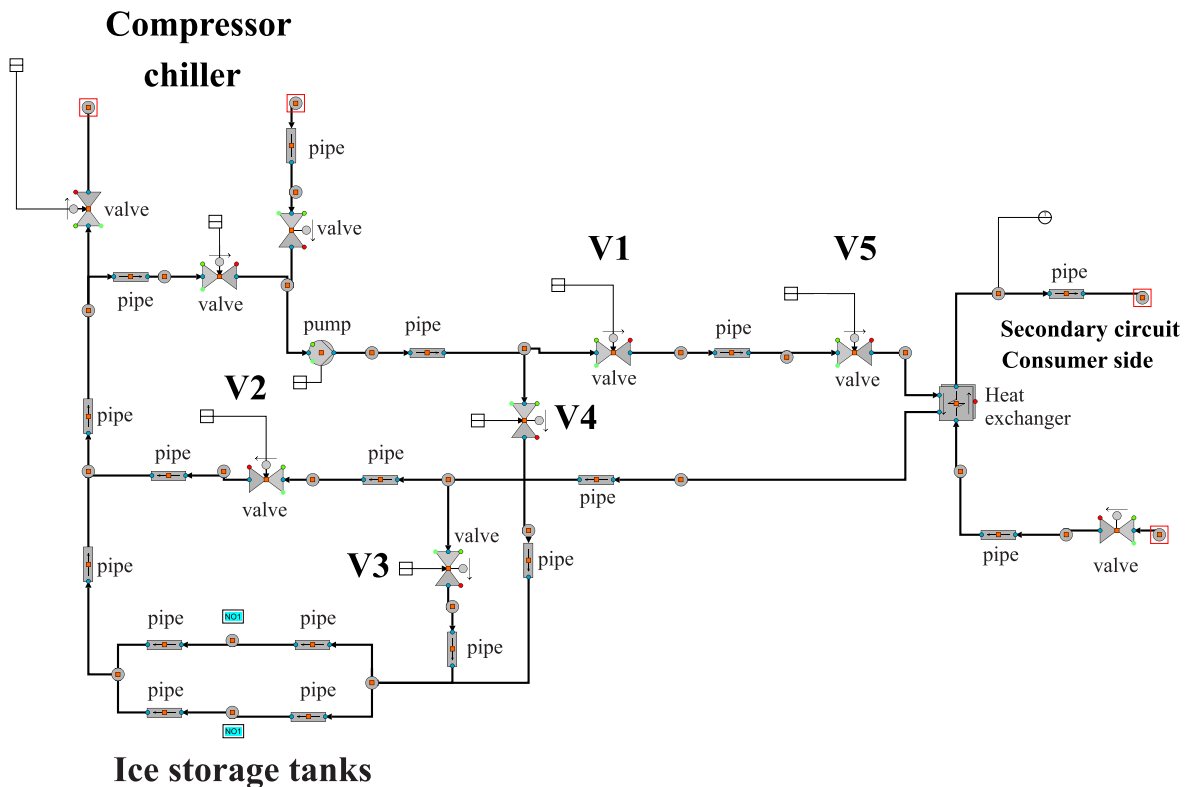


Figure 6.37: Apros model of the cooling energy centre.

6.3.5 Simulation results

The cooling energy centre aims to provide chilled water to the consumer at a constant temperature. For this purpose, a temperature PI controller is designed (see Appendix H). The cold HTF supplied by the compressor chiller and the TES tanks is used to decrease the temperature of the consumer side. The PI controller regulates the cold HTF's mass flow rate using valve 5 to achieve the cold water demands. Similar to case study 1, a thermal load profile (Q_{CS}) is injected into the secondary circuit of the heat exchanger. The profile given in

kW is converted to temperature (T_{CS}) using equation (3.20), where the output temperature and the mass flow rate of the consumer circuit are set to 7°C and 5 kg/s , respectively. The temperature profile is given by

$$T_{CS} = 7 - \left(\frac{Q_{CS}}{5 \cdot 4180} \right). \quad (6.9)$$

Figure 6.38 shows the thermal load profile used. During the night (first eight hours), there is no thermal load because the cooling energy centre exclusively operates in charging mode.

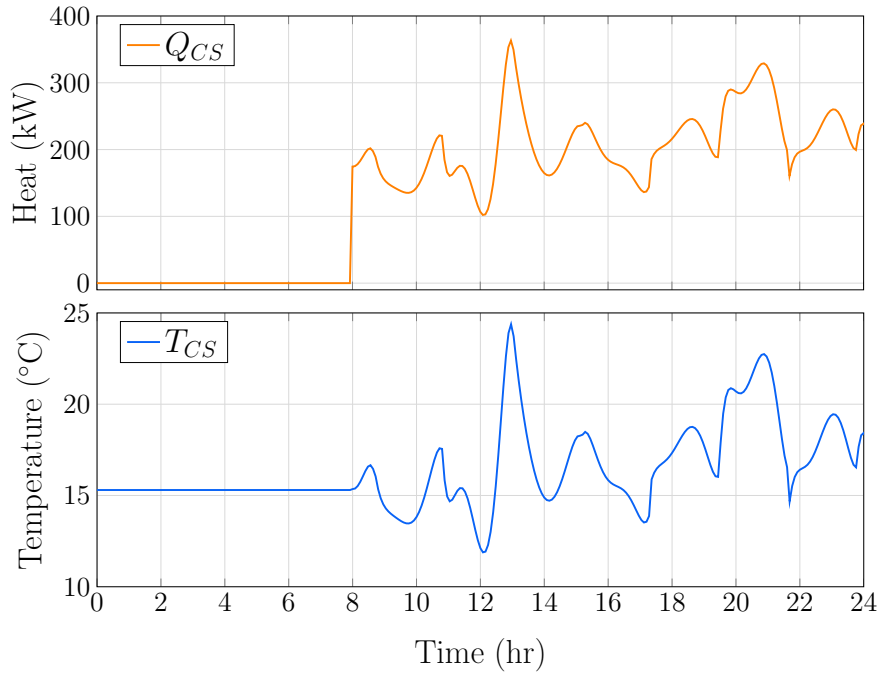


Figure 6.38: Thermal load of heat exchanger given in cooling power (top) and temperature (bottom) variations.

Two different scenarios are simulated: (1) the ice tank-based TESs only supplies the cold HTF and (2) the compressor chiller is turned on to share the cold fluid supply process with the TES tanks.

Cold supplied only by the TES tank

Figure 6.39 shows the performance of the temperature controller. As it can be observed, the temperature reference is only followed during 5 hours. Afterwards, the controller is not able to keep the output temperature of the secondary circuit constant as the TES tanks have discharged. No more cold HTF is provided by the energy cooling centre, neither by the TES tanks nor compressor chiller. A comparison between the thermal load and the heat transferred by the heat exchanger shows that the load is only met while the TES tanks can provide cold HTF.

A detailed description of the energy centre operating modes is shown in Figure 6.40. The charging mode, where only valve 4 is open, allows to flow the HTF through the TES tanks as shown at the bottom of Figure 6.40. For clarity, only the temperatures and mass flow rate of one TES tank are shown. As they are connected in parallel, the same conditions are obtained

6.3. Case study 2

for both. A mass flow rate \dot{m}_{v4} of 21 kg/s provides the cold water at -6°C to the TES tanks. As it can be observed, the mass flow rate of the TES tank 1 (\dot{m}_{T1}) is exactly half of \dot{m}_{v4} .

The cooling energy centre changes to the discharging mode by opening valves 1 and 3 and closing valve 4. The HTF flows through the heat exchanger ($\dot{m}_{v1} = \dot{m}_{v3}$) and returns to the TES tanks with a higher temperature. Each TES tank receives the half of \dot{m}_{v3} as it can be observed in the bottom of Figure 6.40.

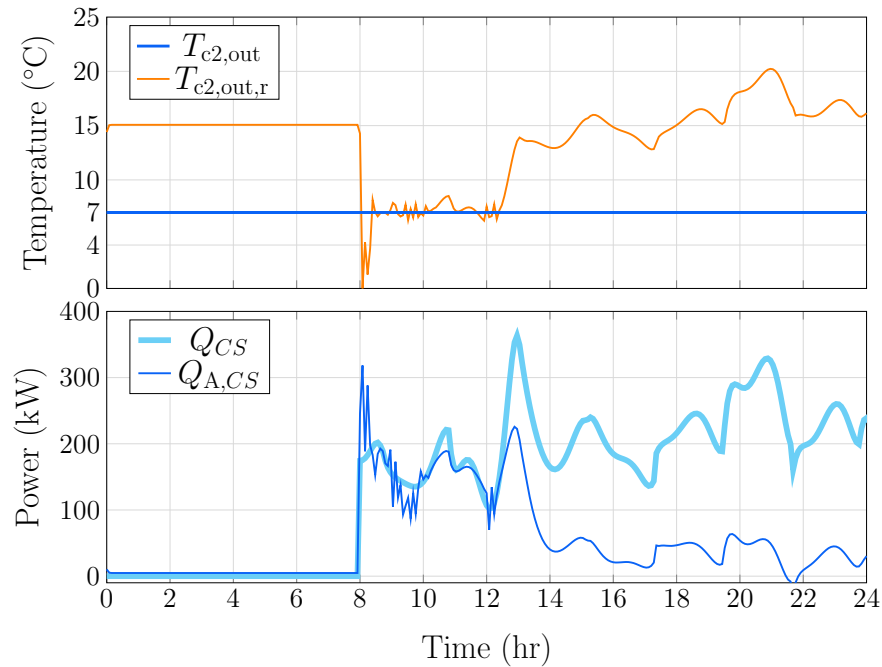


Figure 6.39: Output temperature of the secondary circuit of the heat exchanger (top) and thermal load injected and cooling power transferred by heat exchanger (bottom).

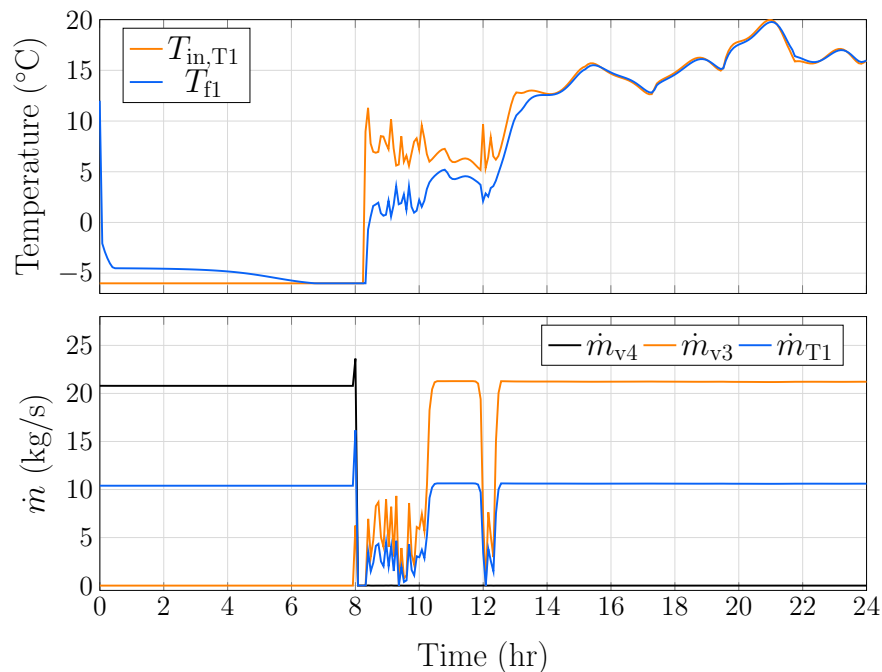


Figure 6.40: Input and output temperatures of TES tank 1 (top) and mass flow rates during charging and discharging modes (bottom).

Figure 6.41 shows the temperatures of the ice nodes and the SoC of one TES tank. The method proposed in Chapter 4 provides information of the SoC, which agrees with the thermal behaviour of the storage tank. The limits of SoC are 0% and 100%, which are reached when the T_{fi} is equal to $T_{in,T1}$.

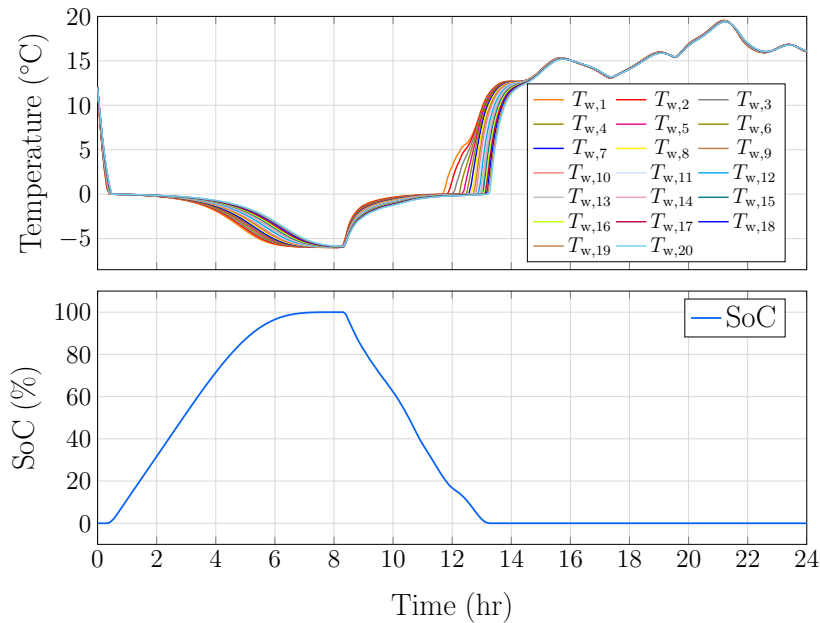


Figure 6.41: Ice nodes temperatures (top) and SoC (bottom) of one ice tank-based TES model.

The heat transferred to one TES tank is shown in Figure 6.42. During the charging process, the compressor chiller provides $E_{ch} = 335$ kWh. Each TES tank supplies a total energy of $E_{dch} = 330$ kWh when it is discharged. The fluctuations in values of the power presented afterwards the discharging process are due to only sensible thermal energy.

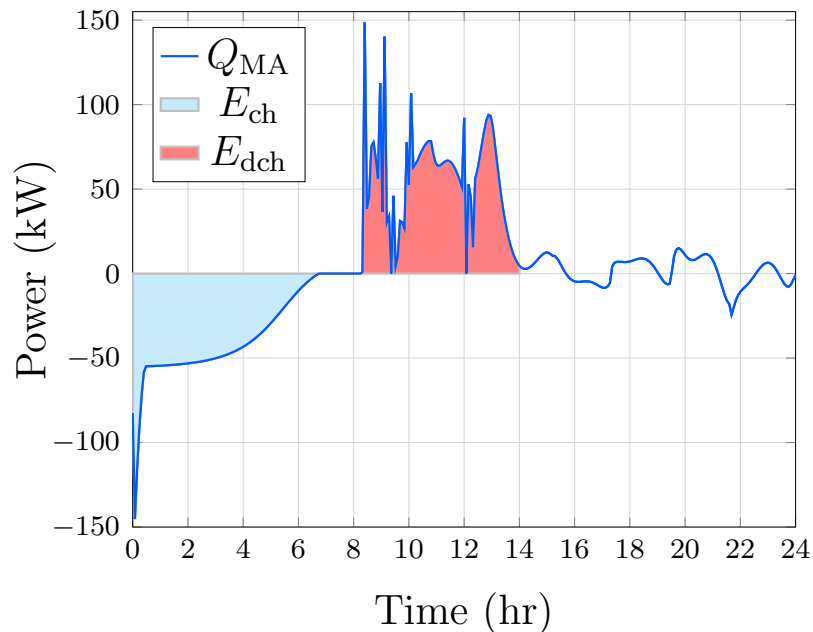


Figure 6.42: Absorbed and released cooling power of one TES tank during the operation of the cooling energy centre.

Cold supplied by TES tanks and compressor chiller

A second scenario is simulated where cold is supplied by the TES tanks and the compressor chiller. The mass flow rate from the heat exchanger (\dot{m}_{v1}) is split into the bypass (\dot{m}_{v2}) and the TES tanks (\dot{m}_{v3}). The streams are mixed after the fluid crosses the tanks. Then, a mass flow rate from the chiller \dot{m}_{ch} at 3°C is added to be supplied to the heat exchanger. This configuration offers more cold HTF to meet the cooling loads. Figure 6.43 shows the performance of the temperature controller. Although high peaks are presented, a better response is obtained compared with the previous scenario. The output temperature of the secondary circuit ($T_{c2,out,r}$) is close to the reference. Therefore, the thermal load is nearly met with the use of the compressor chiller.

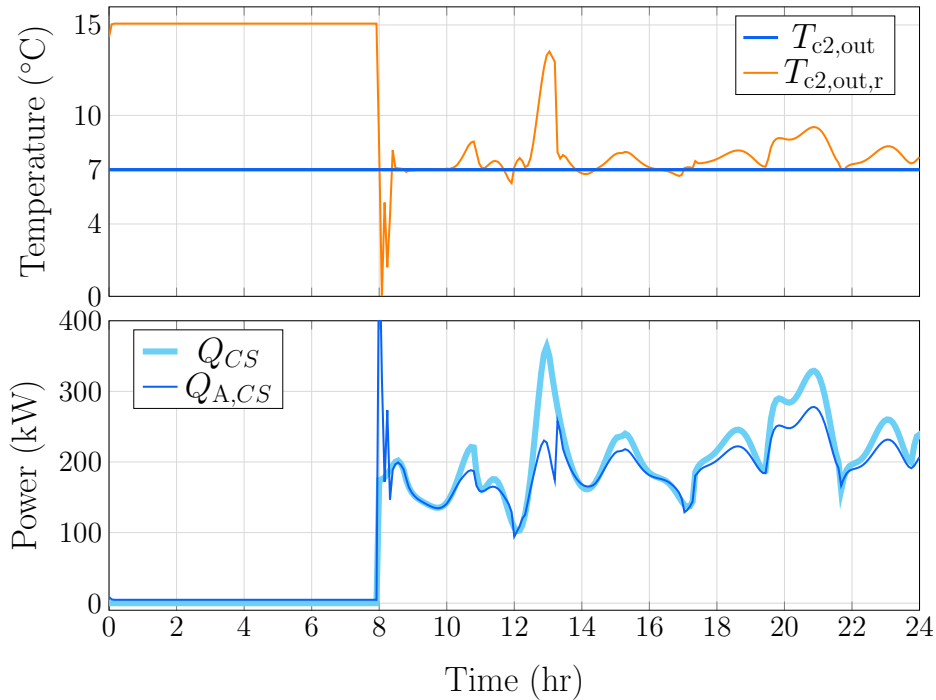


Figure 6.43: Output temperature of the secondary circuit (top), and the thermal load comparison with the heat transferred in the heat exchanger using the compressor chiller (bottom).

Figure 6.44 shows the behaviour of the mass flow rates throughout the cooling energy centre. The TES tanks are charged with a constant mass flow rate (\dot{m}_{ch}) at -6°C . Each TES tank receives half of this flow (\dot{m}_{T1}). When the discharging process starts, the compressor chiller increases the temperature of the HTF to 3°C . Then, valve 1 is open to supply the cold HTF to the heat exchanger (\dot{m}_{v1}). During this stage, the HTF is still split through the by-pass of valve 2 ($\dot{m}_{v2} = \dot{m}_{v3}$). Finally, when the TES tanks are empty, \dot{m}_{v3} is reduced to 1 kg/s and the rest of the fluid goes to the by-pass (\dot{m}_{v2}).

Figure 6.45 shows the temperature of the ice nodes and the SoC of one TES tank. The empty and full states are achieved when the ice nodes temperatures reach 5.7°C and 0°C , respectively. These values are the limits of the phase change transition zone of the ice-water established in Chapter 4. Finally, Figure 6.45 shows the cooling power absorbed and released by one TES tank. The cooling power supplied by each TES tank is $E_{dch} = 320$ kWh. As it can be observed, the TES tanks supply cold HTF one extra hour compared to the previous scenario. However, the amount of \dot{m}_{v1} required for the heat exchanger considerably increases

with respect to the previous scenario. Therefore a deeper analysis is required to establish the best option within the cooling energy centre.

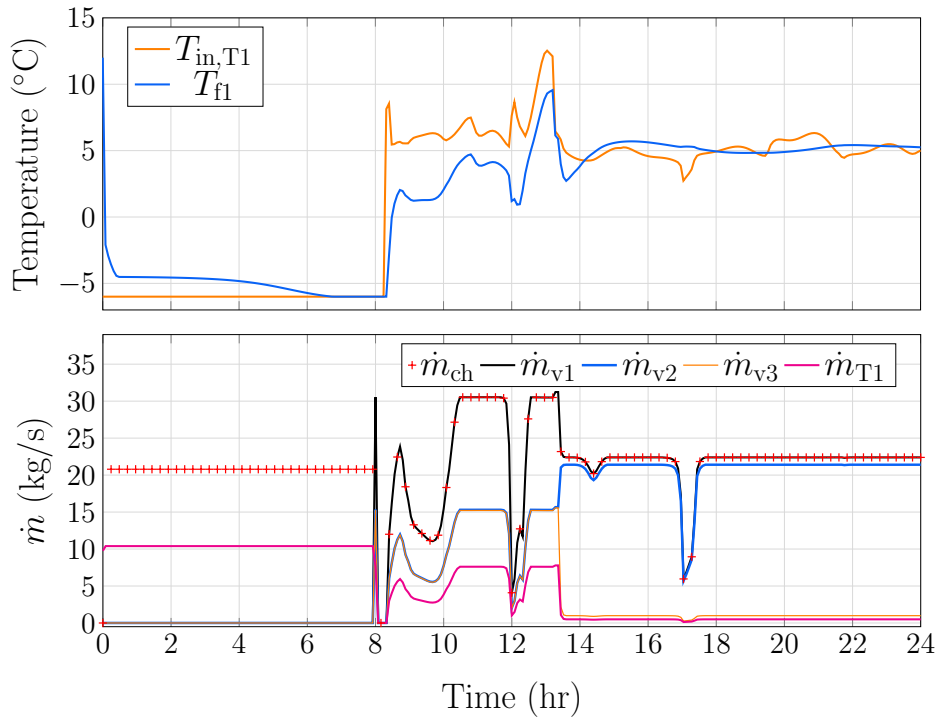


Figure 6.44: Input and output temperatures of TES tank 1 (top) and mass flow rates of the cooling energy centre (bottom).

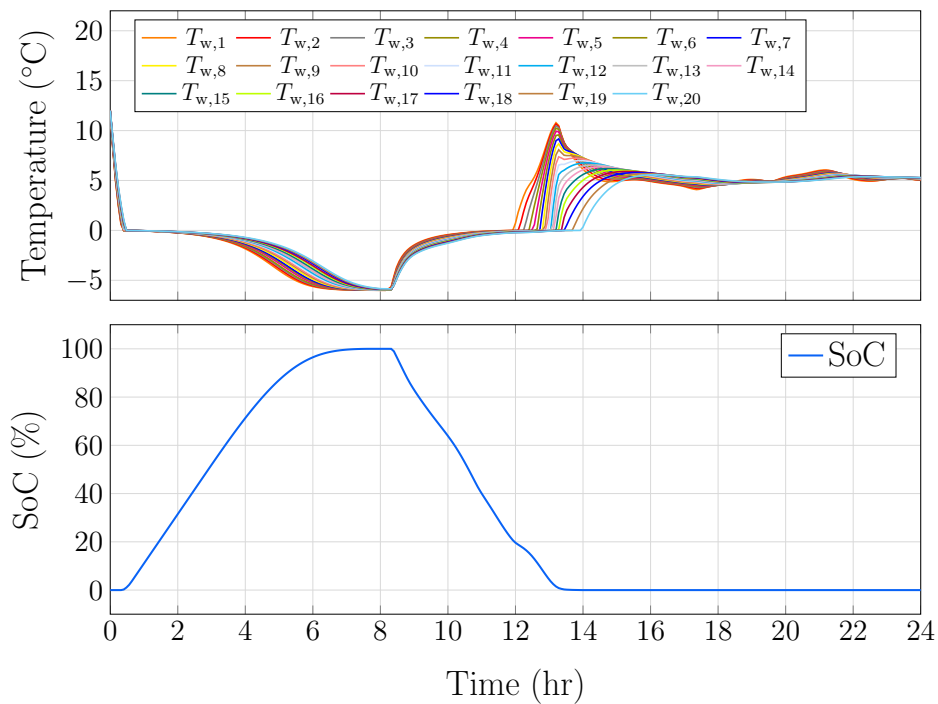


Figure 6.45: Ice nodes temperatures (top) and SoC (bottom) of one TES tank.

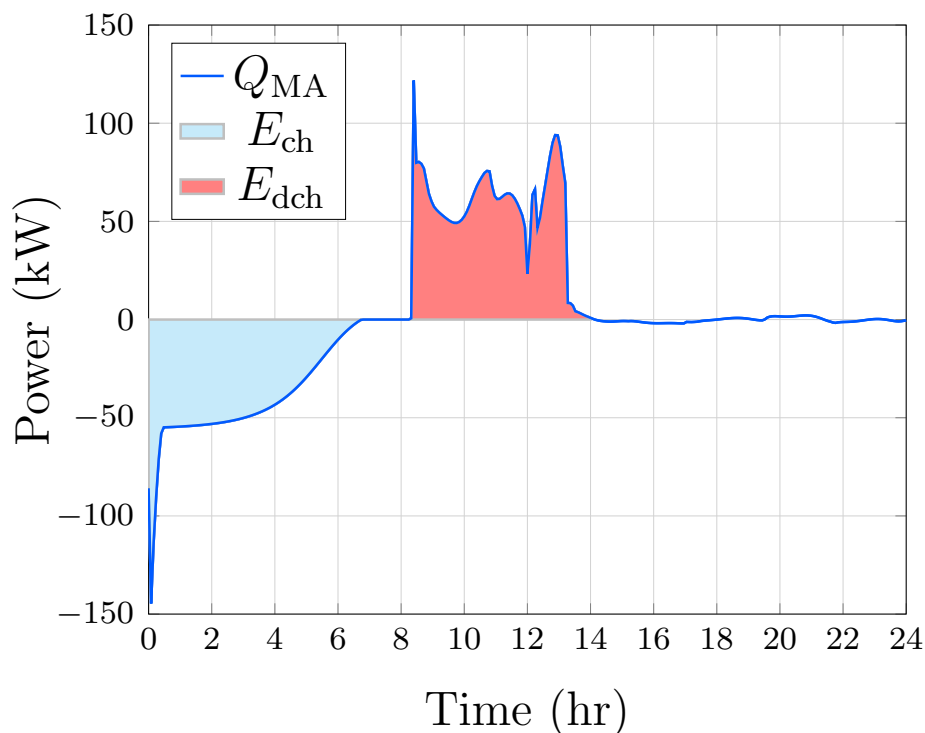


Figure 6.46: Absorbed and released cooling power of one TES tank during the operation of the cooling energy centre.

6.4 Summary

This chapter presents case studies of a DHS and an energy cooling centre. The performances of temperature and differential pressure controllers in a DHS are analysed in case study 1. The use of the 1-D dynamic model of latent TES in the analysis of an energy cooling centre is presented in case study 2.

Case study 1 describes the assessment of PI controllers for a DHS under typical heat demands conditions. The model of the DHS and the PI controllers were built in Apros. The temperature controllers in all DHS's substations and the differential pressure in the farthest substation present successful performances. Sensible TES is included, and its charging process is regulated with a PI controller, which achieves the period of charge established previously.

The 1-D thermal dynamic model of the latent TES is used to analyse an energy centre's performance. Two models of an ice tank-based TES are implemented in MATLAB/Simulink. They are linked to an energy cooling centred built-in Apros via OPC communication protocol. Two scenarios are evaluated: the only use of the TES tanks and the sharing thermal load between TES tanks and the compressor chiller. The SoC calculation method proposed in Chapter 4 is implemented. The phase state (growth and depletion ice) of the TES's water-ice described by the internal temperatures matches with the calculated SoC.

6.5 References

- [1] "HRS Hevac Gasketed Plate Heat Exchangers." <https://www.hrshevac.co.uk/?products=hrs-hevac-gasketed-plate-heat-exchanger>. Accessed: 2021-03-10.

- [2] S. Frederiksen and S. Werner, *District Heating and Cooling*. Studentlitteratur AB, 2013. Google-Books-ID: vH5zngEACAAJ.
- [3] “opc fundation.” <https://opcfoundation.org/>. Accessed: 2021-03-10.
- [4] “Calmac - thermal storage.” <http://www.calmac.com/>. Accessed: 2021-03-10.

Chapter 7

Conclusions

7.1 Conclusions

Dynamic modelling approaches for components of a DHCS were developed to describe their thermal and hydraulic behaviours. The mathematical models of the main components were obtained and classical control theory used for the control system design. A literature review in the modelling of DHCSs was presented in Chapter 2 to identify the gaps bridged in this research. Chapter 3 presented the explanation of the developed modelling approaches. The mathematical model of a pipe network, heat exchangers, TES tanks and a single house (*i.e.*, a thermal load) were described in Chapter 4. Classical PI controllers were designed for critical variables in the operation of DHCSs in Chapter 5. Two case studies were presented in Chapter 6 where controllers for temperature and differential pressure variables were assessed. In addition, the use of latent heat-based TES tanks to support a cooling energy centre was described. Key achievements and conclusions are discussed in the following paragraphs.

Dynamic modelling approaches for thermal and hydraulic behaviours of DHCSs

The dynamic modelling approaches for thermal and hydraulic behaviour of DHCS's components were developed in Chapter 3. The modelling procedures have been framed in step sequences to facilitate their implementation. Moreover, basic examples were presented to exemplify their use. Besides, the electrical to thermal analogy for building dynamic modelling was explained.

Both dynamic modelling approaches allow developing models of DHCS's components to carry out dynamic analyses. They are based on physics principles allowing a better understanding of the dynamic interactions of key variables in the thermal and hydraulic behaviours of a DHCS in a transparent manner. Furthermore, the 1-D approach obtained under modelling assumptions significantly reduces the models' complexity without affecting their accuracy. This was demonstrated in Chapter 4, through the comparison of simulation results against results obtained using commercial software and experimental data provided in articles found in the open literature.

ODEs describe the mathematical models that are obtained employing the modelling approaches. Although these ODEs may be non-linear, they can be coded and solved using any software that has an ODE solver. This is of importance, as it implies that the models are portable and can be implemented on different platforms. The simplicity of the developed 1-D modelling approaches compared with 2-D or 3-D models make them the better option for

the analysis of large and complex DHCSs. Regarding their high accuracy obtained, it can be concluded that it relies in the dynamic computation of critical parameters of the system behaviour such as heat transfer coefficients, frictional factors or head losses. Additionally, the thermophysical properties of the materials involved in the heat transfer process are considered as temperature dependent, which captures the real dynamic behaviour of these properties (*e.g.*, density, specific heat, viscosity).

On the one hand, the dynamic thermal modelling approach uses a stratification/discretisation method to obtain the thermal model of a system. It was demonstrated that with a higher number of nodes a better accuracy is obtained. Nevertheless, there is a limit where the increment of nodes does not significantly improve the model accuracy. There is no rule of thumb for the specification of this number. However, there is a trade off between the computation time and the desired accuracy. For instance, thirty nodes are enough for the heat exchanger models. Nevertheless, a model with only three nodes may be enough for the control design process, as demonstrated in Chapter 5.

On the other hand, the dynamic hydraulic modelling approach has shown that iterative methods are not necessary to obtain the solution of a complex network using steady-state approaches. The hydraulic conditions can be solved through well established dynamic models described through ODEs and system parameters such as pipe's absolute roughness, pump's volumetric flow-head curves or valve's flow coefficient. The electrical to hydraulic analogy significantly simplifies the modelling process, allowing the use of Kirchhoff's laws to solve the hydraulic circuit defined by the pipe network configuration.

Apart from their accuracy, one more advantage of the modelling approach followed in this work is its suitability for control system design. Unlike the steady-state approach, models described through ODEs are adequate to obtain mathematical representations suitable for control. For instance, state-space representations or transfer functions were obtained applying a linearisation method over the non-linear models in Chapter 5. Thus, the design of feedback controllers based on the dynamic behaviour of the system is achieved.

The main advantages of the modelling approaches are their simplicity, accuracy, suitability for control purposes, and portability to be implemented in different programming languages or platforms. On the other hand, the main drawback is the detailed information of the modelled system required to feed the mathematical models. This information is commonly unavailable or incomplete. Overall, the developed modelling approaches offer a good alternative for the dynamic modelling of the DHCS's components. The hydraulic and thermal behaviours are accurately captured through mathematical equations, enabling the analysis of complex DHCSs where variations of operating conditions can be captured, and their effects on each component may be analysed. Moreover, the suitability of dynamic models for control design is a powerful advantage to improve the DHCS's performance.

Dynamic models of DHCS's components

The 1-D dynamic models of a pipe network, heat exchangers, TES tanks and a single house have been developed in Chapter 4, using the dynamic modelling approaches presented in Chapter 3. ODEs describe the hydraulic and thermal behaviour of these DHCS's components. They are implemented in MATLAB/Simulink and solved through s-functions. The models are verified using Apros or experimental data reported in the literature. These verifications

provide confidence in the modelling methodology.

Case study 2 in Chapter 6 demonstrates the implementation of 1-D thermal dynamic model of a latent TES tank for the analysis of a cooling energy centre. Co-simulations between MATLAB/Simulink and Apros were carried out to analyse the cooling supply process using two latent TES tanks and one compressor chiller; charging and discharging processes are included in the analysis. The use of s-functions in MATLAB/Simulink simplifies the implementation process of the TES models. The co-simulation with Apros using the OPC communication protocol showed good synchronization of solver engines .

Chapter 4 presents the development of comprehensive dynamic models of the main DHCS's components. With these, it has been possible to conduct an assessment of different operating conditions, where physics principles were considered. The dynamic description of temperature, pressure and mass flow rate presented in the DHCS given by the developed 1-D models allows obtaining a better understanding of their operational characteristics. The pipe, valve and pump of a DHCS were dynamically modelled considering fluid mechanics principles and their real characteristics such as volumetric-head curves or relative roughness. The most critical model parameters usually neglected in the literature due to their complexity have been here, instead, described in detail: friction factor and loss coefficients. The use of these models to solve a large pipe network configuration has been demonstrated. Pressure and mean velocity, which can be converted to mass flow rate, are obtained successfully, solving non-linear differential equations. Thus, different operating conditions, such as valve opening and pump's speed variations, can be studied by implementing these models. Overall, the confidence of the hydraulic dynamic models and the simplicity of their implementation allow to go further in the modelling of more complex pipe networks.

Concerning the thermal side, the dynamic models of the most common heat exchangers in DHCS have been developed: flat plate and shell-and-tube. The energy balance implementation in a heat exchanger model divided into many nodes yields a set of non-linear differential equations describing the temperature of the heat exchanger fluids in each node. The models with different number of nodes were assessed showing that the increment of nodes increases the model's accuracy. Nevertheless, there is no significant change if this number increases beyond 30. Therefore, it is concluded that a heat exchanger represented by 30 nodes is adequate to render high accuracy. The heat transfer process is dynamically captured in the models through the accurate calculation of the overall heat transfer coefficient, which in turn considers the internal structure of the heat exchangers and the thermophysical properties of the fluids involved in the heat transfer. This parameter has often been overlooked or considered static in steady-state and even in some dynamic models. The transparent manner to obtain this fundamental parameter of the heat exchanger operation gives a physical insight into the energy supply process in the DHCSs. The parallel and counter flow configurations of each type of heat exchanger were modelled. The more efficient performance in terms of the amount of heat transferred of the counterflow configuration has been demonstrated.

Continuing with the thermal models, sensible and latent TES tanks have been modelled dynamically. Similar to the heat exchanger models, 1-D thermal dynamic models of a TES were obtained employing the modelling approach developed in Chapter 4. A water tank-based TES 1-D model has been verified using Apros. The 1-D dynamic models of two latent TES tanks for heating and cooling were verified against experimental data. The agreement between simulation for both types of TES tanks gives confidence in the models.

The water tank-based TES model was divided into 5 nodes (layers), resembling the practical monitoring of a real TES, which usually has 5 temperature sensors located through the tank's height. Thus, only five non-linear differential equations are sufficient to describe the thermal behaviour. The solution of those equations provides the values of the temperatures for each layer. It was shown that this number of internal temperatures is sufficient to calculate the energy stored with enough accuracy. This was concluded by comparing the models with 5, 20 and 50 layers, where a slight difference of the total internal energy of the TES was shown. Thus, discharging and charging process can be simulated only considering the contribution of the hot or cold mass flow rate energy injected into the TES.

Latent types of TES tanks were assessed through the modelling of two TES tanks for heating and cooling applications. The fundamental thermophysical property of PCM used by the latent TES was dynamically included in the modelling process, namely the latent heat value. Usually, this property has been considered as a total amount without a clear description of its value during the phase change. In this research, this property was described as a PDF relating the PCM temperature and its specific heat value. This curve may be obtained from the enthalpy curve of the PCM. Thus, the PCM temperature when it is changing from liquid to solid and vice-versa is known at any moment. Although the mass fraction (*i.e.*, the amount of solid and liquid) during the phase change is neglected, this function provides an accurate value of the specific heat at any moment of the simulation. This was demonstrated by the good agreement of the simulation and experimental data.

A comprehensive explanation of the enthalpy-specific heat relation of the PCM properties is given in Chapter 4. In fact, this proposed curve of the specific heat helps developing a novel and simple method to compute the SoC of the TES using the PCM temperatures. The costly installation of internal temperature sensors in TES tanks has forced manufacturers to use indirect and inaccurate monitoring of the SoC. Therefore, applying the proposed method in a real system through a non-linear observer might help increase the efficiency of the charging process.

Finally, the dynamic thermal model of a single house was developed using electric to thermal analogy. The heat transfer process between ambient conditions and the internal house's space is modelled using conduction and the convection transfer processes. ODEs define the temperature of the house's walls and roof and their corresponding insulators. Although the system modelled is a simple house, this modelling approach can be applied for more complex buildings. The model can dynamically predict the house's internal temperature and describe the insulator's effects under ambient temperature variations.

The developed models can dynamically describe critical parameters. The accuracy of the models is based on this dynamic computation, which is based on heat transfer theory or linear momentum principles. Moreover, the internal structure and thermophysical properties of the medium involved such as water or PCMs are considered by the models, increasing their accuracy. Despite their high accuracy, their main drawback restricting their use is the need for detailed information of the system's parameters. For instance, the hydraulic diameter of a heat exchanger is a value that is usually not provided by manufacturers. The roughness of the pipe represents a similar problem. Due to the complex processes to determine this value, manufacturers do not give this information. Regarding the TES tanks, the enthalpy-specific heat curve of the PCM also has the same problem. Besides, some manufacturers of TES tanks do not offer enough information on the internal structure of the storage tank. For instance,

the dimension of the channels where the fluid flows may not be available. The disadvantage of the lack of parameter's information can be circumvented by adopting an estimation method. As it was done for the ice's enthalpy-specific heat curve ('trial and error' procedure using a comparison with experimental data), a similar process can be followed to estimate the systems' missing parameters.

Overall, the results of the verification process of the models indicate that the 1-D modelling approach of thermal and hydraulic behaviours is sufficiently accurate for modelling real elements of DHCS. Moreover, the suitability of dynamic models for control system design enables simple classical controllers to improve the performance of the DHCS, as it was addressed in Chapter 5 and 6.

Design and assessment of PI controllers for DHCSs

Classical PI controllers have been designed for a pipe network, flat plate heat exchanger, shell-and-tube heat exchanger, sensible TES tank and a single house in Chapter 5. Pressure and temperature have been controlled efficiently by achieving the desired parameters established in the control design process. MATLAB is used for the control design process. The differential pressure control performance for a pipe network, the temperature control for heat exchangers and the charging control of a sensible TES tank are assessed in Apros. Finally, the temperature control of a single house is verified only using MATLAB/Simulink.

The sequence of steps proposed in Appendix G facilitates the control design process of the PI controllers. The loop-shaping process is developed based on the equivalent second-order system with adequate desired parameters defined in the frequency domain. Although the PI controllers are designed for a linearised system based on a specific operating point, they show a successful performance under different operating conditions and subject to disturbances. Thus, it is demonstrated that simple PI controllers can keep the system conditions under the desired control reference. Regarding the accuracy required for the linear model used for control purposes, the control design process of the shell-and-tube heat exchanger illustrates that a simple 3 node division heat exchanger model is sufficient to obtain an accurate linearised model to design a PI controller that can be implemented in a more complex non-linear heat exchanger model with 30 nodes.

The helpful control design tool employed to simplify the high-order transfer functions obtained from the linearisation method simplifies and makes more understandable the control design process. A manageable second-order system facilitates a control design process compared with a higher-order system. For instance, the equations that relate the desired performance in the time domain to the frequency domain are well defined for a second-order system. Thus, the control design process becomes straightforward. These advantages are highlighted in the PI controller design process of the 10 nodes division model of the flat plate heat exchanger whose tenth-order transfer function considerably complicates the loop-shaping process. Likewise, the single house's interior temperature control is designed using a more tractable system defined by the equivalent second-order system of a transfer function set.

A more challenging assessment of the PI controllers was carried out in Chapter 6, where two case studies are defined to assess the designed controllers under typical operating conditions of a complete DHCS. For case study 1, a DHS is built in Apros. The temperature controllers for all substations and the differential pressure controller for the farthest substation are

designed. Although some disturbances are present, the PI controllers keep the temperature of the secondary circuit of the heat exchanger within acceptable tolerances. On the other hand, high disturbances caused by the mass flow rate variations in all substations were managed by a differential pressure controller located in the farthest substation. The pump's speed is regulated through the PI control action, keeping the pressure drop in the last DHS's substation within set point's tolerances. Thus, the hydraulic and temperature conditions of the DHS are ensured through simple PI controllers.

In case study 2, a cooling energy centre is built in Apros and two latent TES tanks are implemented in MATLAB/Simulink. Apart from addressing the feasibility of the latent TES tanks in a cooling centre, this case study also presents the performance of a temperature controller for chilling water. The PI controller can keep the reference of the cold water only if there is enough cold fluid provided by the compressor chiller or the latent heat TES tanks. A detailed analysis of the supply cold HTF coordinated with compressor chiller and TES tanks is necessary.

The main advantage of the control design procedure followed in this work is that the linearisation method allows using classic control design tools based on frequency domain. Thus, simple PI controllers are designed following well-established steps. Nevertheless, it is important to be aware that the robustness of these controllers is limited as the linear model of the system is obtained for a specific operating point.

Overall, it can be concluded that complex controllers are not required to achieve a good performance. Classical PI controllers are sufficient to regulate the differential pressure in a pipe network, the temperature in substations, the charging process of a TES tank, and the internal temperature of a house in the neighbourhood of the operating point used for the linearisation process.

7.2 Future work

The outcomes presented in this thesis can be served as the base of future extended work. Several options with high potential impacts are discussed in the following paragraphs.

Dynamic models of energy technologies and thermal loads

In this work the missing elements of the DHCS have been the different types of energy technologies and the heating and cooling device loads such as HVAC or building radiators. Undoubtedly, the development of dynamic models of all these components will complement this work. These models will allow simulating energy generation process and the use of heat and cold provided by the DHCS substations.

The versatility of the hydraulic and thermal dynamic modelling framework presented in this thesis will help to obtain the 1-D dynamic models of critical systems such as gas boilers and CHP units. Thus, a complete analysis of the DHCS may be achieved.

Dynamic model of the pipe network thermal behaviour

The dynamic model of the pipe network presented in Chapter 4 was restricted to the hydraulic behaviour. The convective and conductive heat transfer processes presented in the pipe network during the transportation of thermal energy are given by the ground (for underground

pipes) and ambient temperatures. Thus, only the ground and the pipe insulator's thermal conductivities are necessary to develop the dynamic model.

Although thermal losses were analysed through simulations in Apros, an accurate dynamic model of the thermal behaviour of the DHCS's pipes is still necessary. This model will allow studying how the potential thermal energy stored in the pipes due to their water volume may provide flexibility to the system. A detailed analysis of the thermal losses and the improvement of the insulator also may be carried out. Moreover, the thermal dynamic model of the pipe also will give the option to develop temperature controllers that use to reduce the thermal losses may be assessed.

Design and implementation of non-linear observer for latent TES tank's SoC

The dynamic model of the latent TES tanks provided an accurate description of the heat transfer process between the HTF and the PCM. Nevertheless, a potential practical use is the development of non-linear observers capable of estimating the PCM's internal temperatures and the SoC only having information about the mass flow rate, input and output temperatures of the HTF. The observer should be based on the dynamic model developed in Chapter 4 which includes the specific heat curve of the PCM. Thus, the temperatures of the PCM can be predicted by the observer and used to compute the SoC.

The feasibility of the sensors implementation to monitor the HTF mass flow rate and temperatures and the current inadequate monitoring systems of SoC prompt the implementation of a better system to increase the efficiency of the charging and discharging process of the latent TES tanks. Thus, the non-linear observer rises as a potential solution for the accurate estimation of the SoC.

More in-depth analysis of TES usage within DHCS

The case studies presented in this thesis included the use of TES where the total discharge of the stored energy was not achieved due to significant changes in the supplied fluid temperature. The blending between the warm temperature of the partially discharged TES and the stream from the energy centre should guarantee an adequate temperature for the stream supplied to the customer.

The development of a temperature controller capable of mixing the remaining energy of the TES at warm temperature with the heat/cold from the energy source is necessary for an effective discharging process.

Appendices

Appendix A

MATLAB/Simulink s-functions

The use of MATLAB/Simulink s-functions to solve the stratified dynamic models of the DHCS's components is exemplified utilizing the system defined by equation 3.61. S-function block of MATLAB/Simulink allows the user to create his own block-function. Thus, the user function block are able to interact with the MATLAB/Simulink engine. The type of algorithms that can be solved in a s-function block include continuous system which are defined by ODEs. The components of the continuous system are illustrated in Figure A.1.

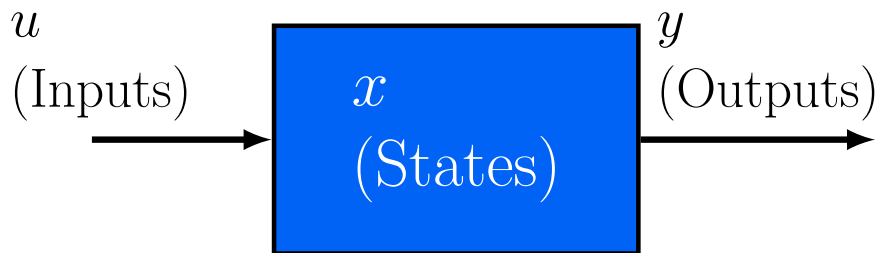


Figure A.1: Schematic of the continuous system.

The relationship between the continuous system elements and the simulation time can be expressed mathematically as

$$y = f_O(t, x, u) \quad (\text{A.1})$$

$$\dot{x} = f_d(t, x, u) \quad (\text{A.2})$$

Equations (A.1) and (A.2) can be defined in the s-function setup. Therefore, it is necessary

to convert the system (3.61) to a state space representation. This conversion yields

$$\begin{bmatrix} \dot{T}_{c,1} \\ \dot{T}_{h,1} \\ \vdots \\ \dot{T}_{c,i} \\ \dot{T}_{c,i} \\ \vdots \\ \dot{T}_{c,N} \\ \dot{T}_{c,N} \end{bmatrix} = \begin{bmatrix} \dot{x}_1 \\ \dot{x}_2 \\ \vdots \\ \dot{x}_i \\ \dot{x}_{i+1} \\ \vdots \\ \dot{x}_{2N-1} \\ \dot{x}_{2N} \end{bmatrix} = \begin{bmatrix} \frac{\dot{m}_c c_{p,c} (T_{c,\text{in}} - x_1) + UA (x_2 - x_1)}{\rho_c V c_{p,c}} \\ \frac{\dot{m}_h c_{p,h} (T_{h,\text{in}} - x_2) + UA (x_1 - x_2)}{\rho_h V c_{p,h}} \\ \vdots \\ \frac{\dot{m}_c c_{p,c} (x_{i-2} - x_i) + UA (x_{i+1} - x_i)}{\rho_c V c_{p,c}} \\ \frac{\dot{m}_h c_{p,h} (x_{i-1} - x_{i+2}) + UA (x_i - x_{i+1})}{\rho_h V c_{p,h}} \\ \vdots \\ \frac{\dot{m}_c c_{p,c} (x_{2N-3} - x_{2N-1}) + UA (x_{2N} - x_{2N-1})}{\rho_c V c_{p,c}} \\ \frac{\dot{m}_h c_{p,h} (x_{2N-2} - x_{2N}) + UA (x_{2N-1} - x_{2N})}{\rho_h V c_{p,h}} \end{bmatrix} \quad (\text{A.3})$$

As it can be observed, the evens and odds states are the cold and hot stream temperatures, respectively. Then, the system defined by (A.3) can be solved implementing the stiff ODEs concept which is suitable for the s-function block. It simplifies the code of the ODEs given by the system stratification in two lines which expresses the sequence of the state variables. The next pseudocode illustrates the employment of stiff ODEs for the system (A.3) where the ODEs from the state variable \dot{x}_3 to \dot{x}_N are defined as

Discretisation 1

- 1: $x(1) = [\dot{m}_c c_{p,c} (T_{c,\text{in}} - x(1)) + UA (x(2) - x(1))] / [\rho_c V c_{p,c}]$
 - 2: $x(2) = [\dot{m}_h c_{p,h} (T_{h,\text{in}} - x(2)) + UA (x(1) - x(2))] / [\rho_h V c_{p,h}]$
 - 3: $i = 3 : 2 : N$
 - 4: $x(i) = [\dot{m}_c c_{p,c} (x(i-2) - x(i)) + UA (x(i+1) - x(i))] / [\rho_c V c_{p,c}]$
 - 5: $x(i+1) = [\dot{m}_h c_{p,h} (x(i-1) - x(i+2)) + UA (x(i) - x(i+1))] / [\rho_h V c_{p,h}]$
-

The system parameters such as volume and heat transfer area (HEX), the thermophysical properties of the water (W) and the initial conditions (IC) of the state variables are given as arguments of the function. Inputs (u) and outputs (sys) should be define to connect the s-function block to other function block in the MATLAB/Simulink environment. For the system ((A.3)) the inputs are the mass flow rate and temperatures of the streams:

$$\begin{aligned} u(1) &= \dot{m}_c, \\ u(2) &= T_{c,\text{in}}, \\ u(3) &= \dot{m}_h, \\ u(4) &= T_{h,\text{in}}. \end{aligned} \quad (\text{A.4})$$

The temperature dependency of the themophysical properties is obtained by employing the MATLAB function for look-up tables called *interp1*. The computation of U is defined as an external function which is called in each simulation step.

The code of the s-function called *system1* is following shown. The setup parts required for the s-function are defined: initialization, derivatives, updates, outputs and termination.

```

function [sys,x0,str,ts,simStateCompliance]=system1(t,x,u,flag,IC,N,W,HEx)
switch flag
% INITIALIZATION
5 case 0
    [sys,x0,str,ts,simStateCompliance] = mdlInitializeSizes(IC,N);
    %IC are the initial conditions of all state variables
    %N is the number of control volumes defined by the stratification process
    % DERIVATIVES
10 case 1
    sys = mdlDerivatives(t,x,u,N,W,HEx);
    % UPDATE AND TERMINATE
    case {2,9}
        sys = []; % do nothing
15 % OUTPUT
    case 3
        sys = mdlOutputs(t,x,N);
    otherwise
        DAStudio.error('Simulink:blocks:unhandledFlag', num2str(flag));
20 end
function [sys,x0,str,ts,simStateCompliance] = mdlInitializeSizes(IC,N)

    sizes = simsizes;
    sizes.NumContStates = N*2;
25 sizes.NumDiscStates = 0;
    sizes.NumOutputs = N*2;
    sizes.NumInputs = 4;
    sizes.DirFeedthrough = 0;
    sizes.NumSampleTimes = 1;
30
    sys = simsizes(sizes);
    str = [];
    x0 = ones(1,N*2)*IC(1);
    x0(2:2:end) = IC(2);
35 ts = [0 0]; % sample time: [period, offset]

    % speicfy that the simState for this s-function is same as the default
    simStateCompliance = 'DefaultSimState';
function sys = mdlDerivatives(t,x,u,N,W,HEx)
40 mf_c = u(1);
    T_c = u(2);
    mf_h = u(3);
    T_h = u(4);
    Nx = N*2;
45 xdot(1) = ((mf_c.*interp1(T,cp,x(1)).*(T_c-x(1)))+(A.*U.*(x(2)-x(1))))./
    (V.*interp1(T,cp,x(1)).*interp1(T,d,x(1)));
    xdot(2) = ((mf_h.*interp1(T,cp,x(2)).*(T_h-x(2)))+(A.*U.*(x(1)-x(2))))./
    (V.*interp1(T,cp,x(2)).*interp1(T,d,x(2)));
    i = 3:2:Nx;
50 xdot(i) = ((mf_c.*interp1(T,cp,x(i)).*(x(i-2)-x(i)))+(A.*U.*(x(i+1)-x(i))))./
    (V.*interp1(T,cp,x(i)).*interp1(T,d,x(i)));
    xdot(i+1) = ((mf_h.*interp1(T,cp,x(i+1)).*(x(i-1)-x(i+1)))+(A.*U.*(x(i)-x(i+1))))
    ./ (V.*interp1(T,cp,x(i+1)).*interp1(T,d,x(i+1)));
    sys = xdot;
55 function sys = mdlOutputs(t,x,N)
    sys = x;
    % end mdlOutputs

```


Appendix B

Conversion factor of valve's flow coefficient

The flow coefficient of a valve can be given in the English (C_v) and International System (SI) of units (K_v)¹. This appendix shows the dimensional analysis of the factor conversion from C_v to K_v .

For (SI) the units of flow coefficient of a valve are:

$$K_v \quad \left[\frac{\text{m}^3}{\text{hr}}, \text{bar} \right].$$

For the English system of units are:

$$C_v \quad \left[\frac{\text{gal}}{\text{min}}, \text{psi} \right]$$

The conversion factors of the units from English to International system of units and the time from min to hr are:

Table B.1: Conversion factors from English to International System.

Variable	English	IS
Volume	264.172, gal	m ³
Pressure	14.5038, psi	bar
Time	60, min	hr

Then, the dimensional analysis is given by

$$K_v \left[\frac{\text{m}^3}{\text{hr}}, \text{bar} \right] = C_v \left[\frac{\text{gal}}{\text{min} \sqrt{\frac{1}{\text{psi}}}} \right] \left[\frac{\text{m}^3}{264.172 \text{gal}} \right] \left[\frac{60 \text{min}}{\text{hr}} \right] \left[\sqrt{\frac{14.5038 \text{psi}}{\text{bar}}} \right] = 0.8651 \left[\frac{\text{m}^3}{\text{hr}}, \text{bar} \right] \tag{B.1}$$

¹bar is most used than Pa unit due to the large number of digits required to express pressure in Pa

Appendix C

Systems' parameters

C.1 Pump's head-volumetric curve and valve's flow coefficient of section 4.2.4

Table C.1: Points of flow-head curve of pump and position-flow coefficient curve of valve.

Pump			Valve			
Q_v (m ³ /h)	Q_v (m ³ /s)	h (m)	o_v (°)	C_v	o_v (%)	K_v
0	0	70.6820	10	4.4	0.1111	3.8064
25	0.0069	70.6022	20	17.1	0.2222	14.7932
50	0.0139	69.1369	30	45.6	0.3333	39.4486
75	0.0208	66.2861	40	84.2	0.4444	72.8414
100	0.0278	62.0498	50	139.2	0.5556	120.4219
125	0.0347	56.4279	60	258.6	0.6667	223.7149
150	0.0417	49.4205	70	422.4	0.7778	365.4182
175	0.0486	41.0276	80	709	0.8889	613.3559
200	0.0556	31.2491	90	845.9	1	731.7881

C.2 Pipe network of section 4.2.5

Table C.2: Parameters of pipes, valves and pump.

Variable	Unit	Value
Pipe, valve and pump diameters (D_k, D_{cv}, D_p)	m	0.11284
Pipe, valve and pump flow Area (A_k, A_{cv}, A_p)	m ²	0.01
Length pipe 1 (L_{k1})	m	500
Length pipe 2 (L_{k2})	m	1
Length pipe 3 (L_{k3})	m	500
Length pipe 4 (L_{k4})	m	300
Length pipe 5 (L_{k5})	m	5
Length pipe 6 (L_{k6})	m	300
Length pipe 7 (L_{k7})	m	150
Length pipe 8 (L_{k8})	m	1
Length pipe 9 (L_{k9})	m	150
Relative roughness (ε/D_k) of pipes 1,3,4,6,7,9	-	1×10^{-5}
Relative roughness (ε/D_k) of pipes 2,5,8	-	1×10^{-4}
Pump's nominal heat (h_p)	m	100
Pump's motor efficiency (η_m)	-	0.90

The total mass of fluid in the branches is computed using the volume of each component and the fluid density. The pump, valve and pipe volumes are shown in Table C.3.

Table C.3: Volumes of elements.

Element	Volume[m ³]	Element	Volume[m ³]
Pipe 1,3 (V_{k1}, V_{k3})	5	Pipe (V_{k2})	0.01
Pipe 4,6 (V_{k4}, V_{k6})	3	Pipe (V_{k5})	0.05
Pipe 7,9 (V_{k7}, V_{k9})	1.5	Pipe (V_{k8})	0.01
Pump (V_p)	0.01	Valve 1,2,3,4 ($V_{cv1}, V_{cv2}, V_{cv3}, V_{cv4}$)	0.01

The total mass of each branch is obtained by

$$m_{T1} = (V_p + V_{cv1} + V_{k1} + V_{cv2} + V_{k2} + V_{k3}) \rho = 10012\text{kg}, \quad (\text{C.1})$$

$$m_{T2} = (V_{cv1} + V_{cv2} + V_{k2} + V_{k4} + V_{k5} + V_{k6}) \rho = 6063\text{kg}, \quad (\text{C.2})$$

$$m_{T3} = (V_{cv2} + V_{cv3} + V_{k5} + V_{k7} + V_{k8} + V_{k9}) \rho = 3071\text{kg}, \quad (\text{C.3})$$

C.3 Flat plate heat exchanger of sections 4.3.1 and 5.2.2

Table C.4: Flat plate heat exchanger parameters of S600+ model.

Variable	Value	Units
gap g	3.1	mm
length plate l	1.5	m
Width plate W	0.6	m
Number of plates N_p	390	-
Cold volumetric capacity V_c	0.5441	m ³
Hot volumetric capacity V_h	0.5441	m ³
Transfer area A_{tf}	351	m ²
Hydraulic diameter D_h	6.2	mm
Cross sectional area A_c	0.3627	m ²
Plate thickness w_p	1	mm
Plate thermal conductivity k_p	16	W/m K

C.4 Shell-and-tube heat exchanger of section 4.3.1

Table C.5: Shell and tubes heat exchanger parameters.

Variable	Value	Units
Internal radius of tube r_i	0.0158	m
External radius of tube r_o	0.0188	m
Tubes length l_t	3	m
Shell length l_s	3	m
Number of tubes N_t	270	
Volumetric capacity (tubes) V_t	0.6353	m ³
Volumetric capacity (shell) V_s	0.6	m ³
Flow area A_f	0.2	m ²
Hydraulic diameter of tubes $D_{h,t}$	0.0316	m
Hydraulic diameter of shell $D_{h,s}$	0.0233	m
Thermal conductivity of tubes k_t	16	W/mK
Heat transfer area	80.4122	m ²

C.5 Water tank-based TES of section 4.4.1

Table C.6: Water tank parameters.

Variable	Value	Units
Radius r	1.8	m
Height h	10	m
Volumetric capacity V_T	101.78	m ³
Cross sectional area A	10.1788	m ²
Total lateral area $A_{tr,T}$	113.0973	m ²

C.6 Latent thermal energy storage tank of section 4.4.2

Table C.7: Parameters of PCM based TES tank for heating application.

Variable	Value	Units
Internal radius of pipe r_i	6.75	mm
External radius of pipe r_o	8.25	mm
PCM radius r_P	24.023	mm
Pipe length l_p	2.5	m
Number of pipes N_p	72	
Volumetric capacity (pipes) V_p	0.0258	m ³
Volumetric capacity (shell) ^a V_P	0.1862	m ³
Hydraulic diameter of tubes $D_{h,p}$	13.5	mm
Thermal conductivity of tubes k_t	50	W/mK
Heat transfer area of single pipe A_{tr}	0.106	m ²

^aThis volume is determined by the imaginary bounds proposed to define the control volumes.

C.7 Latent thermal energy storage tank of section 4.4.2

Table C.8: Parameters of single tube of ice tank model 1098C.

Variable	Value	Units
External radius r_o	7.9375	mm
Internal radius r_i	6.35	mm
Ice radius r_{ice}	22.9235	mm
Pipe length l_p	32.5581	m
Heat transfer area of single tube	1.6238	m ²
Volumetric capacity V_t	0.0041	m ³
Volumetric capacity (water) ^a V_w	0.0473	m ³
Thermal conductivity of tube k_t	0.33	W/mK
Thermal conductivity (water) ^b k_w	1.35	W/mK

^aThis volume is determined by the imaginary bounds proposed to define the control volumes.

^bThe value of this parameter is the average of thermal conductivities of the solid and liquid phase of the water which are approximated by 2.1 W/mK and 0.6 W/mK, respectively.

C.8 Material properties of single house of section 4.5.2

Table C.9: Thermophysical properties, thickness and area of house elements.

Material (Element)	k [W/mK]	c_p [J/kgK]	ρ [kg/m ³]	d [m]	A [m ²]
Aerated Concrete Block (Wall)	0.240	1000	750	0.2	435.95
Asbestos tiles (Roof)	0.550	837	1900	0.02	522.16
Glass (Windows)	0.700	837	2500	0.01	6
Cellulose fill IN13 (Wall Insulator)	0.039	1381	48	0.2	435.95
Mineral wool/fibre fill IN01 (Roof Insulator)	0.043	837	10	0.2	522.16

Table C.10: Equivalent resistances of house without insulator.

R	Value [°C/W]	R	Value [°C/W]	R	Value [°C/W]
R_1	[0.0023 0.0031]	R_2	[0.007 0.0140]	R_3	[0.0171 0.026]
R_4	[0.0706 0.1514]	R_5	[0.0012 0.0018]	R_6	[0.0051 0.0109]

Table C.11: Equivalent resistances of house with insulator.

R	Value [°C/W]	R	Value [°C/W]	R	Value [°C/W]
$R_{I,1}$	[0.0073 0.008]	$R_{I,2}$	0.0068	$R_{I,3}$	[0.007 0.014]
$R_{I,4}$	[0.0171 0.0260]	$R_{I,5}$	[0.0706 0.1514]	$R_{I,6}$	[0.0012 0.0018]
$R_{I,7}$	0.0045	$R_{I,8}$	[0.0095 0.0154]		

C.9 Shell-and-tube heat exchanger of section 5.2.3

Table C.12: Shell and tubes heat exchanger parameters.

Variable	Value	Units
Internal radius of tube r_i	0.010	m
External radius of tube r_o	0.013	m
Tubes length l_t	4	m
Shell length l_s	4	m
Number of tubes N_t	3000	
Volumetric capacity (tubes) V_t	3.76	m ³
Volumetric capacity (shell) V_s	0.8	m ³
Flow area A_f	0.2	m ²
Hydraulic diameter of tubes $D_{h,t}$	0.010	m
Hydraulic diameter of shell $D_{h,s}$	0.0032	m
Thermal conductivity of tubes k_t	16	W/mK
Heat transfer area	753.9822	m ²

Appendix D

Coefficient of the matrices of linearised heat exchanger model

Table D.1: List of coefficient of matrix **A** and **B**.

Coefficient	value	Coefficient	value	Coefficient	value	Coefficient	value
a_1	-0.7881	a_2	0.0601	a_3	0.0605	a_4	-0.4844
a_5	0.4239	a_6	0.7286	a_7	-0.7901	a_8	0.0615
a_9	0.0620	a_{10}	-0.4863	a_{11}	0.4244	a_{12}	0.7292
a_{13}	-0.7922	a_{14}	0.0630	a_{15}	0.0635	a_{16}	-0.4885
a_{17}	0.4250	a_{18}	0.7298	a_{19}	-0.7944	a_{20}	0.0646
a_{21}	0.0652	a_{22}	-0.4911	a_{23}	-0.4911	a_{24}	0.7304
a_{25}	-0.7968	a_{26}	0.0663	a_{27}	0.0670	a_{28}	-0.4935
a_{29}	0.4265	a_{30}	0.7312	a_{31}	-0.7994	a_{32}	0.0683
a_{33}	0.0689	a_{34}	-0.4963	a_{35}	0.4273	a_{36}	0.7320
a_{37}	-0.8024	a_{38}	0.0704	a_{39}	0.0712	a_{40}	-0.4996
a_{41}	0.4284	a_{42}	0.7328	a_{43}	-0.8056	a_{44}	0.0728
a_{45}	0.0737	a_{46}	-0.5033	a_{47}	0.4296	a_{48}	0.7338
a_{49}	-0.8088	a_{50}	0.0750	a_{51}	0.0759	a_{52}	-0.5068
a_{53}	0.4309	a_{54}	0.7348	a_{55}	-0.8123	a_{56}	0.0774
a_{57}	0.0785	a_{58}	-0.5110	b_1	0.0530	b_2	0.0572
b_3	0.0618	b_4	0.0670	b_5	0.0728	b_6	0.0793
b_7	0.0868	b_8	0.0953	b_9	0.1044	b_{10}	0.1149

Appendix E

Calculation of thermal resistance on shell-and-tube heat exchanger

For the verification of the shell and tube heat exchanger model, a different method to compute the thermal resistance is also included in the comparison between MATLAB and Apros models. Unlike, the equation (4.78) which is defined by the proper method of the heat transfer process through different layers. The computation of R_T is simplified only considering the external area of the tubes (A_{etr}) as

$$R_T = \frac{1}{A_{itr}U_{cv,t}} + \frac{1}{A_{etr}U_{cd}} + \frac{1}{A_{etr}U_{cv,s}}. \quad (E.1)$$

$$R_{T2} = \frac{1}{A_{etr}(U_{cv,t} + U_{cd} + U_{cv,s})} \quad (E.2)$$

the results of the Apros simulation are shown in Figure E.2, it includes the input temperatures and mass flow rate conditions. The subscript A stands for Apros results.

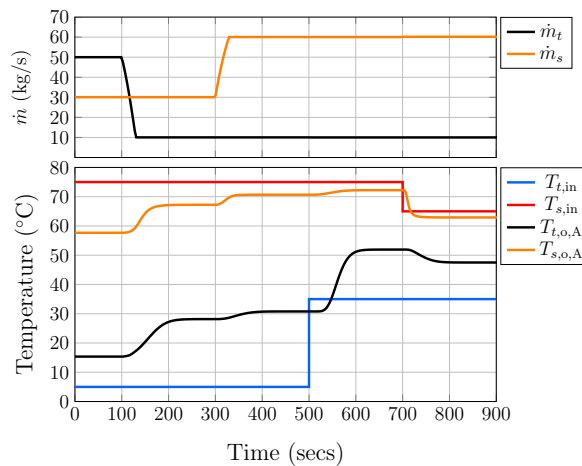


Figure E.1: Apros simulation of shell-and-tube with 10 nodes

Then, the same conditions are implemented in the built-in MATLAB/Simulink models. The simulation results are compared in Figure E.2. The subscripts M1 and M2 stands for the

models which uses the R_T and R_{T2} , respectively. The error between the developed model and the Apros element is reduced up to one degree in some temperature of the fluids. For instance the difference of the output temperature of the shell during the first 100 seconds is around 1 °C between Apros and M1 meanwhile the difference between M2 is 0 °C. Afterwards, the error starts to be reduced for both methods, nevertheless, the method 2 is still showing a smaller error as it is shown in the a zoom effect over the plots. The differences are quantified by the mean square error and shown in Table E.1.

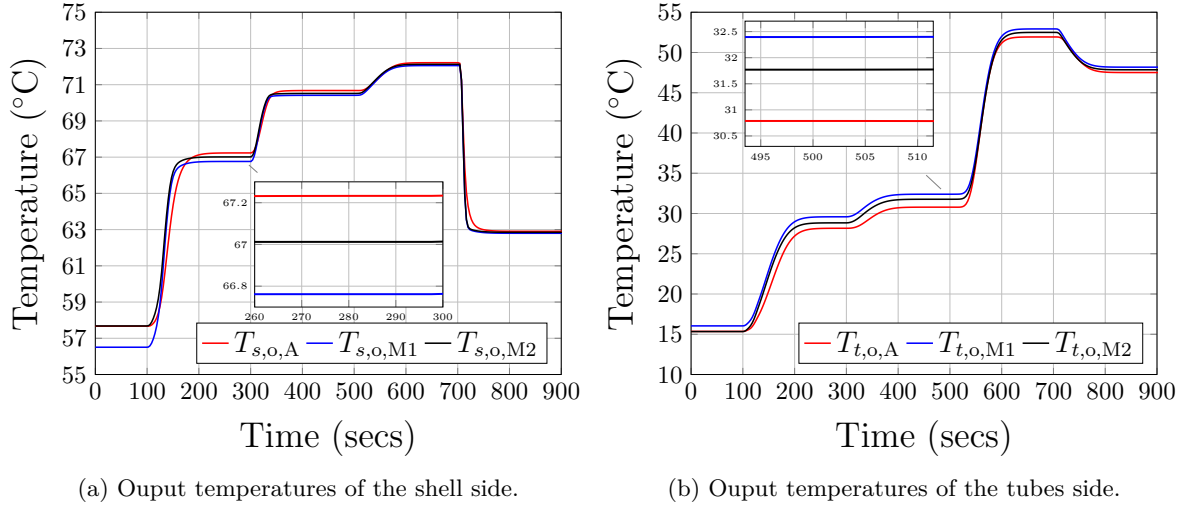


Figure E.2: Comparison simulation of the output temperatures of the built-in Apros system and the developed model using method 1 (M1) and 2 (M2) to compute the heat exchanged.

Table E.1: Mean square Errors of comparison between both methods and Apros simulation.

Method	Heat transfer equation	Error of shell side	Error of tubes side
1	$(T_s - T_t) / R_t$	1.6556	0.4196
2	$UA_{\text{ctr}} (T_s - T_t)$	0.5654	0.1878

Appendix F

Thermophysical properties of Glycol 34%

The thermophysical properties of the Glycol 34% fluid are given as function of temperature T . Polynomial function are used to define the density, thermal conductivity, dynamic viscosity and specific heat properties as

The density ρ [kg/m³]:

$$\rho = C_1T^4 + C_2T^3 + C_3T^2 + C_4T + C_5, \quad (\text{F.1})$$

where $C_1 = -1.42 \times 10^{-7}$, $C_2 = 3.66 \times 10^{-5}$, $C_3 = -0.0038$, $C_4 = -0.374$ and $C_5 = 1063.3$.

The thermal conductivity k [W/mK]:

$$k = C_6T^4 + C_7T^3 + C_8T^2 + C_9T + C_{10}, \quad (\text{F.2})$$

where $C_6 = 2.3674 \times 10^{-11}$, $C_7 = -3.1566 \times 10^{-10}$, $C_8 = -7.8598 \times 10^{-7}$, $C_9 = 1.9683 \times 10^{-4}$ and $C_{10} = 0.4662$.

The dynamic viscosity μ [N/sm²]:

$$\mu = C_{11}T^4 + C_{12}T^3 + C_{13}T^2 + C_{14}T + C_{15}, \quad (\text{F.3})$$

where $C_{11} = 2.4811 \times 10^{-10}$, $C_{12} = -5.9628 \times 10^{-8}$, $C_{13} = 5.166 \times 10^{-6}$, $C_{14} = -2.1234 \times 10^{-4}$ and $C_{15} = 0.0049$.

The specific heat c_p [J/kgK]:

$$c_p = C_{16}T^2 + C_{17}T + C_{18}, \quad (\text{F.4})$$

where $C_{16} = -5.9524 \times 10^{-4}$, $C_{17} = 2.7976$ and $C_{18} = 3564.3$.

Control design procedure

A system that needs to be controlled must comprise the minimum amount of devices or equipment necessary to accomplish the control function. For instance, the secondary circuit's output temperature in a heat exchanger is controlled by modifying the heat flow provided by a stream flowing in the primary circuit. To achieve this task, the mass flow rate should be regulated. A sensor measures the temperature to be used by the controller. A control signal is sent to change a valve opening to modify the fluid's mass flow rate in the primary circuit. Thus, the model of the system should include the dynamics of the valve and sensor. For the control design process, once the system has been identified, the desired performance should be established. These functional requirements must be determined based on the well-known system dynamics and reasonable system operating conditions [1].

Suitable mathematical models are thus required for the proper design of the controller. For instance, classical techniques such as loop-shaping analysis may not be possible if differential equations do not describe the system. These equations may be non-linear, which in turn require advanced control laws, such as robust control [2]. Nevertheless, linearisation methods can be implemented to obtain a linear model of the system allowing the use of classical control design tools. It is crucial to highlight that the linearised model is restricted to a specific operating point. Finally, it is necessary to analyse the controller performance when the system operates under different conditions or when disturbances are present. This analysis requires computer design tools to test the designed controllers using simulations. For this task, MATLAB is used due to its popularity and availability for system controls analysis. The steps of the control design process can be summarised as [1]

1. Establishing the desired system performance specifications.
2. Defining the mathematical model of the physical system.
3. A control theory design approach plus computer-aided-design tool such as MATLAB.
4. Performing a simulation of the designed feedback controller.
5. Implementing and testing of the controller in the actual system.

Following this set of steps and in agreement with the structure of this thesis, a control design process is proposed. Figure G.1 shows the sequence of the steps necessary to design the PI controllers presented in this Thesis.

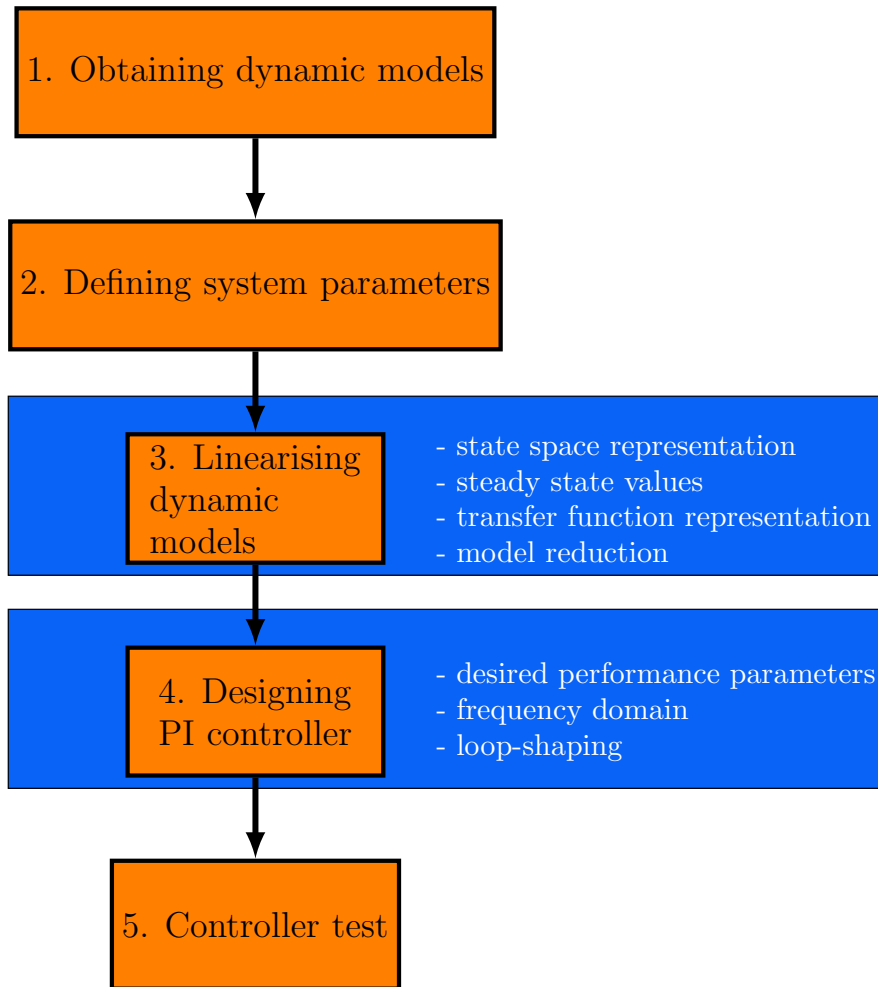


Figure G.1: Steps of the proposed control design process.

G.1 System linearisation

All models of the DHCS's elements developed in Chapter 4 are described by non-linear differential equations. For instance, the pump's dynamic models, valve and pipe imply quadratic terms of the system variables such as v^2 . These non-linearities do not allow to apply classical control design tools, which for simplicity require a linear time-invariant model. Nevertheless, the typical operation of a system may be around an operating point. In terms of control theory, this operational condition is called the equilibrium point [1, 2]. If the system operates around an equilibrium point, it is possible to obtain a linear system approximation of its non-linear behaviour. It is important to notice that this linear system may be equivalent to the non-linear system considering a limited operating range.

A DHCS operates under different operating conditions, which in turn are defined by specific system setups. For instance, precise values of differential pressure or temperatures set points are established in substations during specific operating points. This chapter addresses the performance of a designed PI controller for a specific operating point of DHCS's elements under disturbances and under an extended operating range.

The linearisation method used in this work is based on the expansion of the non-linear functions into a Taylor series around an operating point but keeping only the linear terms. Thus, to obtain a linear mathematical model for a non-linear system, we assume that the

G.1. System linearisation

variables deviate only slightly from the operating condition. Consider a system whose variables states are x , input u and output y . Then, the system can be defined by a non-linear state equation as

$$\dot{\mathbf{x}} = f(\mathbf{x}, u) \quad (\text{G.1})$$

Applying the Taylor series expansion method, the linearised state equation is given by

$$\Delta \dot{\mathbf{x}} = \begin{bmatrix} \frac{\partial f_1(x, u)}{\partial x_1} & \frac{\partial f_1(x, u)}{\partial x_2} & \dots & \frac{\partial f_1(x, u)}{\partial x_n} \\ \frac{\partial f_2(x, u)}{\partial x_1} & \frac{\partial f_2(x, u)}{\partial x_2} & \dots & \frac{\partial f_2(x, u)}{\partial x_n} \\ \vdots & \vdots & \ddots & \vdots \\ \frac{\partial f_n(x, u)}{\partial x_1} & \frac{\partial f_n(x, u)}{\partial x_2} & \dots & \frac{\partial f_n(x, u)}{\partial x_n} \end{bmatrix}_{x=x_0, u=u_0} [\Delta \mathbf{x}] + \begin{bmatrix} \frac{\partial f_1(x, u)}{\partial u} \\ \frac{\partial f_2(x, u)}{\partial u} \\ \vdots \\ \frac{\partial f_n(x, u)}{\partial u} \end{bmatrix}_{x=x_s, u=u_s} [\Delta u] \quad (\text{G.2})$$

where x_s and u_s are the states' values and input at the equilibrium point, namely steady-state values. It is important to notice that the system defined by equation (G.2) has a single input as the systems modelled in Chapter 4. Nevertheless, multiple-input multiple-output systems can be linearised by adding the PDEs of the outputs. The control design process presented in this chapter is restricted to single-input single-output systems. Matrix representation of the state-space linearised system once the steady-state values are evaluated is defined by

$$\begin{aligned} \Delta \dot{\mathbf{x}} &= \mathbf{A} \Delta \mathbf{x} + \mathbf{B} \Delta u \\ \Delta y &= \mathbf{C} \Delta \mathbf{x} + \mathbf{D} \Delta u \end{aligned} \quad (\text{G.3})$$

where matrix \mathbf{C} determines which of the states in \mathbf{x} defines the output of the system. For the sake of clarity, operator Δ is removed from the equation (G.3) and it is assumed that the linearisation method has been applied and the linear system is well-defined by \mathbf{x} . The direct transmission matrix \mathbf{D} is zero in the models because there is no direct feed-through in the system. Then, the state-space representation of the linear system is re-written as

$$\begin{aligned} \dot{\mathbf{x}} &= \mathbf{A} \mathbf{x} + \mathbf{B} u \\ y &= \mathbf{C} \mathbf{x} \end{aligned} \quad (\text{G.4})$$

The linearised system model requires the steady-state values of the system variables (states and input). Dynamic simulations of the non-linear models play an important role in obtaining these values. The dynamic models of the DHCS's elements provide a detailed description of each state of the system. Therefore, steady-state values can be obtained simulating the desired operating conditions. This process is done by 'trial and error' over the system in open loop without feedback control.

A state-space representation may be useful when each system state needs to be monitored or when modern controllers, such as state-space feedback, are designed. Moreover, stability or the analysis of the internal dynamics can be carried out with this representation. Although these type of studies are highly desirable, they are out of the scope of this thesis. However, the control design process needs a direct description of the system's input and output. Thus, the transfer function relating the input and the output is defined from the linearised system

by

$$\frac{Y(s)}{U(s)} = \mathbf{C}(s\mathbf{I} - \mathbf{A})^{-1} \mathbf{B} \quad (\text{G.5})$$

The steps explained so far are exemplified with an illustrative fictional non-linear system which does not represent a practical system. Let a system be defined by

$$\begin{aligned} \dot{x}_1 &= 0.1 \left[(u - x_1)^2 + x_2 - x_1 \right] \\ \dot{x}_2 &= 0.1 \left[(x_1 - x_2)^2 - x_4 \right] \\ \dot{x}_3 &= 0.1 (x_1 - 2x_3 - x_4) \\ \dot{x}_4 &= 0.1 (x_3^2 - x_4) \end{aligned} \quad (\text{G.6})$$

The linearisation method is used to obtain the state-space representation of the system defined by (G.6) as

$$\begin{bmatrix} \Delta \dot{x}_1 \\ \Delta \dot{x}_2 \\ \Delta \dot{x}_3 \\ \Delta \dot{x}_4 \end{bmatrix} = \begin{bmatrix} -0.2(u - x_1) & 0.1 & 0 & 0 \\ 0.2(x_1 - x_2) & -0.2(x_1 - x_2) & 0 & -0.1 \\ 0.2x_1 & 0 & -0.2 & -0.1 \\ 0 & 0 & 0.2x_3 & -0.1 \end{bmatrix} \begin{bmatrix} \Delta x_1 \\ \Delta x_2 \\ \Delta x_3 \\ \Delta x_4 \end{bmatrix} + \begin{bmatrix} 0.2(u - x_1) \\ 0 \\ 0 \\ 0 \end{bmatrix} [u] \quad (\text{G.7})$$

The steady-state values are obtained from the implementation of (G.6) in MATLAB/Simulink without feedback control. The operating point selected is $x_{s,2} = 1$. This condition is achieved when $u = 3.55$. The remaining steady-state values are: $x_1 = 2.378$, $x_3 = 1.885$ and $x_4 = 1.885$. Removing the operator Δ and evaluating the steady-state values, the state-space representation of the linear system is given by

$$\begin{aligned} \dot{\mathbf{x}} &= \begin{bmatrix} -0.3344 & 0.1 & 0 & 0 \\ 0.2756 & -0.2756 & 0 & -0.1 \\ 0.4756 & 0 & -0.2 & -0.1 \\ 0 & 0 & 0.1 & -0.1 \end{bmatrix} [\mathbf{x}] + \begin{bmatrix} 0.2344 \\ 0 \\ 0 \\ 0 \end{bmatrix} [u], \\ y &= \begin{bmatrix} 0 & 1 & 0 & 0 \end{bmatrix} [\mathbf{x}]. \end{aligned} \quad (\text{G.8})$$

Using equations (G.5) and (G.8), the following transfer function is obtained:

$$G(s) = \frac{0.0646s^2 + 0.01938s + 0.0008232}{s^4 + 0.91s^3 + 0.2776s^2 + 0.03768s + 0.002414} \quad (\text{G.9})$$

Equation (G.9) is used in the next steps of the proposed control design process.

G.2 PI controller design

The definition of the desired performance parameters of the feedback control scheme is required to carry out the PI controller design process. These specifications should be based

on the knowledge of the system dynamics. Experimental data or simulation results under operating conditions give an insight into the system behaviour. Thus, reasonable control design specifications can be defined within the operating range of the system. For instance, a controller that generates a high input to achieve a fast response in a real system may be unfeasible. Thus, it is crucial to notice that the priority is accuracy at steady-state operation rather than a fast transient response. Therefore, this step should be done considering the capabilities and restrictions of the system.

Usually, these desired performance parameters are given in the time-domain. Nevertheless, the frequency domain allows using powerful control design tools, such as the Bode diagram, to tune PI controllers based on the system's frequency response. The Bode diagram is comprised of two graphs: the magnitude plot in decibels [dB] and phase angle plot in degrees [°] of the sinusoidal response of a transfer function. The base of the graphs is the frequency [rad/s] in logarithm scale, which allows to analyse a wide range of frequencies within the same graph. The Bode diagram could be built from experimental data, where the transfer function of a system is determined by the shape of its magnitude and phase graphs. The Bode diagram also gives information about the time response of the system. For instance, the magnitude graph of a second-order system could show if it is under, critically or over-damped, which defines whether there is overshoot in the time response.

Hence, the conversion of the time domain performance parameters into the frequency domain is implemented within the design process. Although the response of feedback control systems is described by many parameters, typically the settling time and a zero or limited steady-state error are required [2]. Two specific parameters are used in the PI controllers designed in this chapter: settling time t_s [s], which is defined as the time required for the system to achieve the 95% of the reference and maximum overshoot o_s [%] that is the allowed peak of the system in its closed-loop step response. The latter guarantees the safety conditions of the system, avoiding high overshoots, that might cause system damage.

It is necessary to convert the design parameters from the time domain to the frequency domain. On one hand, t_s is related to the bandwidth of the system (ω_{bw}) [rad/s]. This parameter is the frequency at which the magnitude of the closed-loop frequency response is 3 dB below its zero frequency value. This relationship for a second-order system is given by

$$\omega_{bw} = \frac{3}{\zeta t_s} \quad (\text{G.10})$$

where ζ is a dimensionless parameter, called the damping ratio. For a second-order system, ω_{bw} is calculated by

$$\omega_{bw} = \omega_n \sqrt{1 - 2\zeta^2 + \sqrt{2 - 4\zeta^2 + 4\zeta^4}}, \quad (\text{G.11})$$

where ω_n [rad/s] is the natural frequency of the system. On the other hand, for a second-order system, o_s is related to the phase margin ϕ_m of the frequency response as

$$\phi_m = \text{atan} \left(\frac{2\zeta}{-2\zeta^2 + \sqrt{1 + 4\zeta^4}} \right), \quad (\text{G.12})$$

where ζ is obtained from

$$\zeta = \frac{-\log(o_v/100)}{\sqrt{\pi^2 + \log(o_v/100)^2}}, \quad (\text{G.13})$$

Thus, ϕ_m and ω_{bw} are the frequency domain parameters used to loop-shape the linearised system's frequency response to determine the gains of the PI controllers. It should be noticed that equations (G.10)-(G.13) are only valid for second-order systems. Therefore, it is necessary to define an equivalent system to carry out the loop-shaping using the discussed procedure. Afterwards, the designed PI controller may be tested in the original linearised system.

G.3 Second-order equivalent system

The linearisation of systems with several states yields high-order linear systems, making the loop-shaping process difficult. An equivalent second-order system of the linearised system must be defined to facilitate meeting the control design requirements. The standard form of a second-order system is given by

$$G_e(s) = \frac{A_1 \omega_n^2}{s^2 + 2\zeta \omega_n s + \omega_n^2}. \quad (\text{G.14})$$

The following values define the equivalent second-order system of (G.13): $\omega_n=0.42$ rad/s, $\zeta=0.25$ and $A_1=0.35$, as

$$G_{so}(s) = \frac{0.06174}{s^2 + 0.21s + 0.1764}. \quad (\text{G.15})$$

Figure G.2a shows the frequency and time responses of both systems.

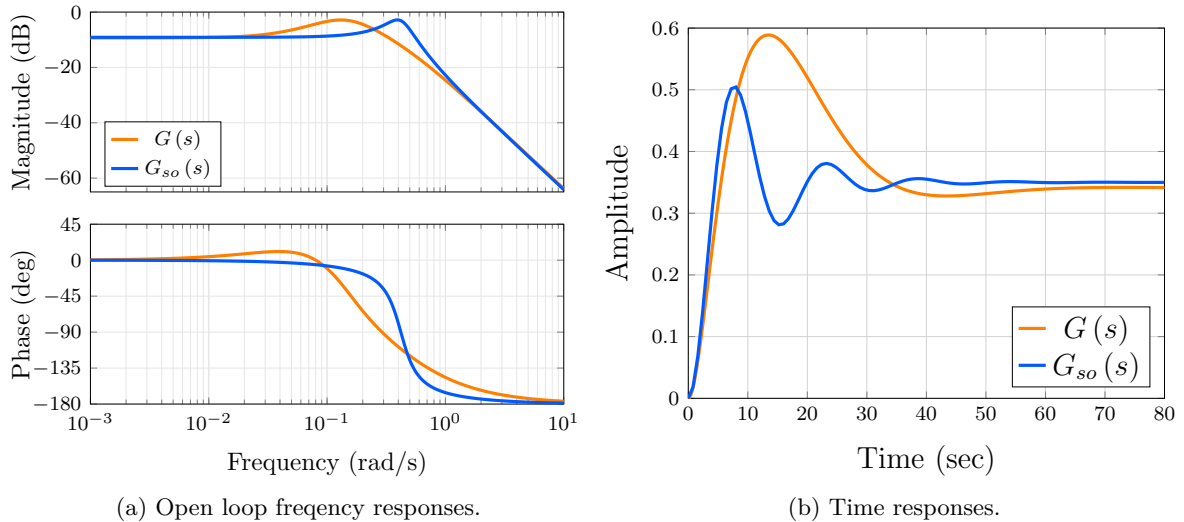


Figure G.2: (a) Open-loop Bode plots and (b) closed-loop step responses of the $G(s)$ and $G_{so}(s)$.

G.4 Loop-shaping

Loop-shaping using the Bode diagram is carried out over the equivalent system $G_{so}(s)$ and subsequently assessed in the original linear system $G(s)$. This consists of adding and modifying

the integral and proportional gains of the PI controller until the shape of the frequency response of the system achieves the bandwidth and the phase margin established previously, as shown in Fig. G.3a. The design parameters for the system are $t_s = 160$ seconds and $o_s = 1\%$. Using equations (G.10)-(G.13), the design specifications are translated to the frequency domain as a $\zeta = 0.8261$, ϕ_m of at least 70.9° and a minimum bandwidth $\omega_{bw} = 0.0271$ rad/s. The following PI controller meets these parameters:

$$C(s) = \frac{0.06358s + 0.0533}{s}, \quad (\text{G.16})$$

where the controller proportional k_p and integral k_i gains are 0.06358 and 0.0533, respectively.

Figure G.3a shows the open-loop frequency response of the system. A phase margin of 90° is achieved, which means that no overshoot will be presented in the closed-loop step response. A bandwidth ω_{bw} of 0.0265 rad/s is obtained, which is very close to the desired value: 0.0271 rad/s. The next step is to verify if the time domain desired parameters are reached. Figure G.3b shows the closed-loop step responses of the equivalent ($G_{so}(s)$) and of the original linear system ($G(s)$). As it can be observed, the settling time and overshoot conditions are achieved in both step responses.

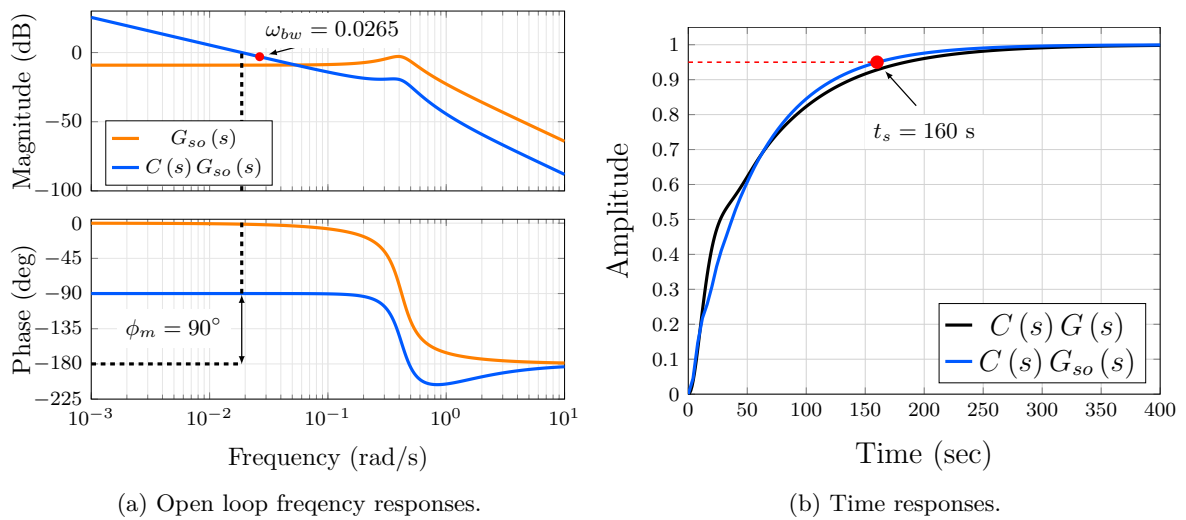


Figure G.3: (a) Open-loop Bode plots of $G_{so}(s)$ and $C(s)G_{so}(s)$. (b) Closed-loop step responses of the equivalent and original linear system.

G.5 Controller test

The final step is to assess the performance of the designed PI controller on the non-linear system defined by (G.6). The operating point chosen for the control design process is set up and disturbances are injected into the system as shown in Figure G.4a. Step changes in the reference are carried out, with results shown in Figure G.4b.

As it can be observed, the PI controller works successfully under disturbances and for different operating points even when it was specifically designed for $x_2 = 1$. The desired specification values for settling time and overshoot are achieved in all simulated conditions.

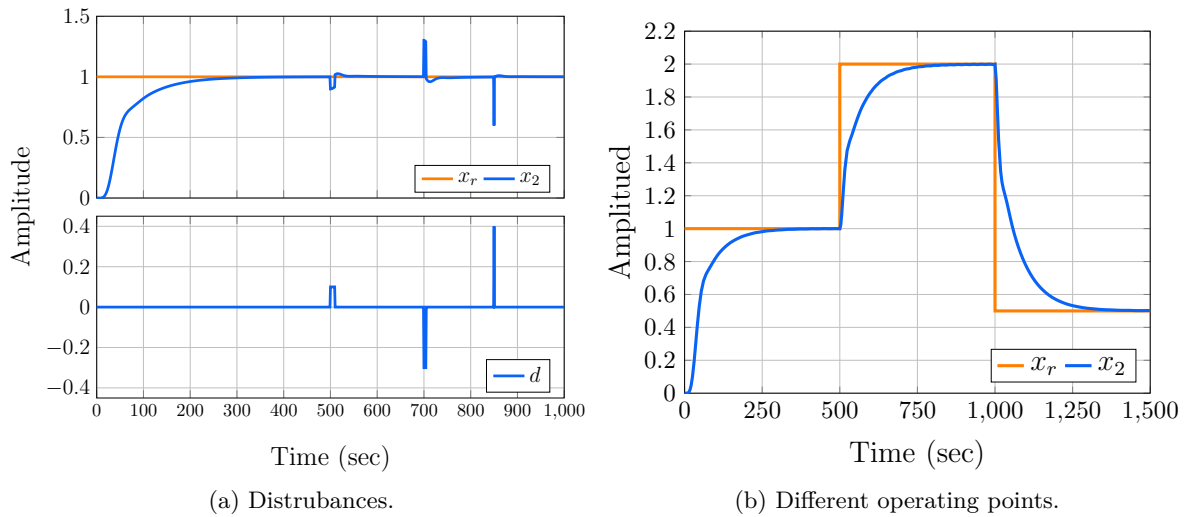


Figure G.4: Simulation results of the non-linear system controlled by the designed PI controller.

G.6 References

- [1] C. H. Houpis, S. N. Sheldon, and J. J. D'Azzo, *Linear Control System Analysis and Design: Fifth Edition, Revised and Expanded*. New York: CRC Press, 5th edition ed., Aug. 2003.
- [2] K. Ogata, *Modern Control Engineering*. Boston: Prentice Hall, 2009.

Appendix H

Design of PI controllers for case studies

H.1 Differential pressure control for DHS

The PI controller design for the differential pressure control scheme shown in Figure 6.8 is described in this appendix. The design control procedure presented in Appendix G is followed to obtain the gains of the PI controller (equation 6.2) used in case study 1. The modelling process of the complex pipe network shown in Figure 6.4 is a challenging task. Therefore, the pipe network model is simplified, considering only the long supply and return pipes of the farthest substation. Moreover, the pressure drop of the heat exchanger is so low that it is neglected. Thus, the simplified pipe network is shown in Figure H.1.

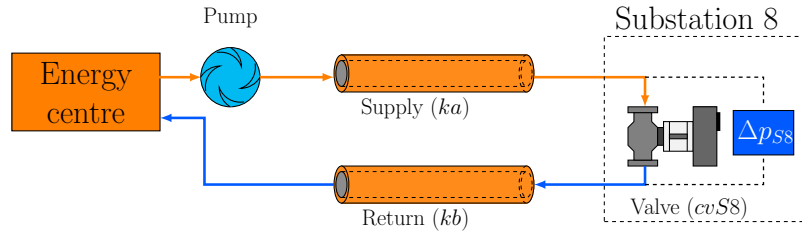


Figure H.1: Schematic of the simplified pipe network.

The parameters of the pipes are shown in Table H.1. The flow coefficient values of the valve and the head-volumetric flow curve of the pump are given in Appendix C.

Table H.1: Pipe parameters of simplified pipe network.

Pipe label	Length [m]	D_i [m]	ε/D_i	Flow area A_k [m ²]
k_a	3800	0.148	1×10^{-7}	0.0172
k_b	3800	0.148	1×10^{-7}	0.0172

Thus, the dynamic model of the pipe network is defined by

$$\dot{v} = [A_p \Delta p(\omega_{sp}, v) - A_{k_a} \Delta p_{k_a}(v) - A_{cvSS} \Delta p_{cvSS}(v) - A_{k_b} \Delta p_{k_b}(v)] / V_T \rho, \quad (\text{H.1})$$

where v [m/s] is the velocity of the fluid, V_T [m³] is the total volume of the hydraulic circuit,

A_p is the flow area of the pump and A_{cvS8} is the flow area of the valve. These values are equal to A_{ka} and A_{kb} .

The controlled variable is the pressure drop in the substation valve (Δp_{S8}). Therefore, it is necessary to add this state variable to the system defined by equation (H.1). The valve pressure drop is defined by

$$\Delta p_{cvS8} = \frac{(1 \times 10^{-5}) (3600 A_{cvS8} v)^2}{k_{cvS8} (o_{vS8})} \quad (\text{H.2})$$

Using the state-space notation, the state variables are defined as $x_1 = v$ and $x_2 = \Delta p_{cvS8}$. The pressure drop in the valve should be established in a differential form as

$$\dot{x}_2 = \left[\frac{2 (1 \times 10^5) (3600 A_{cv4})^2 x_1}{K_{cvS8} (o_{vS8})} \right] \dot{x}_1. \quad (\text{H.3})$$

Then, the state-state representation of the pipe network model is given by

$$\begin{aligned} \dot{x}_1 &= (A_p \Delta p (\omega_{sp}, x_1) - A_{ka} \Delta p_{ka} (x_1) - A_{cvS8} \Delta p_{cvS8} (x_1) - A_{kb} \Delta p_{kb} (v)) \\ \dot{x}_2 &= \left[\frac{2 (1 \times 10^5) (3600 A_{cv4})^2 x_1}{K_{cvS8} (o_{vS8})} \right] (A_p \Delta p (\omega_{sp}, x_1) - A_{ka} \Delta p_{ka} (x_1) - x_2 - A_{kb} \Delta p_{kb} (x_1)) \end{aligned} \quad (\text{H.4})$$

The model is implemented in MATLAB/Simulink and the steady state values of the state variables are obtained setting the maximum pump's speed (100%) and the opening valve to $o_{vS8} = 29\%$. These values are : $x_1 = 1.371$ m/s and $x_2 = -50000$ Pa. The system is programmed in MATLAB code using equations (4.15), (4.19) and (4.35) to compute the Taylor expansion through symbolic variables and evaluate the steady state values. Then, the linearised model is defined by

$$\begin{aligned} \begin{bmatrix} \dot{x}_1 \\ \dot{x}_2 \end{bmatrix} &= \begin{bmatrix} -0.4499 & 0 \\ 20.8512 & -0.0025 \end{bmatrix} \begin{bmatrix} x_1 \\ x_2 \end{bmatrix} + \begin{bmatrix} 0.6169 \\ 202.2646 \end{bmatrix} u \\ y &= \begin{bmatrix} 0 & 1 \end{bmatrix} \begin{bmatrix} x_1 \\ x_2 \end{bmatrix} \end{aligned} \quad (\text{H.5})$$

Using equation (G.5) the transfer function of the system (H.5) is obtained as

$$G(s) = \frac{202.3s + 103.9}{s^2 + 0.4524s + 0.001131}. \quad (\text{H.6})$$

There is a gain of the pressure sensor shown in Figure 5.4 which is considered in the system transfer function as

$$G(s) = \frac{0.0002023s + 0.0001039}{s^2 + 0.4524s + 0.001131}. \quad (\text{H.7})$$

The next step of the control design procedure is to find an equivalent second-order system for G . The state-space representation has only two state variables; thus, the transfer function is a second-order system with a zero. Therefore, the equivalent second-order system is obtained

H.2. Temperature control for DHS and energy cooling centre

neglecting the effect of the zero in the transfer function as

$$G_{so}(s) = \frac{0.0001039}{s^2 + 0.4524s + 0.001131}. \quad (\text{H.8})$$

Figure H.2 shows the frequency and the time step responses of G and G_{so} .

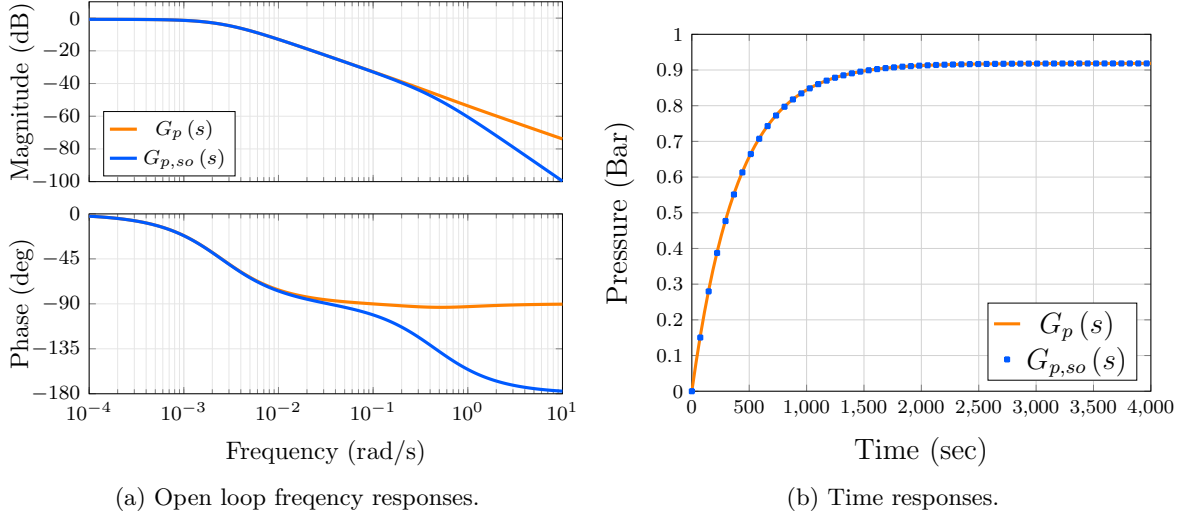


Figure H.2: (a) Open-loop Bode plots and (b) step responses of the $G_p(s)$ and $G_{p,so}(s)$.

The desired performance parameters are defined as a 1% overshoot and a settling time of $t_s=50$ s. A small t_s is established due to an aggressive PI controller response is necessary to face the potential disturbances provoked by the other pipe network substations. These time performance specifications are translate to the frequency domain using equations (G.11-G.13) as $\zeta = 0.8261$, a minimum margin phase $\phi_m=70.9048^\circ$ and a minimum bandwidth $\omega_{bw} = 0.0759$ rad/s. The design requirements are met with

$$C_p = \frac{23.95 + 0.057s}{s}, \quad (\text{H.9})$$

where the proportional k_p and the integral k_i gains are 23.95 and 0.057, respectively.

Figure H.3 shows the open-loop frequency response of the system controlled. As it can be observed, the desired parameters are achieved. For frequency domain: a larger phase margin than 70.9048° ($\phi_m = 83.2^\circ$) and a bandwidth value close to 0.0759 rad/s ($\omega_{bw} = 0.0769$). For the time domain: no overshoot and a settling time of 50 s are achieved.

H.2 Temperature control for DHS and energy cooling centre

The temperature control scheme of the DHS' substations is shown in Figure 6.6. The PI controller design is described in the following paragraphs. The design procedure presented in Appendix G is followed. A 3 node division model of the heat exchanger is used to obtain the linearised model. The parameters of the S450+ heat exchanger model are shown in Appendix C. The dynamic thermal model of the heat exchanger is defined by

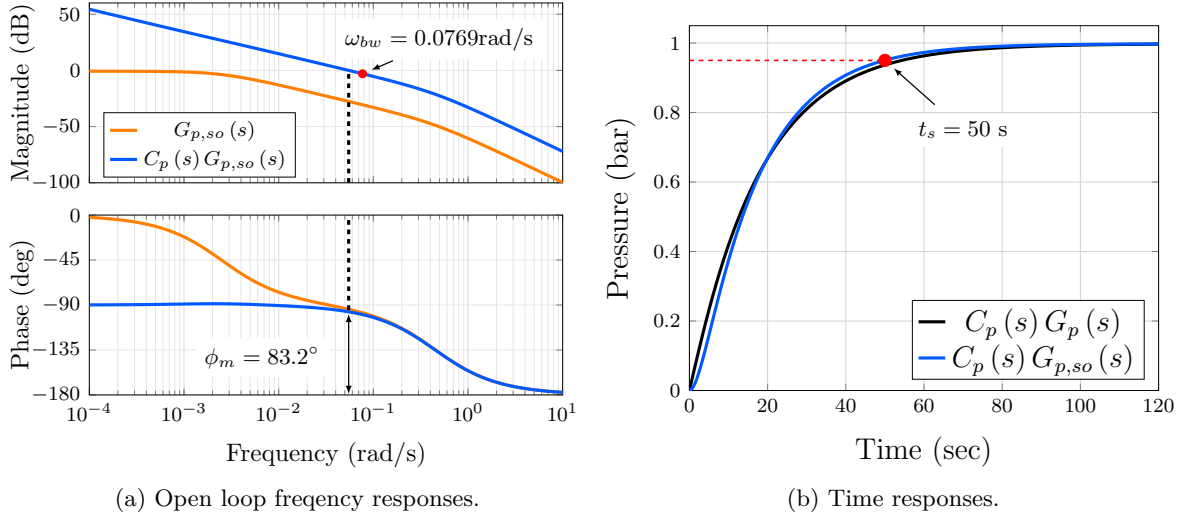


Figure H.3: (a) Open-loop Bode plots of the equivalent second-order system and the loop-shaped obtained with $C_p(s)$. (b) Time step responses of the closed-loop system with $G_{p,so}(s)$ and $G_p(s)$.

$$\begin{aligned} m_{c,1}c_{p,c1}\dot{T}_{c,1} &= \dot{m}_c c_{p,c1} (T_{c,\text{in}} - T_{c,1}) + U_1 A_{tr} (T_{h,1} - T_{c,1}), \\ m_{h,1}c_{p,h1}\dot{T}_{h,1} &= \dot{m}_h c_{p,h1} (T_{h,2} - T_{h,1}) + U_1 A_{tr} (T_{h,1} - T_{c,1}). \end{aligned} \quad (\text{H.10})$$

$$\begin{aligned} m_{c,2}c_{p,c2}\dot{T}_{c,2} &= \dot{m}_c c_{p,c2} (T_{c,1} - T_{c,2}) + U_2 A_{tr} (T_{h,2} - T_{c,2}), \\ m_{h,2}c_{p,h2}\dot{T}_{h,2} &= \dot{m}_h c_{p,h2} (T_{h,3} - T_{h,2}) + U_2 A_{tr} (T_{c,2} - T_{h,2}). \end{aligned} \quad (\text{H.11})$$

$$\begin{aligned} m_{c,3}c_{p,c3}\dot{T}_{c,3} &= \dot{m}_c c_{p,c3} (T_{c,2} - T_{c,3}) + U_3 A_{tr} (T_{h,3} - T_{c,3}), \\ m_{h,3}c_{p,h3}\dot{T}_{h,3} &= \dot{m}_h c_{p,h3} (T_{h,\text{in}} - T_{h,3}) + U_3 A_{tr} (T_{c,3} - T_{h,3}), \end{aligned} \quad (\text{H.12})$$

where \dot{m} [kg/s] and T_{in} are the mass flow rates and input temperatures of cold (c) and hot (h) streams, respectively.

Using the state-space notation where the state variables are the node temperatures, the model is defined as

$$\dot{x}_1 = [\dot{m}_c c_{p,x_1} (T_{c,\text{in}} - x_1) + U_1 A_{tr} (x_2 - x_1)] / (m_{c,1} c_{p,x_1}), \quad (\text{H.13})$$

$$\dot{x}_2 = [\dot{m}_h c_{p,x_2} (x_4 - x_2) + U_1 A_{tr} (x_2 - x_1)] / (m_{h,1} c_{p,x_2}), \quad (\text{H.14})$$

$$\dot{x}_3 = [\dot{m}_c c_{p,x_3} (x_1 - x_3) + U_2 A_{tr} (x_4 - x_3)] / (m_{c,2} c_{p,x_3}), \quad (\text{H.15})$$

$$\dot{x}_4 = [\dot{m}_h c_{p,x_4} (x_6 - x_4) + U_2 A_{tr} (x_3 - x_4)] / (m_{h,2} c_{p,x_4}), \quad (\text{H.16})$$

$$\dot{x}_5 = [\dot{m}_c c_{p,x_5} (x_3 - x_5) + U_3 A_{tr} (x_6 - x_5)] / (m_{c,3} c_{p,x_5}), \quad (\text{H.17})$$

$$\dot{x}_6 = [\dot{m}_h c_{p,x_6} (T_{c,\text{in}} - x_6) + U_3 A_{tr} (x_5 - x_6)] / (m_{h,3} c_{p,x_6}), \quad (\text{H.18})$$

The steady-state values required to linearise the system are shown in table H.2 and are obtained simulating the system defined by equations (H.10-H.12) with the next operating conditions: $T_{\text{in},c} = 20^\circ\text{C}$, $T_{\text{in},h} = 90^\circ\text{C}$, $\dot{m}_c = 8 \text{ kg/s}$ and $\dot{m}_h = 8.7 \text{ kg/s}$.

H.2. Temperature control for DHS and energy cooling centre

Table H.2: Steady-state values for heat exchanger linearisation.

Node	Cold stream (°C)	Hot stream (°C)	U (W/m ² K)	$m_c c_{p,T_c}/n$	$m_h c_{p,T_h}/n$
1	$x_1 = 29.6004$	$x_2 = 62.4706$	$U_1 = 465.3273$	1.3538×10^5	1.3373×10^5
2	$x_3 = 39.6515$	$x_4 = 71.2764$	$U_2 = 505.9358$	1.3484×10^5	1.3318×10^5
3	$x_5 = 50.0276$	$x_6 = 80.4927$	$U_3 = 543.1952$	1.3437×10^5	1.3269×10^5

The next step of the control design procedure is to linearise the system applying the Taylor linearisation method on equations (H.13-H.18) and using the steady state values. Thus, the state-space representation is given by

$$\dot{\mathbf{x}} = \begin{bmatrix} -0.3191 & 0.0721 & 0 & 0 & 0 & 0 \\ 0.0730 & -0.3454 & 0 & 0.2723 & 0 & 0 \\ 0.2479 & 0 & -0.3267 & 0.0787 & 0 & 0 \\ 0 & 0 & 0.0797 & -0.3535 & 0 & 0.2738 \\ 0 & 0 & 0.2489 & 0 & -0.3338 & 0.0848 \\ 0 & 0 & 0 & 0 & 0.0859 & -0.3612 \end{bmatrix} [\mathbf{x}] + \begin{bmatrix} 0 \\ 0.2757 \\ 0 \\ 0.2900 \\ 0 \\ 0.3008 \end{bmatrix} u \quad (\text{H.19})$$

$$y = \begin{bmatrix} 0 & 0 & 0 & 0 & 1 & 0 \end{bmatrix} [\mathbf{x}],$$

where u is the mass flow rate of the hot stream (\dot{m}_h).

The next step is to obtain the transfer function applying equation (G.5) to (H.19):

$$G_H = \frac{0.02552s^4 + 0.04s^3 + 0.02567s^2 + 0.007935s + 0.001051}{s^6 + 2.04s^5 + 1.714s^4 + 0.7591s^3 + 0.1861s^2 + 0.02369s + 0.001177}. \quad (\text{H.20})$$

Similar to the PI controller designed in section 5.2.2, the dynamic of the actuator to regulate \dot{m}_h should be added to G_H as

$$G_{v,H} = \frac{100}{5s + 1} G_H. \quad (\text{H.21})$$

Then, the equivalent second-order system is obtained by defining the parameters of the equation (G.14) as $A1 = 89$, $\zeta = 0.9$ and $\omega_n = 0.11$ rad/s. The transfer function of the equivalent system is defined by

$$G_{v,H,so} = \frac{1.077}{s^2 + 0.198s + 0.0121}. \quad (\text{H.22})$$

Figure H.4 shows the frequency and the step time responses of $G_{v,H}$ and $G_{v,H,so}$.

The desired performances parameters are a settling time of $t_s = 40$ s and a maximum overshoot of $o_v = 1\%$. A small value of t_s is defined to face the disturbances provoked by the pressure variations of the whole pipe network. Thus, a fast response of the PI controller guarantees a constant output temperature of the secondary circuit of the heat exchanger. The time desired parameters are translated to the frequency domain using equations (G.11-G.13)

as $\phi_m = 70.9^\circ$, $\zeta = 0.8261$ and $\omega_{bw} = 0.0759$. The obtained PI controller through the loop-shaping of the system frequency response is define by

$$C_H = \frac{0.0066s + 0.00057}{s}, \quad (\text{H.23})$$

where the proportional gain is $k_p = 0.0066$ and the integral gain is $k_i = 0.00057$.

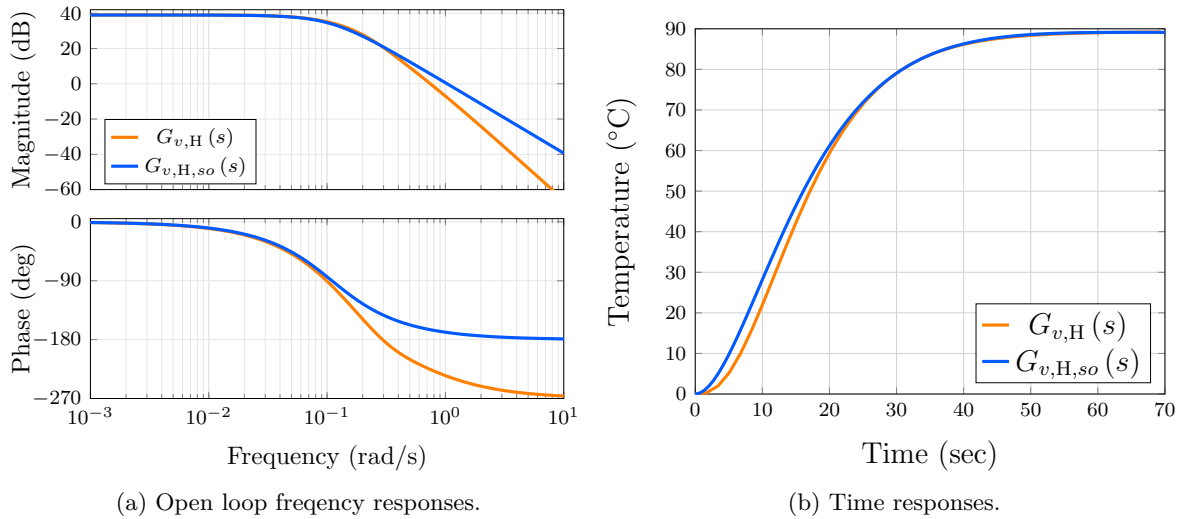


Figure H.4: (a) Open-loop Bode plots and (b) step responses of the $G_{v,H}(s)$ and $G_{v,H,so}(s)$.

Figure H.5 shows the open-loop frequency responses of the equivalent second-order system ($G_{H,so}$) and the PI controller action over it. As it can be observed the margin phase condition is achieved. Although there is a slight difference of the system bandwidth, the t_s and the no overshoot time conditions are met with the PI controller for the original linearised system $G_{v,H}$.

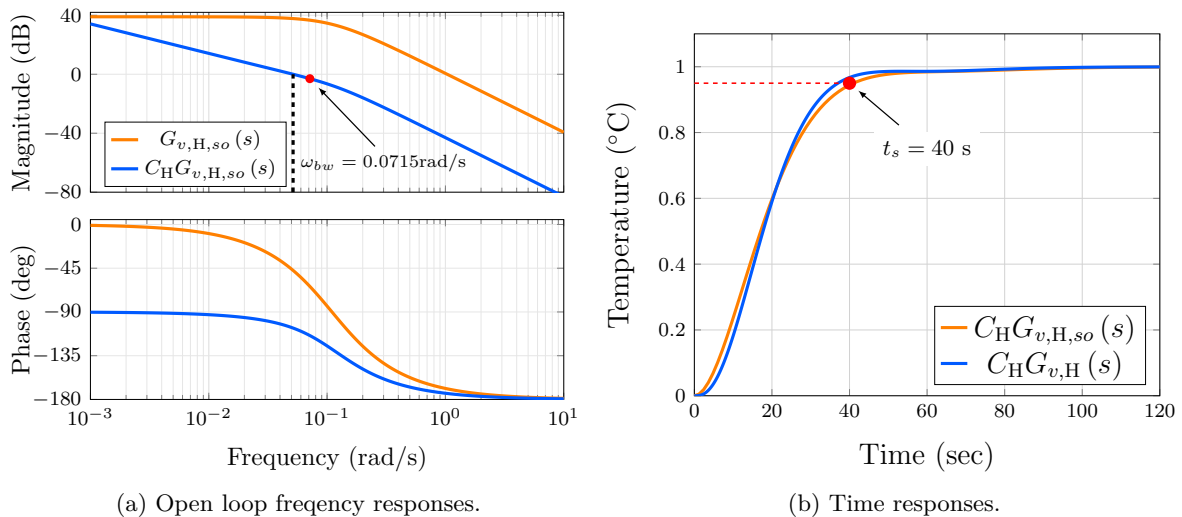


Figure H.5: (a) Open-loop Bode plots of the equivalent second-order system and the loop-shaped obtained with $C_H(s)$. (b) Time step responses of the closed-loop system with $G_{v,H,so}(s)$ and $G_{v,H}(s)$.